frontiers | Research Topics

Physico-mechanical properties and treatment technology of hazardous geomaterials

Edited by
Bing Bai, Riyadh Al-Raoush, Wei Hu and Xianze Cui

Published in
Frontiers in Materials

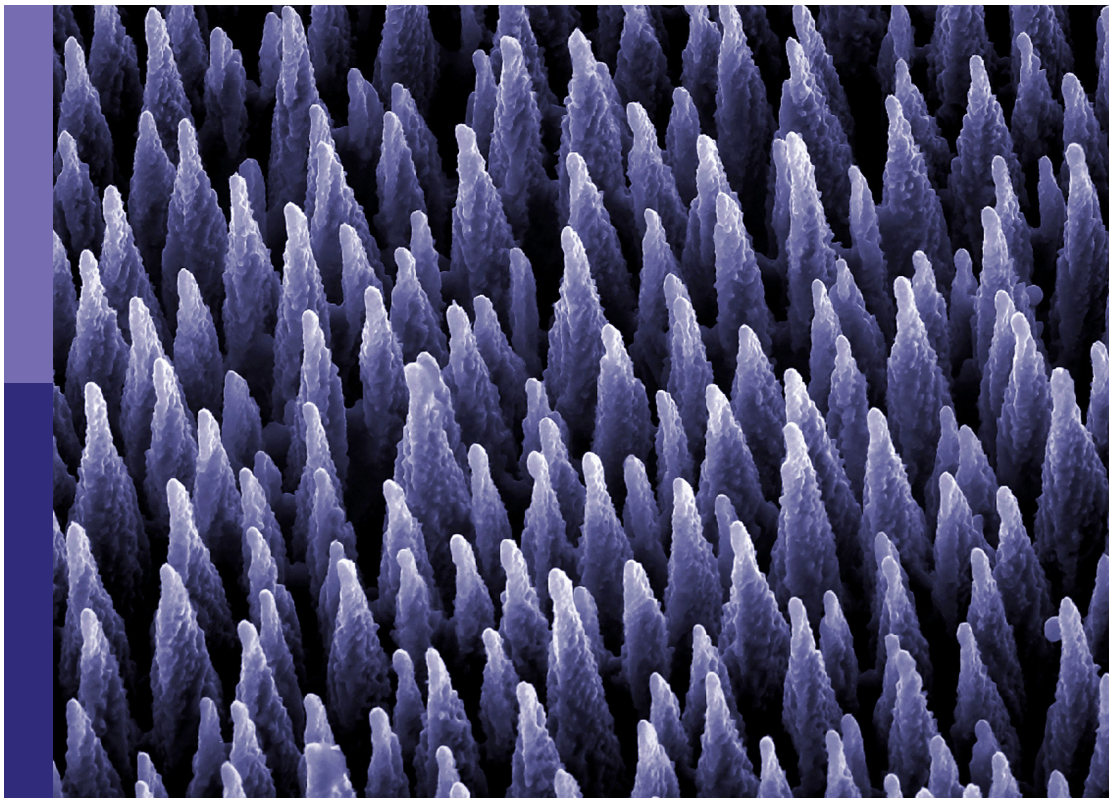

FRONTIERS EBOOK COPYRIGHT STATEMENT

The copyright in the text of individual articles in this ebook is the property of their respective authors or their respective institutions or funders. The copyright in graphics and images within each article may be subject to copyright of other parties. In both cases this is subject to a license granted to Frontiers.

The compilation of articles constituting this ebook is the property of Frontiers.

Each article within this ebook, and the ebook itself, are published under the most recent version of the Creative Commons CC-BY licence. The version current at the date of publication of this ebook is CC-BY 4.0. If the CC-BY licence is updated, the licence granted by Frontiers is automatically updated to the new version.

When exercising any right under the CC-BY licence, Frontiers must be attributed as the original publisher of the article or ebook, as applicable.

Authors have the responsibility of ensuring that any graphics or other materials which are the property of others may be included in the CC-BY licence, but this should be checked before relying on the CC-BY licence to reproduce those materials. Any copyright notices relating to those materials must be complied with.

Copyright and source acknowledgement notices may not be removed and must be displayed in any copy, derivative work or partial copy which includes the elements in question.

All copyright, and all rights therein, are protected by national and international copyright laws. The above represents a summary only. For further information please read Frontiers' Conditions for Website Use and Copyright Statement, and the applicable CC-BY licence.

ISSN 1664-8714
ISBN 978-2-83252-083-3
DOI 10.3389/978-2-83252-083-3

About Frontiers

Frontiers is more than just an open access publisher of scholarly articles: it is a pioneering approach to the world of academia, radically improving the way scholarly research is managed. The grand vision of Frontiers is a world where all people have an equal opportunity to seek, share and generate knowledge. Frontiers provides immediate and permanent online open access to all its publications, but this alone is not enough to realize our grand goals.

Frontiers journal series

The Frontiers journal series is a multi-tier and interdisciplinary set of open-access, online journals, promising a paradigm shift from the current review, selection and dissemination processes in academic publishing. All Frontiers journals are driven by researchers for researchers; therefore, they constitute a service to the scholarly community. At the same time, the *Frontiers journal series* operates on a revolutionary invention, the tiered publishing system, initially addressing specific communities of scholars, and gradually climbing up to broader public understanding, thus serving the interests of the lay society, too.

Dedication to quality

Each Frontiers article is a landmark of the highest quality, thanks to genuinely collaborative interactions between authors and review editors, who include some of the world's best academicians. Research must be certified by peers before entering a stream of knowledge that may eventually reach the public - and shape society; therefore, Frontiers only applies the most rigorous and unbiased reviews. Frontiers revolutionizes research publishing by freely delivering the most outstanding research, evaluated with no bias from both the academic and social point of view. By applying the most advanced information technologies, Frontiers is catapulting scholarly publishing into a new generation.

What are Frontiers Research Topics?

Frontiers Research Topics are very popular trademarks of the *Frontiers journals series*: they are collections of at least ten articles, all centered on a particular subject. With their unique mix of varied contributions from Original Research to Review Articles, Frontiers Research Topics unify the most influential researchers, the latest key findings and historical advances in a hot research area.

Find out more on how to host your own Frontiers Research Topic or contribute to one as an author by contacting the Frontiers editorial office: frontiersin.org/about/contact

Physico-mechanical properties and treatment technology of hazardous geomaterials

Topic editors

Bing Bai — Beijing Jiaotong University, China
Riyadh Al-Raoush — Qatar University, Qatar
Wei Hu — Youngstown State University, United States
Xianze Cui — China Three Gorges University, China

Citation

Bai, B., Al-Raoush, R., Hu, W., Cui, X., eds. (2023). *Physico-mechanical properties and treatment technology of hazardous geomaterials*. Lausanne: Frontiers Media SA. doi: 10.3389/978-2-83252-083-3

Table of contents

frontiers | Frontiers in Materials

TYPE Editorial
PUBLISHED 20 March 2023
DOI 10.3389/fmats.2023.1179876

Check for updates

OPEN ACCESS

EDITED AND REVIEWED BY
John L. Provis,
The University of Sheffield,
United Kingdom

*CORRESPONDENCE
Bing Bai,
bbai@bjtu.edu.cn

SPECIALTY SECTION
This article was submitted to Structural Materials,
a section of the journal
Frontiers in Materials

RECEIVED 05 March 2023
ACCEPTED 13 March 2023
PUBLISHED 20 March 2023

CITATION
Bai B and Cui X (2023), Editorial: Physico-mechanical properties and treatment technology of hazardous geomaterials.
Front. Mater. 10:1179876.
doi: 10.3389/fmats.2023.1179876

COPYRIGHT
© 2023 Bai and Cui. This is an open-access article distributed under the terms of the Creative Commons Attribution License (CC BY). The use, distribution or reproduction in other forums is permitted, provided the original author(s) and the copyright owner(s) are credited and that the original publication in this journal is cited, in accordance with accepted academic practice. No use, distribution or reproduction is permitted which does not comply with these terms.

Editorial: Physico-mechanical properties and treatment technology of hazardous geomaterials

Bing Bai[1]* and Xianze Cui[2]

[1]School of Civil Engineering, Beijing Jiaotong University, Beijing, China, [2]College of Hydraulic and Environmental Engineering, China Three Gorges University, Yichang, China

KEYWORDS

geomaterial, mechanical property, special soil, purification, constitutive model

Editorial on the Research Topic
Physico-mechanical properties and treatment technology of hazardous geomaterials

Introduction

New materials and technologies are emerging in every branch of geotechnical engineering, such as high-speed railway subgrade, soil improvement and remediation, ground energy storage, tunnel waterproof engineering, and marine engineering. In addition to the common infrastructure construction materials, it also includes the treatment of hazardous geomaterials, resource utilization of industrial wastes, geopolymer materials, contaminated soils related to geo-environmental engineering as well as other newly developed materials. The advancement of new materials has promoted the development of geotechnical engineering and its close intersection with other disciplines. Scholars have done fruitful work, but the understanding of many new materials is not very clear. Moreover, the external environment (e.g., heat, water, external force) borne by various materials is becoming more and more complex. The newly developed geotechnical materials involve the multiple field actions such as physics, mechanics, chemistry and even biology.

The Research Topic aims to bring together original research and review articles on the recent developments in natural geotechnical material improvement, hazardous geomaterials, synthetic materials, energy geotechnical materials and contaminated soil treatment. A total of twenty-two articles are presented in this Research Topic, which include theoretical description, numerical simulation, laboratory experiments and field tests. The Editorial includes the following:

- Physico-mechanical properties of hazardous soils
- Mechanical characteristics of composite geomaterials
- Soil remediation and purification technology
- New geotechnical materials and the application

Physico-mechanical properties of hazardous soils

The physico-mechanical properties of the hazardous soils affected by external complex environment have received great attention. Yi et al. investigated the effect of lateral surcharge loading on the existing adjacent pile in extensively soft soils, which indicated that the surcharge loading zone showing obvious downward displacements, while the soft soils close to the loading zone showing upward displacements. Dai et al. performed the wetting deterioration and uniaxial compression tests to discuss the influence of different interlayer orientations on the hygroscopic deterioration characteristics of rock and analyzed the wetting cracking and deformation of dolomite with interlayer in different directions from the time effect of rock micro-expansion. Cao et al. reported an experimental study of the unconfined compressive strength of cement-solidified clay with respect to its initial water content, cement incorporation ratio, organic matter content, curing temperature, and curing duration.

Zhang et al. investigated various advantages of applying cement fly-ash gravels (CFG) pile treatment to the soft foundation, which demonstrated that the reinforcement effect of the CFG pile significantly weakens the influence of vehicle dynamic load on roadbeds. Yuan et al. carried out one-dimensional consolidation creep tests and SEM tests of the Nansha soft soil. Yuan et al. also discussed the macroscopic mechanical properties and the evolution mechanism of soft soil in microscope during consolidation creep, and also to discuss the rheological phenomena by establishing an energy scale method. Chen et al. started with the microscopic force of particles and explored the influence of particle composition and geometric scale on the particle surface and interface state, then developed an energy multiscale method to explain the internal mechanism of the soil scale effect.

Mechanical characteristics of composite geomaterials

The recycling and application of waste geotechnical materials is a promising development direction of geo-environmental engineering. Combined with the soil-rock mixture in a slag dump site, Zhang et al. investigated the influence of different fillers on the gravel soil shear characteristics through a large-scale triaxial test of coarse-grained soil, and analyzed the slope stability of the slag dump site. Zhou et al. presented a method for determining the shear strength of the soil-rock mixture taking the size effect into account, and discussed the size effect on the uniaxial compressive strength from the macroscopic and mesoscopic views in two dimensions, and also proposed a quantitative relationship between the shear strength and particle size.

Xu et al. performed a 3D simulation under simulated field conditions and compared with actual monitoring data, and compared with simulation findings of spatial effects under alternative load conditions to verify the effectiveness of the equation correction to establish a connection between asymmetric loads and the spatial effects of foundation pits. Gu et al. presented a series of model tests on floating stone columns under vertical incremental loads, investigated the influence of floating stone columns in terms of load-displacement behavior, bulging deformation, load transfer mechanism, and the radial stress of the geogrid encasement. Ma et al. established a mechanical model of coordinated deformation and overall stability of supporting structures using the elastic fulcrum method by considering the internal force and stability of the supporting slope with a crown-beam cooperative pile–anchor structure and compared with numerical simulation, and then studied the cooperative action mechanism of the pile, anchor, and top beams in pile–anchor supporting structures.

Yi and Gu used the three-dimensional finite different method to conduct a parametric study of passive piles subjected to adjacent surcharge load to investigate the effect of four important factors (pile bending stiffness, distance between the long edge of the loading area and the pile, embankment height, and cushion thickness) on the behavior of a single steel pipe pile installed in extensively soft soil and subjected to adjacent surcharge loading. Jiang et al. proposed a damage constitutive model to replace the traditional elastic constitutive model in the numerical analysis of pile–slope stability by a damage constitutive model, which can reflect the plastic deformation of the pile and the factors of pile position and reinforcement ratio on a slope factor of safety.

Soil remediation and purification technology

The remediation and purification technology of soils have been intensely researched in recent years. Based on a ground-penetrating radar method, Lv et al. examined the reflection characteristics of ground-penetrating radar waves at different lithological interfaces, which provided a theoretical basis and technical support for the actual detection of water erosion deterioration of loess in similar projects. Li et al. employed the fatigue loading tests combined with real-time acoustic emission monitoring technique to investigate the influence of water content on the deformation, damage, and fracture characteristics, which showed that rock fatigue life decreases with increasing water content, and the hysteresis curve changes regularly with time.

Hu et al. proposed an external regulatory system with the adsorbent (ERSA) and investigated the effect of electrode type, ERSA, and cation exchange membrane on the Electrokinetic remediation of an artificially Cu^{2+} and Pb^{2+} contaminated loess, which can well reflect the adsorption mechanism of the Bai model (Bai et al., 2021) widely used in purification technology. Based on the systematic analysis of vegetation and soil characteristics under different vegetation restoration models, Zhao et al. constructed a vegetation-soil coupling coordination model combined with the coupling coordination degree correction model, which tried to provide a scientific reference for revealing the interaction between habitat materials and vegetation in a disturbed area. These results are helpful to understand the fatigue mechanical responses of water-sensitive soft rock, as well as the slope stability of the open-pit mine.

New geotechnical materials and the application

New materials and technologies are emerging in geotechnical engineering, which is the necessary way to treat the geotechnical engineering disasters. Huang et al. established the relationship between the tunnel stability index and construction factors according to Taylor's theorem, which reveals the coupling relationship between tunnel stability, physico-mechanical properties of clay, and tunnel construction conditions. Chen et al. analyzed the reasons and main distribution positions of lining cracking and the influence of different positions of lining cracking on the stress and deformation of lining structure by numerical simulation, which improved the understanding of the influence of lining crack diseases. Chen et al. investigated the damage evolution of concrete-based tunnels by the proposed static finite element method, which provided better suggestions for engineering design and predicting the weak surface of the tunnel through the fault to avoid the adverse effects of faults on the tunnel. Based on the finite element limit analysis method, Luo et al. analyzed the stability of the face in case of active failure under three constitutive models (Mohr-Coulomb, modified Cambridge model and Drucker-Prager) to discuss the ultimate support pressure of the face and the influence of factors such as different burial depth ratios, cohesion and friction angle, *etc*.

Although the submissions for this Research Topic has been closed, more in-depth research in the field of soil pollution and geotechnical environment continues to address the challenges. All of the selected contributions help to discover innovative theories, advanced technologies, and application examples. We would like to thank all the editors, reviewers and authors for their crucial contributions.

Author contributions

All authors listed have made a substantial, direct, and intellectual contribution to the work and approved it for publication.

Conflict of interest

The authors declare that the research was conducted in the absence of any commercial or financial relationships that could be construed as a potential conflict of interest.

Publisher's note

All claims expressed in this article are solely those of the authors and do not necessarily represent those of their affiliated organizations, or those of the publisher, the editors and the reviewers. Any product that may be evaluated in this article, or claim that may be made by its manufacturer, is not guaranteed or endorsed by the publisher.

Reference

Bai, B., Nie, Q., Zhang, Y., Wang, X., and Hu, W. (2021). Cotransport of heavy metals and SiO2 particles at different temperatures by seepage. *J. Hydrol.* 597, 125771. doi:10.1016/j.jhydrol.2020.125771

frontiers | Frontiers in Materials

ORIGINAL RESEARCH
published: 11 July 2022
doi: 10.3389/fmats.2022.965975

Strength Properties and Prediction Model of Cement-Solidified Clay Considering Organic Matter and Curing Temperature

Yupeng Cao[1,2]*, *Jing Zhang*[3], *Guizhong Xu*[4], *Mingdong Li*[5] and *Xia Bian*[6]

[1]College of Civil Engineering and Architecture, Weifang University, Weifang, China, [2]Key Laboratory of Ministry of Education for Geomechanics and Embankment Engineering, Hohai University, Nanjing, China, [3]Zibo Planning and Information Center, Zibo, China, [4]Geotechnical Research Institute, Yancheng Institute of Technology, Yancheng, China, [5]School of Civil Engineering and Architecture, East China University of Technology, Nanchang, China, [6]Key Laboratory of Ministry of Education for Geomechanics and Embankment Engineering, Hohai University, Nanjing, China

Cement-solidified clay (CSC) is an important filler material in land reclamation projects. Its strength is greatly affected by its organic matter content and curing temperature. This work reports an experimental study of the unconfined compressive strength (UCS) of CSC with respect to its initial water content w, cement incorporation ratio A_w, organic matter content C_o, curing temperature T, and curing duration. A model (UCSOT) for predicting the UCS of CSC is established considering the influence of organic matter and curing temperature. A procedure to implement the model is proposed, and the accuracy of the model is verified. The results show that for a given curing duration, UCS decreases with increases in C_o and w, and increases with increases in T and A_w. The influence of organic matter on the UCS is greatly affected by A_w, with a threshold of A_w = 15%. High-temperature curing increases the early and ultimate strengths of CSC, and organic matter increases this temperature sensitivity. Multiple regression characterization using cement content, w, and C_o as independent control parameters accurately reflects the UCS at the reference temperature. On this basis, the UCSOT model established here considering the influence of organic matter and curing temperature has universal applicability.

Keywords: organic matter, curing temperature, unconfined compressive strength, cement solidified clay, prediction model

OPEN ACCESS

Edited by:
Xianze Cui,
China Three Gorges University, China

Reviewed by:
Zi Ying,
École des ponts ParisTech (ENPC), France
Jianwen Ding,
Southeast University, China

***Correspondence:**
Yupeng Cao
paradise456917@163.com

Specialty section:
This article was submitted to Structural Materials, a section of the journal Frontiers in Materials

Received: *10 June 2022*
Accepted: *20 June 2022*
Published: *11 July 2022*

Citation:
Cao Y, Zhang J, Xu G, Li M and Bian X (2022) Strength Properties and Prediction Model of Cement-Solidified Clay Considering Organic Matter and Curing Temperature. Front. Mater. 9:965975. doi: 10.3389/fmats.2022.965975

INTRODUCTION

Abundant silt is deposited in waterways, rivers, lakes, and harbors, and it must be dredged to maintain adequate channel depth, expand storage capacity, and improve water quality (Cao et al., 2019, 2020; 2021a). Dredged silt has high initial contents of water and clay (Cao et al., 2021b) and contains considerable quantities of salts and organic matter (Grubb et al., 2010; Huang et al., 2017; Ying et al., 2021, 2022), resulting in poor dehydration, difficult processing, and high soil lateral pressure (Zhang et al., 2022). A practical and reasonable solution is to improve the physical and mechanical properties of dredged silt through cement solidification, then use the solidified clay to fill structures such as embankments, banks, and artificial islands (Zhang et al., 2020). Examples include artificial island No. 13 at the Central Japan International Airport, the embankment surrounding Tekong Island in Singapore, and the

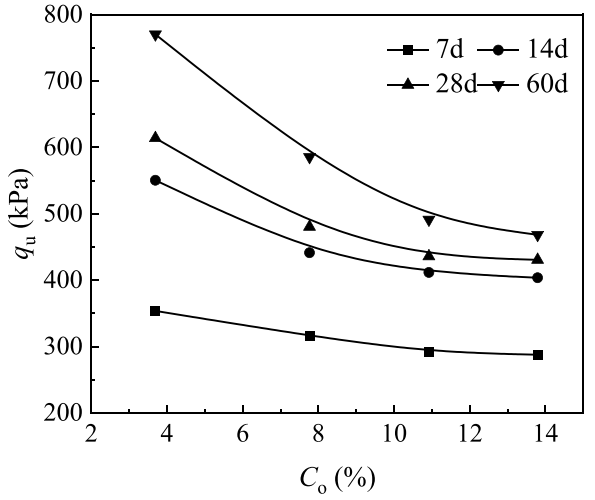

FIGURE 1 | Strength q_u plotted with respect to organic matter content C_o.

dike in the Songhua River Trunk Canal in northeast China (Kitazume and Satoh, 2003; Tan et al., 2011).

Cement solidified clay (CSC) is used as a filler in construction when the construction speed is fast and there is a large pouring volume; the heat released by cement hydration accumulates in the solidified body, raising the internal solidified temperature of the CSC significantly above the ambient temperature (Zhang et al., 2020). As the on-site curing temperature varies among different regions and by season (Yun et al., 2006), it is necessary to consider the influence of temperature on CSC packing. Relevant studies have shown that temperature can not only affect the mechanical properties of material such as deformation, consolidation, infiltration and migration (Bai et al., 2021a; 2021b), but also greatly increase the strength gain of gelled materials (Zhang et al., 2014). For concrete and mortar, the early strength is usually higher after hotter curing, but the long-term strength will decrease. The Arrhenius equation describes the effect of curing temperature on concrete and mortar, with a hotter curing reaction being faster; the equation does not model any change in the ultimate strength of cementitious materials as the curing temperature changes (Chitambira, 2004). For CSC, it is generally believed that increasing the curing temperature will increase both the early and long-term strengths. Zhang et al. (2014) modified the Arrhenius equation to include a temperature enhancement factor; the modified equation considered both the accelerated reaction rate caused by a higher curing temperature and the influence of temperature on the ultimate strength of cementitious materials. Bi and Chian (2021) proposed a universal method to evaluate the temperature sensitivity of cement-based systems by assuming changes in the reaction mechanism and incorporating the effect of temperature through the Arrhenius equation; the method can standardize the evaluation of strength development in various cementitious materials. However, there is no widely accepted model for predicting the temperature–strength characteristics of CSC. Research on the influence of curing temperature on the development of strength in different cementing materials, especially CSCs, remains rare.

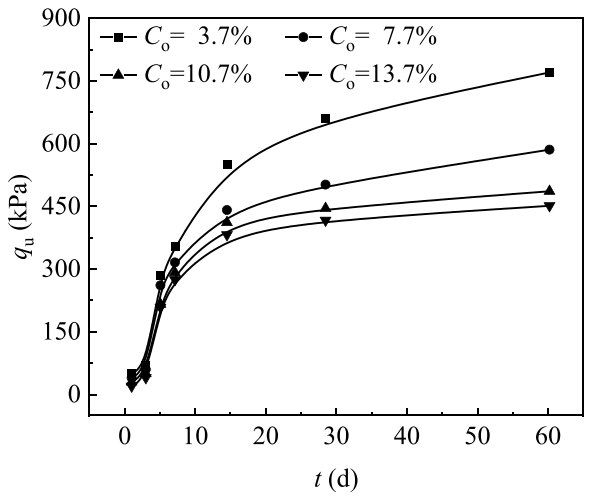

FIGURE 2 | Hyperbolic model for different C_o values.

Previous studies of the effect of temperature have focused mainly on concrete materials, granular soil, and fine clay (Chitambira, 2004; Bai et al., 2019, 2022), but few have examined soft clay containing organic matter. Gu et al. (2018) reported silt in a river beach in Shenzhen, China, to contain up to 15.6% organic matter. Du et al. (2020) also highlighted the important influence of organic matter on the development of strength in cement-stabilized clay. Therefore, it is of great practical significance to extend the temperature-dependent strength-development model to consider the solidification of dredged silt containing organic matter.

This paper reports unconfined compressive strength (UCS) tests of CSC with respect to its initial water content w, cement incorporation ratio A_w, organic matter content C_o, and curing temperature T. Applying multivariate fitting analysis to the UCS data leads to the development of a model to calculate strength at a reference temperature using w, cement content C_m, and C_o as independent control parameters. Introducing the theory describing the effects of temperature then extends the model to predict UCS considering both organic matter and curing temperature. The final model, called UCSOT, and its implementation are put forward here. The proposed model's accuracy is also verified via comparison with independent data sets reported in the literature to provide a theoretical basis for predicting the strength of solidified silt containing organic matter while considering the influence of temperature.

LABORATORY EXPERIMENT

Test Materials

The silt tested here is lake sediment that came from the bank of the Huaihe River at Hekou Village, Zhuding Town, Wuhe County, Bengbu City, Anhui Province, China. The silt is gray in the initial state, and the natural water content is 73.9%. The

content of organic matter is 3.7% using potassium dichromate method. Dredged silt consists of 4.4% fine sand, 60.5% silt and 35.1% clay, with plastic limit of 26.9% and liquid limit of 58.8%. Under the ASTM D2487 classification, the silt is classified as clay with high liquid limit (ASTM, 2010). The curing agent selected here is Portland blast furnace cement with a slag content of 65%. CaO and SiO_2 are the main oxides, with a total content of 79%. The content of MgO in cement is less than 2%. Humic acid powder with a purity of 95% (Jinan Luhui Chemical Co., Ltd., Shandong Province, China) is used as an organic additive.

Sample Preparation and Test Procedure

To analyze the influence of mixing ratio and organic matter content on the evolution of the strength of the CSC, UCS tests with different w, A_w, C_o, and curing age t are conducted. The A_w of CSC is 10, 13, 15, and 20%, and the water content of CSC is $1.5w_L$, $1.75w_L$, $2.0w_L$, and $2.25w_L$ (w_L is liquid limit of soil), respectively. The selection of each ratio is based on previous work (Zhang et al., 2013). With A_w = 15% cement content and 1.5 w_L water content as the benchmark, the method of adding humic acid is used to prepare the silt (Suits et al., 2002). By referring to the organic matter content in the silt of different regions and the solidification tests of the silt containing organic matter (11%, Detzner et al., 1998; 15.6%, Gu et al., 2018; 3.9%, Schmidt et al., 2010; 0–21%, Du et al., 2020), the corresponding organic matter content is determined to be 3.7, 7.7, 10.7, and 13.7%, respectively. The CSC samples are prepared in batches according to the curing temperature. Temperatures of 15, 20, 35, and 45°C are selected with reference to previously studied curing temperatures (10–50°C, Porbaha et al., 2001; 10–25°C, Van Impe and Verastegui Flores, 2006; 10–40°C, Marzano et al., 2009). The curing period of the samples is 3–60 days. After the samples are cured to a specific age (3d, 7d, 14d, 28d, and 60d), they are taken out for the strength test. A total of 640 sample groups are

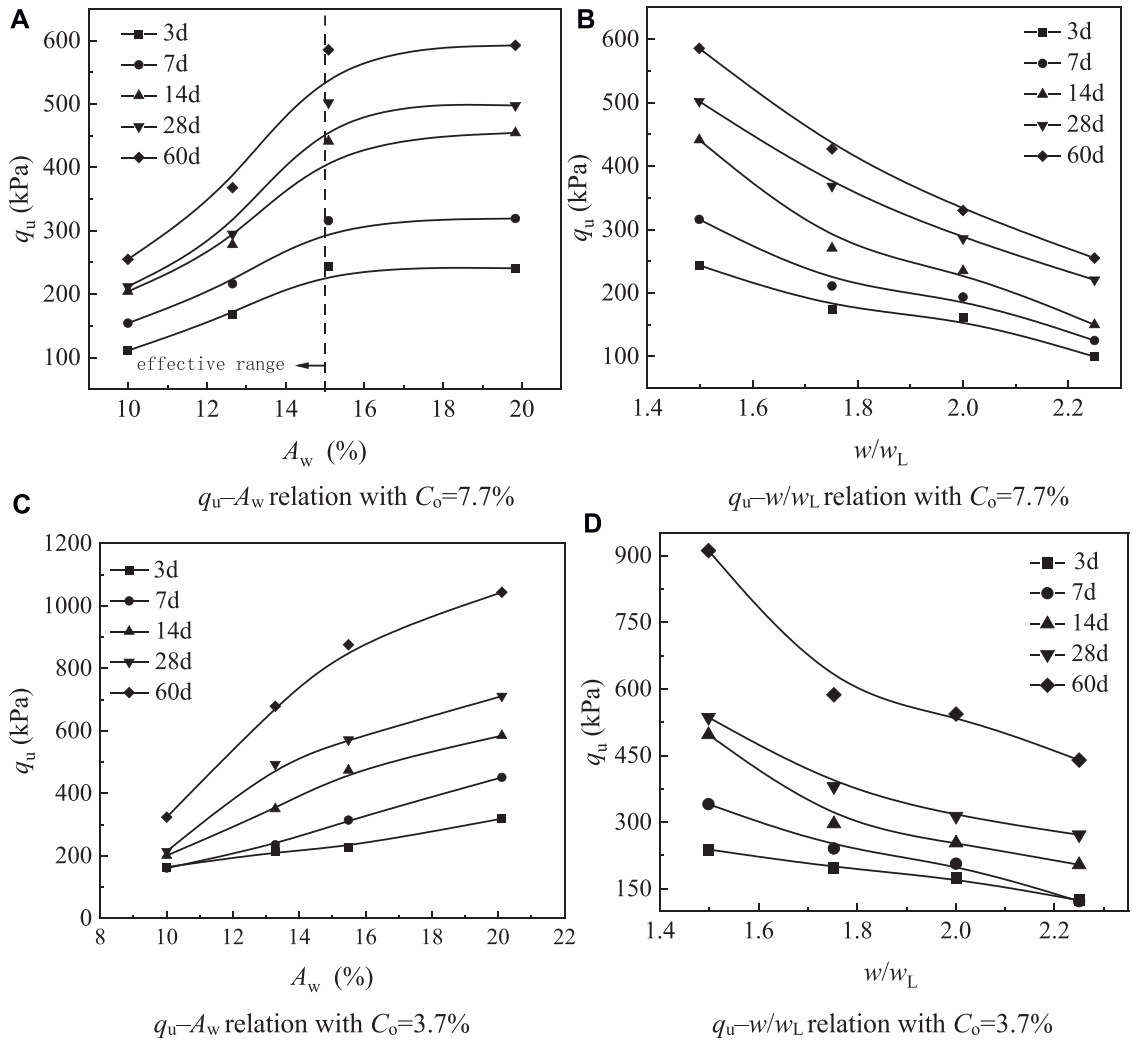

FIGURE 3 | Compressive strength q_u plotted with respect to cement incorporation ratio A_w and initial water content w. **(A)** q_u–A_w relation with C_o = 7.7% **(B)** q_u–w/w_L relation with C_o = 7.7%. **(C)** q_u–A_w relation with C_o=3.7% **(D)** q_u–w/w_L relation with C_o=3.7%.

TABLE 1 | Strength $q_{u,\infty}$ under different physical properties.

C_o (%)	C_m (kg/m^3)	w (%)	μ	σ	$q_{u,\infty}$ (kPa)
3.7	79	88.2	2.02	1.02	771
7.7	79	88.2	1.94	0.93	586
10.7	79	88.2	1.88	0.88	487
13.7	79	88.2	1.86	0.85	452
3.7	53	88.2	1.97	1.30	252
3.7	68	88.2	2.01	1.30	623
3.7	104	88.2	2.03	1.32	784
3.7	79	102.9	1.94	1.33	521
3.7	79	117.6	1.94	1.34	394
3.7	79	132.3	1.97	1.33	372

used for the UCS test. Each group have two parallel samples, and the average value of strength is obtained.

The samples are processed as follows. First, calculate the amounts of material for each group according to the test design, then weigh a certain quantity of silt, add pure water to the required content (for samples containing organic matter, humic acid powder is fully mixed with the water in advance), and stir for even mixing. Then, weigh the required quantity of cement, add it to the well-stirred soil–water mixture, and continue mixing for 6–8 min. Pour the evenly mixed soil–cement mixture into a PVC mold in three layers. To eliminate the influence of bubbles, after pouring each layer, vibrate the mold on a vibration table for 30 s. After filling the mold, place it in a standard curing box; remove the sample from the mold after 6 h. In actual land reclamation projects, the fillers solidify underwater, so the samples are cured here in a curing tank. They are removed for UCS testing after a specified duration. Testing is on an YYW-2 (Nanjing Soil Instrument Factory, China) strain controlled UCS tester, and the strain element is measured by a TMR-200 multi-data acquisition system (Bestech, Australia).

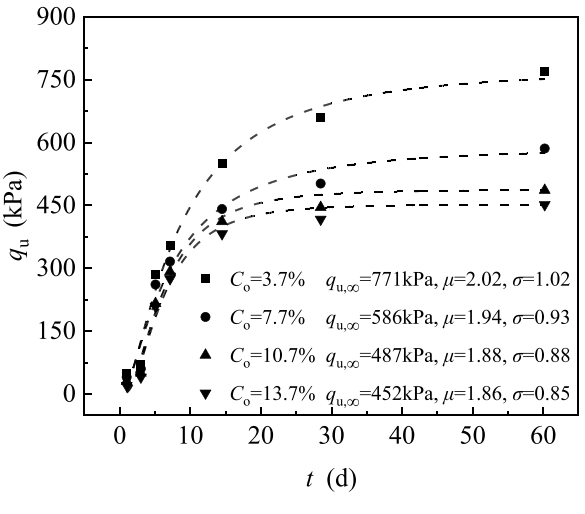

FIGURE 4 | Strength models for different C_o values (A_w = 15%, w = 1.5w_L).

ANALYSIS OF EXPERIMENTAL RESULTS

Strength Development of Cement-Solidified Clay at the Reference Temperature

Figure 1 shows the variation with C_o of the compressive strength q_u of the CSC samples after different curing durations; the figure shows decreasing strength with increasing C_o at each age. The changing trend can be divided into two stages: for C_o between 3.7 and 10.7%, the decreasing trend is linear; for C_o > 10.7%, the curve changes little, and the strength tends to a constant value. The strength of CSC with C_o = 13.7% is only about 60% of that with C_o = 3.7% after curing for 60 days. The observed variation is consistent with the experimental results of Du et al. (2020). The longer the curing age, the more obvious the decreasing trend of strength with changing C_o. The ratios of the strengths of samples with C_o = 13.7 and 3.7% at 14, 28, and 60 d are 0.88, 0.72, and 0.66, respectively, indicating an increasing influence of organic matter on the strength of CSC with increasing aging. Organic matter reduces the strength of CSC cured for a long duration, mainly because in the alkaline environment of cement hydration, humic acid will exchange ions with calcium, magnesium, iron, aluminum, and other metal ions, resulting in a reduction of OH^- in the pores of the solidified soil, making it difficult to activate the pozzolanic reaction (Kipton et al., 1992; Pan et al., 2019).

Hyperbolic modeling is widely used to describe the change of strength with aging of pure cement solidified soil (Ma, 2017). The hyperbolic model $q_u = t/(at + b)$ accurately describes the development of the compressive strength q_u of CSC with low cement content during aging for time t. The correlation coefficients are all greater than 0.9 (**Figure 2**). The strength data in **Figure 2** come from tests with A_w = 15% and w = 1.5w_L. However, when A_w < 15%, the q_u–A_w curve for a CSC sample with C_o = 7.7% shows a nonlinear increase, similar to that for a pure cement solidified soil sample (C_o = 3.7%), and when A_w > 15%, the q_u–A_w curve levels off, as shown in **Figure 3**. This indicates that when A_w > 15%, the hyperbolic model does not accurately describe the development of strength with age for CSC containing organic matter. **Figure 3** also shows that for CSC samples with C_o = 7.7%, the variation of q_u with w/w_L is

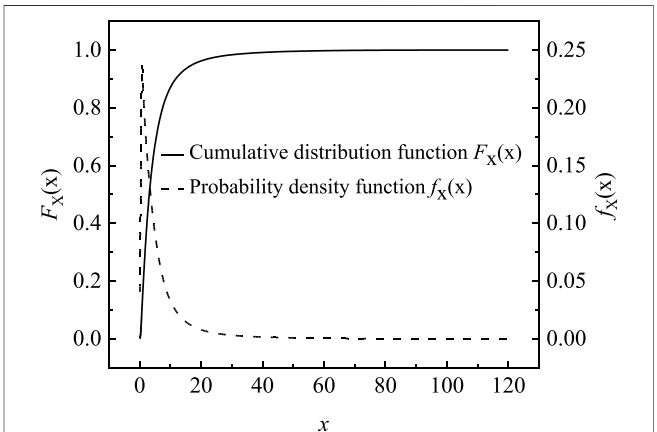

FIGURE 5 | Log-normal distribution function [$x\epsilon$ (0.120), (μ = 1, σ = 1)].

consistent with that of ordinary CSC (C_o = 3.7%); that is, with increasing w, the strength gradually decreases. When w increases, the water distributed in the pores of soil particles and cemented products increase, resulting in the interaction between particle clusters in CSC sample decreases, and the strength decreases.

Figure 4 plots the development with curing time of the strength of CSC with different C_o. The data points represent the measured data. The figure shows similar overall trends for CSC samples with different C_o: that is, a rapid early development of strength, which slows later during curing. Therefore, the variation of q_u with t for CSC samples with different C_o values can be expressed as a function that has a small initial convex surface followed by a long concave surface shape and a platform appearing as t→∞. Referring to an existing strength prediction model (Bi and Chian, 2020), the probability density function of a log-normal distribution (**Figure 5**) can describe the variation with t of q_u for CSC samples with different C_o.

The parameters μ, σ, and $q_{u,\infty}$ in **Figure 4** are obtained by fitting the relative strength model under different values of C_o. The values of the constants μ and σ are positively correlated with the rate of strength development, and the theoretical ultimate strength of CSC (i.e., $q_{u,\infty}$) depends on the mixing ratio. The figure shows good consistency between the experimental results and the model prediction, with correlation coefficients greater than 0.97. Overall, the relative strength model appears appropriate to predict the strength development of CSC samples.

Modeling the Strength of Cement-Solidified Clay at a Reference Temperature Considering the Influence of Organic Matter

To introduce w, A_w, and C_o into the model to calculate the relative strength of samples containing organic matter, the fitting parameters μ, σ, and $q_{u,\infty}$ of CSC with different physical properties are analyzed (**Table 1**). Note that solidified soil with a high water content and a low cement-incorporation ratio has a relationship between A_w and C_m (defined as the mass of cement

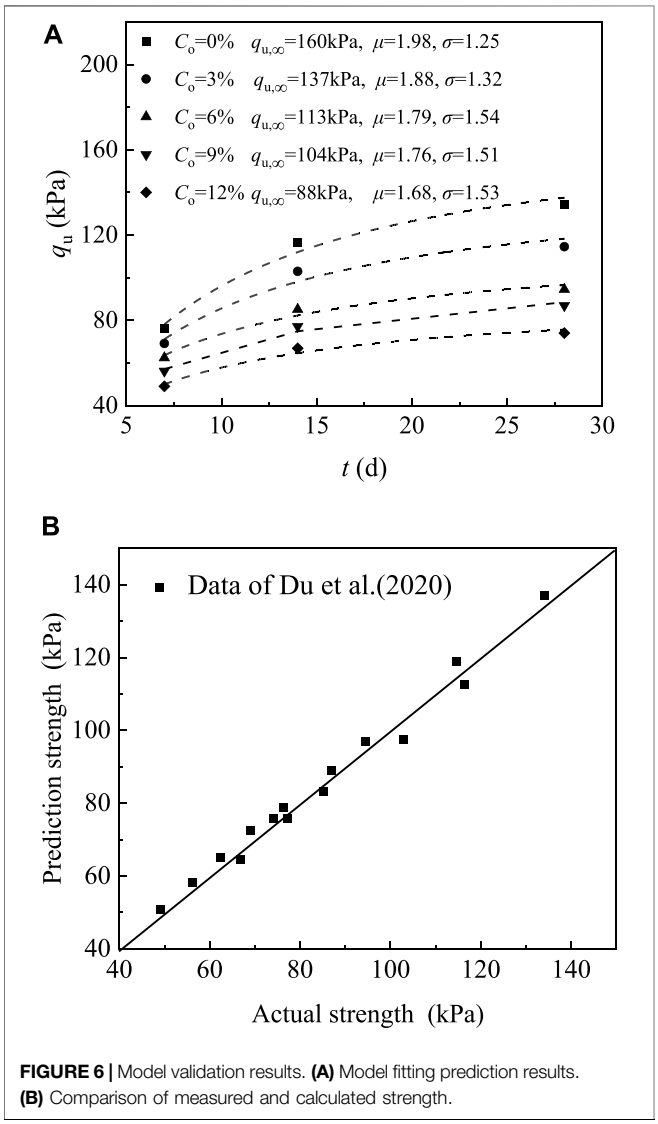

FIGURE 6 | Model validation results. **(A)** Model fitting prediction results. **(B)** Comparison of measured and calculated strength.

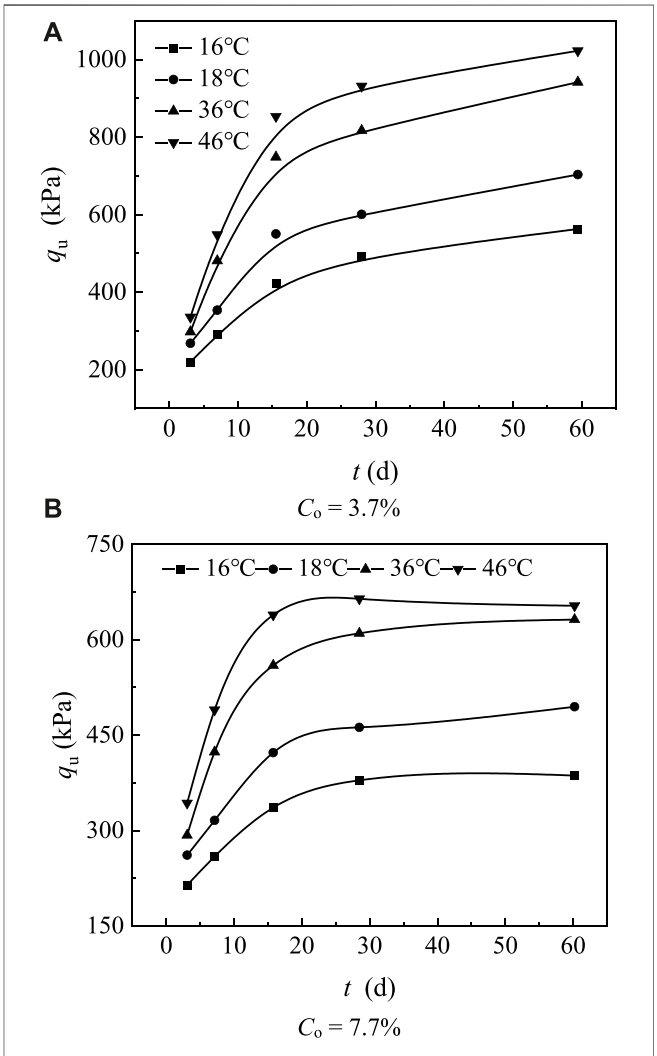

FIGURE 7 | Development of strength q_u with curing time t for samples with different C_o values cured at different temperatures. **(A)** C_o = 3.7% **(B)** C_o = 7.7%.

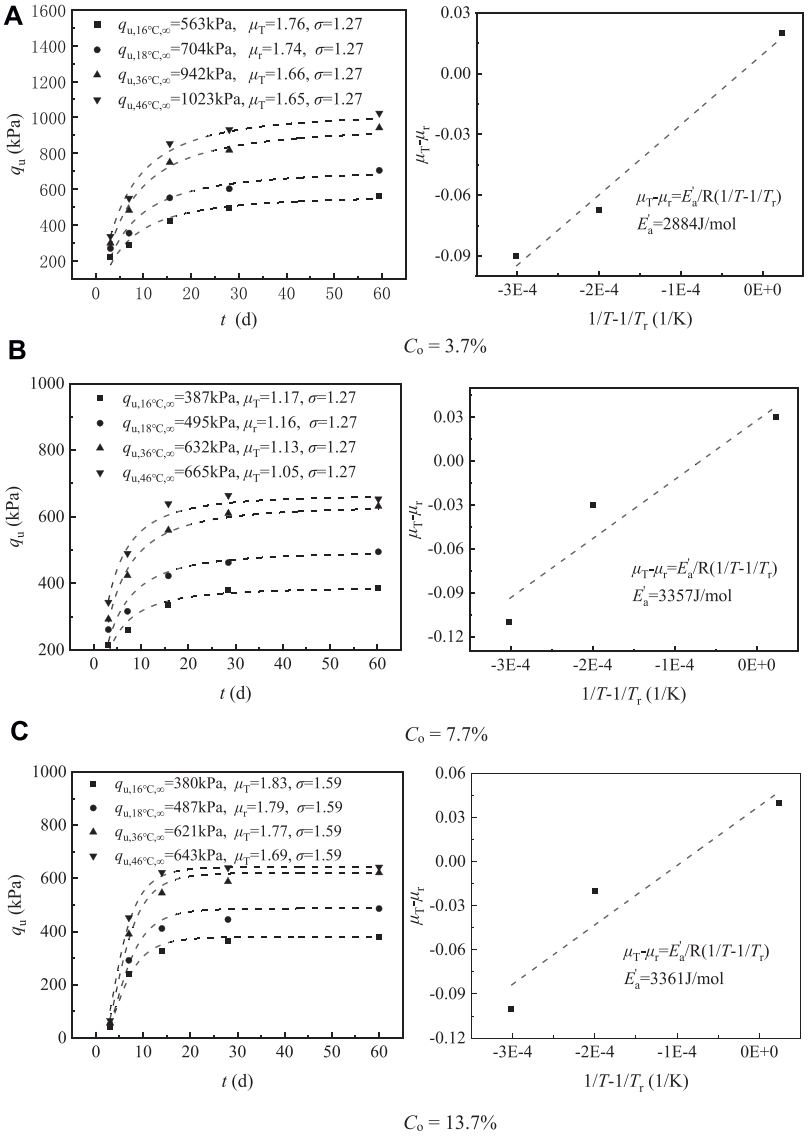

FIGURE 8 | Strength development curves of CSC samples affected by temperature. **(A)** C_o = 3.7% **(B)** C_o = 7.7% **(C)** C_o = 13.7%.

added per cubic meter of soil) that varies with w. To eliminate the influence of water content in different mixing ratios on cement content, A_w (%) is converted to C_m (kg/m^3), i.e., the A_w values of 10, 13, 15, and 20% respectively become C_m values of 53, 68, 79, and 104 kg/m^3 (**Table 1**). **Table 1** shows no significant variation of μ and σ for different values of w, C_m, and C_o: their ranges are 1.86–2.03 and 0.85–1.34, respectively, and their mean standard errors are 0.19 and 0.32, respectively. This indicates that μ and σ have a low correlation with the physical properties of the actual data, consistent with the results reported by Bi and Chian (2021). However, $q_{u,\infty}$ varies markedly (with a range of 532 kPa) as the physical properties change (**Table 1**), with much greater variation than that shown by μ and σ. Therefore, the fitting parameters for $q_{u,\infty}$ have the greatest correlation with the soil properties of CSC, indicating that the soil properties constitute the most important factor affecting the development of q_u with t.

Based on the above analysis, multivariate fitting analysis is conducted on $q_{u,\infty}$ and the indexes for physical property (**Table 1**) to obtain the relationship between the fitting parameters for $q_{u,\infty}$ and the physical properties:

$$q_{u,\infty} = -18.335 \times C_o + 9.700 \times C_m - 6.679 \times w + 523.833, \quad R^2 = 0.78 \tag{1}$$

Combining the probability density function of the log-normal distribution gives.

$$\frac{q_u}{q_{u,\infty}} = F_X(x) = F_T(t) = \frac{1}{2}\left[1 + erf\left(\frac{\ln(t) - \mu}{\sqrt{2}\sigma}\right)\right] \tag{2}$$

where t is curing age (in d) and T is curing temperature (in K).

The model to calculate the strength of CSC samples containing organic matter given w, C_m, and C_o is thus obtained:

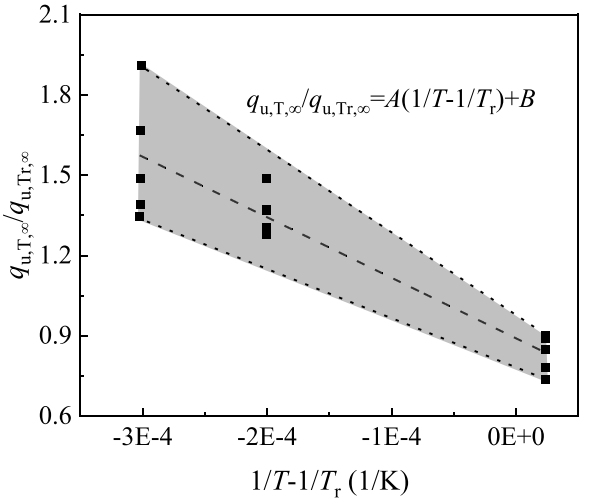

FIGURE 9 | Relation between $q_{u,T,\infty}/q_{u,Tr,\infty}$ and $1/T - 1/T_r$.

$$q_u = \frac{1}{2}\left[1 + erf\left(\frac{\ln(t) - \mu}{\sqrt{2}\sigma}\right)\right](-18.335C_o + 9.700C_m - 6.679w + 523.833) \quad (3)$$

Note that the correlation between fitting parameters for $q_{u,\infty}$ and physical property indexes are obtained from the best selection from among a linear, power, and second-order polynomial function. Fitting for the power and polynomial functions does not converge, while a linear fitting function shows a high correlation coefficient.

To assess the accuracy of the above prediction model, independent data are collected from published literature, and the measured strengths are compared with the corresponding calculated values. As this model is based on CSC samples with high water content and low cement content, the considered mixing ratios should be within the applicable range for CSC (i.e., $A_w \leq 15\%$, $C_m \leq 79\ kg/m^3$, and $C_o < 13.7\%$). In this paper, partial data from literature Du et al. (2020) are collected and

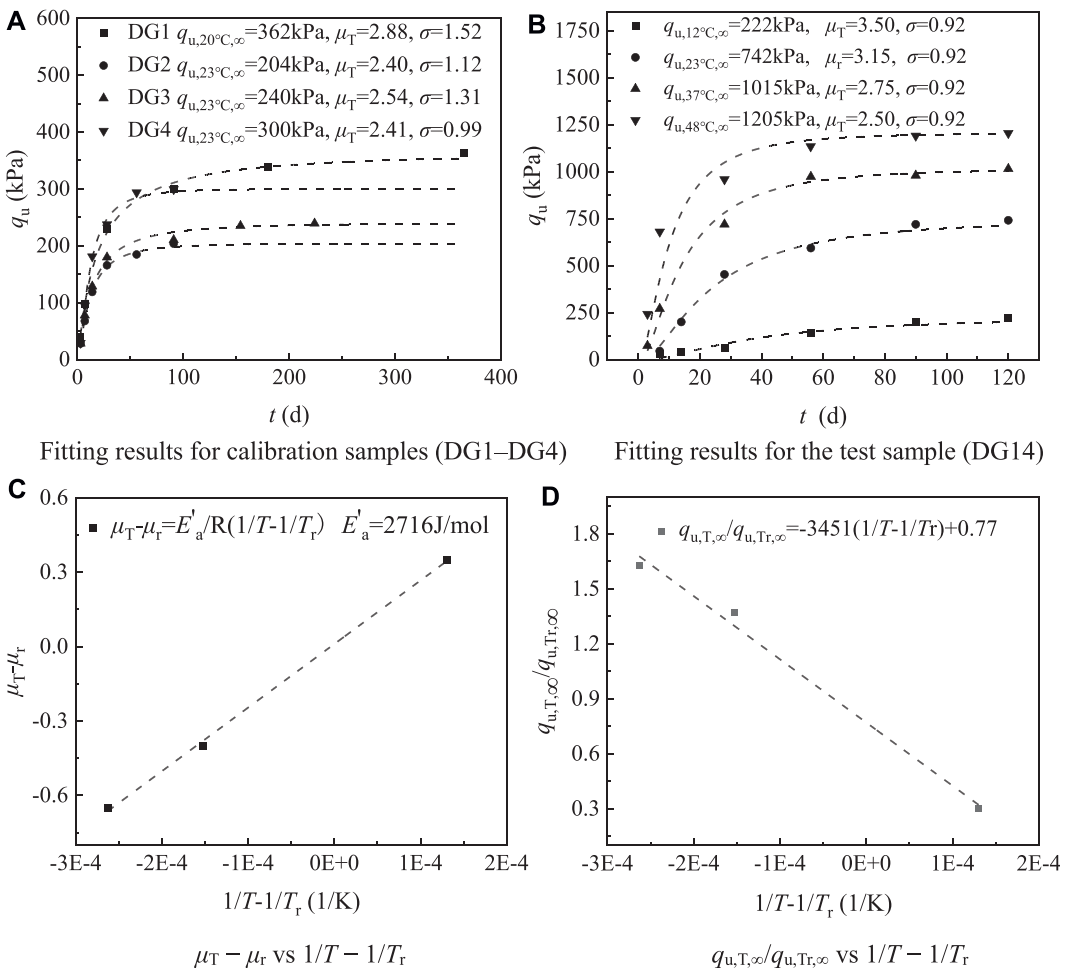

FIGURE 10 | Verification of the model using data from Zhang et al. (2014). **(A)** Fitting results for calibration samples (DG1–DG4) **(B)** Fitting results for the test sample (DG14) **(C)** μ_T–μ_r vs. $1/T$–$1/T_r$ **(D)** $q_{u,T,\infty}/q_{u,Tr,\infty}$ vs. $1/T$–$1/T_r$.

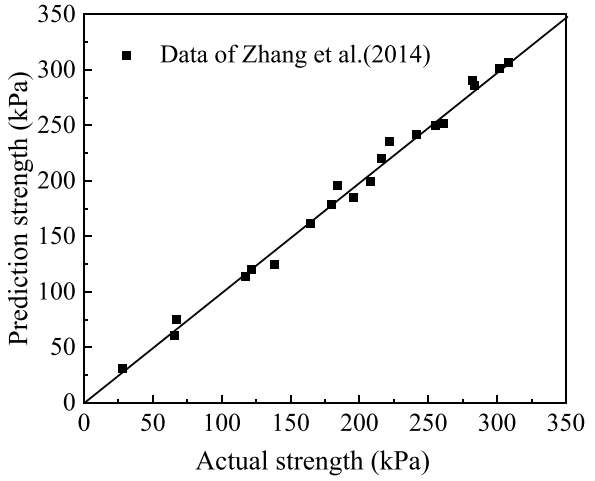

FIGURE 11 | Comparison of measured and predicted strengths.

verification is carried out based on the data. The verification results are shown in **Figure 6**. **Figure 6A** shows the curves of solidified soil samples under different C_o values obtained by fitting model. It can be seen that the established model is in good agreement with the actual test data. The verification results in **Figure 6B** show only a small error between the predicted and measured strength, indicating the applicability of the strength model proposed here to predict the strength of cement-solidified soils with different C_o values.

UCSOT MODEL

Cement-Solidified Clay Strength Characterization Model Considering the Effect of Temperature

Figure 7 plots the development with time of the strength of the CSC samples with different C_o values at different temperatures. For a given mixing ratio and curing age, increasing the curing temperature always raises the UCS in both the short- and long-term. The early increase in strength is due to the increase in the polymerization rate of silicate products and the formation of denser gelling products, while the long-term strength increases because high temperature is more conducive to the dissociation of silicate and aluminate, which will allow more Ca $(OH)_2$ to participate in the pozzolanic reaction, resulting in more enhanced products.

Modeling Strength Development in Cement-Solidified Clay Samples Cured at Different Temperatures

Existing models assume that the effect of temperature is closely related to the acceleration of the chemical reaction during strength development; they link the temperature and degree of reaction using the Arrhenius equation and maturity theory (Zhang et al., 2014). Accordingly, based on prior research, this paper directly links the curing temperature T with the degree of reaction by considering maturity, and then extends the strength prediction model proposed by Bi and Chian (2021) to a strength–time model for $q_{u,T}/q_{u,\infty}$ for any curing temperature T.

Bi and Chian's (2021) strength prediction model is

$$q_{u,T} = \frac{1}{2}\left[1 + erf\left(\frac{\ln t - \mu}{\sqrt{2}\sigma}\right)\right]q_{u,\infty} \tag{4}$$

t_r and t_T are the curing time required to reach a certain maturity M at the reference temperature T_r and any curing temperature T, respectively. The relative strength at any temperature T and the reference temperature T_r are D_T and D_r, respectively, and are given as follows.

$$D_T = \frac{q_{u,T}}{q_{u,T,\infty}} = \frac{1}{2}\left[1 + erf\left(\frac{\ln t - \mu_T}{\sqrt{2}\sigma_T}\right)\right] \tag{5}$$

$$D_r = \frac{q_{u,T_r}}{q_{u,T_r,\infty}} = \frac{1}{2}\left[1 + erf\left(\frac{\ln t - \mu_r}{\sqrt{2}\sigma_r}\right)\right] \tag{6}$$

Maturity theory gives maturity M as $M = \int_0^t k dt = k_{T_r} t_r = k_T t_T$; from this equation, the following formula can be obtained (Chitambira, 2004):

$$\frac{t_T}{t_r} = \frac{k_{T_r}}{k_T} = \exp\left(\frac{E'_a}{R}\left(\frac{1}{T} - \frac{1}{T_r}\right)\right) \tag{7}$$

where k_{Tr} and k_T are the rate constants at temperature T_r and T, respectively, E'_a is the apparent activation energy, and R is the ideal gas constant (8.3144 J/mol). Taking logarithms of both sides of **Eq. 7**, subtracting μ_r from both sides, and dividing by $2\sigma_r$ gives

$$\frac{\ln t_T - \left(\frac{E'_a}{R}\left(\frac{1}{T} - \frac{1}{T_r}\right) + \mu_r\right)}{\sqrt{2}\sigma_r} = \frac{\ln t_r - \mu_r}{\sqrt{2}\sigma_r} \tag{8}$$

Maturity theory assumes that any CSC samples with the same maturity have the same strength. Considering **Eqs 5**, **6**, this leads to

$$\frac{1}{2} + \frac{1}{2}erf\left[\frac{\ln t_T - \mu_T}{\sqrt{2}\sigma_T}\right] = \frac{1}{2} + \frac{1}{2}erf\left[\frac{\ln t_r - \mu_r}{\sqrt{2}\sigma_r}\right] \tag{9}$$

Both sides of **Eq. 9** are cumulative distribution functions of a log-normal distribution, and therefore increase monotonically. The following relationship can be obtained:

$$\frac{\ln t_T - \mu_T}{\sqrt{2}\sigma_T} = \frac{\ln t_r - \mu_r}{\sqrt{2}\sigma_r} \tag{10}$$

Combining this with **Eq. 8** gives

$$\sigma_T = \sigma_r \tag{11}$$

$$\mu_T = \frac{E'_a}{R}\left(\frac{1}{T} - \frac{1}{T_r}\right) + \mu_r \tag{12}$$

Therefore, the model predicting the development relative strength at any curing temperature T is

$$D_T = \frac{q_{u,T}}{q_{u,T,\infty}} = \frac{1}{2}\left[1 + erf\left(\frac{\ln t - \mu_T}{\sqrt{2}\sigma_T}\right)\right] = \frac{1}{2}\left[1 + erf\left(\frac{\ln t - \mu_r - \frac{E'_a}{R}\left(\frac{1}{T} - \frac{1}{T_r}\right)}{\sqrt{2}\sigma_r}\right)\right] \quad (13)$$

where $q_{u,T,\infty}$ and μ_T are the fitting parameters of temperature T; they respectively characterize the theoretical ultimate strength and strength development speed at temperature T. The fitting parameters μ_r and σ_r are obtained from the reference temperature T_r, and respectively represent the strength development rate at reference temperature T_r and a fitting constant independent of curing temperature.

Figure 8 plots strength fitting curves for CSC cured at different temperatures obtained from **Eq. 13**. It shows that the established model agrees well with the actual test data, and thus indicates the model's appropriateness. **Eq. 12** of the temperature model shows a clear linear relationship between the difference of reciprocal temperature ($1/T - 1/T_r$) and the difference of fitting parameter μ ($\mu_T - \mu_r$) for any temperature T and the reference temperature T_r. The slope of this relationship is the apparent activation energy. **Figure 8** shows that this linear relationship fitted by actual test data is stable and that there is a positive correlation between measured E'_a and C_o. The apparent activation energy E'_a corresponding to C_o = 3.7, 7.7, and 13.7% is 2284, 3357, and 3361 J/mol, respectively, indicating that organic matter increases the temperature sensitivity of the CSC samples.

The relative theoretical ultimate strength $q_{u,T,\infty}/q_{u,Tr,\infty}$ is introduced to establish the relationship between the relative theoretical ultimate strength and the difference of reciprocal temperature ($1/T - 1/T_r$), as shown in **Figure 9**. It has a clear linear relationship with $1/T - 1/T_r$, which can be expressed as

$$\frac{q_{u,T,\infty}}{q_{u,T_r,\infty}} = A\left(\frac{1}{T} - \frac{1}{T_r}\right) + B \quad (14)$$

where A and B are fitting coefficients.

Combining **Eqs 12**, **14** obtains the unconfined compressive strength prediction model for arbitrary curing temperature T based on a reference temperature:

$$q_{u,T} = \left(A\left(\frac{1}{T} - \frac{1}{T_r}\right) + B\right) \times q_{u,T_r,\infty} \times \frac{1}{2}\left[1 + erf\left(\frac{\ln t - \mu_r - \frac{E'_a}{R}\left(\frac{1}{T} - \frac{1}{T_r}\right)}{\sqrt{2}\sigma_r}\right)\right] \quad (15)$$

Eq. 15 can predict the strength development of the CSC at any curing temperature (within the relevant range of 15–45°C), given that the relevant parameters $q_{u,Tr,\infty}$ and μ_r for the sample at the reference temperature are determined in advance according to the selected curing age. As $\mu_T - \mu_r$ and $q_{u,T,\infty}/q_{u,Tr,\infty}$ both have a significant linear relationship with the temperature parameters $1/T - 1/T_r$, the accuracy of the model's prediction will be greatly affected by whether the estimation of the relevant parameters at the reference temperature is accurate. For solidified soils with high organic matter content, small differences can lead to large variations. To ensure the stability of the model and decrease the error caused by deviation of the reference temperature parameters, more strength development data for CSC samples containing organic matter at the reference temperature are needed.

The development of strength in CSC samples containing organic matter can be accurately fitted by the cumulative distribution function of the log-normal distribution. The theoretical ultimate strength $q_{u,\infty}$ is linearly correlated with the physical property indexes C_o, C_m, and w (**Eq. 3**). Any lack of data due to errors or omitted tests can be corrected and predicted by the CSC strength calculation model. Therefore, the corresponding temperature model **Eq. 15** becomes **Eq. 16**, which is the UCSOT model for CSC that considers the influences of organic matter and curing temperature:

$$q_{u,T} = \left(A\left(\frac{1}{T} - \frac{1}{T_r}\right) + B\right) \times (aC_o + bC_m + cw + d) \times \frac{1}{2}\left[1 + erf\left(\frac{\ln t - \mu_r - \frac{E'_a}{R}\left(\frac{1}{T} - \frac{1}{T_r}\right)}{\sqrt{2}\sigma_r}\right)\right] \quad (16)$$

where a, b, c, and d are linear fitting coefficients for the theoretical ultimate strength $q_{u,Tr,\infty}$ and the physical property indexes C_o, C_m, and w at temperature T_r.

Procedure for the UCSOT Model

Based on the established UCSOT model, a methodology to predict the strength development of organic CSC samples at arbitrary temperature T is proposed by revising the method of Zhang et al. (2014).

The sample is prepared from the target material with a representative mixing ratio and cured at a minimum of three temperatures, i.e., the reference temperature and the expected maximum and minimum temperatures. The unconfined compressive strengths of the samples are measured at 3, 7, 14, 28, and 60 d.

1) The theoretical ultimate strength $q_{u,Tr,\infty}$ and the fitting parameter μ_r at the reference temperature T_r are fitted by the formula $\frac{q_{u,T_r}}{q_{u,T_r,\infty}} = \frac{1}{2}\left[1 + erf\left(\frac{\ln t - \mu_r}{\sqrt{2}\sigma_r}\right)\right]$. For cement-solidified soil samples containing organic matter, the theoretical ultimate strength $q_{u,Tr,\infty}$ is calculated as $q_{u,Tr,\infty} = aC_o + bC_m + cw + d$.
2) The theoretical ultimate strength $q_{u,T,\infty}$ and the fitting parameter μ_T at the maximum and minimum temperatures are fitted as $\frac{q_{u,T}}{q_{u,T,\infty}} = \frac{1}{2}\left[1 + erf\left(\frac{\ln t - \mu_T}{\sqrt{2}\sigma_T}\right)\right]$.
3) The difference of the fitting parameters $\mu_T - \mu_r$ and the relative theoretical ultimate strength $q_{u,T,\infty}/q_{u,Tr,\infty}$ at the maximum and minimum temperatures are calculated. The corresponding apparent activation energy and ultimate strength parameters A and B are obtained from $\mu_T - \mu_r = \frac{E'_a}{R}\left(\frac{1}{T} - \frac{1}{T_r}\right)$ and $\frac{q_{u,T,\infty}}{q_{u,Tr,\infty}} = A\left(\frac{1}{T} - \frac{1}{T_r}\right) + B$.
4) For different mixing ratios of a given cured material, step (1) is repeated to obtain the theoretical ultimate strength $q_{u,Tr,\infty}$ and μ_r at the reference temperature. The parameters E'_a, A, and B

remain unchanged. Based on the temperature–strength prediction model $q_{u,T} = (A(\frac{1}{T} - \frac{1}{T_r}) + B) \times q_{u,T_r,\infty} \times \frac{1}{2}[1 + erf(\frac{\ln t - \mu_r - \frac{E'_a}{R}(\frac{1}{T} - \frac{1}{T_r})}{\sqrt{2}\,\sigma_r})]$, the strength of the CSC at any temperature T in the specified range can be obtained.

Note that the CSC samples must have C_o < 13.7%. If C_o exceeds this limit, new tests should be carried out to determine the relationship between the theoretical ultimate strength $q_{u,Tr,\infty}$ and the physical properties.

Validation of UCSOT Model

From the data of Zhang et al. (2014), the results for samples DG1 to DG4 are used to calibrate the theoretical ultimate strength $q_{u,Tr,\infty}$ at the reference temperature, and the data for sample DG14 is used to evaluate the accuracy of the temperature–strength model. The considered soils are all Singapore marine soft clay, and the curing agent is slag cement. **Figure 10** shows the verification results.

The figure shows that $q_{u,Tr,\infty}$ for DG1 to DG4 is linearly correlated with the physical properties C_o, C_m, and w: $q_{u,Tr,\infty} = -154.538C_o + 18.835C_m - 1.546w + 222.175$. Therefore, the theoretical limit of the calibrated strength of DG14 at the reference temperature is 742 kPa. Using this strength to fit the UCSOT model gives predicted results that are in good agreement with the actual data. Plots of $1/T$—$1/T_r$ with respect to μ_T–μ_r (**Figure 10C**) and $q_{u,T,\infty}/q_{u,Tr,\infty}$ (**Figure 10D**) obtained from the fitting model are clearly linear. **Figure 11** compares the predicted and actual strengths; it shows their consistency, and thus indicates the appropriateness of the UCSOT model proposed here. As the model fully considers the influence of temperature and organic matter on the strength of solidified silt, it is generally applicable in engineering.

CONCLUSION

Through a series of laboratory tests, this paper discusses the influence of A_w, C_o, w, and T on the q_u of CSC. A model characterizing the compressive strength of CSC considering the effects of organic matter and curing temperature is proposed. The accuracy of the model is verified by comparing its predictions with reported experimental data. The main conclusions are as follows.

1) The UCS of CSC decreases with increasing C_o (between 3.7 and 13.7%) and w (between 1.5 and 2.25w_L) and increases with increasing A_w (between 10 and 20%) and T (between 15 and 45°C). Hotter curing raises both the early and long-term strengths of CSC.
2) A_w greatly affects the influence of organic matter on the UCS of CSC. For A_w > 15%, the UCS does not increase as the cement incorporation ratio increases, and the traditional hyperbolic model cannot accurately predict UCS. The multiple regression model using C_m, w, and C_o as independent control parameters can accurately reflect the UCS at the reference temperature.
3) Organic matter increases the temperature sensitivity of CSC samples. A model to characterize strength while considering the influence of organic matter and curing temperature is established. Its predictions fit well the experimental data and the strength data reported in the literature: $\mu_T - \mu_r$ and $1/T - 1/T_r$ have good linear relationship.
4) A procedure for using the UCSOT model is presented. It easily determines the parameters for the established temperature–strength model, thus allowing prediction of the strength development of CSC at any curing temperature T within the relevant range (15–45°C).

DATA AVAILABILITY STATEMENT

The original contributions presented in the study are included in the article/supplementary material, further inquiries can be directed to the corresponding author.

AUTHOR CONTRIBUTIONS

YC: conceptualization, methodology, writing—original draft. JZ: investigation, formal analysis, validation. GX: resources. ML: writing—review and editing. XB: methodology.

FUNDING

This research is supported by the National Natural Science Foundation of China (Grant No. 52178347), project ZR2021ME068 supported by Shandong Provincial Natural Science Foundation, Key Laboratory of Ministry of Education for Geomechanics and Embankment Engineering, Hohai University (Grant No. 2021006), Excellent Doctor Young Teacher Support Program of Weifang University, Scientific Research Foundation of Weifang University (Grant No.2021BS32).

REFERENCES

ASTM (2010). *Standard Practice for Classification of Soils for Engineering Purposes (Unified Soil Classification System)*. Montgomery County, PA: West Conshohocken. ASTM D2487-10.

Bai, B., Wang, Y., Rao, D. Y., and Bai, F. (2022). The Effective Thermal Conductivity of Unsaturated Porous Media Deduced by Pore-Scale SPH Simulation. *Front. Earth Sci* 10. doi:10.3389/feart.2022.943853

Bai, B., Nie, Q., Zhang, Y., Wang, X., and Hu, W. (2021a). Cotransport of Heavy Metals and SiO_2 Particles at Different Temperatures by Seepage. *J. Hydrology* 597, 125771. doi:10.1016/j.jhydrol.2020.125771

Bai, B., Yang, G.-c., Li, T., and Yang, G.-s. (2019). A Thermodynamic Constitutive Model with Temperature Effect Based on Particle Rearrangement for Geomaterials. *Mech. Mater.* 139, 103180. doi:10.1016/j.mechmat.2019.103180

Bai, B., Zhou, R., Cai, G., Hu, W., and Yang, G. (2021b). Coupled Thermo-Hydro-Mechanical Mechanism in View of the Soil Particle Rearrangement of Granular Thermodynamics. *Comput. Geotechnics* 137 (8), 104272. doi:10.1016/j.compgeo.2021.104272

Bi, J., and Chian, S. C. (2020). Modelling of Three-phase Strength Development of Ordinary Portland Cement- and Portland Blast-Furnace Cement-Stabilised Clay. *Géotechnique* 70 (1), 80–89. doi:10.1680/jgeot.18.p.087

Bi, J., and Chian, S. C. (2021). Modelling Strength Development of Cement-Stabilised Clay and Clay with Sand Impurity Cured under Varying Temperatures. *Bull. Eng. Geol. Environ.* 80 (8), 6275–6302. doi:10.1007/s10064-021-02281-8

Cao, Y., Ding, J., Zhang, R., and Xu, G. Z. (2021b). Effect of Vertical Flow on Consolidation Degree of Foundation with Vertical Drains in Large-Strain Consolidation Theory. *KSCE J. Civ. Eng.* 25 (1), 3264–3272. doi:10.1007/s12205-021-1558-8

Cao, Y., Xu, J., Bian, X., and Xu, G. (2019). Effect of Clogging on Large Strain Consolidation with Prefabricated Vertical Drains by Vacuum Pressure. *KSCE J. Civ. Eng.* 23 (10), 4190–4200. doi:10.1007/s12205-019-1884-2

Cao, Y., Zhang, J., Xu, J., and Xu, G. (2020). A Large-Strain Vacuum-Assisted Radial Consolidation Model for Dredged Sludge Considering Lateral Deformation. *KSCE J. Civ. Eng.* 24 (12), 3561–3572. doi:10.1007/s12205-020-1854-8

Cao, Y., Zhang, R., Xu, G., and Xu, J. (2021a). Axisymmetric Large Strain Consolidation by Vertical Drains Considering Well Resistance under Vacuum Pressure. *Arab. J. Geosci.* 14 (19), 2016. doi:10.1007/s12517-021-08354-y

Chitambira (2004). *Accelerated Ageing of Cement Stabilised/solidified Contaminated Soils with Elevated Temperatures*. University of Cambridge.

Detzner, H. D., Schramm, W., Döring, U., and Bode, W. (1998). New Technology of Mechanical Treatment of Dredged Material from Hamburg Harbour. *Water Sci. Technol.* 37 (6-7), 337–343. doi:10.2166/wst.1998.0770

Du, C., Zhang, J., Yang, G., and Yang, Q. (2020). The Influence of Organic Matter on the Strength Development of Cement-Stabilized Marine Soft Clay. *Mar. Georesources Geotechnol.* 1 (7), 1–11. doi:10.1080/1064119x.2020.1792593

Grubb, D. G., Chrysochoou, M., Smith, C. J., and Malasavage, N. E. (2010). Stabilized Dredged Material. I: Parametric Study. *J. Geotech. Geoenviron. Eng.* 136 (8), 1011–1024. doi:10.1061/(asce)gt.1943-5606.0000254

Gu, Z., Hua, S., Zhao, W., Li, S., Gao, Z., and Shan, H. (2018). Using Alkali-Activated Cementitious Materials to Solidify High Organic Matter Content Dredged Sludge as Roadbed Material. *Adv. Civ. Eng.* 2018 (10), 1–10. doi:10.1155/2018/2152949

Huang, Y., Dong, C., Zhang, C., and Xu, K. (2017). A Dredged Material Solidification Treatment for Fill Soils in East China: A Case History. *Mar. Georesources Geotechnol.* 35 (6), 865–872. doi:10.1080/1064119x.2016.1257669

Kipton, H., Powell, J., and Town, R. M. (1992). Solubility and Fractionation of Humic Acid; Effect of pH and Ionic Medium. *Anal. Chim. Acta* 267 (1), 47–54. doi:10.1016/0003-2670(92)85005-q

Kitazume, M., and Satoh, T. (2003). Development of a Pneumatic Flow Mixing Method and its Application to Central Japan International Airport Construction. *Proc. Institution Civ. Eng. - Ground Improv.* 7 (3), 139–148. doi:10.1680/grim.2003.7.3.139

Ma, C. (2017). *Study on High Efficiency Curing Agent for Saturated Soft Soil and Strength Characteristics of Solidified Soil*. Shanghai: Shanghai Jiaotong University

Marzano, I. P., Al-Tabbaa, A., and Grisolia, M. (2009). Influence of Curing Temperature on the Strength of Cement-Stabilised Artificial Clays." in Proceedings of the 2nd International Workshop on Geotechnics of Soft Soils, Glasgow, Scotland, September 03–September 05, 2008, 257–262.

Pan, Y., Rossabi, J., Pan, C., and Xie, X. (2019). Stabilization/solidification Characteristics of Organic Clay Contaminated by Lead when Using Cement. *J. Hazard. Mater.* 362, 132–139. doi:10.1016/j.jhazmat.2018.09.010

Porbaha, A., Raybaut, J.-L., and Nicholson, P. (2001). State of the Art in Construction Aspects of Deep Mixing Technology. *Proc. Institution Civ. Eng. - Ground Improv.* 5 (3), 123–140. doi:10.1680/grim.2001.5.3.123

Schmidt, F., Hinrichs, K. U., and Elvert, M. (2010). Sources, Transport, and Partitioning of Organic Matter at a Highly Dynamic Continental Margin. *Mar. Chem.* 118 (1-2), 37–55. doi:10.1016/j.marchem.2009.10.003

Suits, L. D., Sheahan, T. C., Tan, T. S., Goh T Land Yong, K. Y. (2002). Properties of Singapore Marine Clays Improved by Cement Mixing. *Geotechnical Test. J.* 25 (4), 422–433. doi:10.1520/gtj11295j

Tan, T. S., Lu, Y. T., Phoon, K. K., and Karthikeyan, M. (2011). Innovative Approaches to Land Reclamation in Singapore. *Int. Symposium Adv. Ground Technol. Geo-Information*, 85–102. doi:10.3850/978-981-07-0188-8_p176

Van Impe, W. F., and Flores, R. D. V. (2006). Deep Mixing in Underwater Conditions: A Laboratory and Field Investigation. *Proc. Institution Civ. Eng. - Ground Improv.* 10 (1), 15–22. doi:10.1680/grim.2006.10.1.15

Ying, Z., Cui, Y. J., Duc, M., and Benahmed, N. (2022). Effect of Salt Solution on the Optimum Lime Contents of Bentonite and Silt. *Acta Geotech.*, 1–15. doi:10.1007/s11440-022-01488-7

Ying, Z., Cui, Y.-J., Benahmed, N., and Duc, M. (2021). Drying Effect on the Microstructure of Compacted Salted Silt. *Géotechnique*, 1–9. doi:10.1680/jgeot.20.p.319

Yun, J.-M., Song, Y.-S., Lee, J.-H., and Kim, T.-H. (2006). Strength Characteristics of the Cement-Stabilized Surface Layer in Dredged and Reclaimed Marine Clay, Korea. *Mar. Georesources Geotechnol.* 24 (1), 29–45. doi:10.1080/10641190600559499

Zhang, J., Li, M., Ke, L., and Yi, J. (2022). Distributions of Lateral Earth Pressure behind Rock-Socketed Circular Diaphragm Walls Considering Radial Deflection. *Comput. Geotechnics* 143, 104604. doi:10.1016/j.compgeo.2021.104604

Zhang, R. J., Lu, Y. T., Tan, T. S., Phoon, K. K., Asce, F., and Santoso, A. M. (2014). Long-term Effect of Curing Temperature on the Strength Behavior of Cement-Stabilized Clay. *J. Geotechnical Geoenvironment Eng.* 140 (8), 04014045. doi:10.1061/(asce)gt.1943-5606.0001144

Zhang, R. J., Qiao, Y. Q., Zheng, J. J., and Dong, C. Q. (2020). A Method for Considering Curing Temperature Effect in Mix Proportion Design of Mass Cement-Solidified Mud at High Water Content. *Acta Geotech.* 16 (12), 1–23. doi:10.1007/s11440-020-00961-5

Zhang, R. J., Santoso, A. M., Tan, T. S., Phoon, K. K., and Asce, F. (2013). Strength of High Water-Content Marine Clay Stabilized by Low Amount of Cement. *J. Geotech. Geoenviron. Eng.* 139 (12), 2170–2181. doi:10.1061/(asce)gt.1943-5606.0000951

Conflict of Interest: The authors declare that the research was conducted in the absence of any commercial or financial relationships that could be construed as a potential conflict of interest.

Publisher's Note: All claims expressed in this article are solely those of the authors and do not necessarily represent those of their affiliated organizations, or those of the publisher, the editors and the reviewers. Any product that may be evaluated in this article, or claim that may be made by its manufacturer, is not guaranteed or endorsed by the publisher.

Copyright © 2022 Cao, Zhang, Xu, Li and Bian. This is an open-access article distributed under the terms of the Creative Commons Attribution License (CC BY). The use, distribution or reproduction in other forums is permitted, provided the original author(s) and the copyright owner(s) are credited and that the original publication in this journal is cited, in accordance with accepted academic practice. No use, distribution or reproduction is permitted which does not comply with these terms.

frontiers | Frontiers in Materials

TYPE Original Research
PUBLISHED 05 August 2022
DOI 10.3389/fmats.2022.980375

Check for updates

OPEN ACCESS

EDITED BY
Bing Bai,
Beijing Jiaotong University, China

REVIEWED BY
Yongchao Tian,
Henan Polytechnic University, China
He Liu,
University of South China, China

*CORRESPONDENCE
Bingqin Zhao,
bingqinzhao@163.com

SPECIALTY SECTION
This article was submitted to Structural Materials,
a section of the journal
Frontiers in Materials

RECEIVED 28 June 2022
ACCEPTED 11 July 2022
PUBLISHED 05 August 2022

CITATION
Zhang H, Liu L, Feng W, Zhou Y, Zheng W and Zhao B (2022), Design selection and dynamic response analysis of CFG pile composite foundation in soft soil areas.
Front. Mater. 9:980375.
doi: 10.3389/fmats.2022.980375

COPYRIGHT
© 2022 Zhang, Liu, Feng, Zhou, Zheng and Zhao. This is an open-access article distributed under the terms of the Creative Commons Attribution License (CC BY). The use, distribution or reproduction in other forums is permitted, provided the original author(s) and the copyright owner(s) are credited and that the original publication in this journal is cited, in accordance with accepted academic practice. No use, distribution or reproduction is permitted which does not comply with these terms.

Design selection and dynamic response analysis of CFG pile composite foundation in soft soil areas

Huahua Zhang[1,2,3], Liming Liu[1,2], Wei Feng[4], Yuru Zhou[3], Wei Zheng[1,2] and Bingqin Zhao[1,2]*

[1]Hubei Provincial Engineering Research Center of Slope Habitat Construction Technique Using Cement-based Materials, China Three Gorges University, Yichang, China, [2]College of Civil Engineering and Architecture, China Three Gorges University, Yichang, China, [3]Housing and Urban-Rural Development Bureau, Yichang, China, [4]The Seventh Geological Brigade of Hubei Geological Bureau, Yichang, China

The construction of roads along rivers plays a crucial role in the construction of economic belts and social and economic development along rivers. Roadbeds are the foundation of highway construction, while the soft soil foundation is widely distributed on both sides of rivers, resulting in some difficulties for roadbed construction and highway use. Despite diverse technical methods for the treatment of general roadbeds, the treatment of soft soil roadbeds should be further explored. In this paper, various advantages of applying CFG (Cement Fly-ash Gravels) pile treatment to the soft foundation in Bailinhe Road, Yichang are investigated. Specifically, the soft soil roadbed treated by CFG pile is numerically simulated, the changes in engineering index response before and after foundation treatment are analyzed, and then the dynamic analysis under vehicle dynamic load is performed. The results demonstrate that the reinforcement effect of the CFG pile significantly weakens the influence of vehicle dynamic load on roadbeds.

KEYWORDS

soft foundation treatment, CFG, foundation settlement, dynamic load, dynamic response

1 Engineering background

Influenced by the rise and fall of river water level, the roadbed of Bailinhe Road in Yichang City has complicated geological and hydrological conditions (Cui et al.,2022). If the roadbed is treated by the conventional roadbed treatment method, it would not reach the design bearing capacity during construction and compaction, and it is easy to cause uneven settlement after construction (Bai et al., 2021a). The existing data theory and processing methods have some limitations (Bai et al., 2021b). Nevertheless, the requirements of national general norms are still adopted, and the targeted theoretical research and analysis are not conducted in the combination with the particularity of the region (Jones Jr, 1981; Cui et al.,2019). Therefore, a comprehensive theoretical analysis

based on engineering geology and hydrology conditions in Yichang should be conducted to propose corresponding treatment measures and lay a theoretical basis for the treatment of similar special soil foundations (Peng et al., 2016; Yin and Yu, 2009; Bai et al.,2022). Besides, the roadbed, as the foundation of the road, is the prerequisite to guarantee the high-speed, smooth, comfortable, and safe operation of vehicles. Hence, the deformation and dynamic issues of soft soil roadbeds under dynamic loads are crucial in road roadbed engineering (Tan, 1995; Bai et al.,2019).

Currently, researchers around the world have conducted a lot of studies on the dynamic response and reinforcement of roadbeds under dynamic loads and achieved a series of achievements (Derbyshire et al., 1994; Bai et al.,2020). For example, Zhao Guotang and Liang Bo et al. simplified the superstructure and established a roadbed model under the consideration of the relationship between each structure layer and the dynamic response characteristics of roadbeds. Xu Peng et al. investigated the dynamic response caused by vehicles' dynamic loads using the dynamic model and then provided the longitudinal and transverse distribution of dynamic deformation and dynamic stress along roadbeds. Chen Renpeng et al. discussed the influence of vehicle speed on the mean value and variation coefficient of dynamic stress based on the roadbed roughness and then established two-dimensional and three-dimensional analysis models of roadbed structures. Since the particularity of soft soil engineering properties makes the dynamic characteristics of soft soil roadbeds complicated, the stability induced by dynamic response is also concerned (Terzaghi, 1943; Habibagahi and Mokhberi, 1998). Although many research achievements on the dynamic response of roadbeds have been obtained, there are few studies on the reinforcement effect of soft roadbeds (Alamgir et al., 1996; Otani et al., 1998). Moreover, the roadbeds built on soft soil generally need reinforcement in the actual engineering due to an insufficient foundation bearing capacity, and CFG pile reinforcement is one of the effective methods (Jung et al.,2001; Lai et al., 2016). The three-dimensional finite element method was employed to analyze the effect after CFG pile reinforcement and the variation rules of vertical velocity, acceleration, and compressive stress based on the roadbed reinforcement engineering of Bailinhe Road, Yichang City. The simulation results are of great significance for promoting the development of foundation treatment technology for soft soil roadbed engineering (Ye and Gong, 2017; Cheng et al., 2018).

2 Roadbed settlement calculation

Soil masses are compressible, and foundation settlement is inevitable during construction. Foundation settlement generally includes three parts: Instantaneous settlement, primary consolidation settlement, and secondary consolidation settlement. Instantaneous settlement occurs in the initial stage and is provoked by the deformation of the soil skeleton and elastic deformation of the soil. Secondary consolidation settlement occurs in the final stage and results from the creep of soil. Primary consolidation settlement is the most concerned. The settlement in a general sense indicates the primary consolidation settlement and is generated by the drainage of excess pore water in the soil particle clearance and the change in the soil void. In practice, the three kinds of settlements are not completely independent, and there are frequently multiple settlement components simultaneously, while one of them occupies a higher proportion.

The deformation settlement of soft soil roadbeds has two characteristics: A large amount of deformation and a long duration of deformation settlement. Instantaneous settlement and secondary consolidation settlement usually adopt estimation, while main consolidation settlement adopts more theoretical calculation methods. Appropriate calculation methods should be employed to handle specific issues. Under the Winkler model, the settlement of a certain point on the foundation is related to the pressure of soil action at that point, rather than the pressure of other points. With regard to the foundation with similar mechanical properties to water, such as the semi-liquid soil with very low shear strength (such as silt, soft clay) or the plastic zone under a relatively large foundation, the winkle elastic foundation beam method is considered to be more appropriate for soft foundation reinforcement treatment, and the composite stiffness method is more suitable for the composite foundation treatment.

In China, the calculation of foundation settlement is primarily performed by the layerwise summation method, which is clear in theory, simple in the calculation, and easy to obtain the calculation parameters. The calculation results are consistent with the actual situation. Unfortunately, the influence of soil lateral deformation is neglected.

The volume of soil particles for single-layer soil masses remains unchanged before and after compression, as Formula (1):

$$V_s = \frac{1}{1+e_1} HA = \frac{1}{1+e_2} (H-s)A \tag{1}$$

Therefore, the settlement value can be obtained following the e-p curve as Formula (2):

$$s = \frac{e_1 - e_2}{1+e_1} H = \frac{a\Delta p}{1+e_1} H = \frac{\Delta p H}{E_s} \tag{2}$$

Finally, the sum of all layers of soil is utilized to acquire the final settlement expression, as Formula (3)

$$s = \sum_{i=1}^{n} \frac{\Delta p_i H_i}{E_{csi}} \tag{3}$$

Where Vs. represents the initial volume, e1 indicates the initial porosity ratio, e2 denotes the compressed pore ratio, H refers to

the thickness of the soil, A means the area of the soil, s stands for the height of settlement, a represents the compression coefficient, Δp means the average additional stress applied to the soil layer, and Es denotes the amount of compressed soil.

3 Cement fly-ash gravels pile reinforcement mechanism

Cement Fly-ash Gravel (CFG) pile is a high-strength bonded pile formed by cement, gravel, fly ash, stone debris, and water through the long Auger pipe pump pressure into the pile in the foundation drilling perfusion. CFG pile composite foundation is composed of the pile body, the soil between piles, and the cushion layer. CFG piles are widely used in the treatment of soft soil foundations owing to their characteristics of simple construction, significant improvement of foundation bearing capacity, green environmental protection, low economic cost, and strong applicability.

CFG pile generally reinforces the foundation through compaction, restraint, and drainage consolidation between piles and the soil.

1) CFG pile body. Since the pile strength and elastic modulus in the CFG pile composite foundation are significantly greater than those of the soil between piles, the CFG pile body shares most of the upper pile load, improves the overall foundation stiffness, and reduces the roadbed settlement.
2) Compaction. The soil particles become compact through the construction vibration and impact of the CFG pile, leading to a decrease in the soil pore ratio and water content, an increase in the soil weight, and an improvement in the bearing capacity of the foundation.
3) Constraint effect. CFG piles can limit the lateral deformation of the soil between piles, maintain the interaction between piles and the soil, and weaken the roadbed settlement.
4) Drainage consolidation. CFG pile body and cushion, with good water permeability, can be used as the foundation drainage channel to accelerate the consolidation settlement after foundation construction.
5) Cushion. The cushion can lower the stress concentration of the bottom of the foundation, adjust the proportion of pile to soil to share the upper load, provide conditions for CFG pile penetration, and assure the cooperation of the pile body and the soil between the piles.

4 Analysis of reinforcement effect of cement fly-ash gravels pile on soft foundation

Foundation survey data reveal that the foundation soil contains silty clay, silt soil, gravel soil, and containing-gravel silty clay from shallow and deep. Based on the comprehensive consideration of the engineering geology, the replacement has not been economic enough and fails to satisfy the requirement of the time limit for engineering. Therefore, CFG pile treatment can be employed to guarantee the construction progress and make the roadbed rapidly consolidate. The depth of soft soil in highway roadbeds is 5–10 m, and it is brown soft clay, with high moisture content and large compressibility. Hence, there is a large settlement and risk of embankment instability.

4.1 Establishment and parameter selection of finite element model

Foundation survey data suggest that the foundation soil contains silty clay, silt soil, gravel soil, and containing-gravel silty clay from shallow and deep. Based on the comprehensive consideration of the engineering geology, the replacement has not been economic enough and cannot meet the requirement of the time limit for engineering. Therefore, it is feasible to adopt CFG pile treatment to guarantee the construction progress and make the roadbed rapidly consolidate.

Plaxis software was used for two-dimensional numerical modeling. Method 1: Plate element method is adopted. The disadvantage of this method is that it ignores the seepage in plate element, but it is relatively easy to calculate the bending moment, shear force and axial force. Method 2: Solid element method is adopted to calculate the solid element parameters of 2-days pile based on the equivalence of stiffness, weight and permeability coefficient. Besides, permeability is taken into account. However, the bending moment, shear force and axial force are not obtained directly. They can only be calculated by using the stress on the pile. Considering that the highway has a symmetrical structure, half of the structure was used for modeling analysis, and the actual design values were selected for the geometric parameters of the model. The 2D model of the highway cross-section was established with a 10 m-deep soft soil base and a 10 m-deep bearing layer foundation. The sheet element was utilized to simulate the pile, and the pile length was 11 m according to the design. Then, it traversed the soft soil area and was embedded in 1 m under the bearing layer. The pile spacing was 1.4m, and the pile diameter was 0.4 m. The mechanical properties of the CFG pile are presented in Table. 1. The geological survey report did not provide the more detailed parameters of the foundation soil. Thus, the highway filling was filled with gravel soil, the stratified construction with a thickness of 0.5 m was conducted, and the bottom of the embankment adopted a 0.4 m-thick gravel cushion, so as to simplify the model and fully consider the unfavorable factors of the soft soil foundation. The parameters of the highway soil body are listed in Table. 2. Moore-coulomb soil constitutive model and Goodman contact element without thickness were utilized to simulate pile-soil interaction, and then the strength reduction was used for the interface element.

The highway embankment is 5 m high, 27 m wide at the top, and 42 m wide at the bottom. The embankment slope rate is 1:1.5.

TABLE 1 Mechanical parameters of CFG pile.

Axial rigidity (kN•m^{-1})	Flexural rigidity (kN•m^{-1})	Equivalent thickness (m)	Volume weight (kN•m^{-3})	Poisson's ratio
3.2e+6	7e+4	0.512	23	0.167

TABLE. 2 Parameters of the soil mass.

Soil mass	Gravity density/ (kN•m^{-3})	Osmotic coefficient (m•d^{-1})	Elasticity modulus (kN•m^{-2})	Poisson's ratio	Cohesive force (kN•m^{-2})	Frictional angle (°)	Interface reduction factor
Gravel filling	18.5	0.25	3e+4	0.28	2.4	28.0	0.67
Gravel cushion	20	0.5	5e+4	0.25	1.2	38.0	0.67
Reinforced layer	17	4e-4	3.1e+3	0.35	8.0	10.5	0.58
Bearing stratum	18	1e-5	5e+3	0.31	3.0	40.0	0.58

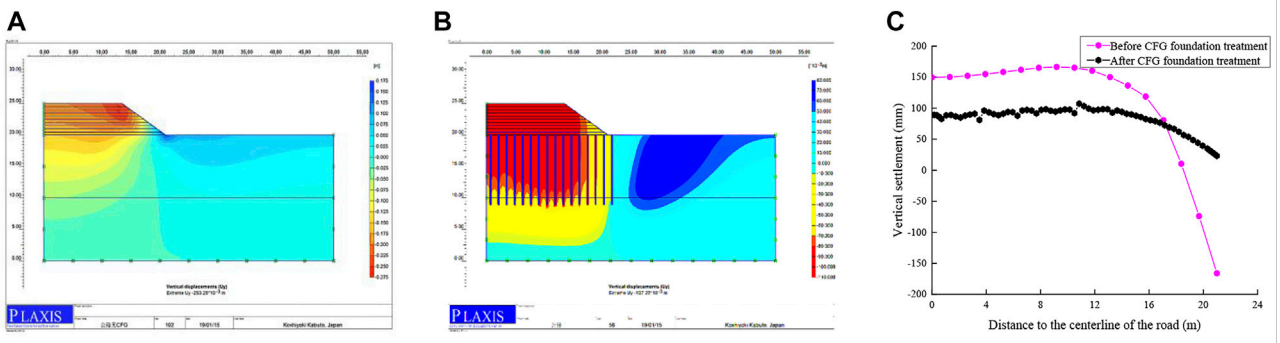

FIGURE 1
Settlement calculation results before and after foundation treatment: **(A)** Vertical settlement of the road without foundation treatment; **(B)** Vertical settlement of the road after CFG pile foundation treatment; **(C)** Distribution of vertical settlement of pile top along the width of the embankment before and after foundation treatment.

Besides, the modeling range is 50 m in width and 25 m in depth to avoid any influence on numerical results due to the geometric size of the model. Standard boundary conditions were applied to the boundary, with horizontal constraints for the left and right sides, and complete constraints for the bottom. Meanwhile, the influence of water level on the model was ignored.

4.2 Displacement result analysis of reinforced foundation

As demonstrated in Figure 1A, B, the foundation settlement after CFG pile treatment decreased from 253.25mm to 107.23mm, with a decrease of about 57.66%. In other words, the CFG pile significantly improved the stiffness of the soft soil foundation and effectively reduced the settlement caused by insufficient foundation stiffness. In Figure 1C, compared with the case without foundation treatment, the uneven settlement has been slowed down under the CFG pile group effect, and the settlement was more integrated, leading to the lowered potential risk of upper structure damage induced by uneven settlement. Without CFG pile foundation treatment, the embankment even produced uplift near the slope angle, presenting a slope deformation form and even instability risks.

As demonstrated in Figure 2. Regarding the horizontal displacement of the roadbed, the embankment load was

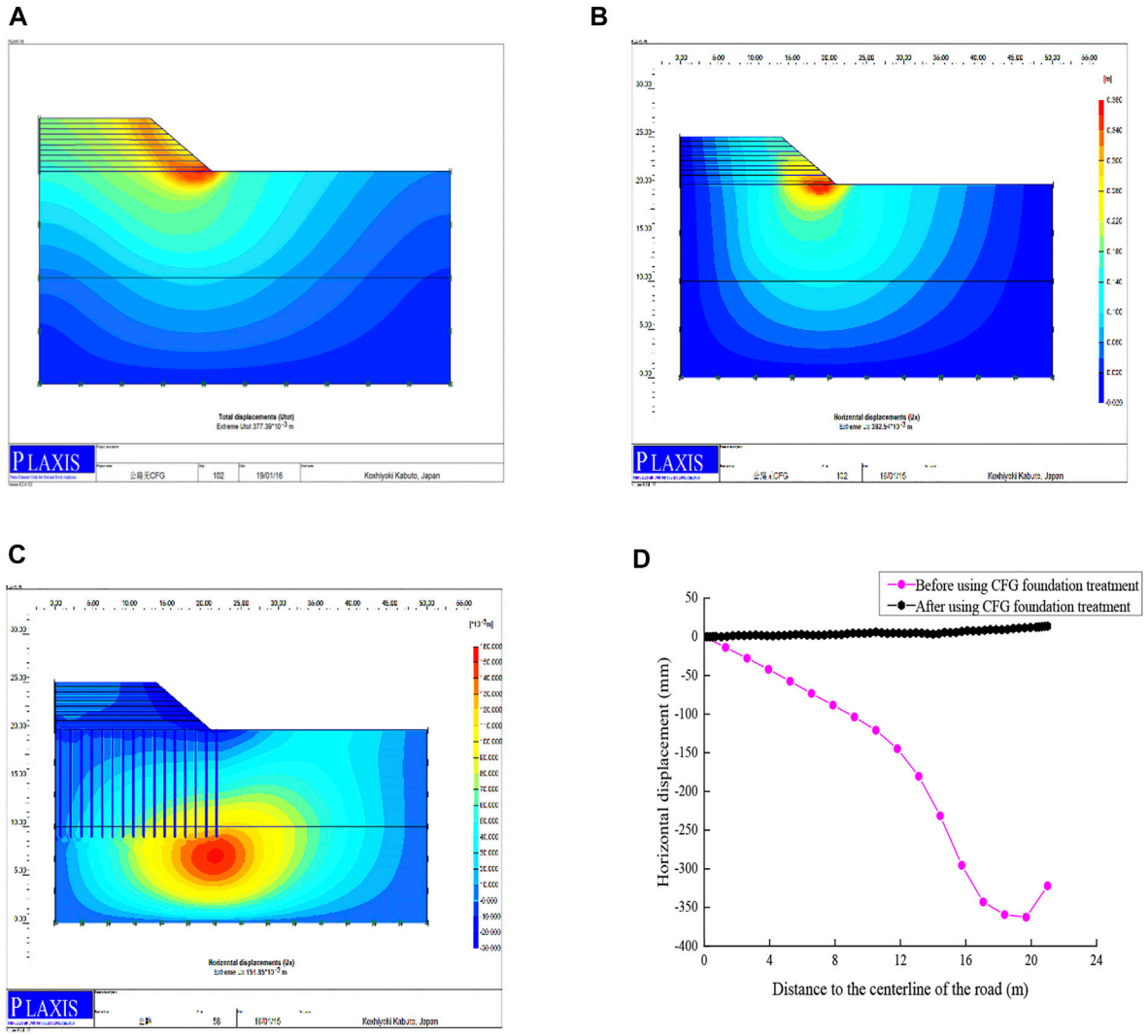

FIGURE 2
Calculation results of horizontal displacement before and after foundation treatment: **(A)** Deformation form of embankment without foundation treatment; **(B)** Horizontal displacement of the highway without foundation treatment; **(C)** Horizontal displacement of the highway after CFG pile foundation treatment; **(D)** Distribution of horizontal displacement of pile top along the width of the embankment before and after foundation treatment.

transferred to the deeper soil layer given the reinforcement of piles. The shallow soil mass exhibited no significant horizontal displacement, while the deep soil mass possessed a certain horizontal displacement (the horizontal displacement is positive toward the center of the embankment). The shallow horizontal displacement decreased from 362.54mm to 151.85mm, transferring the shallow horizontal displacement to the deep layer and guaranteeing the safety of the structure. After CFG pile foundation treatment, the horizontal displacement of the pile top was small and directed towards the center of the embankment.

Generally, the highway embankment after CFG pile foundation treatment was significantly reinforced and demonstrated significantly improved structural performance compared with the original embankment. To summarize, the following effects can be achieved:

1) The settlement was significantly reduced. The maximum settlement decreased from 253.25mm to 107.23mm, with a decrease of about 57.66%.
2) The uneven settlement effect was significantly improved. At the pile top position, the settlement was evenly distributed

along the width of the embankment, and there was no significant change.

3) The horizontal displacement was effectively lowered. Since the embankment load was transferred to the deeper soil layer, the horizontal displacement was transferred from the shallow layer to the deep soil layer, decreasing from 362.54mm to 151.85 mm. As a result, safety was strengthened.
4) The horizontal displacement of the embankment was effectively controlled. Under the action of the pile body, the horizontal displacement of the pile top was controlled to a small value, and the displacement to both sides of the road was avoided.

5 Analysis of factors influencing the reinforcement effect of cement fly-ash gravels pile composite foundation

The CFG pile had a significant reinforcement effect on the highway embankment, while it was affected by multiple factors. Clarifying the influence factors of CFG pile composite foundation treatment was of great significance to explore its reinforcement mechanism. In this study, parameter analysis of pile length and pile distance of the CFG pile composite foundation, as well as the thickness of gravel cushion under the embankment, was performed using the numerical method to understand the main factors and changing laws of the reinforcement effect of the CFG pile composite foundation.

5.1 Influence of pile length on the composite foundation

With pile length as a variable quantity, 11, 13, and 15 m were selected to obtain the changes in the vertical settlement and horizontal displacement of the embankment at the pile top along the embankment width resulting from the change in pile length. Figure 3 suggested that the vertical settlement was significantly affected when the pile length changed from 11m to 15m, and the horizontal displacement was different depending on the pile length. The maximum settlement was 107mm and 41.86 mm when the pile length was 11m and 15m, respectively. The horizontal displacement trend and size distribution were similar when the pile length was 11m and 13 m. The horizontal displacement was significantly controlled when the pile length was 15 m. Therefore, the improvement effect of the CFG pile length on the settlement was significantly stronger than that of horizontal displacement, and the change was more linear with pile length. However, the horizontal displacement was different with different pile lengths. The horizontal displacement was effectively controlled when the pile length exceeded 13 m. The pile length had little effect on the horizontal displacement when it was less than 13 m. Hence, when CFG pile was used for highway soft foundation reinforcement, an appropriate pile length should be considered to ensure that settlement could be controlled, while the influence of pile length can be overlooked for the relatively minor horizontal displacement.

Standard working conditions:(1) pile length: 11 m, pile distance: 1.4 m, cushion: 0.4 m; (2) pile length: 13 m, pile distance: 1.4 m, cushion: 0.4 m; (3) pile length: 15 m, pile distance: 1.4 m, cushion: 0.4 m. As shown in Figure 4.

The statistical diagrams of the horizontal and vertical soil pressures of the roadbed under different pile lengths are shown in the figures below:

5.2 Influence of pile distance on composite foundation

With pile distance as the variable quantity, 1.2, 1.4, and 1.6 m were selected to obtain the changes in the vertical settlement and horizontal displacement of the embankment at the pile top along the embankment width owing to the changes in the pile distance. As implied in Figure 5, the changes in the pile distance slightly affected the vertical settlement, because the change of pile distance has little impact on the replacement rate of pile and the vertical elastic modulus of composite foundation, with barely any change in the vertical settlement. But significantly affected the horizontal displacement. As the pile distance changed from 1.2 m to 1.6 m, the vertical settlement distribution and size were almost the same without significant difference, and the pile distance had a limited effect on the vertical settlement change. However, the changes in the pile distance significantly improved the soil stiffness in the horizontal direction. With the decrease in the pile distance, the horizontal stiffness of the soil mass increased, and the horizontal displacement decreased. The maximum horizontal displacement was 22.84mm and 3.85 mm when the pile distance was 1.2 m and 1.6 m, respectively. Therefore, the changes in the pile distance effectively influenced the horizontal displacement change in the design process of the CFG pile.

Standard working conditions: (1) pile length: 11m, pile distance: 1.2m, cushion: 0.4 m; (2) pile length: 11 m, pile distance: 1.4 m, cushion: 0.4 m; (3) pile length: 11m, pile distance: 1.6 m, cushion: 0.4 m. As shown in Figure 6.

The statistical diagrams of the horizontal and vertical soil pressures of the roadbed under different pile distances are shown in the figures below:

5.3 Influence of gravel cushion on composite foundation

With the cushion thickness as the variable quantity, 0.4, 0.6, and 0.8 m were selected to obtain the changes in the vertical

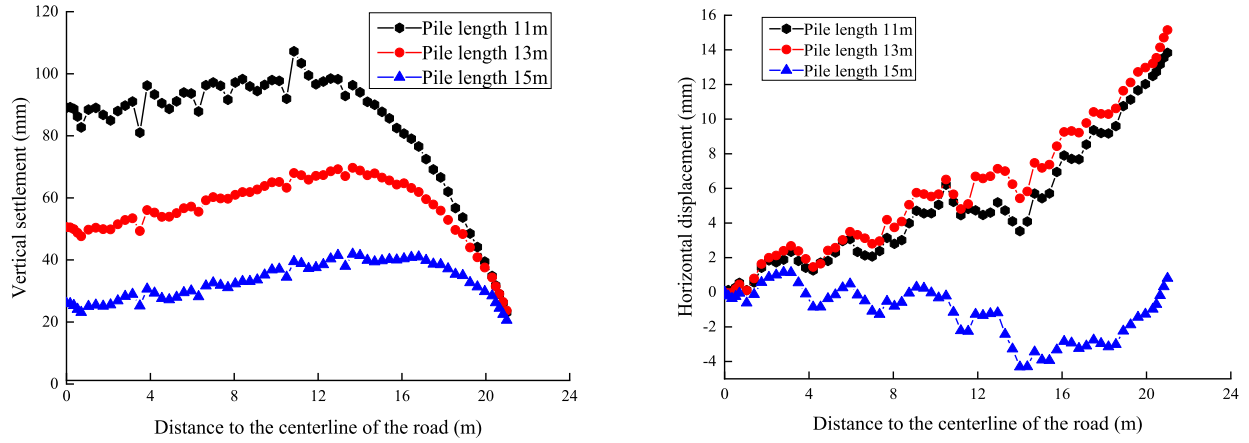

FIGURE 3
Influence of pile length change on reinforcement effect of CFG pile composite foundation:**(A)** Vertical settlement affected by pile length; **(B)** horizontal displacement affected by pile length.

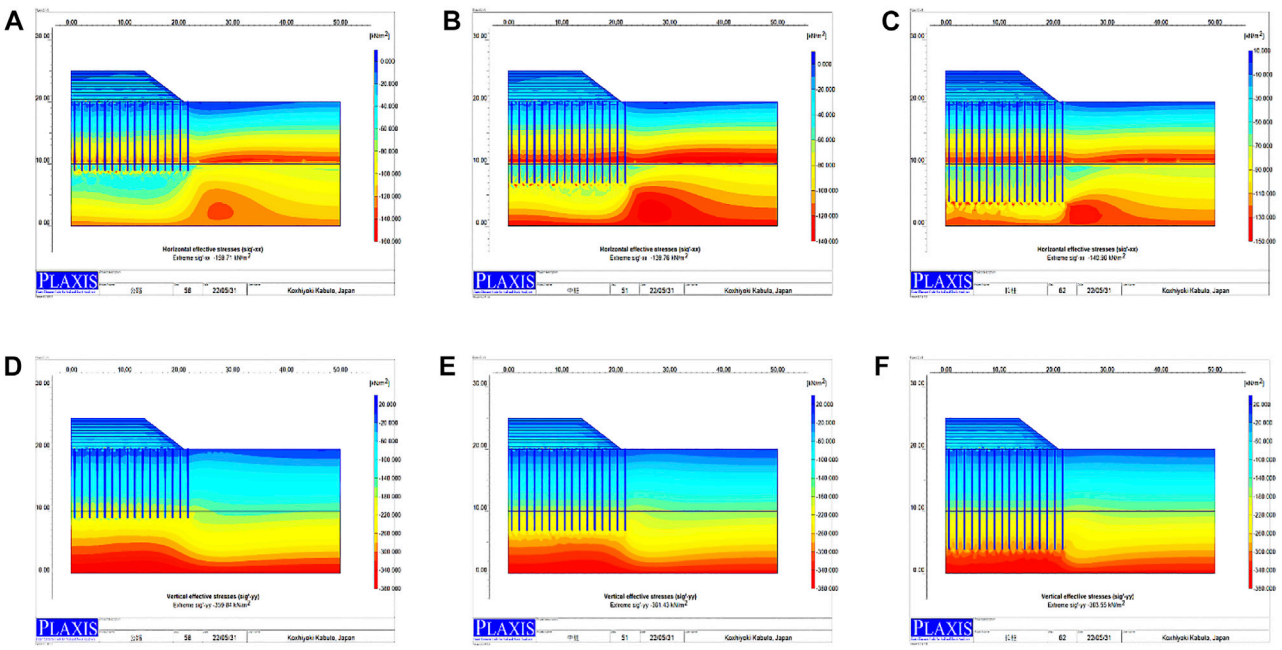

FIGURE 4
Horizontal soil pressure of pile length: **(A)** 11m; **(B)** 13m; **(C)** 15 m. Vertical soil pressure of pile length: **(D)** 11m; **(E)** 13m; **(F)**: 15 m

settlement and horizontal displacement of the embankment at the pile top induced by the cushion thickness changes along the embankment width. As demonstrated in Figure 7 the gravel cushion exerted no impact on the structural deformation due to the large embankment height and equivalent load. Moreover, the changes in the cushion thickness did not cause significant differences in the structural response.

Standard working conditions: (1) pile length: 11 m, pile distance: 1.4m, cushion: 0.4m; (2) pile length: 11 m; (3) pile distance: 1.4m, cushion: 0.6 m pile length: 11 m, pile distance: 1.4 m, cushion: 0.8 m. As shown in Figure 8.

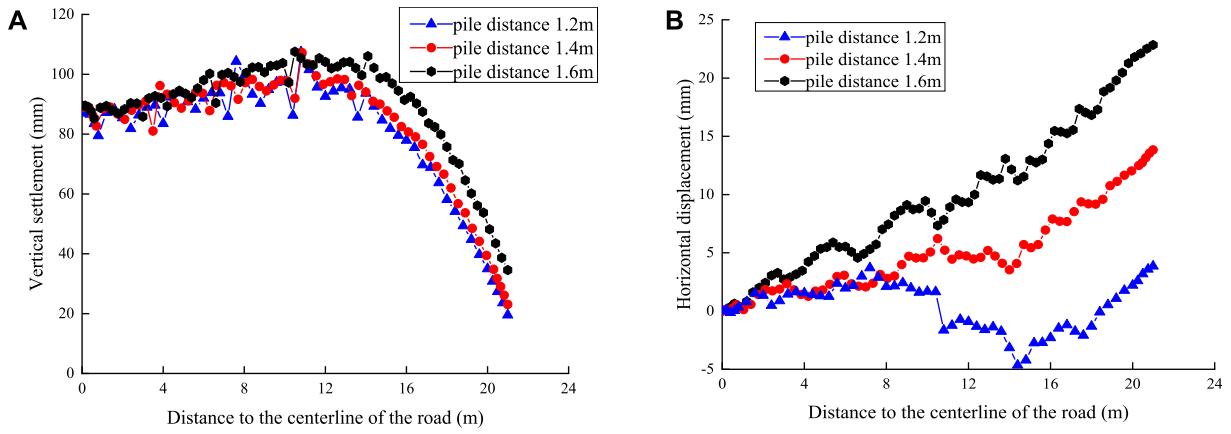

FIGURE 5
Influence of pile distance change on reinforcement effect of CFG pile composite foundation: **(A)** Vertical settlement affected by pile distance; **(B)** horizontal displacement affected by pile distance.

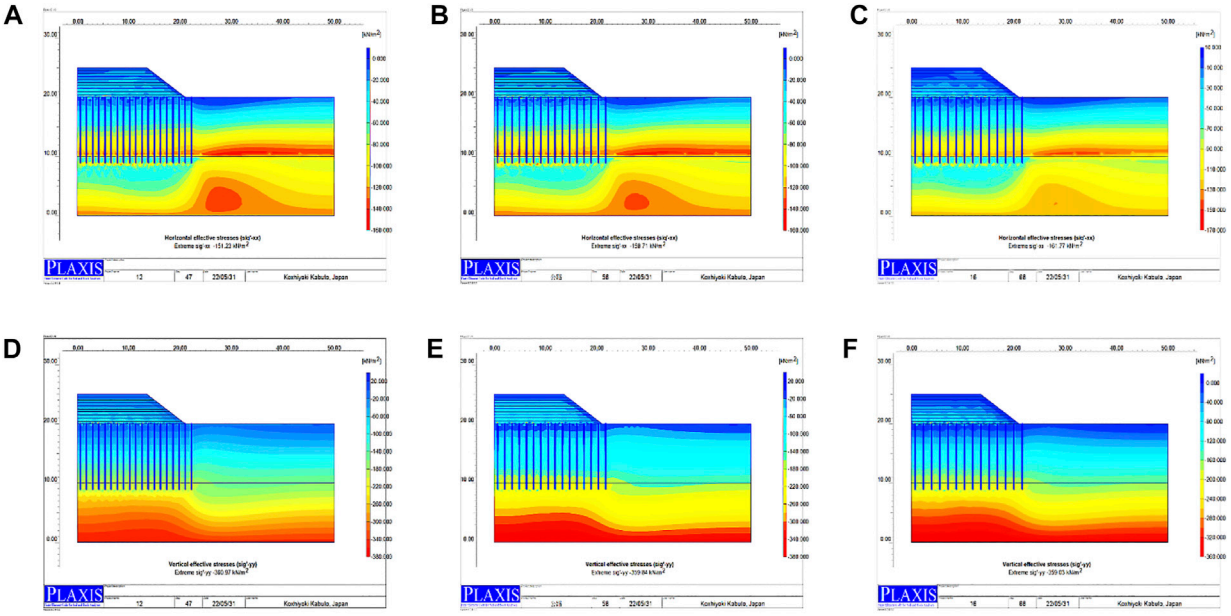

FIGURE 6
Horizontal soil pressure of pile distance: **(A)** 1.2m; **(B)** 1.4m; **(C)** 1.6 m. Vertical soil pressure of pile distance: **(D)** 1.2m; **(E)** 1.4m; **(F)** 1.6 m

The statistical diagrams of the horizontal and vertical soil pressures of the roadbed under different cushions are shown in the figures below:

The numerical method was used to analyze the pile length, pile distance, and the thickness of the gravel cushion of the CFG pile composite foundation. The changes in the pile length had a significant impact on the vertical settlement of the embankment, and the settlement decreased significantly with the increase in the pile length. The changes in the pile distance had a significant impact on the horizontal displacement of the embankment, and the horizontal displacement of the soil was reduced with the increase in the horizontal stiffness of the pile distance. The influence of

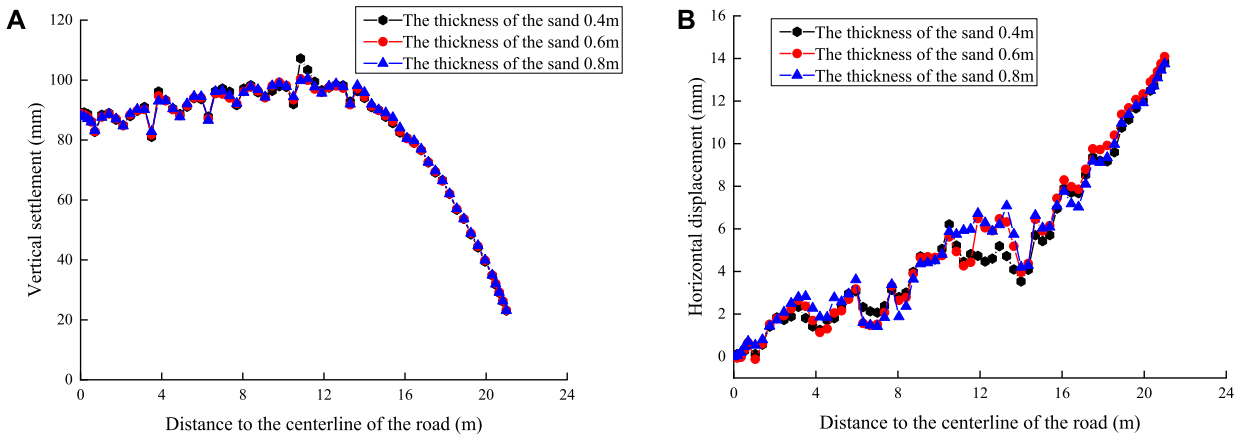

FIGURE 7
Influence of cushion thickness change on reinforcement effect of CFG pile composite foundation: **(A)** Vertical settlement affected by cushion thickness; **(B)** horizontal displacement affected by cushion thickness.

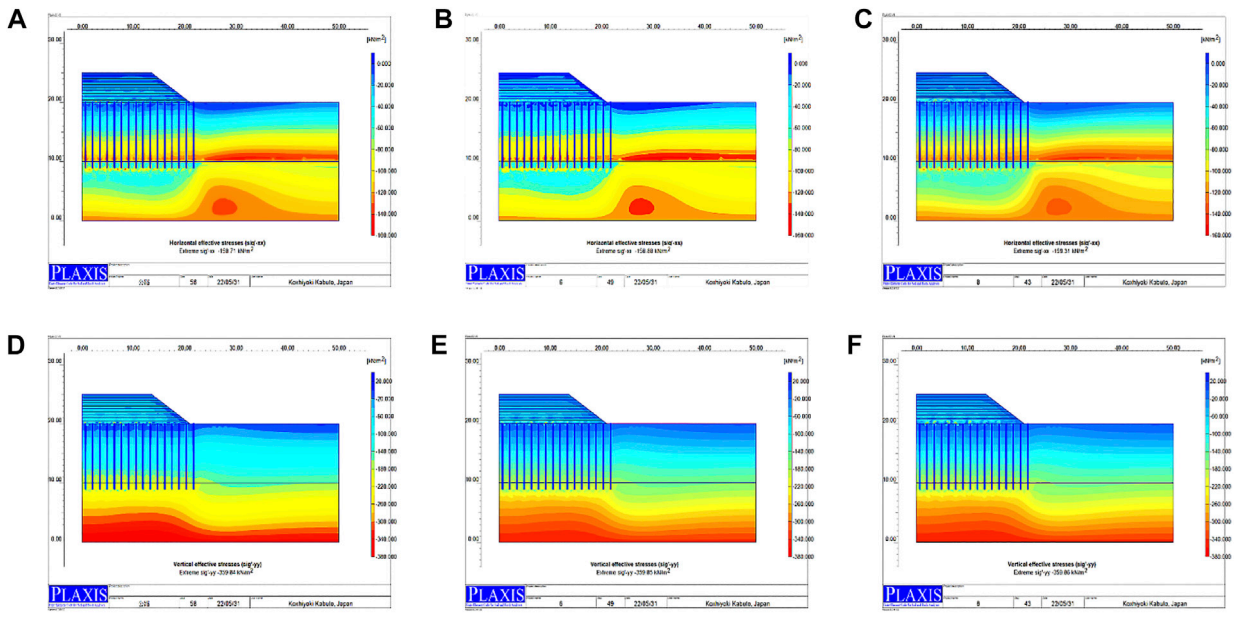

FIGURE 8
Horizontal soil pressure of cushion thickness: **(A)** 0.4m; **(B)** 0.6m; **(C)** 0.8 m. Vertical soil pressure of cushion thickness: **(D)** 0.4m; **(E)** 0.6m; **(F)** 0.8 m

cushion thickness on the vertical settlement and horizontal displacement of the embankment was small and can be ignored. In the design process, the pile length is considered with the vertical settlement as the main control variable, the horizontal displacement of the embankment is controlled through appropriate pile distance, and the cushion is not the focus of the structural design.

As revealed by the above analysis, the CFG pile can improve highway soft foundation, reflected in the following aspects. (1) The settlement was significantly reduced; (2) The effect of uneven settlement was significantly improved; (3) the horizontal displacement was effectively reduced; (4) the horizontal displacement of the embankment was controlled. After CFG

pile treatment, the service performance of the highway embankment was improved, and its safety and stability were guaranteed.

6 Dynamic response of vehicle load of roadbed

The design concept of current roadbeds in China is based on statics theory, which is slightly different from the actual situation, especially with low embankments. Since vehicle load is a dynamic load, it is insufficient to replace its effect on roadbeds with static force (Song et al., 2021; Milne et al., 2017). Various dynamic loads such as earthquake and vehicle vibration may cause the liquefaction, instability and subsidence of saturated soft soil subgrade. By increasing the external load, the soft foundation can be compressed, which causes lateral and vertical deformation to the soft foundation. If this deformation occurs in the bridge, it can lead to bridge jump, the uneven settlement in the middle of the road, transverse cracking and so on. Therefore, the theory of roadbed design must develop from a static method to a dynamic method. It is of practical significance to explore the dynamic effect of vehicle loads on highway roadbeds (Li and Selig, 1996; Liu et al., 2021).

The 3D finite element method and Midas gts nx were employed to establish the composite foundation model after CFG pile treatment. Then, the dynamic load of the vehicle was utilized to analyze the variation rule of vertical velocity and acceleration of the roadbed. The simulation results are of great significance to the development of foundation treatment technology for soft soil roadbed engineering.

This model simulated a vehicle fleet with a speed of 40km/h on the road. It was assumed that moving vehicles passed each node of the model in a short time, the impact load was applied to the node, and the impact load was idealized into a triangle. The simulation of automobile load adopted the built-in train load function, with wheelbase and axle weight parameters being modified. The axle weight and axle base parameters were set according to *The General Code for Highway Bridge and Culvert Design* (JTG D60-2015). Among them, the duration of applying train dynamic loading was 3s, and the time increment was 0.03s.

Representative nodes and model cross-sections were selected to analyze the dynamic characteristics of the roadbed. Three nodes were selected as the research working condition points at the starting point, midpoint, and end point of the central axis of the roadbed surface.

The following assumptions will be made during the simulation. (1) All materials in the model are homogeneous, continuous and isotropic. (2) The Mohr coulomb yield condition is used to simulate each soil layer. CFG pile is simulated by beam element. (3) Ignoring the relative slip between CFG pile and soil, composite foundation is used for simulation. (4) Considering the mutual space effect, a THREE-DIMENSIONAL model is used for numerical simulation. The model is exhibited in Figure 9.

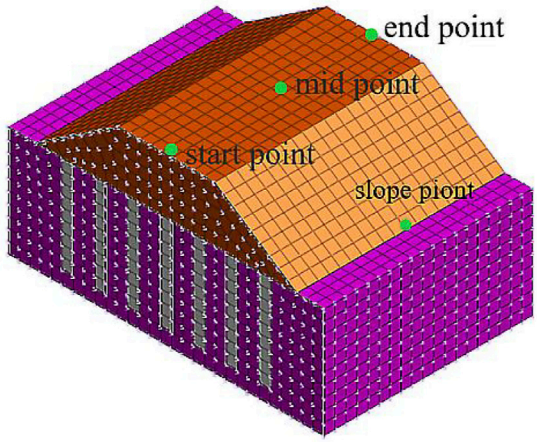

FIGURE 9
CFG pile composite foundation model.

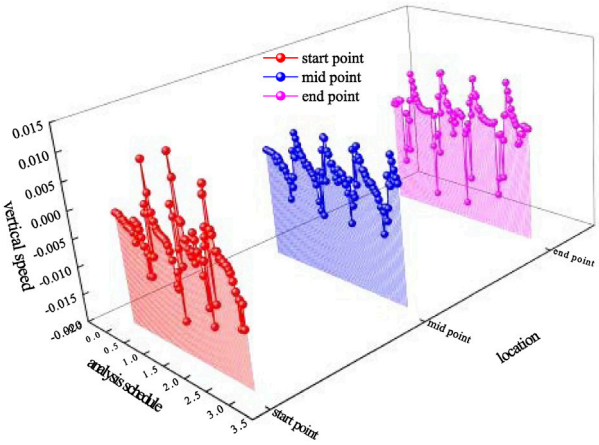

FIGURE 10
Vibration rule of the vertical velocity along with different road surface feature points in driving direction.

6.1 Distribution rule of the vertical velocity of road surface along the longitudinal roadbed surface

With time as the abscissa and vertical velocity response value as the ordinate, the simulation results were drawn into the variation curve of the vertical velocity of the roadbed surface. As implied by the vibration velocity in Figure 10, the vibration of each point in the roadbed had a certain response time with the movement of the train. The variation of the vertical velocity of each part of the roadbed surface exhibited regular vibration.

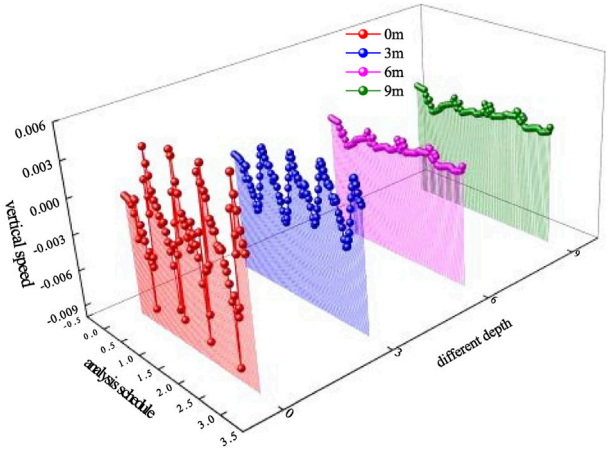

FIGURE 11
Vibration rule of the vertical velocity of feature points at different depths of midpoint cross-section of the roadbed.

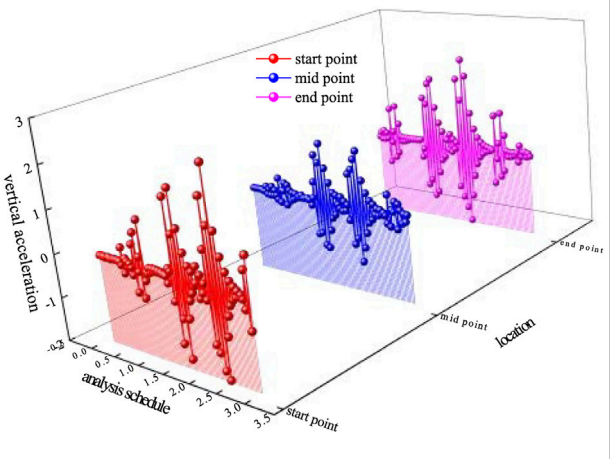

FIGURE 12
Vibration rules of vertical acceleration of feature points along different road surfaces in driving directions.

At the starting point of the road surface, the positive and negative maximum values of the vertical vibration velocity were 0.01427 m/s and -0.01397m/s, respectively, with relatively close absolute values. At the midpoint of the road surface, the positive and negative maximum values of the vertical vibration velocity were 0.00617 m/s and -0.00877 m/s, respectively, with an absolute value difference of about 30%. At the endpoint of the road surface, the positive and negative maximum values of the vertical vibration velocity are 0.00832m/s and -0.01681 m/s, respectively, presenting an absolute value difference of around 50%.

According to the time travel curves of each feature point, the vibration law of each feature point is the same, demonstrating a periodic motion with different peak values and periods.

6.2 Distribution rule of the vertical velocity of roadbed points at different depths on the cross-section of roadbed midpoint

With time as the abscissa and vertical velocity response value as the ordinate, the simulation results were drawn into the variation curve of the vertical velocity of the roadbed surface. As unveiled from the vibration velocity in Figure 11, the variation of the vertical velocity of each part of the roadbed surface exhibited regular vibration with the movement of the train.

It can be observed that at the midpoint of the roadbed, the positive and negative maximum values of the vertical vibration velocity were 0.00622m/s and -0.00886m/s, respectively, with an absolute value difference of about 30%. The positive and negative maximum values of the vertical vibration velocity were 0.00257m/s and -0.00408m/s, respectively, at 3 m below the midpoint of the roadbed, and the absolute value difference was around 50%. At 6 m below the road surface at the midpoint of the roadbed, the positive and negative maximum values of the vertical vibration velocity were 0.000606m/s and -0.00199m/s, respectively, displaying an absolute value difference of approximately 70%. At 9 m under the road surface at the midpoint of the roadbed, the positive and negative maximum values of the vertical vibration velocity were 0.000605m/s and -0.00199m/s, respectively, demonstrating an absolute value difference of roughly 70%.

As the depth increased, the peak value of the vertical vibration velocity at the feature point gradually decreased, the additional stress in the subgrade gradually decreases to zero, and the vertical vibration velocity at 6m and 9 m below the road surface was the same. Therefore, as the depth increases, the additional stress generated by dynamic load in the soil layer declines continuously, and the vibration generated by vehicle driving has diminishing influence on the roadbed. When it is below 6m, the additional stress becomes extremely low, its effect is almost uniform, and its absolute value is negligible.

The time travel curves of each feature point uncovered that the vibration laws of each feature point were the same. In other words, they presented a periodic motion with different peak values. With the increase in the depth of feature points, the vibration peak decreased gradually, while the period was the same.

6.3 Distribution rule of vertical acceleration of roadbed surface along the longitudinal road surface

With time as the abscissa and vertical velocity response value as the ordinate, the simulation results were drawn into the variation curve of the vertical acceleration of the roadbed surface. The vibration acceleration in Figure 12 suggested that the vibration of the roadbed exhibited a certain response time with

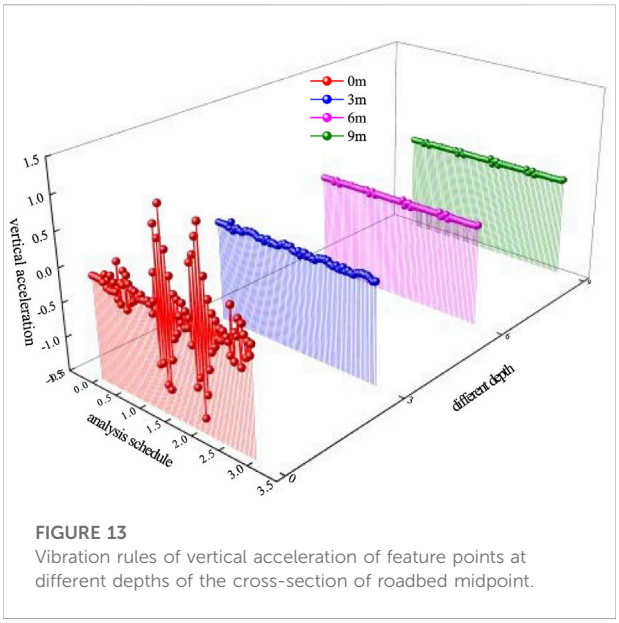

FIGURE 13
Vibration rules of vertical acceleration of feature points at different depths of the cross-section of roadbed midpoint.

the movement of the train. Meanwhile, the variation of the vertical velocity of each part of the roadbed surface changed regularly.

At the midpoint of the roadbed, the positive and negative maximum values of the vertical vibration acceleration were 2.511m/s^{-2} and -1.949m/s^{-2}, respectively, and the absolute value difference was about 22%. At the midpoint of the roadbed, the positive and negative maximum values of the vertical vibration acceleration were 1.3471m/s^{-2} and -1.2708m/s^{-2}, respectively, with an absolute value difference of roughly 6%. At the endpoint of the roadbed, the maximum positive and negative values of the vertical vibration acceleration were 2.1971m/s^{-2} and -1.9319m/s^{-2}, respectively, demonstrating an absolute value difference of around 12%.

According to the time travel curves of each feature point, the vibration law of each feature point was the same, showing a periodic motion with different peak values and periods. Moreover, the time point of peak acceleration at each point was delayed owing to the difference in the arrival time of vehicle loads. The peak value of acceleration at the starting point was relatively close to that at the endpoint, while the acceleration value at the midpoint of the roadbed remarkably differed from the first two because the first two were at the model boundary and affected by the boundary constraints.

6.4 Distribution rules of vertical acceleration of roadbed points at different depths on the cross-section of roadbed midpoint

With time as the abscissa and vertical acceleration response value as the ordinate, the simulation results were drawn into the variation curve of the vertical acceleration of the roadbed surface. The vibration speed in Figure 13 revealed that the variation of the vertical acceleration of each part of the roadbed surface changed regularly with the movement of the train.

At the midpoint of the roadbed, the positive and negative maximum values of the vertical vibration acceleration were 1.3471m/s and -1.2708m/s, respectively, and the absolute value difference was about 6%. The positive and negative maximum values of the vertical vibration velocity were 0.07482m/s and -0.0583m/s, respectively, at 3 m below the midpoint of the roadbed, with an absolute value difference of roughly 22%. At 6 m below the road surface at the midpoint of the roadbed, the positive and negative maximum values of the vertical vibration acceleration were 0.03922m/s and -0.04671m/s, respectively, presenting an absolute value difference of approximately 19%. At 9 m under the road surface at the midpoint of the roadbed, the positive and negative maximum values of the vertical vibration acceleration were 0.03926m/s and -0.04674m/s, respectively, and the absolute value difference was around 19%.

On the road surface, the vertical vibration acceleration of the feature point was the largest. The peak value of the vertical vibration acceleration of the feature point sharply decreased to about 1/20 of that of the road surface feature point when the depth increased by 3 m. The maximum positive vertical vibration acceleration at 6 m below the road surface was reduced to about 1/2 of that at 3 m below the road surface. The vertical vibration acceleration at 6m and 9 m below the road surface was the same. Therefore, the acceleration transfer depth of roadbed vibration caused by the vibration of vehicle driving was relatively small, which mainly affected the road surface and the range of about 4 m under the road surface. Additionally, the influence was almost the same from 6 m below the depth, and its absolute value can be overlooked.

6.5 Distribution rule of vertical vibration acceleration of roadbed slope point

With time as the abscissa and vertical acceleration response value as the ordinate, the simulation results were drawn into the variation curve of the vertical acceleration of the roadbed slope point. As suggested by the vibration acceleration in Figure 14, the vertical vibration of slope points presented certain rules with the movement of trains. The positive and negative maximum values of the vertical vibration acceleration were 0.002314m/s and -0.00265m/s, respectively, with an absolute value difference of about 14%.

The time interval between the peak accelerations was about 0.69s. If it was calculated according to the set vehicle speed, the driving distance was exactly the distance between the front and rear axles of a standard vehicle. The roadbed slope point demonstrated irregular vibrations when the vehicle distance was irregular.

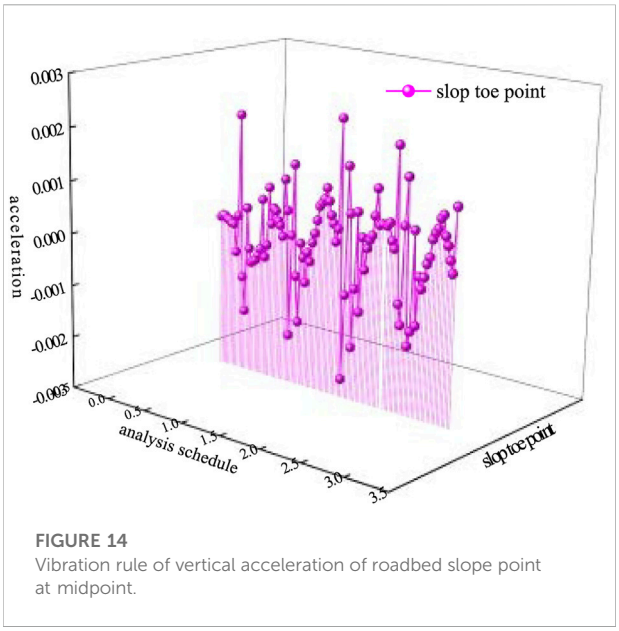

FIGURE 14
Vibration rule of vertical acceleration of roadbed slope point at midpoint.

7 Conclusion

1) The settlement was significantly reduced; The effect of uneven settlement was significantly improved; the horizontal displacement was effectively reduced; the horizontal displacement of the embankment was controlled. After CFG pile treatment, the service performance of the highway embankment was improved, and its safety and stability were guaranteed.
2) The vertical velocity and acceleration of the roadbed were significantly reduced after the roadbed section was strengthened by the CFG pile. The dynamic issue induced by roadbed moving with trains' dynamic load was improved to effectively ensure the normal and safe operation of the road.
3) Under the action of the dynamic load of vehicles, the vertical velocity and acceleration of the roadbed decreased slightly within 0.3 m below the roadbed surface, and the attenuation speed was relatively fast within 0.3–3 m. The values of the two were very small, basically close to 0, when it was below 3 m. This suggested that the influence range of vehicle dynamic load was mainly concentrated in the roadbed surface below 3 m. Therefore, this point should be fully considered in the design, construction, and reinforcement of engineering.
4) After the CFG pile reinforcement, the stress of the upper layers of soil mass and roadbed was effectively improved. In addition to guaranteeing the roadbed settlement, the foundation reinforced by the pile also bore the downward load of moving vehicles to a great extent, contributing to bettering the working properties of the roadbed and prolonging its service life (Bai et al., 2021b).

Data availability statement

The original contributions presented in the study are included in the article/supplementary material, further inquiries can be directed to the corresponding author.

Author contributions

HZ is responsible for referencewriting and calculation LL is responsible for establishing finite elementmodel WF is responsible for making pictures and tables YZ is responsible for collecting site data WZ is responsible for model building and data analysis BZ is responsible for collecting site samples and conceiving the framework of the paper.

Funding

This research was funded by the Hubei Provincial Engineering Research Center of Slope Habitat Construction Technique Using Cement-based Materials (China Three Gorges University) Open Research Program (2022SNJ07、2022SNJ04), and the Nei Monggol Autonomous Region Science and Technology Major Project (2021ZD0007-03).

Conflict of interest

The authors declare that the research was conducted in the absence of any commercial or financial relationships that could be construed as a potential conflict of interest.

Publisher's note

All claims expressed in this article are solely those of the authors and do not necessarily represent those of their affiliated organizations, or those of the publisher, the editors and the reviewers. Any product that may be evaluated in this article, or claim that may be made by its manufacturer, is not guaranteed or endorsed by the publisher.

References

Alamgir, M., Miura, N., Poorooshasb, H. B., and Madhav, M. (1996). Deformation analysis of soft ground reinforced by columnar inclusions. *Comput. Geotechnics* 18 (4), 267–290. doi:10.1016/0266-352x(95)00034-8

Bai, B., Yang, G., Li, L., and Yang, G. (2019). A thermodynamic constitutive model with temperature effect based on particle rearrangement for geomaterials. *Mech. Mater.* 139, 103180. doi:10.1016/j.mechmat.2019.103180

Bai, B., Xu, T., Nie, Q., and Li, P. (2020). Temperature-driven migration of heavy metal Pb2+ along with moisture movement in unsaturated soils. *Int. J. Heat Mass Transf.* 153, 119573. doi:10.1016/j.ijheatmasstransfer.2020.119573

Bai, B., Zhou, R., Cai, G., Hu, W., and Yang, G. (2021a). Coupled thermo-hydro-mechanical mechanism in view of the soil particle rearrangement of granular thermodynamics. *Comput. Geotechnics* 137 (8), 104272. doi:10.1016/j.compgeo.2021.104272

Bai, B., Nie, Q., Zhang, Y., Wang, X., and Hu, W. (2021b). Cotransport of heavy metals and SiO2 particles at different temperatures by seepage. *J. Hydrology* 597, 125771. doi:10.1016/j.jhydrol.2020.125771

Bai, B., Wang, Y., Rao, D., and Bai, B. (2022). The effective thermal conductivity of unsaturated porous media deduced by pore-scale SPH simulation. *Front. Earth Sci.* 10, 943853. doi:10.3389/feart.2022.943853

Liu, B., Lin, J., Ku, X., et al. (2021). Particle migration induced by hydrodynamic interparticle interaction in the Poiseuillel fow of a Giesekuslfuid[J]. *J. Brazilian Soc. Mech. Sci. Engg.* 43 (2), 2852–2856.

Cheng, X. S., Jing, W., Yin, C., and Li, C. (2018). Stability parameter analysis of a composite foundation of an oil storage tank in a loess area treated with compaction piles[J]. *Soils Found.* 58, 306. doi:10.1016/j.sandf.2018.02.004

Peng, Y. Z., Bing, B., and Si, C. J. (2016). Coupled effects of hydrodynamicforces and pore structure on suspended particle transport and deposition in a saturated porous medium[J]. *Rock and Soil Mechanics* 37 (5), 1307–1316.

Cui, X., Fan, Y., Wang, H., and Huang, S. (2019). Experimental investigation of suspended particles transport in porous medium under variable temperatures. *Hydrol. Process.* 33 (7), 1117–1126. doi:10.1002/hyp.13390

Cui, X., Wu, D., Wang, H., Ding, S., and Fan, Y. (2022). Pore features and seepage characteristics of natural gap-graded sand with two size distributions. *Géotechnique*, 1–12. doi:10.1680/jgeot.21.00213

Derbyshire, E., Dijkstra, T. A., Smalley, I. J., and Li, Y. (1994). Failure mechanisms in loess and the effects of moisture content changes on remoulded strength. *Quat. Int.* 24 (24), 5–15. doi:10.1016/1040-6182(94)90032-9

Habibagahi, G., and Mokhberi, M. (1998). A hyperbolic model for volume change behavior of collapsible soils. *Can. Geotech. J.* 35 (2), 264–272. doi:10.1139/t97-089

Jones Jr, J. S. (1981). State-of-the-art report — Engineering practice in artificial ground freezing[J]. *Eng. Geol.* 18 (1-4), 313–326. doi:10.1016/B978-0-444-42010-7.50034-7

Jung, J. B., Lee, K. I., Lee, J. S., and Chang, Y. C. (2001). Numerical analyses of composite ground improved by fully and partly penetrated sand compaction piles. *KSCE J. Civ. Eng.* 5 (2), 165–173. doi:10.1007/bf02829072

Lai, J., Liu, H., Qiu, J., and Chen, J. (2016). Settlement analysis of saturated tailings dam treated by CFG pile composite foundation. *Adv. Mater. Sci. Eng.* 2016 (6), 1–10. doi:10.1155/2016/7383762

Li, D., and Selig, E. T. (1996). Cumulative plastic deformation for fine-grained subgrade soils. *J. Geotech. Engrg.* 122 (12), 1006–1013. doi:10.1061/(asce)0733-9410(1996)122:12(1006)

Milne, D. R. M., Le Pen, L. M. L., Thompson, D. J., and Powrie, W. (2017). Properties of train load frequencies and their applications. *J. Sound Vib.* 397, 123–140. doi:10.1016/j.jsv.2017.03.006

Otani, J., Ochiai, H., and Yamamoto, K. (1998). Bearing capacity analysis of reinforced foundations on cohesive soil. *Geotext. Geomembranes* 16 (4), 195–206. doi:10.1016/s0266-1144(98)00005-3

Tan, S. (1995). Validation of hyperbolic method for settlement in clays with vertical drains.[J]. *Soils Found.* 35 (31), 125–131. doi:10.3208/sandf1972.35.101

Terzaghi, K. (1943). *Theoretical soil mechanics[M]*. New York, NY: Wiley.

Song, W., Liu, X., Zheng, C., et al. (2021). Migration-deposition characteristics of exogenous particles near the injection well in a groundwater heat pump system[J]. *Geothermics* 94 (1), 102097.

Ye, S. H., and Gong, X. N. (2017). "Static load test of a project CFG pile composite foundation[C]," in *International conference on mechanics and architectural design*, 175–180.

Yin, Y., and Yu, X. J. (2009). "Research on applying glass fiber cement soil to strengthen soft soil subgrade[C]," in Procedding of the Geohunan International Conference, Changsha, Hunan, China, August, 2009, 7–13.

frontiers | Frontiers in Materials

ORIGINAL RESEARCH
published: 11 August 2022
doi: 10.3389/fmats.2022.962372

Shear Characteristics of Gravel Soil With Different Fillers

*Huahua Zhang[1,2], Yi Luo[3], Siyu Yuan[4], Yuru Zhou[2], Qiong Zhou[2], Fanrong Zeng[5] and Wei Feng[6]**

[1]Huazhong University of Science and Technology, Wuhan, China, [2]Housing and Urban-Rural Development Bureau, Yichang, China, [3]Hubei Communications Planning and Design Institute CO., LTD., Yichang, China, [4]Hubei Institute of Geosciences, Wuhan, China, [5]China Nuclear Industry 22ND Construction Co., LTD., Wuhan, China, [6]The Seventh Geological Brigade of Hubei Geological Bureau, Yichang, China

In recent years, China has established many large water conservancy projects in the western mountainous areas. However, dam foundation excavation produces a huge amount of waste rock mixture. A soil-rock mixture with unique structural characteristics can easily cause geological disasters, such as collapse, landslide, and debris flow following an earthquake, rainfall, and engineering disturbance. Therefore, research on the strength and shear characteristics of the soil-rock mixture is beneficial to avoiding soil-rock mixture disasters. In this study, the soil-rock mixture in the slag dump site of Jinping Hydropower station is taken as the research object. The influence of different fillers on the gravel soil shear characteristics is investigated through a large-scale triaxial test of coarse-grained soil. The slope stability of the slag dump site is analyzed using Midas GTS. Then, the most unfavorable sliding surface of the slag dump site is discovered and the slope stability coefficient under the most unfavorable conditions is calculated. The results lay a scientific foundation for the design and construction of a slag dump slope.

Keywords: shear characteristics, soil-rock mixture, cohesion, friction angle, triaxial test

OPEN ACCESS

Edited by:
Xianze Cui,
China Three Gorges University, China

Reviewed by:
Yongshui Kang,
Institute of Rock and Soil Mechanics (CAS), China
Yalong Jiang,
East China Jiaotong University, China

***Correspondence:**
Wei Feng
fw500@163.com

Specialty section:
This article was submitted to Structural Materials, a section of the journal Frontiers in Materials

Received: *06 June 2022*
Accepted: *20 June 2022*
Published: *11 August 2022*

Citation:
Zhang H, Luo Y, Yuan S, Zhou Y, Zhou Q, Zeng F and Feng W (2022) Shear Characteristics of Gravel Soil With Different Fillers. Front. Mater. 9:962372. doi: 10.3389/fmats.2022.962372

1 INTRODUCTION

China's geological disaster situation is complex (Cui et al.,2022) and can easily cause geological disasters, such as landslides and debris flow under poor geological conditions and extreme weather. In particular, China has a significant number of soil-rock aggregate slopes (Bai et al.,2021a). These slopes are generally composed of white collapse deposits, residual deposits, landslide deposits, moraine deposits, and slope deposits. The solid component of these loose slopes is usually a mixture of soil and gravel, which is called the soil-rock mixture in China (Cui et al.,2019; Medley, 1994). The soil-rock mixture is ubiquitous. It is not only widely used in human production practice but has also become a source of many habitats for human production and life (Paduana, 1966; Georgiannou et al.,1990; Bai et al.,2022). Additionally, the soil-rock mixture is widely used in practical project construction because of the easy access to materials (Lupini et al.,1981; Bai et al.,2019). For example, the soil-rock mixtures obtained by local mountain excavation and dam foundation excavation are broadly applied to slope engineering and soil-rock dam filling when road subgrade is built in mountainous areas (Cheng et al., 2018; Bai et al., 2020).

The solid phase of the soil-rock mixture is composed of coarse particles and fine particles, with great differences in mechanical properties, particle size, and chemical composition (Schlosser and Long, 1974). Its physical and mechanical properties have a bigger difference than those of single soil and rock. In practical engineering, the physical and mechanical properties of the soil-rock mixture

should be analyzed under the consideration of not only the main composition of soil-rock-mixture physical and mechanical performance but also the stone spatial distribution (Hall, 1951; Donaghe and Townsend, 1976), material composition, particle morphology, and other meso-structure characteristics. The special engineering characteristics of the soil-rock mixture lead to several related engineering issues, such as the soil-rock slope mixture collapsing (Lindquist and Goodman, 1994). Specifically, under adverse geological conditions, a shallow accumulation composed of soil and rock mixture is prone to adverse geological disasters, such as collapse, landslide, and debris flow (Strack and Cundall, 1978; Kaneko et al.,2003).

Soil-rock mixture is a kind of special rock mass with certain safety risks and should be properly handled in actual engineering (Chang et al., 2016). At present, engineers usually assume that the mechanical strength of a soil-rock mixture is equal to a matrix material (Cundall, 1971b; Drescher and De Jong, 1972). However, this assumption can only be realistic when the content of the coarse phase in the soil-rock mixture is low. The soil-rock mixture will exhibit completely different mechanical behavior when the content of its coarse phase is high (Jefferies and Ben, 2015).

While the research theory of soil-rock mixture has become more mature worldwide, the test equipment is getting ever more sophisticated. Moreover, there are some deficiencies and defects in the present test methods (Cundall, 1971a; Bagi, 2005). For example, the traditional direct shear instrument artificially controls the shear surface, which leads to certain errors in the test results (Simoni and Houlsby, 2006). Large triaxial apparatus can overcome the shear stress concentration and uneven shear stress distribution in the energetic test, while strictly controlling the drainage condition in the test process (Mulilis et al.,1977). Thus, researchers are increasingly interested in this area. Furthermore, there is no fixed failure surface in the large-scale triaxial test and the test result is better than the direct shear test (Marsal, 1973; Bai et al., 2021b). Therefore, a large-scale triaxial test is adopted in this study to investigate the shear behavior of a soil-rock mixture (Nemat-Nasser and Tobita, 1982).

Jinping hydropower station dam is the highest arch dam in the world, with a dam height of 305 m. The storage capacity below normal water level is 760 million cubic meters, which forms the Yalong River hydropower development control reservoir. The dam foundation excavation waste volume of Jinping hydropower station is 14.44 million cubic meters, and the strata at the dam site are marble.

The Yinbazi Slag site is located about 6 km from the Jinping hydropower station dam site and is the main slag field of Jinping hydropower station. It is expected to pile up about 14 million cubic meters. According to the topographic map, the slope height will exceed 250 m and the scale of the slope is unusual. Additionally, it is located in a high earthquake incidence area. Therefore, the slope's safety needs a special design, and the slope design requires friction Angle φ and cohesion c of the mixture. The dam's foundation and the geological conditions of the two sides of the slope are different. Dam foundation excavation and slope excavation are performed by blasting in different ways. The slag that is abandoned after blasting is mainly soil-rock mixture, gravel soil, and sand-soil mixture. As a result, its composition, particle size, and grading are complex. Field soil samples are collected for an indoor triaxial experiment. Following the experimental results, the influence of the composition in different mixtures on the shear properties of the material is analyzed to reveal the slag with the best mechanical properties, which provides a theoretical basis for design and construction.

2 RESEARCH STATUS

In recent years, gravel soil research methods have mainly concentrated on field tests, laboratory tests, and numerical simulations. Xinhua You prepared soil-rock mixture *in situ* horizontal shear test and obtained different stone content, moisture content, size, and failure mode under stress state, as well as the change law of shear strength parameters. Weishu Li performed *in situ* direct shear test and researched the variation of shear strength parameters of a soil-rock mixture under different water contents. The relationship between the shear strength index and water content was established based on extensive experiments, and the weakening formula of the shear strength index with water content was derived. Mingjian Hu conducted a large indoor triaxial test of a soil-rock mixture, and calculated its shear strength index and shear strength with the stone content, moisture content, and confining pressure. Xingrui Li compared the trend differences of stress-strain curves and designed a method to destroy a turning point to define the way. Jincheng Ning obtained the regular decay of the soil-rock mixture's shear strength by changing these indexes. Zhenhua Ouyang conducted large-scale shear tests under flexible boundary conditions to explore the effects of stone content, stone size, and stone arrangement. The stone arrangement affected the performance of soil-rock mixture shear: the stone size had the greatest influence, followed by stone content, and then stone arrangement. Jiacheng Wang studied the influence of the soil-rock shear strength parameters on moisture content and particle level matching through laboratory large-scale direct shear tests. Xianming Hu researched the residual strength of gravel soils with water content and shear rate under different conditions through the indoor ring shear test, and set up the residual strength criteria of gravel soils under different shear rates based on the Bingham model. Xiuli Ding performed biaxial numerical tests of different samples using the PFC program and depicted the stress-strain curves of the soil-rock mixture, most of which exhibited "stepped" distribution.

The research on accumulated gravel soil is not comprehensive enough at present. Moreover, the construction speed is fast, and the final filling slope height exceeds the limit. These are the design principles for slope safety. In this study, unconsolidated and undrained shear tests are performed. In combination with the representative grading of abandoned gravel soil in the Jinping hydropower station, the law, failure mode, and corresponding shear strength index of the soil-rock principal differential stress-strain curve under different rock contents and confining pressures are analyzed to further reveal the complex, discontinuous, and non-uniform material shear properties.

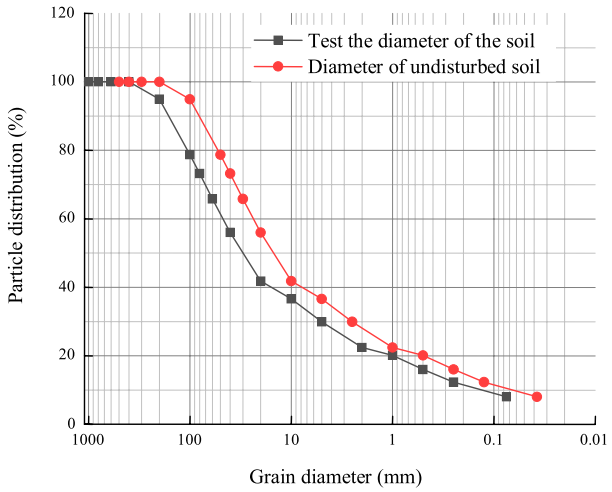

FIGURE 1 | Grading curve of whole stone slag diagram.

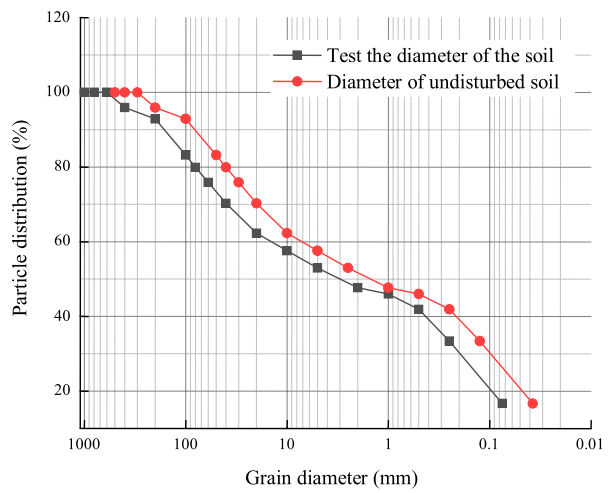

FIGURE 2 | Gradation curve of gravel slag and sand-soil mixture diagram.

The results of this research can help to lay a theoretical foundation for landslide prevention and the control of similar projects.

3 LABORATORY TRIAXIAL TEST

3.1 Test for Grading

Because the particle size of the soil sample collected on site is too large, a larger triaxial compression test apparatus is required. The test result will be inaccurate when the maximum particle size of the sample exceeds the maximum allowed by the instrument. When the maximum particle size of the material used for laboratory testing is limited, it is necessary to scale down the mixture above the maximum allowable size in the test. The

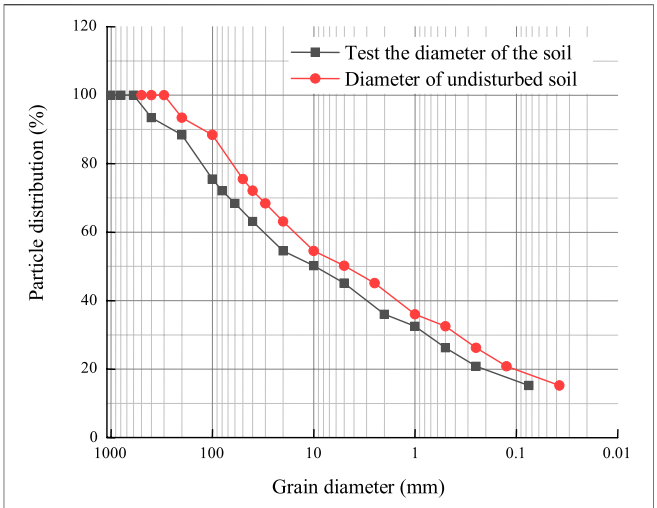

FIGURE 3 | Gradation curve of slag-soil mixture diagram.

mechanical properties of the actual material are then determined from the scaled-down material. The commonly used coarse-grain scaling method is described as follows: following the provisions of "soil test code" SL 237-1999, there are four kinds of elimination method, equivalent substitution method, similar gradation method, and mixture method. The elimination method removes the overdrawn diameter particles, which is simple and convenient. However, some super-particle size particles are removed, leading to increased fine grain content. The equivalent substitution method suggests that soil particles larger than 5 mm are allowed according to the maximum size of the instrument. Supersized particles are replaced with equal mass in proportion. The advantage of the equivalent substitution method is to keep the original coarse-grain content, fine material content, and properties unchanged. In this experiment, the equivalent substitution method is used. The gradation of the three mixtures is illustrated in **Figures 1–3**.

3.2 Preparation of Dry Density

Laboratory test sample loading dry density should be consistent in the field sampling dry density in principle, and the dry density of samples in this test is the average dry density of the three pits sampled on site. The samples are prepared in accordance with the requirements of the specification "Standard for Geotechnical Test Methods". The average density of the whole-rock slag was 2.15 tons per cubic meter, the average density of the rock ballast-sand mixture was 2.10 tons per cubic meter, and the average density of the rock ballast-soil mixture was 1.81 tons per cubic meter.

3.3 Shear Strength Test Method

Shear strength test method: slag dump site construction speed is fast, and the final filling slope height exceeds the limit. These are the design principles for slope safety. Besides, the test method should adopt non-consolidation and non-drainage shear to finally determine the total strength of the filling material. The test equipment and materials are shown in **Figure 4**.

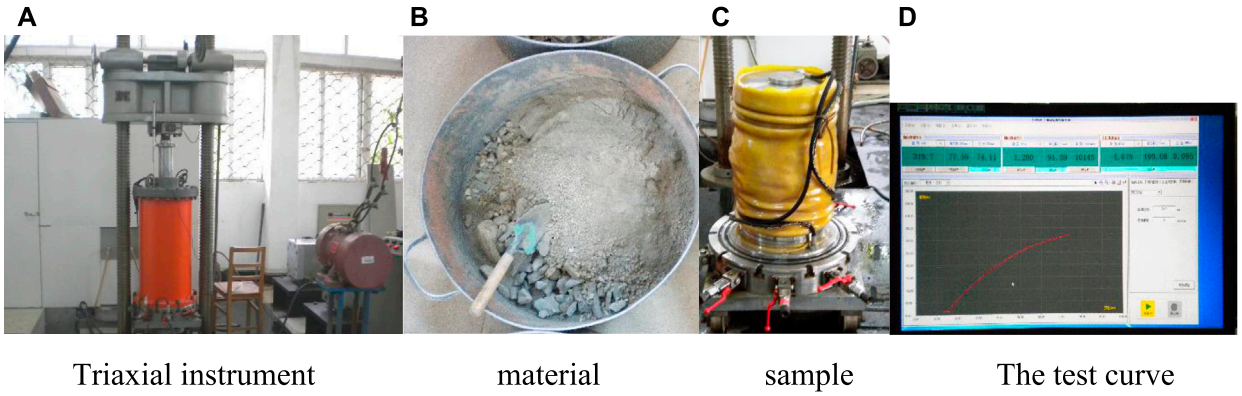

FIGURE 4 | Testing equipment: **(A)** Triaxial instrument; **(B)** material; **(C)** sample; **(D)** The test curve.

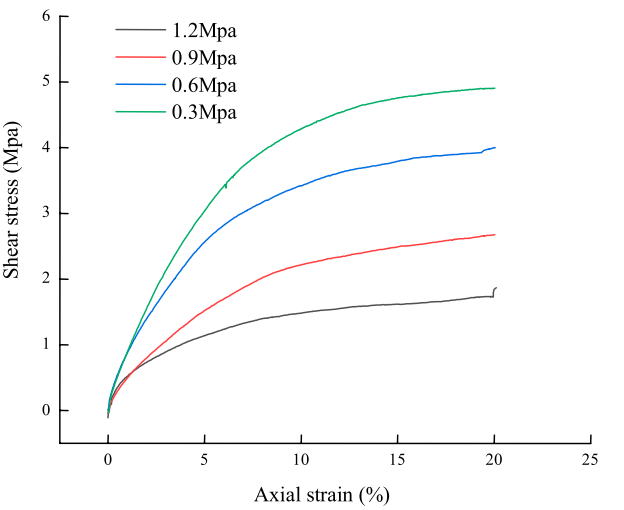

FIGURE 5 | Results of unconsolidated and undrained shear triaxial test of whole stone slag diagram.

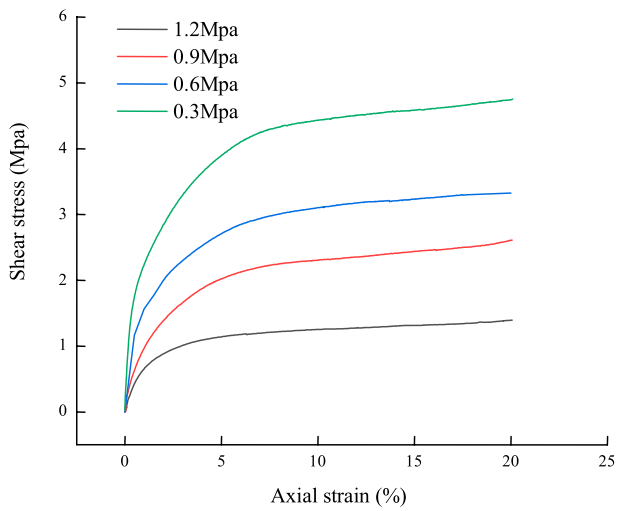

FIGURE 6 | Results of unconsolidated and undrained shear triaxial test of gravel slag and sand-soil mixture diagram.

1) Test equipment: the test adopts a microcomputer with a size of φ300 × 600 mm to control the 1000 kN triaxial instrument.
2) Test confining pressure selection: the maximum ambient pressure is preliminarily determined to be 1,200 kPa, and the ambient pressure of the remaining samples is 300, 600, and 900 kPa.
3) Rate selection: axial shear is performed at the rate of 0.5%–1% axial strain per minute, and the shear rate is 2 mm per minute.

3.4 Triaxial Test Results

3.4.1 Stress-Strain Test Curve

The results of the unconsolidated and undrained shear triaxial test are presented in **Figures 4–6**. In this figure, the horizontal axis is the axial strain ε_a and the vertical axis is the shear strain q, $q = \sigma_1 - \sigma_3$, where σ_1 and σ_3 denote the axial stress and the confining pressure, respectively. The test curves demonstrate the confining pressures of 0.3, 0.6, 0.9, and 1.2 mpa. The test results of the three mixtures are illustrated in **Figures 5–7**.

3.4.2 Mohr Circle

According to the unconsolidated and undrained shear tests of three kinds of abandoned slag materials, the Mohr circles are provided in **Figures 7–9**. The horizontal axis is axial stress σ, and the vertical axis is shear stress τ. The molar circles of the three mixtures are shown in **Figures 8–10**.

3.4.3 Cohesion and Friction Angle

Cohesion C and friction Angle φ of the three mixtures can be obtained from **Figures 7–9**, as listed in **Table.1**.

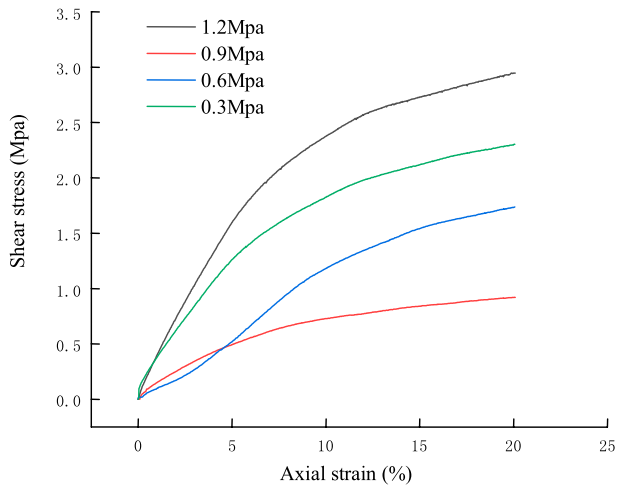

FIGURE 7 | Results of unconsolidated and undrained shear triaxial test of rock-slag and soil mixture diagram.

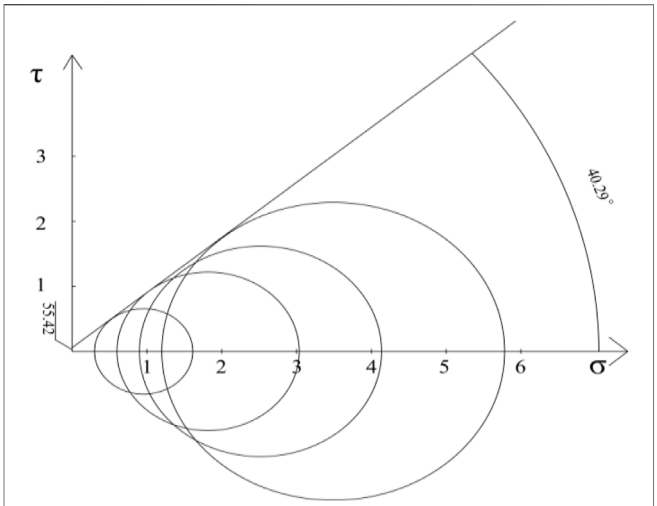

FIGURE 9 | Mohr circle of stone slag and sand mixture diagram.

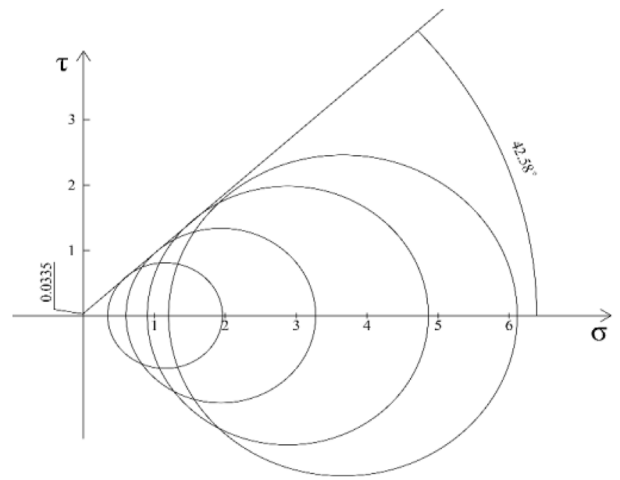

FIGURE 8 | Mohr circle of whole stone slag diagram.

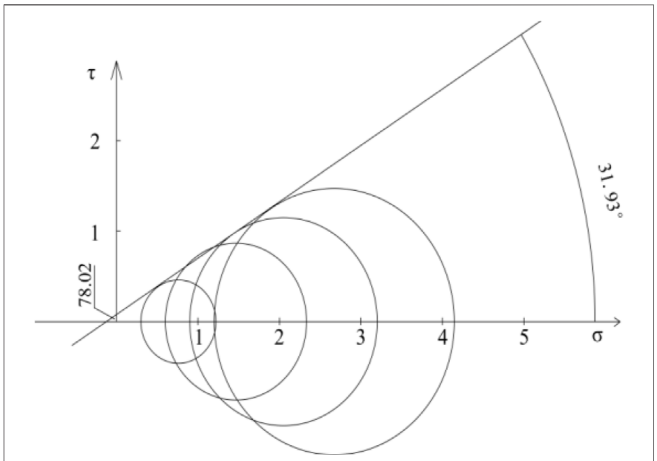

FIGURE 10 | Mohr circle of rock-slag and soil mixture diagram.

TABLE.1 | Statistical table of cohesion and friction angle of three kinds of abandoned slag.

Parameter material	Density	Cohesion	Friction angle
Whole stone slag	2.15	0.034	42.58
Stone slag and sand	2.10	0.055	40.29
Rock-slag and soil	1.81	0.080	31.93

According to the above experimental data, the following conclusions can be drawn:

1) Density has a great influence on cohesion and friction angle. The greater the original density of the soil, the stronger the interlocking action between soil materials. The occlusal action must be overcome when the shear is applied to produce relative sliding. The high density of the soil indicates that the pores between soil grains are small, the contact is close, and the original cohesion is large. Therefore, the original density has a significant influence on the shear strength. The higher the density of the soil, the greater the friction angle and cohesion. Finally, the particle size of coarse aggregate in the mixture is bigger, its shape is more irregular, the surface is coarser, and the friction angle is larger. Generally, the thicker the particle, the more irregular the shape, the worse the degree of grinding and polishing, and the larger the friction angle.
2) Although the gradation of whole stone slag, stone slag, and sand-soil mixture is different, the friction angles are close because the densities are close.
3) According to the test results, adding sand can improve the cohesion of slag. The density of the slag-sand mixture is lower than that of slag, while its cohesion is slightly higher compared

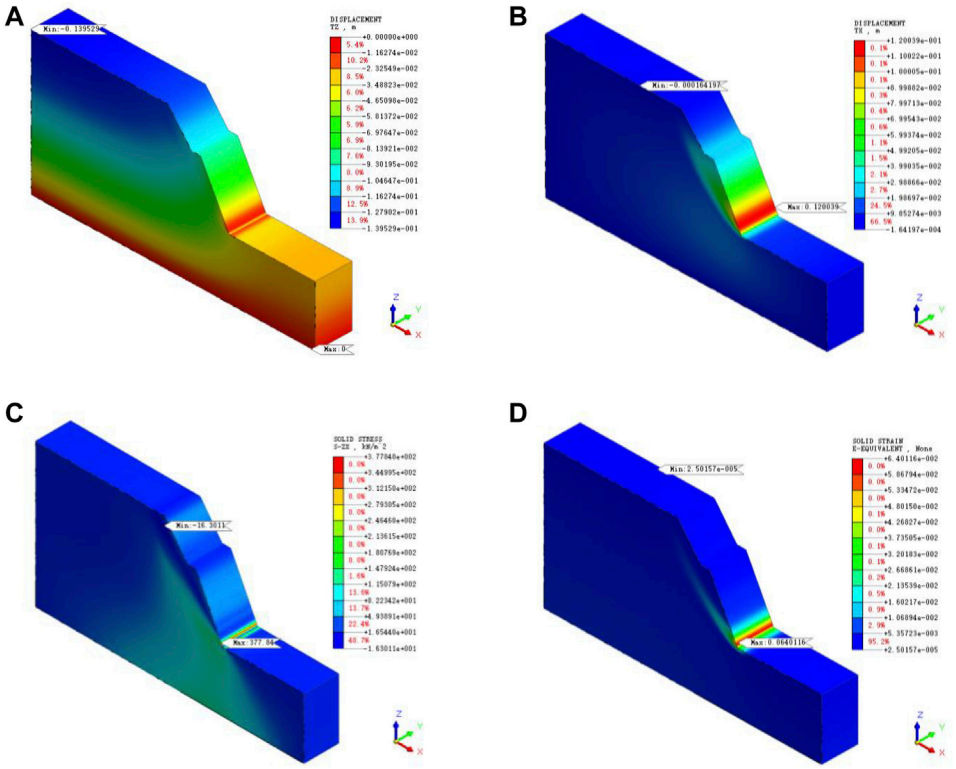

FIGURE 11 | Rock-slag slope model calculates results: **(A)** vertical displacement diagram of whole-rock slag; **(B)** horizontal displacement diagram of whole-rock slag; **(C)** XZ plane strain diagram of whole-rock slag; **(D)** plastic strain diagram of whole stone slag.

to stone slag. Because it is mixed with fine aggregate, fine aggregate surface-bound water and electrical molecular forces are different, resulting in increased cohesion. It can be concluded from **Table 1** that adding an amount of sand to the slag can reduce the friction angle. This is favorable for relative sliding between coarse aggregates because the fine aggregate provides some lubrication between the coarse aggregate skeletons. The friction angle is remarkably reduced when fine aggregates are replaced with silt or finer materials. Moreover, the fine aggregate strength is lower, and the fine aggregate is closer to a spherical shape, contributing to the relative sliding between the coarse aggregate.

4) The test results of three different slag discarding materials are accurate, and the cohesion and friction angles obtained by the Mohr circle are regular.

4 THEORY OF SHEAR STRENGTH REDUCTION COEFFICIENT METHOD

The traditional slope stability analysis methods are mainly various stability analysis methods based on the limit equilibrium theory. These methods ignore the internal stress-strain relationship of soil, making it impossible to analyze the occurrence and development process of slope failure. The finite difference method can not only satisfy the balance condition of the force but can also consider the stress-strain relation of material, generating more accurate and reasonable calculation results. Finite element software is widely used in geotechnical engineering numerical simulation, and traditional analysis methods are adopted to predict the stability of gravel soil slope. Starting from the physical and mechanical properties of slope soil, the relationship between physical and mechanical parameters and slope stability safety factors is explored to provide an effective theoretical basis for slope optimization design and safety construction. The failure envelope of the model corresponds to the Mol Coulomb criterion (shear yield function) and the upper tensile separation point (tensile stress yield function). This is related to the tensile stress flow law but not to the shear flow. Midas GTS NX numerical software based on the strength reduction method is feasible in slope stability analysis. The calculation results of safety factors are closer to those obtained by the traditional Bishop method and better than those obtained by the traditional method.

4.1 The Concept of the Shear Strength Reduction Coefficient Method

The definition of the Shear Strength Reduction Factor is the ratio of the maximum shear strength exerted by the soil on the slope to the actual shear stress generated by the external load on the slope when the external load remains unchanged. The shear strength reduction factor defined in this article is consistent with the slope stability safety factor defined in the limit equilibrium analysis.

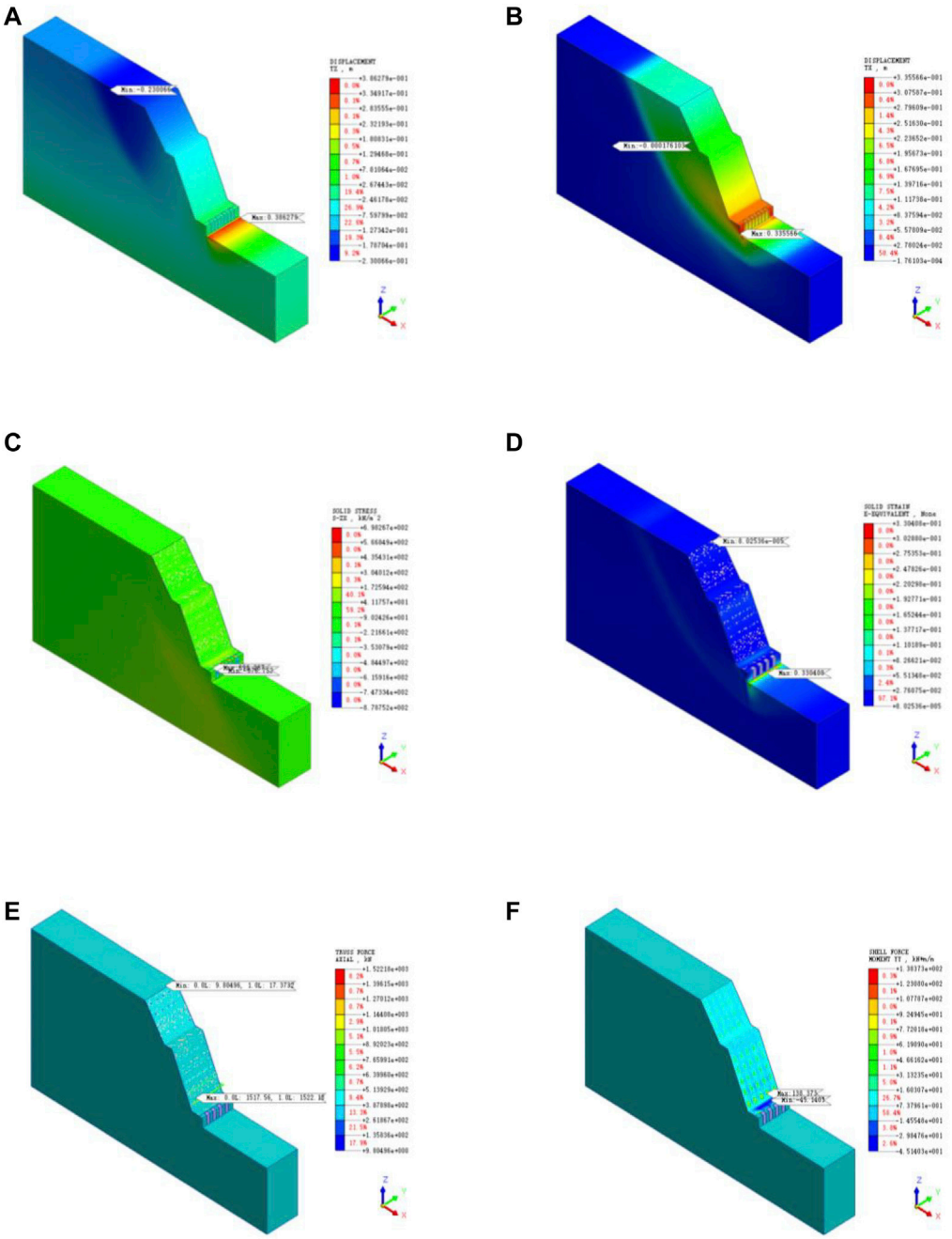

FIGURE 12 | Calculation results of rock-slag slope after construction of supporting structure: **(A)** vertical displacement diagram of whole-rock slag support; **(B)** horizontal displacement diagram of whole-rock slag support; **(C)** strain diagram in XZ plane after rock cinder slope construct support; **(D)** plastic strain diagram of rock-slag slope after construct support; **(E)** axial diagram of anchor bolt after construct support of rock cinder slope; **(F)** bending moment diagram of shotcrete on rock-slag slope.

4.2 Specific Content of the Shear Strength Reduction Coefficient Method

The shear strength reduction technique of shear strength of soil is based on indexes c and Φ. The reduction coefficients F, σ and τ represent the normal stress and the shear stress reduction, respectively, such as **Eqs 1**, **2** in the form of reduction. Then, use virtual shear strength indexes $c^{'}$ and φ' after reduction instead of shear strength indexes c and Φ. σ' and φ' denote the normal stress and shear stress after reduction, respectively, as expressed in **Eq. 3**:

$$c' = \frac{c}{F_s} \tag{1}$$

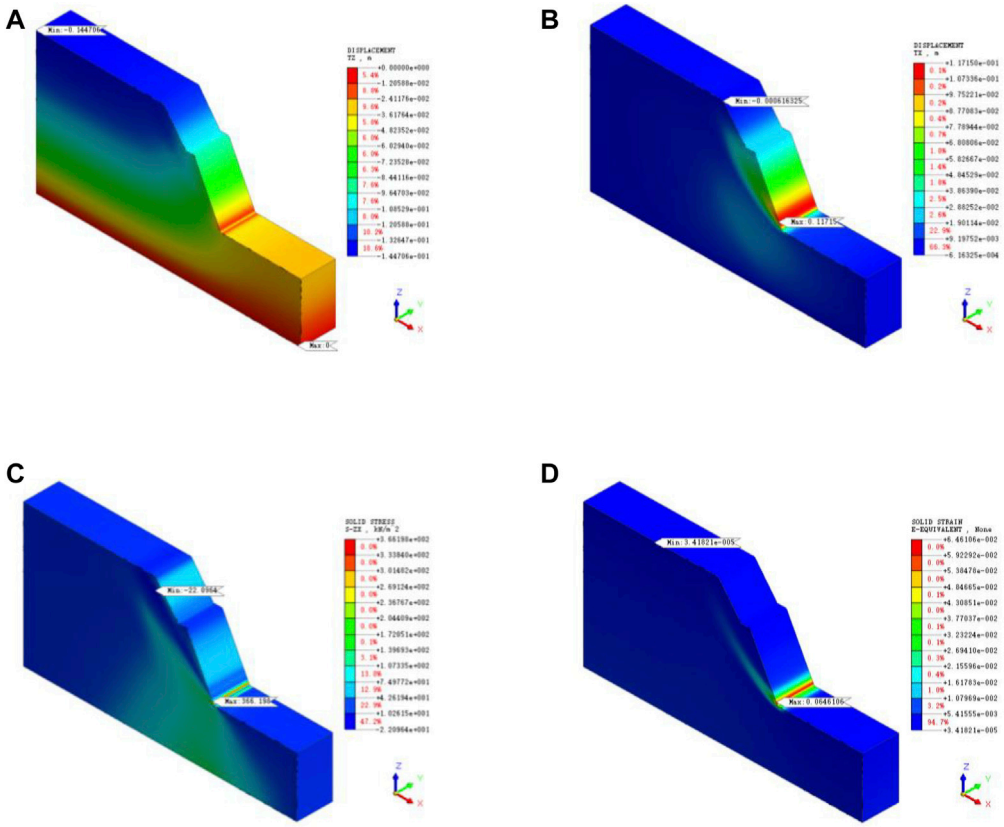

FIGURE 13 | Rock-slag and sand slope model calculate results: **(A)** vertical displacement diagram of rock-slag and sand soil without support; **(B)** horizontal displacement diagram of whole-rock slag; **(C)** XZ plane strain diagram of whole-rock slag; **(D)** plastic strain diagram of whole stone slag.

$$\varphi' = \arctan\left(\frac{\tan\varphi}{F_s}\right) \tag{2}$$

$$\text{Among: } F_s = \frac{\int_0^l c+\sigma\tan\varphi dl}{\int_0^l \tau dl}$$

$$\tau' = c' + \sigma\tan\varphi' \tag{3}$$

4.3 Advantages of the Shear Strength Reduction Coefficient Method

The shear strength reduction coefficient method combined with the finite difference method has the following advantages when compared with the traditional method:

1) It can calculate the slope with complex geomorphology and geology.
2) The constitutive relation of soil and the effect of deformation on stress are considered.
3) It can simulate the slope process of soil slope and the shape of slip surface (usually the shape and position of slip surface are determined by sheer strain increment or displacement increment).
4) It can simulate the joint action of soil and support structure (advance support, soil nail, and surface layer).
5) When solving the safety factor, it is not necessary to assume the shape of the slip surface nor perform striping.

The core idea of the strength reduction method in finite element calculation of slope stability has been widely accepted. It is not necessary to assume a sliding surface, while the computer can find the most unfavorable sliding surface and the minimum slope stability factor through multiple calculations.

The criterion of slope failure calculated by the finite element method is detailed as follows:

1) Complete transfixion of a plastic zone on the sliding surface: the beginning of progressive failure.
2) The displacement and strain on the sliding surface change abruptly, resulting in a large and unlimited plastic flow.
3) Double convergence criterion of force and displacement: the model calculation does not converge from the convergence criterion of force or displacement.

According to the comparative analysis, two kinds of materials (stone slag and stone slag) and sand soil are employed to analyze the stability of the slope of the slag discarding site. The Midas GTS NX model is utilized to investigate the stability of the two kinds of the

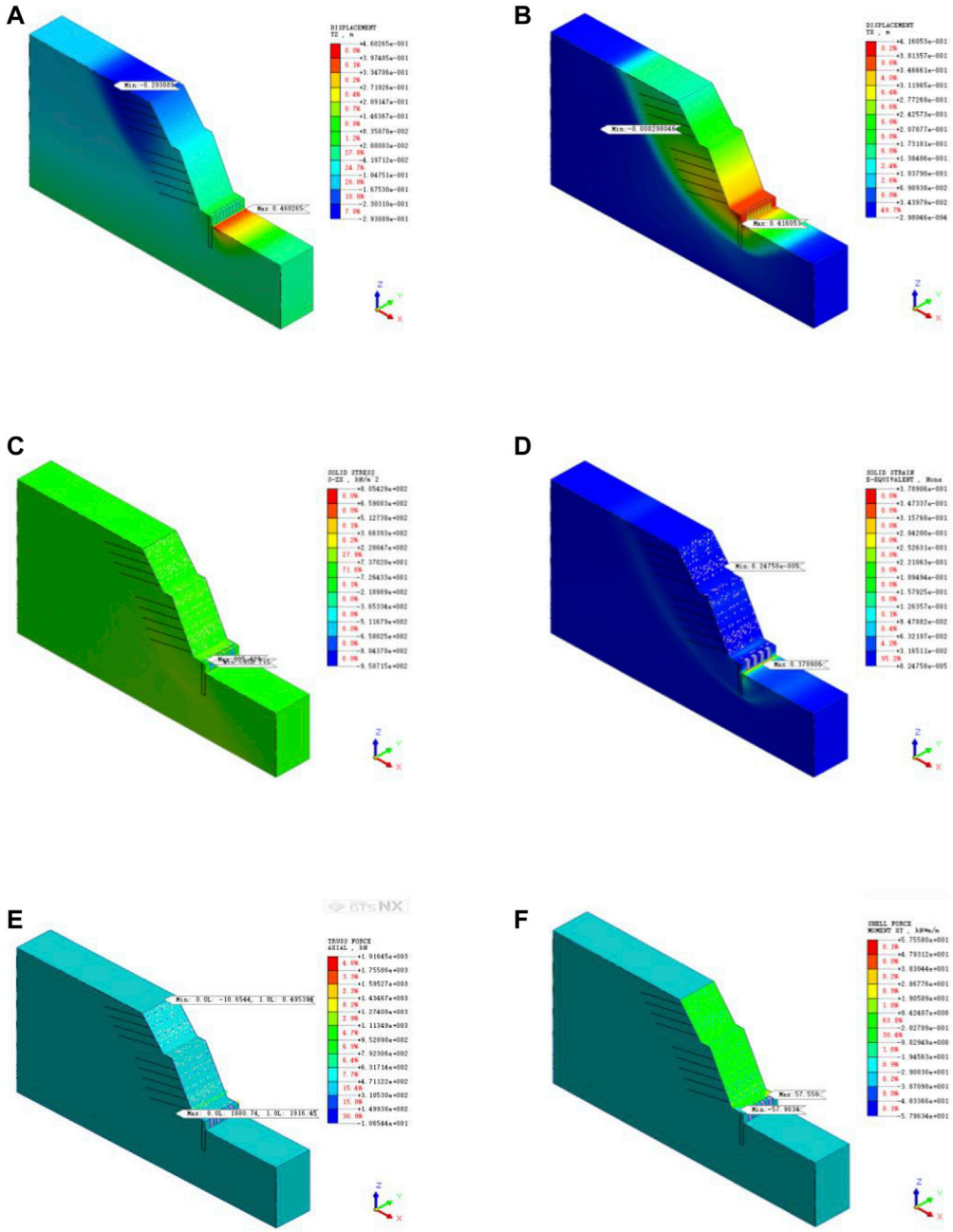

FIGURE 14 | Calculation results after construction of supporting structure of rock-slag and sand slope: **(A)** vertical displacement diagram of rock-slag and sand slope after construct support; **(B)** horizontal displacement diagram of rock-slag and sand slope after construct support; **(C)** axial diagram of anchor bolt after construct support of rock-slag and sand slope; **(D)** plastic strain diagram of rock-slag and sand slope after construct support; **(E)** axial diagram of anchor bolt after construct support of rock-slag and sand slope; **(F)** bending moment diagram of shotcrete on a slope.

mixture. The analysis results of the whole rock slag slope model are illustrated in **Figure 11**.

The calculation results demonstrate that the maximum vertical displacement of the slope is 0.14 m, the maximum horizontal displacement is 0.12 m, and the maximum stress in the XZ plane is 377.84 kPa. The plastic zone of the slope is completely through and the slope safety factor of 1.3 does not meet the requirements of the code. Thus, a special design for the slope is needed. Anti-slide piles with a side length of 1.2 m were added to the slope toe, 1.2 m intervals were arranged, and anchor bolts with a length of 15 m were added to the slope surface, with longitudinal intervals of 3 m and transverse intervals of 1.2 m. The results of slope stability analysis after the establishment of the finite element model are presented in **Figure 12**.

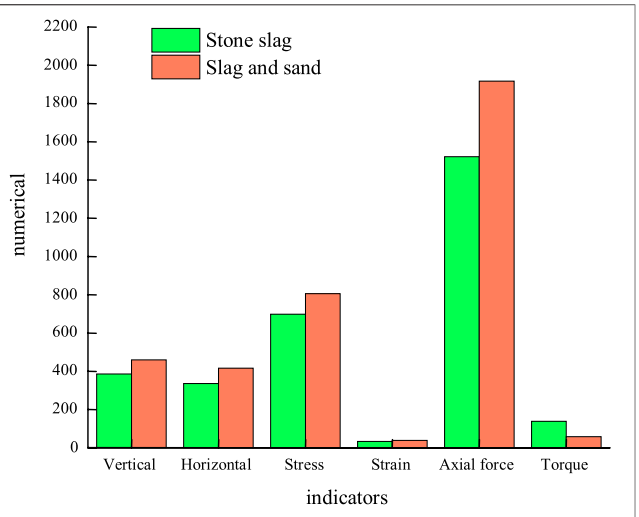

FIGURE 15 | Comparison chart of each index of the two materials.

The calculation results reveal that the maximum vertical displacement of the slope is 0.386 m, the maximum horizontal displacement is 0.336 m, and the maximum stress in the XZ plane is 698.27 kPa. The plastic zone of the slope is not completely through and the safety factor of the slope is 2.35, which meets the requirements of the code. The mechanical characteristics of the rock-slag and sand mixture are modeled and analyzed. The analysis results are illustrated in **Figure 13**.

The calculation results suggest that the maximum vertical displacement of the slope is 0.148 m, the maximum horizontal displacement is 0.117 m, and the maximum stress in the XZ plane is 336.198 kPa. The slope plastic zone is completely through and the slope safety factor is 1.58, which fails to meet the requirements of the code. The friction angle of the whole stone slag is slightly larger than that of the mixture of stone slag and stone powder, while the cohesion is slightly smaller than that of the latter. Hence, the same slope support scheme with whole stone slag is adopted to establish the finite element model for slope stability after support. The analysis results are provided in **Figure 14**.

The calculation results imply that the maximum vertical displacement of the slope is 0.460 m, the maximum horizontal displacement is 0.416 m, and the maximum stress in the XZ plane is 805.43 kPa. Due to the failure of the plastic zone in the slope, the slope safety factor is 2.67, which meets the requirements of the code. The indicators after the construction of the supporting structure of the two materials are exhibited in **Figure 15**.

It can be concluded from this figure that the maximum bending moment of the shotcrete panel of the rock-slag material slope is greater than that of the rock-slag and sand-soil mixture, while other engineering indexes are smaller than the latter. The friction angle of stone slag is higher than that of stone slag and sand mixture, and the cohesion is smaller than the latter. The numerical simulation results show that the stability of the coarse-grained soil slope is significantly affected by the friction angle of the material and is less affected by the cohesion of the material; that is, the friction angle directly affects the slope sliding fracture angle. The smaller the friction angle, the smaller the slope sliding fracture angle, the further the sliding surface extension, and the stronger the cohesion of the resistance. Nonetheless, the coarse-grained soil friction angle is extremely large, and the cohesion is relatively small. Thus, the stability of the coarse-grained soil slope is mainly affected by the friction angle and stone slag should be selected as the pile material of the abandoned soil site (Simoni and Houlsby, 2006).

5 CONCLUSION

1) Influence of stone content on cohesion: when water content remains unchanged, the cohesion decreases as the stone content increases, and the decrease in cohesion increases. The cohesion of accumulated gravel soil mainly depends on sample density and fine soil content. The cohesion increases as the density increases, and decreases as the fine soil content decreases. Due to the increase in stone content, the decrease in cohesion caused by the decrease in fine particle content is much larger than the increase in cohesion caused by density increase. The hydraulic and electric force molecules on the surface of the fine aggregate increase the cohesion, which is far greater compared to increasing the density to enhance the interlocking (interlocking) effect between soils.
2) Influence of stone content on internal friction angle: when the water content is unchanged, the internal friction angle increases with the increase in stone content, and the increase in the internal friction angle increases. Rubble acts as a skeleton and fine-grained soil coats the surface of the gravel. Hence, it plays the lubrication function. When the water content remains unchanged, with the increase in stone content, fine soil content decreases, more gravel is in direct contact, and the friction angle increases.
3) The influence of initial dry density on strength: under different confining pressures, with the increase in initial dry density, the ability of coarse-grained soil to resist shear increases gradually because the coarse-grained soil becomes more compact. Macroscopically, this demonstrates relatively large strength. Meanwhile, the greater the confining pressure, the stronger the lateral constraint of soil, the longer the contraction phaser, the stronger the capability of the soil to resist shear, and the higher the value of $(\sigma_1\text{-}\sigma_3)_{max}$.

DATA AVAILABILITY STATEMENT

The original contributions presented in the study are included in the article/Supplementary Material; further inquiries can be directed to the corresponding author.

AUTHOR CONTRIBUTIONS

HZ, responsible for reference writing and calculation. YL, responsible for contacting lab to do test and record data. QZ, responsible for making pictures and tables. FZ, responsible for making test samples and testing.

FUNDING

This research was supported by the Open Research Program of MOE Key Laboratory of Groundwater Circulation and Environmental Evolution, China University of Geosciences (Beijing) (Grant No. 2021-001). The data used in this article are available upon request from the corresponding author.

REFERENCES

Bagi, K. (2005). An Algorithm to Generate Random Dense Arrangements for Discrete Element Simulations of Granular Assemblies. *Granul. Matter* 7 (1), 31–43. doi:10.1007/s10035-004-0187-5

Bai, B., Yang, G.-c., Li, T., and Yang, G.-s. (2019). A Thermodynamic Constitutive Model with Temperature Effect Based on Particle Rearrangement for Geomaterials. *Mech. Mater.* 139, 103180. doi:10.1016/j.mechmat.2019.103180

Bai, B., Xu, T., Nie, Q., and Li, P. (2020). Temperature-driven Migration of Heavy Metal Pb2+ along with Moisture Movement in Unsaturated Soils. *Int. J. Heat Mass Transf.* 153, 119573. doi:10.1016/j.ijheatmasstransfer.2020.119573

Bai, B., Zhou, R., Cai, G., Hu, W., and Yang, G. (2021a). Coupled Thermo-Hydro-Mechanical Mechanism in View of the Soil Particle Rearrangement of Granular Thermodynamics. *Comput. Geotechnics* 137 (8), 104272. doi:10.1016/j.compgeo.2021.104272

Bai, B., Nie, Q., Zhang, Y., Wang, X., and Hu, W. (2021b). Cotransport of Heavy Metals and SiO2 Particles at Different Temperatures by Seepage. *J. Hydrology* 597, 125771. doi:10.1016/j.jhydrol.2020.125771

Bai, B., Wang, Y., Rao, D., and Bai, F. (2022). The Effective Thermal Conductivity of Unsaturated Porous Media Deduced by Pore-Scale SPH Simulation. *Front. Earth Sci.* 10, 943853. doi:10.3389/feart.2022.943853

Cui, X., Fan, Y., Wang, H., and Huang, S. (2019). Experimental Investigation of Suspended Particles Transport in Porous Medium under Variable Temperatures. *Hydrol. Process.* 33 (7), 1117–1126. doi:10.1002/hyp.13390

Cui, X., Wu, D., Wang, H., Ding, S., and Fan, Y. (2022). Pore Features and Seepage Characteristics of Natural Gap-Graded Sand with Two Size Distributions. *Géotechnique*, 1–12. doi:10.1680/jgeot.21.00213

Chang, I., Im, J., and Cho, G. C. (2016). Geotechnical Engineering Behaviors of Gellan Gum Biopolymer Treated Sand. *Can. Geotech. J.* 53 10, 1658–1670. doi:10.1139/cgj-2015-0475

Cheng, S. Y., Fu, M. Y., and Kulacki, F. A. (2018). Characterization of a Porous Transducer Using a Capillary Bundle Model: Permeabilityand Streaming Potential Prediction. *Int. J. Heat Mass Transf.* 118, 349–354.

Cundall, P. A. (1971b). *The Measurement and Analysis of Accelerations in Rock Slopes*. London: Imperial College of Science and Technology.

Donaghe, R. T., and Townsend, F. C. (1976). "Scalping and Replacement Effects on the Compaction Characteristics of Soil-Rock Mixtures," in *Soil Specimen Preparation for Laboratory Testing* (Vicksburg, Miss: ASTM International), 248.

Drescher, A., and de Josselin de Jong, G. (1972). Photoelastic Verification of a Mechanical Model for the Flow of a Granular Material. *J. Mech. Phys. Solids* 20 (5), 337–340. doi:10.1016/0022-5096(72)90029-4

Georgiannou, V. N., Burland, J. B., and Hight, D. W. (1990). The Undrained Behaviour of Clayey Sands in Triaxial Compression and Extension. *Géotechnique* 40 (3), 431–449. doi:10.1680/geot.1990.40.3.431

Hall, E. (1951). "A Triaxial Apparatus for Testing Large Soil Specimens," in *Triaxial Testing of Soils and Bitminous Mixtures* (Sausalito, Calif: ASTM International), 152.

Jefferies, M., and Been, K. (2015). *Soil Liquefaction: A Critical State Approach*. Beijing, China: CRC Press.

Kaneko, K., Terada, K., Kyoya, T., and Kishino, Y. (2003). Global-local Analysis of Granular Media in Quasi-Static Equilibrium. *Int. J. Solids Struct.* 40 (15), 4043–4069. doi:10.1016/s0020-7683(03)00209-9

Lindquist, E. S., and Goodman, R. E. (1994). *Strength and Deformation Properties of a Physical Model Melange: 1st North American Rock Mechanics Symposium*. Austin, Texas: American Rock Mechanics Association.

Lupini, J. F., Skinner, A. E., and Vaughan, P. R. (1981). The Drained Residual Strength of Cohesive Soils. *Géotechnique* 31 (2), 181–213. doi:10.1680/geot.1981.31.2.181

Marsal, R. J. (1973). *Mechanical Properties of Rockfill*. Incorporated: Publication of: Wiley John and Sons, 109–200.

Medley, E. W. (1994). *The Engineering Characterization of Melanges and Similar Block-In-Matrix Rocks (Bimrocks)*. Berkeley: California.

Mulilis, J. P., Seed, H. B., Chan, C. K., Mitchell, J. K., and Arulanandan, K. (1977). Effects of Sample Preparation on Sand Liquefaction. *J. Geotech. Engrg. Div.* 103 (2), 91–108. doi:10.1061/ajgeb6.0000387

Nemat-Nasser, S., and Tobita, Y. (1982). Influence of Fabric on Liquefaction and Densification Potential of Cohesionless Sand. *Mech. Mater.* 1 (1), 43–62. doi:10.1016/0167-6636(82)90023-0

Paduana, J. A. (1966). *The Effect of Type and Amount of Clay on the Strength and Creep Characteristics of Clay-Sand Mixtures*. Berkeley: California.

Schlosser, F., and Long, N.-T. (1974). Recent Results of French Research on Reinforced Earth. *J. Constr. Div.* 100, 223–237. doi:10.1061/jcceaz.0000429

Simoni, A., and Houlsby, G. T. (2006). The Direct Shear Strength and Dilatancy of Sand-Gravel Mixtures. *Geotech. Geol. Eng.* 24 (3), 523–549. doi:10.1007/s10706-004-5832-6

Strack, O., and Cundall, P. A. (1978). *The Distinct Element Method as a Tool for Research in Granular Media*. Minnesota, United States: Department of Civil and Mineral Engineering, University of Minnesota.

Conflict of Interest: Author YL is employed by Hubei Communications Planning and Design Institute CO. LTD. Author FZ is employed by China Nuclear Industry 22ND Construction CO. LTD.

The remaining authors HZ, SY, QZ, YZ and WF declare that the research was conducted in the absence of any commercial or financial relationships that could be construed as a potential conflict of interest.

Publisher's Note: All claims expressed in this article are solely those of the authors and do not necessarily represent those of their affiliated organizations, or those of the publisher, the editors, and the reviewers. Any product that may be evaluated in this article, or claim that may be made by its manufacturer, is not guaranteed or endorsed by the publisher.

Copyright © 2022 Zhang, Luo, Yuan, Zhou, Zhou, Zeng and Feng. This is an open-access article distributed under the terms of the Creative Commons Attribution License (CC BY). The use, distribution or reproduction in other forums is permitted, provided the original author(s) and the copyright owner(s) are credited and that the original publication in this journal is cited, in accordance with accepted academic practice. No use, distribution or reproduction is permitted which does not comply with these terms.

frontiers | Frontiers in Materials

TYPE Original Research
PUBLISHED 12 August 2022
DOI 10.3389/fmats.2022.976489

Check for updates

OPEN ACCESS

EDITED BY
Bing Bai,
Beijing Jiaotong University, China

REVIEWED BY
Yalong Jiang,
East China Jiaotong University, China
Zichao Zhao,
Shandong Academy of Agricultural Sciences, China

*CORRESPONDENCE
Ruzhang Gao,
871746519@qq.com

SPECIALTY SECTION
This article was submitted to Structural Materials,
a section of the journal
Frontiers in Materials

RECEIVED 23 June 2022
ACCEPTED 13 July 2022
PUBLISHED 12 August 2022

CITATION
Zhao B, Shen Y, Hu X, Wu Y, Zhang L, Xia D, Xu W and Gao R (2022), Evaluation of coupling coordination relationship between different habitat materials and vegetation system in the engineering disturbed area.
Front. Mater. 9:976489.
doi: 10.3389/fmats.2022.976489

COPYRIGHT
© 2022 Zhao, Shen, Hu, Wu, Zhang, Xia, Xu and Gao. This is an open-access article distributed under the terms of the Creative Commons Attribution License (CC BY). The use, distribution or reproduction in other forums is permitted, provided the original author(s) and the copyright owner(s) are credited and that the original publication in this journal is cited, in accordance with accepted academic practice. No use, distribution or reproduction is permitted which does not comply with these terms.

Evaluation of coupling coordination relationship between different habitat materials and vegetation system in the engineering disturbed area

Bingqin Zhao[1,2], Yuanyang Shen[2], Xinkai Hu[2], Yuhang Wu[2], Lun Zhang[1,2], Dong Xia[1,2], Wennian Xu[1,2] and Ruzhang Gao[1,2]*

[1]Hubei Key Laboratory of Disaster Prevention and Mitigation, China Three Gorges University, Yichang, China, [2]Hubei Provincial Engineering Research Center of Slope Habitat Construction Technique Using Cement-based Materials, China Three Gorges University, Yichang, China

In order to explore the coupling coordination relationship between habitat materials and vegetation system in the engineering disturbed area, six different vegetation restoration patterns in Xiangjiaba engineering disturbed region were utilized as research objects. An evaluation system of 14 habitat materials indicators and 10 vegetation indicators was established. The weight of each indicator was determined by Principal Component Analysis (PCA), and the interrelationship between habitat material and vegetation system was investigated using the Partial Least Square Path model (PLS-PM). Finally, a model for the degree of coupling coordination between habitat materials and vegetation system under different vegetation restoration modes was constructed. The results showed that: 1) habitat materials and vegetation system are closely related, and the habitat materials have a stronger impact on ecosystem restoration. Artificial vegetation restoration technologies can effectively improve soil conditions in engineering disturbed areas, allowing for vegetation restoration in a healthy environment. 2) Under different vegetation restoration patterns, the habitat materials and vegetation coupling coordination index of natural forest plots, frame beam filling soil plots, thick layer base material spraying plots, guest external soil spray seeding plots, vegetation concrete plots, and abandon slag slope plots was 0.767, 0.673, 0.669, 0.625, 0.557, and 0.400, respectively. The development of habitat materials and vegetation in guest external soil spray seeding plots was of a synchronous type. The vegetation development lagged behind habitat materials in thick layer base material spraying plots, vegetation concrete plots, and abandon slag slope plots, while habitat materials lagged behind vegetation development in natural forest plots, frame beam filling soil plots. The model for the degree of coupling coordination between habitat materials and vegetation constructed in this study can serve as a scientific reference for evaluating the impact of ecological restoration engineering in other similar projects.

KEYWORDS

engineering disturbance area, habitat materials and vegetation system, coupling coordination, evaluation model, ecological restoration

Introduction

The Chinese infrastructure industry is experiencing rapid growth. Engineering construction alters the surface structure on a massive scale and causes vegetation damage, causing the environment to be severely disrupted (Chen et al., 2019; Cui et al., 2020; Bai et al., 2021; Kong D. L. et al., 2021). In this context, vegetation ecological restoration technology arose, combining the safety of traditional slope treatment methods with vegetation reconstruction ecology. It has since become widely utilized and developed (Yang et al., 2015; Zhao et al., 2017). In vegetation ecological restoration techniques, habitat materials are employed to form a soil environment that is favorable for the growth of plants. The characteristics and succession process of vegetation communities, soil quality of habitat materials often have a direct impact on its benefits after the adoption of vegetation ecological restoration technique (Zhou et al., 2017; Bai et al., 2020). Meanwhile, vegetation and habitat materials interact with each other, as vegetation needs the soil of habitat materials for growth and soil fertility of habitat materials is also changed by vegetation. Therefore, the focus of research for vegetation restoration has shifted from soil quality assessments of habitat materials and simple vegetation diversity alone to the investigation of the vegetation-soil system coupling relationship (Jiang et al., 2010; Du et al., 2013; Bai et al., 2019; Cui et al., 2022).

Yan et al., applied the "spatio-temporal substitution approach" to investigate the law of synergistic succession of vegetation and soil in sample plots with different vegetation restoration patterns. In this field, it has been discovered that soil bulk density, organic matter, and water content could be employed as characteristic indexes of soil development, and various vegetation metrics revealed different synergistic laws in vegetation community succession and soil formation (Yan 2012). Xue et al., constructed a vegetation-soil coupling model for multiple highway slope protection modes based on grey correlation degree. The findings demonstrated that soil physical and chemical parameters accounted for the most variation in vegetation. The soil slope has a higher coupling coordination degree than the rock slope (Xue et al., 2016). Yin et al., discovered various degrees of correlation between different vegetation types and soil properties, and there was a substantial correlation between species diversity of herbaceous plants and soil water content, phosphatase activity, and protease activity. While there was a substantial correlation between species diversity of woody plants and soil total phosphorus level and protease activity. We should pay attention to dynamic changes in the vegetation regeneration of rock slopes and Proposing control methods (Yin et al., 2012). Through research of the relationship between vegetation and soil features in 20 typical slope protection plots, Zhang et al. discovered that the vegetation restoration effect of soil slopes and the coordinated development between vegetation and soil are both better than those of rock slopes (Zhang H. F. et al., 2013). It is clear that vegetation and soil have a complicated and nonlinear dynamic coupling connection, and the interaction and organic combination of the vegetation system and the soil system results in the establishment of a sustainable vegetation restoration system (Wang et al., 2021; Jiao et al., 2005; Zhou et al., 2016). Due to the clear spatial heterogeneity of vegetation and soil features, the investigation of the soil-vegetation coupling connection of vegetation restoration in a specific area is the premise and basis for the evaluation and regulation guidance of targeted vegetation restoration effects.

The vegetation system and habitat materials system are important subsystems in vegetation ecological restoration, and their coupling and coordination directly affect the effect of vegetation ecological restoration. The soil quality of the habitat materials and vegetation restoration have received the majority of attention in recent years in academic studies on the ecological environment of Xiangjiaba Hydropower Station, but there has been a dearth of research on the coupling relationship between habitat materials and vegetation system (Zeng et al., 2009; Zhao et al., 2020). As a result, this paper takes representative sample plots under different vegetation restoration patterns in the disturbed area of Xiangjiaba Hydropower Station as the research object, and the vegetation-soil coupling coordination model is constructed based on the systematic analysis of vegetation and soil characteristics under different vegetation restoration models, combined with the coupling coordination degree correction model. The goal of this study is to provide a scientific reference for revealing the interaction between habitat materials and vegetation in a disturbed area, as well as a theoretical foundation for enhancing the scientific management level of similar vegetation ecological restoration projects.

Materials and methods

Overview of the research area

The right bank of the dam site of Xiangjiaba Hydropower Station is located in Shuifu County, Yunnan Province, and the

TABLE 1 Basic situation of sample plots.

Sample	Dominant species	Geographic coordinates	Altitude (m)	Slope (°)	Slope property	Vegetation restoration time
A1	*Pennisetum alopecuroides (L.) Spreng*	N28°38′15.75″ E104°24′51.74″	328.5	63	Excavated slope	2004.12
A2	*Imperata cylindrica (L.) Beauv*	N28°38′23.65″ E104°24′42.08″	288.9	40	Abandoned slag slope	2004.11
A3	*Leucaena leucocephala (Lam.) de Wit*	N28°38′21.99″ E104°26′16.22″	388.9	51	Excavated slope	2004.12
A4	*Lagerstroemia indica L*	N28°39′00.30″ E104°23′40.28″	473.9	30	Excavated slope	2005.06
A5	*Setaria viridis (L.) Beauv*	N28°38′59.45″ E104°24′10.14″	520.5	42	Abandoned slag slope	
A6	*Alnus cremastogyne Burk*	N28°39′07.14″ E104°23′38.82″	502.4	45		

left bank is located in Yibin County, Sichuan Province. It has a subtropical monsoon climate with an average annual temperature of 18°C. The reservoir region and adjacent counties have a maximum frost-free duration of 320 days and a minimum of 266 days. The annual average precipitation is 1030.5 mm, the annual average evaporation is 1001.1 mm, and the relative humidity ranges from 74% to 83%. In the project region, the soil layer is generally thin, the texture is harsh, and the organic matter level is low. Soil erosion is particularly severe in the project location, which is a crucial erosion control area in the Yangtze River's upper reaches. The slope area of the real construction disturbance area accounts for more than 50 percent of the overall construction area at Xiangjiaba Hydropower Station. The disturbed area's slope vegetation types include primarily shrubs and grasses, with more dryland agriculture vegetation, artificial greening ornamental vegetation, and commercial fruit trees, and less forest vegetation (Ye, 2016; Xu et al., 2017).

In the disturbed area of the Xiangjiaba Hydropower Station project, different vegetation restoration method sample plots were selected for vegetation survey and soil sampling. This survey included six sample plots: vegetation concrete plots (A1), frame beam filling soil plots (A2), thick layer base material spraying plots (A3), guest external soil spray seeding plots (A4), abandon slag slope plots (A5), and natural forest plots (A6). The project's disturbed area was mostly formed in 2004, and the artificial vegetation restoration patterns were mostly implemented between November 2004 and June 2005. To avoid the effects of rainfall and other climatic conditions on soil parameters, the sampling period should include at least 1 week without rain, and the sampling work should be performed during that time. Table 1 depicts the basic circumstances of each plot.

Investigation and analysis of vegetation

The vegetation community study was conducted in all plots using a combination of field survey and quadrat sampling method. According to the type of vegetation, 5 m × 5 m quadrats of tree and shrub layer or 1 m × 1 m quadrats of herb layer was built up in each sample plot, and the sample was repeated 5 times (Zhang and Shangguan, 2016). The total vegetation coverage, plant name, split coverage, average height, number of plants were recorded, and the species diversity index, richness index, and evenness index were calculated by the following equation in Table 2 (Xia 2010).

Collection and analysis of soil samples

Three soil repeated sampling plots were set up in each sample plot at the same time as the vegetation research, and soil samples were collected by circular knife method and bisect method. Because the overlaying soil layer in the vegetation restoration sample was roughly 10 cm thick, soils within 0–10 cm of the soil surface layer were obtained from each plot, sealed, and returned to the laboratory after debris removal (Li et al., 2018). Each soil sample was split into two parts: one was air-dried, crushed, and screened (2 mm pore size) for physical and chemical analysis, while the other was kept fresh in a refrigerator at 4°C as soon as feasible for biological features examination.

Physical and chemical indicators of habitat materials mainly include

Water content, organic matter, available nitrogen, total phosphorus, accessible phosphorus, and available potassium. The drying method was used to measure water content, the potassium dichromate volumetric method was used to estimate

TABLE 2 Formula used to calculate vegetation community diversity index.

Vegetation community diversity index		Formula
The species diversity index of vegetation community	*Shannon-Wiener* diversity index (*SW*)	$SW = -\sum_{i=1}^{S} P_i \ln P_i$
	Simpson diversity index (*SP*)	$SP = 1 - \sum_{i=1}^{S} (P_i)^2$
	McIntosh diversity index (*MI*)	$MI = \frac{N - \sqrt{\sum_{i=1}^{s} (N_i)^2}}{N - \sqrt{N}}$
The species richness index of vegetation community	*Margalef* richness index (*MA*)	$MA = (S-1)/\ln N$
	Menhinick richness index (*ME*)	$ME = S/\sqrt{N}$
	Monk richness index (*MO*)	$MO = S/N$
The species evenness index of vegetation community	*Pielou* evenness index (J_{SW})	$J_{SW} = SW/\ln S$
	Alatato evenness index (J_A)	$J_A = \frac{(\sum_{i=1}^{s} (P_i)^2) - 1}{exp(SW) - 1}$
	Simpson evenness index (J_S)	$J_S = \frac{SP}{1 - 1/S}$

organic matter. The available nitrogen, total phosphorus, available phosphorus, and available potassium were determined by Spectrophotometer method based on the modified Berthelot reaction with an Skalar San++ continuously flowing autoanalyzer (Bao 2000; Chen 2005; Zhang et al., 2006; Zhang 2007; Zhang, 2011).

Biological indicators of habitat materials mainly include

Urease, neutral phosphatase, sucrase, polyphenol oxidase, microbial biomass nitrogen, microbial biomass phosphorus, and microbial diversity. The indophenol colorimetry method was used to measure urease, while the disodium phenyl phosphate method was used to determine neutral phosphatase, sucrase was determined by DNS (3,5-dinitrosalicylic acid) method, and polyphenol oxidase was determined by pyrogallol colorimetry. The chloroform fumigation method was used to evaluate the nitrogen, and phosphorus content of microbial biomass (Shen 1998; Chen 2005). The average color change rate per well (AWCD) was utilized to reflect the metabolic level of microorganisms to a single carbon source, and the BIOLOG-ECO microplate method was employed to quantify microbial diversity. 10 sugars, 7 carboxylic acids, 6 amino acids, 4 poly polymers, 2 phenols, and 2 amines are among the carbon sources of BIOLOG-ECO microplates employed in this work, for a total of 31 carbon sources (Choi and Dobbs 1999; Zhang W. et al., 2013; Xiang et al., 2014).

Coupling model construction

Highly sensitive evaluation index reflecting the effect of vegetation restoration in the Xiangjiaba Project's affected region was developed. The vegetation integrated subsystem includes 10 indicators such as vegetation coverage (CO), Species diversity index [*Shannon-Wiener* diversity index (*SW*), *McIntosh* diversity index (*MI*), and *Simpson* diversity index (*SP*)], richness index [*Margalef* richness index (*MA*), *Menhinick* richness index (*ME*), and *Monk* richness index (*MO*)], and evenness index (*Simpson* evenness index (J_S), *Pielou* evenness index (J_{SW}) and *Alatato* evenness index (J_A). The habitat materials integrated subsystem includes 14 indicators such as water content (WAT), organic matter (SOM), available nitrogen (AN), total phosphorus (TP), available phosphorus (AP), available potassium (AK), urease (URE), neutral phosphatase (NEP), sucrase (INV), polyphenoloxidase (PPO), microbial biomass nitrogen (MBN), microbial biomass phosphorus (MBP), microbial entropy (qMBC), AWCD. Because different indexes have varying dimensions and magnitudes, the range standardization method is used to standardize the data, and the principal component analysis method is utilized to estimate each index's weight (Xie et al., 2017; Zheng and Yang, 2022). Figure 1 depicts the weight findings for each index.

The coupling degree (*C*) is a useful metric to qualitatively evaluate the degree of interaction between systems or elements. Other domestic researchers have conducted extensive research on coupling degree, believing that the value of coupling degree is 0–1, with the value being closer to 1 when the coordination among the system's elements is stronger and closer to 0 when the coordination is weaker (Peng et al., 2011; Zhang H. F. et al., 2013; Zhang Y. et al., 2013; Luo et al., 2018; Li et al., 2019). The coupling degree can only represent the strength and size of the system's interaction, and it can't fully reflect the overall synergistic effect between systems or between elements within the system. A habitat materials and vegetation system coupling coordination model after vegetation restoration in the disturbed area of Xiangjiaba Project was constructed with reference to the coupling model in physics and Wang Shujia's

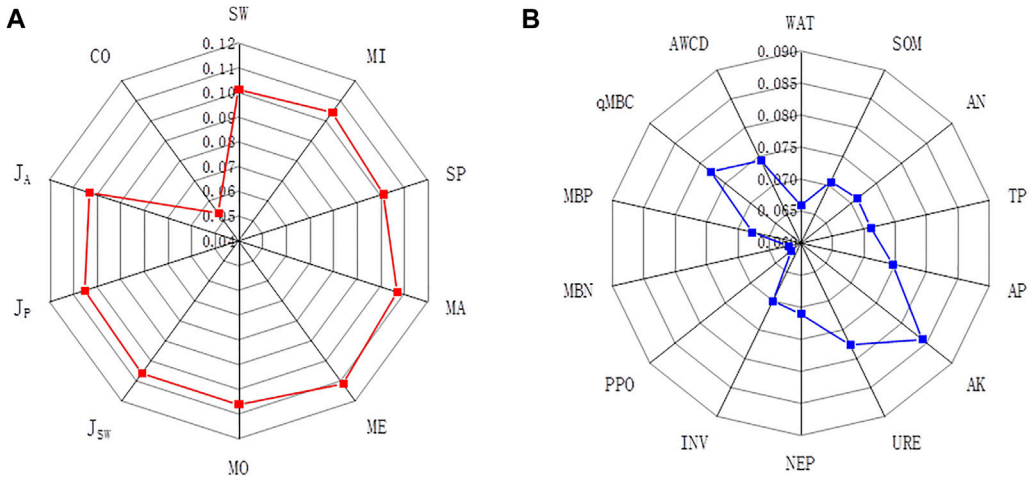

FIGURE 1
Radar map of coupling coordination index and weight between vegetation system **(A)** and soil system **(B)**.

modification of the domestic coupling model in order to more objectively and accurately reflect the coupling and coordination relationship between habitat materials and vegetation system in the process of vegetation restoration in the study area (Liu and Song 2005; Wang et al., 2021). The following is the calculating formula:

$$C = \frac{2\sqrt{\delta}}{1+\delta} \quad (2-1)$$

$$\delta = \frac{min[S(x), P(x)]}{max[S(x), P(x)]} \subset [0,1] \quad (2-2)$$

$$P(x) = \sum_{i=1}^{p} a_i x_i \quad (2-3)$$

$$S(x) = \sum_{j=1}^{q} b_j x_j \quad (2-4)$$

In the formula: C is the coupling degree of the habitat materials and vegetation system, $0 \le C \le 1$. a_i and b_j are the weights of the i habitat material indicator and j vegetation indicator, x_i and x_j are the standardized values of the i habitat material indicator and j vegetation indicator, $S(x)$ is the habitat materials comprehensive evaluation function, and $P(x)$ is the vegetation comprehensive evaluation function. The coupling coordination degree of the habitat materials and vegetation system was evaluated in order to further evaluate the overall "synergistic" effect of habitat materials and vegetation subsystems in the evaluation of ecological restoration effect, and to avoid the error caused by only relying on the evaluation of coupling degree. The following is the calculating formula:

$$C_d = \sqrt{C \times T} \quad (2-5)$$

$$T = \alpha S(x) + \beta P(x) \quad (2-6)$$

In the formula: C_d is the coupling coordination degree of habitat materials and vegetation system, $0 \le C_d \le 1$. The closer the C_d value is to 1, the closer it is to the high-quality coupling coordination state between habitat materials and vegetation system; T is the comprehensive coordination index of habitat materials and vegetation system; α and β are the contribution rates of habitat materials and vegetation subsystems. In the process of vegetation restoration in the disturbed area, habitat materials and vegetation subsystems influence and depend on each other, and the importance coefficients of ecological restoration are the same for both, so α and β take the average value of 0.5.

If $P(x)/S(x)$ is greater than 1, the growth and development of vegetation is faster than that of habitat material; if $P(x)/S(x)$ is less than 1, the growth and development of vegetation is slower than that of habitat material, and vegetation does not make full use of habitat materials fertility resources; and the closer the ratio is to 1, the more synchronous and coordinated the succession between them tends to develop (Luo et al., 2018). In summary, the coordinated evaluation criteria of habitat materials and vegetation system coupling for ecological restoration in the disturbed area of Xiangjiaba project are established as shown in Table 3.

Data processing and analysis

The data were subjected to a general statistical analysis using the programs SPSS and Excel, which were created by IBM Corporation and Microsoft Corporation, respectively. SmartPLS and RStudio tools, created by SmartPLS GmbH and RStudio, respectively, were used to analyze the partial least

TABLE 3 Classification of habitat materials and vegetation system coupling coordination types.

Habitat materials and vegetation system coupling coordination degree	Coordination state	*P(x)/S(x)*	Coupling coordination type
0.00 < *Cd* ≤ 0.20	Low-level coordination (LC)	*P(x)/S(x)* > 1.2	LC- habitat materials lag
		0.8 ≤ *P(x)/S(x)* ≤ 1.2	LC- habitat materials and vegetation system balance
		P(x)/S(x) < 0.8	LC-Vegetation lag
0.20 < *Cd* ≤ 0.40	Primary coordination (PC)	*P(x)/S(x)* > 1.2	PC- habitat materials lag
		0.8 ≤ *P(x)/S(x)* ≤ 1.2	PC- habitat materials and vegetation system balance
		P(x)/S(x) < 0.8	PC-Vegetation lag
0.40 < *Cd* ≤ 0.60	Intermediate coordination (IC)	*P(x)/S(x)* > 1.2	IC- habitat materials lag
		0.8 ≤ *P(x)/S(x)* ≤ 1.2	IC- habitat materials and vegetation system balance
		P(x)/S(x) < 0.8	IC-Vegetation lag
0.60 < *Cd* ≤ 0.80	Advanced coordination (AC)	*P(x)/S(x)* > 1.2	AC- habitat materials lag
		0.8 ≤ *P(x)/S(x)* ≤ 1.2	AC- habitat materials and vegetation system balance
		P(x)/S(x) < 0.8	AC-Vegetation lag
0.80 < *Cd* ≤ 1.0	Superior coordination (SC)	*P(x)/S(x)* > 1.2	SC- habitat materials lag
		0.8 ≤ *P(x)/S(x)* ≤ 1.2	SC- habitat materials and vegetation system balance
		P(x)/S(x) < 0.8	SC-Vegetation lag

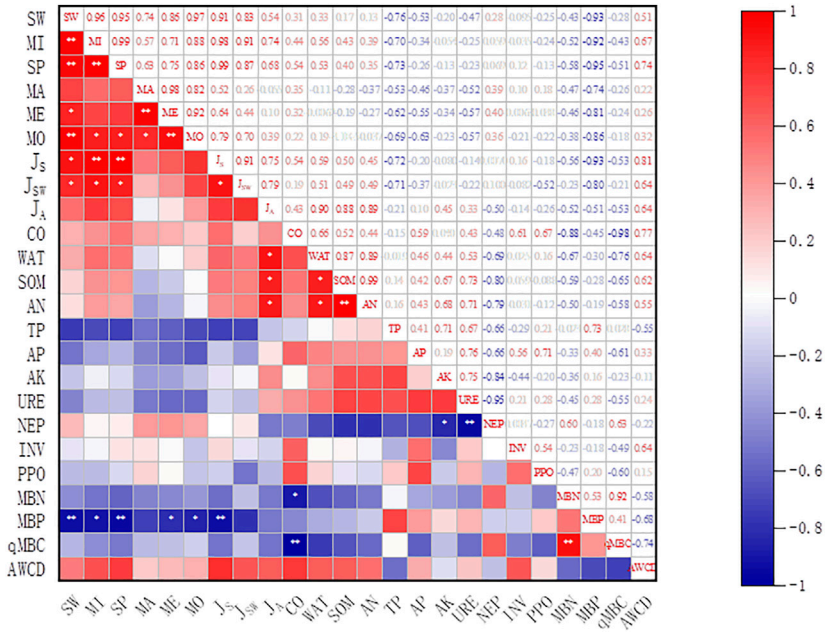

FIGURE 2
Correlation between indicators of habitat materials and vegetation system under different vegetation restoration models. Notes: * indicates significant correlation ($p < 0.05$), and ** indicates highly significant correlation ($p < 0.01$).

square path model (PLS-PM). SmartPLS and SPSS were used to evaluate the relationships between the indicators; Origin was used to depict the relationships between the vegetation and soil systems; and Canoco was used to process the weights between the indicators and the BIOLOG data using Principal Component Analysis (PCA). Software called Origin and Canoco were created by OriginLab Inc. and Microcomputer Power Inc.

TABLE 4 Coupling coordination of habitat materials and vegetation system in different areas.

Sample plot	*P(x)*	*S(x)*	*P(x)/S(x)*	*C*	C_d	Coupling coordination type
A1	0.1611	0.5981	0.2694	0.8177	0.5572	IC-Vegetation lag
A2	0.7101	0.2885	2.4614	0.9065	0.6728	AC- habitat materials lag
A3	0.3280	0.6092	0.5383	0.9539	0.6686	AC-Vegetation lag
A4	0.3572	0.4279	0.8346	0.9959	0.6253	AC- Vegetation and habitat materials balance
A5	0.0815	0.3129	0.2605	0.8099	0.3996	LC-Vegetation lag
A6	0.9028	0.3828	2.3586	0.9145	0.7667	AC- habitat materials lag

Results

Analysis of correlation between vegetation and habitat materials indicators

The examination of the correlation between the aforesaid indicators (Figure 2) revealed that the vegetation system and the habitat materials system had varying degrees of correlation discrepancies. Vegetation cover and microbial biomass carbon showed highly significant negative correlation, and it showed significant negative correlation with microbial biomass nitrogen. The water content, organic matter, and available nitrogen all demonstrated a strong positive association with Alatato evenness index. The microbial biomass phosphorus showed highly significant negative correlation with Shannon-Wiener diversity index, Simpson diversity index, Simpson evenness index, and it showed significant negative correlation with McIntosh diversity index, Menhinick richness index, and Monk richness index. Many indexes in the vegetation integrated subsystem had a substantial negative correlation with the level of microbial biomass phosphorus, indicating that improving the transformation ability of microorganisms to phosphorus would impede the development of vegetation community variety.

Analysis of habitat materials and vegetation system coupling coordination characteristics of different vegetation restoration patterns

The coupling coordination degree is a numerical index that describes the degree of interdependence between the system's constituents (Pu et al., 2021; Nan et al., 2021; Xu et al., 2016). The coupling coordination degree of habitat materials and vegetation system can scientifically and precisely depict the relative development levels and interactions of the two systems. In the disturbed area of the Xiangjiaba Project, the calculation results of habitat materials comprehensive evaluation index, vegetation comprehensive evaluation index, habitat materials and vegetation system coupling degree, and habitat materials and vegetation system coupling coordination degree of 6 different vegetation restoration models were shown in Table 4. The vegetation comprehensive assessment index was ranked A6 > A2 > A4 > A3 > A1 > A5, while the habitat materials comprehensive evaluation index was ranked A3 > A1 > A4 > A6 > A6 > A5 > A2. The coupling degree of habitat materials and vegetation system varied from 0.8099 to 0.9959, with A4 > A3 > A6 > A2 > A1 > A5 as the order of coupling degree. The change of coupling coordination degree was 0.3996–0.7667, with A6 > A2 > A3 > A4 > A1 > A5. The findings reveal that the comprehensive assessment index and coupling coordination features of habitat materials and vegetation system in the disturbed region change significantly with the difference in vegetation restoration model, and the overall coordination type is better than abandoned land.

Analysis on influencing factors of habitat materials and vegetation system coupling coordination

Partial least squares path model (PLS-PM) is a comprehensive analysis model for analyzing multivariable causal relationships. This model can not only handle the problem of indicator multicollinearity, but also calculate the direct and indirect effects of various variables on response variables. 25 observation variables were selected to construct PLS-PM in order to study the relationship between vegetation community characteristics and physical and chemical properties of habitat materials under different vegetation restoration patterns, as shown in Figure 3. The R^2 of the vegetation system is 0.832, the R^2 of the habitat materials system is 0.959, and the R^2 of the habitat materials and vegetation coupling coordination system is 0.838, all of which are more than 0.6 in the PLS-PM calculation. As a result, the dependent variables in this model are effectively explained by the independent variables. The number of external models loads of observed variables greater than 0.7 under each latent variable is 76%, which is within an acceptable range, indicating that the characteristic index used is appropriate for evaluating the habitat materials and vegetation system coupling coordination model

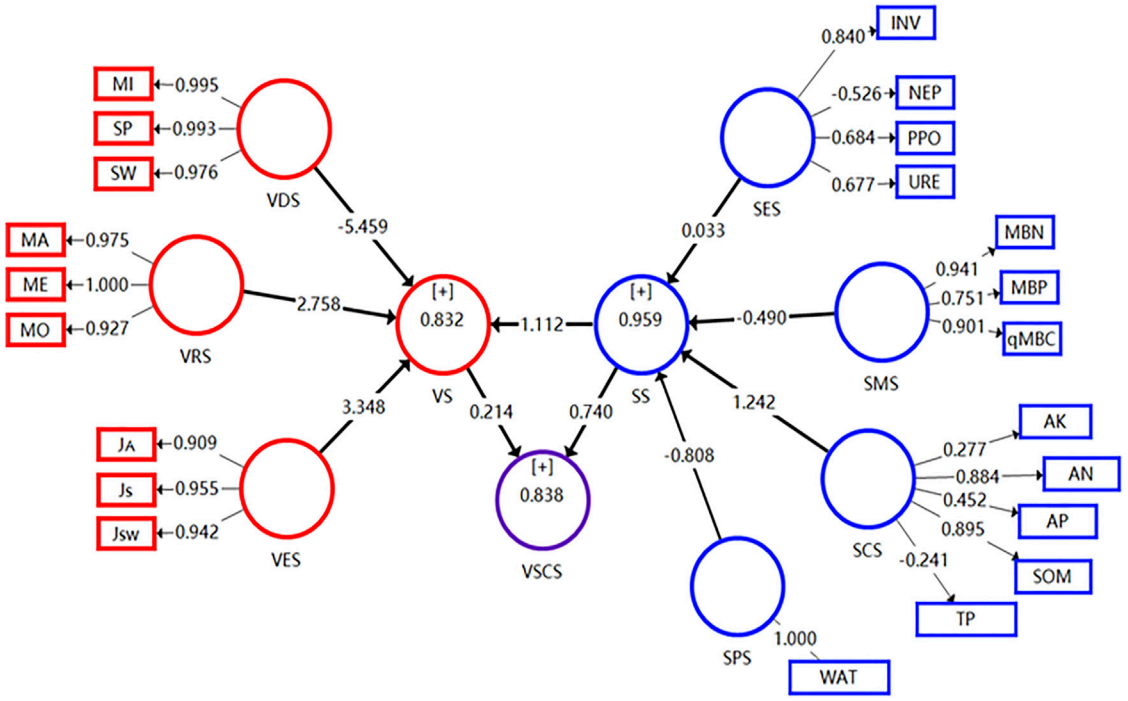

FIGURE 3
PLS-PM analysis map under different vegetation restoration models. Notes: VDS: vegetation diversity subsystem; VRS: vegetation richness subsystem; VES: vegetation uniformity subsystem; VS: total vegetation system; SS: habitat materials total system; SES: habitat materials enzyme subsystem; SMS: habitat materials microorganism subsystem; SCS: habitat materials chemistry subsystem; SPS: habitat materials physics subsystem; VSCS: habitat materials and vegetation system coupling coordination system.

(Qi and Kong 2017; Yang et al., 2017; Kim et al., 2021; Kong W. B. et al., 2021; Ma et al., 2021; Zhao et al., 2022).

When the vegetation system and the habitat materials system act on the coupling coordination system, the influence of the habitat materials system on the overall coupling coordination system was higher than that of the vegetation system, as determined by decomposing the direct effect, indirect effect, and total effect among the latent variables and analyzing the relationship between the latent variables and their influence on the habitat materials and vegetation system. The reason for the follow-up analysis could be that the vegetation in the disturbed area has been severely damaged, and the vegetation community has not evolved to the top community after some degree of ecological restoration, so the vegetation system's influence on the coupling coordination system is weaker than the habitat materials system's during the same time period.

The path coefficients of the habitat materials physics and chemistry subsystems were −0.808 and 1.242, respectively, both of which were greater than 0.7 and had a large direct influence on the habitat materials system, followed by the indirect coefficient of the habitat materials microorganism subsystem, which calculated as −0.490, and the path coefficient of the habitat materials enzyme subsystem was 0.033, which had the least direct effect on the habitat materials system. However, enzymes indirectly affect the habitat materials system throughout the ecological cycle by changing the transformation of nutrient content in habitat materials chemistry and habitat materials microbial indices. The content of microbial carbon, microbial nitrogen and microbial phosphorus can also indirectly reflect the nutrient content of the habitat materials. The path coefficients of the diversity subsystem, evenness subsystem, and richness subsystem in the vegetation system were −5.495, 3.348, and 2.758, respectively, all greater than 0.7, showing that they have a significant impact on the vegetation system. The diversity index, evenness index, and richness index are chosen to better intuitively describe the vegetative system. In the early stages of vegetation restoration, we should focus on factors that directly affect the habitat materials system, such as water content and available nutrients in habitat materials, while in the middle and later stages of vegetation restoration, we should focus on the content of enzymes and the influence of microbial carbon, microbial nitrogen and microbial phosphorus on the nutrient content of the habitat materials, in order to achieve better ecological restoration results.

Discussion

The structure and components of vegetation community will gradually become stable during the process of vegetation community succession due to intraspecific and interspecific competition (Zhang et al., 2015). Because they are not disturbed by external disturbances, natural forest plots are more likely to form a stable structure with trees and shrubs as dominating species in this study than other plots, which is consistent with He et al.'s studies on *southern hemlock* (He et al., 2010). The niche dynamics of a *Pinus massoniana* plantation were studied by Li et al.(2021) who found that as the community matures, the interaction among species becomes more stable, niche differentiation increases, the niche overlap index falls, and the struggle between species is waning. As a result, it is assumed that the intense succession stage in the early stage of vegetation development in natural forest sample plots has ended, and the succession trend has begun to slow down. However, the early succession stage consumes a lot of nutrients in the habitat materials and vegetation system, and the content of organic matter in the original soil in the Xiangjiaba area is generally low, and soil erosion in the project site is more serious, so the soil is difficult to work with. This is consistent with the results of Xu et al. on the current status of soil lag in *Caragana* and grassland ditches caused by intense succession (Xu et al., 2016).

The *P(x)* value of abandon slag slope was significantly lower than that of other plots, because the dominant species were mostly annual or perennial grass like *Setaria viridis (L.) Beauv.* after the primary stage of secondary succession, with a single vegetation type, low species richness, low utilization of habitat materials nutrients by vegetation, and an unstable community as a whole. Those indicated that the coupled habitat materials and vegetation system was in a weakened state and the vegetation lags behind, which is consistent with Jian et al.'s result on the quantitative classification and structure of grassland communities in small watersheds of the loess hilly region (Jian et al., 2022). Although the soil quality and vegetation coverage of the thick layer base material spraying plots were improved over the abandoned area, the *Medicago sativa L., Festuca elata Keng ex E. Alexeev,* and *Cynodon dactylon (L.) Pers.* sown in the early stages of restoration entirely withdrew from the succession sequence due to the invasion of *Leucaena leucocephala (Lam.).* The important value of *Leucaena leucocephala (Lam.)* in the sample plot was 57.14%, which was significantly greater than that of other linked species, indicating that there was a single dominant population of *Leucaena leucocephala (Lam.)* (Zhao et al., 2021). The invasion of foreign species diminishes the complexity of the vegetation community structure, which is harmful to the ecological community's stability (Xia 2010). As a result, vegetation development continues to lag behind habitat materials.

Prior research on the early succession process and community stability on the disturbed slope of Xiangjiaba Hydropower Station discovered that the multi-level structure of tree, shrub, grass, and vine was beneficial to community stability (Xu et al., 2016). The vegetation communities of vegetation concrete technical plots and frame beam filling soil plots both evolved from the initial configuration of pure herbs to a multi-layer community structure of herb-shrub-vine combination after more than 10 years of succession, but the coupling state of habitat materials and vegetation system has changed. The frame beam filling soil plots used a lot of habitat materials nutrients in the early stages of community secondary succession, and the sampling period was concentrated in August during the summer, when the demand for habitat materials nutrients in the multi-level community of tree, shrub, herb and vine was significantly higher than other periods. Because the humus created by falling leaves and litter, as well as other nutrients given by the external environment, was less, the habitat materials system was generally barren at this time, causing the habitat materials system to lag behind. During the initial species allocation, the vegetation concrete plots added organic materials and organic fertilizers. Although habitat materials fertility was rapidly depleted during the early stages of vegetation succession, there is still a surplus in the overall fertility following the establishment of a stable structure, indicating that the sample plot is experiencing vegetation lag (Xia 2010). The original establishment of the vegetation community in the guest external soil spray seeding plots was still dominated by *Lagerstroemia indica L.* after a period of secondary succession, while the *Cynodon dactylon (L.) Pers.* was completely destroyed. In comparison to other restoration models, the guest external soil spray seeding plots had a balanced habitat materials and vegetation system development, indicating that the vegetation system composed of woody plants like *Lagerstroemia indica L.* and herbaceous plants like *Imperata cylindrica (L.) Beauv.* and *Diplopterygium glaucum (Thunberg ex Houttuyn) Nakai* had the best coordination with the habitat materials system. To some extent, habitat materials fertility regulation and restoration species selection based on local conditions can encourage the joint development of plants and habitat materials.

To summarize, the four restoration plots chosen in the project's disturbed area are in a state of coordinated development, indicating that various habitat materials and vegetation systems are in the process of transitioning to high-quality and coordinated development at this time, and significant ecological restoration progress has been made. However, there is still much room for improvement in maintaining balanced habitat materials and vegetation development. The development and succession of vegetation communities will be aided by improved habitat materials' soil quality during the ecological restoration and vegetation reconstruction process.

Simultaneously, as natural succession progresses, the vegetation community will have a greater level of community structure, which will be more favourable to the accumulation of organic matter and improve habitat materials' soil quality progressively (Han et al., 2010; Yang et al., 2018; Hu et al., 2021). As a result, when selecting an ecological restoration method, it is necessary to tailor measures to local conditions in order to improve not only the coupling and coordination relationship between vegetation growth and the habitat materials environment, but also to promote their common development and increase the ecological benefits of vegetation restoration.

Conclusion

Habitat materials variables play a bigger role in the habitat materials and vegetation coupling coordination system. The correlation between the system indicators were significantly varied, and organic matter, water content, available nitrogen, AWCD, microbial biomass phosphorus and microbial biomass nitrogen were among the habitat materials system indicators that had substantial effects on vegetation community succession and growth.

The growth of habitat materials and vegetation system coupling and coordination in the four artificial vegetation restoration patterns is varied after vegetation restoration, and the ecological restoration effect of them is impressive when compared to abandon slag slope plots. The natural forest sample plot has the highest habitat materials and vegetation system coupling coordination index, whereas frame beam filling soil plots, thick layer base material spraying plots and guest external soil spray seeding plots are all well-coordinated. The distinction lies in the balanced state of habitat materials and vegetation system development in the secondary classification, and the vegetation concrete plots are the intermediate coordinated state vegetation lag type.

To achieve sustainable development, species should be selected from multiple niches as much as possible for sample sites with lagging vegetation. In addition, in subsequent monitoring, alien species invasion should be avoided. According to the results of the PLS-PM analysis, the amounts of organic matter, available nitrogen, and available phosphorus can be suitably raised in the lagging sample plots to improve the habitat materials lag.

Data availability statement

The original contributions presented in the study are included in the article/supplementary material, further inquiries can be directed to the corresponding author.

Author contributions

BZ conceived and designed the experiment. RG and BZ contributed to the writing of the first draft, review and editing. YS, XH, and YW conduct data analysis, LZ, DX, and WX provided conceptual advice for the experimental program. All authors contributed critically to the drafts and gave final approval for publication.

Funding

This research was funded by the Hubei Provincial Engineering Research Center of Slope Habitat Construction Technique Using Cement-based Materials (China Three Gorges University) Open Research Program (2022SNJ07), the Nei Monggol Autonomous Region Science and Technology Major Project (2021ZD0007-03), and the National Natural Science Foundation of China (51979147).

Conflict of interest

The authors declare that the research was conducted in the absence of any commercial or financial relationships that could be construed as a potential conflict of interest.

Publisher's note

All claims expressed in this article are solely those of the authors and do not necessarily represent those of their affiliated organizations, or those of the publisher, the editors and the reviewers. Any product that may be evaluated in this article, or claim that may be made by its manufacturer, is not guaranteed or endorsed by the publisher.

References

Bai, B., Xu, Tao., Nie, Q., and Li, P. (2020). Temperature-driven migration of heavy metal Pb2+ along with moisture movement in unsaturated soils. *Int. J. Heat Mass Transf.* 153, 119573. doi:10.1016/j.ijheatmasstransfer.2020.119573

Bai, B., Yang, G. C., Li, T., and Yang, G. S. (2019). A thermodynamic constitutive model with temperature effect based on particle rearrangement for geomaterials. *Mech. Mater.* 139, 103180. doi:10.1016/j.mechmat.2019.103180

Bai, B., Zhou, R., Cai, G. Q., Hu, W., and Yang, G. (2021). Coupled thermo-hydro-mechanical mechanism in view of the soil particle rearrangement of granular thermodynamics. *Comput. Geotechnics* 137 (8), 104272. doi:10.1016/j.compgeo.2021.104272

Bao, S. D. (2000). *Soil agrochemical analysis*. 3rd Edition. Beijing: China Agricultural Press.

Chen, F. H., Fu, B. J., Xia, J., Wu, T., Wu, S. H., Zhang, Y. L., et al. (2019). Major advances in studies of the physical geography and living environment of China

during the past 70 Years and future prospects. *Sci. China Earth Sci.* 49 (11), 1665–1701. doi:10.1007/s11430-019-9522-7

Chen, L. X. (2005). *Soil experiment practice course*. Harbin: Northeast Forestry University Press.

Choi, K. H., and Dobbs, F. C. (1999). Comparison of two kinds of biolog microplates (GN and ECO) in their ability to distinguish among aquatic microbial communities. *J. Microbiol. Methods* 36 (3), 203–213. doi:10.1016/S0167-7012(99)00034-2

Cui, X. Z., Fan, Y., Wang, H. X., and Huang, S. B. (2020). Ground environment characteristics during the operation of GWHP considering the particle deposition effect. *Energy Build.* 206, 109593. doi:10.1016/j.enbuild.2019.109593

Cui, X. Z., Wu, D., Wang, H., Ding, S., and Fan, Y. (2022). Pore features and seepage characteristics of natural gap graded sand with two size distributions. *Géotechnique*, 1–12. doi:10.1680/jgeot.21.00213

Du, H., Peng, W. X., Song, T. Q., Wang, K. L., Zeng, F. P., Lu, S. Y., et al. (2013). Plant community characteristics and its coupling relationships with soil in depressions between karst hills, north guangxi, China. *Chin. J. Plant Ecol.* 37 (3), 197–208. doi:10.3724/sp.j.1258.2013.00020

Han, L., Wang, H. Z., Peng, J., Chen, J. L., and Peng, M. (2010). Soil physical and chemical properties under succession of plant community in desert riparian forest of the tarim river. *Ecol. Environ. Sci.* 19 (12), 2808–2814. doi:10.16258/j.cnki.1674-5906.2010.12.030

He, J. Y., Rong, H., Wu, Y. Y., Chen, C., Ke, X. S., Xu, Z. K., et al. (2010). Study on interspecific association of main population in arborous layer of A *tsuga tchekiangensis* community in wuyishan national nature reserve of fujian Province. *J. Fujian Coll. For.* 30 (2), 169–173. doi:10.13324/j.cnki.jfcf.2010.02.003

Hu, P. L., Zhao, Y., Xiao, D., Xu, Z. H., Wang, K. L., Xiao, J., et al. (2021). Dynamics of soil nitrogen availability following vegetation restoration along A climatic gradient of A subtropical karst region in China. *J. Soils Sediments* 21 (6), 2167–2178. doi:10.1007/s11368-021-02915-0

Jian, C. X., Lai, S. B., Zhou, J. J., Chen, Z. F., Yang, Q., Chen, Yang., et al. (2022). Quantitative and structure characteristics and the influencing factors of grassland communities in A typical watershed at loess hilly-gully region. *ACTA Ecol. SIN.* 42 (4), 1381–1392. doi:10.5846/stxb202010272753

Jiang, Y., Zhang, Y. P., Yang, Y. G., Xu, J. Y., and Li, Y. P. (2010). Impacts of grazing on the system coupling between vegetation and soil in the alpine and subalpine meadows of wutai mountains. *Acta Ecol. Sin.* 30 (4), 837–846. doi:10.3969/j.issn.1002-8692.2014.20.020

Jiao, J. Y., Ma, X. H., Bai, W. J., Jiao, F., and Wen, Z. M. (2005). Correspondence analysis of plant community and soil environmental factors in reclaimed farmland in loess hilly and gully region. *ACTA PEDOL. SIN.* 42 (5), 42–50. doi:10.11766/trxb200411110506

Kim, M. S., Lee, S. H., and Kim, J. G. (2021). Evaluation of factors affecting arsenic uptake by Brassica juncea in alkali soil after biochar application using partial least squares path modeling (PLS-PM). *Chemosphere* 275, 130095. doi:10.1016/j.chemosphere.2021.130095

Kong, D. L., Zhang, H. T., He, X., Ren, H. W., Hu, Q. Z., Xiao, S. Y., et al. (2021). Influencing factors of farmland soil pH in southwest Hubei based on PLSPM model. *Soils* 53 (4), 809–816. doi:10.13758/j.cnki.tr.2021.04.019

Kong, W. B., Yin, Y. M., Peng, E. R., Wu, P. J., Mao, Z. M., Liu, Q., et al. (2021). Dynamic study on restoration of slope plant community disturbed by river engineering in mountainous area. *Environ. Monit. Manag. Technol.* 33 (6), 19–23+34. doi:10.19501/j.cnki.1006-2009.2021.06.005

Li, H., Lu, J. Y., Wei, T. X., and Zhu, Q. K. (2019). Evaluation on coupling characteristics of vegetation and soil systems under different microrelief in loess plateau of northern shaanxi Province. *J. Sichuan Agric. Univ.* 37 (2), 192–198+214. doi:10.16036/j.issn.1000-2650.2019.02.007

Li, L., Wang, Y. Q., Ma, J. M., Zhang, H., Huang, L. X., Mo, Y. H., et al. (2021). Niche dynamics of understory woody plants during the near-natural restoration of *Pinus massoniana* plantations in southern subtropics. *Guangxi Sci.* 28 (5), 499–510. doi:10.13656/j.cnki.gxkx.20211203.001

Li, R. R., Kan, S. S., Zhu, M. K., Chen, J. J., Ai, X. Y., Chen, X. Y., et al. (2018). Effect of different vegetation restoration types on fundamental parameters structural characteristics and the soil quality index of artificial soil. *Soil Tillage Res.* 184, 11–23. doi:10.1016/j.still.2018.06.010

Liu, Y. B., and Song, X. F. (2005). Coupling degree model and its forecasting model of urbanization and ecological environment. *J. China Univ. Min. Technol.* 34 (1), 94–99. doi:10.3321/j.issn:1000-1964.2005.01.019

Luo, Q. H., Ning, H. S., and Chen, Q. M. (2018). Relation between vegetation and soil of haloxylon ammodendron plantation in the process of sand-fixation. *J. Desert Res.* 38 (4), 780–790. doi:10.7522/j.issn.1000-694X.2017.00037

Ma, H. F., Hu, H., Li, Y., Guo, Y. X., Ren, C. J., Zhao, F. Z., et al. (2021). Stability of soil aggregates at different altitudes in qinling mountains and its coupling relationship with soil enzyme activities. *Environ. Sci.* 42 (9), 4510–4519. doi:10.13227/j.hjkx.202101236

Nan, G. W., Zhao, M. X., Wang, Y. Y., Rong, H. Q., and Dai, L. S. (2021). Evaluation of coupling coordination relationship between soil and vegetation systems in different afforestation types. *J. Arid Land Resour. Environ.* 35 (5), 157–162. doi:10.13448/j.cnki.jalre.2021.142

Peng, W. X., Song, T. Q., Zeng, F. P., Wang, K. L., Du, H., and Lu, S. Y. (2011). Models of vegetation and soil coupling coordinative degree in grain for green project in depressions between karst hills. *Trans. CSAE* 27 (9), 305–310. 1002-6819(2011)-09-0305-06. doi:10.3969/j.issn.1002-6819.2011.09.053

Pu, Y. X. H., Wang, Y. L., Zhao, Z. J., Huang, J., and Yang, Y. (2021). Coupling relationships between vegetation and soil in different vegetation restoration models in the loess region of northern shanxi Province. *Acta Prataculturae Sin.* 30 (5), 13–24. doi:10.11686/cyxb2020458

Qi, W. T., and Kong, L. (2017). Path analysis of PPP project performance based on SEM model. *J. WUT(Information Manag. Eng.* 39 (2), 202–207. doi:10.3963/j.issn.2095-3852.2017.02.017

Shen, S. M. (1998). *Soil fertility in China*. Beijing: China Agriculture Press.

Wang, S. J., Kong, J., Ren, L., Zhi, D. D., and Dai, B. T. (2021). Research on misuses and modification of coupling coordination degree model in China. *J. Nat. Resour.* 36 (3), 793. doi:10.31497/zrzyxb.20210319

Wang, H. Y., Guo, Y. F., Xu, Y. J., Qi, W., Bu, F. J., and Qi, H. J. (2021). Coupling relationship between vegetation and soil system in ecological restoration of different stand types in Jiufeng mountain. *Int. J. Ecol. Environ. Sci.* 30 (12), 2309–2316. doi:10.16258/j.cnki.1674-5906.2021.12.005

Xia, Z. Y. (2010). *Research on the initial succession process and stability of artificial vegetation community on disturbed slope of Xiangjiaba hydropower station*. Wuhan, China: Wuhan University.

Xiang, Z. Y., Zhang, L., Zhang, F. Q., Liu, W., Wang, G. X., Wang, Z. T., et al. (2014). Soil nutrients and microbial functional diversity of different stand types in qinghai Province. *Sci. Silvae Sin.* 50 (4), 22–31. doi:10.11707/j.1001-7488.20140404

Xie, Y. X., Zhang, L. B., Luo, S. H., Yang, J., Li, F., and Wang, D. W. (2017). Evaluating the level of provincial ecological civilization development in China using the double-benchmark progressive method. *Strategic Study CAE* 19 (4), 60–66. doi:10.15302/J-SSCAE-2017.04.010

Xu, M., Zhang, J., Liu, G. B., Qiu, T. T., and Zheng, M. Q. (2016). Analysis on vegetation-soil coupling relationship in gullies with different vegetation restoration patterns. *J. Nat. Resour.* 31 (12), 2137–2146. doi:10.11849/zrzyxb.20150736

Xu, W. N., Xia, D., and Zhao, B. Q. (2017). *Research on vegetation ecological restoration technology in disturbed areas of hydropower projects*. Beijing: Science Press.

Xue, O., Wei, T. X., Liu, F., and Li, Y. Y. (2016). Modeling the degree of coupling and interaction between plant community diversity and soil properties on highway slope. *J. Beijing For. Univ.* 38 (1), 91–100. doi:10.13332/j.1000-1522.20150235

Yan, D. F. (2012). *Mechanism of synergistic succession of vegetation and soil under different vegetation restoration measures in the low hilly area of taihang mountains*. Zhengzhou: Henan Agricultural University.

Yang, H. W., Li, J., Xiao, Y. H., Gu, Y. B., Liu, H. W., Liang, Y. L., et al. (2017). An integrated insight into the relationship between soil microbial community and tobacco bacterial wilt disease. *Front. Microbiol.* 8, 2179. doi:10.3389/fmicb.2017.02179

Yang, W. T., Miao, J. Q., Wang, X. W., Xu, J. C., and Li, Z. X. (2018). Corn-soybean intercropping and nitrogen rates affected crop nitrogen and carbon uptake and C: N ratio in upland red soil. *J. Plant Nutr.* 41 (15), 1890–1902. doi:10.1080/01904167.2018.1476540

Yang, Y. S., Xia, Z. Y., Xiao, H., Chen, Y., Zhang, L., and Yao, X. Y. (2015). Application of restoration ecology to slopes ecological protection in disturbed areas of hydropower projects. *J. Changjiang Acad. Sci.* 32 (7), 52–57. doi:10.3969/j.issn.1001-5485.2015.07.010

Ye, W. (2016). A study on the environmental protection and management supervision of the Xiangjiaba hydro power station in Jinsha River. Master's thesis. Changsha (China): Hunan University.

Yin, J. Z., Zhu, K. H., Shi, X. Y., Han, C., and Gu, B. (2012). Vegetation restoration and soil properties on rocky slope in qingfeng quarry. *Bull. Soil Water Conservation* 32 (1), 144–149+155. doi:10.13961/j.cnki.stbctb.2012.01.013

Zeng, X., Chen, F. Q., Xu, W. N., Wang, J. Z., and Xia, Z. Y. (2009). Vegetation restoration in disturbance area of large hydropower project — a case study of Xiangjiaba hydropower project. *Resour. Environ. Yangtze Basin* 18 (11), 1074–1079. doi:10.3969/j.issn.1004-8227.2009.11.014

Zhang, H. F., Li, G., Song, X. L., Yang, D. L., Li, Y. J., Qiao, J., et al. (2013). Changes in soil microbial functional diversity under different vegetation restoration patterns for hulunbeier sandy land. *Acta Ecol. Sin.* 33 (1), 38–44. doi:10.1016/j.chnaes.2012.12.006

Zhang, J. E. (2007). *Commonly used experimental research methods and techniques in ecology*. Beijing: Chemical Industry Press.

Zhang, M. X., Wang, D. X., Kang, B., Zhang, G. G., Liu, P., Du, Y. L., et al. (2015). Interspecific associations of dominant plant populations in secondary forest of *Pinus armandii* in qinling mountains. *Sci. SILVAE SINCAE* 51 (1), 12–21. doi:10.11707/j.1001-7488.20150102

Zhang, W. (2011). *Soil, water, and plant physicochemical analysis tutorial*. Beijing: China Forestry Publishing House.

Zhang, W., Zhou, Y. Y., and Hu, G. W. (2013). Coupling mechanism and space-time coordination of new-approach urbanization, new-approach industrialization and service industry modernization in megacity behemoths: A case study of ten cities in China. *Sci. Geogr. Sin.* 33 (5), 562–569. doi:10.13249/j.cnki.sgs.2013.05.007

Zhang, Y. L., Xu, A. M., Shang, H. B., and Ma, A. S. (2006). Study on the method of determination of total nitrogen in soil and plants by AA3 continuous flow analyzer. *J. Northwest Sci-Tech Univ. Agri (Nat. Sci. Ed.).* 34 (10), 128–132. doi:10.13207/j.cnki.jnwafu.2006.10.026

Zhang, Y. W., and Shangguan, Z. P. (2016). The coupling interaction of soil water and organic carbon storage in the long vegetation restoration on the loess plateau. *Ecol. Eng.* 91, 574–581. doi:10.1016/j.ecoleng.2016.03.033

Zhang, Y., Zhao, T. N., Shi, C. Q., Wu, H. L., Li, D. X., and Sun, Y. K. (2013). Evaluation of vegetation and soil characteristics during slope vegetation recovery procedure. *Trans. Chin. Soc. Agric. Eng.* 29 (3), 124–131. doi:10.3969/j.issn.1002-6819.2013.03.017

Zhao, B. Q., Gao, R. Z., Xia, D., Xia, L., Zhu, W. Q., Xu, W. N., et al. (2021). Vegetation community characteristics under different vegetation eco-restoration techniques at Xiangjiaba hydropower station. *Nat. Environ. Pollut. Technol.* 20 (4), 1381–1392. doi:10.46488/NEPT.2021.v20i04.001

Zhao, B. Q., Xia, D., Xia, L., Xia, Z. Y., and Xu, W. N. (2020). Assessment of vegetation restoration soil quality in disturbed area in Xiangjiaba hydropower project. *China Environ. Sci.* 40 (3), 1224–1234. doi:10.19674/j.cnki.issn1000-6923.2020.0085

Zhao, B. Q., Xia, Z. Y., Xu, W. N., Yang, S., Xia, D., and Wang, Z. G. (2017). Review on research of slope eco-restoration technology for engineering disturbance area. *Water Conservancy Hydropower Technol.* 48 (2), 130–137. doi:10.13928/j.cnki.wrahe.2017.02.022

Zhao, Y. Q., Shen, J., Feng, J. M., and Wang, X. Z. (2022). Relative contributions of different sources to DOM in erhai lake as revealed by PLS-PM. *Chemosphere* 299, 134377. doi:10.1016/j.chemosphere.2022.134377

Zheng, C. C., and Yang, S. J. (2022). Research on the development of rural E-commerce based on principal component analysis- taking longnan city as an example. *Logist. Sci-Tech.* 45 (3), 56–59. doi:10.13714/j.cnki.1002-3100.2022.03.035

Zhou, J., Fu, B. J., Gao, G. Y., Lv, Y. H., Liu, Y., and Lv, N. (2016). Effects of precipitation and restoration vegetation on soil erosion in A semi-arid environment in the loess plateau, China. *Catena* 137, 1–11. doi:10.1016/j.catena.2015.08.015

Zhou, Y., Ma, H. B., Jia, X. Y., Zhang, R., Shu, T. T., and Zhou, J. J. (2017). Soil quality evaluation of typical grassland in the loess hills of ningxia under different ecological restoration measures. *Trans. Chin. Soc. Agric. Eng.* 33 (18), 102–110. doi:10.11975/j.issn.1002-6819.2017.18.014

frontiers | Frontiers in Materials

TYPE Original Research
PUBLISHED 12 August 2022
DOI 10.3389/fmats.2022.971485

Check for updates

OPEN ACCESS

EDITED BY
Xianze Cui,
China Three Gorges University, China

REVIEWED BY
Yao Xiao,
Guangdong University of Technology, China
Dan Chang,
Sun Yat-sen University, China

*CORRESPONDENCE
Jianmei Liu,
liujianmei@dtsjy.com

SPECIALTY SECTION
This article was submitted to Structural Materials, a section of the journal Frontiers in Materials

RECEIVED 17 June 2022
ACCEPTED 05 July 2022
PUBLISHED 12 August 2022

CITATION
Yi S and Liu J (2022), Field investigation of steel pipe pile under lateral loading in extensively soft soil.
Front. Mater. 9:971485.
doi: 10.3389/fmats.2022.971485

COPYRIGHT
© 2022 Yi and Liu. This is an open-access article distributed under the terms of the Creative Commons Attribution License (CC BY). The use, distribution or reproduction in other forums is permitted, provided the original author(s) and the copyright owner(s) are credited and that the original publication in this journal is cited, in accordance with accepted academic practice. No use, distribution or reproduction is permitted which does not comply with these terms.

Field investigation of steel pipe pile under lateral loading in extensively soft soil

Shixuan Yi[1] and Jianmei Liu[2]*

[1]Structural Engineer, Guangzhou Metro Design & Research Institute Co., Ltd., Guangzhou, China, [2]Director of Structure Institute, Guangzhou Metro Design & Research Institute Co., Ltd., Guangzhou, China

The construction of railway and highway embankments has a significant influence on the behavior of existing pile foundations, especially in the situation of high embankments and extensively soft soils, which are commonly encountered in coastal areas. A high embankment might produce large lateral movement and bending moment to the existing adjacent piles, which would cause the failure of the pile if the surcharge loading is not properly considered. A field test was designed and performed to investigate the effect of lateral surcharge loading on the existing adjacent pile in extensively soft soils. A 4 m high embankment was constructed in five lifts and was close to the existing adjacent steel pipe pile with a length of 35 m. The deformation of the pile and the soft soils, the excess pore water pressure, and lateral earth pressures were measured during the surcharge loading test. The test results showed that the lateral displacement of the steel pipe pile at the ground surface exceeded 229.9 mm and could not maintain constant due to the surcharge loading. The lateral displacement decreased along with the pile depth and was relatively small when the pile depth exceeded 10 m. Large lateral displacements were observed in the soft soils at different locations. The surcharge loading zone showed obvious downward displacements, while the soft soils close to the loading zone showed upward displacements. The excess pore water pressure changed regularly with the construction of the embankment, and its maximum value reached 53.6 kPa. The lateral earth pressures that acted on the pile continuously increased with the increase in the embankment height, which caused large deformation of the pile.

KEYWORDS

steel pipe pile, lateral surcharge loading, field test, extensively soft soils, embankment

Introduction

Lateral soil movement caused by self-weight or external factors known as the passive pile differs from lateral loads applied at the pile head, which is an active pile for the lateral bearing modes of pile foundations. In many cases, the design and failure of piles are governed by lateral performance. Examples of passive piles include existing piles near piling (Poulos, 1994), piles for stabilizing slopes (Ito et al., 1982; Bai et al., 2021), piles adjacent to the tunneling and excavation project (Poulos and Chen, 1997; Madhumathi

TABLE 1 Geological profiles.

Soil no.	Soil type	Description	Frictional resistance (kPa)	Thickness of each layer (m)
①	Fill	Loose to medium dense gravel	—	1
②	Marine deposit	Sea-land sedimentary silt	40	5.2
③	Marine deposit	Mud	70	31.8
④	Alluvium	Round gravel containing clay	300	2.7
⑤	Completely decomposed granite	Sandy silt, silty sand	450	7.8

TABLE 2 Physical and mechanical properties of the soil.

Soil no.	Cohesion (kPa)	Friction angle (°)	Wet density (g/cm^3)	Young's modulus (Pa)	Poisson ratio
①	0	34	1.65	1e7	0.35
②	8.4	0.5	1.59	0.3e6	0.46
③	13.6	6.8	1.69	8e6	0.32
④	3.0	32	2.05	5.2e8	0.30
⑤	60	45	2.25	1e9	0.30

and Ilamparuthi, 2018; Ong, 2018; Madhumathi and Abisha, 2020; Li et al., 2021), and piles close to surcharge (Bransby and Springman, 1996; Bai et al., 2022). The interaction between piles and moving soil is very complicated. For the bridge pile adjacent to an embankment to be built, the pile may face the following challenges: 1) the external vertical loads (for example, superstructure objects and vehicles) applied to the pile head, 2) external lateral loads (for example, wind load and earthquake load) applied to the pile head (that is, active loading), and 3) the additional soil pressures acting on the pile shaft due to the surcharge (that is, passive loading).

Several studies have been conducted to evaluate the lateral response of the pile adjacent to surcharge loading, such as laboratory tests (Al-abboodi et al., 2020; Karkush et al., 2020; Karkush and Jaffar, 2020; Toma Sabbagh et al., 2020), finite element method (Xu and Poulos, 2001; Karim, 2013; Al-abboodi and Sabbagh, 2019), and theoretical approach (Springman, 1989; Zhang et al., 2020a; Bellezza, 2020; Zhang et al., 2020b). The laboratory tests, numerical method, and theoretical analysis (Chen and Poulos, 1997; Ellis and Springman, 2001; Abo-Youssef et al., 2021; Ramalakshmi, 2021) proved that the effect of movement soil would lead to large deformation or even failure of the pile. However, numerical models, laboratory tests, and theoretical derivation wherein unidentified in actual conditions (properties of soil and shape of stratum) might not entirely reflect the field's authenticity and directly calibrate the results. Field monitor in actual cases is an effective and reliable method to analyze the soil-pile interaction caused by the surcharge. Field data can be used to investigate the interaction effect of soil–piles–surcharge and support the design procedure.

The mechanical behavior of passively loaded piles with nearby inclined bedrock was tested in the laboratory, and the result concluded that under the low load condition, the pile far from the load boundary was mainly in a tensile state (Xie et al., 2018). Heyman (1965) adopted the resistance strain gauges to record the pile's displacement and stress and roughly used the pile's displacement to estimate the pile's bending moment. The error between the test and the calculated bending moment was 20%. Nicu et al. (1971) measured the lateral displacement of six piles and the abutment on 13.5 m thick hard clay and found that the undrained shear strength of soft soil equaled three times the limit value of the abutment. Karkush and Kareem (2021) studied the behavior of axially loaded piles in contaminated clay soil adjacent to the construction of embankments, finding that the increase of embankment settlement led to the increase of lateral displacement of the soil surface. Poulos (1972) listed different engineering cases and showed that the measured settlement is consistent with the settlement predicted by FEM. The predicted displacement was much more sensitive than the vertical displacement, and the predicted value at the foot of the subgrade slope was even more than 1.5 times the measured value. Tavenas et al. (1979) analyzed the lateral displacement of soft soil during the construction and consolidation of 21 embankments. The results showed that the magnitude of the lateral displacement was very difficult to predict when the

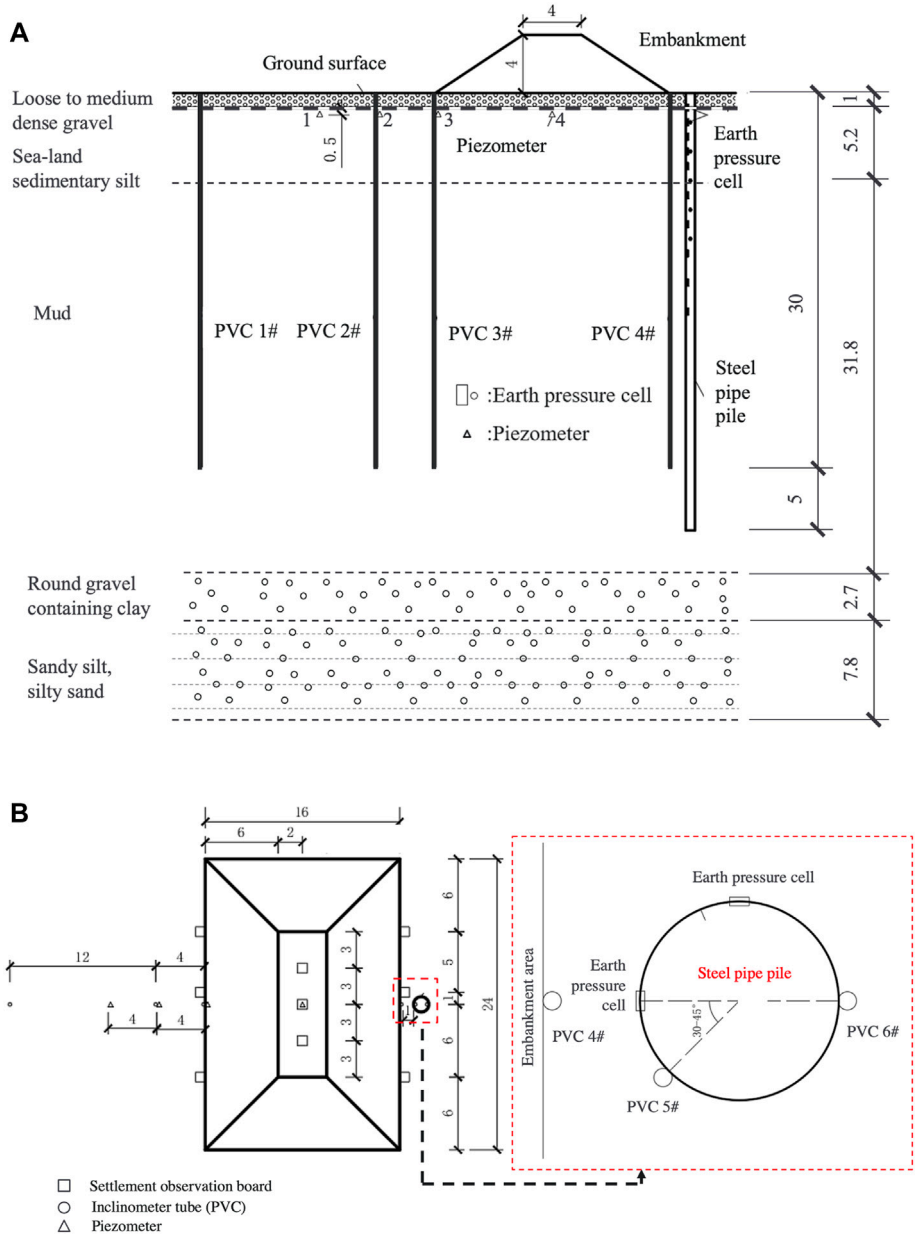

FIGURE 1
Instrumentation layout of the field test: **(A)** sectional view and **(B)** plan view (unit: m).

construction was completed. It depended mainly on the drainage of the foundation, the geometric characteristics, the mechanical properties, the loading rate, and the consolidation rate.

The field test was important for the analysis of passively loaded piles. The construction of railway and highway embankments has a significant influence on the behavior of existing pile foundations, especially in the situation of high embankments and extensively soft soils, which are commonly encountered in coastal areas. The mechanism of soil–pile interaction due to the construction of the embankment in extensively soft soils was not fully understood and needed further investigation. The high embankment might produce large lateral movement and bending moment to the existing adjacent piles, which would cause the failure of the pile if the surcharge loading is not properly considered. A field test was designed and performed to investigate the effect of lateral surcharge loading on the existing adjacent pile in extensively soft soils. The deformation of the pile and the soft soils, the excess pore water pressure, and lateral earth pressures were measured during the surcharge loading test and presented as follows.

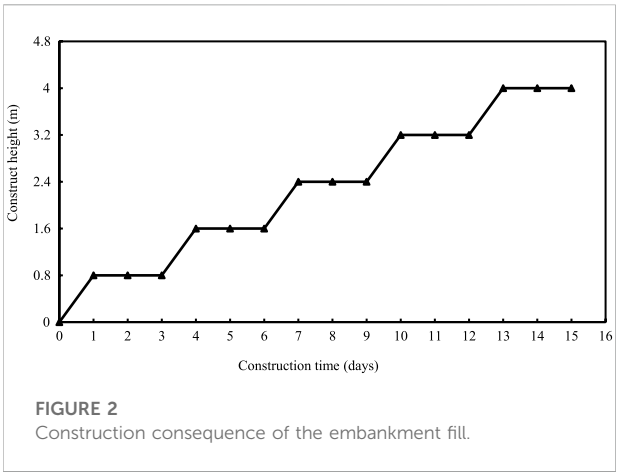

FIGURE 2
Construction consequence of the embankment fill.

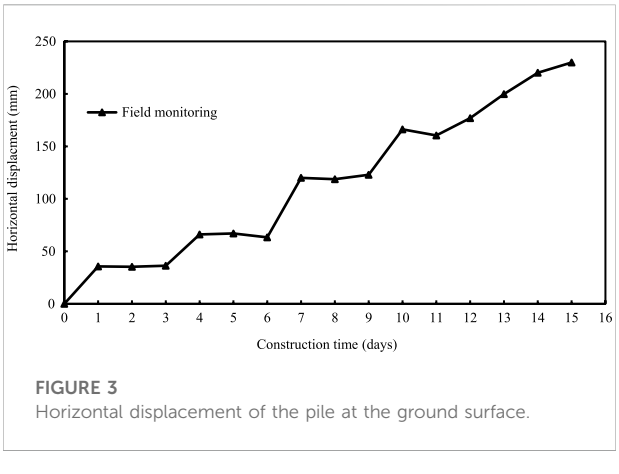

FIGURE 3
Horizontal displacement of the pile at the ground surface.

Project overview

The field test was performed in Guangdong Province, China. The region represented the geological characteristic of the Pearl River Delta alluvial plain in the coastal area of South China. This region is typically composed of farmland, ponds, and rivers. Pile foundations with elevated caps for the bridge are commonly used to solve the geotechnical problems in this region. Table 1 shows the geological profiles based on borehole logs. The soil is mainly composed of fill, marine deposits, alluvium, and completely decomposed granite. The soft soil with a large thickness was distributed in the whole field for this project. Table 2 shows the physical properties of the soil based on experimental tests.

Instrumentation and measurement

The test pile was a steel pipe pile with an outer diameter of 610 mm, a wall thickness of 10 mm, and a length of 35 m. The bottom of the pile was open for the convenience of piling construction. The bending stiffness of the steel pipe pile used in the field test was 1.611×10^9 N/m^2. Figure 1 shows the instrumentation layout of the field test. The area of the embankment fill was 24 m in length and 16 m in width. The slope gradient of the fill was 1:1.5. In order to investigate the response of pile foundations under lateral surcharge loading, a 4 m high embankment was constructed in five lifts (each lift was 0.8 m thick) close to an existing single pile. The deformation of the pile and the soft soils, the excess pore water pressure, and lateral earth pressures were measured during the surcharge loading test. The detail of the instrumentation and the test procedures were as follows.

1) The vibration piling method was used in the field test to ensure that the pile penetrated the extensively soft soil. The steel pipe pile was 35 m long, and the bottom of the pile floated in the mud soil.
2) Four inclinometer tubes (PVCs) were installed at different distances from the fill in the foundation soil (with a label of 1#, 2#, 3#, and 4#, respectively, from left to right, as shown in Figure 1, to measure the lateral movement of the soil. In addition, two inclinometer tubes (PVCs) were constructed along the outer surface of the steel pipe pile to measure the horizontal displacement of the pile (with labels of 5# and 6#, as shown in Figure 1). The length of each PVC tube was 30 m. The outer and inner diameters of the tube were 70 and 60 mm, respectively. After the installation of the inclinometer tubes, the initial readings were measured before the construction of the embankment fill.
3) A total of 15 earth pressure cells were installed at the surface of the steel pipe pile at different depths. The test surface of the earth pressure cells was kept flush with the outer surface of the pile in order to measure the lateral earth pressure accurately. The earth pressure cell was supported by a rigid bracket welded on the steel pipe. The earth pressure cell contained precise test elements and some necessary protection measures that were taken to reduce the vibration effect during the piling construction of the steel pipe pile. Figure 1 shows that ten Earth pressure cells were installed in the direction facing the embankment. Five earth pressure cells within a depth of 5 m were located with a vertical interval of 1 m. Other earth pressure cells were located with a vertical interval of 2 m. At the normal direction of the steel pipe pile, five earth pressure cells were installed in the vertical direction with an interval of 2 m.
4) The pore-water pressure transducers (PPTs) were buried in soft soil at four locations with a depth of 1.5 m from the ground surface. The PPT was put into the hole formed by drilling equipment, and the holes were filled with fine sand. The data acquisition system was connected and recorded the pore water pressures automatically. The initial reading was measured before the construction of the embankment fill.
5) The total station and level instrument were used to measure the horizontal displacement of the pile and the vertical deformation of the ground surface, respectively. The marks were set at the corresponding locations of the pile and the

TABLE 3 Comparison of the increment of the horizontal displacement measured by different methods.

Construction sequence	1st lift	2nd lift	3rd lift	4th lift	5th lift
The inclinometer (mm)	36.3	30.7	55.9	54.0	53.0
The total station (mm)	32.6	26.1	58.7	47.7	43.8
Error (%)	−10.2	−15.0	5.0	−11.7	−17.4

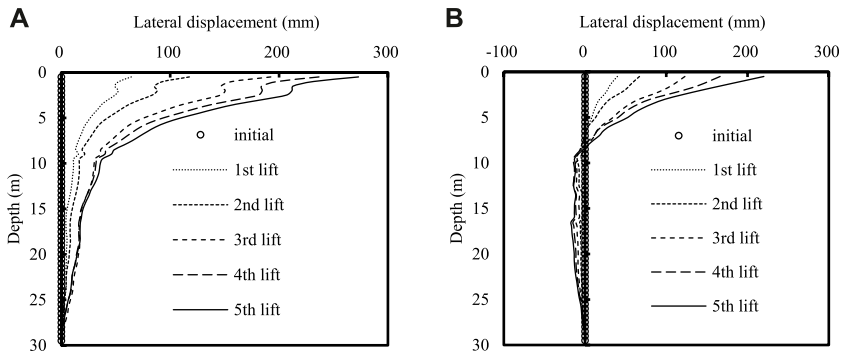

FIGURE 4
Horizontal displacement along the pile depth measured by **(A)** PVC 5# and **(B)** PVC 6#.

ground surface. Nine settlement observation plates with an area of 40 cm × 40 cm were placed at different locations. Three plates were placed at the top surface of the embankment. Three plates were placed on the embankment toe close to the pile. Three plates were placed on the embankment toe far away from the pile.

After the construction of the steel pipe pile and the instrumentation, the embankment fill was placed in five lifts. Each lift was compacted and had a thickness of 0.8 m. Figure 2 shows the construction consequence of the embankment fill. The embankment height was kept constant for three days, and the next lift was placed on the top of the embankment. The deformation of the pile and the soft soils, the excess pore water pressure, and lateral earth pressures were measured and recorded at different embankment heights. This procedure would be repeated until the embankment height reached 4 m.

Results and discussion

Horizontal displacement of the pile

Figure 3 shows the horizontal displacement of the pile at the ground surface obtained by the inclinometer (PVC 6#). The horizontal displacement of the pile increased with the increase of the embankment height. The horizontal displacement increased rapidly after the placement of a new lift. The displacement then remained relatively constant during the observation period of three days for the first three lifts. The pile was capable of withstanding the lateral surcharge loading. However, the horizontal displacement of the pile continued to increase with time and could not maintain constant when the embankment height reached 3.2 m. After the construction of five lifts, the horizontal displacement of the pile rapidly increased with time and showed an unstable state. The observed maximum horizontal displacements of the pile under each lift were 36.3, 67.0, 122.9, 176.9, and 229.9 mm, respectively.

The horizontal displacement of the pile measured by the total station was compared with that measured by the inclinometer. Table 3 illustrates the increment of the horizontal displacement under each lift. It can be seen that the results measured by different methods were relatively close, and the maximum error was −17.4%, which was acceptable in the field investigation. The error of the horizontal displacement measurement was defined as follows.

$$Error = \frac{Value\ of\ the\ total\ station - Value\ of\ the\ \text{inclinometer}}{Value\ of\ the\ \text{inclinometer}} \times 100\% \quad (1)$$

The embankment construction caused the stress redistribution and displacement of the pile and soil caused,

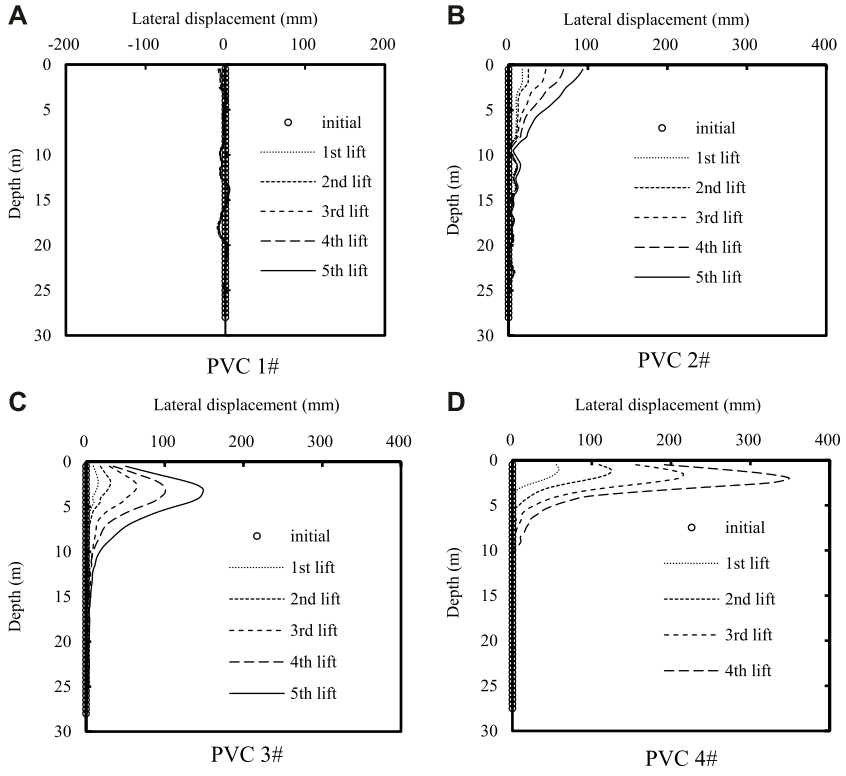

FIGURE 5
Horizontal displacement of the soil measured by **(A)** PVC 1#, **(B)** 2#, **(C)** 3#, and **(D)** 4# with depth under different surcharge loading stages.

which would make the pile–soil interaction more complicated if the lift was close to the pile. The embankment produced a vertical load on the ground surface and resulted in the displacement of the soil moving away from the surcharge area. The soil movement would apply additional pressure on the pile. The horizontal displacement of the pile depended on the lateral movement of the soil and was time-dependent, as shown in Figure 3. The movement of the soil was also time-dependent and would result in a continuous increase in pile displacement (Abo-Youssef et al., 2021). The observed results in this field investigation demonstrated that the pile close to the surcharge failed after the fourth lift (the construction time of the 11th day).

Pile bending

The inclinometer of the PVC 5# and 6# were used to investigate the horizontal displacement along the pile depth. Figure 4 shows that the horizontal displacement of the pile was significant with the increase of the load for both PVC 5# and 6#. The horizontal displacement of the pile decreased rapidly along the pile depth at each surcharge loading. The data measured by PVC 5# showed that the major displacement occurred within a depth of 10 m. The horizontal displacements of the pile at the ground surface measured by PVC 5# were 64.3, 117.6, 192.5, 236.7, and 273.0 mm, respectively, corresponding to each surcharge loading. The data measured by PVC 6# showed some difference compared with the data from PVC 5#. The horizontal displacement of the pile decreased rapidly with the increase of the depth in the shallow layer of about 7.5 m. The horizontal displacements of the pile at the ground surface measured by PVC 5# were 39.8, 67.0, 122.9, 166.2, and 220.1 mm, respectively, corresponding to each surcharge loading.

It is of note that the pile bending developed since the first surcharge loading. Figure 4 shows that PVC 6# occurred in a contraflexure, and the main positive displacement developed for the depth of 7.5 m. The PVC 5# did not occur in the contraflexure, and the main region of displacement exceeded 7.5 m to the deeper position. The aforementioned difference was caused by the different installation locations of the PVC. The PVC 5# was installed on the opposite side of the pile, which was different from the location of PVC 6# (as shown in Figure 1). The PVC 5# may develop additional bending and movement during each surcharge loading. The soil movement forced the pile to

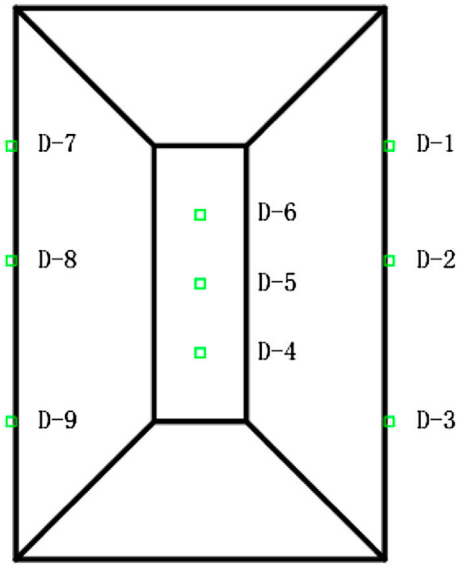

FIGURE 6
The location of settlement observation plates.

carry additional lateral earth pressure, which caused the unexpected lateral deformation of the PVC.

Lateral displacement of the soft soil

Figure 5 shows the horizontal displacement of the soil measured by PVC 1#, 2#, 3#, and 4# at different locations. The horizontal displacement of the soil was more significant with the increase of the load at the location of PVC 2#, 3#, and 4#. The horizontal displacement of the soil measured by PVC 2# decreased with the increase of the depth. The horizontal displacement of the soil measured by PVC 3# and PVC 4# increased with the increase of the depth for the shallow layers (the depth varied from 2 to 4 m) and then decreased with the increase of the depth. The horizontal displacement of the soil measured by PVC 1# changed slightly with the increase of the load. The displacement measured by PVC 1# and 4# showed negative values. The maximum value of the displacement measured by PVC 1# was −9.6 mm, which indicated that the effect of the surcharge loading was negligible for the soil far away from the center of the loading area (the distance was 24 m in this case). The horizontal displacements at the location of PVC 2# developed the maximum value at the ground surface and were 17.3, 25.1, 47.0, 69.2, and 93.7mm, respectively, for different surcharge loading stages. The maximum displacements of the soil measured by PVC 3# and 4# were 148.2 and 348.8mm, respectively.

Figure 5 shows that the lateral displacement of the soil at the edge of the surcharge loading area was larger than that for the soil far away from the surcharge and was smaller for the soil closer to the ground surface (the location of PVC 3# and 4#). The displacement increased with the decrease of the distance from the loading area in the sequence of PVC 1#, 2#, and 3#. The displacement measured by PVC 4# was larger than other locations measured by PVC 1#, 2#, and 3#. The pile provided more resistance to the earth pressure which was caused by soil movement and surcharge loading. The lateral thrust of the soil could not be neglected for the design of the passively loaded pile. The shape of the displacement profile in the PVC 3# was different from the profile of the PVC 2#, which indicated that the movement of soil diffused outward with the increase of the distance between the soil and the loading area.

Settlement of the embankment

The settlement of the embankment during construction was monitored by nine settlement observation plates placed at different locations. Figure 6 shows the location of settlement observation plates. Three plates were placed at the top surface of the embankment fill. Three plates were placed at the embankment toe close to the pile. Three plates were placed at the embankment toe far away from the pile. Figure 7 shows the settlement of the embankment versus construction time at different loading stages. The settlement at the center of the loading area (D-4, D-5, and D-6) increased with the increase of the embankment height. On the contrary, the soil on both sides of the surcharge area developed negative settlement (the soil heave) and the deformation changed with time irregularly. The average settlement of D-4, D-5, and D-6 was 0.2, 13.7, 22.5, 46.0, and 64.2 cm, respectively, for different surcharge loading stages. The maximum heave height for the side without steel pipe pile (D-7, D-8, and D-9) and with steel pipe pile (D-1, D-2, and D-3) were 29.4 and 77.2 cm, respectively, after the completion of the embankment construction. The vertical deformation of the embankment soil was significant compared with the lateral movement of the soil. The soil at the center of the loading area showed downward vertical deformation. The soil at the edge of the loading area showed upward vertical deformation. The maximum vertical deformation occurred at the edge with the steel pipe pile and was larger than the settlement at the center of the loading area. The existence of the steel pipe pile constrained the lateral movement of the soft soil; therefore, the soil close to the pile moved upward and resulted in larger heave deformation than the soil on the other side without the pile.

Excess pore-water pressure

The water table of the site was 1 m below the ground surface. The excess pore-water pressure (EPP) of the soil was measured by the pore-water pressure transducers (PPTs), which were buried

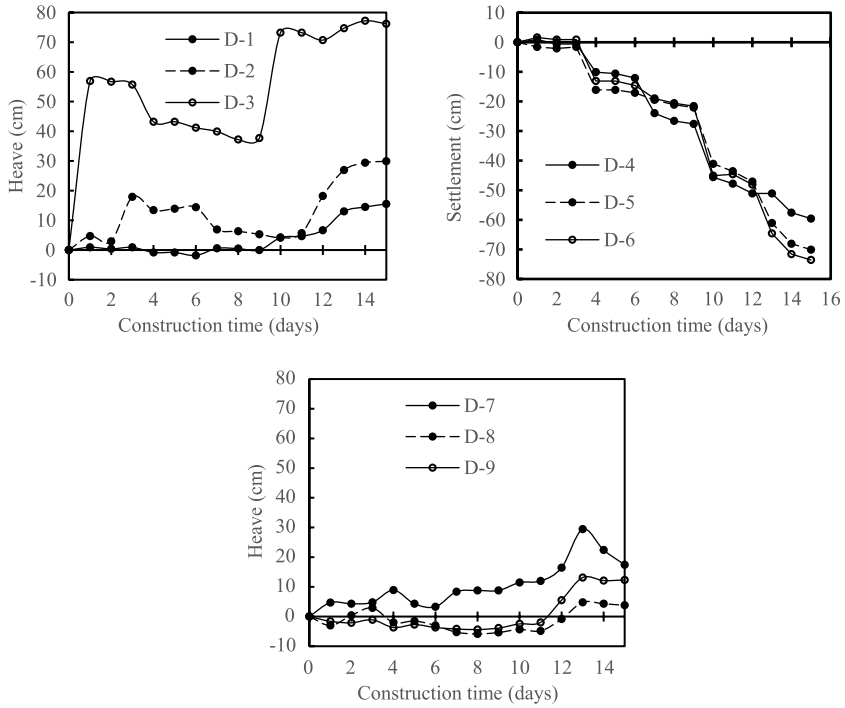

FIGURE 7
Settlement of the embankment versus construction time at different loading stages.

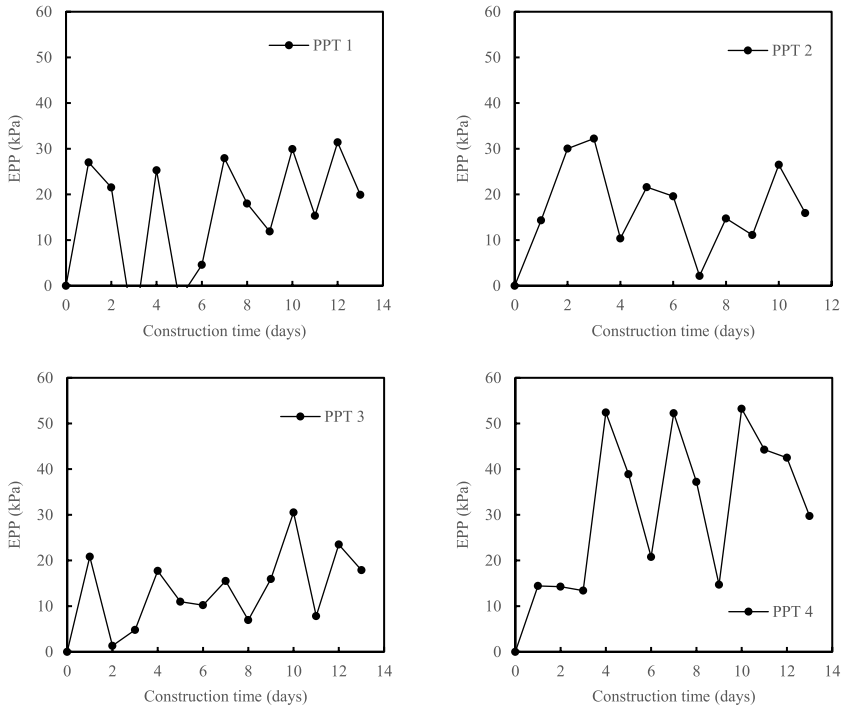

FIGURE 8
Excess pore-water pressure (EPP) of the soil versus the construction time.

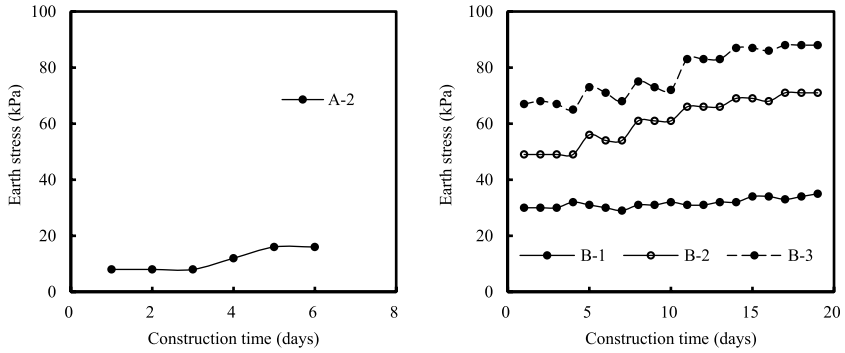

FIGURE 9
The lateral earth pressure at different pile depths versus the construction time.

in soft soil at four locations with a depth of 1.5 m from the ground surface. The location of PPTs was presented in Figure 1. Figure 8 shows the value of the EPP measured by PPTs varied with time. It can be seen from Figure 8 that the EPP increased rapidly after the placement of each lift and then gradually dissipated with time before the next lift. The PPT 4# was located in the center of the loading area and was significantly affected by the surcharge loading. Its maximum value of EPP reached 52 kPa for the placement of the second to the fourth lift. The dissipation of the EPP with the time was obvious for each placement of the lift. The rapid increase of the EPP indicated that the soft soil carried additional vertical stress due to the surcharge loading, which would result in the shear failure of the foundation soil if the surcharge loads was inappropriately high or the dissipation of the EPP was not well considered in the embankment construction.

Lateral earth pressure on the pile

The lateral earth pressure that acted on the pile was measured by the earth pressure cells installed in the steel pipe pile (as presented in Figure 1). Ten earth pressure cells directly facing the surcharge were labeled as A-1 to A-10 and located along the pile depth. Five earth pressure cells were labeled as B-1 to B-5 in the normal direction. Some earth pressure cells did not work properly during the test due to construction damages and complicated measurement environments. Figure 9 shows test results of the lateral earth pressure at different pile depths versus the construction time. A-2 was buried at a depth of 2 m. Its initial earth pressure (measured before the first lift) was 8 kPa and increased to 16 kPa after the placement of the first lift. A-2 was damaged, and there was no more reading. The depth of the B-1, B-2, and B-3 were 2, 4, and 6 m, respectively, in another direction. The initial earth pressure for the B-1, B-2, and B-3 were 32, 49, and 65 kPa, respectively. The earth pressure increased with the increase of the embankment thickness for the B-1, B-2, and B-3. The earth pressures of the B-1 were 29, 32, 32, 34, and 35 kPa, respectively, for the placement of each lift. The change of earth pressure at this location was small due to the increase of the surcharge load. The earth pressures of the B-2 were 54, 61, 66, 68, and 71 kPa, respectively, for the placement of each lift. The earth pressures of the B-3 were 68, 72, 83, 86, and 88 kPa, respectively, for the placement of each lift. The earth pressure of B-2 and B-3 changed obviously with the increase of the surcharge load. The earth pressures eventually increased up to 3, 22, and 23 kPa, respectively, for the B-1, B-2, and B-3 after the completion of the embankment construction. The increased lateral earth pressure put additional horizontal loads on the steel pipe pile, which caused a disadvantageous situation for the pile foundation.

Conclusion

In this research study, an embankment of 4.0 m in thickness was constructed in five lifts to investigate the performance of the steel pipe pile under lateral surcharge loading. The deformation of the pile and the soft soils, the excess pore-water pressure, and lateral earth pressures that acted at the pile were measured during the test. Based on the results obtained from the field test, the following conclusions were drawn:

1) The maximum horizontal displacement of the pile reached 229.9 mm due to the surcharge loading. The displacement increased rapidly and was unable to maintain for the fourth and fifth lifts. The lateral displacement decreased along with the pile depth. The displacement was relatively small when the pile depth exceeded 10 m.
2) The lateral displacement of the soft soil increased with the decrease of the distance from the loading area. The influence area of a 4 m high embankment surcharge in this field test

was about 24 m from the surcharge center based on the consideration of the negligible lateral displacement of the soil.

3) The surcharge loading zone developed downward vertical displacement (settlement), while the soft soils at the edge of the loading zone developed upward vertical displacement (heave deformation). The maximum vertical deformation occurred at the edge with the steel pipe pile and was larger than the settlement at the center of the loading area.
4) The excess pore-water pressure changed regularly with the construction of each lift, and the maximum value reached 53.6 kPa. The lateral earth pressures that acted on the pile continuously increased with the increase of the embankment height, which caused large deformation of the pile.

Data availability statement

The original contributions presented in the study are included in the article/Supplementary Material; further inquiries can be directed to the corresponding author.

Author contributions

SY was the first author and was in charge of the field test and analysis. JL was the corresponding author and was in charge of the test plan and writing.

Conflict of interest

Authors SY and JL were employed by the Guangzhou Metro Design & Research Institute Co., Ltd.

Publisher's note

All claims expressed in this article are solely those of the authors and do not necessarily represent those of their affiliated organizations, or those of the publisher, the editors, and the reviewers. Any product that may be evaluated in this article, or claim that may be made by its manufacturer, is not guaranteed or endorsed by the publisher.

References

Abo-Youssef, A., Morsy, M. S., ElAshaal, A., and ElMossallamy, Y. M. (2021). Numerical modelling of passive loaded pile group in multilayered soil. *Innov. Infrastruct. Solut.* (6), 101. doi:10.1007/s41062-021-00464-6

Al-abboodi, I., Sabbagh, T. T., and Al-salih, O. (2020). Response of passively loaded pile groups-an experimental study. *Geomechanics Eng.* 20, 333–343.

Al-abboodi, I., and Sabbagh, T. T. (2019). Numerical modelling of passively loaded pile groups. *Geotech. Geol. Eng. (Dordr).* 2747 (37), 2747–2761. doi:10.1007/s10706-018-00791-z

Bai, Bing, Nie, Qingke, Zhang, Yike, Wang, Xiaolong, and Hu, Wei (2021). Cotransport of heavy metals and SiO_2 particles at different temperatures by seepage. *J. Hydrology* 597, 125771. doi:10.1016/j.jhydrol.2020.125771

Bai, Bing, Wang, Yan, Rao, Dengyu, and Fan, Bai (2022). The effective thermal conductivity of unsaturated porous media deduced by pore-scale SPH simulation. *Front. Earth Sci. (Lausanne).* 10. doi:10.3389/feart.2022.943853

Bai, Bing, Zhou, Rui, Cai, Guoqing, Hu, Wei, and Yang, Guangchang (2021). Coupled thermo-hydro-mechanical mechanism in view of the soil particle rearrangement of granular thermodynamics. *Comput. Geotechnics* 137 (8), 104272. doi:10.1016/j.compgeo.2021.104272

Bellezza, I. (2020). Closed-form expressions for a rigid passive pile in a two-layered soil. *Géotechnique Lett.* 242 (10), 242–249. doi:10.1680/jgele.19.00250

Bransby, M., and Springman, S. (1996). 3-D finite element modelling of pile groups adjacent to surcharge loads. *Comput. Geotechnics* 19, 301–324. doi:10.1016/0266-352x(95)00001-q

Chen, L., and Poulos, H. (1997). Piles subjected to lateral soil movements. *J. Geotech. Geoenviron. Eng.* (123), 802–811. doi:10.1061/(asce)1090-0241(1997)123:9(802)

Ellis, E., and Springman, S. (2001). Full-height piled bridge abutments constructed on soft clay. *Geotechnique* (51), 3–14. doi:10.1680/geot.2001.51.1.3

Heyman, L. (1965). *Measurement of the influence of lateral earth pressure on pile foundations*. Toronto: Soil Mech & Fdn Eng Conf Proc/Canada/.

Ito, T., Matsui, T., and Hong, W. P. (1982). Extended design method for multi-row stabilizing piles against landslide. *Soils Found.* (22), 1–13. doi:10.3208/sandf1972.22.1

Karim, M. R. (2013). Behaviour of piles subjected to passive subsoil movement due to embankment construction – a simplified 3D analysis. *Comput. Geotechnics* 1 (53), 1–8. doi:10.1016/j.compgeo.2013.04.004

Karkush, M. O., Aljorany, A. N., and Jaffar, G. S. (2020). Behavior of passive single pipe pile in sandy soil. *IOP Conf. Ser. Mat. Sci. Eng.* (737), 012106. doi:10.1088/1757-899x/737/1/012106

Karkush, M. O., and Jaffar, G. S. (2020). Simulation the behavior of passive rigid pile in sandy soil. *J. Eng. Technol. Sci.* 449 (52), 449–467. doi:10.5614/j.eng.technol.sci.2020.52.4.1

Karkush, M. O., and Kareem, Z. A. (2021). Investigation the impacts of fuel oil contamination on the behaviour of passive piles group in clayey soils. *Eur. J. Environ. Civ. Eng.* 485 (25), 485–501. doi:10.1080/19648189.2018.1531790

Li, H., Liu, S., Yan, X., Gu, W., and Tong, L. (2021). Effect of loading sequence on lateral soil-pile interaction due to excavation. *Comput. Geotechnics* 104134 (134). doi:10.1016/j.compgeo.2021.104134

Madhumathi, R., and Abisha, R. (2020). Experimental investigation of axially loaded pile group subjected to ground movement. *Mater. Today Proc.* 2238 (24), 2238–2243. doi:10.1016/j.matpr.2020.03.750

Madhumathi, R., and Ilamparuthi, K. (2018). Laboratory study on response of single pile adjacent to supported cut. *Geotech. Geol. Eng. (Dordr).* 3111 (36), 3111–3133. doi:10.1007/s10706-018-0524-9

Nicu, N. D., Antes, D. R., and Kessler, R. S. (1971). "Field measurements on instrumented piles under an overpass abutment," in *Highway research record*.

Ong, D. (2018). Detrimental effects of lateral soil movements on pile behaviour. *Geotech. Eng.* 85 (49), 85–95.

Poulos, H. (1994). Effect of pile driving on adjacent piles in clay. *Can. Geotech. J.* 31, 856–867. doi:10.1139/t94-102

Poulos, H. G., and Chen, L. T. (1997). Pile response due to excavation-induced lateral soil movement. *J. Geotech. Geoenviron. Eng.* (123), 94–99. doi:10.1061/(asce)1090-0241(1997)123:2(94)

Poulos, H. G. (1972). Difficulties in prediction of horizontal deformations of foundations. *J. Soil Mech. Found. Div.* 843 (98), 843–848. doi:10.1061/jsfeaq.0001774

Ramalakshmi, M. (2021). Force-displacement response of bridge abutments under passive push. *Mater. Today Proc.* 883 (43), 883–887. doi:10.1016/j.matpr.2020.07.202

Springman, S. M. (1989). *Lateral loading on piles due to simulated embankment construction*. Cambridge, United Kingdom: University of Cambridge.

Tavenas, F., Mieussens, C., and Bourges, F. (1979). Lateral displacements in clay foundations under embankments. *Can. Geotech. J.* 16, 532–550. doi:10.1139/t79-059

Toma Sabbagh, T., Al-Salih, O., and Al-Abboodi, I. (2020). Experimental investigation of batter pile groups behaviour subjected to lateral soil movement in sand. *Int. J. Geotechnical Eng.* 14, 705–716. doi:10.1080/19386362.2019.1585596

Xie, Y., Zhang, S.-h., and Zhou, D.-q. (2018). Experimental study of mechanical behavior of passive loaded piles adjacent to piled foundation. *KSCE J. Civ. Eng.* 3818 (22), 3818–3826. doi:10.1007/s12205-018-0565-x

Xu, K., and Poulos, H. (2001). 3-D elastic analysis of vertical piles subjected to "passive" loadings. *Comput. Geotechnics* (28), 349–375. doi:10.1016/s0266-352x(00)00024-0

Zhang, H., Shi, M., and Guo, Y. (2020a). Semianalytical solutions for abutment piles under combined active and passive loading. *Int. J. Geomech.* 20, 04020171. doi:10.1061/(asce)gm.1943-5622.0001804

Zhang, H., Shi, M., Yang, L., and Guo, Y. (2020b). A semianalytical solution for passively loaded piles adjacent to surcharge load. *Adv. Civ. Eng.* 1 (2020), 1–19. doi:10.1155/2020/2398389

frontiers | Frontiers in Materials

TYPE Original Research
PUBLISHED 23 August 2022
DOI 10.3389/fmats.2022.980851

Check for updates

OPEN ACCESS

EDITED BY
Xianze Cui,
China Three Gorges University, China

REVIEWED BY
Xin Tan,
Hunan University, China
Xiaohui Sun,
Shenzhen University, China

*CORRESPONDENCE
Jie Yuan,
yuanj@gzhu.edu.cn

SPECIALTY SECTION
This article was submitted to Structural Materials,
a section of the journal
Frontiers in Materials

RECEIVED 29 June 2022
ACCEPTED 18 July 2022
PUBLISHED 23 August 2022

CITATION
Gu M, Mo H, Qiu J, Yuan J and Xia Q (2022), Behavior of floating stone columns reinforced with geogrid encasement in model tests.
Front. Mater. 9:980851.
doi: 10.3389/fmats.2022.980851

COPYRIGHT
© 2022 Gu, Mo, Qiu, Yuan and Xia. This is an open-access article distributed under the terms of the Creative Commons Attribution License (CC BY). The use, distribution or reproduction in other forums is permitted, provided the original author(s) and the copyright owner(s) are credited and that the original publication in this journal is cited, in accordance with accepted academic practice. No use, distribution or reproduction is permitted which does not comply with these terms.

Behavior of floating stone columns reinforced with geogrid encasement in model tests

Meixiang Gu[1], Haizhao Mo[2], Jianlin Qiu[3], Jie Yuan[4]* and Quan Xia[3]

[1]School of Civil Engineering, Guangzhou University, Guangzhou, China, [2]China Construction Fourth Engineering Division Corp. Ltd, Guangzhou, China, [3]School of Civil Engineering, Guangzhou University, Guangzhou, China, [4]School of Civil Engineering, Guangzhou University, Guangzhou, China

The bearing capacity and deformation characteristics of floating stone columns were complicated and are not thoroughly understood. In the present study, a series of experimental model tests of floating stone columns under vertical plate loading was performed. This study investigated the influence of geogrid encasement on the behavior of floating stone columns and provided valuable insight into the load-displacement behavior, bulging deformation, load transfer mechanism, and the radial stress of the geogrid encasement. The test results show that the bearing capacity of the floating stone column was significantly improved due to the geogrid encasement. The column with longer encasement showed higher stiffness at large settlements. The bulging deformation pattern of the column changed with different encasement lengths. More vertical pressure transferred from the top of the column to the bottom of the column due to the existence of the geogrid encasement. The fully encased stone columns developed high radial stress and achieved effective confinement of the column. The bearing capacities of the floating-encased stone columns with different encasement lengths were controlled by bulging deformation instead of penetration failure, which gave confidence that the floating-encased stone columns were an effective method for field construction in extensive soft soils.

KEYWORDS

geosynthetics, model tests, floating stone column, geogrid encasement, bulging deformation

Introduction

Stone columns were an effective ground improvement technique and were extensively used to deal with soft clay deposits by increasing bearing capacities, controlling settlements, and accelerating the consolidation rate (Han, 2015a; Han, 2015b). In geotechnical design and construction application, the column typically penetrated through the soft clay and rested on a strong stratum, which was called an end-bearing stone column. However, in the situation of vertically extensive soft soils (commonly encountered in coastal areas), it was unnecessary to penetrate through the entire soft soil deposits. The effective column length was suggested not to exceed 10 times

the column diameter based on the consideration of performance and economy. Therefore, the column may not reach a strong stratum and float in the soft clay deposits, which were called floating stone columns. In some instances, the construction of floating stone columns was found to be more economical and technically feasible than the end-bearing stone columns.

The ordinary stone columns may not be effective when soft soils are extremely weak (e.g., undrained shear strength less than 15 kPa). The surrounding soft soils may not provide sufficient confining pressure in the shallow depth. The stone column was likely to bulge and failed to carry additional loads. Geosynthetics (such as geogrid and geotextile) were introduced and used to reinforce the stone columns vertically. The geosynthetic encasement can provide additional confining pressure and improve the stiffness and bearing capacity of the columns (Bai et al., 2019; Bai et al., 2021; Bai et al., 2022; Gniel and Bouazza, 2010; Ghazavi and Afshar, 2013; Almeida et al., 2014; Chen et al., 2015; Zhang and Zhao, 2015; Gu et al., 2016; Chen et al., 2018; Gu et al., 2020; Tan et al., 2020).

However, most previous studies focused on either floating stone columns unreinforced with geosynthetics (Ng and Tan, 2014; Shahu and Reddy, 2014; Zhou et al., 2017; Ong et al., 2018; Shan et al., 2022; Zhao et al., 2021), or geosynthetic-encased stone columns that reached a strong stratum (Murugesan and Rajagopal, 2010; Pulko et al., 2011; Yoo and Lee 2012; Gu et al., 2017a; Gu et al., 2017b; Mohapatra and Rajagopal 2017; Schnaid et al., 2017; Kadhim et al., 2018; Kong et al., 2018; Zhou and Kong, 2019a; Zhou and Kong, 2019b; Zhang et al., 2020; Tan et al., 2021). There are limited studies on the performance of floating stone columns reinforced with geosynthetic encasement. Ali et al. (2012) carried out model tests on floating and end-bearing stone columns and found that the full column length gives higher failure stress than encasement over the top half or quarter of the column length. Dash and Bora (2013) investigated the performance of end-bearing stone columns and floating stone columns reinforced with window-mesh encasement (the geosynthetic was called geomesh to model the geogrid). The material properties of the window-mesh were significantly different from those of the geogrid in terms of tensile stiffness and rib width. The widow-mesh was difficult to model the actual behavior of the geogrid, especially the interaction effect between the aggregates and the geogrid. Hasan and Samadhiya (2016) investigated the bearing capacities of vertical encased granular piles by experimental and numerical analysis. Sarvaiya and Solanki (2017) conducted experimental tests on floating stone columns with different encasement lengths. It was suggested that the full length of the encasement was not necessary based on the consideration of the columns' bearing capacity. Debnath and Dey (2017) suggested that the optimum column length and optimum encasement length of floating stone columns with a geogrid-reinforced sand bed were six and three times the diameter of the column, respectively, using finite element analyses. Kahyaoğlu and Vaníček (2019) presented the behavior of the embankment supported by floating-encased columns using the finite element method. The effect of the encasement stiffness, the basal reinforcement stiffness, and the embankment fill height was investigated. The effective encasement length depended on the surcharge and the strength properties of the column and the soil. Thakur et al. (2021) compared the load capacities of the vertically and horizontally reinforced floating stone columns in model tests. The results indicated that the fully encased stone column had a lower load capacity than the horizontal reinforced stone column using geotextile encasement.

The deformation and load transfer mechanisms were complicated for the floating stone columns reinforced with geogrid encasement and are not thoroughly understood. The bulging deformation controlled the bearing capacity of floating-ordinary stone columns (F-OSC, unreinforced with geosynthetics) if the column was sufficiently long. The failure mode of the floating-encased stone columns (F-ESC, reinforced with geogrid encasement) may change because the large bulging deformation would be limited to a relatively small value due to the geogrid encasement. Moreover, the interaction between the aggregates and the geogrid was important and needed to be investigated further. This study presented a series of model tests on floating stone columns under vertical incremental loads. The influence of geogrid encasement on the behavior of floating stone columns was investigated in terms of load-displacement behavior, bulging deformation, load transfer mechanism, and the radial stress of the geogrid encasement.

Description of the experiment

To investigate the behavior of floating stone columns reinforced with the geosynthetic encasement, a series of plate loading tests was conducted based on unit cell assumption. Table 1 summarizes the model test parameters. The thickness of the clay bed was kept at 1,000 mm in all tests and represents the situation of vertically extensive clay beds. Two parameters (i.e., the column length and the encasement length) were investigated and varied in different tests. The column length varied from 200–800 mm; therefore, the column was floated in the clay beds. The encasement length varied from 0–600 mm and represented the cases of floating-ordinary stone columns (F-OSC) and floating-encased stone columns (F-ESC). Figure 1 shows that the floating stone column was constructed in vertically extensive clay beds and subjected to vertical pressure.

Materials properties

The soft clay was obtained from a deep excavation project of a subway station in Guangzhou Higher Education Mega Center, located in the Pearl River Delta near the coastal areas of south

TABLE 1 Summary of model test parameters.

Test No.	Test type	Test description	Column length (mm)	Encasement length (mm)	Thickness of clay bed (mm)
1	Floating ordinary stone columns (without encasement)	F-OSC2D	200	0	1,000
2		F-OSC4D	400	0	1,000
3		F-OSC6D	600	0	1,000
4		F-OSC8D	800	0	1,000
5	Floating-encased stone columns (with encasement)	F-ESC6D-2D	600	200	1,000
6		F-ESC6D-4D	600	400	1,000
7		F-ESC6D-6D	600	600	1,000
8	Unreinforced clay	Clay	—	—	1,000

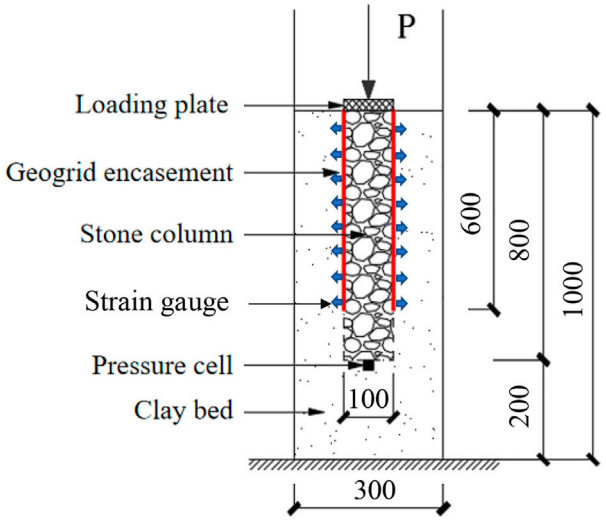

FIGURE 1
Plate loading test on floating-encased stone columns in vertically extensive clay beds.

TABLE 2 Properties of the soft clay.

Parameters	Value
Liquid limit	40%
Plastic limit	22%
Plastic index	18
Moisture content	36%
Specific gravity	2.7
Undrained shear strength (kPa)	4.1
USCS classification	CL

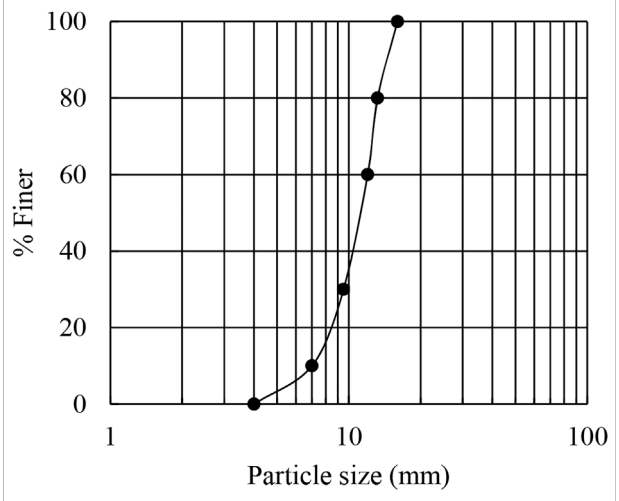

FIGURE 2
Particle size distribution of the aggregates.

China. The soil was classified as CL based on the USCS. Undrained triaxial tests were conducted to determine its undrained shear strength and the corresponding moisture content. Table 2 summarizes the detailed properties of soft clay. The aggregates used in the experimental test were angular crashed stones and Figure 2 shows the particle size distribution. The internal friction of the aggregates was determined as 42.9^0 at a relative density of 62%.

The tensile properties and rib dimension of the biaxial geogrid were carefully considered and properly modeled in the model test. A 1-mm thick polypropylene sheet was cut to the aperture size of 10 × 10 mm by using a laser cutting machine. The rib width of the geogrid was 5 mm in this study. The geogrid encasement was formed by rolling the geogrid sheet

TABLE 3 Tensile properties of the biaxial geogrid.

Parameters	Geogrid with cable ties	Geogrid without cable ties
Tensile strength at 1% elongation (kN/m)	2.69	2.82
Tensile strength at 2% elongation (kN/m)	4.51	4.74
Ultimate tensile strength (kN/m)	6.81	6.22
Secant stiffness at 1% elongation (kN/m)	269.1	282.2
Secant stiffness at 2% elongation (kN/m)	225.6	237.3

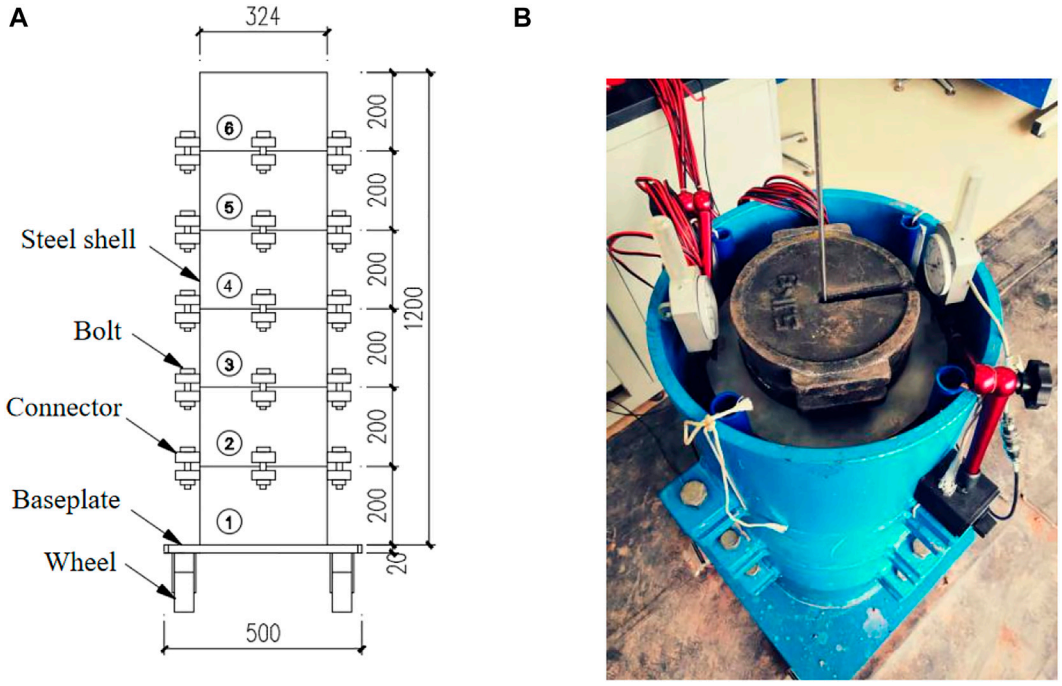

FIGURE 3
Testing set-up: **(A)** schematic of the test tank; **(B)** photograph of the plate loading test.

into a cylinder and fixed with nylon cable ties in the circumferential direction. Three rows of nylon cable ties were used at the joint interface to guarantee an effective connection. Multi-rib tensile tests were conducted for the geogrid samples with and without nylon cable ties according to ASTM D6637 standard (ASTM 2015). Secant stiffness can be calculated as $J = \frac{F}{\varepsilon}$, where F and ε are the tensile strength and the elongation of the geogrid, respectively. Table 3 shows the test results and tensile properties of the geogrid. The tensile strengths of the geogrid with and without nylon cable ties were close, which demonstrated that the connection method used to fix the joint interface was reliable and effective.

Preparation of floating-encased stone columns

A cylindrical steel tank was manufactured with an inner diameter and a height of 300 and 1,200 mm, respectively. To facilitate the preparation of the model test, the test tank was uniformly divided into six sections in height. Each section had a height of 200 mm and was connected with the neighboring sections by bolts. Figure 3 shows the testing setup of the model test. Plastic sheets were covered on the inner wall surface of the test tank to reduce friction at the soil–wall interface. The soft clay at a desired moisture content of 36% was filled into the tank by layers. Each layer had a

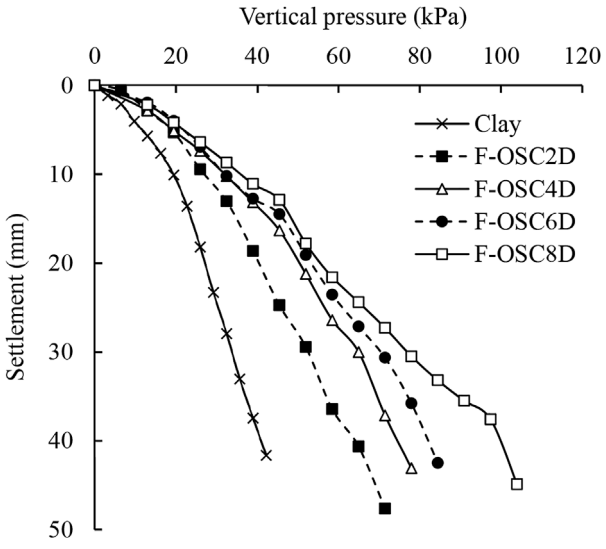

FIGURE 4
Load-displacement curve of floating-ordinary stone columns with different column lengths.

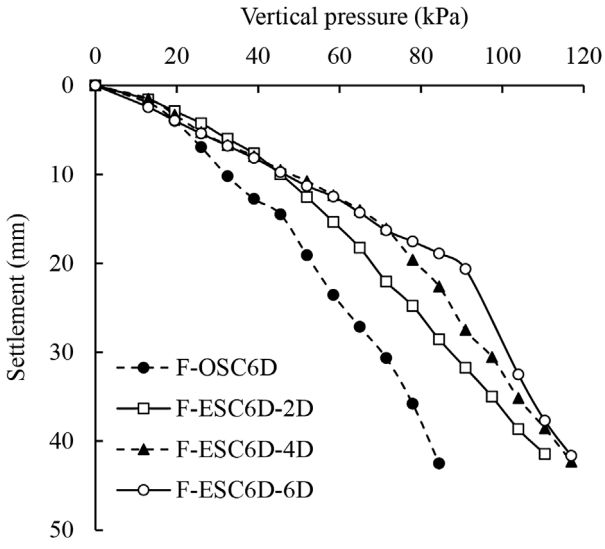

FIGURE 5
Load-displacement curve of floating-encased stone columns with different encasement lengths.

thickness of 50 mm and compacted uniformly. The test tank was covered with a plastic sheet to prevent water evaporation and stood for 3 days after the clay bed reached a thickness of 1,000 mm.

A replacement method was adopted for the construction of floating stone columns. An open-ended plastic pipe with an outer diameter of 100 mm was used and located at the center of the test tank. The bottom of the pipe was first placed on the surface of the soil instead of the bottom of the tank. In the case of a floating-ordinary stone column with a column length of 600 mm (F-OSC6D), the plastic pipe was placed on the soil after the clay bed reached a thickness of 400 mm. After the clay bed reached a thickness of 600 mm, the aggregates of the calculated amount were filled into the pipe to form the stone column 200 mm high and well compacted. The pipe was then pulled up gently by 100 mm in the vertical direction so that the pipe had a minimum embedment depth of 100 mm within the surrounding soil. The pipe was pulled up again after the next 200 mm thick soil was placed and the next stone column section was installed. The aforementioned procedure was repeated until the entire stone column was constructed. In the case of floating-encased stone columns, the geogrid encasement was slid down to the designed depth along the outer surface of the pipe. The encasement was kept in a fixed location during the pulling up of the pipe by additional downward resistance applied by hand and the interlock forces between the aggregates and the geogrid.

Load tests on stone columns

A plate loading test was performed on a single column using the maintained pressure test method. Vertical pressure was applied on the top of the column in 8–10 increments and measured by the mass of the standard weight. The pressure was maintained constant until the rate of the settlement was less than 0.1 mm/h and then the next pressure increment was applied. The loading test was terminated when the settlement exceeded 40 mm, where the vertical pressure may not be maintained and the column failed. Strain gauges were used to measure the hoop strains in the geogrid encasement. The strain gauges were oriented along the circumferential direction of the encasement and fixed onto the geogrid just after a cylindrical geogrid sleeve was formed. An earth pressure cell was installed at the bottom of the column to measure the pressure transferred to the bottom of the column.

Results and discussion

Load-displacement behavior

Figure 4 shows the load-displacement response of floating-ordinary stone columns with different column lengths. The bearing capacity of the clay bed was considerably improved by the F-OSC. The ultimate bearing capacity of the column was defined as the vertical pressure applied at the settlement of 20% of the loading plate diameter (i.e., 20 mm). The ultimate bearing

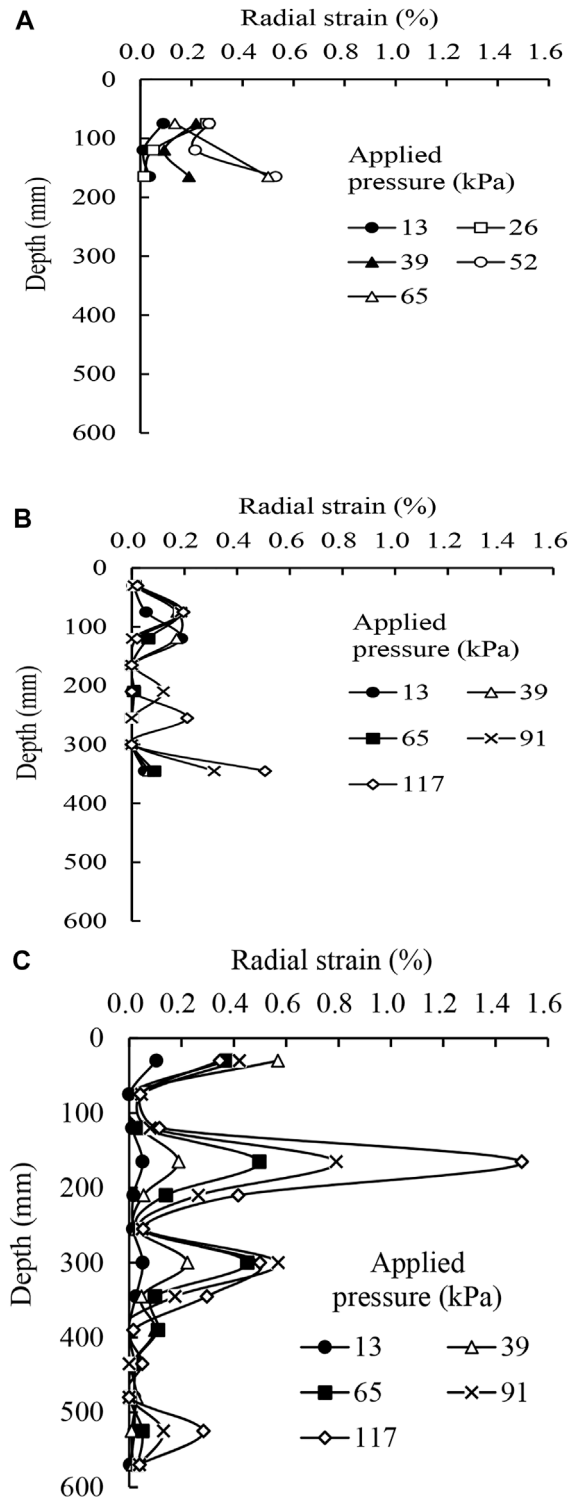

FIGURE 6
Bulging deformation of floating-encased stone columns with different encasement lengths: **(A)** 200 mm, **(B)** 400 mm, and **(C)** 600 mm.

capacity of the F-OSC was 40.4, 50.3, 53.3, and 55.7 kPa for the column lengths at 200, 400, 600, and 800 mm, respectively. The bearing capacity of the clay bed (e.g., 27.1 kPa at the same settlement) was improved by 1.9 times due to the existence of the F-OSC with a column length of 400 mm. It was observed that the bearing capacity may not be improved linearly with the increasing column lengths. The increment of the bearing capacity was small for the column length varying from 400 to 800 mm. An effective column length of 600 mm was determined in this study based on the consideration of the bearing capacity. Therefore, the floating stone column with a length of 600 mm was selected as a baseline case for the investigation of the influence of the geogrid encasement on floating stone columns.

Figure 5 shows the load-displacement response of floating-encased stone columns with different encasement lengths. The bearing capacity of the floating stone column was significantly improved due to the geogrid encasement. The ultimate bearing capacities of the F-ESC were 68.0, 78.8, and 88.5 kPa for the encasement lengths at 200, 400, and 600 mm, respectively. At the beginning loading stage (e.g., the settlement was less than 10 mm), the F-ESC with different encasement lengths showed similar vertical pressure-settlement behavior. The granular aggregates moved laterally and the column mobilized bulging deformation gradually at this stage. The column stiffness decreased with the increase in the settlement due to the discrete nature of the granular material. Figure 5 shows that the F-ESC with longer encasement maintained higher stiffness at large settlements. The fully encased column (F-ESC6D-6D) showed good bearing capacity and its stiffness began to decrease until the settlement reached 20 mm.

Bulging deformation

The strain gauges were attached to the surface of the geogrid encasement to measure the circumferential strains. The value of circumferential strains was equal to the radial strains of the column due to the axial symmetry of the cylindrical stone columns. Figure 6 shows the bulging deformation profiles of floating-encased stone columns with different encasement lengths subjected to vertical pressures.

Figures 6A,B show that the radial strain of the F-ESC increased with the applied pressure. The recorded maximum value of the radial strain was 0.53 and 0.51%, respectively, for the columns with the encasement length of 200 and 400 mm. The strain gauges in the F-ESC6D-2D test malfunctioned after the applied pressure exceeded 65 kPa; therefore, no more data were recorded in this test. Large radial strains happened near the base of the encasement sleeve in these two tests. The bulging deformation of the column in the reinforced section was limited due to the encasement. The unreinforced section (i.e., the column below the reinforcement base) may develop large bulging deformation. Bulging failure in

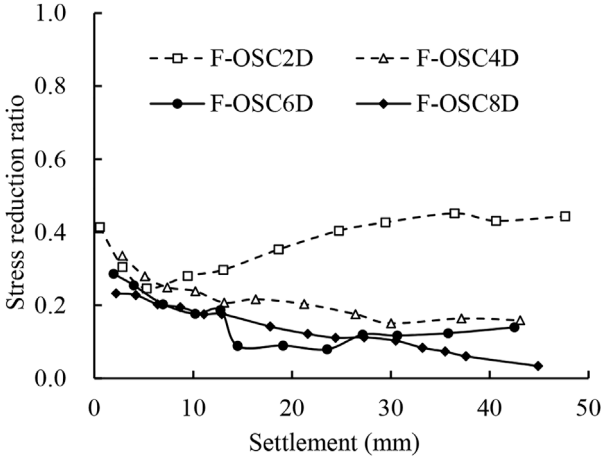

FIGURE 7
Stress reduction ratio of floating-ordinary stone columns with different column lengths.

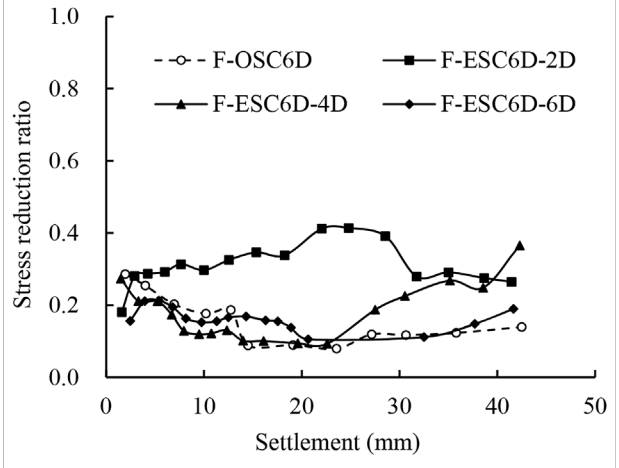

FIGURE 8
Stress reduction ratio of floating-encased stone columns with different encasement lengths.

the unreinforced section controlled the ultimate bearing capacity of the partially encased stone column, which was similar to that of the end-bearing encased stone column (Gu et al., 2016). The fully encased stone column (F-ESC6D-6D) shows a different bulging deformation pattern along the column depth. Figure 6C shows that large bulging deformation happened at a column depth of 165 mm instead of the base of the encasement sleeve. The recorded maximum value of the radial strain was 1.5%, which was close to the ultimate tensile strain of the geogrid. The column developed bulging failure in the upper reinforced section (within a depth of 2 times the column diameter), which was similar to that of the end-bearing encased stone column.

The bulging deformations of the partially and fully floating-encased stone column were similar to those of the corresponding end-bearing stone columns. This demonstrated that the floating-encased stone column was an effective and reliable method to improve the vertically extensive soft clay deposits.

Load transfer mechanism

To evaluate the applied pressure transferred from the top of the column to the bottom of the column, a ratio of the stress at the bottom to that at the top, referred to as the stress reduction ratio can be calculated. The pressure transferred to the bottom of the stone column was measured using the earth pressure cell installed at the bottom of the column. Figure 7 shows the stress reduction ratio plotted against the settlement for the floating ordinary stone columns with different column lengths. The stress reduction ratio was less than 0.5 for all tests. The value of the stress reduction ratio typically decreased with the increase in the settlement except for the case of F-OSC2D. The short column may penetrate the soft clay instead of bulging failure. The long column (e.g., F-OSC4D, F-OSC6D, and F-OSC8D) showed a smaller stress reduction ratio and less pressure transferred to the bottom of the column. The applied pressure transferred to the bottom of the long column was less than 20% after the column reached a settlement of 20 mm. The bulging deformation dominated the failure mechanism of the floating ordinary stone columns.

Figure 8 shows the stress reduction ratio plotted against the settlement for the floating encased stone columns with different encasement lengths. The stress reduction ratio of the encased stone column was higher than that of the ordinary stone column. The encased column had good stiffness due to the effective confinement provided by the encasement sleeve. More pressure was transferred from the top of the column to the bottom of the column. The stress reduction ratio of the fully encased stone column (e.g., F-ESC6D-6D) showed a similar trend with that of the ordinary stone column (e.g., F-OSC6D) because of their same location of bulging deformation. The bulging failure of these two columns both happened within a column depth of 2 times the column diameter. The partially encased column (e.g., F-ESC6D-2D and F-ESC6D-4D) showed a high stress reduction ratio at large settlements. A new shear zone developed in the bulging section (i.e., the unreinforced section below the reinforcement base); thus, the column acted like a pile and more pressure was transferred to the bottom.

Radial stress of the encasement

The circumferential strains of the geogrid encasement were measured by using strain gauges. The hoop force (T) provided by

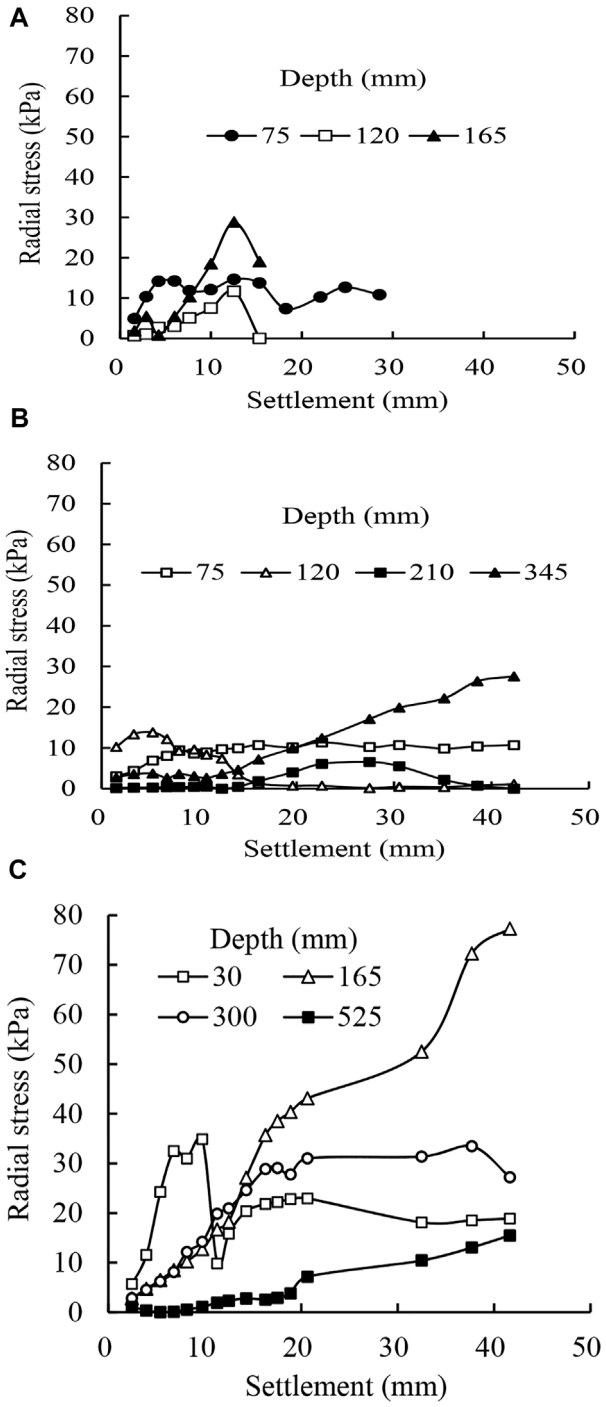

FIGURE 9
Radial stress of floating-encased stone columns with different encasement lengths: **(A)** 200 mm, **(B)** 400 mm, and **(C)** 600 mm.

the encasement can be calculated as $T = J\varepsilon$, where J and ε are the secant stiffness and radial strain of the geogrid encasement, respectively. The secant stiffness at 1 and 2% tensile strain was 269.1 and 225.6 kN/m, respectively. The radial stress (σ_r) provided by the geogrid encasement was then determined as , where r is the radius of the stone column. Figure 9 shows the radial stress of floating encased stone columns with different encasement lengths plotted against the settlement. Three or four locations (at different column depths) were selected in each case to illustrate the change in the radial stresses with the increase in the settlement. The radial stresses provided by the encasement sleeve were not constant and varied with the settlement. The maximum radial stresses were 28.9, 27.6, and 77.3 kPa, respectively, for the columns with encasement lengths of 200, 400, and 600 mm. Figure 9 (c) shows that the fully encased stone columns (F-ESC6D-6D) developed high radial stress, and therefore achieved effective confinement of the aggregates. As illustrated in the section on bulging deformation$\sigma_r = T/r$, the fully encased column developed bulging failure in the shallow section instead of in the bottom unreinforced section in the case of the partially encased column. The bulging deformation of the fully encased column was significantly smaller than that of the partially encased column. Less volume change of the fully encased column was anticipated during the loading process. The floating stone column with a long encasement length was stiffer and more robust than that with a short encasement sleeve.

Conclusion

In the present study, experimental model tests were performed on floating stone columns reinforced with a geogrid encasement. The following conclusions can be made from this study.

1) The bearing capacity of the floating stone column was significantly improved due to the geogrid encasement. The column with longer encasement showed high stiffness at large settlements.
2) The partially and fully encased stone column showed different bulging deformation patterns and developed large radial strains near the base of the encasement sleeve and at a shallow depth of 2 times the column diameter, respectively.
3) The floating-encased stone column showed good stiffness and more vertical pressure transferred from the top of the column to the bottom of the column due to the effective confinement provided by the geogrid encasement.
4) The radial stresses provided by the encasement sleeve were not constant and varied with the settlement. The fully encased stone columns (F-ESC6D-6D) developed high radial stress and achieved effective confinement of the column.
5) The bulging deformation controlled the bearing capacities of the floating-encased stone columns with different encasement lengths, which gave confidence that the geosynthetic-encased stone columns floated in extensive soft soils was an effective method for field construction.

Data availability statement

The original contributions presented in the study are included in the article/Supplementary Material; further inquiries can be directed to the corresponding author.

Author contributions

MG was in charge of the whole research and model tests. JY was in charge of the model tests and paper preparation. HM, JQ, and QX were in charge of the model tests and data analysis.

Funding

This research was funded by the National Natural Science Foundation of China (Grant Nos. 51908150 and 51908151) and the Guangzhou City Technology and Science Program (202102010456). The aforementioned support was appreciated.

Conflict of interest

Author HM was employed by China Construction Fourth Engineering Division Corp. Ltd.

The remaining authors declare that the research was conducted in the absence of any commercial or financial relationships that could be construed as a potential conflict of interest.

Publisher's note

All claims expressed in this article are solely those of the authors and do not necessarily represent those of their affiliated organizations, or those of the publisher, the editors, and the reviewers. Any product that may be evaluated in this article, or claim that may be made by its manufacturer, is not guaranteed or endorsed by the publisher.

References

Ali, K., Shahu, J. T., and Sharma, K. G. (2012). Model tests on geosynthetic-reinforced stone columns: A comparative study. *Geosynth. Int.* 19 (4), 292–305. doi:10.1680/gein.12.00016

Almeida, M. S., Hosseinpour, I., Riccio, M., and Alexiew, D. (2014). Behavior of geotextile-encased granular columns supporting test embankment on soft deposit. *J. Geotech. Geoenviron. Eng.* 141 (3), 04014116. doi:10.1061/(asce)gt.1943-5606.0001256

ASTM (2015). *Standard test method for determining tensile properties of geogrids by the single or multi-rib tensile method* (ASTM International: West Conshohocken, PA). D6637/D6637M-15.

Bai, B., Wang, Y., Rao, D., and Bai, F. (2022). The effective thermal conductivity of unsaturated porous media deduced by pore-scale SPH simulation. *Front. Earth Sci. (Lausanne).* 10. doi:10.3389/feart.2022.943853

Bai, B., Yang, G., Li, T., and Yang, G. (2019). A thermodynamic constitutive model with temperature effect based on particle rearrangement for geomaterials. *Mech. Mater.* 139, 103180. doi:10.1016/j.mechmat.2019.103180

Bai, B., Zhou, R., Cai, G., Hu, W., and Yang, G. (2021). Coupled thermo-hydro-mechanical mechanism in view of the soil particle rearrangement of granular thermodynamics. *Comput. Geotechnics* 137 (8), 104272. doi:10.1016/j.compgeo.2021.104272

Chen, J. F., Li, L. Y., Xue, J. F., and Feng, S. Z. (2015). Failure mechanism of geosynthetic-encased stone columns in soft soils under embankment. *Geotext. Geomembranes* 43 (5), 424–431. doi:10.1016/j.geotexmem.2015.04.016

Chen, J. F., Wang, X. T., Xue, J. F., Zeng, Y., and Feng, S. Z. (2018). Uniaxial compression behavior of geotextile encased stone columns. *Geotext. Geomembranes* 46 (3), 277–283. doi:10.1016/j.geotexmem.2018.01.003

Dash, S. K., and Bora, M. C. (2013). Influence of geosynthetic encasement on the performance of stone columns floating in soft clay. *Can. Geotech. J.* 50, 754–765. doi:10.1139/cgj-2012-0437

Debnath, P., and Dey, A. K. (2017). Bearing capacity of geogrid reinforced sand over encased stone columns in soft clay. *Geotext. Geomembranes* 45 (6), 653–664. doi:10.1016/j.geotexmem.2017.08.006

Ghazavi, M., and Afshar, J. (2013). Bearing capacity of geosynthetic encased stone columns. *Geotext. Geomembranes* 38 (1), 26–36. doi:10.1016/j.geotexmem.2013.04.003

Gniel, J., and Bouazza, A. (2010). Construction of geogrid encased stone columns: A new proposal based on laboratory testing. *Geotext. Geomembranes* 28 (1), 108–118. doi:10.1016/j.geotexmem.2009.12.012

Gu, M., Han, J., and Zhao, M. (2020). Three-dimensional dem analysis of axially loaded geogrid-encased stone column in clay bed. *Int. J. Geomech.* 20 (3), 04019180. doi:10.1061/(asce)gm.1943-5622.0001595

Gu, M., Han, J., and Zhao, M. (2017b). Three-dimensional DEM analysis of single geogrid-encased stone columns under unconfined compression: A parametric study. *Acta Geotech.* 12 (3), 559–572. doi:10.1007/s11440-017-0547-z

Gu, M., Han, J., and Zhao, M. (2017a). Three-dimensional discrete-element method analysis of stresses and deformations of a single geogrid-encased stone column. *Int. J. Geomech.* 17 (9), 04017070. doi:10.1061/(asce)gm.1943-5622.0000952

Gu, M., Zhao, M., Zhang, L., and Han, J. (2016). Effects of geogrid encasement on lateral and vertical deformations of stone columns in model tests. *Geosynth. Int.* 23 (2), 100–112. doi:10.1680/jgein.15.00035

Han, J. (2015a). *Principles and practice of ground improvement*. Hoboken, New Jersey, USAJune: Wiley, 418.

Han, J. (2015b). Recent research and development of ground column technologies. *Proc. Institution Civ. Eng. - Ground Improv.* 168 (4), 246–264. doi:10.1680/grim.13.00016

Hasan, M., and Samadhiya, N. K. (2016). Experimental and numerical analysis of geosynthetic-reinforced floating granular piles in soft clays. *Int. J. Geosynth. Ground Eng.* 2, 22. doi:10.1007/s40891-016-0062-6

Kadhim, S. T., Parsons, R. L., and Han, J. (2018). Three-dimensional numerical analysis of individual geotextile-encased sand columns with surrounding loose sand. *Geotext. Geomembranes* 46 (6), 836–847. doi:10.1016/j.geotexmem.2018.08.002

Kahyaoğlu, M. R., and Vaníček, M. (2019). A numerical study of reinforced embankments supported by encased floating columns. *Acta Geotech. Slov.* 2, 25–38. doi:10.18690/actageotechslov.16.2.25-38.2019

Kong, G., Zhou, Y., and Liu, H. (2018). Nonlinear model analysis of radial bulging deformation of geosynthetic-encased stone columns. *Int. J. Geomech.* 18 (10), 06018022. doi:10.1061/(asce)gm.1943-5622.0001195

Mohapatra, S. R., and Rajagopal, K. (2017). Undrained stability analysis of embankments supported on geosynthetic encased granular columns. *Geosynth. Int.* 24 (5), 465–479. doi:10.1680/jgein.17.00015

Murugesan, S., and Rajagopal, K. (2010). Studies on the behavior of single and group of geosynthetic encased stone columns. *J. Geotech. Geoenviron. Eng.* 136 (1), 129–139. doi:10.1061/(asce)gt.1943-5606.0000187

Ng, K. S., and Tan, S. A. (2014). Design and analyses of floating stone columns. *Soils Found.* 54, 478–487. doi:10.1016/j.sandf.2014.04.013

Ong, D. E. L., Sim, Y. S., and Leung, C. F. (2018). Performance of field and numerical back-analysis of floating stone columns in soft clay considering the influence of dilatancy. *Int. J. Geomech.* 18 (10), 04018135. doi:10.1061/(asce)gm.1943-5622.0001261

Pulko, B., Majes, B., and Logar, J. (2011). Geosynthetic-encased stone columns: Analytical calculation model. *Geotext. Geomembranes* 29 (1), 29–39. doi:10.1016/j.geotexmem.2010.06.005

Sarvaiya, H. K., and Solanki, C. H. (2017). A study on effect of length of geosynthetic encasement material on floating stone column. *Int. J. Civ. Eng. Technol.* 8 (6), 977–985.

Schnaid, F., Winter, D., Silva, A. E. F., Alexiew, D., and Küster, V. (2017). Geotextile encased columns (GEC) used as pressure-relief system. Instrumented bridge abutment case study on soft soil. *Geotext. Geomembranes* 45 (3), 227–236. doi:10.1016/j.geotexmem.2017.02.003

Shahu, J. T., and Reddy, Y. R. (2014). Estimating long-term settlement of floating stone column groups. *Can. Geotech. J.* 51, 770–781. doi:10.1139/cgj-2012-0477

Shan, Y., Liang, J., Tong, H., Yuan, J., and Zhao, J. (2022). Effect of different fibers on small-strain dynamic properties of microbially induced calcite precipitation–fiber combined reinforced calcareous sand. *Constr. Build. Mater.* 322, 126343. doi:10.1016/j.conbuildmat.2022.126343

Tan, X., Hu, Z., Chen, C., and Zhao, M. (2021). 3D DEM-FDM coupled analysis of the behavior of an isolated geogrid-encased stone column under axial loading. *J. Geotech. Geoenviron. Eng.* 147 (6), 04021028. doi:10.1061/(asce)gt.1943-5606.0002516

Tan, X., Zhao, M., Hu, Z., and Feng, L. (2020). Failure process of a single stone column in soft soil beneath rigid loading: Numerical study. *Int. J. Geomech.* 20 (8), 04020130. doi:10.1061/(asce)gm.1943-5622.0001776

Thakur, A., Rawat, S., and Gupta, A. K. (2021). Experimental and numerical investigation of load carrying capacity of vertically and horizontally reinforced floating stone column group. *Geotech. Geol. Eng. (Dordr).* 39, 3003–3018. doi:10.1007/s10706-020-01674-y

Yoo, C., and Lee, D. (2012). Performance of geogrid-encased stone columns in soft ground: Full-scale load tests. *Geosynth. Int.* 19 (6), 480–490. doi:10.1680/gein.12.00033

Zhang, L., Xu, Z., and Zhou, S. (2020). Vertical cyclic loading response of geosynthetic-encased stone column in soft clay. *Geotext. Geomembranes* 48 (6), 897–911. doi:10.1016/j.geotexmem.2020.07.006

Zhang, L., and Zhao, M. (2015). Deformation analysis of geotextile-encased stone columns. *Int. J. Geomech.* 15 (3), 198–210. doi:10.1061/(asce)gm.1943-5622.0000389

Zhao, J., Tong, H., Shan, Y., Yuan, J., Peng, Q., and Liang, J. (2021). Effects of different types of fibers on the physical and mechanical properties of MICP-treated calcareous sand. *Materials* 142, 268. doi:10.3390/ma14020268

Zhou, H., Diao, Y., Zheng, G., Han, J., and Jia, R. (2017). Failure modes and bearing capacity of strip footings on soft ground reinforced by floating stone columns. *Acta Geotech.* 12, 1089–1103. doi:10.1007/s11440-017-0535-3

Zhou, Y., and Kong, G. (2019a). Deformation analysis of a geosynthetic-encased stone column and surrounding soil using cavity-expansion model. *Int. J. Geomech.* 19 (5), 04019036. doi:10.1061/(asce)gm.1943-5622.0001418

Zhou, Y., and Kong, G. (2019b). Deformation analysis of geosynthetic-encased stone column-supported embankment considering radial bulging. *Int. J. Geomech.* 19 (6), 04019057. doi:10.1061/(asce)gm.1943-5622.0001426

frontiers | Frontiers in Materials

TYPE Original Research
PUBLISHED 23 August 2022
DOI 10.3389/fmats.2022.967871

Check for updates

OPEN ACCESS

EDITED BY
Bing Bai,
Beijing Jiaotong University, China

REVIEWED BY
Chen Peipei,
Beijing University of Civil Engineering and Architecture, China
Haiqing Zhang,
Hebei University, China

*CORRESPONDENCE
Wen-Chieh Cheng,
w-c.cheng@xauat.edu.cn

SPECIALTY SECTION
This article was submitted to Structural Materials,
a section of the journal *Frontiers in Materials*.

RECEIVED 13 June 2022
ACCEPTED 14 July 2022
PUBLISHED 23 August 2022

CITATION
Hu W, Cheng W-C, Wen S and Kang N (2022), Revealing underlying mechanisms affecting electrokinetic remediation of an artificially Cu- and Pb-contaminated loess using the external regulatory system with adsorbent.
Front. Mater. 9:967871.
doi: 10.3389/fmats.2022.967871

COPYRIGHT
© 2022 Hu, Cheng, Wen and Kang. This is an open-access article distributed under the terms of the Creative Commons Attribution License (CC BY). The use, distribution or reproduction in other forums is permitted, provided the original author(s) and the copyright owner(s) are credited and that the original publication in this journal is cited, in accordance with accepted academic practice. No use, distribution or reproduction is permitted which does not comply with these terms.

Revealing underlying mechanisms affecting electrokinetic remediation of an artificially Cu- and Pb-contaminated loess using the external regulatory system with adsorbent

Wenle Hu[1,2], Wen-Chieh Cheng[1,2,3]*, Shaojie Wen[1,2] and Nongbo Kang[1,2]

[1]Xi'an Key Laboratory of Geotechnical and Underground Engineering, Xi'an University of Science and Technology, Xi'an, China, [2]School of Civil Engineering, Xi'an University of Architecture and Technology, Xi'an, China, [3]Shaanxi Key Laboratory of Geotechnical and Underground Space Engineering (XAUAT), Xi'an, China

Considering extensive metallurgical mining activities in the northwest of China, handling Cu- and Pb-rich wastewater is a challenging task. Inappropriate handling of the Cu- and Pb-rich wastewater can lead to accumulation of Cu and Pb in the surrounding environment, thereby posing a serious threat to human health. Electrokinetic (EK) technology is an increasingly popular alternative to traditional approaches for contaminated soil remediation owing to its high effectiveness and low risk of secondary pollution. This study first proposed an external regulatory system with the adsorbent (ERSA) and investigated the effect of electrode type, ERSA, and cation exchange membrane (CEM) on the EK remediation of an artificially Cu- and Pb-contaminated loess. An EK reactor incorporating ERSA was applied to the EK experiments to circulate the electrolyte, not only making pH surrounding the cathode lower, but also preventing the formation of precipitation. The electrokinetic geosynthetics electrode released H^+ and OH^- faster and promoted their migration toward the specimen. However, because of the faster precipitation near the cathode, the boost in the remediation efficiency was hindered. Furthermore, considering the ERSA use, a decrease in soil pH near the cathode reduced the precipitation, thereby enhancing the EK remediation efficiency. In contrast, the use of CEM lowered the soil pH, increased the soil electrical conductivity (EC) and electric current, and aggravated the electroosmotic flow. The Cu remediation efficiency using the modified EK reactor was largely lifted to 85.52%, while the Pb remediation efficiency increased to 75.51%. These results shed light on an enhancement on the EK remediation efficiency and the potential of applying the modified EK reactor to remedy Cu- and Pb-rich water bodies.

KEYWORDS

loess soil, electrokinetic remediation, heavy metal, electrokinetic geosynthetics, external regulatory system with adsorbent

1 Introduction

With the rapid development of metallurgy, land contamination resulting from metallurgy industry wastewater poses serious threats to the surrounding environment and human health, raising sustainable development concerns. Heavy metals are major chemicals causing soil pollution. In the northwest (NW) of China, loess bears the greatest burden of environmental contamination (Hu et al., 2021a; Hu et al., 2021b). Because of industrial or agricultural waste, it is contaminated by various toxic elements such as copper, lead, mercury, cadmium, and arsenic (Saha and Orvig, 2011; Ghosh et al., 2015; Begum et al., 2022). Heavy metals are toxic, carcinogenic, and strongly adsorbed onto the loess, which can be transported into the human body and accumulated with time eventually affecting human, animal, and plant health (Bai et al., 2019, 2020; Bai et al., 2021c). More importantly, heavy metal contamination is difficult to handle because of its long residual time, strong concealment, toxicity, and other characteristics. Furthermore, artificial remediation or soil self-purification needs long time to degrade contaminants. The remediation of soil contaminated by heavy metals is still a challenge. Therefore, feasible and efficient measures for remediation of soil contaminated by heavy metals are necessary.

The currently available measures for the remediation of soil contaminated by heavy metals mainly include phytoremediation (Caparrós et al., 2022; He et al., 2022; Liu et al., 2022; Wu et al., 2022), thermal desorption (Ding et al., 2019; Liu et al., 2019, 2020), biosorption (Saha et al., 2011; Mukherjee et al., 2013), soil replacement (Du et al., 2011), curing stabilization (Kalantari and Prasad, 2014; Zhou et al., 2017; Wang et al., 2019), chemical precipitation (Lu Y. S. et al., 2019; Muddanna and Baral, 2019), and microbial remediation (Garcia-Sanchez et al., 2018; Lu C. et al., 2019; Wang et al., 2022a; Xue et al., 2022). Among the remediation measures, electrokinetic (EK) remediation has recently come under the spotlight and is considered a promising innovative remediation technology, especially for low permeability soils. Moreover, EK remediation displays better behaviors in terms of metal mobilization and low repeated contamination (Zhou et al., 2021) by inserting the electrodes into the soils and applying a low direct-current (DC) voltage gradient to the electrodes. During EK remediation, the applied electric gradient induces a pH gradient across the soil chamber because of water electrolysis reactions that produce protons at the anode and hydroxyl ions at the cathode. The process also leads to electric effects, including electroosmosis, electromigration, and electrophoresis. Among these, electroosmosis and electromigration are the main removal mechanisms in most instances (Beyrami, 2020; Zhou et al., 2021). Furthermore, the acidic environment generated at the anode aids in the desorption and dissolution of heavy metals from the soil particle surface. It is unfortunate that, the alkalization near the cathode is considered the main barrier to the migration of heavy metal ions from the soil. Moreover, it is not conducive to the desorption and migration of heavy metal ions because of the weak alkaline conditions of loess itself (Hu et al., 2021a), limiting the development and application of EK remediation technology. Moreover, loess is extremely important and covers 630,000 km^2 in China. Clay minerals in loess have complex chemical composition, high specific surface areas, and high negative charge (Xue et al., 2021a, 2021b; Duan et al., 2021; Bai B. et al., 2021, 2021b). The forming of water during the EK remediation process can cause the swelling and dispersion of clays in loess toward increasing the thickness of the electric double layer and causing a reduction in the suction (Hu et al., 2021a; Hu et al., 2022a; Wang et al., 2022a). The reduced suction deteriorates the metastable structure of the loess, accompanied by the collapse deformation (Wang et al., 2020; Hu et al., 2021a), which makes the channel of the pore decrease and further limits the application of EK remediation technology.

Previous studies have shown that the EK remediation technology has the potential to effectively remove heavy metals from soil (Chen et al., 2020; Wang et al., 2021), especially in sandy soil (Baker et al., 2018; Puppala et al., 1997), soft soil (Wang et al., 2021), black soil (Yuan et al., 2017), and kaolin (Li et al., 2019). A significant body of research conducted over the past few years has greatly improved our understanding of the removal of heavy metals and their influencing factors when using EK technology. For instance, Kim et al. (2005) evaluated the potential of EK technology enhanced by an ion-exchange membrane (IEM) for remediating heavy metal contaminated soils. The experimental results indicated that the effectiveness of EK technology was increased by an enhancement scheme using an IEM. Xu et al. (2020) found that applying the cation exchange membrane (CEM) to the cathode could increase the removal efficiency by decreasing soil pH near the cathode. Ling et al. (2021) confirmed the effectiveness and feasibility of electrokinetic geosynthetics (EKG) electrodes in long-term subgrade improvement technology based on electroosmosis. Compared to the traditional graphite electrode, both laboratory and field tests indicated that the EKG electrode is more suitable for long-term electroosmosis treatment because of the lower

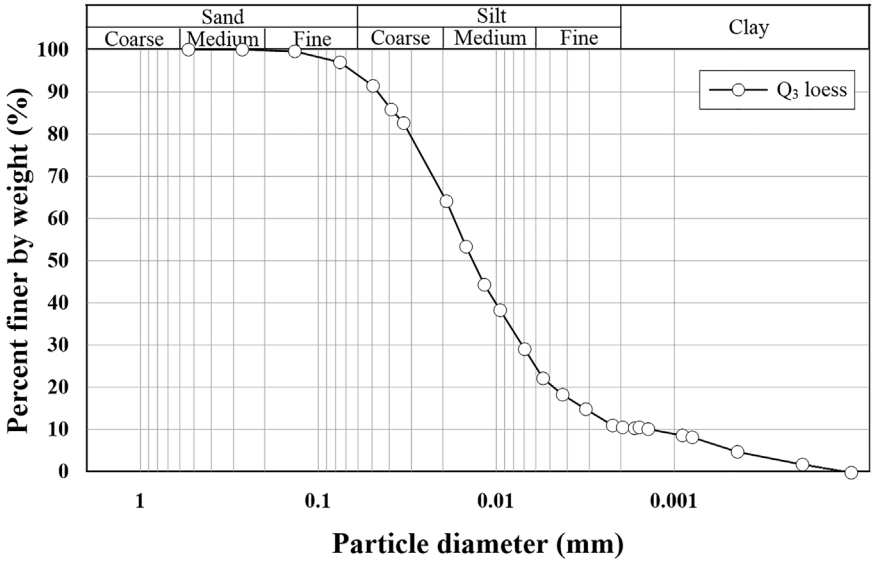

FIGURE 1
Particle-size distribution of the loess.

energy cost of the EKG electrode. Chang et al. (2018) proposed that applying the circulation-enhanced electrokinetic system can maintain a relatively neutral pH of treated soils and make the removal efficiency of Cd and Pb achieve 91 and 85%, respectively. Mohadi et al. (2019) illustrated that contaminated soil remediation could be affected by the operating conditions of the EK process, including pH control, refreshing electrolytes, and changing voltage gradient. Fan et al. (2021) found that the EK coupled with acidic permanganate of the regular oxidant supplement is appropriate for mass removal of heavy metals and polycyclic aromatic hydrocarbons, especially in low-buffered soils. Zhou et al. (2021) and Wang et al. (2021) noted that coupling the EK with other remediation technologies could improve the efficiency of EK remediation or decrease energy costs. Handling Cu- or Pb-rich wastewater, induced by metallurgical activities, is deemed a challenging task, especially in the NW of China. Permeation of Cu and Pb into ground soils can decrease plants' photosynthetic activities (Bilal et al., 2013; Mwandira et al., 2017; Meseldzija et al., 2019) and cause their accumulation. Their accumulation could lead to great harm to organisms or even to humans through food chain (Zu et al., 2004; Tak et al., 2013; Hu et al., 2021a; Hu et al., 2022b; Wang et al., 2022b).

A number of questions regarding the underlying mechanisms affecting the EK remediation efficiency remain (e.g., effect of electrode polarization, heavy metal precipitation surrounding the cathode, etc.). The main objectives of this study are 1) to investigate the effect of electrode types, the external regulatory system with adsorbent (ERSA), and CEM on the removal of copper and lead; 2) to reveal the underlying mechanisms affecting the EK remediation efficiency; and 3) to shed light on the potential of applying the modified EK reactor to remedying the Cu- and Pb-rich water bodies.

TABLE 1 Physicochemical properties of the loess.

Physical parameter	Value
Sand (%)	3.3
Silt (%)	87.4
Clay (%)	9.3
Void ratio, e	0.898
Bulk unit weight, γ (kN/m^3)	16.2
Specific gravity, G_s	2.69
Water content, ω_n (%)	16.5
Liquid limit, ω_L (%)	31.6
Plastic limit, ω_P (%)	19.5
USCS symbol	CL
Permeability (m s^{-1})	2.55×10^{-6}
Organic matter (mg g^{-1})	4.1
pH	8.3
Electrical conductivity (S m^{-1})	0.244
BET specific surface area (m^2 kg^{-1})	2.41×10^4
Ca^{2+} (mg/kg)	126
Mg^{2+} (mg/kg)	40
Na^+ (mg/kg)	103
K^+ (mg/kg)	4.6

TABLE 2 Experimental design of the enhanced electrokinetic remediation of Cu- and Pb-contaminated loess.

Test	Electrode type	Contaminant	Voltage gradient/V·cm^{-1}	Adsorbent	Catholyte	Cation exchange membrane
Exp-01	Graphite	Cu + Pb	1.5	/	/	/
Exp-02	EKG	Cu + Pb	1.5	/	/	/
Exp-03	EKG	Cu + Pb	1.5	Biochar	A to C	/
Exp-04	EKG	Cu + Pb	1.5	Graphene	A to C	/
Exp-05	EKG	Cu + Pb	1.5	Biochar	A to C	The cathode side
Exp-06	EKG	Cu + Pb	1.5	Graphene	A to C	The cathode side

"/" indicates that the corresponding test was not used in the treatment. "A to C" indicates that the anodic electrolyte was pumped out from the anodic chamber and injected into the cathode chamber using a peristaltic pump following adsorption of the adsorbing device.

2 Materials and methods

2.1 Sampling and specimen preparation

In NW China, dust and sand brought by wind are deposited in the Loess Plateau, and loess is formed after three stages of leaching, illuviation, and accumulation of the aeolian materials. There are three major geomorphologic features present in the Loess Plateau: loess ridges, hills, and bedrock gullies. Boreholes data indicate that the strata overlying the sandstone bedrock consist of Palaeosol and the overlying Malan (Q_3) loess, and their thickness varies between 22 and 31 m and 2 and 5 m, respectively (Zhu et al., 2011; Hu et al., 2021a). A series of Q_3 loess block samples from Lantian, Shaanxi Province, were used in this work, approximately 22 km southeast of Xi'an, with a sampling depth of 3.0–4.5 m. In addition, samples retrieved from the sampling site and used in this study have not detected Cu and Pb. The particle-size distribution curve of Q_3 loess is shown in Figure 1. The basic physical and chemical properties of the loess used in this study were determined immediately upon the delivery of the loess blocks according to the (Ministry of Water Resources of the People's Republic of China, 2019) and summarized in Table 1, such as initial water content, void ratio, pH, EC, and element composition.

Previous studies (Zeng et al., 2020; Zheng et al., 2021) have indicated that the process of loess contaminated by heavy metals causes changes in the microstructural characters because of the loess–water–chemical interactions. Furthermore, the process of EK remediation again changes the microstructure of the contaminated loess by the electroosmosis of pore water and electromigration of cations and heavy metal ions. Considering this, compared with the test on real contaminated matrices, the spiked matrices can better ensure the uniformity of the distribution of contaminants. They might be more appropriate in exploring the main contributor to the enhanced remediation efficiency and revealing the improved mechanism of leading the higher remediation efficiency. According to the National Bureau of Statistics (2001) data, Cu and Pb were selected as spiked contaminants for the soil treatment tests. The concentration of Cu and Pb was selected as 500 mg/kg, respectively, according to the previous study (Yuan et al., 2017; Zang et al., 2019) and the data of the National Bureau of Statistics (2018).

The natural loess was air-dried, pulverized, sieved (2 mm), and stored in a sealed glass cylinder. Our previous work took three degrees of compaction (0.8, 0.85, and 0.9) and three moisture contents (15, 20, and 25%) into account while remedying the Cu- and Pb-contaminated loess through the EK remediation technology. The experimental results indicated that the lower degree of compaction (i.e., 0.8) promoted the formation of the agglomerate structure, and therefore, causes the electromigration path wider and straighter, elevating the percentage removal of heavy metals. Furthermore, the slippage of the Gouy layer aggravates the electromigration of the cations and heavy metal ions when subjected to the higher initial water content (i.e., 25%), thereby enhancing the removal of heavy metals. These two parameters were subsequently applied to the testing scheme. The mass of the Cu nitrate [$Cu(NO_3)_2$] and Pb nitrate [$Pb(NO_3)_2$] with a purity >99% were calculated following the quality of air-dried loess. Then the Cu nitrate [$Cu(NO_3)_2$] and Pu nitrate [$Pb(NO_3)_2$] were dissolved in the given amount of deionized water. The solution containing copper and lead ions was sprayed into the loess in layers according to the Ministry of Water Resources of the People's Republic of China (2019). When the loess soil is exposed to a solution containing Cu and Pb ions, the initial adsorption reaction of heavy metals entering the soil is swift. This reaction is usually completed within a few hours and no longer exists later. The ecotoxicity of Cu and Pb in soil decreasing slowly with time is called aging treatment. The prepared Cu- and Pb-contaminated loess was sealed and stored in a moisturizing tank for 72 h to simulate the time effect of on-site contamination and ensure the even distribution of toxicity.

In all cases, the specimens were compacted in five layers to control the degree of compaction of contaminated loess on the reactor after aging treatment. After every layer preparation was completed, the surface of the layers was treated with a knife to make the two layers of soil come into close contact until the fifth

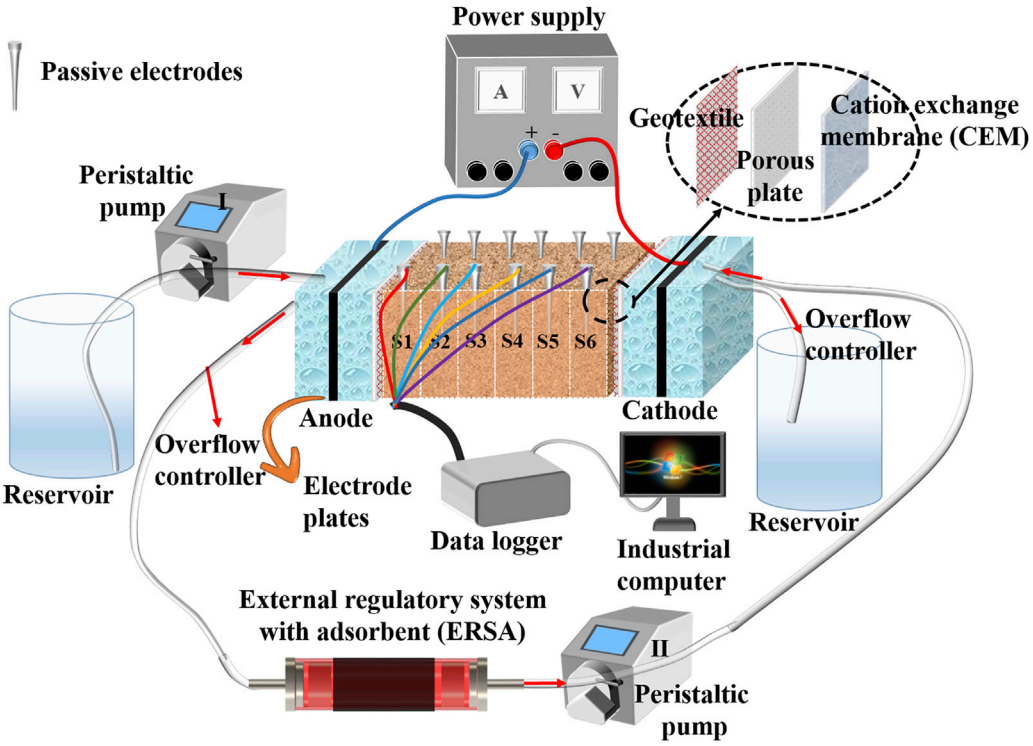

FIGURE 2
Schematic illustration of the electrokinetic reactor.

layer. The EK reactor and experimental details after the sample is prepared will be introduced in the following section.

2.2 Modified electrokinetic reactor and experimental design

A modified EK reactor applied to EK experiments in the present study mainly consists of one soil chamber made of plexiglass, two electrode cells, a pair of electrodes, two electrolyte reservoirs, two peristaltic pumps, one DC regulated power supply, the ERSA and data acquisition system, as shown in Figure 2. Dimensions of the soil chamber are 500 mm (length) × 150 mm (width) × 150 mm (height). Furthermore, the dimensions of the electrode cell are 100 mm (length) × 150 mm (width) × 150 mm (height). The two electrode cells are attached to both sides of the soil compartment containing six parts (termed S1 to S6 hereafter) and separated from the soil compartment using a geotextile and porous plate. The filling height of the soil in the soil chamber should be slightly higher than the liquid level of electrolyte in the electrode compartment, while the liquid level of electrolyte in the electrode compartment should be equal to the height of the lower end of the overflow controller. The setting of the overflow controller is used to ensure a constant liquid level of electrolyte in the electrode cell. A pair of electrodes were deployed to electrode compartments toward developing the electric field using a DC power supply. The two electrolyte reservoirs are connected respectively to the two electrode compartments. Moreover, the ERSA was used to adsorb the heavy metals in the anodic electrolyte and ensure that the purified anodic electrolyte was circulated the cathode cell using two peristaltic pumps. The two peristaltic pumps were opened throughout the EK remediation. The anodic electrolyte was circulated to the cathode cell to prevent pH surrounding the cathode from going higher. Measurements of pH, electrical conductivity (EC), electric current, and electroosmosis were done in each part (S1 to S6) using the data acquisition system during the EK remediation.

Material selection of the electrode itself is crucial in mitigating the effect of electrode polarization, and it has focused on EC and electrochemical activity. In light of this, higher current density and corrosion resistance were deemed as the main criteria for determining an appropriate material of electrodes applied to the EK remediation (Han et al., 2021; Wang et al., 2021). There are two types of electrodes present in this study: graphite and EKG (Wen et al., 2021). Both meet the said requirements. A pair of EKG electrodes were used as the modified electrodes, and a pair of graphite electrodes were

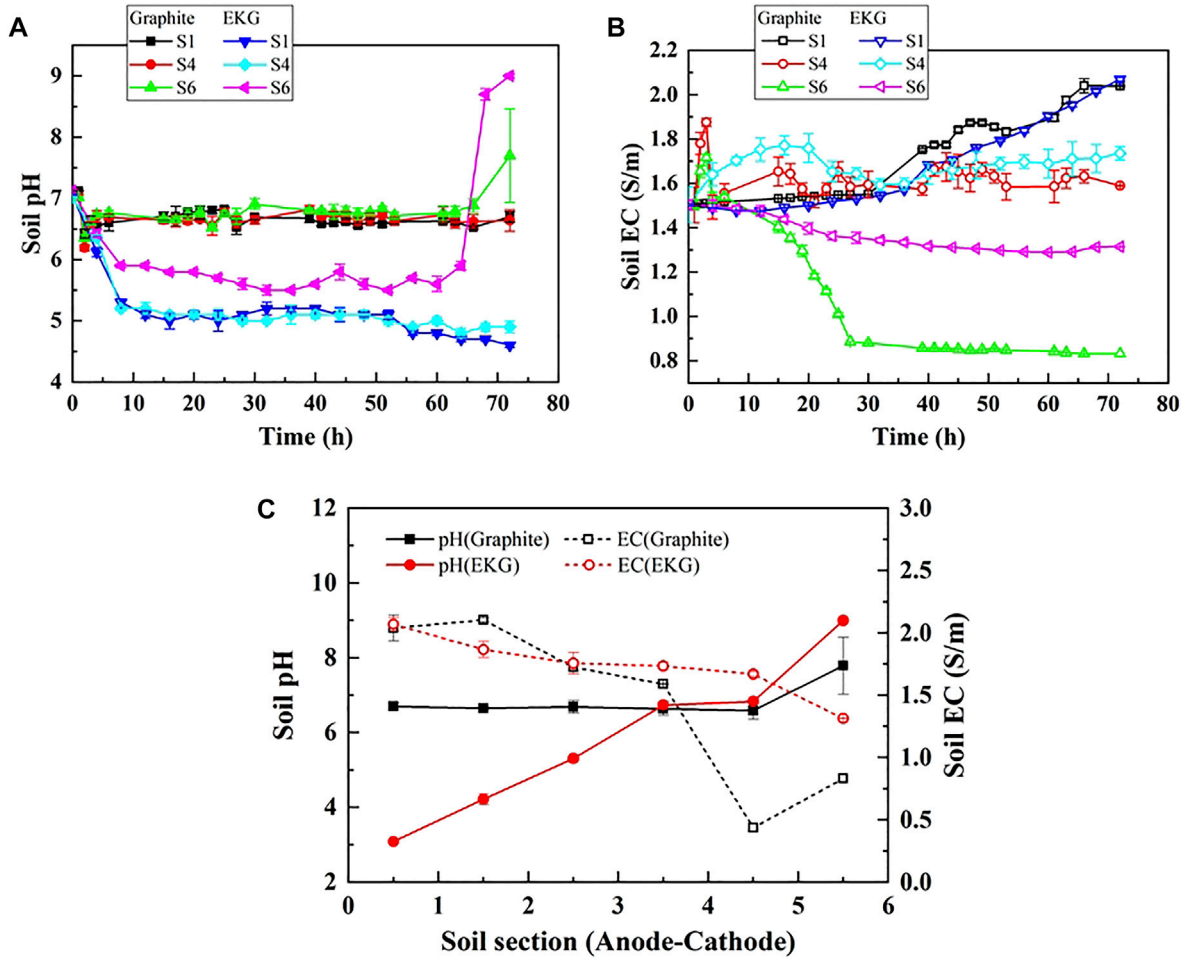

FIGURE 3
(A) soil temporal relationship, **(B)** soil EC temporal relationship, and **(C)** relationship of soil pH versus soil section.

used as the reference electrodes (see Table 2). According to the nitrogen adsorption method, it is essential to point out that the specific surface area (SSA) of the graphite electrode and EKG electrode was 1.12×10^3 m^2/kg and 8.90×10^3 m^2/kg, respectively. Furthermore, the theoretical SSA of graphene particles was nearly three times greater than biochar particles. The larger the SSA, the stronger the adsorption capacity. The adsorbent may affect the performance of the external regulatory system in the circulation of anolyte. To this end, two different types of high-efficiency adsorbents were considered, including biochar and graphene. Moreover, the CEM was used to evaluate its utility and mechanism in EK remediation. At the end of each EK experiment, the Cu and Pb removal was analyzed and compared against other EK experiments. All EK experiments had three replicates. An error bar has already been added to figures where necessary. Statistical analysis indicates that the coefficient of variance for the EK experiments is <15%, which is within the requirement being the coefficient of variance for usual, accessible experimental measurements.

3 Results

3.1 Effect of electrode type

Soil pH is a critical factor affecting the EK remediation efficiency. EK treatment changes pH through the electrolysis reaction at the electrodes and the migration of H^+ and OH^-. The changes of pH against different sections of the modified EK reactor applied to the present work are presented in Figure 3. Acar and Alshawabkeh (1993) found that the H^+ dominates the EK remediation efficiency because the mobility of H^+ is 1.75 times faster than that of OH^- (Bala et al., 2015). In the present work, the electrolysis unit consists of the electrodes for

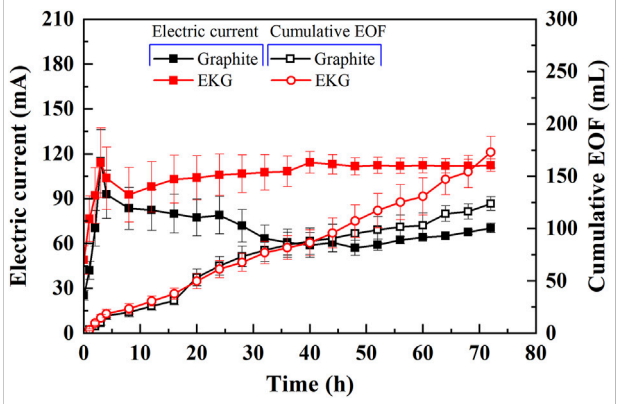

FIGURE 4
Variation of electric current and electroosmotic flow (EOF) versus time during the electrokinetic experiment subjected to the effect of electrode type.

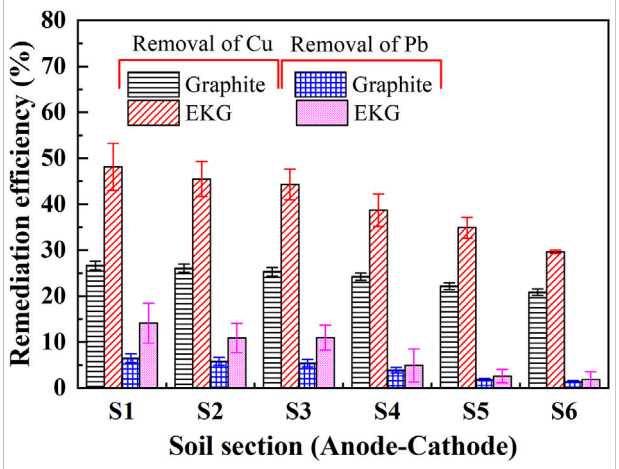

FIGURE 5
Removal of Cu and Pb after the electrokinetic experiment subjected to the effect of electrode type.

electrolysis, during which the modified EK reactor causes pH to increase sequentially from anode to cathode, while EC however behaves in a manner against pH (Figures 3A,B). When graphite is considered as the electrode, the pH surrounding the anode decreases to 6.70 and the pH surrounding the cathode increases to 7.79. Considering EKG as the electrode, the pH surrounding the anode decreases to 3.09 and the pH surrounding the cathode increases to approximately 9 (Figure 3C). Compared to the graphite electrode, the EKG electrode for a given soil section made pH surrounding the anode lower and the one surrounding the cathode remained nearly the same. This causes the hydrogen ions to adsorb on the soil particle surfaces, and the hydroxide ions leave behind, elevating pH surrounding the cathode. In contrast, the EC surrounding the anode is the highest and the one surrounding the cathode is the lowest. The acidic environment surrounding allows more ions to be desorbed from the loess, which causes EC to increase.

It is well known that the changes in the electric current and electroosmotic flow (EOF) have significant effects on the remediation efficiency of heavy metals. In general, the variation of electric current against the time can be characterized as two stages (Stages I and II) (Figure 4). Stage I can be characterized as an initially sharply increasing curve. Stage II can be described as a subsequently gently decreasing curve with the exception of EKG. H^+ ions and OH^- ions are discharged from the anode and cathode respectively throughout the EK remediation, which leads to an increasing number of ions migrated. Apart from that, H^+ also causes the soluble salts and minerals of the loess to dissolve, which further increases the number of ions migrated. The migration of H^+ promotes the desorption of heavy metals from the loess surface. Electric current increases quickly with the elapsed time as a result, as indicated by Stage I of Figure 4. The alkaline front is responsible for the precipitation surrounding the cathode, thereby causing the electrical resistance to increase and electric current to decrease. The electric current for EKG remains at a relatively high level, most likely because of the reduced effect of electrode polarization. Furthermore, gas bubbles, while using the graphite electrode, are constantly present on the electrodes' surface throughout the EK remediation, causing some difficulty in discharging more ions and lifting up EC. Moreover, the concentration polarization simultaneously presents in the anode and cathode cells, which also leads to a decrease in electric current. Compared to the graphite electrode, a higher SSA of the EKG electrode leads to lower current density on the surface and reduces the concentration polarization toward causing larger potential differences and higher EC. A higher electric current implies that H^+ and OH^- are discharged faster. These results provide testimony to the main cause leading to the EOF curve for EKG lying above the graphite curve, given a more significant heavy metal precipitation following a certain period of time (here it is 40 h) (Figure 4).

EOF depends highly on soil zeta potential, and the zeta potential depends on the interfacial chemistry between the pore fluid and particles. The zeta potential is negative under neutral and alkaline conditions (Acar and Alshawabkeh, 1993). As discussed, the EKG electrode causes H^+ and OH^- to be discharged manner and turns the most areas of the specimen into acidic environments, causing higher EC and EOF (Figure 4). Cationic metal is generally transferred to the cathode by electromigration and electroosmosis (Acar and Alshawabkeh, 1993). The Cu and Pb remediation efficiency against different soil sections is presented in Figure 5. Compared to the graphite electrode, the EKG electrode for a given soil section made

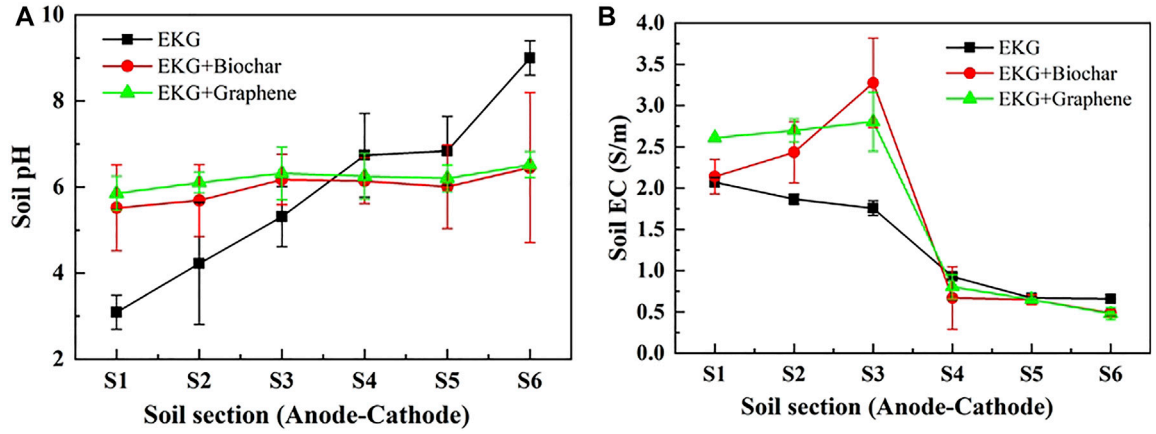

FIGURE 6
Variation of pH and EC after the electrokinetic experiment subjected to the effect of the adsorbed material: **(A)** pH and **(B)** EC.

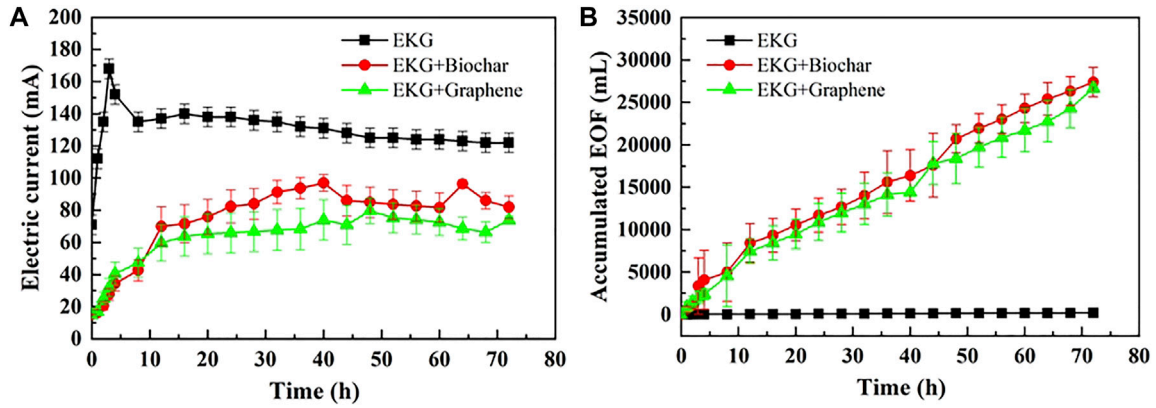

FIGURE 7
Variation of electric current and EOF versus time during the electrokinetic experiment subjected to the effect of the adsorbed material: **(A)** electric current and **(B)** accumulated EOF.

pH surrounding the anode lower. The migration of H^+ promotes the desorption of heavy metals from the surface of the loess improving the remediation efficiency. Such advantage is reduced with the increase in the distance from the anode. Furthermore, the Cu remediation efficiency is higher than the Pb remediation efficiency. Considering the ionic radius of Cu^{2+} is smaller than the ionic radius of Pb^{2+} (0.073 vs. 0.119 nm), the hydrated ion radius of Pb^{2+} is smaller than that of Cu^{2+}. That is, Pb^{2+} is much more difficult to desorb compared to Cu^{2+}. This is, therefore, deemed as the main cause that leads to the higher Cu^{2+} removal.

In short, pH surrounding conditions play a crucial role while introducing the EK remediation using the modified EK reactor. The EKG electrode makes H^+ and OH^- to be discharged faster compared to the graphite electrode, turning most areas of the specimen into acidic environments. The lower the pH surrounding, the more ions to be desorbed, and the higher the EC toward elevating EOF. Considering more cations are discharged while using the EKG electrode, the cations, in turn, reduce the zeta potential, forming an agglomerated structure. The agglomerated structure shortens the migration path of Cu^{2+} and Pb^{2+} and then elevates EOF and the remediation efficiency.

3.2 Effect of the external regulatory system with the adsorbent

Despite the advantages of the EKG electrode, precipitation surrounding the cathode is still notable, causing an inability of elevating the EK remediation efficiency. In the control group

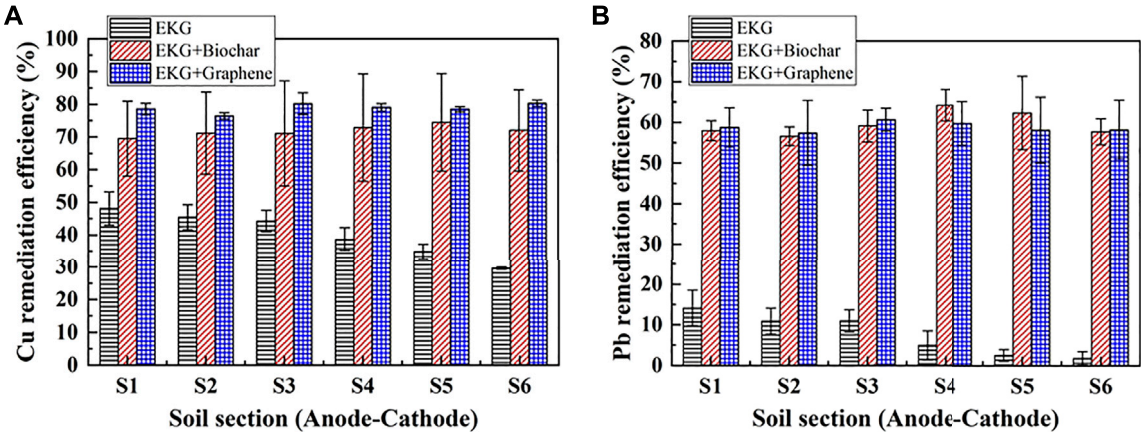

FIGURE 8
Removal of Cu and Pb after the electrokinetic experiment subjected to the effect of the adsorbed material: **(A)** Cu and **(B)** Pb.

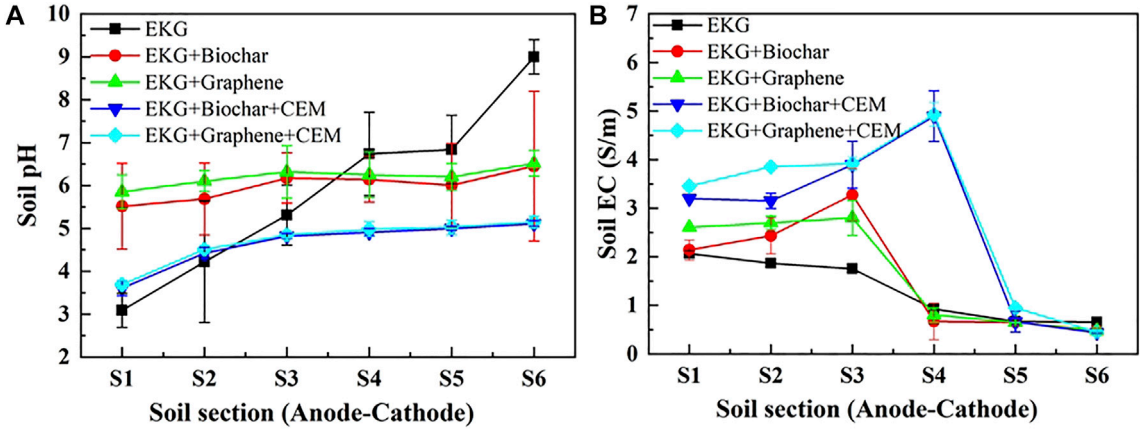

FIGURE 9
Variation of pH and EC after the electrokinetic experiment subjected to the effect of the different treatments: **(A)** pH and **(B)** EC.

(using EKG only), pH varies from 3.1 to 9.0 (Figure 6A). In the other test group (considering EKG and biochar), pH varies from 5.3 to 6.6, while in another test group (considering EKG and graphene), pH is further decreased. The increase in EC for the test groups is more significant compared to the control group, especially for the soil Sections S1–S4 (Figure 6B). These results provide testimony regarding the above argument.

The variation of electric current and EOF versus time during the EK remediation using the modified EK reactor is illustrated in Figure 7. The control and test groups behave in a similar manner concerning the change in electric current (Figure 7A). Notwithstanding, the EOF of the test groups increases very quickly compared to that of the control group, implying that precipitation surrounding the cathode is eased using the ERSA system (Figure 7B). The Cu and Pb remediation efficiency following the EK remediation is presented in Figure 8. The highest Cu remediation efficiency of 78.8% is attained using the EKG electrode with graphene, while the highest Pb remediation efficiency of approximately 59.6% is attained using the same approach. Furthermore, the EK remediation using the EKG electrode performs the worst among the three approaches, most likely because of the formation of precipitation surrounding the cathode. These results indicate that the accumulated EOF is the main cause leading to an improvement in the remediation efficiency rather than the electric current. The higher the accumulated EOF, the larger the number of heavy metals migrated, and the higher the remediation efficiency.

In summary, although the EKG electrode can ease the effect of electrode polarization and aggravate the discharge of

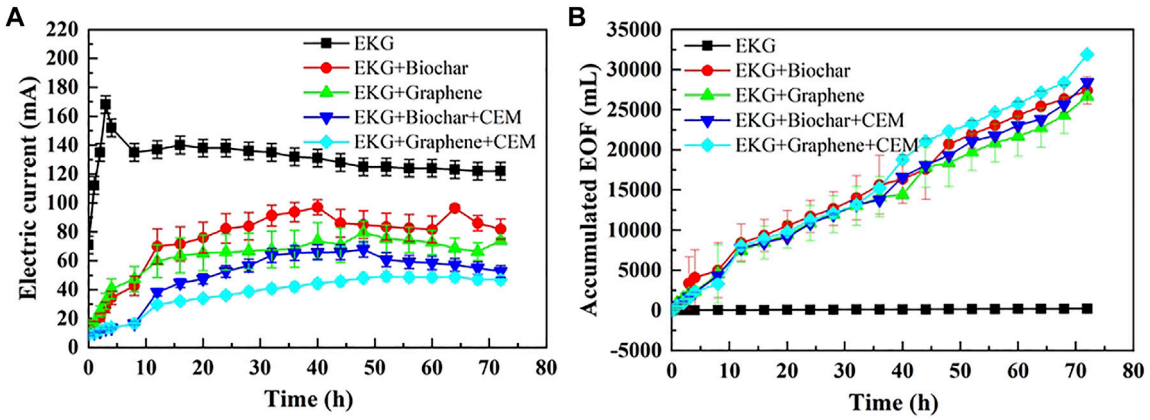

FIGURE 10
Variation of electric current and EOF versus time during the electrokinetic experiment subjected to the effect of the different treatments: **(A)** electric current and **(B)** accumulated EOF.

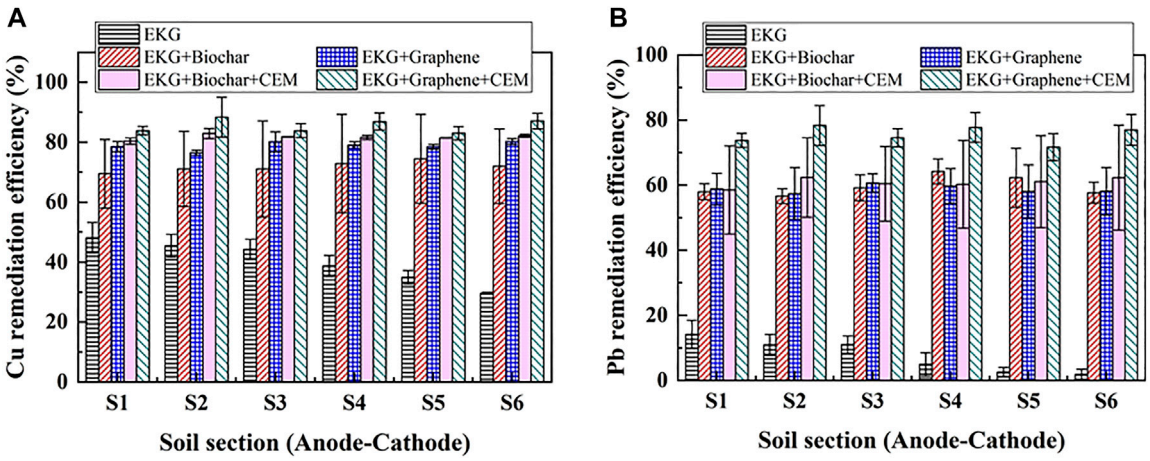

FIGURE 11
Removal of Cu and Pb after the electrokinetic experiment subjected to the effect of the different treatments: **(A)** Cu and **(B)** Pb.

H^+ and OH^- in the EK remediation, there is a significant shortcoming concerning the formation of precipitation surrounding the cathode, thereby reducing the remediation efficiency. The ERSA system is considered effective in mitigating the formation of precipitation where the electrolyte extracting from the anode cell and injecting into the cathode cell reduces the pH surrounding the cathode. The lower the pH surrounding the cathode, the more unlikely the formation of precipitation, and the higher desorption possibility of Cu^{2+} and Pb^{2+}. This is considered as the main cause leading to the highest remediation efficiency while using a combination of the EKG electrode and graphene.

3.3 Effect of cation exchange membrane

The variations of pH and EC against six soil sections under the CEM effect are presented in Figure 9. The use of CEM not only prevents a migration of OH^- to the specimen, but also further reduces pH over the entire specimen. In light of this, EC uses a combination of EKG and graphene as well as CEM that is higher compared to EC either using EKG or using a combination of EKG and graphene. A higher EC causes the electric current to go higher, leading to a higher EOF (Figure 10A). It is worth noting that the highest electric current is attained using EKG, while the lowest electric current is attained via a combination of EKG and graphene as well as CEM. This contradicts the above

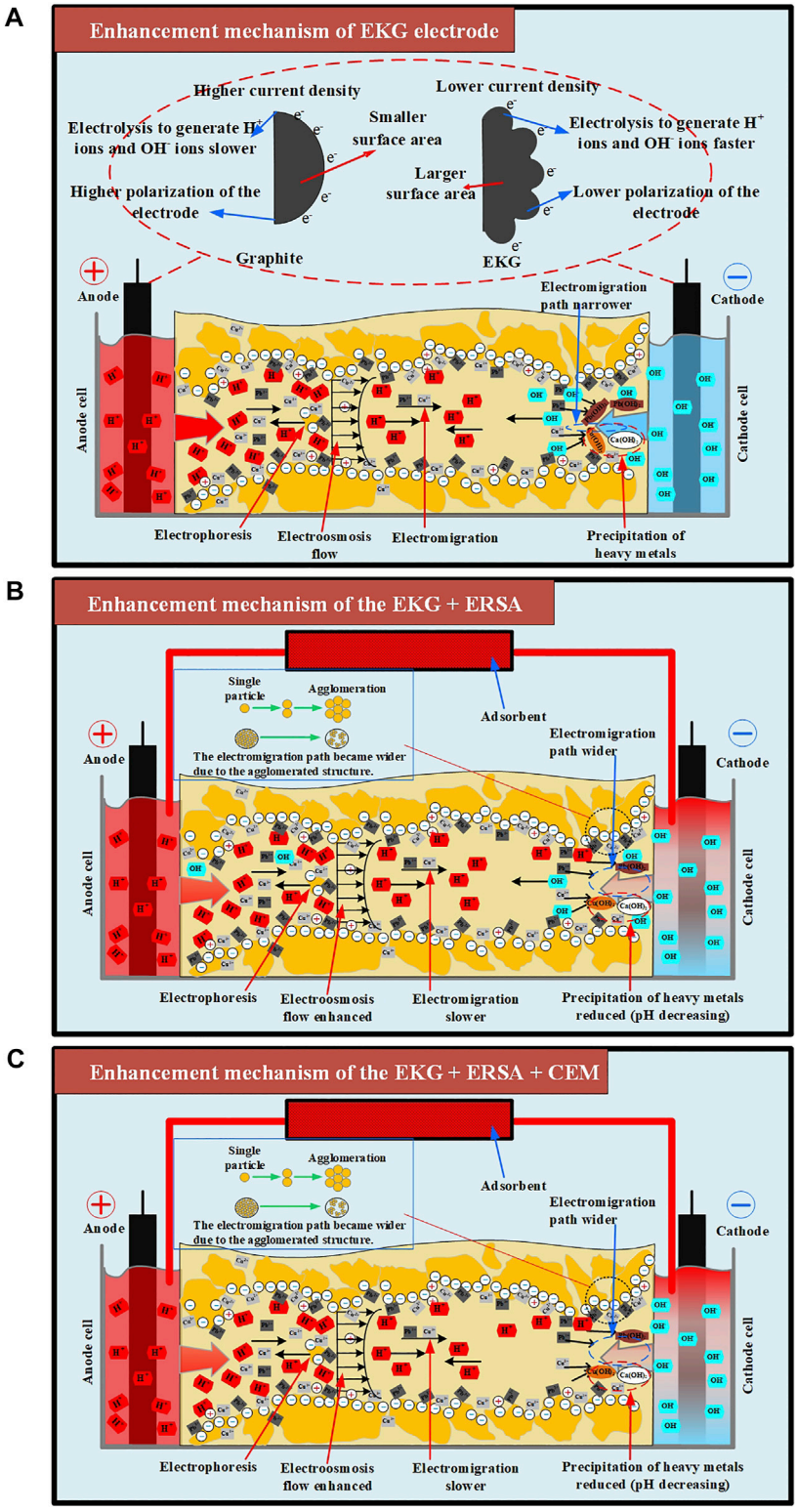

FIGURE 12
The enhancement mechanisms for Cu and Pb removal in loess: **(A)** enhancement mechanism of EKG electrode, **(B)** enhancement mechanism of the EKG + ERSA, **(C)** enhancement mechanism of the EKG + ERSA + CEM.

argument. This is because although the use of ERSA system can ease the formation of precipitation surrounding the cathode, it also circulates the anodic electrolyte to the cathode cell toward reducing the number of ions and causing a reduction in the electric current. In contrast, the number of ions in the anodic electrolyte does not show a drop when the ERSA system is neglected in the EK remediation, causing the highest electric current. The lower pH reduces the zeta potential and causes the formation of agglomerated structure toward lifting up the EOF (Figure 10B). The highest EOF is attained using a combination of EKG and ERSA (graphene), as well as CEM, most likely because of a reduction in the heavy metal precipitation, induced by the higher graphene's adsorption capacity. The variations of Cu and Pb remediation efficiency against six soil sections are shown in Figures 11A,B respectively. Overall, the Cu remediation efficiency is higher than the Pb remediation efficiency. Furthermore, the remediation efficiency using the modified EK reactor can be ordered as follows: EKG < EKG + ERSA (Biochar) < EKG + ERSA (Graphene) < EKG + ERSA (Biochar)+CEM < EKG + ERSA (Graphene)+CEM.

4 Discussion

It is well known that electric current flows through electrodes, leading to the polarization of the anode and cathode (Yuan et al., 2017; Wang et al., 2021). In this study, the use of graphite electrodes reduces not only the electric current, but also the EOF because of its polarization (Figure 4). Compared to the graphite electrode, the EKG electrode has a larger SSA and lower current density, and therefore, the migration of heavy metals is faster (Figure 12A). The discharge of H^+ and OH^- from the anode and cathode, respectively, is faster. This also indicates the faster acidification of the soil surrounding the anode and the faster precipitation surrounding the cathode. Therefore, the EKG electrode outperforms the graphite electrode regarding the removal of Cu and Pb (Figure 5).

Previous studies have emphasized the formation of precipitation surrounding the cathode. It impedes the development of electric current and then EOF toward degrading the remediation efficiency. To tackle such difficulty, the ERSA system was applied in this work to mitigate the formation of precipitation by circulating the anodic electrolyte to the cathode cell (Figure 12B). The pH surrounding the cathode was reduced as a result, preventing the formation of precipitation from occurring (Figure 6A). To this end, desorption of the heavy metals becomes easier than before, and an agglomerated structure can be formed because of the reduced pH surrounding. The agglomerated structure widens the electromigration path and indicates a higher EOF and a better remediation efficiency (Figures 7B, 8).

Although the ERSA use of is considered effective in reducing pH over the entire specimen, the formation of precipitation surrounding the cathode because of the soil alkalization remains to be addressed. In the present work, the use of CEM aims to further address the said issue by preventing the migration of OH^- to the specimen from the cathode (Figure 12C). A reduction in pH surrounding the cathode provides testimony regarding the above argument (Figure 9A). The smaller number of OH^- migrated, the lower potential of the formation of precipitation, and the higher the remediation efficiency. The thinner diffuse double layer, induced by the reduced pH, decreases the tortuosity of the electromigration path of cations and heavy metal ions. This also increases the electric current and EOF, indicating an improvement in the remediation efficiency (Figures 10, 11).

Overall, the use of EKG tackles the effect of electrode polarization. However, the effect of soil alkalization surrounding the cathode remains to be addressed. The ERSA system applied to the present work satisfactorily addresses the effect of soil alkalization surrounding the cathode by circulating the electrolyte from the anode cell to the cathode cell. Notwithstanding, the migration of OH^- to the specimen still causes some difficulty in easing the formation of precipitation surrounding the cathode. The combination of EKG electrode and ERSA, as well as CEM, is applied to the EK remediation and found to be effective in tackling the said problems (i.e., soil alkalization and heavy metal precipitation). The remediation efficiency as high as >85% verifies the applicability of the combination of EKG electrode and ERSA system, as well as CEM. The findings shed light on the potential of applying the EK technology in contaminated site remediation.

5 Conclusion

This study investigated the underlying mechanisms affecting the Cu and Pb remediation using the EK technology. The modified EK reactor was considered effective in improving the removal of Cu and Pb. Based on the results and discussion, some main conclusions can be drawn as follows:

1) The EKG electrode has a larger SSA and a lower current density, preventing the effect of electrode polarization and causing higher electric current. This further increases the EOF and causes an improvement in the removal of Cu and Pb. Notwithstanding, the formation of heavy metal precipitation surrounding the cathode still has to be addressed.
2) The ERSA system aims to reduce pH surrounding the cathode by circulating the anodic electrolyte to the cathode cell. The reduced pH eases the formation of heavy metal precipitation. The same reason also indicates easier desorption of Cu^{2+} and Pb^{2+} and a formation of the agglomerated structure. The agglomerated structure not only widens the electromigration

path, but indicates a higher EOF and better remediation efficiency.

3) The use of CEM intends to prevent the migration of OH^- to the specimen, thereby attaining the lowest pH and tackling the formation of precipitation surrounding the cathode. Such very low pH causes the diffuse double layer to become even thinner and decreases the tortuosity of the electromigration path of cations and heavy metal ions, indicating an increase in the electric current and EOF and improvement in the remediation efficiency. These results stand out as the relative merits of the modified EK reactor, namely, mitigating the effect of electrode polarization and easing the heavy metal precipitation surrounding the cathode. The findings shed light on the potential of applying the modified EK reactor to remedying the Cu- and Pb-rich water bodies.

Data availability statement

The original contributions presented in the study are included in the article/supplementary material, further inquiries can be directed to the corresponding author.

Author contributions

WH: data curation, formal analysis, validation, software, writing—original draft. W-CC: conceptualization, methodology, writing—review and editing, supervision, funding acquisition. SW: data curation, formal analysis, validation, software, writing—original draft. NK: formal analysis, validation, software.

Funding

This work would not have been possible without support from the Special Fund for Xi'an Key Laboratory of Geotechnical and Underground Engineering, Xi'an University of Science and Technology, under Grant no. XKLGUEKF20-02.

Conflict of interest

The authors declare that the research was conducted in the absence of any commercial or financial relationships that could be construed as a potential conflict of interest.

Publisher's note

All claims expressed in this article are solely those of the authors and do not necessarily represent those of their affiliated organizations, or those of the publisher, the editors, and the reviewers. Any product that may be evaluated in this article, or claim that may be made by its manufacturer, is not guaranteed or endorsed by the publisher.

References

Acar, Y. B., and Alshawabkeh, A. N. (1993). Principles of electrokinetic remediation. *Environ. Sci. Technol.* 27, 2638–2647. doi:10.1021/es00049a002

Bai, B., Nie, Q. K., Zhang, Y. K., Wang, X. L., and Hu, W. (2021a). Cotransport of heavy metals and SiO_2 particles at different temperatures by seepage. *J. Hydrology* 597, 125771. doi:10.1016/j.jhydrol.2020.125771

Bai, B., Xu, T., Nie, Q. K., and Li, P. P. (2020). Temperature-driven migration of heavy metal Pb^{2+} along with moisture movement in unsaturated soils. *Int. J. Heat Mass Transf.* 153, 119573. doi:10.1016/j.ijheatmasstransfer.2020.119573

Bai, B., Yang, G. C., Li, T., and Yang, G. S. (2019). A thermodynamic constitutive model with temperature effect based on particle rearrangement for geomaterials. *Mech. Mater.* 139, 103180. doi:10.1016/j.mechmat.2019.103180

Bai, X. D., Cheng, W. C., and Li, G. (2021b). A comparative study of different machine learning algorithms in predicting EPB shield behaviour: A case study at the xi'an metro, China. *Acta Geotech.* 16 (12), 4061–4080. doi:10.1007/s11440-021-01383-7

Bai, X. D., Cheng, W. C., Sheil, B. B., and Li, G. (2021c). Pipejacking clogging detection in soft alluvial deposits using machine learning algorithms. *Tunn. Undergr. Space Technol.* 113, 103908. doi:10.1016/j.tust.2021.103908

Baker, B., Maria, E., and Adel, H. (2018). Electrokinetic nondestructive *in-situ* technique for rehabilitation of liners damaged by fuels. *J. Hazard. Mater.* 359, 510–515. doi:10.1016/j.jhazmat.2018.07.113

Bala, R. P., Srivastava, R. K., and Mohan, D. (2015). Electrokinetic removal of mixed heavy metals from a contaminated low permeable soil by surfactant and chelants. *Environ. Earth Sci.* 73 (3), 1191–1204. doi:10.1007/s12665-014-3474-4

Begum, W., Rai, S., Banerjee, S., Bhattacharjee, S., Mondal, M. H., Bhattarai, A., et al. (2022). A comprehensive review on the sources, essentiality and toxicological profile of nickel. *RSC Adv.* 12, 9139–9153. doi:10.1039/d2ra00378c

Beyrami, H. (2020). Effect of different treatments on electrokinetic remediation of Zn, Pb and Cd from a contaminated calcareous soil. *Chin. J. Chem. Eng.* 38, 255–265. doi:10.1016/j.cjche.2020.09.011

Bilal, M., Shah, J. A., Ashfaq, T., Gardazi, S. M. H., Tahir, A. A., Pervez, A., et al. (2013). Waste biomass adsorbents for copper removal from industrial wastewater—a review. *J. Hazard. Mater.* 263, 322–333. doi:10.1016/j.jhazmat.2013.07.071

Caparrós, P. G., Ozturk, M., Gul, A., Batool, T. S., Anosheh, H. P., Unal, B. T. I., et al. (2022). Halophytes have potential as heavy metal phytoremediators: A comprehensive review. *Environ. Exp. Bot.* 193, 104666. doi:10.1016/j.envexpbot.2021.104666

Chang, J. H., Wang, Y. L., and Shen, S. Y. (2018). A specific configuration of circulation-enhanced electrokinetics (CEEK) to remediate real-site Cd and Pb contaminated soils. *J. Hazard. Mater.* 359, 408–413. doi:10.1016/j.jhazmat.2018.07.079

Chen, X. Y., Kumari, D., Cao, C. J., Grazyna, P., and Varenyam, A. (2020). A review on remediation technologies for nickel-contaminated soil. *Hum. Ecol. Risk Assess. Int. J.* 26 (3), 571–585. doi:10.1080/10807039.2018.1539639

Ding, D., Song, X., Wei, C., and La, C. J. (2019). A review on the sustainability of thermal treatment for contaminated soils. *Environ. Pollut.* 253, 449–463. doi:10.1016/j.envpol.2019.06.118

Du, Y. J., Jin, F., Liu, S. Y., Chen, L., and Zhang, F. (2011). Review of stabilization/solidification technique for remediation of heavy metals contaminated lands. *Rock Soil Mech.* 32 (1), 116–124.

Duan, Z., Cheng, W. C., Peng, J. B., and Tang, H. (2021). Interactions of landslide deposit with terrace sediments: Perspectives from velocity of deposit movement and apparent friction angle. *Eng. Geol.* 280, 105913. doi:10.1016/j.enggeo.2020.105913

Fan, G. P., Zhang, Z. H., Ai, Y. C., Gao, Y., Zhou, D. M., Cang, L., et al. (2021). Electrokinetical enhanced delivery of acidic potassium permanganate and removal of copper-pyrene compound pollution in a red soil. *Chemosphere* 263, 128085. doi:10.1016/j.chemosphere.2020.128085

Garcia-Sanchez, M., Kosnar, Z., Mercl, F., Aranda, E., and Tlustos, P. (2018). A comparative study to evaluate natural attenuation, mycoaugmentation, phytoremediation, and microbial-assisted phytoremediation strategies for the bioremediation of an aged PAH-polluted soil. *Ecotoxicol. Environ. Saf.* 147 (1), 165–174. doi:10.1016/j.ecoenv.2017.08.012

Ghosh, D., Saha, R., Ghosh, A., Nandi, R., and Saha, B. (2015). A review on toxic cadmium biosorption from contaminated wastewater. *Desalination Water Treat.* 53 (2), 413–420. doi:10.1080/19443994.2013.846233

Han, D., Wu, X. Y., Tang, X. Q., Xiao, S. B., and Scholz, M. (2021). Critical review of electro-kinetic remediation of contaminated soils and sediments: Mechanisms, performances and technologies. *Water Air Soil Pollut.* 232, 335. doi:10.1007/s11270-021-05182-4

He, T., Xu, Z. J., Wang, J. F., Wang, F. P., Zhou, X. F., Wang, L. L., et al. (2022). Improving cadmium accumulation by Solanum nigrum L. via regulating rhizobacterial community and metabolic function with phosphate-solubilizing bacteria colonization. *Chemosphere* 287, 132209. doi:10.1016/j.chemosphere.2021.132209

Hu, W. L., Cheng, W. C., Wang, L., and Xue, Z. F. (2022a). Micro-structural characteristics deterioration of intact loess under acid and saline solutions and resultant macro-mechanical properties. *Soil Tillage Res.* 220, 105382. doi:10.1016/j.still.2022.105382

Hu, W. L., Cheng, W. C., and Wen, S. J. (2022b). Investigating the effect of degree of compaction, initial water content, and electric field intensity on electrokinetic remediation of an artificially Cu- and Pb-contaminated loess. *Acta Geotech.* doi:10.1007/s11440-022-01602-9

Hu, W. L., Cheng, W. C., Wen, S. J., and Rahman, M. M. (2021a). Effects of chemical contamination on microscale structural characteristics of intact loess and resultant macroscale mechanical properties. *Catena* 203, 105361. doi:10.1016/j.catena.2021.105361

Hu, W. L., Cheng, W. C., Wen, S. J., and Yuan, K. (2021b). Revealing the enhancement and degradation mechanisms affecting the performance of carbonate precipitation in EICP process. *Front. Bioeng. Biotechnol.* 9, 750258. doi:10.3389/fbioe.2021.750258

Kalantari, B., and Prasad, A. (2014). A study of the effect of various curing techniques on the strength of stabilized peat. *Transp. Geotech.* 1 (3), 119–128. doi:10.1016/j.trgeo.2014.06.002

Kim, W. S., Kim, S. O., and Kim, K. W. (2005). Enhanced electrokinetic extraction of heavy metals from soils assisted by ion exchange membranes. *J. Hazard. Mater.* B118, 93–102. doi:10.1016/j.jhazmat.2004.10.001

Li, C., Hou, H. J., Yang, J. K., Liang, S., Shi, Y. F., Guan, R. N., et al. (2019). Comparison of electrokinetic remediation on lead-contaminated kaolinite and natural soils. *Clean. –. Soil Air Water* 47 (4), 1800337. doi:10.1002/clen.201800337

Ling, J. M., Li, X., Qian, J. S., and Li, X. Y. (2021). Performance comparison of different electrode materials for electroosmosis treatment on subgrade soil. *Constr. Build. Mater.* 271, 121590. doi:10.1016/j.conbuildmat.2020.121590

Liu, H., Li, J. B., Zhao, M., Li, Y. B., and Chen, Y. M. (2019). Remediation of oil-based drill cuttings using low-temperature thermal desorption: Performance and kinetics modeling. *Chemosphere* 235, 1081–1088. doi:10.1016/j.chemosphere.2019.07.047

Liu, K. H., Guan, X. J., Li, C. M., Zhao, K. Y., Yang, X. H., Fu, R. X., et al. (2022). Global perspectives and future research directions for the phytoremediation of heavy metal-contaminated soil: A knowledge mapping analysis from 2001 to 2020. *Front. Environ. Sci. Eng.* 16 (6), 73. doi:10.1007/s11783-021-1507-2

Liu, T., Yuan, X. X., Zhang, G., Hu, J., An, J., and Chen, T. (2020). Stir bar sorptive extraction and automatic two-stage thermal desorption-gas chromatography-mass spectrometry for trace analysis of the byproducts from diphenyl carbonate synthesis. *Microchem. J.* 153, 104341. doi:10.1016/j.microc.2019.104341

Lu, C., Hong, Y., Liu, J., Gao, Y. Z., Ma, Z., Yang, B., et al. (2019b). A PAH-degrading bacterial community enriched with contaminated agricultural soil and its utility for microbial bioremediation. *Environ. Pollut.* 251, 773–782. doi:10.1016/j.envpol.2019.05.044

Lu, Y. S., Wang, W. B., Wang, Q., Xu, J., and Wang, A. Q. (2019a). Effect of oxalic acid-leaching levels on structure, color and physico-chemical features of palygorskite. *Appl. Clay Sci.* 183, 105301. doi:10.1016/j.clay.2019.105301

Meseldzija, S., Petrovic, J., Onjia, A., Volkov-Husovic, T., Nesic, A., Vukelic, N., et al. (2019). Utilization of agro-industrial waste for removal of copper ions from aqueous solutions and mining-wastewater. *J. Industrial Eng. Chem.* 75, 246–252. doi:10.1016/j.jiec.2019.03.031

Ministry of Water Resources of the People's Republic of China (2019). *Standard for geotechnical test methods, GB/T 50123-2019*. Beijing: China Planning Press.

Mohamadi, S., Saeedi, M., and Mollahosseini, A. (2019). Enhanced electrokinetic remediation of mixed contaminants from a high buffering soil by focusing on mobility risk. *J. Environ. Chem. Eng.* 7 (6), 103470. doi:10.1016/j.jece.2019.103470

Muddanna, M. H., and Baral, S. S. (2019). A comparative study of the extraction of metals from the spent fluid catalytic cracking catalyst using chemical leaching and bioleaching by Aspergillus Niger. *J. Environ. Chem. Eng.* 7 (5), 103335. doi:10.1016/j.jece.2019.103335

Mukherjee, K., Saha, R., Ghosh, A., and Saha, B. (2013). Chromium removal technologies. *Res. Chem. Intermed.* 39, 2267–2286. doi:10.1007/s11164-012-0779-3

Mwandira, W., Nakashima, K., and Kawasaki, S. (2017). Bioremediation of lead-contaminated mine waste by Pararhodobacter sp. based on the microbially induced calcium carbonate precipitation technique and its effects on strength of coarse and fine grained sand. *Ecol. Eng.* 109, 57–64. doi:10.1016/j.ecoleng.2017.09.011

National Bureau of Statistics (2001). *China statistical Yearbook*. Beijing, China: China National Publishing House.

National Bureau of Statistics (2018). *China Statistical Yearbook*. Beijing, China: China National Publishing House.

Saha, B., and Orvig, C. (2010). Biosorbents for hexavalent chromium elimination from industrial and municipal effluents. *Coord. Chem. Rev.* 254, 2959–2972. doi:10.1016/j.ccr.2010.06.005

Saha, R., Nandi, R., and Saha, B. (2011). Sources and toxicity of hexavalent chromium. *J. Coord. Chem.* 64 (10), 1782–1806. doi:10.1080/00958972.2011.583646

Puppala, S. K., Alshawabkeh, A. N., Acar, Y. B., Gale, R. J., and Bricka, M. (1997). Enhanced electrokinetic remediation of high sorption capacity soil. *J. Hazard. Mater.* 55 (1–3), 203–220. doi:10.1016/s0304-3894(97)00011-3

Tak, H. I., Ahmad, F., and Babalola, O. (2013). Advances in the application of plant growth-promoting rhizobacteria in phytoremediation of heavy metals. *Rev. Environ. Contam. Toxicol.* 223, 33–52. doi:10.1007/978-1-4614-5577-6_2

Wang, F., Shen, Z. T., Liu, R. Q., Zhang, Y. H., Xu, J., Al-Tabbaa, A., et al. (2019). GMCs stabilized/solidified Pb/Zn contaminated soil under different curing temperature: Physical and microstructural properties. *Chemosphere* 239, 124738. doi:10.1016/j.chemosphere.2019.124738

Wang, L., Cheng, W. C., and Xue, Z. F. (2022a). Investigating microscale structural characteristics and resultant macroscale mechanical properties of loess exposed to alkaline and saline environments. *Bull. Eng. Geol. Environ.* 81, 146. doi:10.1007/s10064-022-02640-z

Wang, L., Cheng, W. C., and Xue, Z. F. (2022b). The effect of calcium source on Pb and Cu remediation using enzyme-induced carbonate precipitation. *Front. Bioeng. Biotechnol.* 10, 849631. doi:10.3389/fbioe.2022.849631

Wang, L. Q., Shao, S. J., and She, F. T. (2020). A new method for evaluating loess collapsibility and its application. *Eng. Geol.* 264, 105376. doi:10.1016/j.enggeo.2019.105376

Wang, Y. C., Li, A., and Cui, C. W. (2021). Remediation of heavy metal-contaminated soils by electrokinetic technology: Mechanisms and applicability. *Chemosphere* 265, 129071. doi:10.1016/j.chemosphere.2020.129071

Wen, D. D., Fu, R. B., and Li, Q. (2021). Removal of inorganic contaminants in soil by electrokinetic remediation technologies: A review. *J. Hazardous Materials* 401, 123345.

Wu, Y. J., Santos, S. S., Vestergård, M., González, A. M. M., Ma, L. Y., Feng, Y., et al. (2022). A field study reveals links between hyperaccumulating Sedum plants-associated bacterial communities and Cd/Zn uptake and translocation. *Sci. Total Environ.* 805, 150400. doi:10.1016/j.scitotenv.2021.150400

Xu, H. T., Song, Y., Cang, L., and Zhou, D. M. (2020). Ion exchange membranes enhance the electrokinetic *in situ* chemical oxidation of PAH-contaminated soil. *J. Hazard. Mater.* 382, 121042. doi:10.1016/j.jhazmat.2019.121042

Xue, Z. F., Cheng, W. C., and Wang, L. (2021b). Effect of straw reinforcement on the shearing and creep behaviours of Quaternary loess. *Sci. Rep.* 11, 19926. doi:10.1038/s41598-021-99318-5

Xue, Z. F., Cheng, W. C., Wang, L., and Hu, W. L. (2022). Effects of bacterial inoculation and calcium source on microbial-induced carbonate precipitation for lead remediation. *J. Hazard. Mater.* 426, 128090. doi:10.1016/j.jhazmat.2021.128090

Xue, Z. F., Cheng, W. C., Wang, L., and Song, G. Y. (2021a). Improvement of the shearing behaviour of loess using recycled straw fiber reinforcement. *KSCE J. Civ. Eng.* 25, 3319–3335. doi:10.1007/s12205-021-2263-3

Yuan, L. Z., Xu, X. J., Li, H. Y., Wang, Q. Y., Wang, N. N., Yu, H. W., et al. (2017). The influence of macroelements on energy consumption during periodic power electrokinetic remediation of heavy metals contaminated

black soil. *Electrochimica Acta* 235, 604–612. doi:10.1016/j.electacta.2017.03.142

Zang, F., Wang, S. L., Nan, Z. R., Zhao, C. Y., Sun, H. L., Huang, W., et al. (2019). Leachability of heavy metals in loess-amended dredged sediment from Northwest of China. *Ecotoxicol. Environ. Saf.* 183, 109561. doi:10.1016/j.ecoenv.2019.109561

Zeng, X. Y., Li, S. W., Leng, Y., and Kang, X. H. (2020). Structural and functional responses of bacterial and fungal communities to multiple heavy metal exposure in arid loess. *Sci. Total Environ.* 723, 138081. doi:10.1016/j.scitotenv.2020.138081

Zheng, R. J., Feng, X. Z., Zou, W. S., Wang, R. H., Yang, D. Z., Wei, W. F., et al. (2021). Converting loess into zeolite for heavy metal polluted soil remediation based on "soil for soil-remediation" strategy. *J. Hazard. Mater.* 412, 125199. doi:10.1016/j.jhazmat.2021.125199

Zhou, H. D., Liu, Z. Y., Li, X., and Xu, J. H. (2021). Remediation of lead (II)-contaminated soil using electrokinetics assisted by permeable reactive barrier with different filling materials. *J. Hazard. Mater.* 408, 124885. doi:10.1016/j.jhazmat.2020.124885

Zhou, R., Liu, X. C., Luo, L., Zhou, Y. Y., Wei, J. H., Chen, A. W., et al. (2017). Remediation of Cu, Pb, Zn and Cd-contaminated agricultural soil using a combined red mud and compost amendment. *Int. Biodeterior. Biodegrad.* 118, 73–81. doi:10.1016/j.ibiod.2017.01.023

Zhu, C. P., Liu, H. L., and Shen, Y. (2011). Laboratory tests on shear strength properties of soil polluted by acid and alkali. *Chin. J. Geotechnical Eng.* 33 (7), 164–170.

Zu, Y., Yuan, L., Schvartz, C., Langlade, L., and Fan, L. (2004). Accumulation of Pb, Cd, Cu and Zn in plants and hyperaccumulator choice in Lanping lead-zinc mine area, China. *Environ. Int.* 30, 567–576. doi:10.1016/j.envint.2003.10.012

frontiers | Frontiers in Materials

TYPE Original Research
PUBLISHED 01 September 2022
DOI 10.3389/fmats.2022.976696

Check for updates

OPEN ACCESS

EDITED BY
Xianze Cui,
China Three Gorges University, China

REVIEWED BY
Lin LI,
Chang'an University, China
Wenbing Wu,
China University of Geosciences
Wuhan, China

*CORRESPONDENCE
Yalong Jiang,
yalongjiang@whu.edu.cn

SPECIALTY SECTION
This article was submitted to Structural Materials,
a section of the journal
Frontiers in Materials

RECEIVED 23 June 2022
ACCEPTED 28 July 2022
PUBLISHED 01 September 2022

CITATION
Xu C, Lin Z, Jiang Y, Shi Y, Fan X, Xiong Z and Liu Y (2022), Research on the spatial effect of foundation pit under asymmetric loads.
Front. Mater. 9:976696.
doi: 10.3389/fmats.2022.976696

COPYRIGHT
© 2022 Xu, Lin, Jiang, Shi, Fan, Xiong and Liu. This is an open-access article distributed under the terms of the Creative Commons Attribution License (CC BY). The use, distribution or reproduction in other forums is permitted, provided the original author(s) and the copyright owner(s) are credited and that the original publication in this journal is cited, in accordance with accepted academic practice. No use, distribution or reproduction is permitted which does not comply with these terms.

Research on the spatial effect of foundation pit under asymmetric loads

Changjie Xu[1,2,3], Zhaorui Lin[1,2], Yalong Jiang[1,2]*, Yufeng Shi[1,2], Xiaozhen Fan[4], Zheng Xiong[1,2] and Yangfeng Liu[1,2]

[1]Institute of Geotechnical Engineering, School of Civil Engineering and Architecture, East China Jiaotong University, Nanchang, China, [2]Jiangxi Key Laboratory of Infrastructure Safety and Control in Geotechnical Engineering, East China Jiaotong University, Nanchang, China, [3]State Key Laboratory of Performance MonitoringProtecting of Rail Transit Infrastructure, East China Jiaotong University, Nanchang, China, [4]Zhejiang University City College, Hangzhou, China

Abstract: This research describes the evolution of the spatial effects of foundation pits considering internal support and external loads. Based on the existing concept of "plane strain ratio", the term "plane strain ratio considering maximum surface settlement" is proposed to characterize the spatial effects of an asymmetric foundation pit. A series of finite element model calculations were carried out using the Nanchang Aixi Lake foundation pit, including 1) the calculation of simulated actual conditions, 2) the calculation of simulated full symmetric load, and 3) the calculation of simulated asymmetric load. The results indicate that for the symmetric condition at 20 kPa and below, the spatial effect range increases as the load increases. For the symmetric condition above 20 kPa, the load has a negligible impact on the spatial effect range. On the side with a larger load under asymmetric loading conditions, the spatial effect of the working condition below 30 kPa is smaller than the corresponding symmetric load. On the side with a smaller load, the spatial effect of the working condition above 80 kPa increases compared with that of the corresponding symmetrical load. Given and verified are the modified fitting equations that take into account the influence range of spatial effect on both sides of the foundation pit under symmetrical and asymmetrical loads.

KEYWORDS

asymmetrical foundation pit, ground settlement, spatial effects, 3D FEM, range of influence

1 Introduction

Due to the construction and development of cities, the limited urban space and heavy traffic make the environment surrounding deep foundation pits exceedingly complicated (Zhang J. et al., 2018). Growing concern exists regarding the impact of deep foundation pit excavation on the surrounding environment and neighboring existing buildings (Chang et al., 2013; Xu et al., 2013; Mangushev et al., 2016; Xu et al., 2016; Zhang X. et al., 2018; Luo et al., 2018; Zeng et al., 2018; Sun et al., 2019; Bai et al.,

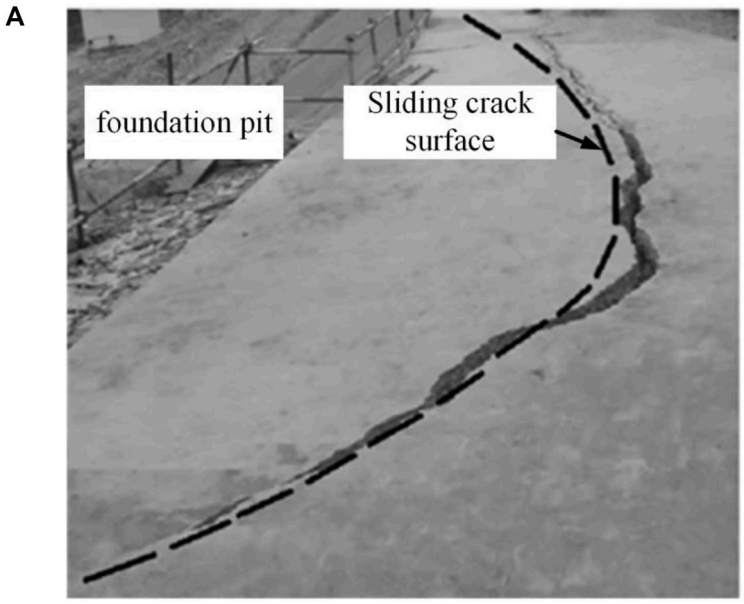

A residential building foundation pit accident site in Mianyang.

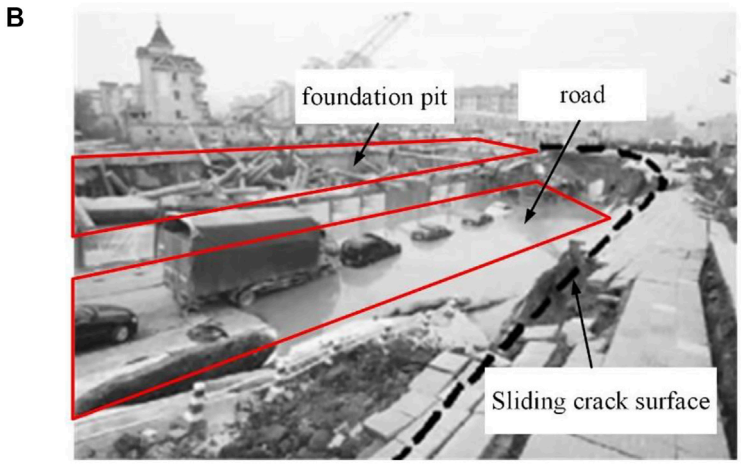

Accident site of deep foundation pit in Hangzhou subway station

FIGURE 1
Typical example of the influence of a foundation pit on its interaction with the surrounding environment (Li et al., 2014). **(A)** A residential building foundation pit accident site in Mianyang. **(B)** Accident site of deep foundation pit in Hangzhou subway station..

2020; Fan et al., 2021). Figure 1 depicts a typical scenario in which the surrounding environment interacts with the foundation pit and generates a disaster. The influence of the surrounding environment on the foundation pit is insufficiently considered, and the deformation of the retaining structure and ground cannot be assessed adequately. Damage to surrounding structures and casualties may result from the excessive movement of retaining structures and earth (Shouhua et al., 2019). Therefore, engineers must give comprehensive consideration to the influence of the surrounding environment on deep foundation pits.

The surrounding environment affects the excavation and deformation of deep foundation pits subjected to a variety type of loads. These loads usually emerge on both sides of the pit in an asymmetrical manner, which can bring uncertainty to the deformation of the pit support. In a foundation pit with an internally braced support system, the effect of the asymmetrical

state is particularly pronounced. Due to the existence of internal bracing, which can lead to complex force transfer issues, the support structures on both sides of the foundation pit may be affected. The available engineering empirical data indicate that asymmetric loads can lead to inconsistent foundation pit deformation on both sides. In the case of small load differences or strict displacement control by the support design, the deformation patterns of the support structures on all sides may be similar, but the amplitudes will vary (Yao and Zhang, 2011; Guo et al., 2019). More frequently than not, asymmetric loads can create a "push-back displacement" toward the exterior of the foundation pit on the side with the smaller load (Xu et al., 2013; Shouhua et al., 2019; Ou et al., 2020; Wang et al., 2021). This means that the top of the support structure on that side may show a reverse displacement towards the outside of the pit. Existing foundation design theories are based on a single side, which cannot logically account for such a condition. Some scholars have also attempted to undertake theoretical research (Xu et al., 2013; Liu et al., 2019), but due to the unique peculiarities of the working condition, these studies have always lacked practical relevance.

With the growth of numerical computation methods and computer technology, numerical simulation has been widely used as a common method in areas that are difficult to be explained by theory. The design of an asymmetric pit is a typical example. Some scholars have utilized numerical modeling techniques to optimize the design of each side in asymmetric pits. On the side with greater loads, especially in projects with special requirements for displacement control, it is required to optimize the deformation situation based on the results of numerical simulations to meet the requirements (Liu et al., 2019; Ou et al., 2020). On the smaller loaded side, it is possible to reduce the reinforcement of the supporting structure appropriately (Lin et al., 2010). This prevents waste because the design is based on the least desirable side. Nevertheless, these optimization efforts are constrained by existing foundation pit design theories. They continue to rely on the plane strain theory, which reduces the foundation pit to 2D for optimization purposes (Li et al., 2021; Chen et al., 2022). The support system of the foundation pit is a 3D complex system with length, width, and height. In the case that the length-to-width ratio and length-to-depth ratio are insufficient, this will inevitably bring a significant mistake. Using 3D numerical simulation approaches, some of the most intricate engineering research has avoided these errors (Guo et al., 2019; Shouhua et al., 2019; Wang et al., 2021). These works are extremely innovative, however, due to the complexity of the studied works, no general experience and guiding principles have been synthesized. The 3D numerical simulations were performed without analyzing and summarizing the deformation of the support structure at the spatial level, and the value of these works was not fully exploited.

To clarify the impact of the foundation pit on the surrounding environment, it is vital to comprehend the spatial deformation of the foundation support system. Past accidents involving foundation pits that have occurred and resulted in damage patterns at the spatial level, demonstrating the necessity of these studies (e.g., Figure 1). The work done by (Chang-Yu et al., 1996; Chang-Yu and Bor-Yuan, 1998; Chang-Yu et al., 2000) is very classical and valuable. They used a 3D nonlinear finite element method based on computer programming techniques to simulate the excavation process of a foundation pit. The concept of "plane strain ratio" (PSR) was initially proposed to quantitatively measure the development of the spatial effect of the foundation pit, and the parametric analysis determined the relationship equation between the 2D calculation results and the 3D calculation results. On the basis of their research, other 3D numerical simulation-based studies with varying focuses were conducted. For instance, (Roboski and Finno, 2006; Finno et al., 2007; Tanner Blackburn and Finno, 2007), established a database covering 150 finite element models and summarized empirical equations between the geometry, the stiffness of the lateral support system, and the safety factor of the footing uplift and the PSR. In addition, the spatial effect cases of different support forms and the spatial distribution of earth pressure (Li and Liang, 2011; Chenghua et al., 2018; Bai et al., 2019; Bai et al., 2020; Bai et al., 2021; Chen and Mo, 2022; Chen and Zhang, 2022) have been investigated. In the majority of studies of spatial effects, plasticity theory has been employed at the theoretical level. These projects include research on sandy soil (Yang et al., 1998) and clay (Mingfeng et al., 2011) foundation pits. In these works, the scope of spatial effects and theoretical calculation methods have been developed. Unfortunately, no research has been conducted on the topic of load in the spatial effect of foundation pits. In addition, due to the limitations of plasticity theory, the application of these theoretical calculation approaches to asymmetric pits is further restricted.

The objective of this paper is to establish a connection between asymmetric loads and the spatial effects of foundation pits. To achieve this purpose, the "plane strain ratio considering the maximum surface settlement" is introduced to quantitatively evaluate the evolution of spatial effects. This is illustrated by the Aixi Lake Tunnel project in Nanchang, Jiangxi, China, where the engineering phenomena "pit within a pit" exists. Firstly, 3D simulation calculations are performed under simulated field conditions and compared with actual monitoring data to validate the accuracy of the parameter selection. Then the development of the spatial effect of the foundation pit under symmetric loads is investigated only for the support of the foundation's outer pit. By fitting data derived from finite element calculations, an empirical formula for the influence range

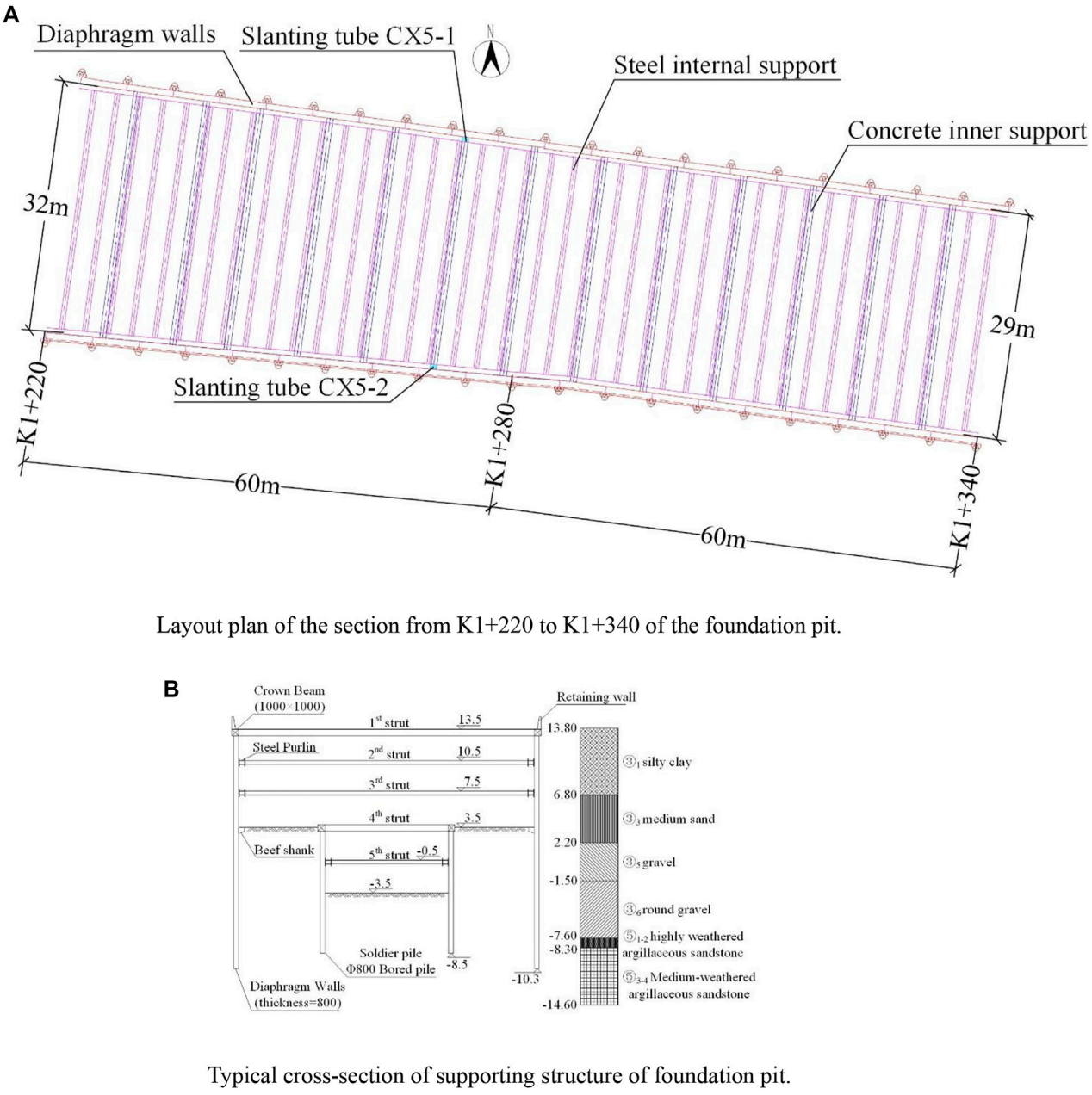

FIGURE 2
Analysis of selected pit project profile. **(A)** Layout plan of the section from K1+220 to K1+340 of the foundation pit. **(B)** Typical cross-section of supporting structure of foundation pit.

of pit spatial effects under symmetric loading considering internal bracing is obtained. Then, the finite element calculations are run for the calculation cases under different load differences and asymmetrical load effects, and the corrections are made again. Finally, the formula calculation results are compared with simulation findings of spatial effects under alternative load conditions to verify the effectiveness of the equation correction.

2 Site characterization

2.1 Project background

The deep foundation pit described in this paper is located in Nanchang, Jiangxi, China, and was excavated for the common construction of the highway crossing Aixi Lake and Nanchang Metro Line 3. A diaphragm wall and three internal supports

TABLE 1 Soil parameters.

Soil layer	h (m)	γ (kN/m^3)	c (kPa)	φ (°)	$\bar{\gamma}$ (kN/m^3)	$\bar{\varphi}$ (°)	E_{50}^{ref} (MPa)	E_{oed}^{ref} (MPa)	E_{ur}^{ref} (MPa)	G_0^{ref} (MPa)
③$_1$ silty clay	7	19	49.92	22.63	19.73	31.93	10.50	10.50	31.50	47.25
③$_3$ medium sand	4.6	19.7	0	32			18.00	18.00	54.00	81.00
③$_5$ gravel	3.7	20	0	35			32.00	32.00	96.00	144.00
③$_6$ round gravel	6.1	20	0	36			35.00	35.00	105.00	126.00
⑤ argillaceous sandstone	2.7	20	40	25			-	-	-	-

comprise the outer pit support system. The first internal support is made of concrete, while the second and third internal supports are made of steel. The inner pit support system is comprised of row piles and two internal supports, the first of which is concrete support and the second of which is steel support. Both sides of the pit's cofferdam provide a specific load to the support structure.

The 120-meter-long section of the pit from K1+220 to K1+340 in the middle of the lake was used for analysis in this research. To measure the horizontal displacement of the diaphragm wall, the slanting tubes were placed on the supporting structure in the center of the foundation pit. Figure 2A depicts the plan layout of the sampled section and the location of the testing instruments. Figure 2B outlines the typical section of the foundation pit support structure.

2.2 Soil profile and parameters

Figure 2B depicts the soil profiles acquired from the geological survey. The main soil layers from the ground to the considered depth are silty clay, medium sand, gravel, round gravel, and argillaceous sandstone. The thickness of each layer can be calculated based on the elevation shown in the soil profile in Figure 2B. The soil parameters for each layer, as determined by field and laboratory experiments, are summarized in Table 1.

3 Standard and assumption

3.1 Criteria for determining spatial effects in the asymmetrical case

In the past, most of the spatial effect studies were undertaken for symmetric foundation pit excavation. Some utilize the "spatial effect coefficient" (Yang et al., 1998; Mingfeng et al., 2011) while others utilize the "plane strain ratio" (PSR) (Chang-Yu et al., 1996; Finno et al., 2007) to describe the extent of the spatial effect. These coefficients are frequently employed to analyze the maximum horizontal displacement of the supporting structure or the amount of the earth pressure. Under the influence of symmetric load, such a discriminative approach is viable. Due to the fact that, under the influence of symmetric excavation, the maximum point of horizontal displacement of the support structure on both sides of the foundation pit is approximately equal, and the action of earth pressure is likewise close. However, under the action of asymmetrical loads, the maximum horizontal displacement point of the support structure on either side of the pit varies. The variation in the deformation of the retaining wall also affects the magnitude and distribution of earth pressure. Therefore, it is necessary to propose a coefficient that can effectively discriminate the development of the spatial effect of the support structure on both sides of the pit when subjected to asymmetrical loads.

The surface soil deformation is a key indicator to focus on in addition to earth pressure and wall displacement (Cui et al., 2020). Heish *et al.* (Pio-Go and Chang-Yu, 1998) offered two possible settlement situations for the settlement of the soil behind the retaining wall: triangular and notched. For these two settlement scenarios, the maximum surface settlement behind the wall occurs at the back of the wall and at 0.5 times the excavation depth, respectively. The position of maximum settlement happens exclusively in relation to the dislocation pattern of the retaining wall. This discrimination method has been frequently utilized due to its simplicity and accuracy.

The original concept of PSR is defined as "maximum wall displacement as the ratio of the maximum wall displacement of a section to the maximum wall displacement of the section under plane strain conditions" (Chang-Yu et al., 1996). In this paper, the "plane strain ratio considering the maximum surface settlement" (PSRS) is proposed as a criterion for identifying the spatial effect development in an asymmetrical foundation pit. PSRS is the ratio of the surface settlement at any point on a line parallel to the pit boundary at the theoretical maximum settlement behind the retaining wall to the maximum surface settlement at that point. The first time the PSRS value hits 0.95 from either side of the foundation pit is considered the boundary between the plane strain zone and the spatial effect zone at that end of the foundation pit. This division approach successfully covers the plane strain area and is easy to implement.

3.2 Simplifications and assumptions in theoretical calculations

To simplify the calculation, the equation fitting and theoretical calculations in this work make the following assumptions and simplifications.

1) The concept of equal-substituted internal friction angle is introduced, the silty clay layer is equal-substituted as a cohesionless soil, and the calculation is performed using the equal-substitution method with equal shear strength of the soil. The specific calculation equation is as follows:

$$\varphi_D = \tan^{-1}\left(\tan\varphi + \frac{c}{\gamma h}\right) \tag{1}$$

where φ_D is the iso-substitutional internal friction angle, φ is the internal friction angle of the soil, c is the cohesion of the soil, γ is the weight of the soil layer, and h is the thickness of the soil layer.

2) It is assumed that the calculation area is filled with a single homogeneous soil layer. For the soil layers discussed above, the sum-of-layers approach is used to homogenize them. The exact expression is as follows:

$$\bar{\varphi} = \sum_{i=1}^{n} \varphi_i h_i \Big/ \sum_{i=1}^{n} h_i \tag{2}$$

$$\bar{\gamma} = \sum_{i=1}^{n} \gamma_i h_i \Big/ \sum_{i=1}^{n} h_i \tag{3}$$

where $\bar{\varphi}$ is the average internal friction angle, φ_i is the internal friction angle of the ith layer of soil, $\bar{\gamma}$ is the average soil weight, γ_i is the ith layer of soil weight, and h_i is the thickness of the ith layer of soil.

The parameters of the soil layer after equal substitution and homogenization are shown in Table 1.

4 Simulation and discussion under symmetric load conditions

4.1 Model establishment

In this paper, plaxis3D is used to simulate the symmetric and asymmetric excavation of the foundation pit in 3D. Figure 3 depicts the 3D model of the deep foundation pit, the mesh division, and the model size. The model size accounts for the avoidance of boundary effects, and the principle of increasing the model size has no effect on the response of the pit excavation.

The soils in the model consist of silty clay, medium sand, gravel, round gravel, highly weathered argillaceous sandstone, and medium-weathered argillaceous sandstone. To accurately describe the force deformation during the excavation of the foundation pit, the Hardening Soil Small (HSS) model is used to simulate the intrinsic relationships of the silty clay, medium sand, gravel, and round gravel layers. The HSS model introduces minor strain properties based on the Hardening Soil model, which can accurately simulate the deformation trend of the support structure and soil during the excavation of the foundation pit but has the disadvantage that the parameters

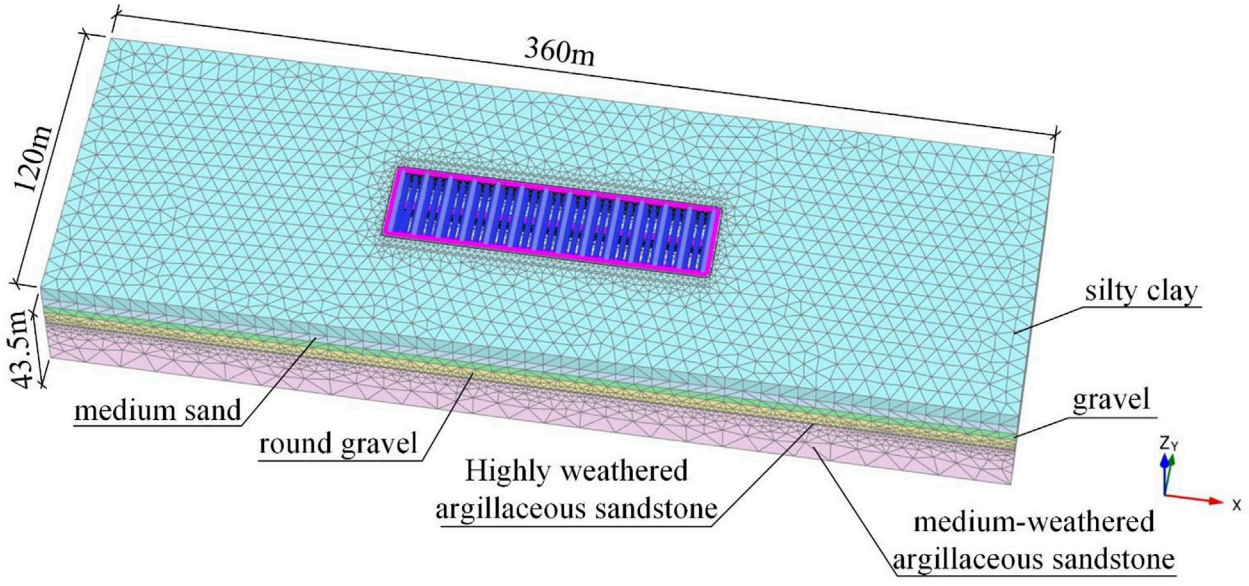

FIGURE 3
Finite element model.

are difficult to be determined. Through lab tests, the values of soil parameters are determined by indoor experiments. Table 1 displays the values. Using the Mohr-Coulomb model, layers of highly weathered argillaceous sandstone and medium-weathered argillaceous sandstone are reproduced. The support structure in the project is simulated by the structure unit, the support in the pit is simulated by the point-to-point anchor, the diaphragm wall and the row pile support are simulated by the plate unit, and the interaction between the soil and the structure is simulated by the interface unit.

4.2 Simulation of excavation under symmetric load

As illustrated in Table 2, the excavation of the foundation pit was simulated. In the first stage, the ground stress was initialized according to the principle of homogeneous, continuous, and isotropic soil layers, and the requisite loads were applied. Prior to the first excavation stage, the displacements and minor strains of the model were reset. The simulation procedures were then followed.

In the calculation of the model parameter check, a 20 kPa asymmetric uniform load is applied on both sides of the pit. The uniform load is applied at a distance of 1 m from the foundation boundary, and the load width is 5m, spanning the entire length of the long side of the foundation pit to imitate the load of the cofferdam on both sides of the foundation pit for the foundation pit enclosure structure at the engineering site. All steps in Table 4 are replicated during the calibration computation.

In the study examining the spatial effects of load, the full load behind the retaining wall was used to determine the typicality of the load factors. From Eq.

TABLE 2 Stages of excavation in FEM analysis.

Excavation stage no.	Description
1	Ground stress initialization and load application
2	Diaphragm wall construction
3	Excavation to 13 m
4	Installation of the first internal support
5	Excavation to 10 m
6	Installation of the second internal support
7	Excavation to 7 m
8	Installation of the third internal support
9	Excavation to 3.5 m
10	Excavation to 3 m
11	Installation of the fourth internal support
12	Excavation to −1 m
13	Installation of the fifth internal support
14	Excavation to −3.5 m

$$x = \frac{H}{\tan\left(45° + \frac{\varphi}{2}\right)} \tag{4}$$

The calculation suggests that the full pile load length outside the foundation pit is approximately 13.32 m, x is the load length outside the foundation pit, H is the length of the support pile, and φ is the angle of internal friction in the equation. In the subsequent load calculation, the load outside the foundation pit was assumed to extend 15 m from the foundation pit's perimeter, spanning the entire length of the foundation pit's long side. The load is measured from 0 to 100 kPa in 10 kPa increments on both sides of the foundation pit and applied symmetrically. In the examination of spatial effects, only the excavation to the bottom of the outer pit is studied, and the effects generated by the piles in the inner pit row are excluded in the simulation. In the subsequent simulations under symmetrical and asymmetrical loads, therefore, just the first nine simulation steps are executed.

4.3 Analysis of FEM results for symmetric load conditions

4.3.1 Analysis of FEM analysis results simulating the realistic condition

The focus must be placed on the horizontal deformation of the support structure in the actual project. When the foundation pit in the calculation example is excavated to the bottom of the inner pit, Figure 4 depicts the horizontal deformation of the outer pit's ground connection wall. In the depth direction, the horizontal displacement of the diaphragm wall is minimal at the top and bottom and abundant in the middle, indicating a "bloated belly" deformation trend. The maximum depth of horizontal displacement is close to the base of the outer pit. Figure 5 depicts a comparison between the monitoring data at CX5 and the maximum wall displacement derived from FEM. The deformation trends and maximum displacements of both are comparable. The peak displacements of the monitoring data looked to be somewhat greater than the FEM results. The realistic force condition of the foundation pit is complex, and the FEM simplification resulted in a certain amount of mistakes. The similar deformation trends and peak displacements of the two indicate that the model parameter selection was fair.

The measured data and numerical calculations result in the deformation of the ground connection wall, which shows the deformation tendency of the "bloated belly" and is consistent with the description of the "concave settlement profile" soil settlement model behind the wall in the literature. Therefore, the PSRS parameter values were determined using the surface settlement value at an excavation depth of 0.5 times behind the retaining wall.

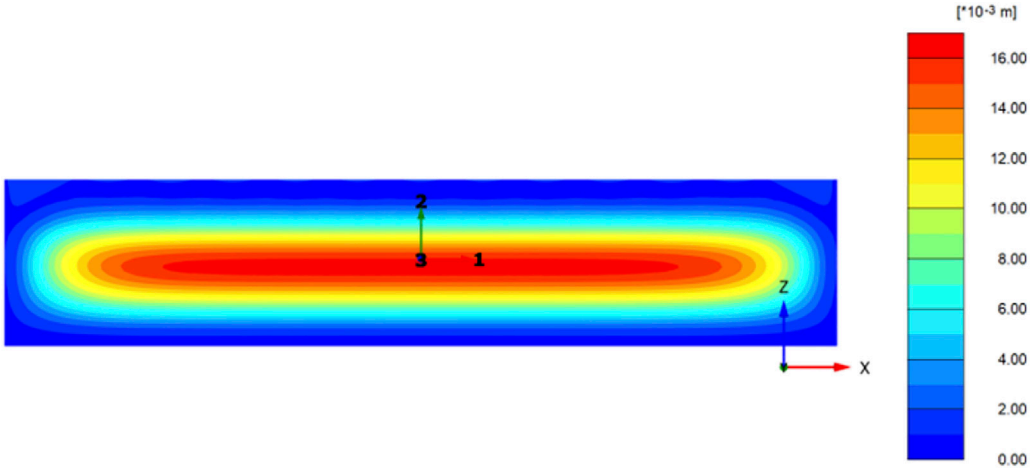

FIGURE 4
Horizontal displacement cloud plot of the external pit diaphragm wall.

4.3.2 Carrying out spatial effects under full symmetric load

Figure 6 depicts the maximum settlement outside the foundation pit along the diaphragm wall direction for the 11 computed symmetry conditions. The maximum settlement values outside the foundation pit exhibit a distinct spatial influence. Near the end, the surface settlement values are much less than those in the middle. The surface settlement values stabilize after a given distance from the terminus. As depicted in Figure 6A, the plane strain zone in the center of the foundation pit displays a "sawtooth" deformation pattern under the minor load. The location of the minor deformation and the first internal support of the foundation pit coincide substantially. Under conditions of low load, the internal support can effectively control the horizontal displacement of the diaphragm wall. In the zone with "sawtooth" deformation, the PSRS = 0.95 criterion can still cover the deformation in the center of the foundation pit, indicating that this criterion is reliable in delineating the plane strain zone and the zone affected by spatial effects. Under working conditions with a load of more than 20 kPa, the deformation of the plane strain zone exhibits a smooth curve, and the deformation in the middle part is close.

Table 3 summarizes the influence range of spatial effects under various operating situations. In the case of no-load action outside the foundation pit, the spatial effect influence range of the foundation pit is greatest. With a rise in the appropriate load value, the spatial effect influence range tends to diminish. When the load exceeds a particular threshold and the load outside the pit is increased, the spatial effect influence range hardly changes. The spatial effect influence range swings between 23.01 and 23.84 m for the eight working conditions with a load value outside the pit between 30 and 100 kPa, and there is no discernible rise or fall. After the load reaches a particular magnitude, the soil of the foundation pit wall may reach a state of equilibrium.

4.4 Correction of the spatial effect range under symmetric load

4.4.1 Equation correction

(Yang et al., 1998) suggested the following equation for estimating the influence range of spatial effects using the theory of plasticity ceiling:

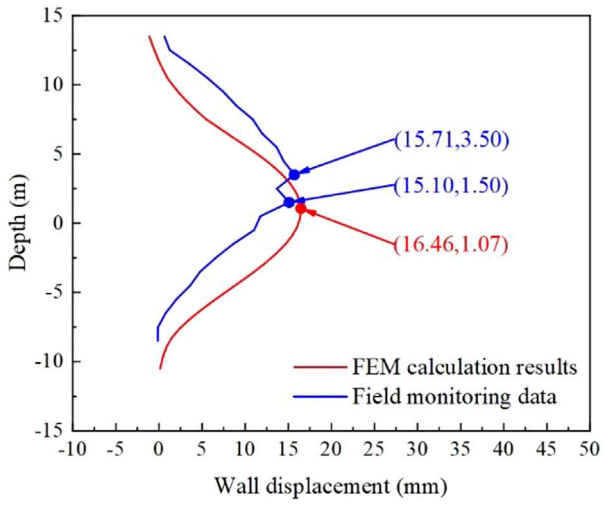

FIGURE 5
Comparison of monitoring data and FEM calculation of horizontal displacement of the diaphragm wall.

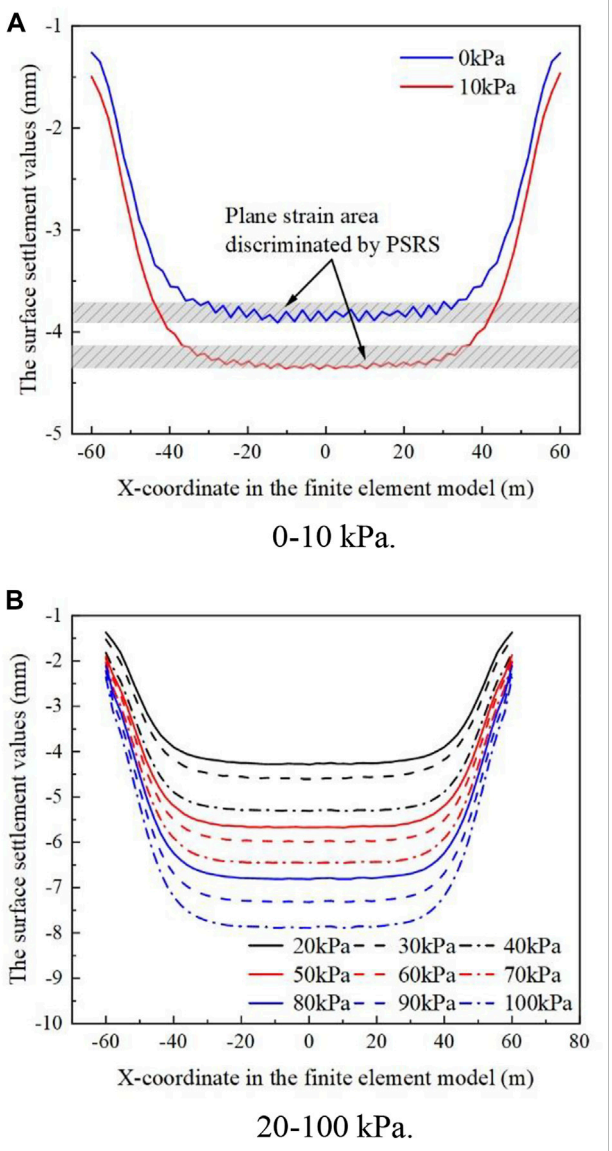

FIGURE 6
Development of spatial effect of the foundation pit under the symmetrical load of 0–100 kPa. **(A)** 0–10 kPa. **(B)** 20–100 kPa.

$$b = H\frac{\tan\varphi}{\sin\beta_{cr}} \tag{5}$$

where b is the spatial effect influence range and β_{cr} is the critical rupture angle of the soil. β_{cr} is obtained from the trial calculation of Eq. 6.

$$E_a = \frac{\sin(\beta_{cr}-\varphi)\cot\beta_{cr}}{\cos(\beta_{cr}-\delta-\varphi)}\left(\frac{1}{2}\gamma BH^2 - \frac{1}{3}\gamma H^3\frac{\tan\varphi}{\sin\beta_{cr}}\right) \tag{6}$$

Where γ is the weight of the soil, and δ is the wall-soil friction angle. It can be found that $\beta_{cr} = 53.4°$ in the calculation of this paper. Substituting the soil parameters and critical rupture angle into Eq. 5, we can determine that b = 18.63 m for this case. This computation result differs significantly from the one provided in Table 3. There are two primary causes for this problem. The first reason is that Eq. 5 does not account for the case of load, and the second reason is that Eq. 5 does not account for the restraining effect of the internal support of the foundation pit on the displacement of the retaining structure. Therefore, the coefficient k_1 considering the loads on both sides of the foundation pit is first introduced, and the first fitting modification to Eq. 5 is made so that it satisfies the requirements for application in inner braced support systems considering the following loads.

TABLE 3 Range of spatial effects under symmetric conditions.

Value of load action outside the foundation pit (kPa)	Range of spatial effects (m)
0	26.77
10	25.06
20	24.53
30	23.63
40	23.01
50	23.68
60	23.24
70	23.41
80	23.43
90	23.56
100	23.84

$$b = [H + k_1]\frac{\tan\varphi}{\sin\beta_{cr}} \tag{7}$$

where P is the load on both sides of the pit.

Considering the calculation results of Table 3, the value of k_1 in Eq. 7 is fitted as shown in Figure 7A.

The spatial effect range of the internally braced support system considering the external load of the foundation pit can be determined using the formula for fitting analysis.

$$b = [H + k_1]\frac{\tan\varphi}{\sin\beta_{cr}} \tag{8}$$

which $k_1 = 4.38609 \times e^{-\frac{\frac{P}{y}}{0.69332}} + 6.14653$

4.4.2 Equation validation

After correcting the resulting Eq. 8, the image is plotted according to the curve in Figure 7B. Take the load value outside the foundation pit 5–95 kPa, every 10 kPa as a kind of condition for calculation, and get 10 sets of validation data, as illustrated in Figure 7B. The difference between the fitted equation calculation results and the trend of the validation

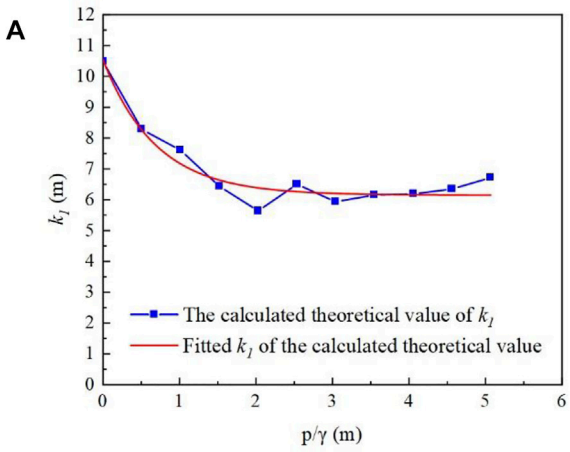

k_1 value fitted curve.

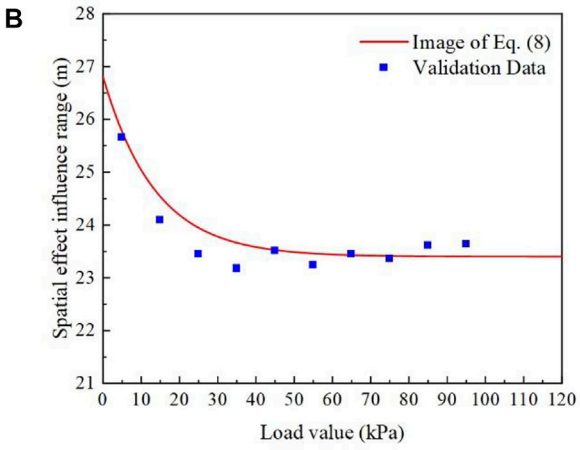

Equation and validation data of the influence range of spatial effect considering symmetric load action.

FIGURE 7
Symmetric case fitted results and validation data. **(A)** k_1 value fitted curve. **(B)** Equation and validation data of the influence range of spatial effect considering symmetric load action.

data is less than 0.5 m. The calculated validity of the fitted equation can be observed.

5 Simulation and discussion under asymmetric conditions

5.1 Simulation of excavation under asymmetric loads

The condition with 0 kPa on the smaller side of an asymmetric load is simulated first. The greater load side is measured from 0 to 100 kPa in 10 kPa increments. The conditions of 20 kPa and 40 kPa on the side with the smaller load are subsequently compared.

5.2 Analysis of FEM results under asymmetric loads

Figure 8 illustrates the vertical deformation in the plane strain zone at 0:20 kPa. The maximum ground surface settlement behind the diaphragm wall is between 5 and 10 m on both sides of the higher and lower loads. The proposed "concave settlement profile" model accurately describes the surface settlement in both cases. It can be demonstrated that

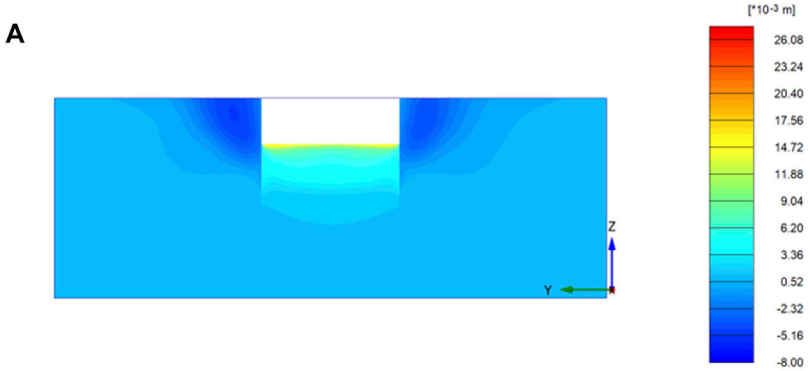

Plane strain zone vertical displacement cloud map.

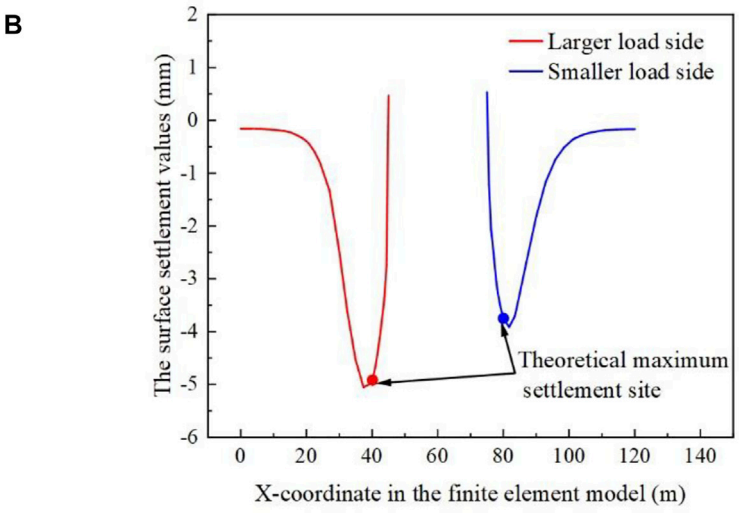

Surface settlement profile after the diaphragm wall in the plane strain section.

FIGURE 8
Vertical deformation under 0:20 kPa condition. **(A)** Plane strain zone vertical displacement cloud map. **(B)** Surface settlement profile after the diaphragm wall in the plane strain section.

the PSRS value is dependable for describing the development of spatial effects on both sides of the asymmetric foundation pit and that the position of its value does not change much when asymmetric pressure occurs.

Table 4 and Figure 9 show the range at which the spatial effects on the greater side of the foundation pit load and the smaller side of the load under the asymmetric load of the deflection condition. Comparing the influence range of the side with greater loads to that of the side with smaller loads under the same working conditions reveals that the influence range of the side with smaller loads is significantly greater. The development of spatial effects on one side of the foundation pit is determined mostly by the loads on that side.

With the application of bias pressure on both sides of the foundation pit, the spatial effect influence range sharply decreases on the greater load side of the foundation pit, reaching an interval between 22.96 and 23.63 m. For the ten conditions with asymmetrically applied loads, the spatial effect influence range on the side with greater loads fluctuates in the interval of 22.96–23.63 m. Comparing with the symmetric load conditions corresponding to the load size in Table 3, the spatial effect influence range is significantly reduced for the three conditions

with smaller load values. In addition, the difference between the two spatial impacts in the seven situations ranging from 40–100 kpa is negligible. To study the cause of this phenomenon, the symmetric 20 kPa load condition and the asymmetric 0:20 kPa load condition were selected for comparison. The diaphragm wall on the bias side of the latter condition is likewise selected for the study. The horizontal displacement value of the diaphragm wall in the symmetric condition (8 mm) is less than the horizontal displacement value of the ground connection wall of the same size in the asymmetric condition (8.5 mm). This situation may occur when the load is not applied to the smaller side of the load, hence preventing the internal support from maximizing the constraining impact of the deformation on the larger side of the load. This situation makes the soil of the foundation pit wall on the side with the greater load to achieve the limit equilibrium more rapidly, which influences the development of the spatial effects. Therefore, Eq. 7 must be corrected by utilizing the greater side value of the load.

On the side of the foundation pit with less load, the spatial effect of the seven conditions with less load has a comparable influence range. In the three operating circumstances when the load is increased, the spatial effect range expands dramatically. This could be owing to the higher value of bias pressure on both sides of the foundation pit, as well as the fact that the soil of the foundation pit wall on the side with the lighter load is not in ultimate equilibrium. As depicted in Figure 9, the deformation on the side with a smaller load reduces as the load difference increases. The constantly shrinking displacement generates a significant difference between the state of the soil when the load difference is minimal. If the bias rises further, it is expected that the side with less load will approach zero displacements. The support structure may even experience a "push-back displacement" toward the outside of the foundation pit, and the soil behind the wall may cause an elevation. It can be seen that on the side with a smaller load, the load difference between the two sides of the foundation pit is an essential determining factor in addition to the load on that side. It can be seen that the cause for the difference in the influence range of the spatial effect of the foundation pit on the side with the greater load and the side with the smaller load is relatively distinct.

Therefore, the corrections for the side with the bigger load and the side with the smaller load must be evaluated individually in the ensuing work.

5.3 Correction of the spatial effect range under asymmetric loads

In the asymmetric state, the factors that lead to the soil of the foundation wall being in non-limiting equilibrium are distinct. To resolve the dilemma, the spatial consequences on both sides of the asymmetric foundation pit are evaluated independently. On the side of the larger load, introduce the coefficient k_2 that considers the load on the larger side of the load, and obtain the following equation for the spatial effect range of the larger side of the load:

$$b = [H + k_1 + k_2] \frac{\tan \varphi}{\sin \beta_{cr}} \tag{9}$$

On the smaller side of the load, the coefficient k_3 that considers the difference of the load on both sides of the foundation pit is introduced, and the following equation is derived for the spatial effect influence range on the smaller side of the load.

TABLE 4 Range of spatial effects on both sides of the foundation pit under asymmetric loads.

Load value in the greater load side (kPa)	Load value in the smaller load side (kPa)	Range of spatial effects on the greater load side (m)	Range of spatial effects on the smaller load side (m)
0	0	26.77	26.77
10	0	23.50	26.22
20	0	23.19	26.45
30	0	22.96	26.47
40	0	23.37	26.68
50	0	23.53	26.94
60	0	23.18	26.48
70	0	23.32	26.97
80	0	23.46	28.11
90	0	23.63	28.56
100	0	23.61	30.48

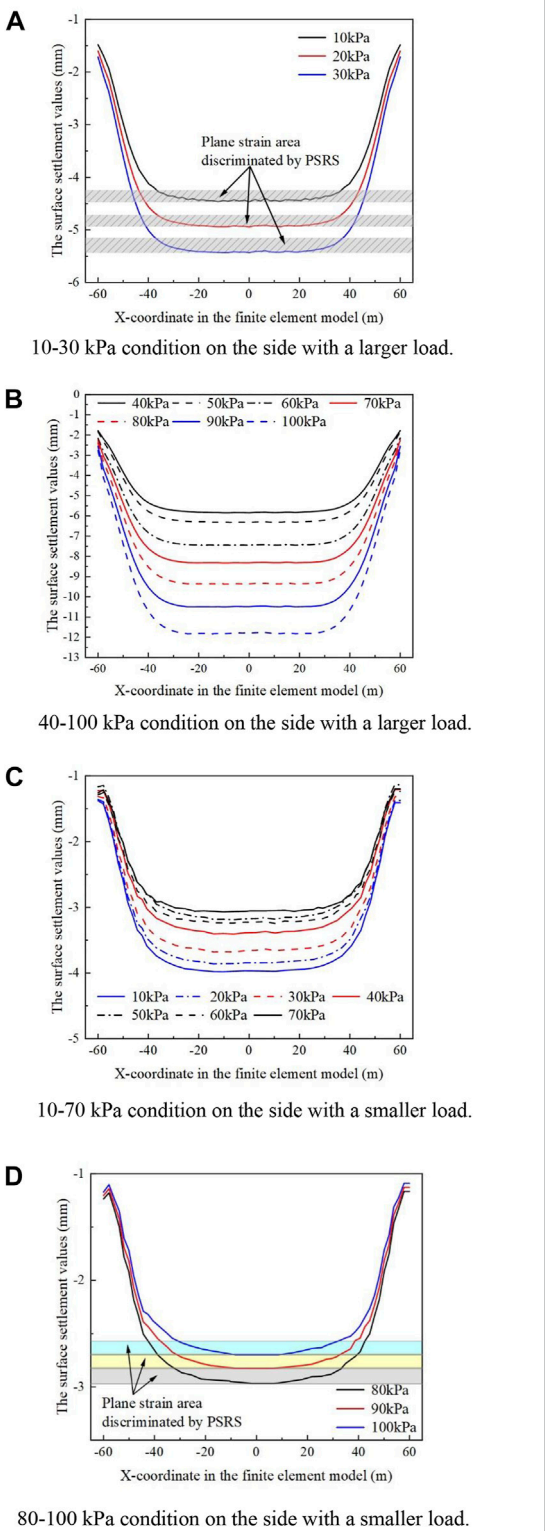

FIGURE 9
Spatial effect influences range when the load is 0 kPa on the smaller side. **(A)** 10–30 kPa condition on the side with a larger load. **(B)** 40–100 kPa condition on the side with a larger load. **(C)** 10–70 kPa condition on the side with a smaller load. **(D)** 80–100 kPa condition on the side with a smaller load.

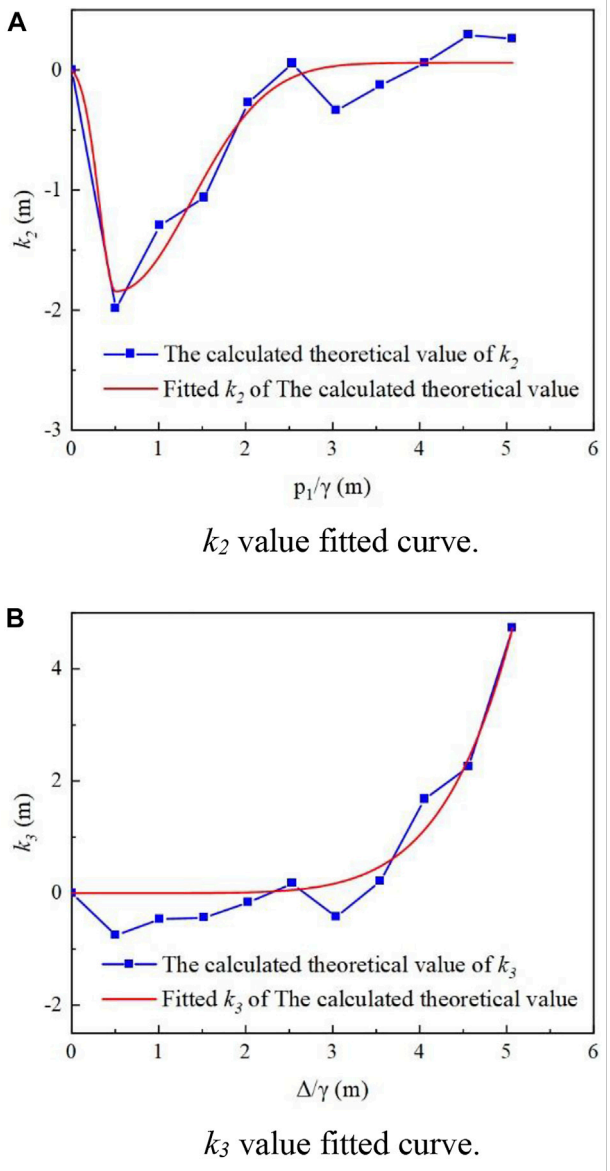

FIGURE 10
The fitting of correction parameters in the asymmetric case. **(A)** k_2 value fitted curve. **(B)** k_3 value fitted curve.

$$b = [H + k_1 + k_3]\frac{\tan\varphi}{\sin\beta_{cr}} \tag{10}$$

Where P_1 is the load value on the larger side of the load, P_2 is the load value on the smaller side of the load, and Δ is the absolute value of the load difference between the two sides of the foundation pit.

5.3.1 Greater load side equation correction

According to the previous analysis, Eq. 8 is again corrected with the ratio of the load value on that side to the soil weight as

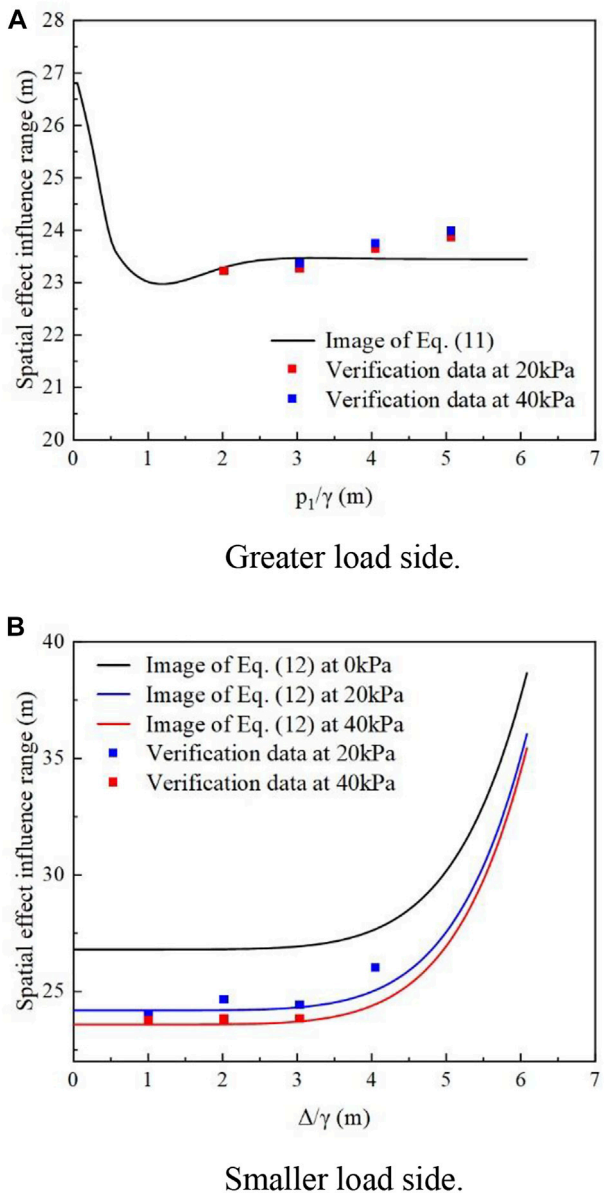

FIGURE 11
Images and validation data of the equation for the influence range of spatial effects under asymmetric loads. **(A)** Greater load side. **(B)** smaller load side.

the independent variable on the side with greater loads. The form of the correction equation is shown in Eq. 9. Considering the calculation results of Table 4 together, the value of k_2 taken in Eq. 9 is fitted, as illustrated in Figure 10A.

By fitting, it is possible to get the following equation for the influence range of the bigger side spatial effect of the load under asymmetric loads:

$$b = [H + k_1 + k_2]\frac{\tan\varphi}{\sin\beta_{cr}} \tag{11}$$

$$\text{Which } k_2 = \begin{cases} 0.0599 - 1.90367e^{-0.5\left(\frac{\frac{P_1}{\gamma}-0.50684}{0.1927}\right)^2}, & \frac{P_1}{\gamma} < 0.5 \\ 0.0599 - 1.90367e^{-0.5\left(\frac{\frac{P_1}{\gamma}-0.50684}{0.86651}\right)^2}, & \frac{P_1}{\gamma} \geq 0.5 \end{cases}$$

5.3.2 Smaller load side equation correction

On the side with a lighter load, the ratio of the load value to the soil weight on this side is the independent variable of the correction factor k_1, while the ratio of the load difference between the two sides of the foundation pit and the soil weight is the independent variable of the correction factor k_3. Eq. 10 depicts the form of the correction equation. Taking into account the findings of Table 4's calculations, the value of k_3 in Eq. 10 is fitted, as depicted in Figure 10B.

By fitting, it is possible to get the following equation for the influence range of the smaller side spatial effect of the load under asymmetric loads:

$$b = [H + k_1 + k_3]\frac{\tan\varphi}{\sin\beta_{cr}} \tag{12}$$

$$\text{Which } k_3 = 1.40054 \times 10^{-4} \times \left(\frac{\Delta}{\gamma}\right)^{6.42495}$$

5.3.3 Equation validation

Equation. 11 produced by correction on the side with the greater load is plotted to obtain the image depicted by the curve in Figure 11A. For calculation and verification purposes, the load values on the side with the smaller load are 20 kPa and 40 kPa, respectively, while the load values on the side with a larger load are altered. As shown in Figures 11A a total of seven sets of validation data were acquired. The validation data basically match the fitted equation.

The smaller side of the load is corrected to obtain Eq. 12, and two variables, the load on the smaller side of the load and the absolute value of the load difference between the two sides of the foundation pit, need to be considered. Three curves are plotted according to Eq. 12 for the load on the smaller side as 0 kPa, 20 kPa, and 40 kPa, as shown in Figure 11B. Verification of the data change trend and the magnitude of the value, as well as the results of the equation computation, are essentially the match. This demonstrates the reliability of the fitted equation.

6 Conclusion

This work proposed the equation of the influence range on the spatial effect of the foundation pit considering the load. A series of numerical computation tests were done in order to examine the three-dimensional deformation of the diaphragm

wall under various loading conditions. The main conclusions obtained are summarized as follows.

1) This study introduces a "notch-type" soil settlement model as a three-dimensional spatial effect discriminator based on the "plane strain ratio". The concept of "plane strain ratio assuming maximum surface settlement" is proposed to quantify the development of spatial effects in asymmetric foundation pits.
2) When the load is small (in the case of 0–20 kPa), the spatial effect of the foundation pit is larger. With the increase of the external load value (in the case of 30–100 kPa), the spatial effect of the foundation pit gradually decreases and stabilizes, fluctuating in the range of 23.01–23.84 m. On this basis, the equation of the influence range of the foundation pit spatial effect considering the internal support and the out-of-pit stacking load is modified and fitted.
3) Under the action of the asymmetric load, the load on one side of the foundation pit governs the spatial effects on that side. When the load on both sides of the foundation pit is small (10–30 kPa for the larger side), the spatial effect of the bias side is reduced. When the load difference between the two sides of the foundation pit is significant (80–100 kPa for the larger side), the spatial effect of the smaller side grows rapidly.

4) For verification purposes, the data obtained from the calculation example were modified to fit the equations for the influence range of spatial effect on the side with a larger load and the side with a smaller load and were compared with the validation conditions. Considering the development of spatial effect of foundation pit from the perspective of out-of-pit settlement can serve as a reference point for the interaction between foundation pit and surrounding environment.

The theory presented in this study is only for pure shear 3D failure mode of pit wall soil mass, for tension crack-shear 3D failure mode of pit wail soil mass is still lack of discussion. At the same time, the validation of the proposed formula needs to be further clarified by field monitoring data or experimental studies for its applicability.

Data availability statement

The original contributions presented in the study are included in the article/supplementary material, further inquiries can be directed to the corresponding author.

Author contributions

CX, ZL, and YJ are the main accomplishers of this work and have completed most of the numerical simulation and theoretical work. YS, XF, ZX and YL assisted in the data processing and geotechnical tests.

Funding

This work was supported by National Science Fund for Distinguished Young Scholars (NSFC Grant No. 51725802), National Natural Science Foundation of China (NSFC Grant No. 51878276) and Jiangxi Natural Science Foundation (No.20212BAB204012).

Conflict of interest

The authors declare that the research was conducted in the absence of any commercial or financial relationships that could be construed as a potential conflict of interest.

Publisher's note

All claims expressed in this article are solely those of the authors and do not necessarily represent those of their affiliated organizations, or those of the publisher, the editors and the reviewers. Any product that may be evaluated in this article, or claim that may be made by its manufacturer, is not guaranteed or endorsed by the publisher.

References

Bai, B., Xu, T., Nie, Q., and Li, P. (2020). Temperature-driven migration of heavy metal Pb2+ along with moisture movement in unsaturated soils. *Int. J. Heat Mass Transf.* 153119573, 119573. doi:10.1016/j.ijheatmasstransfer.2020.119573

Bai, B., Yang, G., Li, T., and Yang, G. (2019). A thermodynamic constitutive model with temperature effect based on particle rearrangement for geomaterials. *Mech. Mater.* 139103180, 103180. doi:10.1016/j.mechmat.2019.103180

Bai, B., Zhou, R., Cai, G., Hu, W., and Yang, G. (2021). Coupled thermo-hydro-mechanical mechanism in view of the soil particle rearrangement of granular thermodynamics. *Comput. geotechnics* 137104272, 104272. doi:10.1016/j.compgeo.2021.104272

Chang, J. X., Yuan, L. X., Hai, H. L., and Feng, M. S. (2013). Influences of vehicle loads on braced excavation in soft clay. *Appl. Mech. Mater.* 2545, 353–356.

Chang-Yu, O., and Bor-Yuan, S. (1998). Analysis of the corner effect on excavation behaviors. *Can. Geotech. J.* 35 (3), 532–540. doi:10.1139/t98-013

Chang-Yu, O., Bor-Yuan, S., and I-Wen, W. (2000). Three-dimensional deformation behavior of the Taipei National Enterprise Center (TNEC) excavation case history. *Can. Geotech. J.* 37 (2), 438–448. doi:10.1139/t00-018

Chang-Yu, O., Dar-Chang, C., and Tzong-Shiann, W. (1996). Three-dimensional finite element analysis of deep excavations. *J. Geotech. Engrg.* 122 (5), 337–345. doi:10.1061/(asce)0733-9410(1996)122:5(337)

Chen, H., Li, L., Li, J., and Sun, D. (2022). A generic analytical elastic solution for excavation responses of an arbitrarily shaped deep opening under biaxial *in situ* stresses. *Int. J. Geomech.* 22 (4). doi:10.1061/(ASCE)GM.1943-5622.0002335

Chen, H., and Mo, P. (2022). An undrained expansion solution of cylindrical cavity in SANICLAY for K0-consolidated clays. *J. Rock Mech. Geotechnical Eng.* 14 (3), 922–935. doi:10.1016/j.jrmge.2021.10.016

Chen, H., and Zhang, L. (2022). *A machine learning-based method for predicting end-bearing capacity of rock-socketed shafts*. Rock Mechanics and Rock Engineering. doi:10.1007/S00603-021-02757-9

Chenghua, W., Xiaoxuan, W., Khu, S., Makropoulos, C., and Nield, D. A. (2018). A quantitative analysis of the spatial effects of retaining structure for slender foundation pits. *IOP Conf. Ser. Earth Environ. Sci.* 189 (2), 022036. doi:10.1088/1755-1315/189/2/022036

Cui, X., Fan, Y., Wang, H., and Huang, S. (2020). Ground environment characteristics during the operation of GWHP considering the particle deposition effect. *Energy Build.* 206109593, 109593. doi:10.1016/j.enbuild.2019.109593

Fan, X., Phoon, K., Xu, C., and Tang, C. (2021). Closed-form solution for excavation-induced ground settlement profile in clay. *Comput. Geotechnics* 137104266, 104266. doi:10.1016/j.compgeo.2021.104266

Finno, R. J., Blackburn, J. T., and Roboski, J. F. (2007). Three-dimensional effects for supported excavations in clay. *J. Geotech. Geoenviron. Eng.* 133133 (1), 301–336. doi:10.1061/(asce)1090-0241(2007)133:1(30)

Guo, P., Gong, X., and Wang, Y. (2019). Displacement and force analyses of braced structure of deep excavation considering unsymmetrical surcharge effect. *Comput. Geotechnics* 113103102, 103102. doi:10.1016/j.compgeo.2019.103102

Li, D., Tang, D., and Yan, F. M. (2014). Mechanics of deep excavation's spatial effect and soil pressure calculation method considering its influence. *J. Zhejiang Univ. Eng. Sci.* 48 (09), 1632–1639+1720.

Li, L., Chen, H., Li, J., and Sun, D. (2021). An elastoplastic solution to undrained expansion of a cylindrical cavity in SANICLAY under plane stress condition. *Comput. Geotechnics* 132, 103990. doi:10.1016/j.compgeo.2020.103990

Li, L. J., and Liang, R. W. (2011). Research on the spatial effect of double row piles structure system in deep foundation. *Adv. Mat. Res.* 374, 2367. doi:10.4028/www.scientific.net/amr.374-377.2367

Lin, G., Xu, C., and Cai, Y. (2010). Research on characters of retaining structures for deep foundation pit excavation under unbalanced heaped load. *Rock Soil Mech.* 31 (08), 2592–2598.

Liu, B., Zhang, D., and XI, P. (2019). Influence of vehicle load mode on the response of an asymmetrically-loaded deep excavation. *KSCE J. Civ. Eng.* 23 (8), 3315–3329. doi:10.1007/s12205-019-0511-6

Luo, Z., Hu, B., Wang, Y., and DI, H. (2018). Effect of spatial variability of soft clays on geotechnical design of braced excavations: A case study of formosa excavation. *Comput. Geotechnics* 103, 103242–103253. doi:10.1016/j.compgeo.2018.07.020

Mangushev, R. A., Osokin, A. I., and Garnyk, L. V. (2016). Experience in preserving adjacent buildings during excavation of large foundation pits under conditions of dense development. *Soil Mech. Found. Eng.* 53 (5), 291–297. doi:10.1007/s11204-016-9401-9

Mingfeng, L. P. C. S., Peng, L. M., Shi, C. H., Zhang, Y. L., and Li, W. H. (2011). A simplified calculation method for spatial effect in large-long-deep foundation pit and its analysis. *Adv. Mat. Res.* 243-249, 2762–2770. doi:10.4028/www.scientific.net/amr.243-249.2762

Ou, X., Zhang, X., Fu, J., Zhang, C., Zhou, X., and Feng, H. (2020). Cause investigation of large deformation of a deep excavation support system subjected to unsymmetrical surface loading. *Eng. Fail. Anal.* 107104202, 104202. doi:10.1016/j.engfailanal.2019.104202

Pio-Go, H., and Chang-Yu, O. (1998). Shape of ground surface settlement profiles caused by excavation. *Can. Geotech. J.* 35 (6), 1004–1017. doi:10.1139/t98-056

Roboski, J., and Finno, R. J. (2006). Distributions of ground movements parallel to deep excavations in clay. *Can. Geotech. J.* 43 (1), 43–58. doi:10.1139/T05-091

Shouhua, L., Junsheng, Y., Jinyang, F., and Xiangcou, Z. (2019). Performance of a deep excavation irregular supporting structure subjected to asymmetric loading. *Int. J. Geomech.* 19 (7). doi:10.1061/(asce)gm.1943-5622.0001468

Sun, H., Chen, Y., Zhang, J., and Kuang, T. (2019). Analytical investigation of tunnel deformation caused by circular foundation pit excavation. *Comput. Geotechnics* 106, 106193–106198. doi:10.1016/j.compgeo.2018.11.001

Tanner Blackburn, J., and Finno, R. J. (2007). Three-dimensional responses observed in an internally braced excavation in soft clay. *J. Geotech. Geoenviron. Eng.* 133133 (11), 136411–141373. doi:10.1061/(asce)1090-0241(2007)133:11(1364)

Wang, K., Li, W., Sun, H., Pan, X., Diao, H., and Hu, B. (2021). Lateral deformation characteristics and control methods of foundation pits subjected to asymmetric loads. *Symmetry* 13 (3), 476. doi:10.3390/sym13030476

Xu, C., Chen, Q., Wang, Y., Hu, W., and Fang, T. (2016). Dynamic deformation control of retaining structures of a deep excavation. *J. Perform. Constr. Facil.* 30 (4). doi:10.1061/(asce)cf.1943-5509.0000819

Xu, C. J., Yin, M., and Lin, G. (2013). Characters analysis of the retaining structure of the foundation pit under local load. *Appl. Mech. Mater.* 477-478, 448–452. doi:10.4028/www.scientific.net/amm.477-478.448

Xu, C., Xu, Y., Sun, H., Chen, Q., and Zhang, X. (2013). Characteristics of braced excavation under asymmetrical loads. *Mathematical problems in engineering*, 20131–12. doi:10.1155/2013/452534

Yang, X., Liu, Z., and He, S. (1998). Research about spatial effect of deep pit supporting. *Chin. J. Geotechnical Eng.* 02, 74–78., No.

Yao, A., and Zhang, X. (2011). Influence of asymmetric load on supporting deformation for deep foundation pit. *Rock Soil Mech.* 32 (S2), 378–382+388.

Zeng, F., Zhang, Z., Wang, J., and Li, M. (2018). Observed performance of two adjacent and concurrently excavated deep foundation pits in soft clay. *J. Perform. Constr. Facil.* 32 (4), 04018040. doi:10.1061/(ASCE)CF.1943-5509.0001184

Zhang, J., Xie, R., and Zhang, H. (2018). Mechanical response analysis of the buried pipeline due to adjacent foundation pit excavation. *Tunn. Undergr. Space Technol.* 78, 78135–78145. doi:10.1016/j.tust.2018.04.026

Zhang, X., Yang, J., Zhang, Y., and Gao, Y. (2018). Cause investigation of damages in existing building adjacent to foundation pit in construction. *Eng. Fail. Anal.*, 83117–83124. doi:10.1016/j.engfailanal.2017.09.016

frontiers | Frontiers in Materials

TYPE Original Research
PUBLISHED 19 September 2022
DOI 10.3389/fmats.2022.988455

Check for updates

OPEN ACCESS

EDITED BY
Bing Bai,
Beijing Jiaotong University, China

REVIEWED BY
Mingxing Zhu,
Southeast University, China
Pengpeng Ni,
Sun Yat-sen University, China

*CORRESPONDENCE
Shuaihua Ye,
yeshuaihua@163.com

SPECIALTY SECTION
This article was submitted to Structural Materials,
a section of the journal
Frontiers in Materials

RECEIVED 07 July 2022
ACCEPTED 18 July 2022
PUBLISHED 19 September 2022

CITATION
Ma T, Zhu Y and Ye S (2022), Simplified calculation method and stability analysis of top beam cooperative pile–anchor supporting slope structure.
Front. Mater. 9:988455.
doi: 10.3389/fmats.2022.988455

COPYRIGHT
© 2022 Ma, Zhu and Ye. This is an open-access article distributed under the terms of the Creative Commons Attribution License (CC BY). The use, distribution or reproduction in other forums is permitted, provided the original author(s) and the copyright owner(s) are credited and that the original publication in this journal is cited, in accordance with accepted academic practice. No use, distribution or reproduction is permitted which does not comply with these terms.

Simplified calculation method and stability analysis of top beam cooperative pile–anchor supporting slope structure

Tianzhong Ma[1,2], Yanpeng Zhu[1,2] and Shuaihua Ye [1,2]*

[1]Key Laboratory of Disaster Mitigation in Civil Engineering of Gansu Province, Lanzhou University of Technology, Lanzhou, China, [2]Western Center of Disaster Mitigation in Civil Engineering, Ministry of Education, Lanzhou University of Technology, Lanzhou, China

Aiming at the problem of insufficient research on the action mechanism and stability calculation method of the top beam in the pile-anchor support structure, firstly the force and deformation model are established based on the elastic fulcrum method and the deformation coordination principle of the pile-anchor structure at the pile top and the anchor end in this paper. Secondly, the calculation model of the support structure under the synergy of the crown and beam and the simplified calculation method of the internal force, displacement and overall stability of the slope are constructed. Finally, combined with an engineering example, a MATLAB program was compiled for calculation, and the pile-anchor structures with crowned beams and without crowned beams were simulated and calculated by the finite element software PLAXIS 3D and Geo Studio. These three aspects are compared and verified. The results show that the internal force, deformation and minimum safety factor calculated by the method in this paper are basically consistent with the numerical simulation calculation results of the top beam condition; the existence of the top beam effectively enhances the bearing capacity of the pile body, and also restricts the displacement of the pile top development; the synergy of the crown and beam makes the safety factor of the slope increase significantly and improves the safety and stability of the slope. The research in this paper can provide a certain reference value for the theoretical calculation and design of the pile-anchor supported slope considering the top beam in engineering practice.

KEYWORDS

slope, pile-anchor support, top beam, cooperative deformation, stability

1 Introduction

As one of the main retaining structures in slope treatment, a pile–anchor supporting structure has been widely used and studied because of its strong anti-sliding ability, flexible layout, safety and reliability, less engineering quantity, and so on (Smethurst and Powrie, 2007; Kang et al., 2009; Song and Cui. 2016; Bai et al., 2019; Bai et al. 2021; Bai et al. 2022). The pile–anchor supporting structure is developed based on an ordinary

supporting pile, and it uses the elastic foundation beam theory for calculation. Furthermore, the main difference between an ordinary supporting pile and the pile–anchor supporting structure is that the former is similar to the cantilever beam structure whereas the latter can be simplified to a simply supported beam or continuous beam structure. Meanwhile, these structures are statically indeterminate structures that require simplification in the calculation (Cai and UGAI 2011; Huang et al., 2013; Chen et al., 2020).

Many scholars have studied the force and deformation of a pile–anchor supporting structure in a foundation pit and in slope engineering. Some scholars first studied the properties of soil particles and the material composition of supporting structures (Satvati et al., 2020; Zheng et al., 2021). However, the traditional design method of a pile–anchor supporting structure is mainly used to solve the problem of soil strength, and the anchor will deform with the pile in the excavation process. At this time, the existence of an anchor makes the internal force and deformation of the supporting structure more complex (Wang and Zhu. 2014; Di et al., 2018; Ye et al., 2019; Ye and Zhao., 2020). Using the strength parameters of the soil deformation state and the stress mode of a pile–anchor structure, Sun et al. (2019) established a design method for the pile–anchor structure of a deep foundation pit based on deformation. In addition, a method was proposed to unify the limit of plastic development of the soil and the checkpoint of soil deformation in a passive area of a deep foundation pit. Using limit equilibrium theory, Dong et al. (2022) established a stability model of a composite structure that considers the interaction of the anchor prestress and pile. In addition, the actual slip lines passing through the pile body, pile bottom, and soil under the pile, as well as the synergistic effect of the pile body and anchor, were further considered. Finally, the dynamic search algorithm of the model was also provided. Li and Zhang (2020) used a centrifuge test as model verification to study the development law of lateral stress and deformation of the passive pile.

Suo et al. (2016) and Wang et al. (2021) used BOTDA distributed optical fiber sensing technology to test the stress of a pile–anchor supporting system in the process of deep foundation pit excavation and studied the deformation law and internal force distribution characteristics of pile–anchor supporting structures. Furthermore, many scholars (Prat, 2017; Shu and Zhang, 2017; Zhao et al., 2018; Zhang et al., 2020) have used finite software—an indispensable research tool in geotechnical engineering—to explore pile–anchor supporting structures in slope engineering. They mainly studies the deformation and internal force of the supporting structure in the pile–anchor structure supporting slope engineering, the stability of the slope, the types and causes of anchoring failure, the influence of cutting some piles on the load transfer trend of the supporting structure, etc.

Although an existing research analysis has revealed that the research on the synergistic effect of the pile and anchor in pile–anchor supporting structures has been mature, a top beam, which influences the deformation and internal force of the supporting pile, remains in these supporting structures (Zeng and Liu, 1995; Chen et al., 2006). Using the matrix displacement method and considering the pile–anchor as a supporting structure with a synergistic action of the pile, anchor, and soil, Ding and Zhang (2012) explored the influence of the construction process on the deformation of the supporting pile, anchor, and passive soil. Li (2011) used the method of structural mechanics to analyze the whole stress system formed by the connection of the top beam and supporting pile, and the influence of the space effect was considered. This shows that the role of top beams in pile–anchor supporting structures cannot be underestimated. However, the existing research on the theoretical research and calculation analysis of crown-beam cooperative pile–anchor slope supporting structures is relatively rare, and most of the tests consider a top beam a type of safety reserve. In addition, only a few studies have explored the deformation of crown-beam cooperative pile–anchor support in theoretical analysis, which failed to provide the theoretical calculation method of the force and deformation of the three cooperative support and the overall stability of the slope.

In this study, the mechanical models of coordinated deformation and overall stability of supporting structures, such as top beams, supporting piles, and anchors, were established using the elastic fulcrum method. A simplified calculation method was derived by considering the internal force and stability of the supporting slope with a crown-beam cooperative pile–anchor structure and was compared with numerical simulation. In addition, the cooperative action mechanism of the pile, anchor, and top beams in pile–anchor supporting structures was further studied. The important role of top beams in pile–anchor supporting structures was clarified, which can provide some theoretical guidance for designing pile–anchor supports in follow-up engineering practice.

2 Calculation of internal force and displacement

2.1 Basic assumptions

1) Supporting piles, top beams, and retaining plates are all linear elastomers.
2) The anchor rod on the side of the pile is simplified to a linear spring with horizontal stiffness.
3) The interaction between the pile and the surrounding soil is replaced by the soil spring, and the bonding force and friction between the pile and the soil are not considered.
4) The earth pressure varies linearly in the same layer of soil.

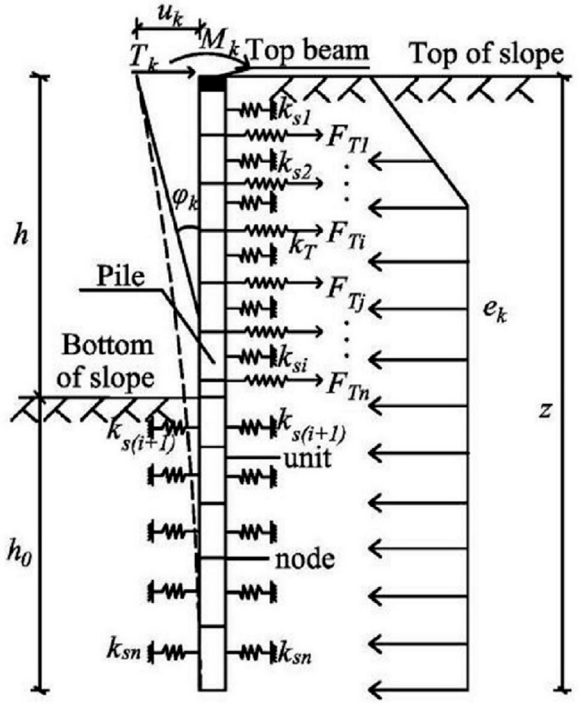

FIGURE 1
Calculation model of a single pile. Where h is the pile's length above the ground, h_0 is the embedded section's length, z is the supporting pile's full length, k_s is the equivalent stiffness of the soil spring, and k_T is the anchor's axial stiffness.

2.2 Establishment and analysis of the mechanical model

On the basis of a single pile's profile, the slope length is L, the number of piles is n, and the kth pile is inspected. The pile above the slope's bottom is considered an elastic beam constrained by a top beam and an anchor, and the pile below the slope's bottom is considered a Winkler elastic foundation beam. Figure 1 shows that the load on the kth pile is e_k and the pile top is subject to the binding T_k, the moment M_k of the top beam to the supporting pile, and the anchor tension F_{Ti} of multiple rows of anchors to the pile. Under the combined action of the above forces, the supporting pile top produces the horizontal displacement u_k and rotation angle θ_k.

2.3 Establishment of computational equations

According to the horizontal displacement u_k and rotation angle φ_k produced at the top of the k supporting pile, the horizontal displacement and rotation angle are caused by the soil pressure on the pile's side and the influence of the top beam and anchor on the supporting pile force. In addition, some horizontal displacement and rotation angles are produced. According to the deformation coordination of the pile top beam and pile top supporting pile under the action of the anchor, to meet the superposition principle, the relationship can be written as follows:

$$\left.\begin{aligned} u_k &= u_{ek} - \delta^u_{ZTkk}T_k - \delta^u_{ZMkk}M_k - \delta^u_{P0_kF_{Ti}}F_{Ti} \\ \varphi_k &= \theta_{ek} - \delta^\theta_{ZTkk}T_k - \delta^\theta_{ZMkk}M_k - \delta^\theta_{P0_kF_{Ti}}F_{Ti} \end{aligned}\right\} \quad (1)$$

where the displacement u_{ek} and the rotation angle θ_{ek} are the horizontal displacement and rotation angle generated at the top of the kth pile under the sole action of earth pressure, respectively. δ^u_{ZTkk} and δ^θ_{ZTkk} are the displacement and rotation angle of the kth top in the axial direction of the vertical pile when a horizontal unit force acts on the pile top. δ^u_{ZMkk} and δ^θ_{ZMkk} are the displacement and rotation angle of the kth pile top in the vertical pile axis when the pile top has a unit external moment. δ^u_{P0kFTi} and δ^θ_{P0kFTi} are the displacement and rotation angle of the kth pile top in the vertical pile axis when the ith row of the anchor rods of the supporting pile has a horizontal unit force.

At the outer end of the anchor rod of the ith anchor rod, its horizontal displacement is caused by the joint action of the top beam and all anchor rods. According to the coordinated deformation of the anchor rod and the supporting pile under the influence of the top beam, the displacements of the outer end of the anchor rod are as follows:

$$u_{ei} - \delta^u_{PiT_k}T_k - \delta^u_{PiM_k}M_k - \sum_{j=1}^{n}\delta^u_{PiF_{Tj}}F_{Tj} = \delta^u_{PiF_{Ti}}F_{Ti}\,(i \neq j) \quad (1.2)$$

where the pile body produces a horizontal displacement u_{ei} under the sole action of earth pressure, δ^u_{PiTk} and δ^u_{PiMk} are the displacements of the horizontal unit force and unit moment acting on the outer end of the ith row of the anchor rods on the kth pile top, respectively, δ^u_{PiFTj} is the displacement of the unit axial force of the anchor rod of the jth row of the supporting pile acting on the outer end of the anchor rod of the ith row of the pile, and δ^u_{PiFTi} is the displacement of the unit axial force of the ith row of the anchor rods of the supporting piles acting on the outer ends of the anchor rods of this row.

2.4 Solutions of equation parameters

In Eq. 1, the calculation ideas of u_{ek}, θ_{ek}, δ^u_{ZTkk}, δ^θ_{ZTkk}, δ^u_{ZMkk}, δ^θ_{ZMkk}, δ^u_{P0kFTi}, and δ^θ_{P0kFTi} are as follows:

2.4.1 Finite element of a structure

The vertical supporting pile is divided into a limited number of elements, and one element is divided every 1–3 m. To facilitate calculation, the nodes on the boundary are used to connect the elements in the cross section of the supporting structure, the action point of the anchor, the sudden change in load, and so on.

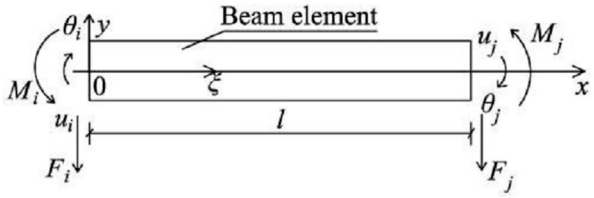

FIGURE 2
Beam element calculation diagram.

On the basis of the principle of no relative displacement in the coordination of the supporting pile, anchor bar, top beam, and soil, the soil stiffness of the element length is equivalent to soil spring k_{si}. The anchor force is F_{Ti}, and the bolt stiffness is k_{Ti} (Figure 1).

2.4.2 Application of the matrix displacement method

The element node load and the element stiffness matrix are generally calculated using the shape function of the compression bar element (Figure 2).

The interpolation of the deflection function $y(\xi)$ in the element is shown below.

$$y(\xi) = \sum_{i=1}^{4} N_i(\xi) a^e \tag{2}$$

In the formula: $N_i = [\,N_1 \quad N_2 \quad N_3 \quad N_4\,]$; $N_1(\xi) \sim N_4(\xi)$ is the shape function simplified as follows: $N_1 = 1 - 3\xi^2 + 2\xi^3$, $N_2 = (\xi - 2\xi^2 + \xi^3)l$, $N_3 = 3\xi^2 - 2\xi^3$, and $N_4 = (\xi^3 - \xi^2)l$; $a^e = [\,u_i \quad \theta_i \quad u_j \quad \theta_j\,]^T$, where u_i is the linear displacement, θ_i is the angular displacement, $\theta_i = (\frac{dy}{dx})_i$, $\xi = \frac{x}{l}$ $(0 \le \xi \le 1)$, and ξ is a certain point in the unit.

2.4.2.1 Joint load of elements

The main loads acting on the supporting pile are the force of the top beam on the supporting pile, the pulling force of the anchor on the supporting pile, and the earth pressure behind the supporting pile, in which the acting force of the top beam on the supporting pile and the pulling force of the anchor on the supporting pile belong to the nodal load. The earth pressure behind the pile belongs to the non-nodal load. According to the calculation rules of the matrix finite element method, the non-nodal load of the earth pressure behind the pile should be transformed into the equivalent nodal load. Therefore, the load concentration degree of the earth pressure behind the pile is assumed to be $p(x)$, and the equivalent nodal load of the load concentration $p(x)$ in the local coordinate system of element node i and node j is as follows:

$$\left\{F_p\right\}^e = \begin{Bmatrix} F_i \\ M_i \\ F_j \\ M_j \end{Bmatrix} = \int_0^1 [N]^T b_0 p(\xi) l d\xi = b_0 l \begin{Bmatrix} \int_0^1 N_1(\xi) p(\xi) d\xi \\ \int_0^1 N_2(\xi) p(\xi) d\xi \\ \int_0^1 N_3(\xi) p(\xi) d\xi \\ \int_0^1 N_4(\xi) p(\xi) d\xi \end{Bmatrix} \tag{3}$$

where b_0 is the beam element width, $p(\xi)$ is the load concentration, l is the element length, F_i is the horizontal load of node i, and M_i is the moment of node i.

When the earth pressure varies linearly in the same soil layer, there are

$$p(\xi) = p_i + \left(p_j - p_i\right)\xi \tag{4}$$

By integrating Eq. 4 into Eq. 3, the equivalent joint load caused by earth pressure is as follows:

$$\{F_P\}^e = \begin{Bmatrix} F_i \\ M_i \\ F_j \\ M_j \end{Bmatrix} = b_0 p_i l \begin{Bmatrix} 1/2 \\ l/12 \\ 1/2 \\ -l/12 \end{Bmatrix} + b_0\left(p_j - p_i\right) l \begin{Bmatrix} 3/20 \\ l/30 \\ 7/20 \\ -l/20 \end{Bmatrix} \tag{5}$$

2.4.2.2 Element stiffness matrix

From the analysis of the supporting pile, the element stiffness matrix comprises three parts: the first is the stiffness $[k_P]^e$ of the row pile, the second is the equivalent stiffness $[k_s]^e$ produced by the soil of the element length, and the third is the anchor axial stiffness $[k_T]^e$. The stiffness $[k]^e$ of the element in the global coordinate system is as follows:

$$[k]^e = [k_P]^e + [k_s]^e + [k_T]^e \tag{6}$$

The element stiffness $[k_P]^e$ of row piles is as follows:

$$[k_P]^e = \frac{EI}{l^3} \begin{bmatrix} 12 & 6l & -12 & 6l \\ 6l & 4l^2 & -6l & 2l^2 \\ -12 & -6l & 12 & -6l \\ 6l & 2l^2 & -6l & 4l^2 \end{bmatrix} \tag{7}$$

where E is the elastic modulus of the pile, I is the moment of inertia of the pile section, and l is the element length.

According to the beam model of the elastic foundation, the following results can be obtained:

$$p(z) = mzw(z) \tag{8}$$

where $p(z)$ is the pressure strength of any point on the pile, $w(z)$ is the horizontal displacement of the pile, m is the horizontal elastic coefficient of the foundation, and z is the pile length.

Eq. 8 can be substituted into Eq. 3 to obtain:

$$\left\{F_p\right\}^e = \int_0^1 [N]^T b_0 p(\xi) l d\xi = b_0 l \int_0^1 mz[N]d\xi\{a^e\} \tag{9.1}$$

$$[k_s]^e = b_0 l \int_0^1 mz[N]^T[N]d\xi \tag{9.2}$$

Through integration, the equivalent stiffness e_{sk} produced by the soil of the element can be obtained as follows:

$$[k_s]^e = mzb_0 l \begin{bmatrix} \frac{13}{25} & \frac{11}{210}l & \frac{9}{70} & -\frac{13}{420}l \\ \frac{11}{210}l & \frac{1}{105}l^2 & \frac{13}{420}l & -\frac{1}{140}l^2 \\ \frac{9}{70} & \frac{13}{420}l & \frac{13}{25} & -\frac{11}{210}l \\ -\frac{13}{420}l & -\frac{1}{140}l^2 & -\frac{11}{210}l & -\frac{1}{105}l^2 \end{bmatrix} \tag{10}$$

where M is the horizontal elastic coefficient of the foundation, l is the element length, and b_0 is the width of the beam element.

The stiffness $[k_T]^e$ of the anchor element is as follows:

$$[k_T]^e = \frac{EA}{l_i} \begin{bmatrix} 1 & 0 & -1 & 0 \\ 0 & 0 & 0 & 0 \\ -1 & 0 & 1 & 0 \\ 0 & 0 & 0 & 0 \end{bmatrix} \tag{11}$$

where E is the elastic modulus of the bolt, $A$is the cross-sectional area of the bolt, and l_i is the bolt length.

2.4.3 Establishing the equilibrium equation

The overall stiffness matrix of the structure is obtained by transforming several element stiffness matrixes, and the following formula can be obtained according to the matrix displacement method:

$$[k]\{\delta\} = \{F\} \tag{12}$$

where $[k]$ is the overall stiffness matrix, $\{\delta\}$ is the overall nodal displacement matrix, and $\{F\}$ is the overall load matrix.

2.4.4 Solving the equilibrium equation

From Eq. 12, it can be obtained that the horizontal displacement u_{ek} and rotation angle θ_{ek} of the kth pile top are produced by the supporting pile under the action of earth pressure alone, and when the horizontal unit force and unit external moment act separately on the kth pile top, the vertical pile axis displacements δ^u_{ZTkk} and δ^θ_{ZTkk} and rotation angles δ^u_{ZMkk} and δ^θ_{ZMkk} occur at the pile top. Using the method of structural mechanics, the flexibility coefficients δ^u_{P0kFTi} and δ^θ_{P0kFTi} at the pile top can be obtained when the row anchor i has a horizontal unit force.

$$\left.\begin{aligned} u_k &= \sum_{m=1}^{n} \delta^u_{LFkm} \cdot T_m \\ \varphi_k &= \sum_{m=1}^{n} \delta^\theta_{LMkm} \cdot M_m \end{aligned}\right\} \tag{13}$$

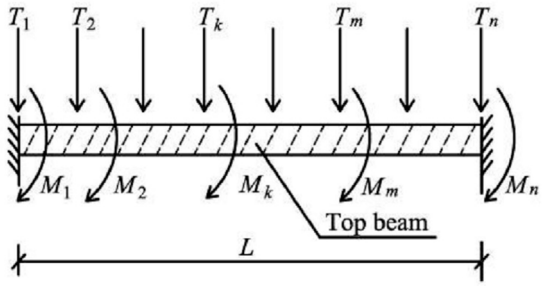

FIGURE 3
Calculation model of the top beam.

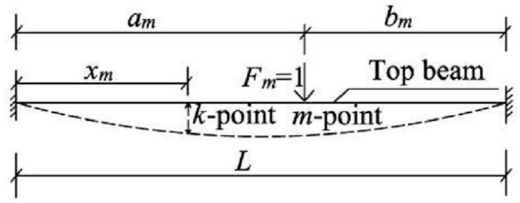

FIGURE 4
Schematic diagram of the calculation of the top beam linear displacement δ^u_{LFkm} under a unit force.

$$\delta^u_{LFkm} = \frac{b_m^2 x_k^2}{6EIL^2}\left[3a_m - \left(1 + \frac{2a_m}{L}\right)x_m\right](k \le m) \tag{14}$$

2.5 Displacement and rotation angle at the kth pile top under the action of the top beam

The top beam can be considered a linear elastic body. On the basis of the analysis of the top beam of the supporting pile, the two ends of the top beam are assumed to be fixed-end constraints (Figure 3), where the length of the top beam is L, the n supporting piles connected to the horizontal force of the top beam have T_1, T_2, T_3,. . ., T_n, and the bending moments produced by the top beam are M_1, M_2, M_3,. . ., M_n. Considering the kth pile top on the top beam for analysis, according to the superposition principle, the displacement u_k and rotation angle φ_k of the kth pile on the top beam can be obtained.where δ^u_{LFkm} is the displacement of the top beam at the kth point when the unit horizontal force at the mth point acts alone and δ^θ_{LMkm} is the rotation angle of the top beam at the kth point when the unit bending moment at the mth point acts alone.

2.5.1 Calculation of the related parameter δ^u_{LFkm} in the top beam calculation formula

Figure 4 shows that when the unit force is applied to a top beam with fixed-end constraints at both ends, the parameter $\delta^u LFkm$ beam can be derived from the knowledge of structural mechanics.where a_m, b_m, x_k, and L have their usual meanings, as in Figure 4, E is the

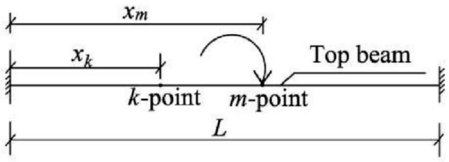

FIGURE 5
Schematic diagram of the calculation of the top beam angular displacement δ^{θ}_{LMkm} under a unit force

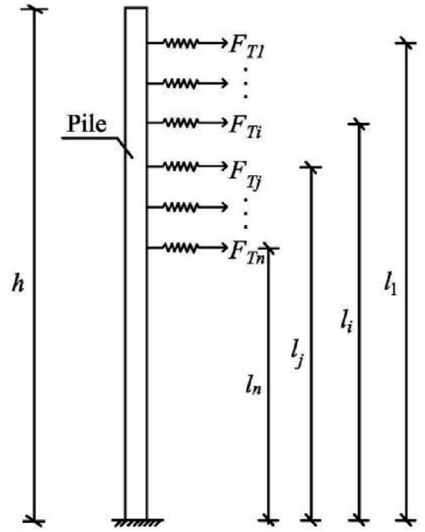

FIGURE 6
Schematic diagram of flexibility coefficient δ^{u}_{PiFTj} calculation.

elastic modulus of the top beam, and I is the section moment of inertia of the top beam.

2.5.2 Calculation of the related parameter δ^{θ}_{LMkm} in the top beam calculation formula

According to the principle of material mechanics, the equation for the parameter δ^{θ}_{LMkm} can be derived. As shown in Figure 5, the calculation formula of the δ^{θ}_{LMkm} equation is shown in Eq. 15. where G is the shear modulus of the top beam, I_t is the polar moment of inertia of the top beam, L is the length of the top beam, a is the calculation factor of the top beam's polar moment of inertia, and b is the short side of the section of the top beam rectangle.

2.6 Displacement of the outer end of the *i*th anchor under the action of the top beam

The horizontal displacement at the anchor end of the i-row anchor under the influence of the top beam is consistent with the deformation of the anchor rod and supporting pile.

$$\left.\begin{aligned} \delta^{\theta}_{LMkm} &= \frac{(L-x_m)\cdot x_k}{GI_tL}\,(k\le m) \\ I_t &= \alpha b^4 \end{aligned}\right\} \tag{15}$$

$$u_{ei} - \delta^{u}_{PiT_k}\cdot T_k - \delta^{u}_{PiM_k}\cdot M_k - \sum_{j=1}^{n}\delta^{u}_{PiF_{Tj}}\cdot F_{Tj} = \delta^{u}_{PiF_{Ti}}\cdot F_{Ti}\,(i\neq j) \tag{16}$$

where the horizontal displacement of the pile is u_{ei} under the action of earth pressure alone. The displacements of the horizontal unit force and the unit moment acting on the kth pile top are, respectively, the displacements of the horizontal unit force and the unit moment acting on the anchor end of the i-row of the pile, the δ^{u}_{PiFTj} pile is the displacement of the jth row anchor unit axial force acting on the i-row anchor end of the pile, and the δ^{u}_{PiFTi} anchor is the displacement of the ith row anchor unit axial force acting on the anchor end of the supporting pile.

Assuming that the pile bottom is the fixed end, the height of the anchor action point to the supporting pile bottom is l_i, and the component of the anchor tension in the horizontal direction is F_{Ti}, the flexibility coefficients of δ^{u}_{PiTk}, δ^{u}_{PiMk}, δ^{u}_{PiFTj}, and δ^{u}_{PiFTi} can be obtained according to the method of structural mechanics. For example, Figure 6 shows the calculation of the δ^{u}_{PiFTj} flexibility coefficient.where E is the elastic modulus of the supporting pile, I is the moment of inertia of the supporting pile section, and l_i, l_j are the heights from the point of action of the ith and jth rows of the anchor rods to the bottom of the supporting pile.

$$\delta^{u}_{P_iF_{Tj}} = \frac{l_j^2}{6EI}\left(3l_i - l_j\right)\quad (i = 1\sim n,\ j = 1\sim n) \tag{17}$$

Simultaneously, Eqs 1, 16 can be used to solve 3n unknown quantities, namely, T_k, M_k, and F_{Ti} $(i\neq j)$.

2.7 Calculating the force between the pile top and anchor end

According to the coordinated deformation of the pile-anchor structure at the top of the pile and the end of the anchor:

$$\begin{cases} u_{ek} - \delta^{u}_{ZTkk}T_k - \delta^{u}_{ZMkk}M_k - \delta^{u}_{p0_kF_{Ti}}F_{Ti} = \sum_{m=1}^{n}\delta^{u}_{LFkm}T_m \\ \theta_{ek} - \delta^{\theta}_{ZTkk}T_k - \delta^{\theta}_{ZMkk}M_k - \delta^{\theta}_{p0_kF_{Ti}}F_{Ti} = \sum_{m=1}^{n}\delta^{\theta}_{LMkm}M_m \\ u_{ei} - \delta^{u}_{PiT_k}T_k - \delta^{u}_{PiM_k}M_k - \sum_{j=1}^{n}\delta^{u}_{PiF_{Tj}}F_{tj} = \delta^{u}_{PiF_{Ti}}F_{Ti} \end{cases} \tag{18}$$

It can be simplified to a system of linear equations in three variables:

$$\begin{cases} a_1x_1 + b_1x_2 + c_1x_3 = d_1 \\ a_2x_1 + b_2x_2 + c_2x_3 = d_2 \\ a_3x_1 + b_3x_2 + c_3x_3 = d_3 \end{cases} \tag{19}$$

Among them:

$$a_1 = \begin{bmatrix} \delta^u_{LF11} + \delta^u_{ZF11} & \cdots & \delta^u_{LF1k} & \delta^u_{LF1m} & \cdots & \delta^u_{LF1n} \\ \cdots & \cdots & \cdots & \cdots & \cdots & \cdots \\ \delta^u_{LFk1} & \cdots & \delta^u_{LFkk} + \delta^u_{ZFkk} & \delta^u_{LFkm} & \cdots & \delta^u_{LFkn} \\ \delta^u_{LFm1} & \cdots & \delta^u_{LFmk} & \delta^u_{LFmm} + \delta^u_{ZFmm} & \cdots & \delta^u_{LFmn} \\ \cdots & \cdots & \cdots & \cdots & \cdots & \cdots \\ \delta^u_{LFn1} & \cdots & \delta^u_{LFnk} & \delta^u_{LFnm} & \cdots & \delta^u_{LFnn} + \delta^u_{ZFnn} \end{bmatrix},$$

$$b_1 = \begin{bmatrix} \delta^u_{LM11} & \cdots & \delta^u_{LM1k} & \delta^u_{LM1m} & \cdots & \delta^u_{LM1n} \\ \cdots & \cdots & \cdots & \cdots & \cdots & \cdots \\ \delta^u_{LMk1} & \cdots & \delta^u_{LMkk} & \delta^u_{LMkm} & \cdots & \delta^u_{LMkn} \\ \delta^u_{LMm1} & \cdots & \delta^u_{LMmk} & \delta^u_{LMmm} & \cdots & \delta^u_{LMmn} \\ \cdots & \cdots & \cdots & \cdots & \cdots & \cdots \\ \delta^u_{LMn1} & \cdots & \delta^u_{LMnk} & \delta^u_{LMnm} & \cdots & \delta^u_{LMmn} \end{bmatrix},$$

$$c_1 = \begin{bmatrix} \delta^u_{P0_1F_{T1}} & \cdots & \delta^u_{P0_1F_{Ti}} & \delta^u_{P0_1F_{Tj}} & \cdots & \delta^u_{P0_1F_{Tn}} \\ \cdots & \cdots & \cdots & \cdots & \cdots & \cdots \\ \delta^u_{P0_iF_{T1}} & \cdots & \delta^u_{P0_iF_{Ti}} & \delta^u_{P0_iF_{Tj}} & \cdots & \delta^u_{P0_iF_{Tn}} \\ \delta^u_{P0_jF_{T1}} & \cdots & \delta^u_{P0_jF_{Ti}} & \delta^u_{P0_jF_{Tj}} & \cdots & \delta^u_{P0_jF_{Tn}} \\ \cdots & \cdots & \cdots & \cdots & \cdots & \cdots \\ \delta^u_{P0_nF_{T1}} & \cdots & \delta^u_{P0_1F_{Ti}} & \delta^u_{P0_1F_{Tj}} & \cdots & \delta^u_{P0_nF_{Tn}} \end{bmatrix},$$

$$a_2 = \begin{bmatrix} \delta^\theta_{LF11} & \cdots & \delta^\theta_{LF1k} & \delta^\theta_{LF1m} & \cdots & \delta^\theta_{LF1n} \\ \cdots & \cdots & \cdots & \cdots & \cdots & \cdots \\ \delta^\theta_{LFk1} & \cdots & \delta^\theta_{LFkk} & \delta^\theta_{LFkm} & \cdots & \delta^\theta_{LFkn} \\ \delta^\theta_{LFm1} & \cdots & \delta^\theta_{LFmk} & \delta^\theta_{LFmm} & \cdots & \delta^\theta_{LFmn} \\ \cdots & \cdots & \cdots & \cdots & \cdots & \cdots \\ \delta^\theta_{LFn1} & \cdots & \delta^\theta_{LFnk} & \delta^\theta_{LFnm} & \cdots & \delta^\theta_{LFnn} \end{bmatrix},$$

$$b_2 = \begin{bmatrix} \delta^\theta_{LM11} + \delta^\theta_{ZM11} & \cdots & \delta^\theta_{LM1k} & \delta^\theta_{LM1m} & \cdots & \delta^\theta_{LM1n} \\ \cdots & \cdots & \cdots & \cdots & \cdots & \cdots \\ \delta^\theta_{LMk1} & \cdots & \delta^\theta_{LMkk} + \delta^\theta_{ZMkk} & \delta^\theta_{LMkm} & \cdots & \delta^\theta_{LMkn} \\ \delta^\theta_{LMm1} & \cdots & \delta^\theta_{LMmk} & \delta^\theta_{LMmm} + \delta^\theta_{ZMmm} & \cdots & \delta^\theta_{LMmn} \\ \cdots & \cdots & \cdots & \cdots & \cdots & \cdots \\ \delta^\theta_{LMn1} & \cdots & \delta^\theta_{LMnk} & \delta^\theta_{LMnm} & \cdots & \delta^\theta_{LMmn} + \delta^\theta_{ZMmn} \end{bmatrix},$$

$$c_2 = \begin{bmatrix} \delta^\theta_{P0_1F_{T1}} & \cdots & \delta^\theta_{P0_1F_{Ti}} & \delta^\theta_{P0_1F_{Tj}} & \cdots & \delta^\theta_{P0_1F_{Tn}} \\ \cdots & \cdots & \cdots & \cdots & \cdots & \cdots \\ \delta^\theta_{P0_iF_{T1}} & \cdots & \delta^\theta_{P0_iF_{Ti}} & \delta^\theta_{P0_iF_{Tj}} & \cdots & \delta^\theta_{P0_iF_{Tn}} \\ \delta^\theta_{P0_jF_{T1}} & \cdots & \delta^\theta_{P0_jF_{Ti}} & \delta^\theta_{P0_jF_{Tj}} & \cdots & \delta^\theta_{P0_jF_{Tn}} \\ \cdots & \cdots & \cdots & \cdots & \cdots & \cdots \\ \delta^\theta_{P0_nF_{T1}} & \cdots & \delta^\theta_{P0_nF_{Ti}} & \delta^\theta_{P0_nF_{Tj}} & \cdots & \delta^\theta_{P0_nF_{Tn}} \end{bmatrix},$$

$$a_3 = \begin{bmatrix} \delta^u_{P1T_1} & \cdots & \delta^u_{P1T_k} & \delta^u_{P1T_m} & \cdots & \delta^u_{P1T_n} \\ \cdots & \cdots & \cdots & \cdots & \cdots & \cdots \\ \delta^u_{PiT_1} & \cdots & \delta^u_{PiT_k} & \delta^u_{PiT_m} & \cdots & \delta^u_{PiT_n} \\ \delta^u_{PjT_1} & \cdots & \delta^u_{PjT_k} & \delta^u_{PjT_m} & \cdots & \delta^u_{PjT_n} \\ \cdots & \cdots & \cdots & \cdots & \cdots & \cdots \\ \delta^u_{PnT_1} & \cdots & \delta^u_{PnT_k} & \delta^u_{PnT_m} & \cdots & \delta^u_{PnT_n} \end{bmatrix},$$

$$b_3 = \begin{bmatrix} \delta^u_{P1M_1} & \cdots & \delta^u_{P1M_k} & \delta^u_{P1M_m} & \cdots & \delta^u_{P1M_n} \\ \cdots & \cdots & \cdots & \cdots & \cdots & \cdots \\ \delta^u_{PiM_1} & \cdots & \delta^u_{PiM_k} & \delta^u_{PiM_m} & \cdots & \delta^u_{PiM_n} \\ \delta^u_{PjM_1} & \cdots & \delta^u_{PjM_k} & \delta^u_{PjM_m} & \cdots & \delta^u_{PjM_n} \\ \cdots & \cdots & \cdots & \cdots & \cdots & \cdots \\ \delta^u_{PnM_1} & \cdots & \delta^u_{PnM_k} & \delta^u_{PnM_m} & \cdots & \delta^u_{PnM_n} \end{bmatrix},$$

$$c_3 = \begin{bmatrix} \delta^u_{P1F_{T1}} & \cdots & \delta^u_{P1F_{Ti}} & \delta^u_{P1F_{Tj}} & \cdots & \delta^u_{P1F_{Tn}} \\ \cdots & \cdots & \cdots & \cdots & \cdots & \cdots \\ \delta^u_{PiF_{T1}} & \cdots & \delta^u_{PiF_{Ti}} & \delta^u_{PiF_{Tj}} & \cdots & \delta^u_{PiF_{Tn}} \\ \delta^u_{PjF_{T1}} & \cdots & \delta^u_{PjF_{Ti}} & \delta^u_{PjF_{Tj}} & \cdots & \delta^u_{PjF_{Tn}} \\ \cdots & \cdots & \cdots & \cdots & \cdots & \cdots \\ \delta^u_{PnF_{T1}} & \cdots & \delta^u_{PnF_{Ti}} & \delta^u_{PnF_{Tj}} & \cdots & \delta^u_{PnF_{Tn}} \end{bmatrix},$$

$$x_1 = \begin{bmatrix} T_1 \\ \cdots \\ T_k \\ T_m \\ \cdots \\ T_n \end{bmatrix}, x_2 = \begin{bmatrix} M_1 \\ \cdots \\ M_k \\ M_m \\ \cdots \\ M_n \end{bmatrix}, x_3 = \begin{bmatrix} F_{T1} \\ \cdots \\ F_{Ti} \\ F_{Tj} \\ \cdots \\ F_{Tn} \end{bmatrix}, d_1 = \begin{bmatrix} u_{e1} \\ \cdots \\ u_{ek} \\ u_{em} \\ \cdots \\ u_{en} \end{bmatrix},$$

$$d_2 = \begin{bmatrix} \theta_{e1} \\ \cdots \\ \theta_{ek} \\ \theta_{em} \\ \cdots \\ \theta_{en} \end{bmatrix}, d_3 = \begin{bmatrix} u_{e1} \\ \cdots \\ u_{ei} \\ u_{ej} \\ \cdots \\ u_{en} \end{bmatrix}$$

To solve Eq. 19, it can be got 3n unknowns, namely, T_k, M_k, and F_{Ti} ($k = i = 1, 2, \ldots, n$).

2.8 Solving the internal force and displacement of the supporting pile

Taking the kth supporting pile as the research object, the loads acting on the supporting pile include the force T_k and moment M_k of method of the top beam on the supporting pile, the earth pressure e_k, and the anchor tension F_{Ti}. The finite elementthe beam system on an elastic foundation is selected to solve the internal force and deformation of the kth root supporting pile. The structural equilibrium equation is as follows:

$$[k]\begin{Bmatrix} u_i \\ \theta_i \\ u_j \\ \theta_j \end{Bmatrix} = \begin{Bmatrix} F_i \\ M_i \\ F_j \\ M_j \end{Bmatrix} (i = 1 \sim n,\ j = 1 \sim n) \tag{20}$$

where $[k]$ is the element stiffness matrix in the global coordinate system, u_i is the linear displacement of node i, and θ_i is the angular displacement of node i.

3 Stability analysis of a slope supported by a top beam combined with a pile and an anchor

3.1 Basic assumptions

1) The form of the slip surface is a circular arc when the whole support system is unstable.
2) The sliding soil zone in the arc is divided into several vertical soil strips, the interaction between the soil strips is ignored, and the arc at the lower end of the soil strip is approximately replaced by a straight line.
3) The shear strength on the slip surface is determined by the Mohr–Coulomb failure criterion.

4) For the pile–anchor supporting system, when the slip surface passes through the anchor and the supporting pile, the supporting structure will provide tensile moment and anti-sliding moment.
5) Search all arc surfaces that may pass through the bottom of the pile and below, and the most dangerous slip surface is the arc surface with the minimum safety factor.

3.2 Establishment of the calculation model

On the basis of the Swedish slice method, without considering the interaction between the two sides of the soil strip, the sliding part of the slope is divided into several soil strips, and the width of the strip b_i is 0.5 m. Taking the point of the top surface of the top beam (corresponding to the pile center) as the origin, the Cartesian coordinate system is established, and the arc center is determined according to the tangent line perpendicular to the port of the slip plane. Then, the value of the overall stability safety factor of the slope is the ratio of the anti-sliding moment to the sliding moment on the potential sliding arc. Figure 7 shows the calculation diagram.

In Figure 7, O_1 is the center of the arc surface, R_1 is the arc radius, q_i is the additional stress, b_i is the i band width, h_i is the i band height, w_i is the soil weight of the i band, l_i is the i band bottom length, β_i is the inclination of the j layer anchor, a_i is the angle between the tangent point of the strip and the arc to the center edge line and the vertical line, and h is the length of the supporting pile.

3.3 Establishment of parameters

1) Determination of the internal force of the top beam and anchor

The internal forces of the top beam and anchor can be solved using Eqs 1, 16 of the matrix stiffness equation mentioned above.

2) Calculation of the antislide moment of the supporting pile

$$M_p = R\cos\alpha_i\sqrt{\frac{2M_c\gamma h_i\left(k_p - k_a\right)}{d + \Delta d}} \tag{21}$$

where M_p is the anti-slide moment produced by the middle pile per meter, R is the arc radius, a_i is the angle between the tangent point of the strip and the arc to the center of the circle and the vertical line, M_c is the bending moment of each pile, h_i is the depth from the arc surface to the slope, γ is the weight of soil within the range of h_i, k_p and k_a are the passive and active earth pressure coefficients of soil, respectively, d is the pile diameter, and Δd is the net spacing between the two piles.

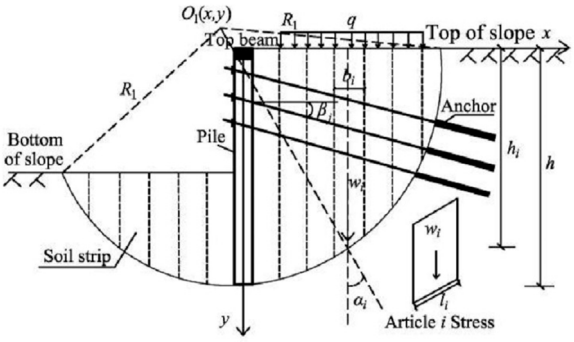

FIGURE 7
Stability calculation diagram.

3.4 Calculation of overall stability of slope

The main difference in stability between the slope supported by the top beam combined with the pile and anchor and the ordinary slope is that when the slip surface passes through the anchor and supporting pile, supporting structures such as the top beam, supporting pile, and anchor will provide tensile moment and anti-sliding moment.

The anti-sliding moments M_{ri}, M_{si}, and M_S produced by the bolt and the anti-sliding moment M_B produced by the top beam on the sliding arc slope of the ith strip are expressed, respectively, as follows:

$$M_{ri} = \sum\left[\left(w_i + q_i b_i\right)\cos\alpha_i\tan\varphi_i + c_i l_i\right]R \tag{22}$$

$$M_{si} = \sum\left(w_i + q_i b_i\right)\sin\alpha_i R \tag{23}$$

$$M_S = \frac{\sum\left[F_{Tj}\sin\left(\theta_j + \beta_j\right)\tan\varphi_i + F_{Tj}\cos\left(\theta_j + \beta_j\right)\right]R}{S_{hj}} \tag{24}$$

$$M_B = \frac{T_k y_0 + M_k}{S_p} \tag{25}$$

The overall stability safety factor of the slope support system is as follows:

$$F_S = \frac{M_{ri} + M_p + M_S + M_B}{M_{si}} \tag{26}$$

where w_i is the soil weight of the soil strip i, l_i is the length of the bottom surface of the soil strip, c_i and φ_i are the cohesion and internal friction angle of the soil layer where the circular sliding surface of the soil strip is located, F_{Tj} is the tension provided by the jth row of anchors, S_{hj} is the horizontal spacing of the jth row of anchors, S_p is the horizontal spacing of the adjacent supporting piles, θ_j is the angle between the jth row anchor axis and the tangent of the failure surface, T_k is the shear force produced by the top beam at the top of the kth pile, y_0 is the vertical distance from the

circle center to the horizontal plane at the pile top, and M_k is the bending moment produced by the top beam at kth pile top.

4 Example analysis

4.1 Project overview

Consider, for example, the slope support project of a crown-beam synergistic pile–anchor structure in Gansu Province, China. A slope with a length of nearly 120 m needs to be supported on the southeast side of the site. The diameter of the supporting pile is 1,500 mm, the distance between piles is 2,000 mm, the length is 26.4 m, the embedded depth is 13.2 m, and the concrete strength grade of the pile body is C40. The anchor adopts an HRB400 Φ 32 mm steel bar as the main reinforcement, which is located at 2 and 4 m below the pile top. The lengths are 16.5 and 15 m, respectively. The inclination angle is 15°, the anchor diameter is 150 mm, the horizontal spacing of the anchor is 2 m, and the designed pulling force is 110 kN. The section size of the top beam is width × height = 1.5 m × 0.8 m, and the strength grade is C40. Figure 8 shows the support scheme.

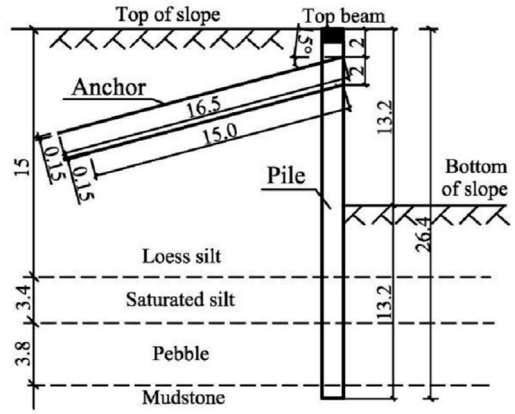

FIGURE 8
Cross section of the supporting structure.

4.2 Establishment of the PLAXIS 3D finite element model

The three-dimensional numerical model of the slope is established using PLAXIS 3D finite element software, and the internal force and displacement of the slope supported by the top beam combined with the pile–anchor structure are calculated. The two sides of the slope are at an angle of 120°, and the lengths of the two sides are 34 and 54 m, respectively. The boundary condition of the model is set according to the actual state of the slope. The upper boundary is free, the surrounding boundary is normally fixed, and the bottom boundary is completely fixed. The distance between the supporting pile and the outer boundary of the slope should be three times or more the height of the slope, and the vertical boundary should be two times or more the height of the slope to avoid the boundary adverse effect on the slope and supporting structure. Usually, the bottom should be taken into hard rock. The dimension of the finite element model is $x \times y \times z$ = 80 m × 105 m × 40 m. Figure 9 shows the model diagram.

The slope support model of the pile–anchor structure with and without a top beam is established, and Table 1 shows the soil parameters. The soil material simulation uses the soil hardening model (referred to as the HS model). In conventional geotechnical engineering numerical analysis, the soil deformation results obtained using the HS model are most consistent with engineering practice and are significantly better than those of other soil constitutive models. In the numerical simulation, the mesh sparse density is set to "fine,"

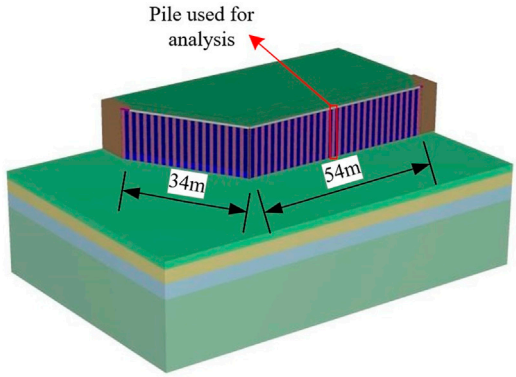

FIGURE 9
Finite element model diagram.

which is divided into 2,30,447 elements and 3,20,183 nodes, and the relative element size is 0.7 m.

The material model of the slope supporting structure is linearly elastic, the pile and full-length anchor are simulated by an embedded beam element (embedded pile), the top beam structure is simulated by a beam element, and the concrete baffle is simulated by a plate element. The interface element is established to simulate the interaction between the pile and soil, and the interface is selected as "partially rough." Table 2 shows the structural design parameters. When the numerical simulation divides the grid, the grid sparse density is set to "fine." Concurrently, the grid within a certain range of the supporting structure is encrypted, and a fine and accurate grid is generated for the parts where large concentrations or large deformations may occur. A total of 77,196 elements and 1,17,771 nodes are divided.

TABLE 1 Soil parameter table.

Soil layer		Loess silt	Saturated silt	Pebble	Mudstone
Thickness/m		15	3.4	3.8	17.8
Severe $\gamma/(kN/m^3)$		15.7	18.7	24	18
Compression modulus (*Mpa*)	E_{50}^{refa}	9.3	4.8	50	20.7
	E_{oed}^{refb}	9.3	4.8	50	20.7
	E_{ur}^{refc}	32.5	17.8	150	62.1
Cohesion *c*/*kpa*		15	18	5	25
Frictional angle $\varphi/(°)$		22	24	28	35

[a]The meaning of the italics is "Secant stiffness"
[b]The meaning of the italics is "Tangent stiffness"
[c]The meaning of the italics is "Unloading/loading stiffness"

TABLE 2 Structural design parameter table.

Envelope structure	Piles	Top beam	Anchor	Retaining plate
Structural model	Embedded beam element	Beam element	Embedded beam element	Plate element
Severe $\gamma/(kN/m^3)$	25	25	25	15.5
Compression modulus *E*/(*Gpa*)	32.5	32.5	32.5	30
Poisson ratio	0.2	0.2	0.2	0.15

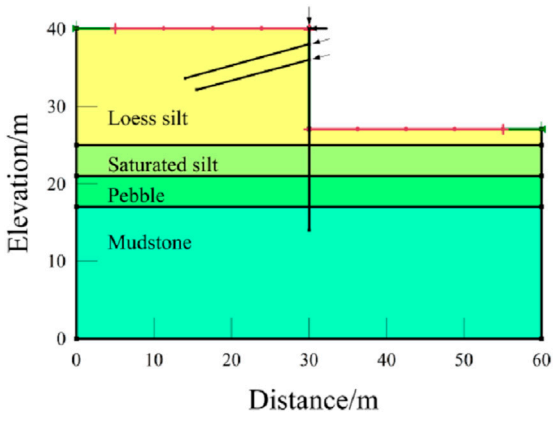

FIGURE 10
Finite element model.

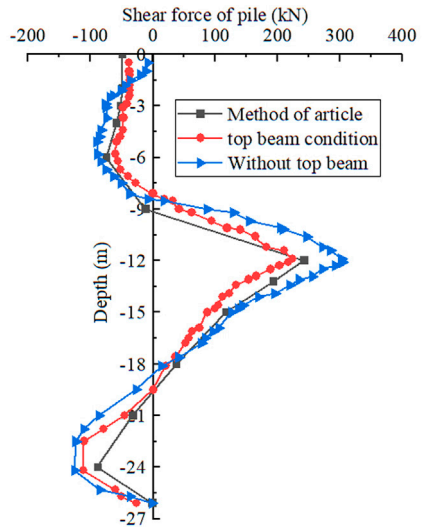

FIGURE 11
Pile shear force comparison chart.

4.3 Establishment of the GeoStudio slope model

The analysis model is established in the SLOPE/W module of GeoStudio. The Morgenstern–Price method is used for slope stability analysis, and the semisine function is selected as the conditional force function. The constitutive relation of soil adopts the Mohr–Coulomb ideal elastic–plastic model, and the parameters of soil and the supporting structure are inputted according to the parameters in Tables 1 and 2. The supporting pile and fully bonded anchor are added by strengthening the load, and the internal force of the top beam is added to the pile top according to the point load. Figure 10 shows that the size of the GeoStudio finite element model is $x \times y$ = 60 m × 40 m.

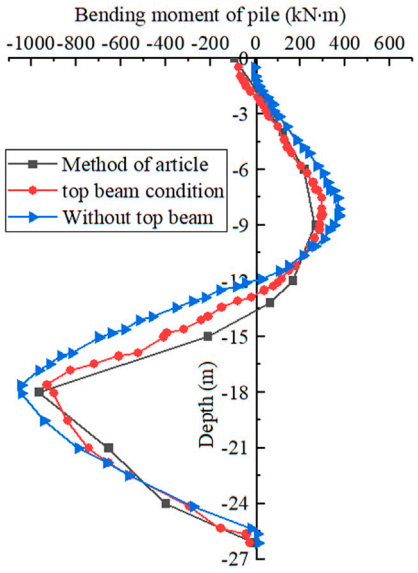

FIGURE 12
Pile body bending moment comparison chart.

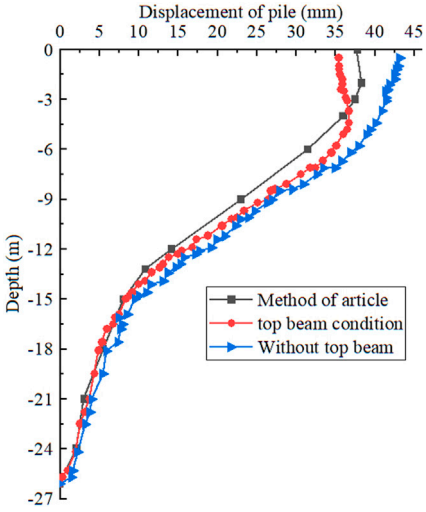

FIGURE 13
Pile displacement comparison chart.

5 Calculation results and analysis

The specific parameters of the project are substituted into the program compiled by MATLAB; the shear force, bending moment, displacement, and minimum safety factor of the slope are calculated; and the results are compared with the simulation results of PLAXIS 3D and GeoStudio software.

5.1 Analysis of the internal force and deformation of a slope supported by a crown-beam cooperative pile–anchor structure

5.1.1 Comparative analysis of the shear force of the pile

From the shear curve of the pile in Figure 11, the calculation results of this method are consistent with the overall stress of the top beam, which verifies the rationality of this method. Under the constraint of the top beam, the shear force at the pile top is similar, but under the condition of no top beam, the shear force at the pile top is −9.78 *kN*. At the maximum positive shear force of the pile, the maximum shear force calculated by this method and that under the condition of the top beam are 346.81 and 320.4 kN, respectively, which differ from the maximum shear force of the nontop beam. The comparison of the shear force between the pile top and the maximum positive shear force of the pile shows that the top beam can prevent the pile from developing to an empty surface.

5.1.2 Comparative analysis of the bending moment of the pile body

From the comparison diagram of the bending moment of the pile body in Figure 12, the bending moment value obtained by this method is similar to that of the bending moment curve with and without the top beam. However, at the position of the pile top, the bending moment of the nontop beam starts to change from zero, whereas the bending moment at the pile top is −92.21 kN m calculated by this method, and it is −73.92 kN m under the condition of the top beam, indicating that the existence of the top beam can effectively enhance the stress state of the pile top. The maximum positive and negative moment values appear near the buried depth of −9 and −18 m, and the comparison of the working conditions with and without the top beam shows that the existence of the top beam effectively reduces the bending moment of the pile.

5.1.3 Comparative analysis of pile displacement

From the variation curve of pile displacement in Figure 13, the method presented in this study is similar to the variation law of pile displacement under the conditions of crown and nontop beams. The calculation result of this method is smaller than that of the top beam as a whole, but the existence of the top beam induces a large difference between the crown and nontop beams at the pile top, and the maximum reaches 5.87 mm, which shows that the top beam can connect both sides of the pile to make the top beam and pile deformation, thus reducing the displacement of the pile top and improving the overall stability of the supporting structure.

5.2 Overall stability analysis of a slope supported by a top beam combined with a pile–anchor structure

On the basis of the calculation and analysis of the above engineering examples, using the overall stability calculation method in this study, the minimum safety factors of the pile–anchor structure supporting slope with and without a top beam are 1.432 and 1.356, respectively, whereas the minimum safety factors of overall stability with and without a top beam cooperative support obtained by GeoStudio simulation are 1.413 and 1.340, respectively. By comparison, it is found that the calculation result of this method is similar to that obtained by numerical simulation, and the overall safety factors of the slope supported by a top beam and a pile–anchor structure are increased by 5.60% and 5.44%, respectively. Hence, the existence of the top beam significantly improves the overall stability; that is, the safety of the slope is significantly improved.

6 Conclusion

In this study, a simplified calculation method for solving the internal force and displacement of supporting structures and the overall stability of the slope was proposed by establishing the calculation model of stress deformation and the overall stability of the slope supported by a top beam combined with a pile and an anchor. By taking a slope project of a crown-beam cooperative pile–anchor support as an example, this method was compared with the numerical simulation with and without a crown-beam cooperative support, and the following conclusion are obtained.

(1) According to the deformation coordination principle of the pile–anchor structure at the pile top and anchor end, the integral matrix equation was established by dividing the supporting pile into finite elements, and the calculation expressions of shear force, bending moment, and pile displacement of the supporting pile were obtained.
(2) On the basis of the Swedish slice method, an overall stability analysis of the slope supported by a top beam and pile–anchor was conducted, and the calculation method of the minimum safety factor of the overall stability of the slope was obtained.
(3) The internal force and displacement values calculated by this method were compared with the internal force distribution and deformation values obtained by PLAXIS 3D numerical simulation, and the law was similar. In addition, the slope overall stability coefficient calculated by this method was compared with that obtained by GeoStudio numerical analysis, and their values were close, thereby confirming the rationality of the proposed method.
(4) The numerical simulation results of crown and nontop beams showed that the existence of a top beam can effectively improve the anti-deformation ability of pile, which can more effectively control slope deformation and can increase its overall stability coefficient. As a result, the anti-sliding ability and safety stability of the slope are improved.

Data availability statement

The original contributions presented in the study are included in the article/supplementary material, further inquiries can be directed to the corresponding author.

Author contributions

TM and SY completed the drafting of the original paper, and YZ made important revisions to the paper. All authors participated in the theoretical research derivation and numerical simulation modeling work of the paper.

Funding

This work was supported by the National Natural Science Foundation of China (Grant No. 52068048) and the Natural Science Foundation of Gansu Province, China (Grant No. 20JR10RA163).

Acknowledgments

The corresponding author would like to acknowledge the National Natural Science Foundation of China (Grant No. 52068048) and the National Natural Science Foundation of Gansu Province, China (Grant No. 20JR10RA163). The financial supports are gratefully acknowledged.

Conflict of interest

The authors declare that the research was conducted in the absence of any commercial or financial relationships that could be construed as a potential conflict of interest.

Publisher's note

All claims expressed in this article are solely those of the authors and do not necessarily represent those of their affiliated organizations, or those of the publisher, the editors and the reviewers. Any product that may be evaluated in this article, or claim that may be made by its manufacturer, is not guaranteed or endorsed by the publisher.

References

Bai, B., Wang, Y., Rao, D., and Bai, F. (2022). The effective thermal conductivity of unsaturated porous media deduced by pore-scale SPH simulation. *Front. Earth Sci. (Lausanne).* 10, 943853. doi:10.3389/feart.2022.943853

Bai, B., Yang, G., Li, T., and Yang, G. (2019). A thermodynamic constitutive model with temperature effect based on particle rearrangement for geomaterials. *Mech. Mater.* 139, 103180. doi:10.1016/j.mechmat.2019.103180

Bai, B., Zhou, R., Cai, G., Hu, W., and Yang, G. (2021). Coupled thermo-hydro-mechanical mechanism in view of the soil particle rearrangement of granular thermodynamics. *Comput. Geotechnics* 137, 104272. doi:10.1016/j.compgeo.2021.104272

Cai, F., and Ugai, K. (2011). A subgrade reaction solution for piles to stabilise landslides. *Geotechnique* 61 (2), 143–151. doi:10.1680/geot.9.p.026

Chen, W. X., Guo, Z. K., and Zhang, W. G. (2006). A calculation method for the internal force and deformation of row piles considering the action of ring beam. *Chin. J. Undergr. Space Eng.* 411–415. (in Chinese).

Chen, F. Y., Zhang, R. H., Wang, Y., Liu, H. L., Böhlke, T., and Zhang, W. G. (2020). Probabilistic stability analyses of slope reinforced with piles in spatially variable soils. *Int. J. Approx. Reason.* 122, 66–79. doi:10.1016/j.ijar.2020.04.006

Di, P. C., Galli, A., Aversa, S., and Maiorano, R. M. S. (2018). "Multi-level design approaches for slope-stabilizing piles," in *Volume 1-3 of landslides and engineered slopes: Experience, theory and practice*. Editors S. Aversa, L. Cascinl, L. Picarelli, and C. Scavia (London: CRC Press), 1-3, 821–826. doi:10.1201/9781315375007-86

Ding, M., and Zhang, Y. X. (2012). Analysis method of pile-anchor structure based on matrix displacement method. *Eng. Mech.* 29 (8), 116–122. (in Chinese). doi:10.6052/j.issn.1000-4750.2010.11.0858

Dong, X. G., Zheng, L. I., Cui, Z., and Zhou, C. (2022). Stability analysis of the pile-prestressed anchor composite structure based on failure mode. *Eng. Fail. Anal.* 137, 106223. doi:10.1016/j.engfailanal.2022.106223

Huang, C., Ren, W., and Kong, L. (2013). New mathematical modelling of stabilizing pile with prestressed tieback anchors. *Math. Problems Eng.* 2013, 1–12. doi:10.1155/2013/601508

Kang, G. C., Song, Y. S., and Kim, T. H. (2009). Behavior and stability of a large-scale cut slope considering reinforcement stages. *Landslides* 6 (3), 263–272. doi:10.1007/s10346-009-0164-5

Li, X. C. (2011). "Large-scale physical model test study on the interaction between landslide and anchor anti-slide pile," (Xi'an: Chang'an University). Dissertation(in Chinese).

Li, Y., and Zhang, W. (2020). Investigation on passive pile responses subject to adjacent tunnelling in anisotropic clay. *Comput. Geotechnics* 127, 103782. (in Chinese). doi:10.1016/j.compgeo.2020.103782

Prat, P. C. (2017). Numerical investigation into the failure of a micropile retaining wall. *Comput. Geotechnics* 81, 262–273. doi:10.1016/j.compgeo.2016.08.026

Satvati, S., Alimohammadi, H., Rowshanzamir, M., and Hejazi, S. M. (2020). Bearing capacity of shallow footings reinforced with braid and geogrid adjacent to soil slope. *Int. J. Geosynth. Ground Eng.* 6 (4), 41–12. doi:10.1007/s40891-020-00226-x

Shu, J., and Zhang, D. (2017). A case study: Observed deformation characteristics and internal force of pile-anchor retaining excavation. *Geotech. Front.* 136–148. doi:10.1061/9780784480458.014

Smethurst, J. A., and Powrie, W. (2007). Monitoring and analysis of the bending behaviour of discrete piles used to stabilise a railway embankment. *Geotechnique* 57 (8), 663–677. doi:10.1680/geot.2007.57.8.663

Song, H., and Cui, W. (2016). A large-scale colluvial landslide caused by multiple factors: Mechanism analysis and phased stabilization. *Landslides* 13 (2), 321–335. doi:10.1007/s10346-015-0560-y

Sun, J., Wang, S., Shi, X., and Zeng, L. (2019). Study on the design method for the deformation state control of pile-anchor structures in deep foundation pits. *Adv. Civ. Eng.* 2019, 1–16. doi:10.1155/2019/9641674

Suo, W. B., Gang, C., Lu, Y., Sun, Y. J., and Shi, B. (2016). Study on distributed monitoring method of deep foundation pit retaining pile based on the brillouin optical time domain technology. *Geol. J. China Univ.* 22 (4), 724–732. (in Chinese). doi:10.16108/j.issn1006-7493.2016165

Wang, D. Q., and Zhu, Y. P. (2014). Additional stress apply to analyzing the stability of prestressed anchor support. *Eng. Mech.* 31 (4), 196–202. (in Chinese). doi:10.6052/j.issn.1000-4750.2012.11.0824

Wang, X., Luo, X. H., Xue, L. W., and Bo, J. (2021). Back analysis of pile and anchor retaining structure based on BOTDA distributed optical fiber sensing technology. *E3S Web Conf.* 248, 01036. doi:10.1051/e3sconf/202124801036

Ye, S. H., Fang, G. W., and Ma, X. R. (2019). Reliability analysis of grillage flexible slope supporting structure with anchors considering fuzzy transitional interval and fuzzy randomness of soil parameters. *Arab. J. Sci. Eng.* 44 (10), 8849–8857. doi:10.1007/s13369-019-03912-9

Ye, S. H., and Zhao, Z. F. (2020). Seismic response of pre-stressed anchors with frame structure. *Math. Problems Eng.* 5, 1–15. doi:10.1155/2020/9029045

Zeng, Q. Y., and Liu, M. C. (1995). Mechanism and calculation analysis of supporting pile ring beam. *Rock Soil Mech.* 16 (2), 74–82. (in Chinese). doi:10.16285/j.rsm.1995.02.009

Zhang, W., Li, Y., Goh, A. T. C., and Zhang, R. (2020). Numerical study of the performance of jet grout piles for braced excavations in soft clay. *Comput. Geotechnics* 124, 103631. doi:10.1016/j.compgeo.2020.103631

Zhao, W., Han, J. Y., Chen, Y., Jia, P. J., Li, S. G., Li, Y., et al. (2018). A numerical study on the influence of anchorage failure for a deep excavation retained by anchored pile walls. *Adv. Mech. Eng.* 10 (2), 168781401875677. doi:10.1177/1687814018756775

Zheng, J., He, H., and Alimohammadi, H. (2021). Three-dimensional Wadell roundness for particle angularity characterization of granular soils. *Acta Geotech.* 16 (1), 133–149. doi:10.1007/s11440-020-01004-9

Nomenclature

Abbreviations

A bolt cross-sectional area

a polar moment of inertia calculation factor for top beams

a_i the angle between the tangent point of the soil strip and the arc to the edge of the circle and the vertical line

b_0 beam element width

b short side of rectangular section of top beam

c_i cohesion

d diameter of pile

E modulus of elasticity of piles or anchors

F_T the tension of the anchor to the pile

G shear modulus of top beams

h_i soil bar height

I moment of inertia of pile section

I_t polar moment of inertia of top beam

k_{si} equivalent stiffness of soil spring

k_{Ti} equivalent stiffness of soil spring

k_a active earth pressure coefficient

k_b passive earth pressure coefficient

L the length of the top beam

l beam element length

l_i the length of the i-th bolt

m horizontal elastic coefficient of foundation

M_k constraint moment of top beam to supporting pile

M_i moment at node i

M_p anti-slide moment produced in pile per meter

M_c bending moment of each pile

M_{ri} anti-slip moment on the slope of the i-th soil strip

M_{si} sliding moment on the slope of the sliding arc of the i-th strip

M_S anti-slip moment generated by anchor

M_B anti-slip moment due to top beam

P pressure strength at any point on the pile

R arc radius

S_h anchor horizontal spacing

S_P support pile horizontal spacing

T_{ki} binding force of top beam to supporting pile

u_{ek} horizontal displacement generated by the k-th pile top

u_{ei} horizontal displacement of pile body under the action of earth pressure alone

w horizontal displacement of pile body

w_i soil strip i with soil weight

z pile length

Greek symbols

θ_j the angle between the axis of the j-th row of anchors and the tangent to the failure surface

γ the weight of soil

θ_{ek} the angle produced by the top of the k-th pile

δ^u_{ZTkk} the horizontal displacement at the top of the pile when the horizontal unit force is applied to the top of the k-th pile.

δ^θ_{ZTkk} the rotation angle at the top of the pile when the horizontal unit force is used at the top of the k-th pile.

δ^u_{ZMkk} the horizontal displacement at the top of the pile when the unit moment acts on the top of the k-th pile.

δ^θ_{ZMkk} the rotation angle at the top of the pile when the unit moment acts on the top of the k-th pile.

δ^u_{P0kFTi} the horizontal displacement of the top of the k-th pile when the unit force is used in the i-row anchor of the supporting pile.

δ^θ_{P0kFTi} when the unit force is used in the i-th row anchor of the supporting pile, the rotation angle at the top of the k-th pile

δ^u_{LFkm} the horizontal displacement at point k when the unit force at point m is applied to the top beam.

δ^θ_{LMkm} when the unit force at the m point is applied to the top beam, the rotation angle at the k point occurs

δ^u_{PiTk} the displacement of the k-th pile at the anchor end of the i-th row when there is a horizontal unit force at the top of the pile.

δ^u_{PiMk} the displacement of the pile at the anchor end of the i-th row when there is a horizontal unit moment at the top of the k-th pile.

δ^u_{PiFTj} displacement of supporting pile at the anchor end of row I under the action of unit axial force of j-row anchor

δ^u_{PiFTi} the displacement at the anchor end of the i-th row anchor of the supporting pile under the action of unit axial force.

φ_i internal friction angle

frontiers | Frontiers in Materials

TYPE Original Research
PUBLISHED 21 September 2022
DOI 10.3389/fmats.2022.1007855

Check for updates

OPEN ACCESS

EDITED BY
Xianze Cui,
China Three Gorges University, China

REVIEWED BY
Jiaqi Guo,
Henan Polytechnic University, China
Zheng Zuo,
Shijiazhuang Tiedao University, China

*CORRESPONDENCE
Song Chen,
chennsongg@163.com
Liufang Li,
lliufun@126.com

SPECIALTY SECTION
This article was submitted to Structural Materials,
a section of the journal
Frontiers in Materials

RECEIVED 31 July 2022
ACCEPTED 22 August 2022
PUBLISHED 21 September 2022

CITATION
Chen S, Yang Z, Liu S, Li L, Zheng Y and Yuan Y (2022), Numerical simulation and analysis of crack disease in tunnel lining structure.
Front. Mater. 9:1007855.
doi: 10.3389/fmats.2022.1007855

COPYRIGHT
© 2022 Chen, Yang, Liu, Li, Zheng and Yuan. This is an open-access article distributed under the terms of the Creative Commons Attribution License (CC BY). The use, distribution or reproduction in other forums is permitted, provided the original author(s) and the copyright owner(s) are credited and that the original publication in this journal is cited, in accordance with accepted academic practice. No use, distribution or reproduction is permitted which does not comply with these terms.

Numerical simulation and analysis of crack disease in tunnel lining structure

Song Chen[1,2]*, Zhao Yang[3], Shuo Liu[2,4], Liufang Li[5]*, Yibo Zheng[2] and Ying Yuan[1,4]

[1]Hebei Key Laboratory of Optoelectronic Information and Geo-detection Technology, Hebei GEO University, Shijiazhuang, China, [2]College of Urban Geology and Engineering, Hebei Geo University, Shijiazhuang, China, [3]Guangdong Hualu Transport Technology Co., Ltd, Guangzhou, China, [4]Hebei Technology Innovation Center for Intelligent Development and Control of Underground Built Environment, Hebei GEO University, Shijiazhuang, China, [5]College of Civil Engineering and Mechanics, Lanzhou University, Lanzhou, China

Tunnel construction in China is increasing year by year. With the passage of time, China will usher in the peak period of tunnel engineering repair, and it is vital to study in advance the influential nature of tunnel lining crack disease as well as management measures. By summarising a large amount of relevant literature, this paper analyses the main locations where cracks are generated in tunnel linings. Through the method of finite element numerical analysis, 24 cases of cracks of different widths and depths were modelled and calculated for each location of lining vaults, shoulders and side walls, respectively, to analyse the influence of different cases on the internal forces and deformation of the lining. The study shows that the stress concentration around the crack tip decreases with the increase of the crack width, while the stress concentration around the crack tip increases with the increase of the crack depth. The stresses in the other main parts of the lining increase after the crack is created, which has a deteriorating effect on the load-bearing capacity and stability of the lining structure. With the increase in crack width and depth, the sinking deformation of the vault and the heaving deformation of the back arch increase, especially when the cracks are large, but lining cracking has less effect on the lateral deformation of the lining. Compared to cracks in the top and shoulder of the arch, cracks in the side walls have a more pronounced effect on the distribution of internal forces around the cracks.

KEYWORDS

road tunnel, lining cracks, numerical simulation, midas-GTS, stress and deformation law

Introduction

In recent years, with the rapid development of China's economy, the construction of road traffic projects in China is increasing year by year. In addition, China's geological conditions are complex and varied, and the southwest region is mountainous and hilly, so a large number of tunnel projects are put into construction. However, due to the complex geological environment of the tunnel and the influence of design and construction, The stability of the project is influenced by many factors. Among them, theoretical analysis (Bai et al., 2019; Bai et al., 2021a; Bai et al., 2022), environmental simulation experiments (Hu et al., 2021), artificial intelligence algorithms (Bai et al., 2021b; Bai et al., 2021c) and other technologies are widely used in the analysis of related issues.

There will be many diseases in the tunnel lining in the later period of use. With the passage of time, China will shift from the peak period of construction to the peak period of maintenance, so it is very important to carry out tunnel disease research before understanding and reserving technology. Among many diseases of tunnel lining, lining

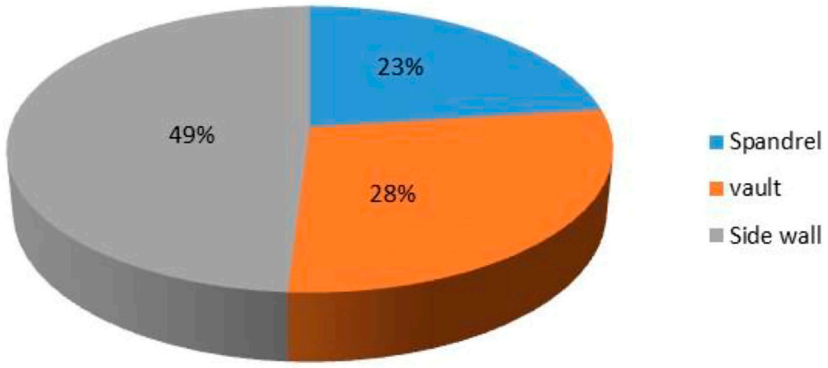

FIGURE 1
Statistical diagram of main distribution positions of lining cracks.

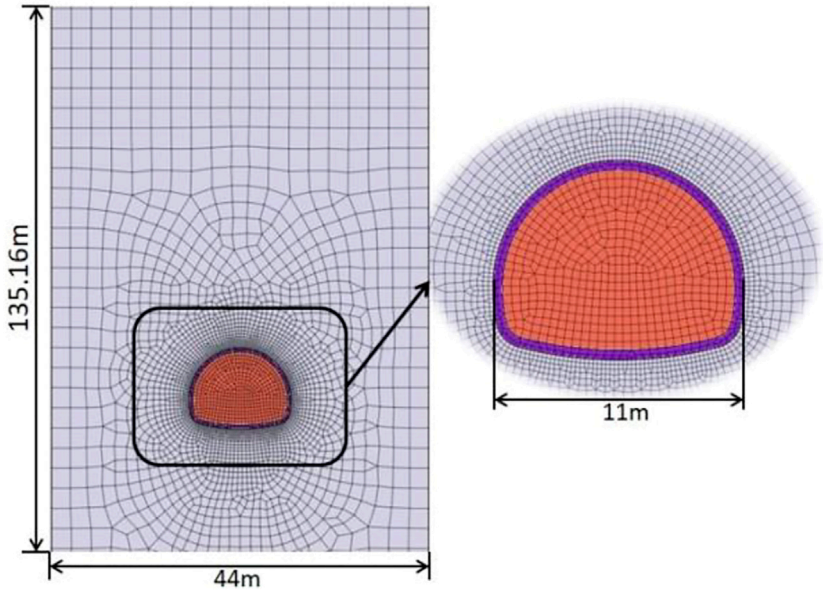

FIGURE 2
Numerical calculation model

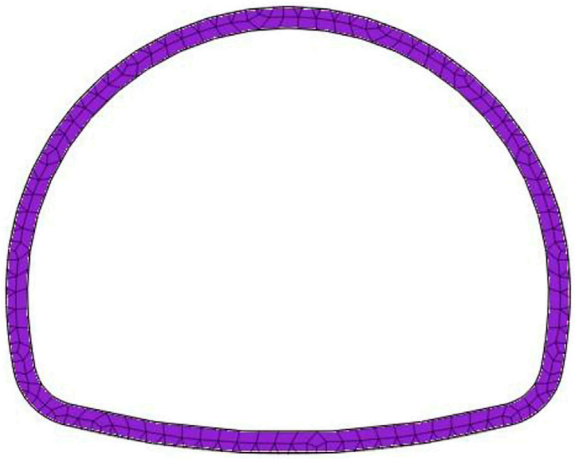

FIGURE 3
Tunnel lining structure

cracks is the most common, which seriously affect the bearing capacity and safety performance of lining. Therefore, the analysis of the causes of tunnel lining cracks and the impact of cracks on the overall stability of lining structure is a hot issue in current research (Zhang et al., 2007).

Scholars had done relevant researches on the problem of lining cracks. Chen and Mo (2009) established the shield tunnel model by finite element method, analyzed the cracking situation of segments in the later tunnel operation, summarized the easy cracking positions of segments and gave prevention suggestions. Ye et al. (2010) made statistics on the crack parameters of a large number of actual tunnels, and combined with design and construction records and numerical analysis results, analyzed various causes of lining cracks, and at the same time, gave safety diagnosis and evaluation for typical crack tracking and monitoring research. Huang et al. (2013) used extended finite element analysis to study the distribution law, cracking mechanism and crack forms of lining cracks under the influence of main causes of highway tunnels in Zhejiang. Briffaut et al. (2016) have studied the sensitivity and influence of different types of fibers on the early cracking of concrete lining through laboratory tests and numerical simulations. The results show that polypropylene coarse fiber and steel fiber can delay the cracking time and reduce the influence of cracking, and changing the fiber type and thickness of secondary lining can help to reduce the transverse cracking. Asad and Majid (2017) has been experimentally demonstrated that building materials such as nylon fiber reinforced concrete can reduce the crack rate in pipeline lining due to alternating wetting and subsidence. Liu et al. (2017) analyzed the lining section defects through the ground penetrating radar (GPR) antenna detection test, summarized the waveform and frequency spectrum characteristics of the defects, and put forward the method of determining the zero line position of radar wave by using the reflection hyperbola of point objects to invert the velocity and then calculate the lining thickness, which can help identify the lining defect types. Fu et al. (2021) conducted experiments and engineering investigations on shrinkage characteristics of lined machine-made sand concrete, gave the differences between machine-made sand concrete and river sand concrete in mechanical properties and shrinkage deformation, and analyzed the causes of circumferential cracking caused by machine-

TABLE 1 Physical and mechanical parameters of materials.

Materials	unit weight of soil (kN/m^3)	Young's modulus (GPa)	Poisson's ratio	Inner friction ange (0)	Cohesion (kN/m^2)
Class IV surrounding rock	22	8.1	0.35	55	210
Concrete (C30)	25	31	0.2		
Spraying concrete (C25)	25	28	0.2		

TABLE 2 Quantitative evaluation criteria of lining cracks.

Criterion	Technical manual of railway public works-tunnels			
Crack grade	Hairy crack	Small crack	Middle crack	Big crack
crack width	≤0.3 mm	0.3–2 mm	2–20 mm	>20 mm

TABLE 3 Simulation schemes.

Cases	Crack position	Crack width (mm)	Cases	Crack position	Crack depth (cm)
1	Lining vault	0.3	13	Lining vault	10
2	Lining vault	2	14	Lining vault	20
3	Lining vault	10	15	Lining vault	30
4	Lining vault	20	16	Lining vault	40
5	Lining spandrel	0.3	17	Lining spandrel	10
6	Lining spandrel	2	18	Lining spandrel	22
7	Lining spandrel	10	19	Lining spandrel	30
8	Lining spandrel	20	20	Lining spandrel	40
9	Lining side wall	0.3	21	Lining side wall	10
10	Lining side wall	2	22	Lining side wall	20
11	Lining side wall	10	23	Lining side wall	30
12	Lining side wall	20	24	Lining side wall	40

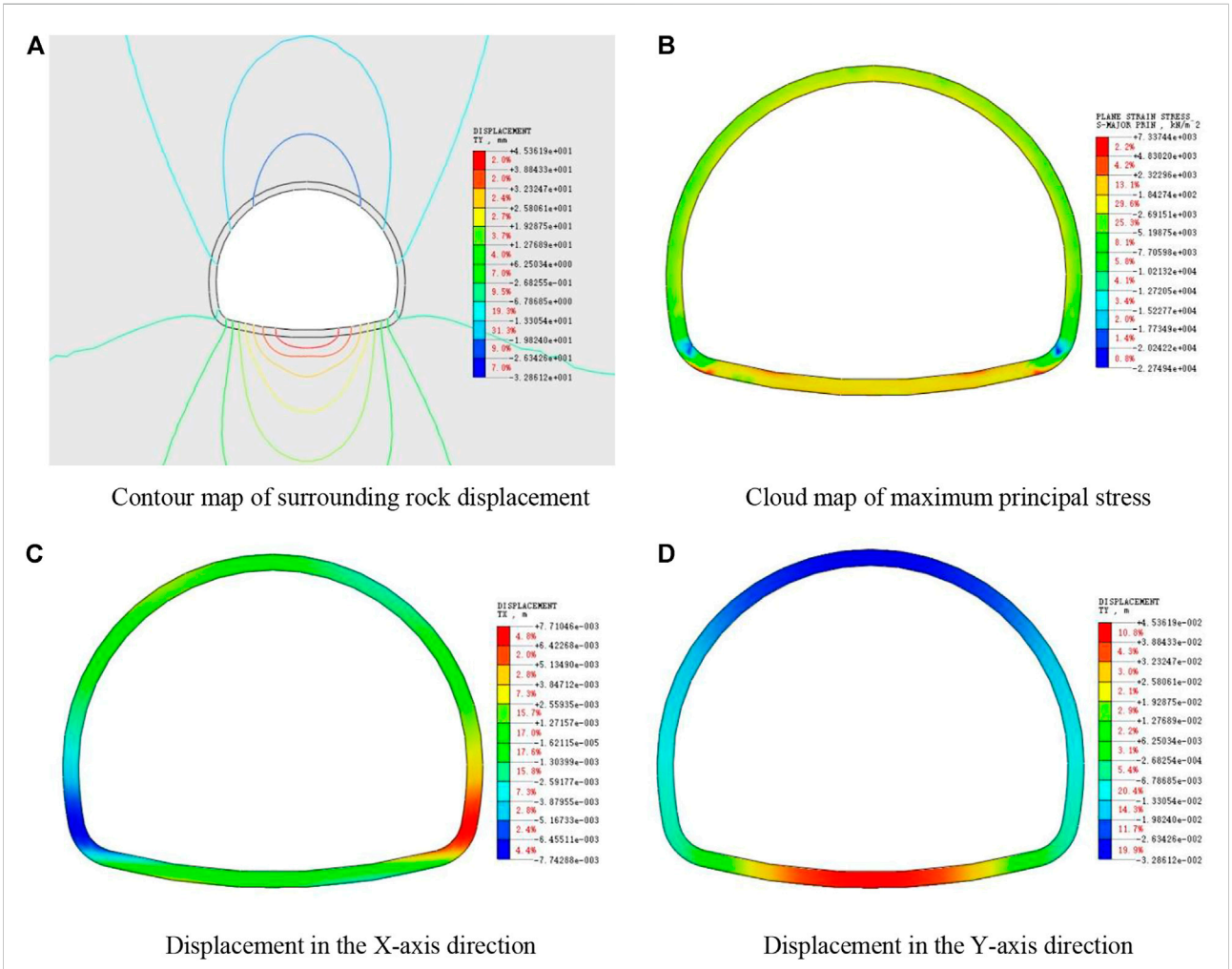

FIGURE 4
Numerical analysis results of undamaged lining model. **(A)** Contour map of surrounding rock displacement. **(B)** Cloud map of maximum principal stress. **(C)** Displacement in the X-axis direction. **(D)** Displacement in the Y-axis direction

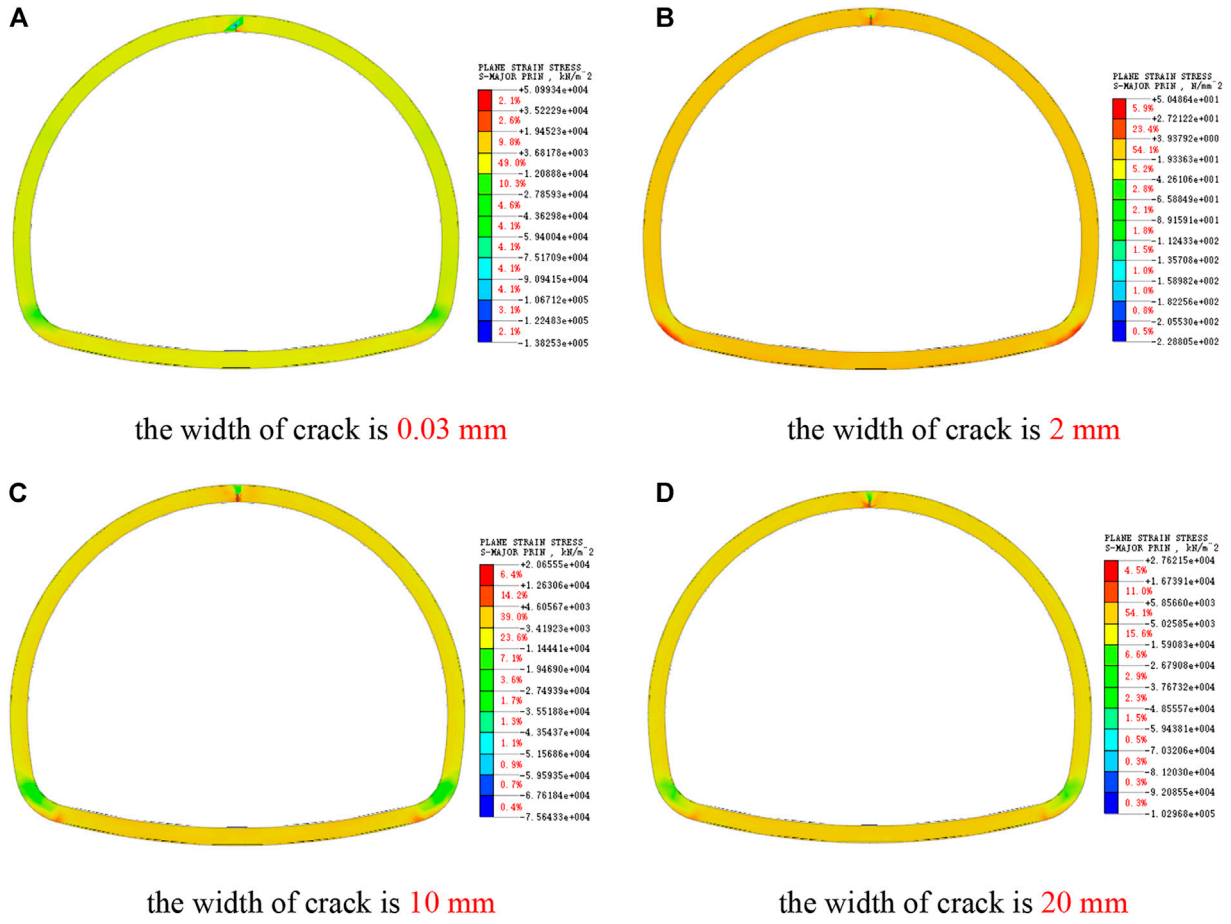

FIGURE 5
Cloud map of major principal stress of vault crack. **(A)** The width of crack is 0.03 mm. **(B)** The width of crack is 2 mm. **(C)** The width of crack is 10 mm. **(D)** The width of crack is 20 mm.

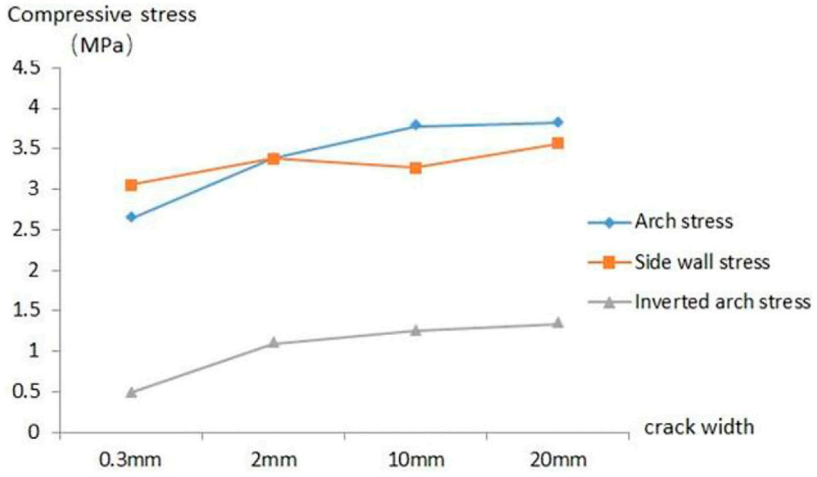

FIGURE 6
Stress variation diagram of main position of cracked lining of vault

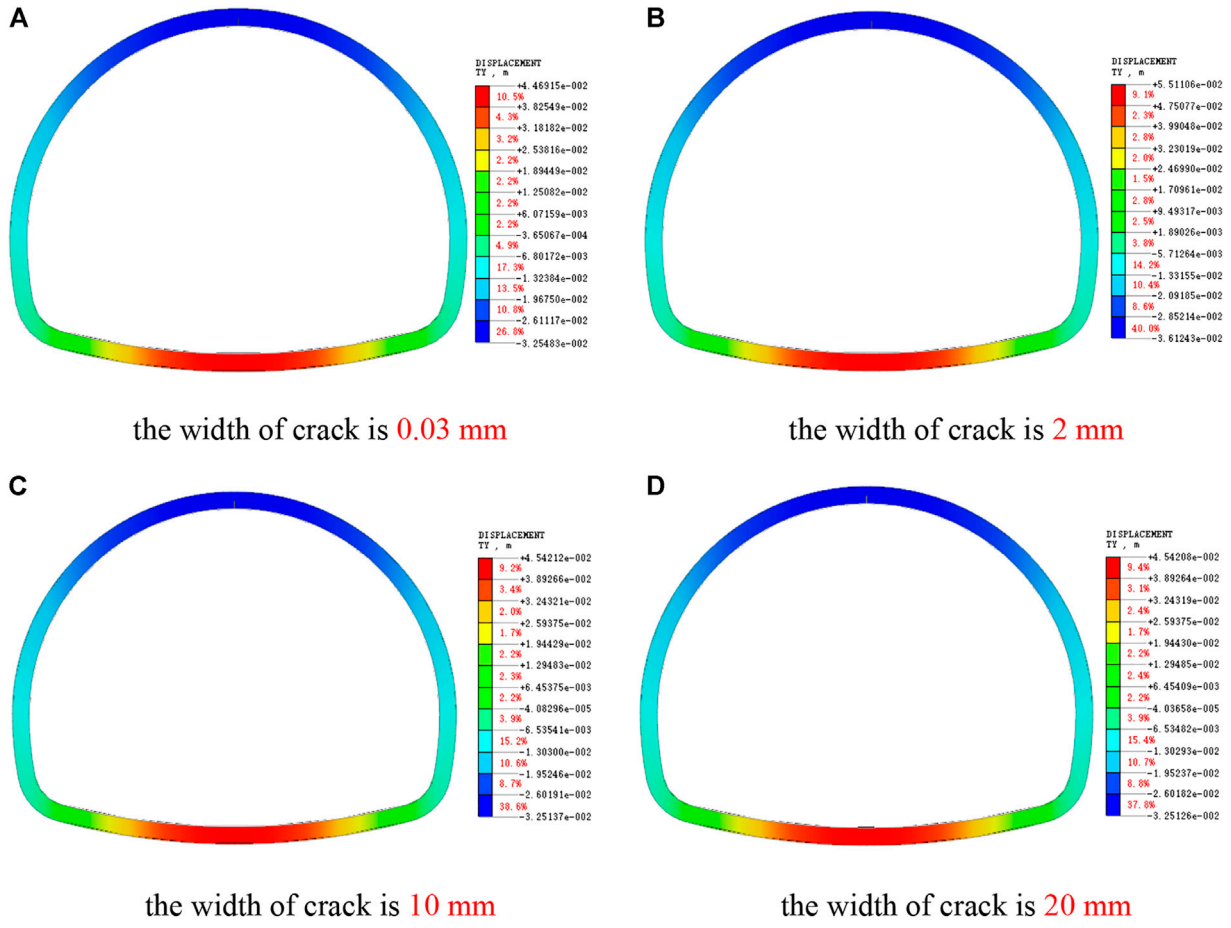

FIGURE 7
Cloud picture of Y-direction displacement of vault crack lining. **(A)** The width of crack is 0.03 mm. **(B)** The width of crack is 2 mm. **(C)** The width of crack is 10 mm. **(D)** The width of crack is 20 mm.

made sand concrete. Xu et al. (2021, 2022) developed a similar material to simulate the cracking of surrounding rock and lining, which can effectively simulate the development and evolution of cracks. Then, the mechanical properties and cracking characteristics of lining under the coupling action of temperature and load were studied by using an independently developed tunnel geomechanics model test system. Zhang et al. (2022a) obtained the damage constitutive parameters required for theoretical research through three kinds of fiber concrete tests combined with DIC technology, and analyzed the influence law of different crack position, inclination angle, vehicle speed and other parameters on the safety and stability of the lined lining with joints under the conditions of conventional concrete and different fiber concrete by finite element displacement method. Zhang Z. Q. et al. (2022) studied the mechanics and deformation characteristics, stress distribution, crack development and failure mechanism of tunnel lining in water-rich layer through large-scale model experiments. Zhang et al. (2022c) studied the deterioration process of tunnel drainage system and the failure mechanism of lining through field investigation and numerical simulation analysis based on cracks.

In this paper, the causes and main distribution positions of lining cracking are analyzed, and the influence of different positions of lining cracking on the stress and deformation of lining structure is analyzed by numerical simulation. This analysis will help to improve the understanding of the influence of lining crack diseases,

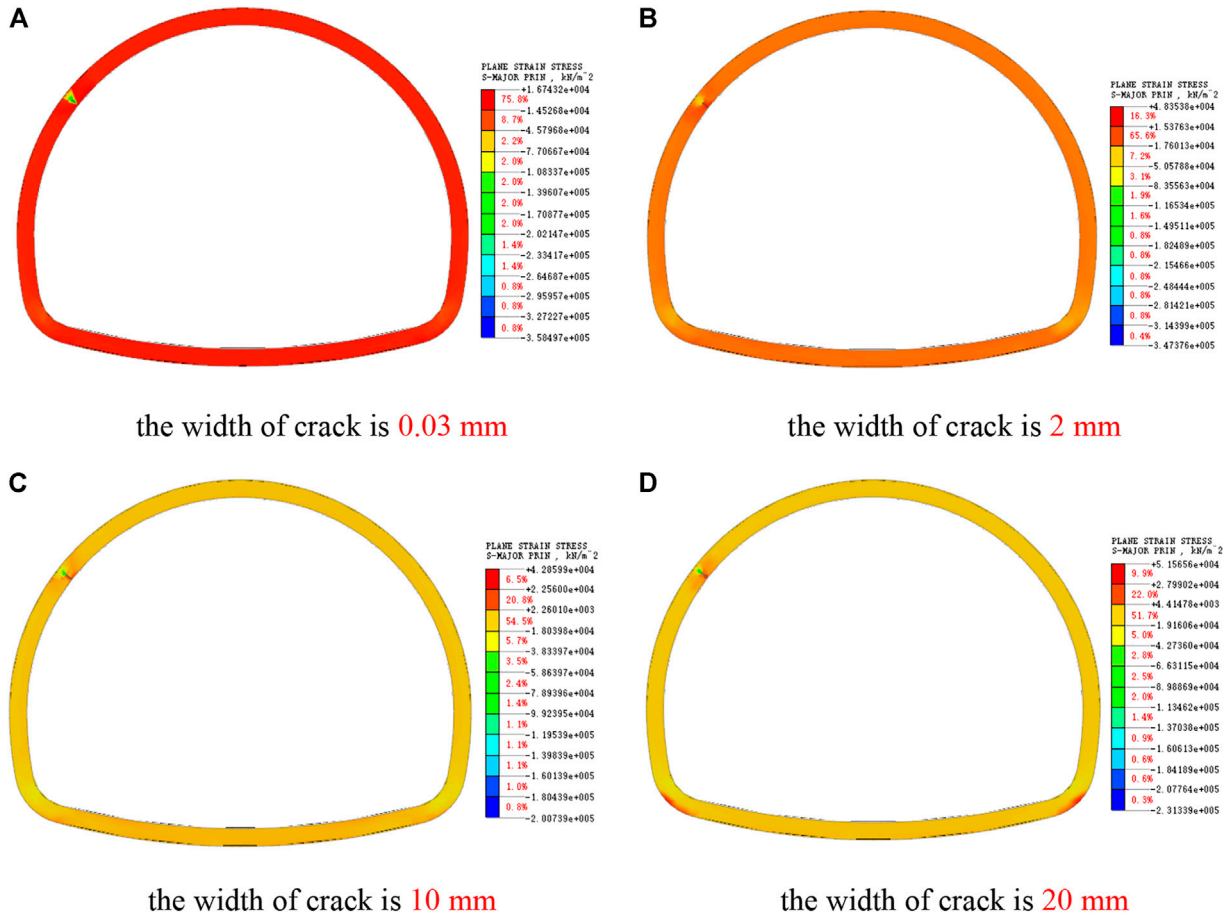

FIGURE 8
Cloud picture of large principal stress of arch shoulder crack, **(A)** the width of crack is 0.03 mm. **(B)** The width of crack is 2 mm. **(C)** The width of crack is 10 mm. **(D)** The width of crack is 20 mm.

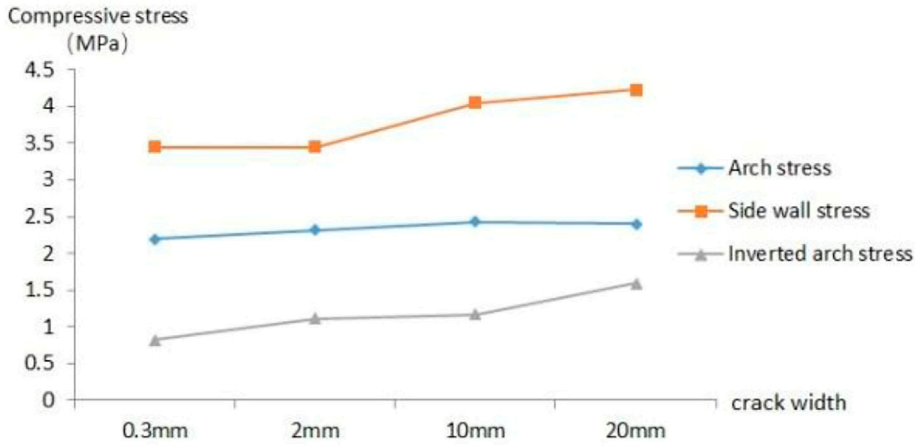

FIGURE 9
Stress variation diagram of main position of arch shoulder cracked lining

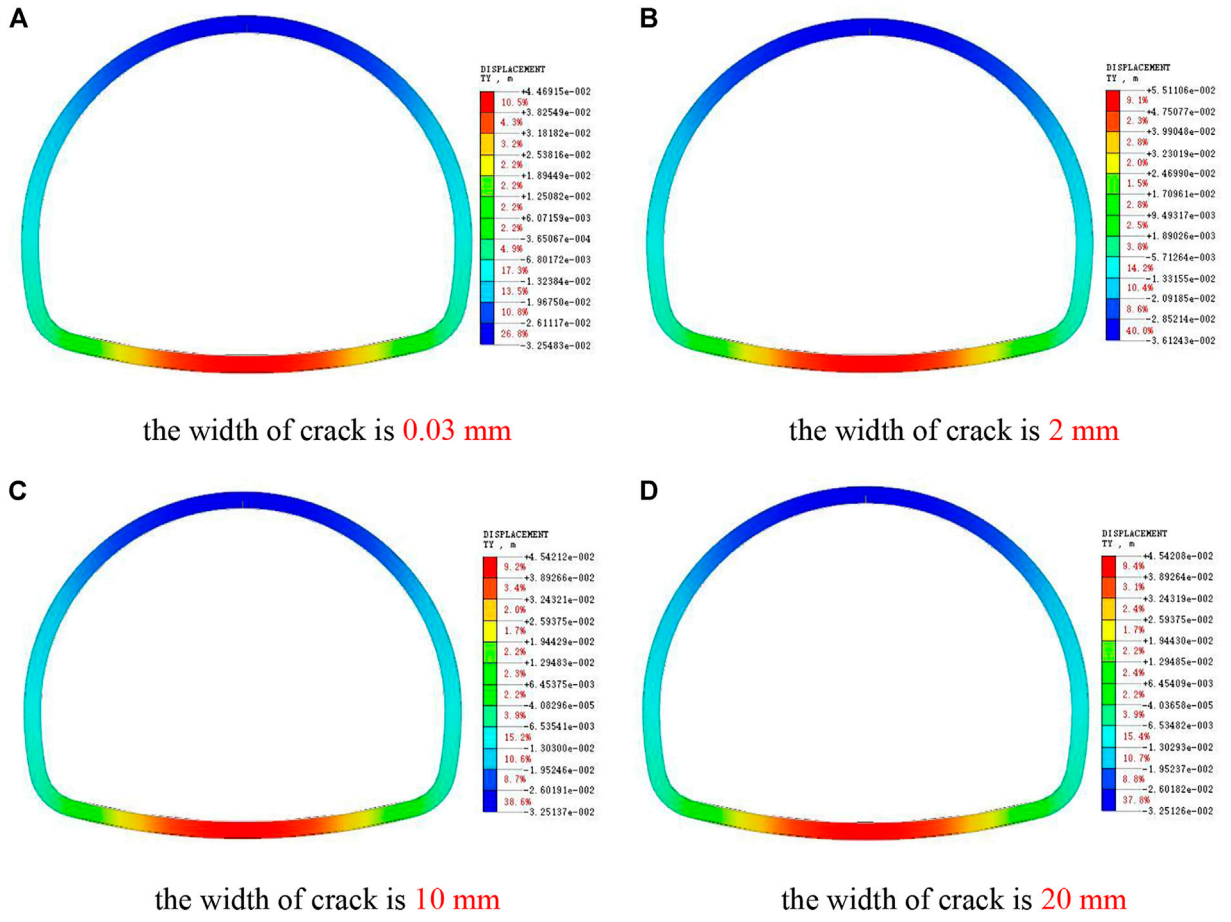

FIGURE 10
Cloud picture of Y-direction displacement of arch shoulder crack lining. **(A)** The width of crack is 0.03 mm. **(B)** The width of crack is 2 mm. **(C)** The width of crack is 10 mm. **(D)** The width of crack is 20 mm.

and give some enlightenment to the later monitoring and maintenance, stability evaluation and reinforcement and repair of tunnel lining.

Numerical calculation models and schemes

Analysis of the distribution of cracks in the lining

Cracks in any part of the lining can affect the safety of the tunnel. Studies have shown that lining cracks are mainly concentrated in the vault, shoulder and sidewall areas, as shown in Figure 1 Cracks in these parts of the tunnel have a more significant impact on the lining forces, and the threat to the overall tunnel lining safety is more obvious when the cracks expand in large numbers (Yuan, 2019).

Numerical models

The “stratum structure” model can better simulate the interaction between stratum and structure than the “load structure” model. This paper mainly studies the influence of the existing cracks on the internal force and deformation of the lining structure. When establishing the model, the boundary situation is considered to be similar to the actual situation as much as possible, so the “stratum structure” model is more appropriate. In the numerical simulations, cracks in the tunnel

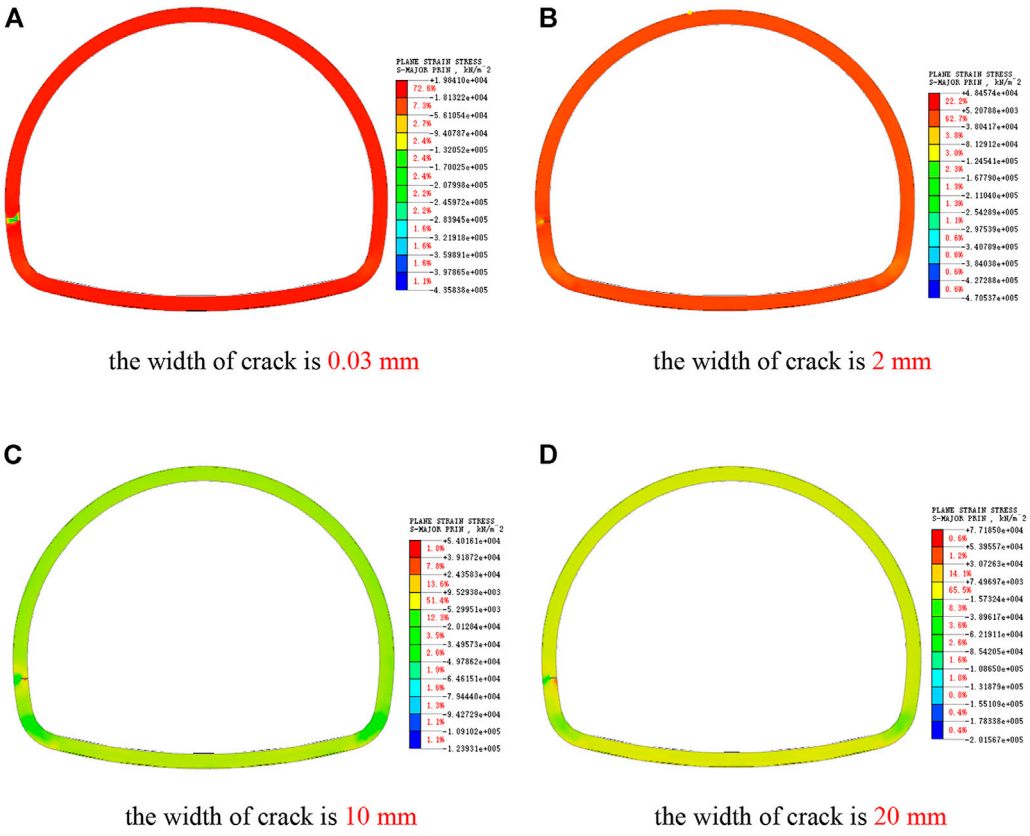

FIGURE 11
Cloud picture of maximum principal stress of side wall cracks. **(A)** The width of crack is 0.03 mm. **(B)** The width of crack is 2 mm. **(C)** The width of crack is 10 mm. **(D)** The width of crack is 20 mm.

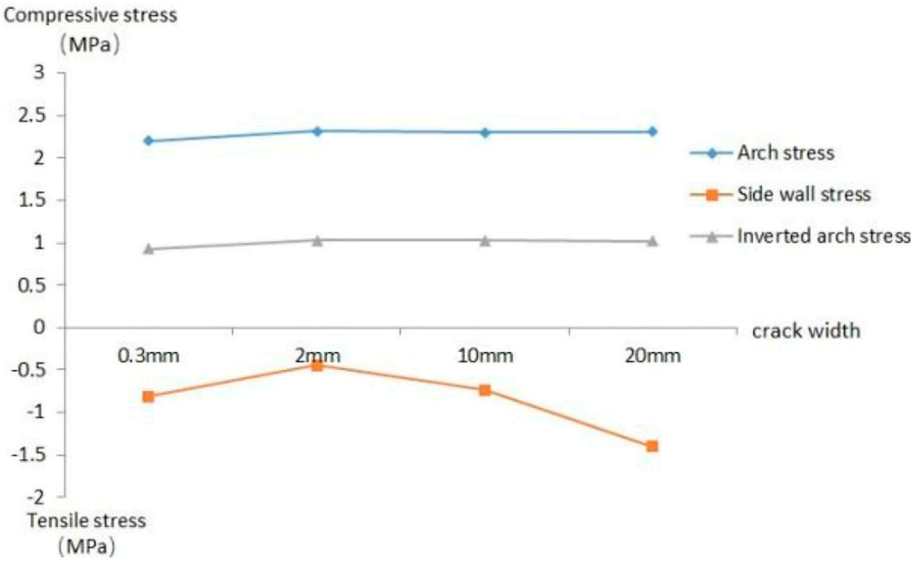

FIGURE 12
Stress variation diagram of main position of cracked lining of side wall

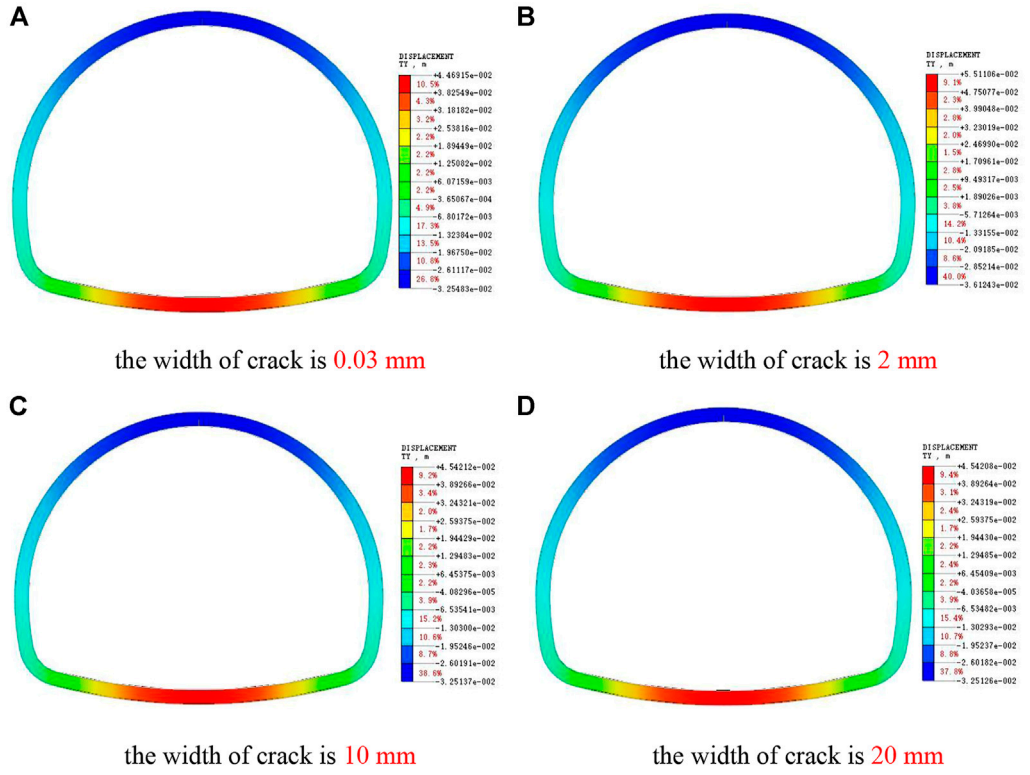

FIGURE 13
Cloud pictures of Y-direction displacement of side wall crack lining. **(A)** The width of crack is 0.03 mm. **(B)** The width of crack is 2 mm. **(C)** The width of crack is 10 mm. **(D)** The width of crack is 20 mm.

lining are simulated by removing the grid cells at the predetermined cracks to achieve a similar effect to the actual situation.

This paper is based on the G4216 Chengdu-Lijiang National Expressway, Huaping-Lijiang section, a deeply buried tunnel in the Yingpan Mountains with complex topography, geology, environment and construction conditions, an average burial depth of about 600 m and a tunnel width of 11 m.

As the spatial effect of the surrounding rock after tunnel excavation is to be considered, the boundary dimensions of the built model contain three times the tunnel bore diameter range (Su, 2012). Taking into account the model's aspect ratio, the tunnel model was determined to have a vault depth of 100m, with the rest of the upper rock being replaced by a corresponding stress boundary, with a model aspect ratio of 44 × 135.16 m. The model is divided into a total of 5,020 meshes, the boundary conditions are set to the left and right boundaries of the horizontal direction constraints, the upper ground constraints for the 500 m surrounding rock self-weight stress 10000 kN/m (Zhang et al., 2018), The lower boundary is fully constrained. The Mohr-Coulomb criterion was chosen for the intrinsic structure of the surrounding rock and the elastic intrinsic structure model was chosen for the tunnel lining intrinsic structure. Figure 2 shows the model and Figure 3 shows the tunnel lining structure. Based on the tunnel design and relevant geological exploration data and relevant national code standards, the material parameters selected for the numerical simulation are shown in Table 1.

Simulation schemes

Firstly, a crack-free lining model is established for numerical analysis as a control group. Then, according to China's Technical Manual of Railway Public Works, the lining cracks are divided into four levels (see Table 2 for details), and the cracks with different widths of 0.3, 2, 10 and 20 mm and different depths of 10, 20, 30 and

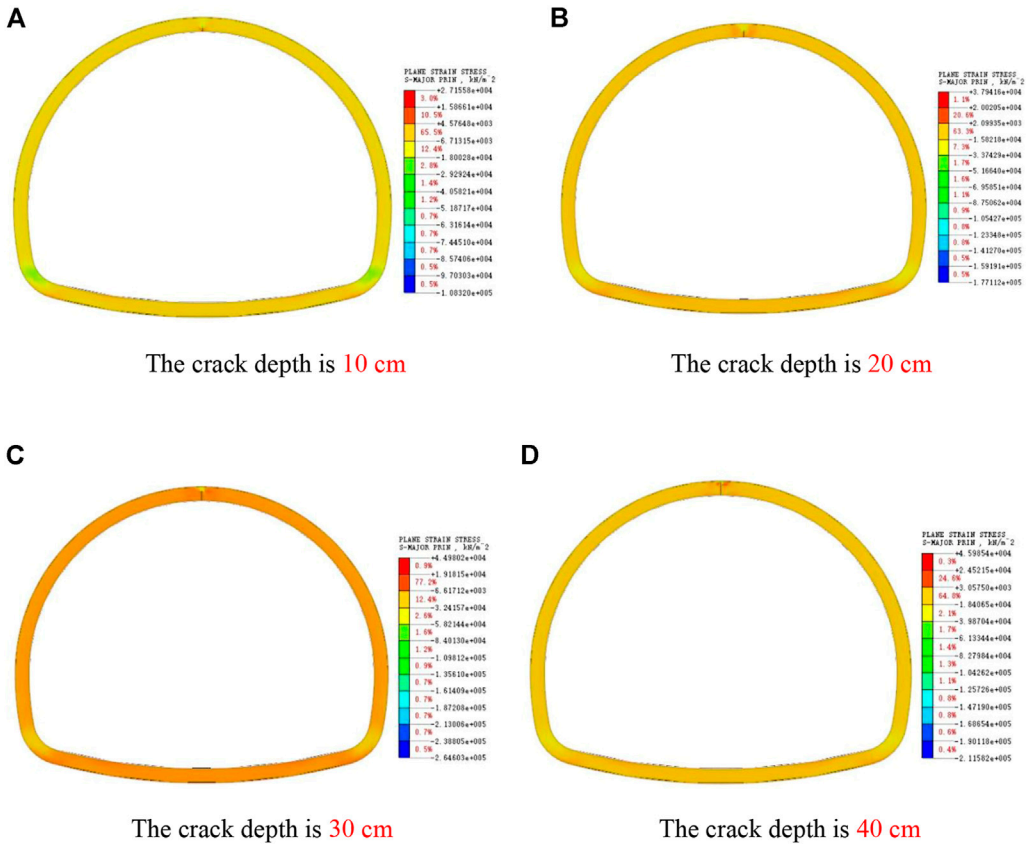

FIGURE 14
Cloud pictures of maximum principal stress of cracks at different depths in vault. **(A)** The crack depth is 10 cm. **(B)** The crack depth is 20 cm. **(C)** The crack depth is 30 cm. **(D)** The crack depth is 40 cm.

40 cm (Xiao et al., 2021) are set on the inside of vault, arch shoulder and side wall respectively. A total of 24 simulation schemes are set according to different positions, widths and depths of lining cracks (see Table 3). The influence of different crack positions, different crack widths and depths on the stress and deformation of tunnel lining structure is analyzed.

Analysis of internal force and deformation of crackless lining

The numerical model of undamaged lining is established, and its internal force and deformation are analyzed as the control group, and compared with the following different lining cracking models.

It can be seen from the numerical simulation cloud chart in Figure 4 that the maximum tensile stress of the undamaged lining is mainly distributed outside the vault and arch shoulder, while the maximum compressive stress is mainly concentrated outside the inverted arch and the wall foot of the tunnel, and the internal force are basically symmetrically distributed. Generally, the stress on the outside of the whole lining structure is higher than that on the inside of the lining, but the maximum tensile stress and the maximum compressive stress do not exceed the tensile strength and compressive strength of concrete, so the lining structure is in a safe and stable state.

From the displacement nephogram, it can be seen that the tunnel lining deformation mainly includes vault subsidence, inverted arch uplift and horizontal deformation of two side walls, and the maximum vertical deformation mainly occurs

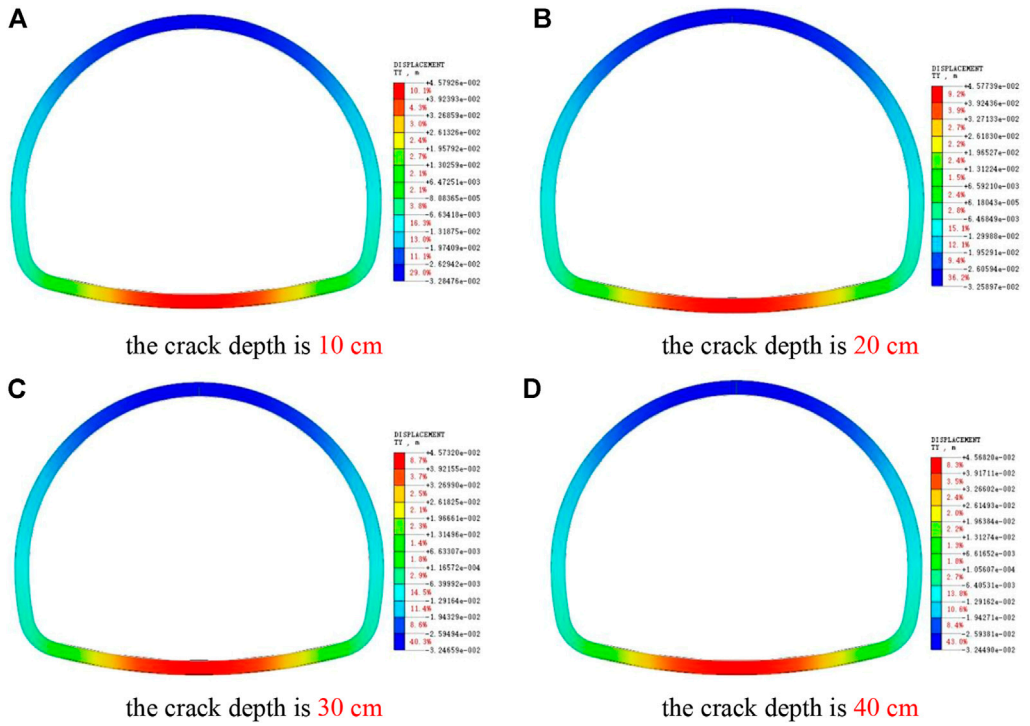

FIGURE 15
Picture of Y-direction displacement of cracked lining at different depths of vault. **(A)** The crack depth is 10 cm. **(B)** The crack depth is 20 cm. **(C)** The crack depth is 30 cm. **(D)** The crack depth is 40 cm.

in the middle of the vault and inverted arch, which accords with the actual deformation of tunnel engineering and verifies the rationality of the model.

Influence analysis of cracks with different widths on lining structure

Analysis of internal force and deformation of lining after vault cracking

As shown in Figures 5, 6, the crack tip of lining mainly bears compressive stress, and both sides of the crack are mainly tensile stress, and the maximum stress value is concentrated at the crack tip, which exceeds the compressive strength of concrete, that is, once cracks are generated in lining, there will be an expansion trend. When the depth of lining crack is constant, with the increase of vault crack width, the tensile stress and compressive stress at the crack are decreasing, because the stress concentration at the crack is weakening with the crack expansion. As shown in Figure 6, with the increase of crack width, the integrity of the lining structure is destroyed to a certain extent, which will weaken the bearing capacity of the lining structure. The stress at the main position of the lining is constantly increasing, especially the internal force at the foot of the wall is significantly increased. Except for the cracks, the whole lining structure is still in a safe working state.

As shown in Figure 7, the vertical displacement of the lining arch increases after the lining vault cracks, which aggravates the phenomenon of vault subsidence, which is not conducive to the stability of the lining. At the same time, with the increase of crack width, compared with the undamaged lining, the vertical displacement of inverted arch slightly increases, which shows that the influence of vault cracking on the vertical deformation of lining is mainly concentrated around the arch of lining.

Analysis of internal force and deformation of lining shoulder after cracking

As shown in Figure 8, the stress value around the arch shoulder crack is obviously larger than that around the vault crack, and the crack tip is damaged by compression, and the

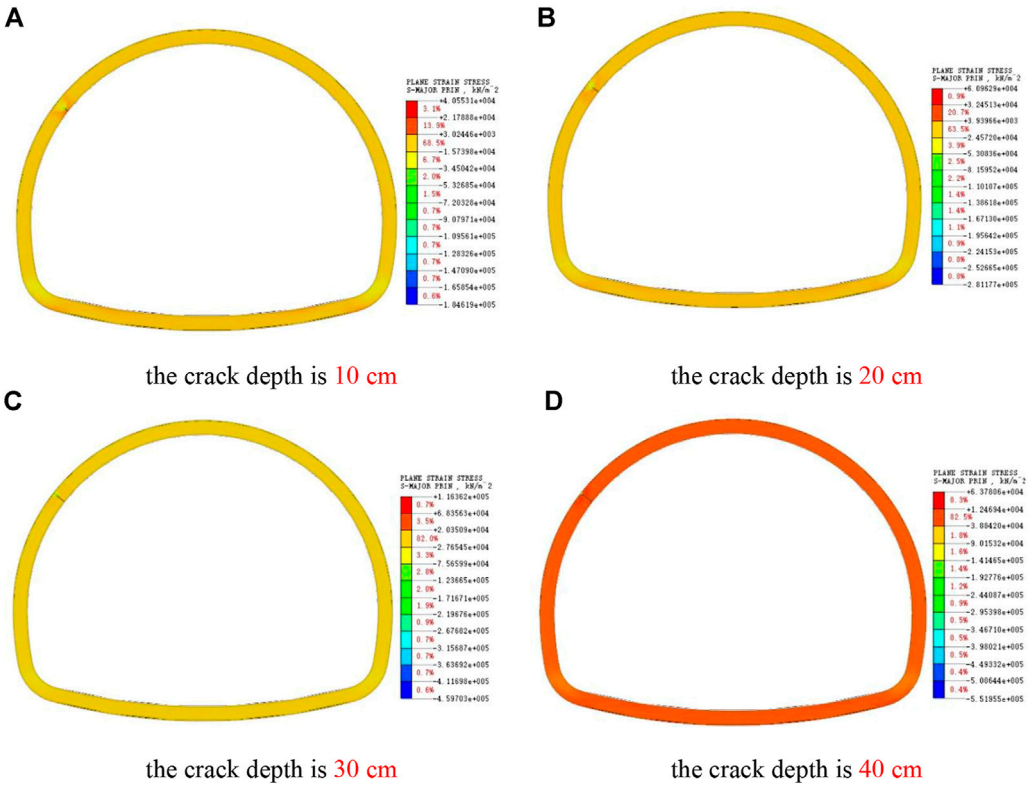

FIGURE 16
Cloud pictures of maximum principal stress of cracks at different depths in arch shoulder. **(A)** The crack depth is 10 cm. **(B)** The crack depth is 20 cm. **(C)** The crack depth is 30 cm. **(D)** The crack depth is 40 cm.

stress concentration range caused by the arch shoulder crack is larger, so the arch shoulder crack damages the lining more than the vault crack. With the increase of crack width, the stress at the crack decreases, and the crack propagation rate will decrease, but the internal forces of other main parts of the lining increase, as shown in Figure 9.

When the crack width is 20 mm, the stress value at the outer edge of the lining at the crack reaches about 20MPa, which is close to the compressive strength of concrete. At this time, the safety of the lining structure has been greatly affected, and the reinforcement and repair measures should be taken in time. When there is a large crack larger than 10mm, the internal force of the cracked side wall is increased by the arch shoulder crack, but the law is not obvious when there is a small crack.

As shown in Figure 10, the cracking of the lining arch shoulder will increase the vertical deformation of the lining and aggravate the arch subsidence and inverted arch uplift. With the continuous expansion of crack width, the vertical settlement deformation of vault and the uplift deformation of inverted arch are increasing, especially when the crack width exceeds 10mm, the deformation is more obvious, which has a certain deterioration effect on the lining structure. At this time, monitoring should be strengthened or repair measures should be taken to ensure the bearing safety.

Analysis of internal force and deformation of lining wall after cracking

As shown in Figure 11, the stress at the crack of the lining side wall is obviously greater than that at other parts of the lining, and the stress concentration phenomenon is very obvious. Comparing Figure 5 and Figure 8, it can be seen that after the lining side wall cracks, the stress around the cracks increases significantly more than that at the lining vault and arch shoulder. When the side wall crack is less than 10 mm, the stress at the bottom of the crack is greater than the strength of the concrete, and the stress at other parts is in a safe bearing state.

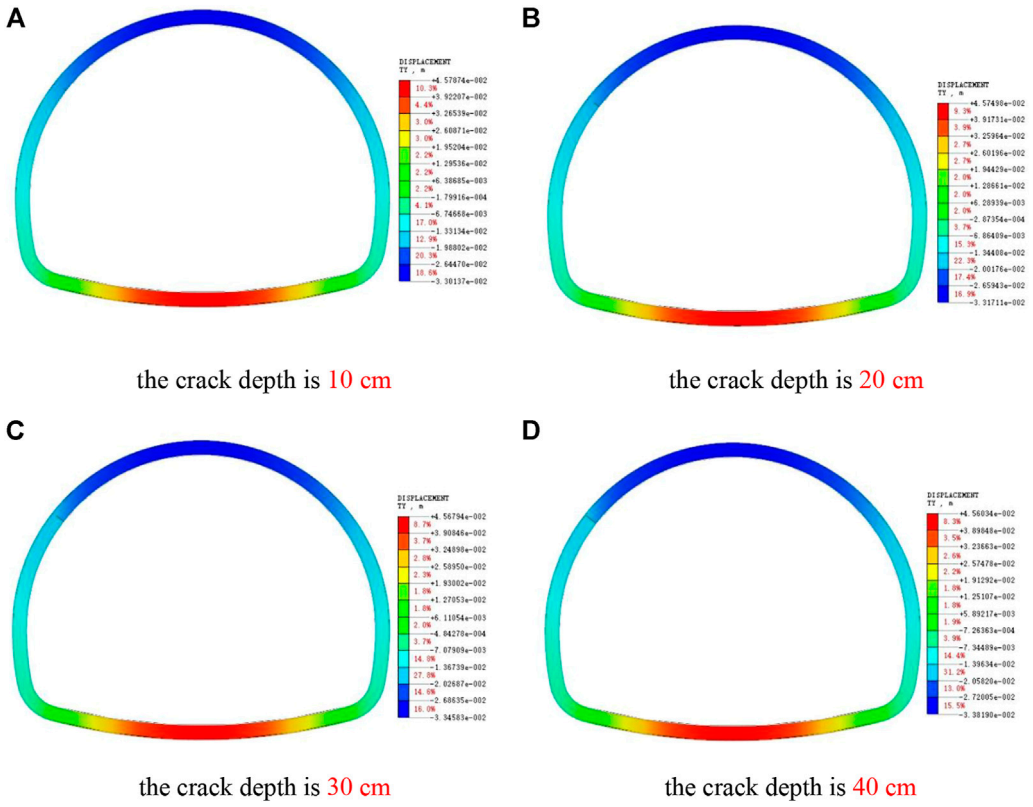

FIGURE 17
Cloud image of Y-direction displacement of lining with cracks at different depths in arch shoulder. **(A)** The crack depth is 10 cm. **(B)** The crack depth is 20 cm. **(C)** The crack depth is 30 cm. **(D)** The crack depth is 40 cm.

As shown in Figure 12, after the side wall cracks, the side wall gradually changes from the compression state to the tension state. When the crack width reaches 20 mm wide, the compressive stress on the outside of the lining and the tensile stress on the side wall of the crack will soon reach the compressive strength and tensile strength of concrete, which indicates that the local concrete at the crack of the lining side wall will be crushed at this time, and the safety of the lining side wall can no longer be guaranteed. Therefore, reinforcement and repair should be carried out in time to prevent the lining structure from being unstable and damaged.

As shown in Figure 13, the vertical settlement deformation of the lining at the crack will be increased after the side wall cracks. For the lining structure, the vertical deformation of other parts has little influence. Compared with the undamaged lining, the side wall cracks will increase the settlement deformation of the vault, but the increased value is very small. It can be seen that the influence of side wall lining cracks on the vertical deformation of lining is mainly concentrated around the cracks.

Influence analysis of cracks with different depths on lining structure

Analysis of internal force and deformation of lining after vault cracking

As shown in Figure 14, when the lining vault cracks, the stress of the lining structure is symmetrically distributed, and obvious stress concentration occurs near the crack tip. With the increase of crack depth, the maximum stress around the crack tip is increasing. When the crack depth is greater than 30 cm, the damage range of compressive stress at the crack tip is close to the lining edge, and the lining stability cannot be guaranteed. Therefore, reinforcement and repair measures should be taken in time.

As shown in Figure 15, with the increase of vault crack depth, the vertical displacement of the lining structure vault increases, but the increased value is relatively small, and the main influence range is concentrated near the vault crack, while the vertical displacement of other main parts has no obvious effect.

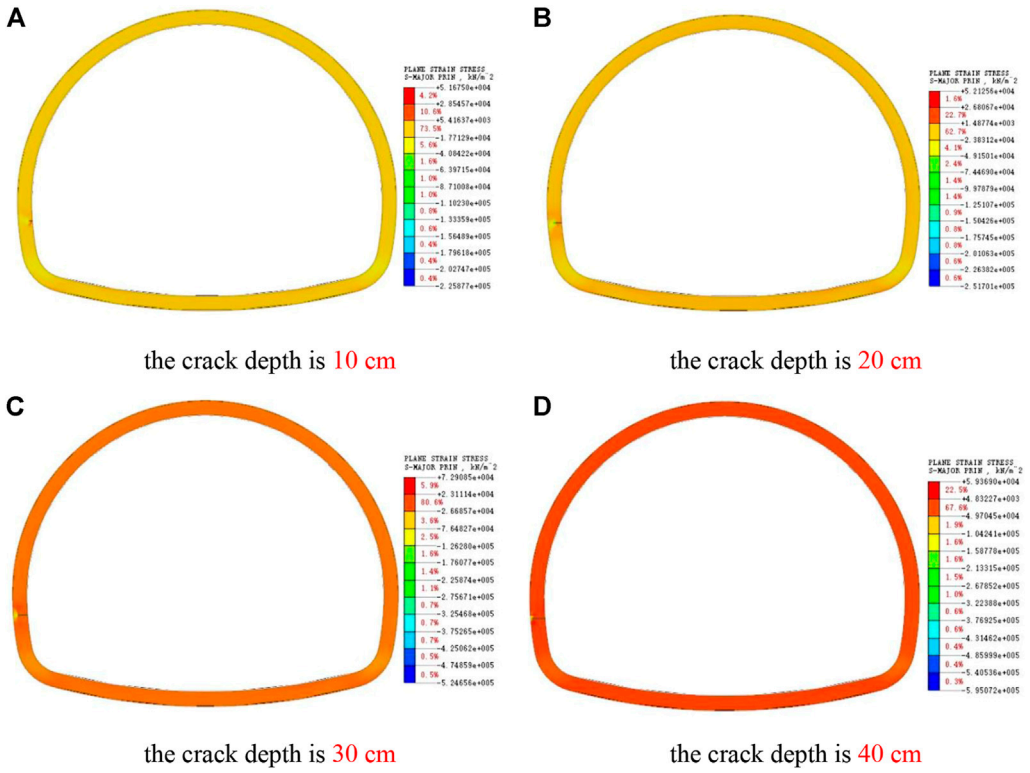

FIGURE 18
Cloud pictures of maximum principal stress of cracks in side walls at different depths. **(A)** The crack depth is 10 cm. **(B)** The crack depth is 20 cm. **(C)** The crack depth is 30 cm. **(D)** The crack depth is 40 cm.

Analysis of internal force and deformation of lining shoulder after cracking

As shown in Figure 16, when the arch shoulder cracks, the stress value around the crack is obviously higher than that of the vault crack, and the stress concentration around the crack is larger, indicating that the arch shoulder is more sensitive to the change of crack depth, that is, the arch shoulder crack is more destructive to the lining than the vault crack. With the increase of crack depth, the stress around the crack increases continuously. When the crack depth is more than 30 cm, the compressive stress of the lining edge near the crack tip has reached the compressive strength of concrete, and the safety and stability of the arch shoulder of the lining structure cannot be guaranteed. Therefore, it is necessary to strengthen the monitoring of the cracks at the arch shoulder to ensure timely repair and reinforcement.

From Figure 17, the vertical deformation of the lining will be increased when cracks appear in the arch shoulder, and the settlement displacement around the vault will increase with the increase of the crack depth, but the increment will be small. Compared with the undamaged lining, the arch shoulder crack also increases the uplift displacement of the inverted arch.

Analysis of internal force and deformation of lining wall after cracking

As shown in Figure 18, the stress around the crack at the side wall increases obviously, and the stress around the crack is larger than that in the vault and arch shoulder, which is more sensitive to the depth factor. When the side wall crack is larger than 30 cm, the stress at the lining edge near the crack tip has reached the limit value, and the lining structure at the side wall has been in a state of destruction.

As shown in Figure 19, with the increase of crack depth, the maximum vertical settlement of lining vault is increasing. Compared with the undamaged lining, the vertical displacement of the inverted arch is increased by the side wall crack, but the change is no longer obvious with the increase of the crack depth.

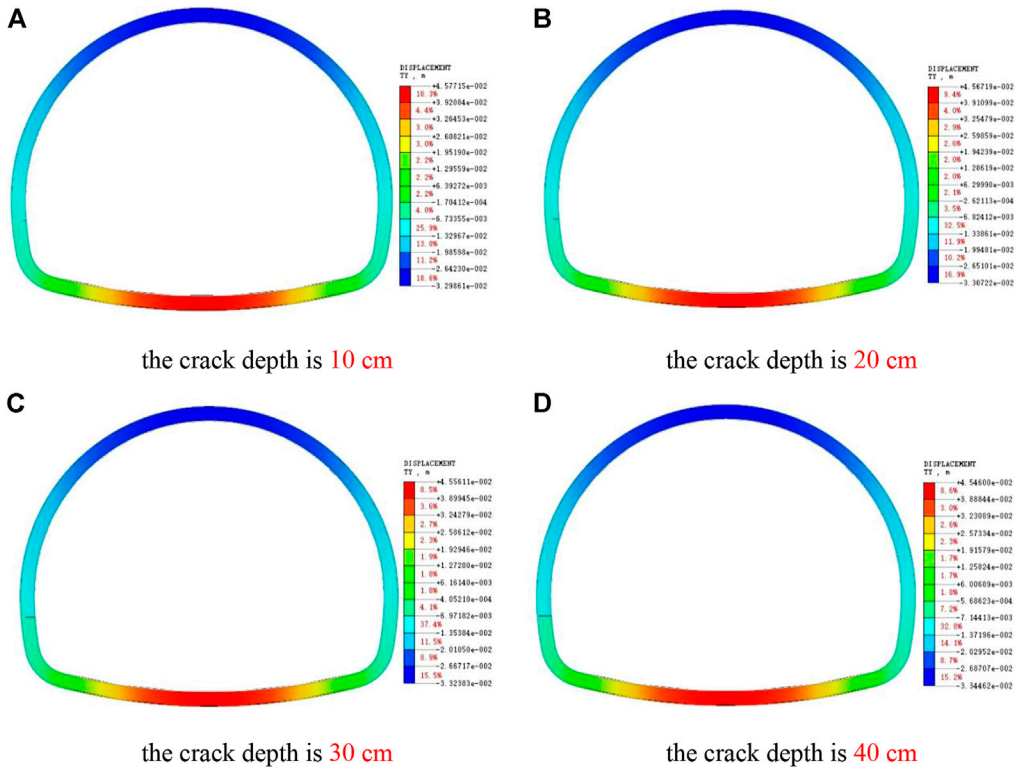

FIGURE 19
Cloud pictures of Y-direction displacement of lining with cracks at different depths of side wall. **(A)** The crack depth is 10 cm. **(B)** The crack depth is 20 cm. **(C)** The crack depth is 30 cm. **(D)** The crack depth is 40 cm.

Conclusion

In this paper, through numerical analysis of the model of lining cracking at different positions, the influence of lining cracking at different positions on the stress of lining structure and the variation law of displacement are summarized. The main conclusions are as follows:

1) Based on the Yingpanshan tunnel, the numerical analysis shows that the internal force of the deep buried tunnel lining is basically symmetrically distributed without damage, and the internal force will be redistributed after the lining cracks.
2) When the lining cracks, with the increase of the crack width, the stress concentration at the crack of the lining decreases continuously; With the increase of crack depth, the stress concentration at the crack of lining increases continuously. And the stress of other main parts of the lining has increased, which has a certain deterioration effect on the bearing capacity and stability of the lining structure.
3) Cracking of lining has little effect on the lateral deformation of lining, and the small lateral deformation is mainly distributed around the crack. With the increase of crack width and depth, the subsidence deformation of vault and the uplift deformation of inverted arch increase continuously, especially when the crack is wide.

Data availability statement

The original contributions presented in the study are included in the article/supplementary material, further inquiries can be directed to the corresponding authors.

Author contributions

Conceptualization: SC and ZY; methodology: SC and ZY; software: SL and LL; validation: YZ and YY; resources: SC and ZY; Data curation: SL and LL; writing—original draft preparation, SL; writing—review and editing: SC and LL; Project administration: SC. All authors have read and agreed to the published version of the manuscript.

Funding

This research is sponsored by the Doctoral research start-up fund of Hebei GEO University and Hebei University Youth Fund Project (QN202105) and Key research and development projects in Hebei Province (22371701D) and Hebei Province Innovation Ability Promotion Program (21567628H).

Conflict of interest

Author ZY was employed by Guangdong Hualu Transport Technology Co., Ltd., China.

The remaining authors declare that the research was conducted in the absence of any commercial or financial relationships that could be construed as a potential conflict of interest.

Publisher's note

All claims expressed in this article are solely those of the authors and do not necessarily represent those of their affiliated organizations, or those of the publisher, the editors and the reviewers. Any product that may be evaluated in this article, or claim that may be made by its manufacturer, is not guaranteed or endorsed by the publisher.

References

Asad, Z., and Majid, A. (2017). Behavior of fiber reinforced concrete for controlling the rate of cracking in canal-lining. *Constr. Build. Mat.* 155, 726–739. doi:10.1016/j.conbuildmat.2017.08.078

Bai, B., Wang, Y., Rao, D. Y., and Bai, F. (2022). The effective thermal conductivity of unsaturated porous media deduced by pore-scale SPH simulation. *Front. Earth Sci. (Lausanne).* 10. 943853, doi:10.3389/feart.2022.943853

Bai, B., Yang, G. C., Li, T., and Yang, G. S. (2019). A thermodynamic constitutive model with temperature effect based on particle rearrangement for geomaterials. *Mech. Mater.* 139, 103180. doi:10.1016/j.mechmat.2019.103180

Bai, B., Zhou, R., Cai, G. Q., Hu, W., and Yang, G. C. (2021a). Coupled thermo-hydro-mechanical mechanism in view of the soil particle rearrangement of granular thermodynamics. *Comput. Geotechnics* 137 (8), 104272. doi:10.1016/j.compgeo.2021.104272

Bai, X. D., Cheng, W. C., and Li, G. (2021b). A comparative study of different machine learning algorithms in predicting epb shield behaviour: A case study at the xi'an metro, China. *Acta Geotech.* 16, 4061–4080. doi:10.1007/s11440-021-01383-7

Bai, X. D., Cheng, W. C., Sheil, B. B., and Li, Ge (2021c). Pipejacking clogging detection in soft alluvial deposits using machine learning algorithms. *Tunn. Undergr. Space Technol.* 113, 103908. doi:10.1016/j.tust.2021.103908

Briffaut, M., Benboudjema, F., and D'Aloia, L. (2016). Effect of fibres on early age cracking of concrete tunnel lining. Part II: Numerical simulations. *Tunn. Undergr. Space Technol.* 59, 221–229. doi:10.1016/j.tust.2016.08.001

Chen, J. S., and Mo, H. H. (2009). Numerical study on crack problems in segments of shield tunnel using finite element method. *Tunn. Undergr. Space Technol.* 24, 91–102. doi:10.1016/j.tust.2008.05.007

Fu, L., Zhang, X. M., Wang, L. C., Hou, G. Q., Wei, M., Gao, X., et al. (2021). Discussion on circumferential cracking of tunnel lining based on shrinkage test of machine-made sand concrete. *J. Railw. Sci. Eng.* 18 (10), 2671–2678. doi:10.19713/j.cnki.43-1423/u.T20210313

Hu, W. L., Cheng, W. C., Wen, S. J., and Rahman, M. M. (2021). Effects of chemical contamination on microscale structural characteristics of intact loess and resultant macroscale mechanical properties. *CATENA* 203, 105361. doi:10.1016/j.catena.2021.105361

Huang, H. W., Liu, D. J., Xue, Y. D., Wang, P. R., and Liu, Y. (2013). Numerical analysis of cracking of tunnel linings based on extended finite element. *Chin. J. Geotechnical Eng.* 35, 266–275. Available at: https://kns.cnki.net/kcms/detail/detail.aspx?FileName=YTGC201302012&DbName=CJFQ2013.

Liu, J., Zhang, Q. L., Du, C., and Liu, Z. Y. (2017). Model test of ground penetrating radar detection for high speed railway tunnel lining with defects. *China Railw. Sci.* 155, 726–739. doi:10.3969/j.issn.1001-4632.2021.05.12

Su, X. K. (2012). Research on choosing boundary range of surrounding rock in numerical simulation of tunnel excavation. *J. Railw. Eng. Soc.* 29 (03), 64–68. doi:10.3969/j.issn.1006-2106.2012.03.014

Xiao, S. L., Li, K., Jiang, X. H., Wu, S. D., and Yao, C. R. (2021). Study on load-bearing safety and crack evaluation standard of cracked lining. *Technol. Highw. Transp.* 37 (S1), 41–47. doi:10.13607/j.cnki.gljt.2021.Supp.007

Xu, Z. L., Chen, J. X., Luo, Y. B., Zhu, H. Y., Liu, W. W., Zhou, S., et al. (2022). Geomechanical model test for mechanical properties and cracking features of Large-section tunnel lining under periodic temperature. *Tunn. Undergr. Space Technol.* 123 (2022), 104319. doi:10.1016/j.tust.2021.104319

Xu, Z. L., Luo, Y. B., Chen, J. X., Su, Z. M., Zhu, T. T., and Yuan, J. P. (2021). Mechanical properties and reasonable proportioning of similar materials in physical model test of tunnel lining cracking. *Constr. Build. Mat.* 300 (2021), 123960. doi:10.1016/j.conbuildmat.2021.123960

Ye, F., He, C., and Xia, Y. X. (2010). Post-construction monitoring and analysis for highway tunnel lining cracks. *China Civ. Eng. J.* 43 (07), 97–104. doi:10.15951/j.tmgcxb.2010.07.004

Yuan, T. F. (2019). A research on the impact of the tunnel lining cracking on the structure force performance. Beijing: Beijing Jiaotong University. Doctoral Dissertation, Available at: https://kns.cnki.net/kcms/detail/detail.aspx?dbcode=CMFD&dbname=CMFD202001&filename=1019214697.nh&uniplatform=NZKPT&v=VeAKMzO1MAHgDNBpXyYBzL7fzZ4QXvdVekRqvBpO2EDwfj3k9erj5MUud6UzFGMR.

Zhang, J. H., Song, J. C., and Ma, Z. Y. (2018). Numerical simulation analysis of the excavation methods of deep tunnels under grade-surrounding rock condition. *Technol. Dev. Enterp.* 37 (11), 5–8. doi:10.14165/j.cnki.hunansci.2018.11.002

Zhang, S. L., Xu, Q., Yoo, C., Min, B., Liu, C., Guan, X. M., et al. (2022c). Lining cracking mechanism of old highway tunnels caused by drainage system deterioration: A case study of liwaiao tunnel, ningbo, China. *Eng. Fail. Anal.* 137 (2022), 106270. doi:10.1016/j.engfailanal.2022.106270

Zhang, W., Li, X. B., Gong, F. Q., and Li, D. Y. (2007). Cause analysis and numerical simulation study of lining cracking of highway tunnel, *Eng. Constr.* 2007(01), 26–29. doi:10.3969/j.issn.1673-8993.2007.01.007

Zhang, Z. G., Zhang, M. X., Feng, J., Ma, W. B., Wang, Z. W., and Cheng, Z. X. (2022a). Analyses on structural stability of fiber concrete tunnel lining considering different characteristics of cracks under train loads. *Chin. J. Rock Mech. Eng.* 41 (S1), 2927–2943. doi:10.13722/j.cnki.jrme.2020.0875

Zhang, Z. Q., Chen, B. K., Li, H. Y., and Zhang, H. (2022b). The performance of mechanical characteristics and failure mode for tunnel concrete lining structure in water-rich layer. *Tunn. Undergr. Space Technol.* 121 (2022), 104335. doi:10.1016/j.tust.2021.104335

frontiers | Frontiers in Materials

TYPE Original Research
PUBLISHED 28 September 2022
DOI 10.3389/fmats.2022.952631

Check for updates

OPEN ACCESS

EDITED BY
Bing Bai,
Beijing Jiaotong University, China

REVIEWED BY
Chunhui Ma,
Xi'an University of Technology, China
Jianyong Han,
Shandong Jianzhu University, China
Chen Peipei,
Beijing University of Civil Engineering and Architecture, China

*CORRESPONDENCE
Gao Lv,
lvgao116@qq.com
Naifei Liu,
liunaifei1985@126.com

SPECIALTY SECTION
This article was submitted to Structural Materials,
a section of the journal
Frontiers in Materials

RECEIVED 25 May 2022
ACCEPTED 10 August 2022
PUBLISHED 28 September 2022

CITATION
Lv G, Liu N, Bao L, Yang B and Zhang Y (2022), Detection of cracks in cemented loess of ancient buildings using remote sensing.
Front. Mater. 9:952631.
doi: 10.3389/fmats.2022.952631

COPYRIGHT
© 2022 Lv, Liu, Bao, Yang and Zhang. This is an open-access article distributed under the terms of the Creative Commons Attribution License (CC BY). The use, distribution or reproduction in other forums is permitted, provided the original author(s) and the copyright owner(s) are credited and that the original publication in this journal is cited, in accordance with accepted academic practice. No use, distribution or reproduction is permitted which does not comply with these terms.

Detection of cracks in cemented loess of ancient buildings using remote sensing

Gao Lv[1,2,3]*, Naifei Liu[2,4]*, Liangliang Bao[5], Bei Yang[6] and Yafei Zhang[1,3]

[1]School of Civil Engineering, Xi'an Shiyou University, Xi'an, China, [2]Shaanxi Key Laboratory of Geotechnical and Underground Space Engineering, XAUAT, Xi'an, China, [3]Xi'an Key Laboratory of Wellbore Integrity Evaluation, Xi'an Shiyou University, Xi'an, China, [4]School of Civil Engineering, Xi'an University of Architecture and Technology, Xi'an, China, [5]School of Civil Engineering, Yulin University, Yulin, China, [6]Architectural Design and Research Institute, Xi'an University of Architecture and Technology, Xi'an, China

The bases of ancient Chinese buildings are prone to deformation, cracks, and other hidden problems due to their age and other reasons. Rainfall and water seepage produce great harm to the cracks of soil plinths. Based on a ground-penetrating radar method, detecting cracks and water erosion defects is important for protecting ancient buildings. This study examines the reflection characteristics of ground-penetrating radar (GPR) waves at different lithological interfaces. Physical experiments and their numerical and physical laws were used to study the reflection characteristics of GPR incidents from brick to air, unsaturated soil, water, and metal interfaces. The model was applied to detect defects of the Xi'an Bell Tower and the main research results are as follows. The echo amplitude of GPR was positively correlated with the relative permittivity of the bedding layer, and its basic law conforms to the positive logarithmic curve. The hyperbolic opening of water erosion imaging of the base-compacted soil is larger, the attenuation effect increases and the signal reflection is obvious. These results provide the theoretical basis and technical support for the actual detection of water erosion deterioration of loess in similar projects, and this provides theoretical and technical references for rapid identification and management of defects in ancient buildings.

KEYWORDS

ground-penetrating radar, relative permittivity, GPR characterization, finite difference time domain method, ancient buildings

Introduction

Ancient Chinese architecture has a long history and is a remarkable architectural style (Xue, 2010). Globally, it has a very high artistic and cultural value. However, the common structure of ancient Chinese architecture consists of wooden buildings and rammed Earth foundations. In particular, the masonry and rammed Earth-based foundations have been subjected to long-term erosion by the natural environment and the influence of human factors (Wang et al., 2017). Therefore, this has led to a series of irreversible damages such

as cracks, breakage, cavitation, collapse, deformation (Liu et al., 2020a; Bai et al., 2021a), and concealed areas. There is an urgent need to implement early detection, early maintenance, early repair, and other measures for the protection of the appearance of ancient buildings and internal hidden problems (Liu et al., 2020b; Bai et al., 2021b).

The evaluation of the masonry footings of ancient buildings is more intuitive. However, identifying and excluding hidden defects of masonry table foundations are more difficult (Wang et al., 2020; Kang et al., 2021). For conservation, it is obvious that measures, such as drilling, cannot be blindly conducted on ancient Chinese buildings. Instead, it is more advantageous and wiser to use non-destructive geophysical methods. The current non-destructive methods for detecting ancient buildings are mainly Pilodyn, Resist graph, Impulse Tomography, GPR, and Hotpoint-line-surface methods (Lv et al., 2018a; Lv et al., 2018b). However, for the detection of water seepage and the location of damage of ancient buildings, GPR has advantages of portability, precision, and low cost (Adachi et al., 2020; Dao et al., 2020; Lieblappen et al., 2020; Khan et al., 2021). GPR can detect the internal structure of ancient buildings, identify possible cracks and cavities in the walls, and determine water seepage areas of ancient buildings (Cappuccio et al., 2020; Ziegler et al., 2020).

Recent research that has advanced GPR for the detection of ancient buildings is described below. Mallorca Cathedral (Elyamani et al., 2017; Elyamani et al., 2018; Elyamani et al., 2019) described the analysis of some structural elements' inner geometries and physical properties by GPR. Different problems, such as the characterization of the masonry, the detection of cracks, and the imaging of metallic reinforcement bars, were examined on three different constructive elements typical of historic buildings (Corradi et al., 2018; Stepinac et al., 2020). An experiment was conducted on samples of sawn timber of different species to study their dielectric responses according to the grain directions using a GPR with a 1.6 GHz antenna to assess the physical properties of wood structures (Fediuk et al., 2020; Wu et al., 2020). Respective signal and image analyses of GPR have enhanced their usefulness in the field of built cultural heritage protection (Solla et al., 2020; Adamopoulos and Rinaudo, 2021; Lombardi et al., 2021). The structure, construction techniques, materials, history, and pathologies in a classified Modern Age building were provided as *a priori* knowledge by GPR (Cardinali et al., 2021; Mishra, 2021). Moisture measurements of porous masonry elements were tested to assess their applicability by a stepped frequency GPR (Agliata et al., 2018; Lai et al., 2018). GPR is a building structure defect detection technology that has accurate and flexible characteristics. The above study uses the visual detection images of GPR as the basis for analysis and evaluation. There are also different frequency detection effect comparisons. However, we want to get more quantitative structural defect characteristics and not just qualitative expressions.

Presently, there are relatively few relevant analyses and studies of GPR imaging characteristics of the basic structure of brick and fill soil such as that at the Xi'an Bell Tower. In particular, there are relatively few studies on the imaging characteristics of problems such as hidden defects in the masonry of ancient buildings. In this study, physical experiments and numerical simulations of the interface between masonry and rammed Earth are used to establish the geoelectric model of the surface and bedding layers under different combinations of relative permittivity. We established an empirical model for the rapid calculation of volumetric moisture content at defect locations. This provides a basis for inference and interpretation during the actual measurement. This study helps to clarify the location and extent of the base breakage and more directly assesses the safety state of the brick and soil of ancient buildings. Additionally, it provides theoretical and technical references for rapid identification and management of defects in ancient buildings.

General description

The Xi'an Bell Tower, which is located in the center of Xi'an, China, is shown in Figure 1A. It was built in 1384 AD, and it is the largest and best-preserved bell tower among the existing bell towers in China (Lv et al., 2018b). In terms of architectural scale, historical value, and artistic value, it is the first of its kind in China. The total height of the Xi'an Bell Tower is 36 m and it covers an area of 1,377 m^2. The overall structure of the Xi'an Bell Tower is divided into three parts, the foundation, the square base, and the wooden building seen in Figure 1B. The foundation is the original pile of loess and residual ancient soil layer. The base is 35.5 m square and 8.6 m in height. The interior is a manually layered and compacted plain fill. The exterior is built with green bricks. The wooden building body is a three-story wooden structure with a height of 27.4 m (Qiu et al., 2020; Xie et al., 2020; Zhu et al., 2020; Hou et al., 2021).

For more than 600 years, there has been a combination of natural environmental erosion (such as wind and rain erosion, humidity and temperature changes), material aging, long-term effects of loading, and fatigue effects. The physical and mechanical properties of the table foundation have been degraded. Inevitably, the accumulation of damage and decay of resistance of the table foundation system (Ma and Wang, 2018; Lu et al., 2021) has occurred. The physical and mechanical properties of the foundation have been degraded. Meanwhile, the Xi'an Bell Tower is located in the traffic hub of Xi'an city. The continuous micro-amplitude vibration caused by long-term surface and underground construction (e.g., underground shopping malls, underground pedestrian passages, and subways) has caused fatigue of the ancient wooden structure and deformation and cracking of the

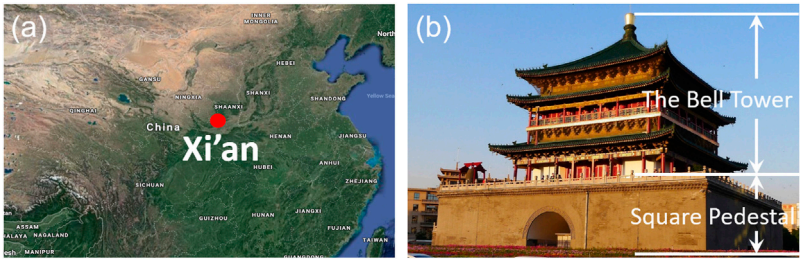

FIGURE 1
Location and the basic structure of the Xi'an Bell Tower.

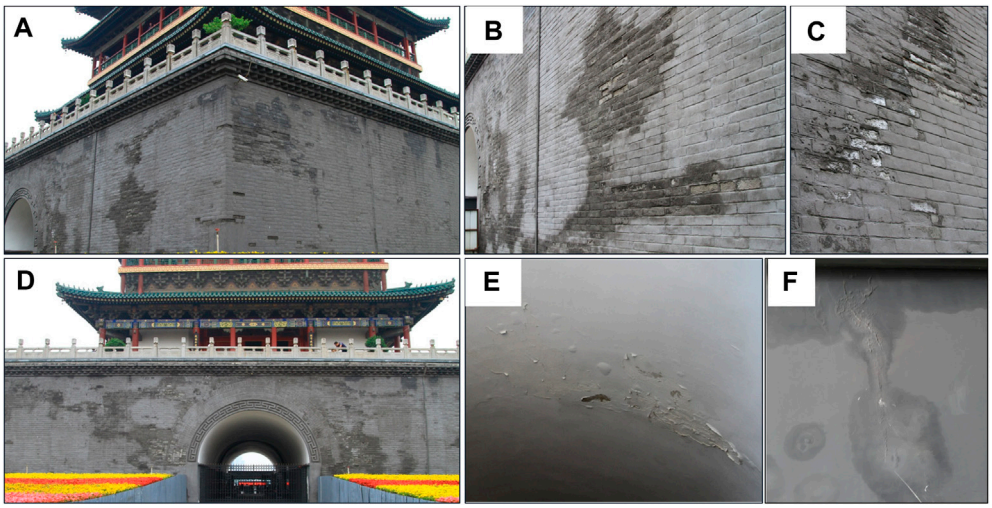

FIGURE 2
Water seepage on the exterior wall of the Xi'an Bell Tower pedestal **(A)** the southwest corner; **(B)** the west pedestal; **(C)** calcium precipitates; **(D)** the south pedestal; **(E)** the west archway; and **(F)** the east archway.

foundation (Luo et al., 2021). The infiltration of rainfall has caused water erosion and deterioration of the city bricks, plasterwork, steps, and rammed Earth layers (Bai et al., 2017; Bai et al., 2019; Bai et al., 2020; Bai et al., 2022). This seriously affects the long-term safety and stability of the Xi'an Bell Tower.

Figures 2A–D show the current condition of water seepage and masonry erosion on the side of the square base, and Figures 2E and F show the condition of water seepage and erosion in the cracks on the top of the archway. From the figures, it can be inferred that cracks exist in the plasterwork, which allows precipitation to seep into the interior of the foundation through the cracks and drain from the outer wall and the top of the archway. This may be due to the foundation's local deformation and uneven settlement caused by the construction of underground facilities and the surrounding traffic environment, which leads to the pulling and expansion of the foundation wall and the internal rammed soil and the formation of internal cracks. Atmospheric precipitation infiltrates into the interior through the sea plaster and external walls. This leads to more significant wetting and deformation of the compacted loess layer. At the same time, the freeze-thaw cycle in winter intensifies the crack expansion process of the external masonry and internal rammed Earth of the foundation. The deterioration process of water and soil erosion in the foundation of the Xi'an Bell Tower is inevitable and progresses from small to large. This causes visible cracking and water seepage on the exterior walls. Table 1 shown he electrical parameters of the bell tower walls vary widely. Therefore, the GPR method is used to detect the integrity of the masonry, and the erosion degree of the

TABLE 1 Dielectric parameters of common construction materials (Lv et al., 2018b).

	ε_r	ρ S/m	α dB/m	v m/ns
Brick	7	5×10^{-2}	0.4–1	0.118
Loess	3–6	1×10^{-3}~0.1	1–100	0.134
Water	81	1×10^{-4}	2×10^{3}	0.033
Air	1	0	0	0.300

internal rammed Earth layer of the Bell Tower foundation is of great importance for the restoration and protection of this tower. Generally, the GPR method is very useful for restoring and conserving the Xi'an Bell tower.

Experiment

Physical experiment

According to the structure of the Bell Tower pedestal and the characteristics of the disease, we established a two-layer experimental model of masonry-rammed Earth with dielectric properties similar to those of ancient wall bricks. The reflection of GPR signals at the interface between the masonry, wall bricks, and the rammed Earth in contact with the ancient building was studied.

A hypothesis of the physical model of the masonry and the community surface was proposed. Both masonry and rammed Earth are semi-infinite space with continuous homogeneous isotropic perfect dielectric models. The reflection and refraction processes of the geophysical radar waves occur in the two-dimensional plane. The dielectric parameters of the geotechnical model involved in this study are shown in Table 1.

We created a physical experiment model considering the possible existence of the masonry-air interface, masonry-unsaturated soil interface and masonry-water interface in ancient buildings. The physical experiment simulates the reflection characteristics of the interface between masonry structure and air, unsaturated soil, and water, and the physical experiment model and experimental scheme are shown in Figure 3.

The thickness of the masonry is 0.10 m (the thickness of the surface layer of Bell Tower sea plaster is 0.10 m). The height of the specimen box of the bedding layer is 0.15 m. The specimens were air, dry soil, volumetric moisture content (MC) 20%, MC 30%, MC 40%, and pure water.

The instrumentation and parameters were as follows: a SIR3000 series mainframe and high identification antenna with a main frequency of 2 GHz from Geophysical Survey Systems Inc. (GSSI) were used as seen in Figure 3A. The parameters of the equipment settings were an emissivity of 100 KHz and an acquisition mode TIME model. The recording length was 10 ns and the automatic gain point was 5. The 2 GHz antenna was placed on the masonry surface and scanned statically from top to bottom.

The original data (after scanning) for the surface modification and automatic gain available GPR imaging is presented in Figure 2.

As shown in Figure 4, a depth of 0.1 m is the interface between the masonry and each medium. The surface occurs at 0.22 m depth. Figures 4B–F shows that the reflected signal of the GPR wave at the interface gradually increases.

The reflected wave amplitudes from small to large are air, dry soil, unsaturated soil, and water. The reflected wave amplitude images are evaluated quantitatively as well as the amplitude value of the reflection part of the interface in the echo curve. The relative reflection wave amplitudes of different interfaces can be obtained as shown in Table 1 (assuming a maximum reflection amplitude of 1 for the masonry-metal interface).

According to Table 2, the relative echo amplitude of the masonry-air interface is the smallest. The relative wave amplitude of the masonry-unsaturated soil interface gradually increases

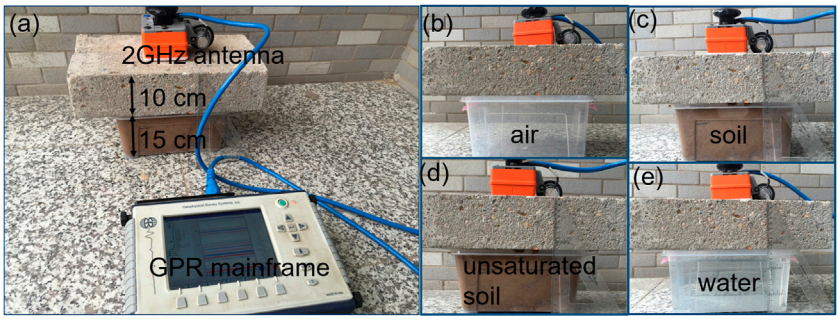

FIGURE 3
Physics experimental equipment and models **(A)** GPR mainframe and physical model; **(B)** concrete-air interface; **(C)** concrete-soil interface; **(D)** concrete-unsaturated soils; and **(E)** concrete-water.

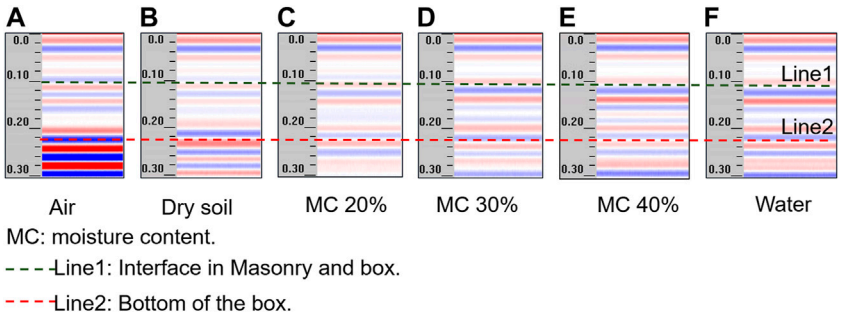

FIGURE 4
Interface reflection result of **(A)** concrete-air; **(B)** concrete-dry soil; **(C)** concrete-MC20% soil; **(D)** concrete-MC30% soil; **(E)** concrete-MC40% soil; and **(F)** concrete-water soil.

TABLE 2 Relative amplitude of the interface reflection (the relative wave amplitude at the masonry-metal interface is 1).

Interface	Air	Dry soil	MC20%	MC30%	MC40%	Water
Amplitude	−0.3531	0.0393	0.2306	0.3348	0.3862	0.492

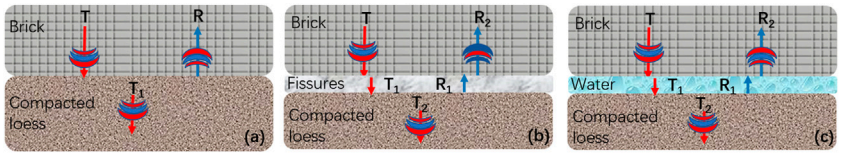

FIGURE 5
Propagation law of electromagnetic waves in **(A)** brick and compacted loess; **(B)** brick and compacted loess with fissures; and **(C)** brick and compacted loess with water fissures.

with an increase of the volumetric water moisture in the specimen. This is because the relative permittivity of the bedding medium gradually increases. Furthermore, the relative permittivity of the surface layer and the relative permittivity of the bedding layer simultaneously change. The variation law of the return amplitude needs more test data, and the physical experimental method is not sufficient to regulate the finer dielectric parameters. Therefore, numerical methods need to be introduced.

Numerical method study of the echo characteristics of the masonry-bedding model

The variation of bedding moisture content in the physical experiments has an effect on the echo amplitude. To reveal the law of change of echo amplitude caused by the change of lithology of the surface layer and the bedding layer, and considering the basic characteristics and properties of the permittivity of the material, an FDTD numerical calculation of the GPR imaging law of the masonry-bedding bilayer media model was conducted. The essential relationship between the material and the echo amplitude and its mechanistic criteria are proposed. A two-layer GPR model was established, and the specific model schematic is shown in Figure 5.

The horizontal distance of this model is 2.0 m and the depth is 0.7 m. The cell size is 0.0025 m by 0.0025. The time depth is 20 ns. The parameters of the first layer are as follows. The permittivity is 0, the electrical conductivity is 0.00 S/m, and the thickness of the first layer is 30 cm. The permittivity of the second layers was 10, 20, 30, 40, and 50. The electrical conductivity is 0.00001 S/m. The thickness of the second layer is 0.4 m. The wavelet frequency is set as 900 MHz, and the excitation source is the Ricker wavelet. In the

TABLE 3 Echo amplitude in the geoelectrical model (the relative wave amplitude at the masonry-metal interface is 1).

Surface cushion	$\varepsilon_1 = 7$	$\varepsilon_1 = 15$	$\varepsilon_1 = 30$	$\varepsilon_1 = 40$
$\varepsilon_2 = 1$	−0.45282	−0.58575	−0.60938	−0.70819
$\varepsilon_2 = 5$	−0.08491	−0.2719	−0.42399	−0.48014
$\varepsilon_2 = 10$	0.09147	−0.10302	−0.27276	−0.33843
$\varepsilon_2 = 15$	0.19338	0	−0.17557	−0.2455
$\varepsilon_2 = 20$	0.26383	0.07406	−0.10377	−0.17597
$\varepsilon_2 = 25$	0.31703	0.13127	−0.04692	−0.12039
$\varepsilon_2 = 30$	0.35939	0.17773	0	−0.07522
$\varepsilon_2 = 35$	0.39436	0.2167	0.04005	−0.03452
$\varepsilon_2 = 40$	0.424	0.25017	0.0748	0
$\varepsilon_2 = 45$	0.44962	0.27942	0.10548	0.03071
$\varepsilon_2 = 50$	0.47212	0.30536	0.13292	0.05822
$\varepsilon_2 = 55$	0.49212	0.32863	0.15772	0.08316
$\varepsilon_2 = 60$	0.5101	0.34969	0.18033	0.10595
$\varepsilon_2 = 65$	0.5256	0.36892	0.20109	0.12693
$\varepsilon_2 = 70$	0.54129	0.3866	0.22026	0.14635
$\varepsilon_2 = 75$	0.55497	0.40293	0.23807	0.16442
$\varepsilon_2 = 80$	0.56764	0.41812	0.25469	0.1813

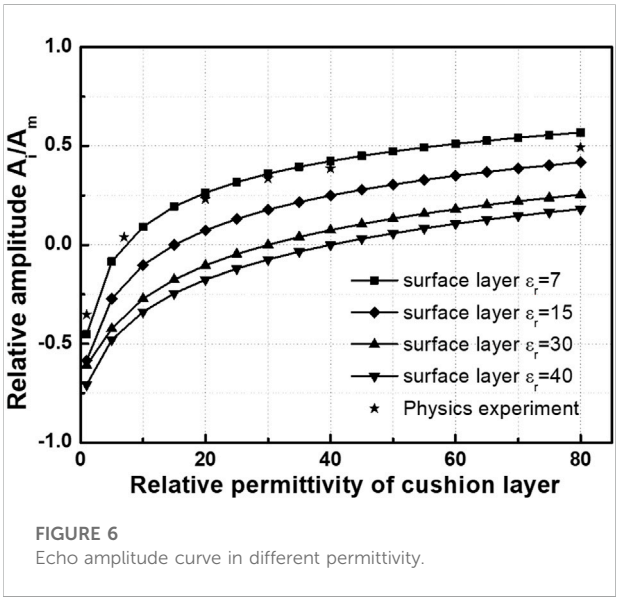

FIGURE 6
Echo amplitude curve in different permittivity.

numerical simulation, there are 180 step calculations and each step calculation contains 3,391 times.

Shown in Table 3. The basic law of echo amplitude is as follows: the surface medium remains unchanged, and when the relative permittivity of the bedding medium increases, the corresponding relative echo amplitude of GPR is also bound to increase. At the same time, when the relative permittivity of the surface layer and the bedding layer are equal, the echo amplitude is 0, which indicates that the electromagnetic wave completely penetrates the interface. According to the wave amplitude characteristics of the two-layer geoelectric model, the basic law can be derived as shown in Figure 6.

In Figure 6, Ai is the GPR echo amplitude, and Am is the GPR echo amplitude at the metal interface. It can be intuitively determined that the smaller the relative permittivity of the surface layer, the larger the relative echo amplitude, which indicates that the imaging characteristics of the bedding defects are more obvious. And comparing the physical experimental data, the basic law and numerical results of the interface reflection test data of physical experiments are the same. Both indicate that the echo amplitude increases as the relative permittivity of the bedding increases. Overall, the results of numerical calculation have high accuracy and a practical application value.

Empirical model of the return amplitude of the double-layer medium

From the findings of physical and numerical experiments, it is clear that the echo amplitude of the double-layered medium is related to the relative permittivity values of both the surface layer and the mat. The echo amplitude of the double-layer medium is related to the relative permittivity values of the surface layer and the bedding layer of the medium. The larger the difference between the relative permittivity of the two sides of the interface, the larger the echo amplitude.

To further directly apply the experimental and numerical results to the field test, this study establishes the mathematical relationship between the difference and the ratio of the relative permittivity and the return amplitude of the double-layer medium and its basic law. An analytical model that is more applicable to the rapid determination of the water moisture of defects in the formation in the field was established.

Figure 7A shows the echo amplitude law of the relative permittivity difference of the media on both sides of the interface. Individual data escapes and the overall law is not obvious. Figure 7B shows the echo amplitude law of the relative permittivity ratio of the media on both sides of the interface. The overall curve is smooth, and there is almost no escape point. This shows that the relative permittivity ratio of the media on both sides of the interface is more accurate than the relative wave amplitude. Therefore, the fitting equation is as follows.

$$A_i/A_m = 0.227 \times \ln(\varepsilon_2/\varepsilon_1) + 0.017 \quad (1)$$

The fill soil of the Bell Tower pedestal bears some of the stress, and the increase in the water moisture of the fill soil must cause a decrease in the mechanical properties of the soil.

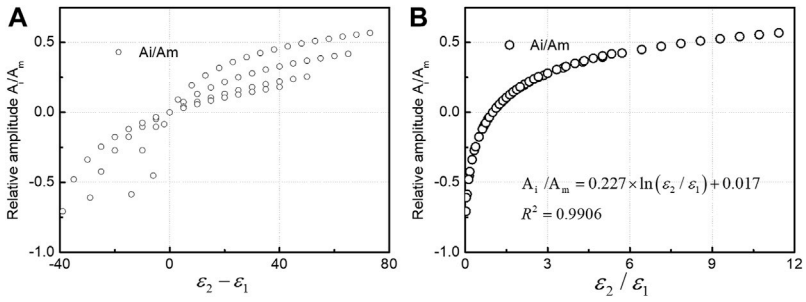

FIGURE 7
Relationship curve of relative amplitude and **(A)** permittivity difference and **(B)** permittivity ratio.

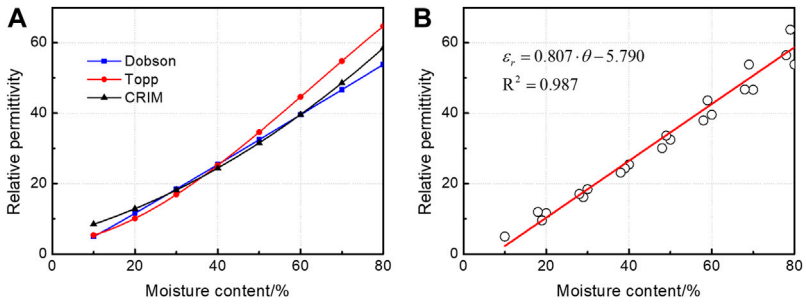

FIGURE 8
(A) Typical empirical relationships curve of permittivity and moisture content and **(B)** relationships curve of permittivity and moisture content of compacted loess.

Water moisture is read more intuitively and quickly from the scanned wave amplitude in this study with the help of Topp's formula (Topp et al., 1980), Dobson's (Dobson et al., 1985) formula, and the Complex Reflective Index Model (CRIM) (Fernandes et al., 2017; Madhousehoush et al., 2021). The laws of water moisture and relative permittivity of soil derived from these commonly used models are compared, and the simple model of water moisture and soil relative permittivity is summarized. These equations are shown in Figure 8A.

Topp's formula

$$\varepsilon_r = 3.03 + 9.3 \times \theta_v + 146.0 \times \theta_v^2 - 76.6 \times \theta_v^3 \quad (2)$$

Dobson's formula

$$\varepsilon_{soil}^{\alpha} = 1 + \frac{\rho_b}{\rho_{ss}}\left(1 - \varepsilon_{ss}^{\alpha}\right) + m_v^{\beta}\left(\varepsilon_{fw}^{\alpha} - 1\right) \quad (3)$$

CRIM formula

$$\sqrt{\varepsilon} = (1 - \phi) \cdot \sqrt{\varepsilon_s} + S_w \cdot \phi \cdot \sqrt{\varepsilon_w} + (1 - S_w) \cdot \phi \cdot \sqrt{\varepsilon_a} \quad (4)$$

In Formula 2, ε_r is the permittivity and θ_v is the volume of moisture content.

In Formula 3, ε_{soil} refers to the soil permittivity. ρ_b and ρ_{ss} refer to the density of dry soil and soil skeleton, respectively. ε_{ss} refers to the solid permittivity. m_v refers to solid quality. ε_{fw} refers to the fluid water permittivity. The empirical coefficient α is 0.65 and β = 1.0 ~ 1.17 (from sandy soil to clay).

In Formula 4, the subscript of *s*, *w*, and *a* represent the soil, water, and air, respectively. φ represents the moisture content, and S_w represents the moisture saturation.

In Figure 8B the relative permittivity of the masonry in the surface layer of the Bell Tower is 7, as measured by calibration, and combined with Eq. 2 and substituted in Eq. 1. The empirical model on water moisture and echo amplitude can be obtained as follows.

$$A_i/A_m = 0.227 \times \ln\frac{0.807 \cdot \theta - 5.790}{7} + 0.017 \quad (5)$$

With Model 5, one can quickly calculate the volumetric water moisture of the soil layer from the relative wave amplitudes in the measured GPR images to observe the water filling of cracks and the dissolution in the loess bedding of the Bell Tower foundation.

TABLE 4 GPR parameter settings.

Parameter	Value
Frequency	400 MHz
Transmit rate	50 kHz
Samp/scan	512
Scans/s	64
Scans/m	20
Ranges	46 ns
Depth	2.0 m
Permittivity	8.0

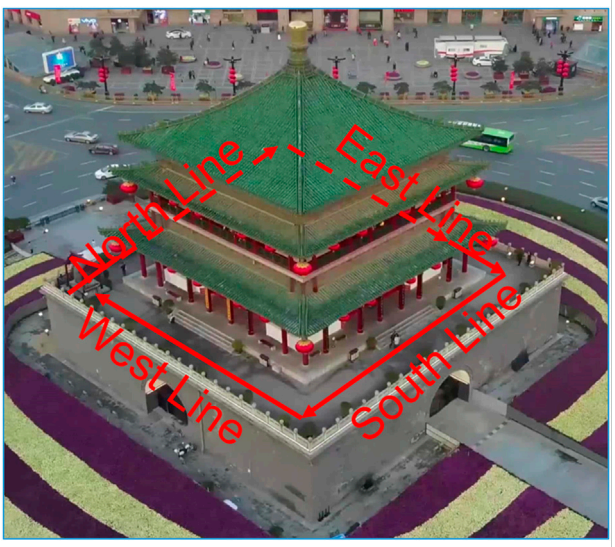

FIGURE 9
Bell Tower abutment survey line layout.

GPR imaging and dielectric property analysis of the Xi'an Bell Tower foundation

Differences in the electromagnetic properties of geotechnical soils are key factors for accurate detection. The water content of the rammed Earth layer at the foundation of the Xi'an Bell Tower tends to be saturated by precipitation. There is a significant difference between the relative permittivity and brick of the rammed soil with saturated water content. Therefore, the conditions for GPR detection are available. In this study, the four sea plasterers of the Xi'an Bell Tower pedestal are scanned by GPR, which can identify and judge the damage of rammed Earth debonding, cracks, and dissolution joints under the masonry structure of the pedestal, and provide accurate information on the location and depth for later repair and maintenance.

GPR field inspection of the Xi'an Bell Tower pedestal

In this study, GSSI's SIR3000 series GPR was used to scan and detect the four sea mantle surfaces of the Bell tower pedestal, and the model and main parameters of the GPR equipment are Shown in Table 4.

The location of the measurement lines is shown in Figure 9, and there are four measurement lines in the southeast and northwest that all have a length of 30 m and a probing depth of 2 m. The measured data were used to analyze the defects in the foundation of the Bell Tower and to investigate the water seepage areas and seepage points inside the foundation of the Bell Tower. The preliminary scanning profile of each mantle surface is shown in Figure 10 by detecting the sea plaster position of the Bell tower foundation.

Figures 10A–D shows the GPR scan profiles of the east, south, west, and north survey lines of the base mantle of Zhong Lou Terrace. Intuitively, there are 16 major anomalous sites among which the anomalous reflections in Figure 10A are: E1~E5; the anomalous reflections in Figure 10B are: S1~S5; the anomalous reflections in Figure 10C are: W1~W3; and the anomalous reflections in Figure 10D are: N1~N3. These significant anomalous reflections can be divided into two categories. The first category as E1, E2, E3, E4, E5, S1, S2, S3, S4, S5, W1, W2, and W3 are hyperbolic winding waves. The reflected waves are discontinuous in the same phase axis and multiple reflections are obvious, which can be inferred to the cavity or the top of the fracture, and the highest point of the hyperbolic curve is the location of the problem. Among them, the hyperbolic curves of E3, E4, S4, W1, W2, and W3 reflect fast attenuation and low frequency and amplitude. The characteristics of fast decay, low frequency, and strong amplitude are reflected in the hyperbolic curves of E3, E4, S4, W1, W2, and W3, and there are a large number of multiple oscillations. The second category as N1, N2, and N3 regions, with intermittent isotropic axes and strong reflections in the region, is inferred to as the area of deglacial anomalies. Among them, the signals at N1 and N2 are disordered and incomplete around the radiated waves with irregular imaging shapes and many prismatic points, which indicates the existence of miscellaneous fillings with high water moisture between the masonry and rammed Earth at this place.

Quantitative analysis of the water moisture of the rammed soil inside the foundation

For data on the four sides of the sea plaster of the Bell Tower foundation, the echo wave amplitude was extracted and substituted into empirical Eq. 5, and the defects and dielectric properties could be inferred as shown in Table 5.

The summary table obtained from the statistics of 16 defects present in the scanned map of the Bell Tower abutment is shown in Table 5. After extracting the wave amplitude values at the top of the

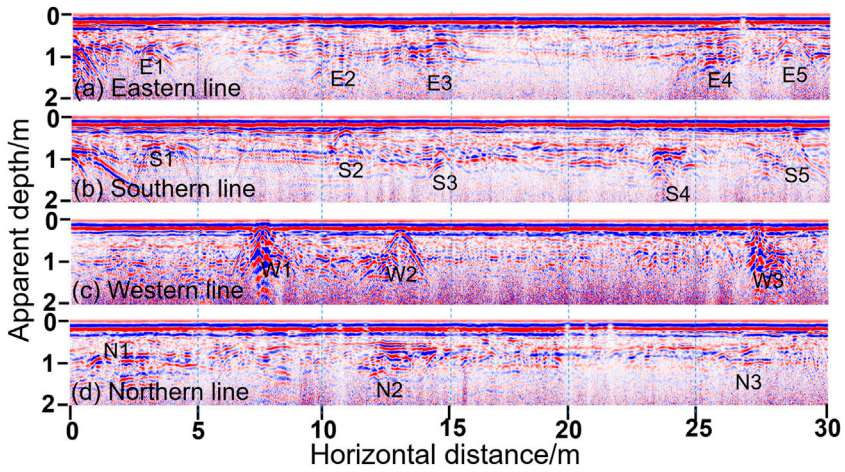

FIGURE 10
(A–D) Scanning profiles of the east, south, west, and north lines of the sea mantle of the Bell Tower.

TABLE 5 Summary of defects and quantification of water moisture of the foundation.

	No.	Horizontal position/m	Relative wave amplitude	Water moisture %
Eastern line	E1	3.0	0.30	38
	E2	10.5	0.05	17
	E3	14.5	0.30	37
	E4	26.0	0.29	36
	E5	29.0	0.02	16
Southern line	S1	3.0	0.24	30
	S2	11.0	0.22	28
	S3	14.5	0.18	25
	S4	24.0	0.29	36
	S5	29.0	0.02	16
Western line	W1	7.5	0.33	42
	W2	13	0.26	33
	W3	27.5	0.32	40
Northern line	N1	2.5	0.28	35
	N2	12.5	0.29	36
	N3	27	0.22	28

anomalous reflection curve and performing the normalization calculation, the quantitative water moisture of the defective parts can be obtained by substituting them into the empirical Model 5. According to the calculated water moisture values of each defect site, it is obvious that the highest volumetric water moisture of more than 40% is found in regions W1 and W3, which indicates that the cracks or cavities have produced larger water seepage channels and water erosion phenomena, and since it is almost impossible for the actual existing cavity defects to be regular in shape, the actual defects are different from the standard hyperbolic features; at E1, E3, E4, N1, N2 and W2, the volumetric water moisture is in the range of 35%–38%, which indicates that the defects also have a greater potential risk, while the volumetric water moisture of the E2 and E5 areas is 16%, which is relatively less risky.

As the Bell Tower was a national key for protection as a culturally famous building, this study only focused on the external wall surface with serious water seepage area photographic evidence, and the most serious internal defects of the western side of the sea plaster position and the external wall water seepage parts coincide.

Conclusion

Through a series of physical experiments and numerical simulation analysis, we obtained the propagation law and characteristics of electromagnetic waves in the double-layer medium and summarized the general empirical formula. The empirical formula was applied to the detection of the Xi'an Bell Tower. A series of structural defects were successfully detected and the main conclusions are drawn as follows.

(1) According to the numerical calculation results of the two-layer geoelectric model, the mathematical and theoretical relationship between the relative permittivity of the mat and the echo amplitude was obtained. We reveal that the laws of the surface layer medium remain unchanged, but the permittivity of the bedding layer medium increases.
(2) The empirical relationship between the permittivity ratio and the echo amplitude has high practicality and accuracy in calculating the water moisture of defects and has a very high application value for the safety evaluation of ancient buildings.
(3) The empirical formula can be considered to have certain practical significance and scientific research value for problem prevention and active monitoring of this type of building. In the next research work, we hope to continuously improve and enrich the accuracy of the empirical formula and perform a practice of validation.

Data availability statement

The raw data supporting the conclusion of this article will be made available by the authors without undue reservation.

Author contributions

GL was in charge of the physical experiments; NL was in charge of the numerical simulations; LB was in charge of collecting field data; and YZ was in charge of the post-processing data and analysis.

Funding

This work was supported by the Shaanxi Key Laboratory of Geotechnical and Underground Space Engineering (Grant no. JT201901), Shaanxi Provincial Urban and Rural Construction Science and Technology Research and Development Program Project (2020-K41), National Natural Science Foundation of China (51806173), Natural Science Foundation of Shaanxi Province (Grant nos. 2021SF-500, 2019M663648, and 2020JM-538), and Open Fund of State Key Laboratory of Road Engineering Safety and Health in Cold and High-altitude Regions (Grant no. YGY2020KYPT-03).

Conflict of interest

The authors declare that the research was conducted in the absence of any commercial or financial relationships that could be construed as a potential conflict of interest.

Publisher's note

All claims expressed in this article are solely those of the authors and do not necessarily represent those of their affiliated organizations, or those of the publisher, the editors and the reviewers. Any product that may be evaluated in this article or claim that may be made by its manufacturer is not guaranteed or endorsed by the publisher.

References

Adachi, S., Yamaguchi, S., Ozeki, T., and Kose, K. (2020). Application of a magnetic resonance imaging method for nondestructive, three-dimensional, high-resolution measurement of the water content of wet snow samples. *Front. Earth Sci. (Lausanne).* 8, 179. doi:10.3389/feart.2020.00179

Adamopoulos, E., and Rinaudo, F. (2021). Close-range sensing and data fusion for built heritage inspection and monitoring—a review. *Remote Sens.* 13 (19), 3936. doi:10.3390/rs13193936

Agliata, R., Bogaard, T. A., Greco, R., Mollo, L., Slob, E. C., and Steele-Dunne, S. C. (2018). Non-invasive estimation of moisture content in tuff bricks by GPR. *Constr. Build. Mater.* 160, 698–706. doi:10.1016/j.conbuildmat.2017.11.103

Bai, B., Yang, G. C., Li, T., and Yang, G. S. (2019). A thermodynamic constitutive model with temperature effect based on particle rearrangement for geomaterials. *Mech. Mater.* 139, 103180. doi:10.1016/j.mechmat.2019.103180

Bai, B., Fei, L., Rao, D., and Xu, T. (2017). The effect of temperature on the seepage transport of suspended particles in a porous medium. *Hydrol. Process.* 31 (2), 382–393. doi:10.1002/hyp.11034

Bai, B., Nie, Q., Zhang, Y., Wang, X., and Hu, W. (2021). Cotransport of heavy metals and SiO2 particles at different temperatures by seepage. *J. Hydrology* 597, 125771. doi:10.1016/j.jhydrol.2020.125771

Bai, B., Wang, Y., Rao, D., and Fan, B. (2022). The effective thermal conductivity of unsaturated porous media is deduced by pore-scale SPH simulation. *Front. Earth Sci.* doi:10.3389/feart.2022.943853

Bai, B., Xu, T., Nie, Q., and Li, P. (2020). Temperature-driven migration of heavy metal Pb2+ along with moisture movement in unsaturated soils. *Int. J. Heat Mass Transf.* 153, 1–12. doi:10.1016/j.ijheatmasstransfer.2020.119573

Bai, B., Zhou, R., Cai, G., Hu, W., and Yang, G. (2021). Coupled thermo-hydro-mechanical mechanism in view of the soil particle rearrangement of granular thermodynamics. *Comput. Geotechnics* 137 (8), 104272. doi:10.1016/j.compgeo.2021.104272

Cappuccio, F., Toy, V. G., Mills, S., and Adam, L., (2020). Three-dimensional separation and characterization of fractures in X-ray computed tomographic images of rocks. *Front. Earth Sci.*, 12, 540. doi:10.3389/feart.2020.529263

Cardinali, V., Castellini, M., Cristofaro, M. T., Lacanna, G., Coli, M., De Stefano, M., et al. (2021). Integrated techniques for the structural assessment of cultural heritage masonry buildings: Application to Palazzo Cocchi-Serristori in Florence. *J. Cult. Herit. Manag. Sustain. Dev.* doi:10.1108/JCHMSD-02-2021-0024

Corradi, M., Di Schino, A., Borri, A., and Rufini, R. (2018). A review of the use of stainless steel for masonry repair and reinforcement. *Constr. Build. Mater.* 181, 335–346. doi:10.1016/j.conbuildmat.2018.06.034

Dao, D. V., Adeli, H., Ly, H. B., Le, L. M., Le, V. M., Le, T. T., et al. (2020). A sensitivity and robustness analysis of GPR and ANN for high-performance concrete compressive strength prediction using a Monte Carlo simulation. *Sustainability* 12 (3), 830. doi:10.3390/su12030830

Dobson, M. C., Ulaby, F. T., Hallikainen, M. T., and El-Rayes, M. A. (1985). Microwave dielectric behavior of wet soil-Part II: Dielectric mixing models. *IEEE Trans. Geosci. Remote Sens.* 23 (1), 35–46. doi:10.1109/tgrs.1985.289498

Elyamani, A., Caselles Magallón, J. O., Roca Fabregat, P., and Clapes, J., (2018). Integrated dynamic and thermography investigation of Mallorca Cathedral. *Mediterr. Archaeol. Archaeom.* 18 (1), 221–236. doi:10.5281/zenodo.1165360

Elyamani, A., Roca Fabregat, P., Caselles Magallón, J. O., and Clapes, J., (2019). Evaluation of Mallorca Cathedral seismic behavior using different analysis techniques. *Mediterr. Archaeol. Archaeom.* 19 (1), 41–60. doi:10.5281/zenodo.2585970

Elyamani, A., Roca, P., Caselles, O., and Clapes, J. (2017). Seismic safety assessment of historical structures using updated numerical models: The case of Mallorca cathedral in Spain. *Eng. Fail. Anal.* 74, 54–79. doi:10.1016/j.engfailanal.2016.12.017

Fediuk, A., Wilken, D., Wunderlich, T., and Rabbel, W. (2020). Physical parameters and contrasts of wooden objects in lacustrine environment: Ground penetrating radar and geoelectrics. *Geosciences* 10 (4), 146. doi:10.3390/geosciences10040146

Fernandes, F. M., Fernandes, A., and Pais, J. (2017). Assessment of the density and moisture content of asphalt mixtures of road pavements. *Constr. Build. Mater.* 154, 1216–1225. doi:10.1016/j.conbuildmat.2017.06.119

Hou, Y., Hu, W., Wang, X., Hou, T., and Sun, C. (2021). Damage identification of ancient timber structure based on autocorrelation function. *Adv. Civ. Eng.*, 2021, 2021–2112. doi:10.1155/2021/6683666

Kang, Y., Fan, J., Jiang, D., and Li, Z. (2021). Influence of geological and environmental factors on the reconsolidation behavior of fine granular salt. *Nat. Resour. Res.* 30 (1), 805–826. doi:10.1007/s11053-020-09732-1

Khan, M. Y., Shafique, M., Turab, S. A., and Ahmed, N., (2021). Characterization of an unstable slope using geophysical, UAV, and geological techniques: Karakoram himalaya, northern Pakistan. *Front. Earth Sci.*, 9, 705. doi:10.3389/feart.2021.668011

Lai, W. W. L., Derobert, X., and Annan, P. (2018). A review of ground penetrating radar application in civil engineering: A 30-year journey from locating and testing to imaging and diagnosis[J]. *NDT E Int.* 96, 58–78.

Lieblappen, R., Fegyveresi, J. M., Courville, Z., and Albert, D. G. (2020). Using ultrasonic waves to determine the microstructure of snow. *Front. Earth Sci. (Lausanne).* 8, 34. doi:10.3389/feart.2020.00034

Liu, N., Li, N., bang, X. C., Li, G., Song, Z., and Yang, M. (2020). Mechanism of secondary lining cracking and its simulation for the dugongling tunnel. *Rock Mech. Rock Eng.* 53 (9), 4539–4558. doi:10.1007/s00603-020-02183-3

Liu, N., Liang, C., and Wang, Y. (2020). Analytical assessment of internal stress in cemented paste backfill. *Adv. Mater. Sci. Eng.* 2020, 1–15. doi:10.1155/2020/6666548

Lombardi, F., Lualdi, M., and Garavaglia, E. (2021). Masonry texture reconstruction for building seismic assessment: Practical evaluation and potentials of Ground Penetrating Radar methodology. *Constr. Build. Mater.* 299, 124189. doi:10.1016/j.conbuildmat.2021.124189

Lu, X., Guan, H., Sun, H., Li, Y., Zhe, Z., Yifan, F., et al. (2021). A preliminary analysis and discussion of the condominium building collapse in surfside, Florida, US, June 24, 2021. *Front. Struct. Civ. Eng.*, 15, 1–14. doi:10.1007/s11709-021-0766-0

Luo, D., Wang, S., Du, X., Zhao, P., Lu, T., Yang, H., et al. (2021). Health detection techniques for historic structures. *Mater. Test.* 63 (9), 855–864. doi:10.1515/mt-2021-0013

Lv, G., Li, N., Yang, J., Yao, X., Hu, D., and Pang, R. (2018). Inversion model of GPR imaging characteristics of point objects and fracture detection of heritage building. *J. Sensors* 2018, 1–10. doi:10.1155/2018/3095427

Lv, G., Yang, J., Li, N., Hu, D., Zhang, Y., and Zhao, F. (2018). Dielectric characteristics of unsaturated loess and the safety detection of the road subgrade based on GPR. *J. Sensors* 2018, 1–8. doi:10.1155/2018/5185460

Ma, G., and Wang, L. (2018). A critical review of preparation design and workability measurement of concrete material for largescale 3D printing. *Front. Struct. Civ. Eng.* 12 (3), 382–400. doi:10.1007/s11709-017-0430-x

Madhousehoush, H., Giannopoulos, A., and Giannakis, I. (2021). "A revised Complex refractive Index model for inferring the permittivity of heterogeneous concrete models," in EGU General Assembly Conference Abstracts. 1-15.

Mishra, M. (2021). Machine learning techniques for structural health monitoring of heritage buildings: A state-of-the-art review and case studies. *J. Cult. Herit.* 47, 227–245. doi:10.1016/j.culher.2020.09.005

Qiu, J., Qin, Y., Feng, Z., Wang, L., and Wang, K. (2020). Safety risks and protection measures for city wall during construction and operation of xi'an metro. *J. Perform. Constr. Facil.* 34 (2), 04020003. doi:10.1061/(asce)cf.1943-5509.0001374

Solla, M., Gonçalves, L., Gonçalves, G., Francisco, C., Puente, I., Providencia, P., et al. (2020). A building information modeling approach to integrate geomatic data for the documentation and preservation of cultural heritage. *Remote Sens.* 12 (24), 4028. doi:10.3390/rs12244028

Stepinac, M., Kisicek, T., Renić, T., Hafner, I., and Bedon, C. (2020). Methods for the assessment of critical properties in existing masonry structures under seismic loads—the ARES project. *Appl. Sci.* 10 (5), 1576. doi:10.3390/app10051576

Topp, G. C., Davis, J. L., and Annan, A. P. (1980). Electromagnetic determination of soil water content: Measurements in coaxial transmission lines. *Water Resour. Res.* 16 (3), 574–582. doi:10.1029/wr016i003p00574

Wang, H., Zhou, B., and Zhang, X. (2017). Research on the remote maintenance system Architecture for the rapid development of smart substation in China. *IEEE Trans. Power Deliv.* 33 (4), 1845–1852. doi:10.1109/tpwrd.2017.2757939

Wang, J., Zhang, Q., Song, Z., and Zhang, Y. (2020). Creep properties and damage constitutive model of salt rock under uniaxial compression. *Int. J. Damage Mech.* 29 (6), 902–922. doi:10.1177/1056789519891768

Wu, X., Senalik, C. A., Wacker, J. P., Wang, X., and Li, G. (2020). Ground-penetrating radar investigation of salvaged timber girders from bridges along route 66 in California. *Wood Fiber Sci.* 52 (1), 73–86. doi:10.22382/wfs-2020-007

Xie, Q., Xu, D., Zhang, Y., Yu, Y., and Hao, W. (2020). Shaking table testing and numerical simulation of the seismic response of a typical China ancient masonry tower. *Bull. Earthq. Eng.* 18 (1), 331–355. doi:10.1007/s10518-019-00731-z

Xue, C. Q. L. (2010). *World architecture in China*. Hong Kong: Joint Publishing.

Zhu, C., Shi, D., Liao, S., He, P., and Jia, R. (2020). Effects of Synechococcus sp. PCC 7942 harboring vp19, vp28, and vp (19 + 28) on the survival and immune response of Litopenaeus vannamei infected WSSV. *Fish. Shellfish Immunol.* 99, 1–8. doi:10.1016/j.fsi.2020.01.028

Ziegler, M. J., Perez, V. J., Pirlo, J., Narducci, R. E., Moran, S. M., Selba, M. C., et al. (2020). Applications of 3D paleontological data at the Florida museum of natural history. *Front. Earth Sci. (Lausanne).* 8, 570. doi:10.3389/feart.2020.600696

frontiers | Frontiers in Materials

TYPE Original Research
PUBLISHED 19 October 2022
DOI 10.3389/fmats.2022.1037771

Check for updates

OPEN ACCESS

EDITED BY
Xianze Cui,
China Three Gorges University, China

REVIEWED BY
Shibing Huang,
Wuhan University of Science and Technology, China
Qing Ai,
Shanghai Jiao Tong University, China

*CORRESPONDENCE
Jie Wu,
jie.voo@gmail.com

SPECIALTY SECTION
This article was submitted to Structural Materials,
a section of the journal
Frontiers in Materials

RECEIVED 06 September 2022
ACCEPTED 20 September 2022
PUBLISHED 19 October 2022

CITATION
Chen Y, Wu J, Zhang S and Teng S (2022), Influence of fault forms on the evolution of concrete damage patterns in tunnels.
Front. Mater. 9:1037771.
doi: 10.3389/fmats.2022.1037771

COPYRIGHT
© 2022 Chen, Wu, Zhang and Teng. This is an open-access article distributed under the terms of the Creative Commons Attribution License (CC BY). The use, distribution or reproduction in other forums is permitted, provided the original author(s) and the copyright owner(s) are credited and that the original publication in this journal is cited, in accordance with accepted academic practice. No use, distribution or reproduction is permitted which does not comply with these terms.

Influence of fault forms on the evolution of concrete damage patterns in tunnels

Yuting Chen[1], Jie Wu[1]*, Shuai Zhang[2] and Shuai Teng[3]

[1]School of Civil and Transportation Engineering, Hebei University of Technology, Tianjin, China, [2]Company of Guangzhou Municipal Engineering Design and Research Institute, Guangzhou, China, [3]Pingdu Municipal Audit Bureau, Qingdao, Shandong, China

Quickly and accurately estimating the seismic weak surface of a fault tunnel is one of the most severe challenges in tunnel seismic design. Therefore, the strong nonlinear response of the Jinping II Hydropower Station under the dislocations of positive, reverse, and slip faults was investigated through the finite element method using a static elastoplastic model. The results reveal the damage and failure mechanism of tunnels under different faults. By using the IDA damage rating index, the damage initiation, evolution, and development process of tunnels under different types of faults are analyzed. The results showed that the affected area of fault dislocation is concentrated and intense, which is mainly distributed along the two sides of the fault surface. The damage of the positive and reverse faults to the tunnel extends from the arch waist to the vault and the invert of the arch, while the influence of the slip fault on the tunnel is the greatest at the vault and invert of the arch and then extends to the arch waist. In terms of the impact range, the reverse fault is the biggest, followed by the slip fault, while the positive fault is the lowest. This study contributes to the design and construction of tunnels through the faults.

KEYWORDS

Jinping II Hydropower Station, fault movement, Rule of damage evolution, FEM, rupture form

Introduction

Three large magnitude earthquakes, namely, those in the Kocaeli, Imperial valley, and Chi-Chi zones (Archuleta, 1984; Ma et al., 1999; Yagi and Kikuchi, 2000; Kelson et al., 2001; Russo et al., 2002), have shown that fault rupture can cause serious damage to the structures, especially tunnels embedded within faults. Interaction of surface faults with surface structures (such as bridges, dams, and buildings) or underground structures (such as tunnels and pipelines) may cause significant damage to them (Ismail and Casas, 2016; Hebbouche et al., 2020; Yp et al., 2020). In recent investigations of tunnel damage cases after strong earthquakes, it has been found that permanent ground deformation from fault dislocations can lead to cracking and even collapse of tunnel linings (Chen et al., 2012; Ma et al., 2019; Ma et al., 2021). However, the researchers of earthquake engineering have focused on the dynamic response of soils and structures than on the dynamic response of the ground with ground displacements caused by rupture of earth faults in the past

four decades (Baziar et al., 2014). Therefore, the potential impact of fault dislocation on the safety of the tunnel structure needs to be considered for tunnels in areas close to the active fracture zones.

The interaction of surface faults with surface structures (e.g., bridges, dams, and buildings) or underground structures (e.g., tunnels and pipelines) may cause significant damage to them (Livaoglu et al., 2019; Rajyaswori et al., 2020; Xuepeng et al., 2020; Zhong et al., 2020; Yi et al., 2022). In order to fully understand this phenomenon, a great deal of research has been carried out on the aspect of tunneling through faults. Peng et al. (2013); Peng et al. (2017) proposed the influence mechanism of ground cracks on the tunnel and the disease prevention and control method through model test and numerical simulation. Rofooei et al. (Jalali et al., 2016; Rofooei et al., 2018) and Tan et al. (Kiani et al., 2016) carried out a detailed parametric analysis of local buckling of buried pipelines under reverse faults through experimental and numerical studies. Sandbox model tests and numerical simulations show that the effect of the reverse fault on the tunnel is closely related to the fault dip and soil stiffness and that the upper plate is more susceptible to deformation and damage than the lower plate phase plate (Baziar et al., 2014; Kiani et al., 2016; Cai et al., 2019). The results of centrifuge experiments show that the concentrated settlement caused by positive faults can cause serious damage to the tunnel (Sabagh and Ghalandarzadeh, 2020). Liu et al. (2015) obtained the relationship between the initial position of the positive fault fracture and the fault dip angle through sandbox experiments. In the case of reverse faults, the tunnel needs to be designed with additional protection against faults in order to reduce the damage caused by the reverse faults (Kieffer et al., 2001; Yan et al., 2020). They investigated the change pattern of the overburden caused by the inverse fault movement based on the two-dimensional discrete element method. Chang et al. (2015) investigated the change pattern of the overburden caused by the inverse fault movement based on the two-dimensional discrete element method. Marchandon et al. (2020) found that the strike-slip fault appears at the top of the fault, and the slip decreases. Experts simulated the internal force and plastic deformation of the tunnel under the dislocation of the walking slip fault by the finite element method (FEM) and finite difference method (FDM) (Zhao et al., 2019; Zaheri et al., 2020).

Most of the current studies focused on the reaction under positive fault, reverse fault, and strike-slip fault dislocation. However, the damage pattern of tunnels under the joint action of multiple forms of staggering still needs further investigation. In this study, the damage evolution of concrete-based tunnels under the action of different fault dislocation forms is investigated by the proposed static FEM method. This article provides better suggestions for engineering design and construction and achieving the purpose of predicting the weak surface of the tunnel through the fault to avoid the adverse effects of faults on the tunnel.

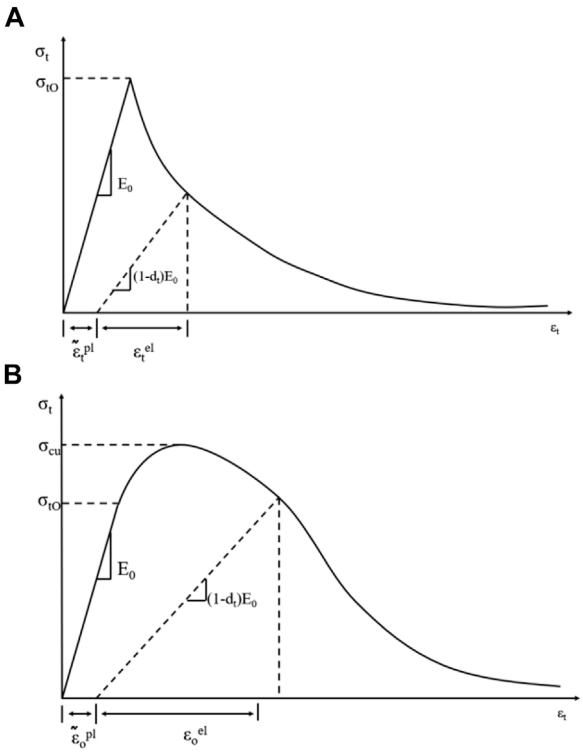

FIGURE 1
Tension and compression curves of concrete. **(A)** Concrete in CDP model tensile cracking strain; **(B)** Concrete in CDP model compression cracking strain.

Project overview

Jinping II Hydropower Station is an important part of China's "West-East Electricity Transmission" and "Sichuan Electricity Transmission". The four diversion tunnels of Jinping II are characterized by large depth of burial, complex environment of crossing strata, super depth of burial, long hole line, and large hole diameter. Such a topographical environment will lead to an unfavorable geological environment, such as rock creep and hydrodynamic seepage (Bai et al., 2021; Bai et al., 2022). The deep buried headrace tunnel is prone to produce fault dislocation due to thermal hydraulic coupling effects (Bai et al., 2019; Cao et al., 2022). Jinping II Hydropower Station is located in the western mountainous region of China, with complex geological conditions such as faults, joints, and fissures development and rock fragmentation. However, how to reduce the impact of active faults on existing tunnels is one of the difficulties in design and construction.

According to the exploration data, the starting and ending piles of the tunnel of the relying project are Citation (1)12 + 261.5~Citation (2)12 + 285, whose fracture zone form is

mainly extrusion fracture zone. The fracture zone is filled with white marble strips, rock chips, and mud, and the rocks in the zone are subject to extrusion and dissolution. Rendering of ferromanganese, the rock is soft and vulnerable to impact such as an earthquake. The dip angle of the fault is about 60°.

Modeling and parameter selection

Concrete tensile and compressive damage model in ABAQUS

The fault movement has two main characteristics of strong nonlinearity and large deformation in the tunnel. In order to describe the damage process ideally, the concrete plastic damage model was chosen for the lining. The model assumes that the uniaxial tensile and compressive response of concrete is characterized by plastic damage, as shown in Figure 1. The response of concrete in tension (a) and in compression (b) to uniaxial loading.

The stress-strain relationship between tension and compression can be expressed as follows:

$$\sigma_t = (1 - d_t)E_0\left(\varepsilon_t - \tilde{\varepsilon}_t^{pl}\right), \tag{1}$$

$$\sigma_c = (1 - d_c)E_0\left(\varepsilon_c - \tilde{\varepsilon}_c^{pl}\right), \tag{2}$$

where the subscripts t and c refer to tension and compression. $\tilde{\varepsilon}_t^{pl}$ and $\tilde{\varepsilon}_c^{pl}$ are the equivalent plastic strains. d_t, d_c is to indicate the degradation of elastic stiffness characterized by two damage variables. E_0 is the initial modulus of the material.

The model assumes that the reduction of the elastic modulus is given by the scalar degenerate variable.

$$E = (1 - d)E_0\,(0 \leqslant d \leqslant 1), \tag{3}$$

where E_0 is the initial (undamaged) modulus of the material.

$$(1 - d) = (1 - s_t d_c)(1 - s_c d_t), \tag{4}$$

where s_t, s_c is the parameter related to the stress state $(0 \leqslant s_t, s_c \leqslant 1)$.

It is defined as follows:

$$\begin{cases} s_t = 1 - w_t r^*(\bar{\sigma}_{11}) & 0 \leqslant w_t \leqslant 1 \\ s_c = 1 - w_c\left[1 - r^*(\bar{\sigma}_{11})\right] & 0 \leqslant w_c \leqslant 1 \end{cases}, \tag{5}$$

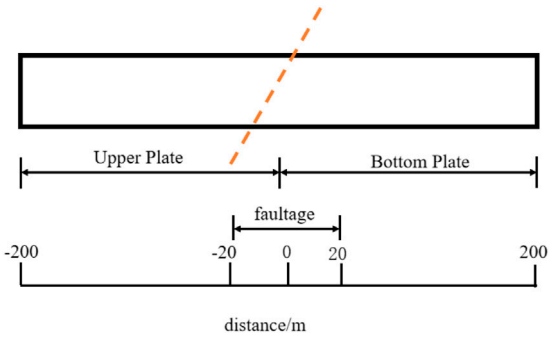

FIGURE 2
Schematic diagram of tunnel and fault location.

$$r^*(\bar{\sigma}_{11}) = H(\bar{\sigma}_{11}) = \begin{cases} 1\,(\bar{\sigma}_{11} > 0) \\ 0\,(\bar{\sigma}_{11} < 0) \end{cases}, \tag{6}$$

where w_t, w_c is the weight factor, related to the material properties, to express the degree of recovery of the material stiffness under the reverse load.

Damage factor calculation

Concrete has a large difference between compression and tension properties due to its inherent properties (Lubliner et al., 1989), so the damage factor d is calculated separately for both compression and tension cases.

From Eqs. 1 and 2, we have

$$d_c = 1 - \sigma_c E_0^{-1} \Big/ \left(\varepsilon_c - \tilde{\varepsilon}_c^{pl}\right). \tag{7}$$

Bringing in $\varepsilon_c = \varepsilon_c^{in} + \varepsilon_{0c}^{el}$ and $\varepsilon_{0c}^{el} = \sigma_c E_0^{-1}$, we get

$$d_c = 1 - \frac{\sigma_c E_0^{-1}}{\varepsilon_c^{pl}\,(1/b_c - 1) + \sigma_c E_0^{-1}}. \tag{8}$$

Among them, $b_c = \tilde{\varepsilon}_c^{pl}/\varepsilon_c^{in}$.

Similarly, we can obtain

$$d_t = 1 - \frac{\sigma_t E_0^{-1}}{\varepsilon_t^{pl}\,(1/b_t - 1) + \sigma_t E_0^{-1}}. \tag{9}$$

Among them, $b_t = \tilde{\varepsilon}_t^{pl}/\varepsilon_t^{ck}$. b_c, b_t are from experimental data.

TABLE 1 Material parameters used in simulation.

Name	Density	Young's modulus	Poisson's ratio	Friction angle	Cohesion
	/(kg·m^{-3})	/(GPa)		/(°)	/(MPa)
Surrounding rocks	2650	20.0	0.25	60	2.0
Fracture zone	2300	4.0	0.3	30	0.5

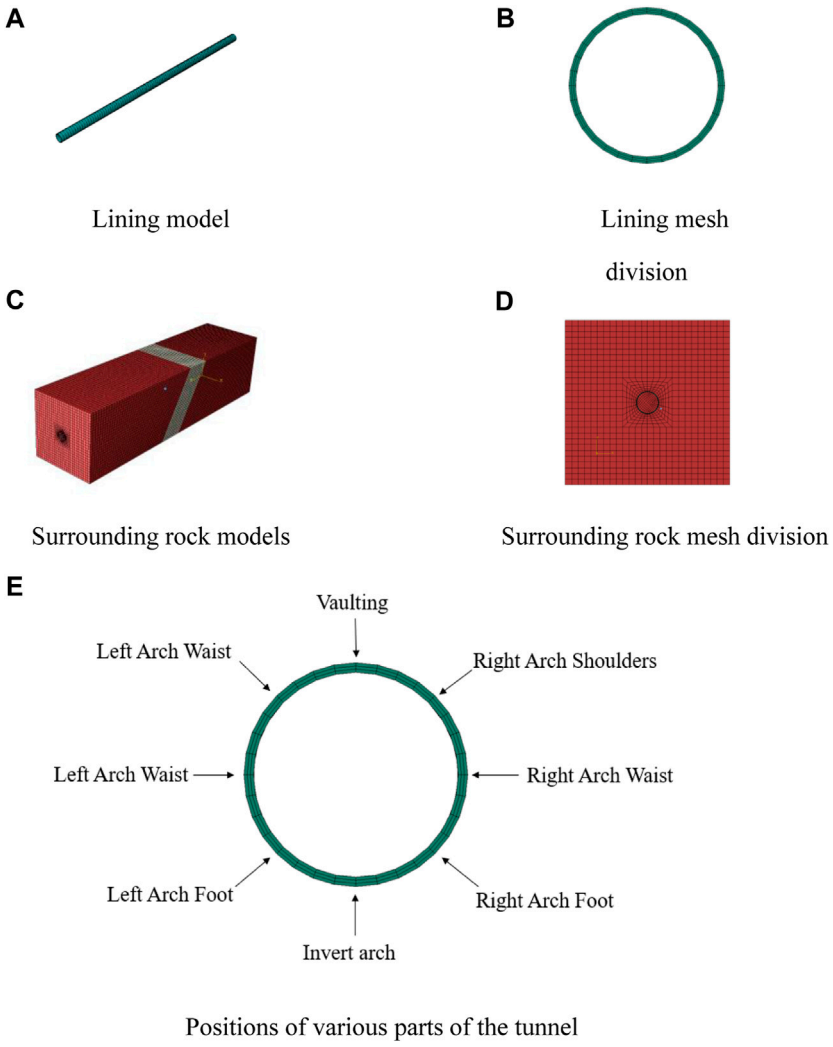

FIGURE 3
Modeling model of tunnel surrounding rock. **(A)** FEM Lining model; **(B)** FEM Lining mesh; **(C)** Surrounding rock models; **(D)** Surrounding rock mesh division.

TABLE 2 Lining material parameters used in simulation.

Name	Density	Young's modulus	Poisson's ratio	Dilatancy angle	Compressive yield stress	Tensile yield stress
	/(kg·m^{-3})	/(GPa)		ψ/(°)	f_c/(MPa)	f_t/(MPa)
Lining	2500	30	0.2	36.31	20.1	2.01

By defining an effective constitutive parameter model (Labibzadeh et al., 2017), we can obtain d_t and d_c. Then, DAMAGEC (compressive damage) is obtained to measure the damage degree of concrete.

Model building and parameter selection

The Jinping II Hydropower Station tunnel adopts the drill and blast construction method, and the lining is a composite

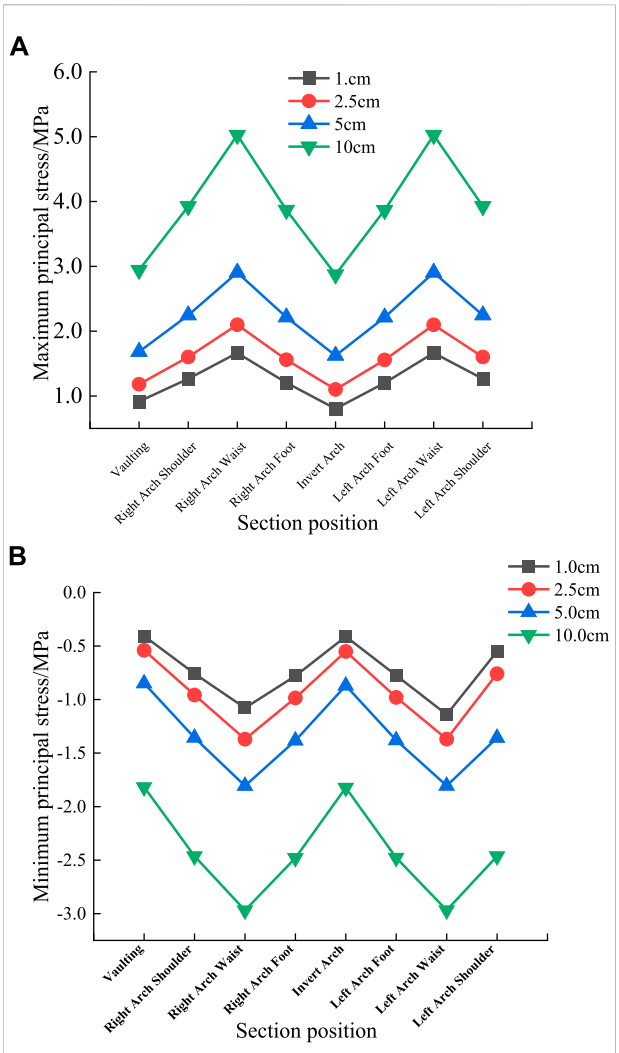

FIGURE 4
Distribution diagram of maximum and minimum principal stresses under elastic constitutive conditions. **(A)** Elastic model lining section maximum principal stress; **(B)** Elastic model lining section Minimum principal stress.

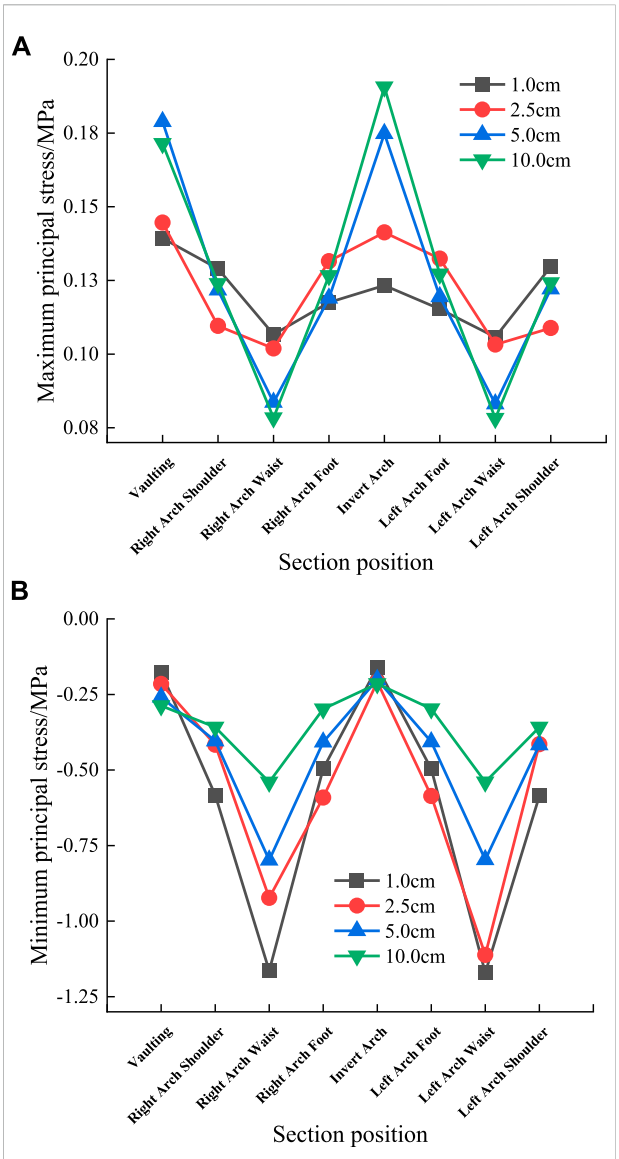

FIGURE 5
Maximum and minimum principal stress distribution under plasticity principal structure. **(A)** Elastic-plastic tunnel section maximum principal stress; **(B)** Elastic-plastic tunnel section minimum principal stress.

lining with initial spray anchor support and secondary mold column support. As the calculation process mainly considers large deformation strong nonlinear analysis, in order to calculate smoothly, the lining is simplified to one layer with a thickness of 0.6 m. The model section size is selected as 100 m × 100 m. The width of the fracture zone is 40 m. In order to simulate the actual situation as much as possible, the fracture surface is set in the fault, as shown in Figure 2, and the simulation is carried out by setting the friction factor of the contact surface. The friction factor in the contact surface was selected as 0.75 (Cheng et al., 2019), and 200 m of the upper and lower sides of the model were selected for research. The model situation and the location of each section are shown in Figure 3.

With reference to the actual exploration engineering data (Wu and Wang, 2011) and combined with the specification requirements, the physical and mechanical parameters of the surrounding rock (marble) and fault and the concrete parameters (C30) of the lining are given in Tables 1 and 2. The CDP (concrete damaged plasticity model) (Lubliner et al., 1989; George et al., 2017) is used for the lining, the elastic-plastic material is used for the surrounding rock and fracture zone (Wang et al., 2022), and the damage criterion used is Mohr–Coulomb's law (Bahmani et al., 2019).

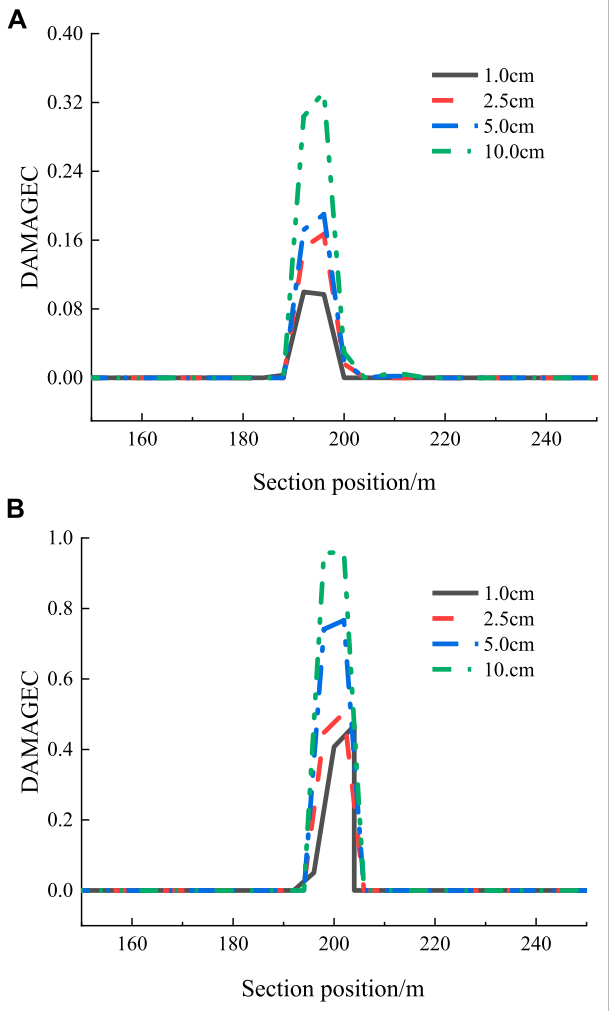

FIGURE 6
Compression damage under positive fault. **(A)** Tunnel cross-section DMAMAGEC at the invert arch; **(B)** Tunnel cross-section DAMAGEC at the arch waist.

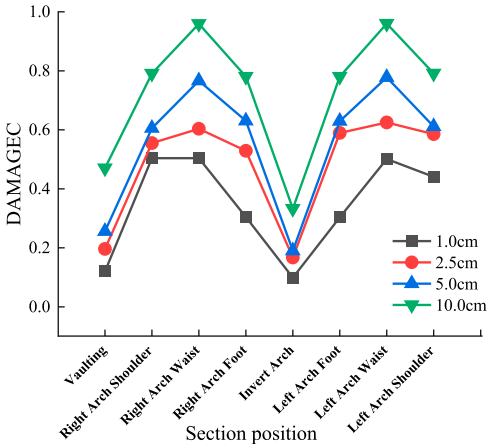

FIGURE 7
Damage parameters of various parts of positive fault section.

In order to calculate the damage response of the tunnel under fault dislocations, a FEM model based on a quasi-static elastoplastic constitutive model is constructed. It is used to calculate the nonlinear damage evolution of the tunnel due to large displacement caused by fault dislocation.

Numerical simulations were carried out using ABAQUS software, and the simulation modeling used the same dimensions as the original ones. The simulation was carried out in three steps: 1) gravity loading was applied to the surrounding rock of the original data, and the ground stress was balanced; 2) the rock excavation was simulated, and the tunnel lining was added; 3) the forced displacement of the upper and lower plates was applied to simulate the fault dislocation. Four working conditions were set, and the amount of dislocation was dislocation 1, 2.5, 5, and 10 cm, respectively. The forced displacement of the corresponding working conditions is applied to the upper and lower plates. The applied displacement is to apply the corresponding displacement along the dislocation direction. Each working condition is individually loaded.

Results and discussion

Analysis of positive fault dislocation

In order to explain the stress of the maximum and minimum principal stress under the damage constitutive of this paper, the elastic model is specially established. In the elastic model, the maximum minimum principal stresses for the four working conditions follow the same trend, as shown in Figure 4. As the amount of dislocation increases, the maximum and minimum principal stress increases accordingly. The maximum and minimum principal stress values in each part of the tunnel increase proportionally with the increase in dislocation. Near the fault plane, the internal force distribution on both sides of the dislocation plane increases sharply, and the influence of the fault on the tunnel is concentrated and strong. The maximum and minimum principal stress peaks appear at the arch waist and gradually extend to the vault and invert arch. The damage pattern is the same as that shown in Figure 6.

In the elastoplastic damage model, as shown in Figure 5, the stress characteristics tend to become more complex as the damage occurs. As the damage at the top of the arch is still relatively small, the stresses at the site still increase with the amount of dislocation. However, the damage at the arch waist is

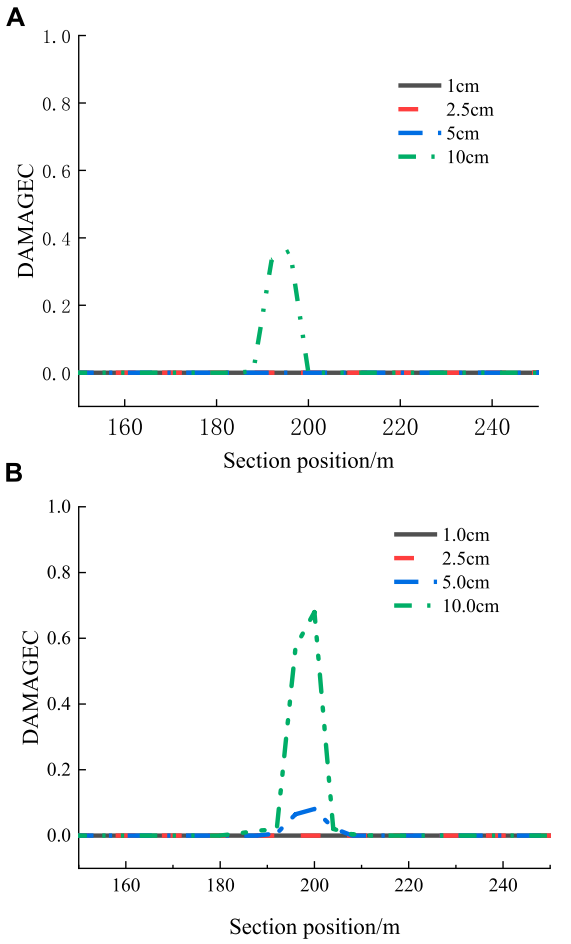

FIGURE 8
Damage evolution under reverse fault. **(A)** Tunnel cross-section DAMAGEC at the foot of the arch **(B)** Tunnel cross-section DAMAGEC at the arch waist.

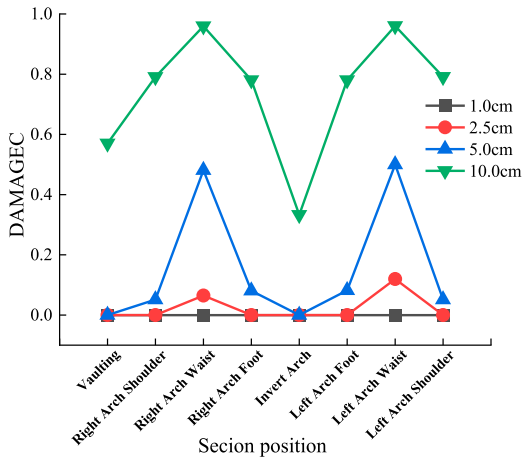

FIGURE 9
Damage parameters of various parts of reverse fault cross-section.

more serious, and the stress decreases with the increase of damage. This is in accordance with the laws of concrete mechanical properties. The damage occurs mainly in the form of tensile damage.

As can be seen from Figure 5, the maximum increase in the maximum principal stress at the top of the arch after the dislocation is 1.23 times, and the maximum increase in the maximum principal stress at the arch shoulder is 1.36 times. The maximum increase in the minimum principal stress at the top of the arch is 1.62 times, and the maximum increase in the minimum principal stress at the arch foot is 1.83 times. The maximum increase of the minimum principal stress at the arch waist is 2.16 times, which shows that the dislocation distance of the positive fault has a greater influence on the section stress, and the influence on the arch waist is greater than that on the arch foot and arch shoulder.

The DAMAGEC at the axial lift interface along the tunnel is extracted, and the DAMAGEC at the arch waist and the invert arch is extracted. The values are shown in Figure 6.

As shown in Figure 6 and Figure 7, in the positive fault action under the four dislocation works trend is basically the same, not affected by the amount of dislocation. The damage increased with the increase of dislocation and reached the peak at 5 m from the dislocation surface; the DAMAGEC at the arch waist was significantly larger than that at the supine arch. The arch waist was the most unfavorable section; the damage extended from the arch waist to the vault and the invert arch. The influence range of dislocation has a slight increase with the increase of dislocation.

The damage value of the upper and lower plates reached the peak at about 5 m from the dislocation surface. However, it rapidly dropped 10 m away from the fracture surface, and the main impact area of the fracture surface was more concentrated. Within 10 m of each of the upper and lower plates on the fracture surface, the increase in dislocation tunnel damage range is not obvious, mainly reflected in the change in the peak value of the damage.

Analysis of inverse fault dislocation

For the four working conditions of the dislocation analysis of the reverse fault, the DAMAGEC of the section at the arch foot and the arch waist along the tunnel axis is extracted, as shown in Figure 8.

From Figure 8 and Figure 9, it can be seen that the change trend under the four dislocation conditions is basically the same and is not affected by the amount of dislocation. The damage

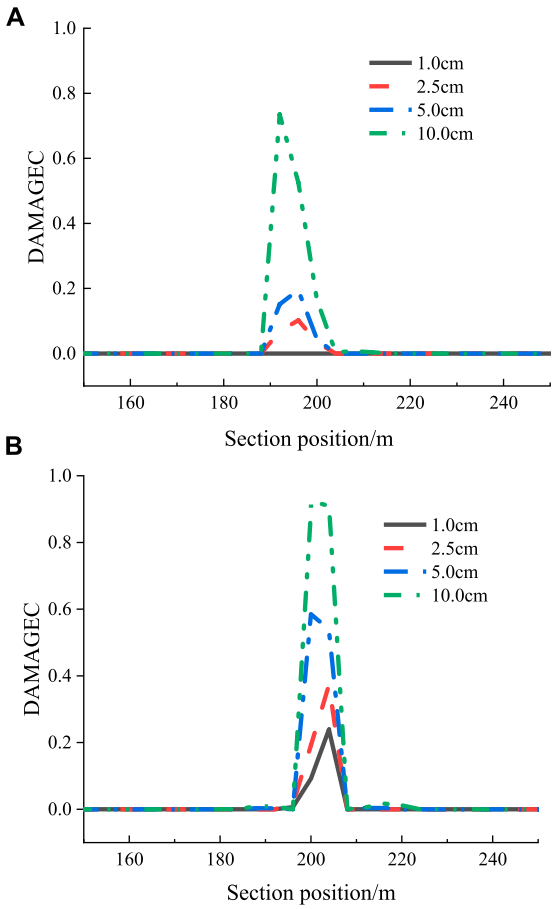

FIGURE 10
Damage evolution of strike-slip faults. **(A)** Tunnel cross-section DAMAGEC at the arch waist; **(B)** Tunnel cross-section DAMAGEC at the arch vault.

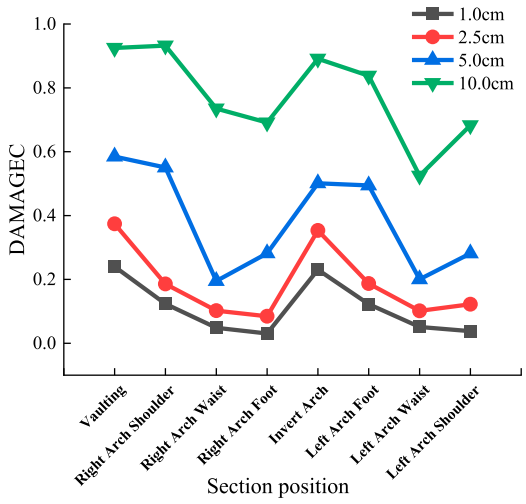

FIGURE 11
Damage parameters of each part of the section.

increases with the amount of dislocation, and the damage at the arch waist under each working condition is the largest and the most unfavorable section. Compared with the positive fault, the reverse fault is mainly damaged by compression (Ghadimi Chermahini and Tahghighi, 2019), so the peak value of DAMAGEC at the same position under the same dislocation is obviously smaller than that of the positive fault. The dislocation face affects the tunnel for about 20 m, and its affected area is larger than the positive fault.

Therefore, the reverse fault is close to the positive fault in the form of a damage extension pattern, both from the waist arch to the vault and the invert of the arch. But the damage value is significantly lower than the positive fault under the same amount of dislocation.

The dislocation surface affects the front and rear of the tunnel for about 20 m, and its affected area is larger than that of the positive fault.

The damage to the tunnel reached a peak at about 8 m from the fracture surface and then declined rapidly. The damage occurred mainly in the form of compression damage.

Analysis of strike-slip fault dislocation

The dislocation analysis of the strike-slip fault is divided into four working conditions, and the DAMAGEC of the arch waist arch top sections along the tunnel axis is extracted, as shown in Figure 10.

From Figure 10 and Figure 11, it can be seen that the trend is basically the same under the four dislocation conditions, which are not affected by the amount of misalignment. Under the action of strike-slip fault, The damage increases with the amount of dislocation.

The strike-slip fault damage pattern is opposite to that of the positive fault and reverse fault. Under each working condition, the DAMAGEC at the vault and invert arch of the tunnel is relatively large, while the damage at the waist arch of the tunnel is relatively small. The damage extends from the vault and invert arch to the waist arch. The damage pattern is different from that of positive and inverse faults. The reason is that the strike-slip fault mainly suffers from transverse shear failure (Karamitros et al., 2007).

The affected area before and after the fault is about 15 m before and after the dislocation surface. The damage to the tunnel reached the peak at 8–10 m from the fracture surface and then decreased rapidly. The structure underwent damage mainly in the form of shear failure.

TABLE 3 Tunnel parameters under different fault dislocation conditions.

Fault form	Peak stress/(MPa)	Peak damage	Location	Distance to the misaligned surface/(m)	Impact scope/(m)
Positive fault	1.90	0.958	Arched waist	5 m	20 m
Inverse fault	1.31	0.898	Arched waist	8 m	40 m
Strike-slip fault	1.67	0.925	Vaulting	8–10 m	30 m

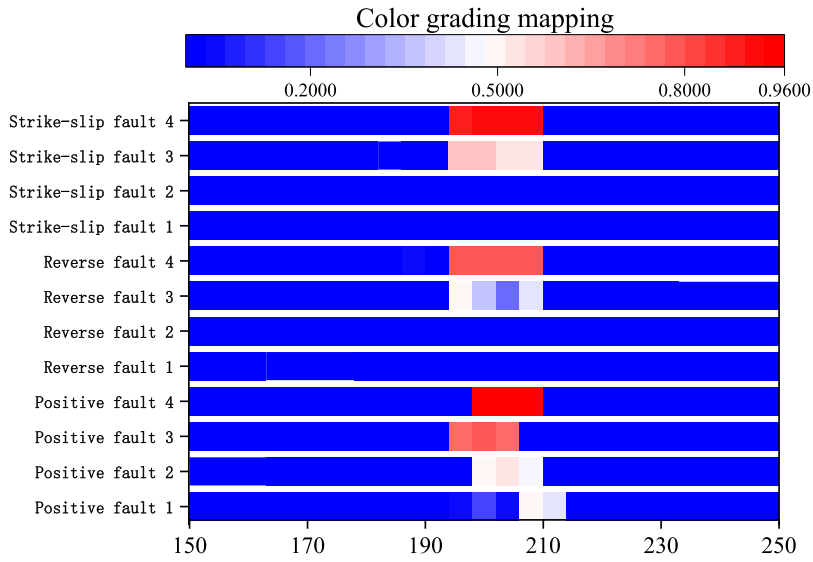

FIGURE 12
Damage proportion under various working conditions.

Tunnel lining response analysis

Tunnel lining response analysis was performed by comparing the response of three different fault dislocation form tunnels, as shown in Table 3 and Figure 12. Due to the influence of fault damage form, by the way the fault is affected by tensile stress is dominant, the maximum stress and damage appeared in the positive fault. The next is strike slip fault, the damage form is shear damage, and the maximum value of damage and stress is between positive fault and reverse fault. Since the reverse fault is mainly damaged by compression, the stress and damage is minimal.

In the CDP model described earlier, the damage indicator is generally characterized by, which takes a value between 0 and 1. When $d = 0$, it is the nondestructive state of the material, and when $d = 1$, it is completely damaged. In order to respond more easily and effectively to the damaged state of the tunnel under the action of dislocation, the IDA-based vulnerability analysis method was introduced (Alembagheri and Ghaemian, 2013; Amirpour and Mirzabozorg, 2014). In this study, the damage of the tunnel is divided into the following states: 1) basically intact: 0–0.05; 2) slightly damaged: 0.05–0.20; 3) moderately damaged: 0.20–0.50; and 4) severely damaged: 0.50–0.80; collapsed: 0.80–1.00

From Figure 12, it can be obtained that the degree of damage of different fault forms varies significantly under the same amount of dislocation. The damage of positive fault is the largest and most concentrated. The reverse fault has the smallest damage value but the widest damage range. The damage peak value and damage range of strike-slip fault are between normal fault and reverse fault. The maximum influence range of positive fault damage value is the smallest. The damage peak value is inversely proportional to the damage range. The reasons are as follows: 1) The tensile fracture energy of concrete is far less than the compressive property. 2) The concrete material loses its tensile property after the tensile damage reaches the limit, while the compression will continue to bear the pressure after the damage, thus, further expanding the damage range. Therefore, under the same amount of dislocation, the damage

peak value and damage growth range present the opposite regulation.

Conclusion

In this article, the influence of different fault dislocations on tunnel damage in Jinping II Hydropower Station was simulated by FEM. A three-dimensional numerical analysis model of the tunnel-rock-fault zone was established to discuss the influence of two factors, fault dislocation form and the amounts, on the tunnel damage distribution. The following conclusions were drawn as follows:

1) The influence of the fault dislocation on the tunnel is more concentrated and intense, and the distribution of internal forces increases sharply on both sides of the dislocation surface. The distribution of the maximum minimum principal stress is affected by the size of the fault dislocation. The maximum minimum principal stress increases monotonically with the amount of dislocation in the elastic and damage initial stage; when the damage begins to the damage limit of the process, the structure can withstand the maximum minimum principal stress extreme value will be reduced.
2) In the model used in this paper, the scope of tunnel damage is less affected by the amount of dislocation momentum and more affected by the form of dislocation.
3) Under the action of strike-slip fault, the most unfavorable section is at the vault and invert of the tunnel. Under the action of the positive fault and reverse fault, the arch waist is the most unfavorable section. The amount of damage to positive faults is greater than that to strike-slip faults than to reverse faults. It can be inferred that the most unfavorable section is on both sides perpendicular to the fault dislocation direction. This damage distribution rule can provide a reference for the seismic design and construction of tunnels through faults.
4) There is a large quantity of joints and discontinuous media in the actual inter-engineering rock, and irregular changes will occur with the dislocation distance. Thus, the physical properties and damage distribution of real faults need to be further considered and explored in the future.

Data availability statement

The original contributions presented in the study are included in the article/Supplementary Material; further inquiries can be directed to the corresponding author.

Author contributions

YC: conceptualization, methodology, software, formal analysis, investigation, resources, writing—original draft preparation, and visualization. JW: methodology, resources, writing—review and editing, visualization, supervision, project administration, and funding acquisition. SZ: supervision and revision. ST: editing and revision. All authors have read and agreed to the published version of the manuscript.

Funding

This research was funded by the National Natural Science Foundation of China (U196520006 and 41807277) and the Natural Science Foundation of Hebei Province (D2019202440).

Conflict of interest

Author SZ was employed by the Company of Guangzhou Municipal Engineering Design and Research Institute.

The remaining authors declare that the research was conducted in the absence of any commercial or financial relationships that could be construed as a potential conflict of interest.

Publisher's note

All claims expressed in this article are solely those of the authors and do not necessarily represent those of their affiliated organizations, or those of the publisher, the editors, and the reviewers. Any product that may be evaluated in this article, or claim that may be made by its manufacturer, is not guaranteed or endorsed by the publisher.

References

Alembagheri, M., and Ghaemian, M. (2013). Damage assessment of a concrete arch dam through nonlinear incremental dynamic analysis. *Soil Dyn. Earthq. Eng.* 44, 127–137. doi:10.1016/j.soildyn.2012.09.010

Amirpour, A., and Mirzabozorg, H. (2014). Quantifying the qualitative limit-states using IDA approach in concrete arch dams. *Arab. J. Sci. Eng.* 39 (11), 7729–7740. doi:10.1007/s13369-014-1393-z

Archuleta, R. J. (1984). A faulting model for the 1979 Imperial Valley earthquake. *J. Geophys. Res.* 89 (B6), 4559–4585. doi:10.1029/jb089ib06p04559

Bahmani, B., Abedi, R., and Clarke, P. L. (2019). A stochastic bulk damage model based on mohr-coulomb failure criterion for dynamic rock fracture. *Appl. Sci.* 9 (5), 830. doi:10.3390/app9050830

Bai, B., Wang, Y., Rao, D., and Bai, F. (2022). The effective thermal conductivity of unsaturated porous media deduced by pore-scale SPH simulation. *Front. Earth Sci. (Lausanne).* 10, 943853. doi:10.3389/feart.2022.943853

Bai, B., Yang, G. C., Li, T., and Yang, G. S. (2019). A thermodynamic constitutive model with temperature effect based on particle rearrangement for geomaterials. *Mech. Mater.* 139, 103180. doi:10.1016/j.mechmat.2019.103180

Bai, B., Zhou, R., Cai, G., Hu, W., and Yang, G. (2021). Coupled thermo-hydro-mechanical mechanism in view of the soil particle rearrangement of granular thermodynamics. *Comput. Geotechnics* 137, 104272. doi:10.1016/j.compgeo.2021.104272

Baziar, M. H., Nabizadeh, A., Lee, C. J., and Hung, W. Y. (2014). Centrifuge modeling of interaction between reverse faulting and tunnel. *Soil Dyn. Earthq. Eng.* 65, 151–164. doi:10.1016/j.soildyn.2014.04.008

Cai, Q., Peng, J., Ng, C. W., Shi, J., and Chen, X. (2019). Centrifuge and numerical modelling of tunnel intersected by normal fault rupture in sand. *Comput. Geotechnics* 111, 137–146. doi:10.1016/j.compgeo.2019.03.010

Cao, Y., Zhang, J., Xu, G., Li, M., and Bian, X. (2022). Strength properties and prediction model of cement-solidified clay considering organic matter and curing temperature. *Front. Mat.* 9, 965975. doi:10.3389/fmats.2022.965975

Chang, Y., Lee, C., Huang, W., Hung, W., Huang, W., Lin, M., et al. (2015). Evolution of the surface deformation profile and subsurface distortion zone during reverse faulting through overburden sand. *Eng. Geol.* 184, 52–70. doi:10.1016/j.enggeo.2014.10.023

Chen, Z., Shi, C., Li, T., and Yuan, Y. (2012). Damage characteristics and influence factors of mountain tunnels under strong earthquakes. *Nat. Hazards (Dordr).* 61 (2), 387–401. doi:10.1007/s11069-011-9924-3

Cheng, X., Ma, C., Huang, R., Huang, S., and Yang, W. (2019). Failure mode analysis of X80 buried steel pipeline under oblique-reverse fault. *Soil Dyn. Earthq. Eng.* 125, 105723. doi:10.1016/j.soildyn.2019.105723

George, J., Rama, J. K., Kumar, M. S., and Vasan, A. (2017). Behavior of plain concrete beam subjected to three point bending using concrete damaged plasticity (CDP) model. *Mater. Today Proc.* 4 (9), 9742–9746. doi:10.1016/j.matpr.2017.06.259

Ghadimi Chermahini, A., and Tahghighi, H. (2019). Numerical finite element analysis of underground tunnel crossing an active reverse fault: A case study on the sabzkouh segmental tunnel. *Geomechanics Geoengin.* 14 (3), 155–166. doi:10.1080/17486025.2019.1573323

Hebbouche, A., Bensaibi, M., Mroueh, H., and Bensalah, M. D. (2020). Seismic fragility curves and damage probabilities of concrete gravity dam under near–far faults ground motions. *Struct. Eng. Int.* 30 (1), 74–85. doi:10.1080/10168664.2018.1531686

Ismail, M., and Casas, J. R. (2016). Evaluation and refinement of closely spaced buildings' performance under near-fault ground motions. *Struct. Infrastructure Eng.* 12 (1), 21–44. doi:10.1080/15732479.2014.993660

Jalali, H. H., Rofooei, F. R., Attari, N., and Samadian, M. (2016). Experimental and finite element study of the reverse faulting effects on buried continuous steel gas pipelines. *Soil Dyn. Earthq. Eng.* 86, 1–14. doi:10.1016/j.soildyn.2016.04.006

Karamitros, D. K., Bouckovalas, G. D., and Kouretzis, G. P. (2007). Stress analysis of buried steel pipelines at strike-slip fault crossings. *Soil Dyn. Earthq. Eng.* 27 (3), 200–211. doi:10.1016/j.soildyn.2006.08.001

Kelson, K. I., Kang, K.-H., Page, W. D., Lee, C.-T., and Cluff, L. S. (2001). Representative styles of deformation along the chelungpu fault from the 1999 chi-chi (taiwan) earthquake: Geomorphic characteristics and responses of man-made structures. *Bull. Seismol. Soc. Am.* 91 (5), 930–952. doi:10.1785/0120000741

Kiani, M., Akhlaghi, T., and Ghalandarzadeh, A. (2016). Experimental modeling of segmental shallow tunnels in alluvial affected by normal faults. *Tunn. Undergr. Space Technol.* 51, 108–119. doi:10.1016/j.tust.2015.10.005

Kieffer, D. S., Caulfield, R. J., and Cain, W. (2001). "Seismic upgrade of the claremont tunnel, northern California," in *2001 proceedings/rapid excavation and tunneling conference: SME)* (San Diego, Calif., USA: Rapid Excavation and Tunneling Conference).

Labibzadeh, M., Zakeri, M., and Shoaib, A. A. (2017). A new method for CDP input parameter identification of the ABAQUS software guaranteeing uniqueness and precision. *Int. J. Struct. Integr.* 8 (2), 264–284. doi:10.1108/ijsi-03-2016-0010

Liu, X., Li, X., Sang, Y., and Lin, L. (2015). Experimental study on normal fault rupture propagation in loose strata and its impact on mountain tunnels. *Tunn. Undergr. Space Technol.* 49, 417–425. doi:10.1016/j.tust.2015.05.010

Livaoglu, H., Irmak, T. S., and Gueven, I. T. (2019). Seismic vulnerability indices of ground for degirmendere (Kocaeli Province, Turkey). *Bull. Eng. Geol. Environ.* 78 (1), 507–517. doi:10.1007/s10064-017-1102-8

Lubliner, J., Oliver, J., Oller, S., and O?Ate, E. (1989). A plastic-damage model for concrete. *Int. J. Solids Struct.* 25 (3), 299–326. doi:10.1016/0020-7683(89)90050-4

Ma, K. F., Lee, C. T., Tsai, Y. B., Shin, T. C., and Mori, J. (1999). The Chi-Chi, Taiwan earthquake: Large surface displacements on an inland thrust fault. *Eos Trans. AGU.* 80 (50), 605–611. doi:10.1029/99EO00405

Ma, S., Zhang, L., Wang, D., Tan, X. R., Li, S., and Liu, Y. (2021). Analysis of tunnel lining failure mechanism under the action of active fault. *Shock Vib.* 2021, 1–11. doi:10.1155/2021/9918021

Ma, Y., Sheng, Q., Zhang, G., and Cui, Z. (2019). A 3D discrete-continuum coupling approach for investigating the deformation and failure mechanism of tunnels across an active fault: A case study of xianglushan tunnel. *Appl. Sci.* 9 (11), 2318. doi:10.3390/app9112318

Marchandon, M., Hollingsworth, J., and Radiguet, M. (2020). Origin of the shallow slip deficit on a strike-slip fault: Influence of elastic structure, topography, data coverage, and noise. *Earth Planet. Sci. Lett.* 554, 116696. doi:10.1016/j.epsl.2020.116696

Peng, J. B., Chen, L. W., Huang, Q. B., Men, Y. M., Fan, W., and Yan, J. K. (2013). Physical simulation of ground fissures triggered by underground fault activity. *Eng. Geol.* 155, 19–30. doi:10.1016/j.enggeo.2013.01.001

Peng, J. B., Huang, Q. B., Hu, Z. P., Wang, M. X., Li, T., Men, Y. M., et al. (2017). A proposed solution to the ground fissure encountered in urban metro construction in Xi'an, China. *Tunn. Undergr. Space Technol.* 61, 12–25. doi:10.1016/j.tust.2016.09.002

Rajyaswori, S., Li, X., Luo, Y., Kumar, M. A., and Xu, K. (2020). The effect of overburden depth on the damage of underground structure during earthquake. *IOP Conf. Ser. Earth Environ. Sci.* 455, 012067. doi:10.1088/1755-1315/455/1/012067

Rofooei, F. R., Attari, N., and Jalali, H. H. (2018). New method of modeling the behavior of buried steel distribution pipes subjected to reverse faulting. *J. Pipeline Syst. Eng. Pract.* 9 (1), 04017029–04017021. doi:10.1061/(ASCE)PS.1949-1204.0000296

Russo, M., Germani, G., and Amberg, W. (2002). "Design and construction of large tunnel through active faults: A recent application," in *Proceedings international conference of tunneling and underground space use* (Istanbul: Turkey: Prague, Czech Republic), 1–14.

Sabagh, M., and Ghalandarzadeh, A. (2020). Centrifugal modeling of continuous shallow tunnels at active normal faults intersection. *Transp. Geotech.* 22, 100325. doi:10.1016/j.trgeo.2020.100325

Wang, J., Sun, K., Hu, Y., Guan, Q., and Li, Q. (2022). The mechanical properties of concrete in water environment: A review. *Front. Mat.* 9, 996650. doi:10.3389/fmats.2022.996650

Wu, S., and Wang, G. (2011). Rock mechanical problems and optimization for the long and deep diversion tunnels at Jinping II hydropower station. *J. Rock Mech. Geotechnical Eng.* 3 (4), 314–328. doi:10.3724/SP.J.1235.2011.00314

Xuepeng, Z., Zhang, Y., Jiang, K., and Maegawa, W. (2020). Mountain tunnel under earthquake force:A review of possible causes of damages and restoration methods. *J. Rock Mech. Geotechnical Eng.* 12 (02), 414–426. doi:10.1016/j.jrmge.2019.11.002

Yagi, Y., and Kikuchi, M. (2000). Source rupture process of the Kocaeli, Turkey, earthquake of August 17, 1999, obtained by joint inversion of near-field data and teleseismic data. *Geophys. Res. Lett.* 27 (13), 1969–1972. doi:10.1029/1999GL011208

Yan, G., Shen, Y., Gao, B., Zheng, Q., Fan, K., and Huang, H. (2020). Damage evolution of tunnel lining with steel reinforced rubber joints under normal faulting: An experimental and numerical investigation. *Tunn. Undergr. Space Technol.* 97, 103223. doi:10.1016/j.tust.2019.103223

Yi, S., Liu, J., and Gu, M. (2022). Field investigation of steel pipe pile under lateral loading in extensively soft soil. *Front. Mat.* 480, 97148. doi:10.3389/fmats.2022.971485

Yp, A., Li, C. A., and Jian, Z. B. (2020). Seismic performance evaluation of fiber-reinforced concrete bridges under near-fault and far-field ground motions. *Structures* 28, 1366–1383. doi:10.1016/j.istruc.2020.09.049

Zaheri, M., Ranjbarnia, M., Dias, D., and Oreste, P. (2020). Performance of segmental and shotcrete linings in shallow tunnels crossing a transverse strike-slip faulting. *Transp. Geotech.* 23, 100333. doi:10.1016/j.trgeo.2020.100333

Zhao, K., Chen, W., Yang, D., Zhao, W., Wang, S., and Song, W. (2019). Mechanical tests and engineering applicability of fibre plastic concrete used in tunnel design in active fault zones. *Tunn. Undergr. Space Technol.* 88, 200–208. doi:10.1016/j.tust.2019.03.009

Zhong, Z., Wang, Z., Zhao, M., and Du, X. (2020). Structural damage assessment of mountain tunnels in fault fracture zone subjected to multiple strike-slip fault movement. *Tunn. Undergr. Space Technol.* 104, 103527. doi:10.1016/j.tust.2020.103527

frontiers | Frontiers in Materials

TYPE Original Research
PUBLISHED 11 November 2022
DOI 10.3389/fmats.2022.1075310

Check for updates

OPEN ACCESS

EDITED BY
Bing Bai,
Beijing Jiaotong University, China

REVIEWED BY
Zhenping Zhang,
Shenyang University of Technology, China
Yuxiang Du,
Jianghan University, China

*CORRESPONDENCE
Yingbo Zhou,
yingbozhou@126.com

SPECIALTY SECTION
This article was submitted to Structural Materials,
a section of the journal
Frontiers in Materials

RECEIVED 20 October 2022
ACCEPTED 27 October 2022
PUBLISHED 11 November 2022

CITATION
Zhou Y, Sheng G, Qiao S, Zhou L, Cai J and Xu H (2022), A determination method for the shear strength of soil-rock mixture considering the size effect and its application.
Front. Mater. 9:1075310.
doi: 10.3389/fmats.2022.1075310

COPYRIGHT
© 2022 Zhou, Sheng, Qiao, Zhou, Cai and Xu. This is an open-access article distributed under the terms of the Creative Commons Attribution License (CC BY). The use, distribution or reproduction in other forums is permitted, provided the original author(s) and the copyright owner(s) are credited and that the original publication in this journal is cited, in accordance with accepted academic practice. No use, distribution or reproduction is permitted which does not comply with these terms.

A determination method for the shear strength of soil-rock mixture considering the size effect and its application

Yingbo Zhou[1]*, Genlin Sheng[2], Shihui Qiao[1], Li Zhou[1], Jie Cai[1] and Hanping Xu[1]

[1]State Grid Hubei Electric Power Company Limited Economic Research Institute, Wuhan, China, [2]State Grid Hubei Electric Power Co., Ltd., Wuhan, China

The shear strength of the soil-rock mixture (S-RM) is the primary mechanical factor influencing the stability of the deposit slope. The particle size range inside the test sample, however, is not the same as that of the S-RM in the deposit slope due to the limitations of the test device, which results in a variation in the mechanical properties. In this study, computer simulation tests were conducted to examine the impact of particle size on mechanical behaviors under the uniaxial compressive condition, and the size effect was analyzed from both macroscopic and mesoscopic perspectives. Results indicate that when the particle size increases, the anisotropy levels of the S-RM sample also rise, causing the particle displacement difference inside the sample to increase and the rounding rock effect to become more pronounced. The quantitative relationship between the uniaxial compressive strength (*UCS*) and the maximum particle size (d_{max}) was proposed, and the accuracy of the prediction formula for the *UCS* value of S-RM that takes the size effect into account has been confirmed. The improvement of the shear strength determination method was achieved by unifying the particle size range corresponding to the uniaxial compressive and shear test results used in the approach, and the determination method was used to evaluate the stability of a typical deposit slope. The study results can be used as a guide for estimating strength parameters of S-RM throughout the design and construction process of the deposit slope.

KEYWORDS

size effect, soil-rock mixture, uniaxial compressive strength, shear strength, deposit slope

Introduction

Soil-rock mixture (S-RM), defined as the combination of the soil matrix with rock blocks of various sizes, presents a large distribution in southwestern China (Fu et al., 2021a; Ji et al., 2021; Zhou et al., 2022). The inclination to use S-RM, for example as the fill material for the high-fill deposit slope and rock-fill dam, is growing in the geotechnical

engineering projects due to the expansion of the highway and building in the mountainous region of southwestern China (Zhang et al., 2021; Du et al., 2022; Fu et al., 2022). The natural S-RM can be divided into landslide deposit, collapse deposit, residual deposit, and other categories depending on how they formed (Xu et al., 2007; Yang et al., 2021). Each of these categories exhibits various particle grading distribution characteristics, particularly the particle sizes (Xu and Hu, 2009; Zhou et al., 2017; Bai et al., 2021). Long-term geological formations and rainfall in the southwestern region of China have resulted in the development of the shallow regions near the deposit slope with considerable weathering impacts, whereas a small range of the particle grading distribution between 40 and 60 mm under weathering effect is typical to be observed in the S-RM due to landslide and residual deposit. Determining the mechanical parameters of the geo-material and the slope stability assessment has been made more difficult by the complex mechanical behaviors of S-RM with different particle size characteristics, which has been a crucial problem to be solved urgently during design and construction of the deposit slope engineering.

It is generally considered that particle size affects the mechanical properties of geotechnical materials, which is called the size effect. As a typical multi-phase material, the threshold size of the "fine" and "coarse" grain material inside S-RM should be determined first using the particle grading distribution. The coarse-grained materials are consistently categorized as rock block components, whereas fine-grained materials are consistently categorized as soil components. The size effect of S-RM has mostly so far been analyzed in terms of how the rock block size affects the mechanical properties in previous researches. The strength of the individual rock block particle and the whole material are both impacted by the size of the rock block (Hong et al., 2020; Ovalle and Dano, 2020). The former changes the pressure range that the rock block can sustain and the likelihood of breaking, while the latter involves the propagation of cracks and the development and dispersion of microcracks (Li, 2013; Lin et al., 2019), speeding up the decomposition of the sample. The S-RM triaxial tests carried out by Zhao and Liu, 2018 demonstrated that the stress-strain curve of the sample with a greater rock size is more varied because of the interaction between the large rock blocks. According to Li et al. (2008), in the triaxial compressive condition, the S-RM sample with a higher d_{max} value exhibits a greater strength, friction angle, and initial tangent modulus. Wu et al. (2020) also suggested the same conclusion in light of the results of the rockfill material testing. Since the widespread use of computers, numerical simulation has been extensively used to investigate how particle size affects the mechanical properties of S-RM from a mesoscopic perspective. Ueda et al. (2011) and Ding et al. (2014) proposed that the bigger size of the rock block causes a greater level of heterogeneity and exacerbates the particle's contribution to the structure and mechanical properties of S-RM. The deformation of S-RM exhibits the size effect as well in terms of crack distribution and shear zone features. Wolinski et al. (1987) reported that the S-RM sample with the smaller d_{max} value (2–4 mm) has a smoother fracture surface than the sample with the greater d_{max} value (8–32 mm). Peng et al. (2017) found that the distribution of the S-RM microcracks with lower particle sizes is more clustered and less uniform, and the formation of the microcracks is connected to the particle size. Lv et al. (2022) and Wang et al. (2022) discovered a strong correlation between the particle size and the shear bandwidth of the granular sample. The characterization quantities of the particle size in previous studies are various, such as the maximum particle size (d_{max}) (Ji et al., 2011; Chaulagai et al., 2017), average particle size (d_{50}) (Giang et al., 2007), and the ratio of the maximum to minimum particle size (d_{max}/d_{min}) (Ding et al., 2014; Vahidi-Nia et al., 2020). However, there is still a need for discussion regarding the quantitative description of the size effect and the quantitative correlations between the mechanical parameters and the representative characterization quantity.

Previous studies have demonstrated the importance of examining the size influence on the mechanical behaviors of S-RM. The maximum allowable particle size of the sample is constrained by the size restrictions of laboratory test apparatus, which also changes with the apparatus size. For example, the maximum allowable particle size of the fixed-size test apparatus often not exceeding 10 mm in certain regular-size laboratory tests, such as the uniaxial compressive test, Brazilian splitting, and compaction tests. However, the maximum allowable particle size has been raised to 40–60 mm in using the large-scale triaxial test apparatus and direct shear test apparatus. Therefore, the mechanical behaviors demonstrated utilizing various test apparatus sizes represent the S-RM samples with the corresponding particle grading properties. It is more challenging to estimate the shear strength characteristics of S-RM using laboratory tests because of the size effect due to the laboratory tests even though the particle size of the S-RM sample is within the range of the allowable size of the test apparatus.

Numerical simulation methods are rapidly being used into the research of the mechanical properties of geotechnical materials as a result of the ongoing advancements in computer technology (Guo et al., 2019; Bai et al., 2022; Bai et al., 2019). The discrete element method based on discontinuous mechanics theory, in contrast to the numerical simulation method for continuous media, can simulate the material multiphase and non-homogeneity of S-RM, providing a tool for the discussion of the mechanical properties of S-RM at various sizes in this paper. However, the low computational efficiency and high computational cost presented by the discrete element calculation method make it more challenging to use in large-size practical engineering. Researchers have lately shown a growing interest in the empirical formula to determine the

strength characteristics of the geotechnical material by using the findings of several mechanical and physical tests. On the one hand, the availability of empirical formulae to describe the mechanical characteristics of geotechnical materials is ensured by the fact that the majority of the empirical formulae are given based on the test results and an established constitutive model. On the other hand, the using empirical formulae can effectively lower the cost required for mechanical tests and eliminate errors in the findings brought on by the unpredictability of the tests. The mechanical parameters can be quickly estimated using the empirical formulae with a small number of physical and mechanical parameters. The theory of the coarse-grained soil is the main source of the typical empirical formulae used to characterize the mechanical properties of S-RM, and the pending parameters are determined from the results of large-scale tests. There are few descriptions of the mechanical parameter calculation method taking the multi-phase components and size effect of S-RM into consideration.

Based on the outcomes of numerical simulation, a method for determining the shear strength of the S-RM taking the size effect into account is presented in this study. The size effect on the uniaxial compressive strength (*UCS*) is discussed from the macroscopic and mesoscopic views using Particle Flow Code in two dimensions (PFC^{2D}), and a quantitative relationship between the *UCS* value and d_{max} is proposed, taking into consideration that the ranges of the particle sizes of the required test data within the formula proposed for calculating the shear strength of S-RM are not uniform. The modified calculation of the *UCS* value taking the size effect into account is used when determining the shear strength parameters of the S-RM. The stability evaluation of a typical deposit slope uses the determination method as a last step, and thus serves as a reference for the estimating the strength parameters of S-RM.

An approach to predicting the shear strength of soil-rock mixture

The multi-phase compositions and structural characteristics of natural S-RM result in complicated and varied mechanical behaviors. The weak soil-rock interface develops as a result of the increase of the rock content, which also damages the integrity of the soil matrix. However, the stronger and more rigid rock blocks can also assist in enhancing the mechanical characteristics of the S-RM. The presence of the negative and positive effects of rock blocks on S-RM make it extremely difficult to calculate its strength parameters.

The relationship between the strength parameters and the rock content, particle size, water content, and other factors has been proposed by a number of researches. The results suggest that the rock content has a significant impact on how the mechanical behaviors of S-RM changes from being comparable to those of soil to being similar to those of broken rocks. Fu et al. (2021b) suggested a method to estimate the strength parameters of S-RM in order to characterize the cooperative influence of the multi-phase compositions on the mechanical properties of the entire material. The calculation for the prediction method is as follows.

$$\tau = A_s \sigma_{c-SRM} \left(\frac{\sigma_n}{\sigma_{c-SRM}} - T_s \right)^n \tag{1}$$

where $\sigma_{c\text{-}SRM}$ is the unconfined compressive strength of the soil-rock mixture, which is used to describe the strength of the contact surface; parameters *Ts* and *n* are material constants, which are related to the rock block proportion, and strength of fine-grained soil and rock blocks; parameter A_s is a nonlinear strength constant of the power-law criterion.

The uniaxial compressive strength of S-RM utilized in Eq. 1 is obtained based on the prediction formula proposed by Kalender et al. (2014) calculated as follows.

$$\sigma_{c-SRM}/\sigma_c = \frac{A - A^{\frac{VBP}{100}}}{A - 1} \tag{2}$$

where σ_c is the *UCS* value of the soil matrix; *VBP* is volumetric rock block proportion, %; characteristic parameter *A* is a constraining variable, which represents the contact strength between the soil and rock blocks and can be determined based on the value diagram using σ_c and the internal friction angle or the roughness of the rock blocks.

Based on Fu et al. (2021b) and Kalender et al. (2014), the precision of the *UCS* and shear strength prediction methods has been confirmed. In Eq. 1, the *UCS* value of the soil matrix and the shape index of rock blocks are used to calculated the influence of the soil-rock interface on the shear strength. The impact of the content and mechanical properties of the soil matrix, rock blocks, and soil-rock interface on the mechanical characteristics of the entire material is thus shown in the shear strength estimation method of Eq. 1. With the multi-component and non-homogeneous characteristics fully considered, the estimation method of S-RM provides a theoretical basis for the following discussions.

According to the results proposed by Kalender et al. (2014), characteristic parameter *A* is chosen based on the results of previous uniaxial compressive experiments. The limitations of the regular-size uniaxial compressive test apparatus result in a constrained range of particle sizes inside the S-RM sample, which typically implies that the maximum particle size of the rock blocks is less than 10 mm. The S-RM sample under regular-size test circumstances is substantially smaller than the typical size of the rock blocks in the shallow region of the deposit slope, which can reach 40–60 mm. To guarantee that the particle size applicable to the prediction technique is fairly close to the

FIGURE 1
Rock blocks inside the S-RM sample used in the laboratory test.

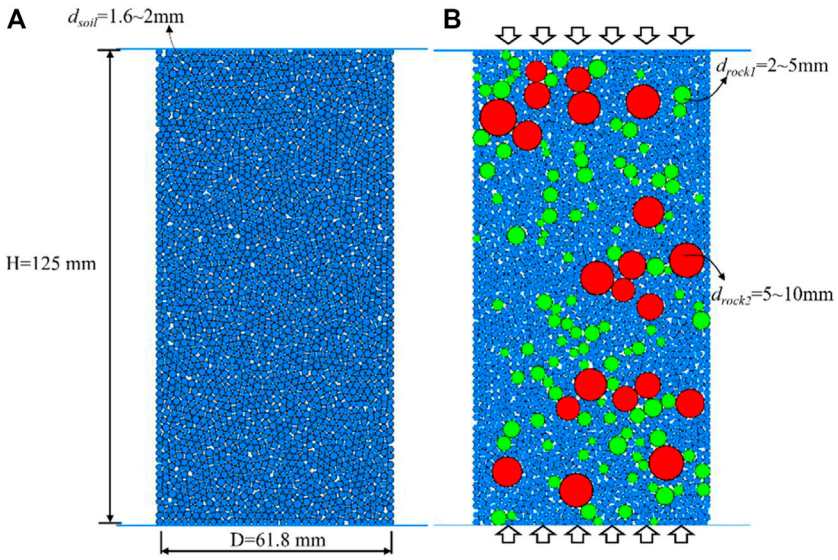

FIGURE 2
S-RM particle models for the calibration.

real circumstances, it is vital to understand how particle size affects mechanical behavior under the uniaxial compressive condition.

Numerical simulations of the size effect on the mechanical behavior of soil-rock mixture

The discussions above indicate that particle size of the S-RM sample is constrained by the size of the laboratory apparatus. In this study, the maximum particle size (d_{max}) of the regular-size uniaxial compressive sample is 10 mm, which is even lower than the value of natural S-RM, and the size effect is numerically simulated using the discrete element method in this study using *PFC*^{2D}.

Model establishment and mesoscopic parameter calibration

The process of the *PFC*^{2D} simulation test is divided into three parts: model establishment, mesoscopic parameter calibration, and simulation process. For the mesoscopic parameter calibration, the S-RM particle model of the same size as the one used in the laboratory test was constructed. The shape of the rock blocks in the natural S-RM is angular-subangular; in contrast, the rock blocks in this study are shown in Figure 1

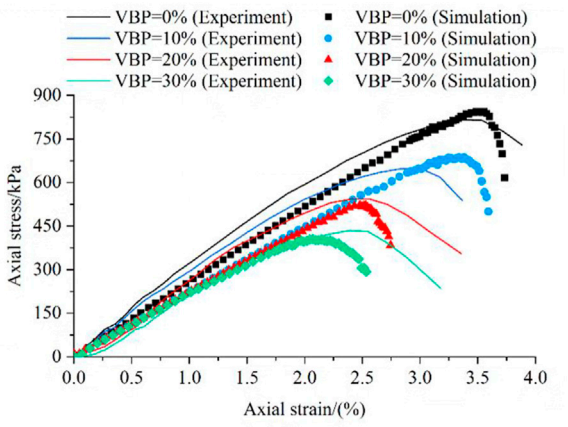

FIGURE 3
Axial stress versus strain curves of the test and simulation results.

as having a round-elliptical shape. Therefore, it is allowed to imitate the rock block using a standard disk element. For the calibration sample, the particle diameter of rock is set as 2–10 mm, and the soil particle diameter is set as 1.6–2 mm. The S-RM particle model used in the calibration procedure is shown in Figures 2A,B.

In *PFC*, the contact model is used to replace the constitutive model to represent the contact force and moment between the particles when an external force is present. An essential step of computer simulation test is the calibration of the precise mesoscopic parameters utilized in the contact models. Different from the continuous numerical calculation method, mesoscopic parameters are utilized to describe the mechanical properties and deformation characteristics. The mesoscopic parameter calibration procedure has thus so far been carried out utilizing several groups of the mesoscopic parameters to make the macro mechanical behaviors of the simulation, such as the *UCS*, strength parameters, and secant modulus, much closer to the test results. The uniaxial compressive test of S-RM in the regular size was carried out in this study as the reference for calibrating the mesoscopic parameters.

The S-RM sample was calibrated at 125 mm in height and 61.8 mm in width. The diameter range of the rock block was specified as 2–10 mm as shown in Figure 1 in accordance with the specification for the geotechnical test, and the d_{max} value of the S-RM sample should be less than 10 mm. In order to determine how the mechanical behaviors of S-RM are affected by the rock block, *VBP* was selected as the controlling factor. Several groups of S-RM uniaxial compressive tests were conducted with a *VBP* range of 0%–30%.

Figure 3 shows the curves of the axial stress and strain of the S-RM samples with various *VBP*s under the test and simulation conditions. The results demonstrate that simulated axial stress exhibits an increasing trend with axial strain identical to the test results, and the peak stress and stress drop are discovered throughout the simulation. As *VBP* increases, the simulated *UCS* value and secant modulus fall, which is line with the variation rule of the test findings. The calibrated mesoscopic parameters can be employed for the S-RM numerical test in this study, according on comparisons in the axial stress between the simulation and test results. The calibrated mesoscopic parameters are listed in Table 1.

TABLE 1 Mesoscopic parameters of the soil and rock particles.

Properties and descriptions	Soil	Rock
Density/(kg/m^3)	1700	2,250
Normal stiffness, k_n/(N/m)	1.8×10^7	3.0×10^7
Normal-to-shear stiffness ratio, k_{rat}	1.0	1.0
Shear strength, cb_strength tensile/(N/m)	4.5×10^5	5×10^4
Tensile strength, cb_strength shear/(N/m)	4.5×10^5	5×10^4
Friction coefficient, Fric	0.3	0.7

Numerical uniaxial compressive simulation test scheme

According to the earlier research, the appropriate D/d_{max} value (ratio of the sample diameter to d_{max}) must be used to avoid the negative effect due to the boundary effect on the simulation and test results. In order to choose an appropriate value range of D/d_{max} for the size effect simulation, the impact of the d_{max} value on the mechanical characteristics of S-RM is first explored.

Seven groups of S-RM samples were constructed at a height and width of 600 and 300 mm, with various d_{max} values. The results of the uniaxial compressive simulation tests show that when the d_{max} is larger than 25 mm, it appears that the variation of *UCS* value is more sensitive to particle size. The relative ratio of *UCS*, denoted by the symbol $\alpha_{\sigma rat}$, is determined in order to better understand the variation law of the *UCS* under various particle size conditions. The calculation of the relative ratio of *UCS* is as follows.

$$\alpha_{\sigma rat} = \frac{UCS_{d\,\max=10mm} - UCS_{d\,\max}}{UCS_{d\,\max=10mm}} \times 100 \quad (3)$$

where $UCS_{dmax\,=\,10mm}$ and UCS_{dmax} is the *UCS* value of the S-RM sample with a d_{max} value of 10 mm and the other value.

The lower value of $\alpha_{\sigma rat}$ indicates that the *UCS* value is substantially closer to that of the S-RM sample with d_{max} = 10mm, which means that the particle size effect and boundary effect area relatively less significant. The fluctuation of $\alpha_{\sigma rat}$ with various D/d_{max} values under different *VBP* conditions is obvious. In contrast to the wave trend of $\alpha_{\sigma rat}$ value in the sample with 60% and 90% *VBP*, the comparisons show that the $\alpha_{\sigma rat}$ exhibits a

TABLE 2 Numerical simulation test scheme.

Test number	Sample size H*L/(mm*mm)	Maximum particle size, d_{max}/mm	The ratio of the sample diameter to maximum particle size, D/d_{max}
B-1	160*80	10	8
B-2	200*100	12.5	
B-3	300*150	18.75	
B-4	400*200	25	
B-5	500*250	31.25	
B-6	640*320	40	

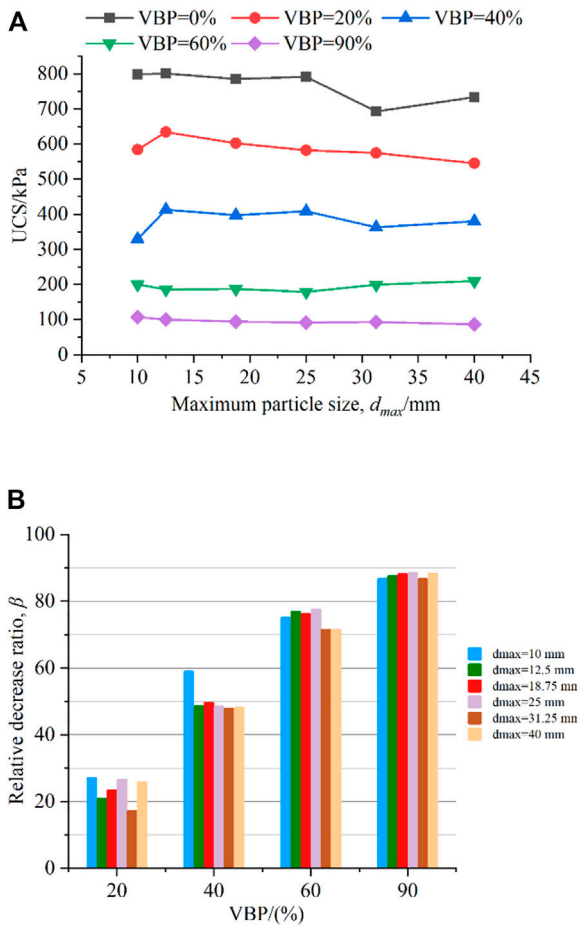

FIGURE 4
(A) *UCS* and **(B)** relative disturbance *UCS* ratio values of S-RM samples with different d_{max} values.

decreasing tendency when D/d_{max} increases from 5 to 8 by 15% and 10% with *VBP* = 20% and 40%. With the exception of the sample with *VBP* = 90%, the $\alpha_{\sigma rat}$ only fluctuates within a limit range of −2.5%–5% as D/d_{max} increases from 8 to 30, indicating that the particle size only little affects the *UCS* value when D/d_{max} is more than 8.0. In this study, an appropriate value of D/d_{max} for the simulation test was determined to be 8, and seven S-RM samples with the corresponding size were carried out. The detailed numerical test scheme is listed in Table 2.

Results and discussions

Figure 4A displays the *UCS* values for S-RM samples with various particle sizes (using d_{max} as the size description index) under different *VBP* conditions. As d_{max} increases from 10 mm to 25 mm, it seems that the *UCS* value almost maintains a value of 800 kPa, and the quick fall in *UCS* appears until d_{max} reaches 25 mm for the soil sample (*VBP* = 0%). In S-RM sample with *VBP* = 20% and 40%, the *UCS* initially rises and then falls with d_{max}, with the maximum *UCS* appearing at a d_{max} value of 12.5 mm. Under a 60% *VBP* condition, the variation range of *UCS* values of the S-RM samples with various d_{max} values is significantly less, and the value is in the range of 179.21–210.07 kPa. The sample with *VBP* = 90% exhibits the most pronounced decreasing trend of *UCS* variation, with the value decreasing from 107.45 to 86.56 kPa as d_{max} increases from 10 mm to 40 mm.

Previous studies indicate that the presence of rock blocks weakens the stability of the soil matrix and reduces the *UCS* value. However, little is yet known about the impact of the different-sized rock blocks. To determine the negative impact of tock block on the soil matrix, the relative disturbance *UCS* ratio, β, is proposed. It is calculated as follows.

$$\beta = \frac{UCS_{soil} - UCS_{S-RM}}{UCS_{soil}} \times 100\% \quad (4)$$

The β values of samples with different d_{max} values under different *VBP* conditions are shown in Figure 4B. Under the *VBP* condition of 20%, the β values of samples are sensitive to changes in the d_{max} value, and are basically greater than 20%. The detrimental effect of the rock block becomes much more

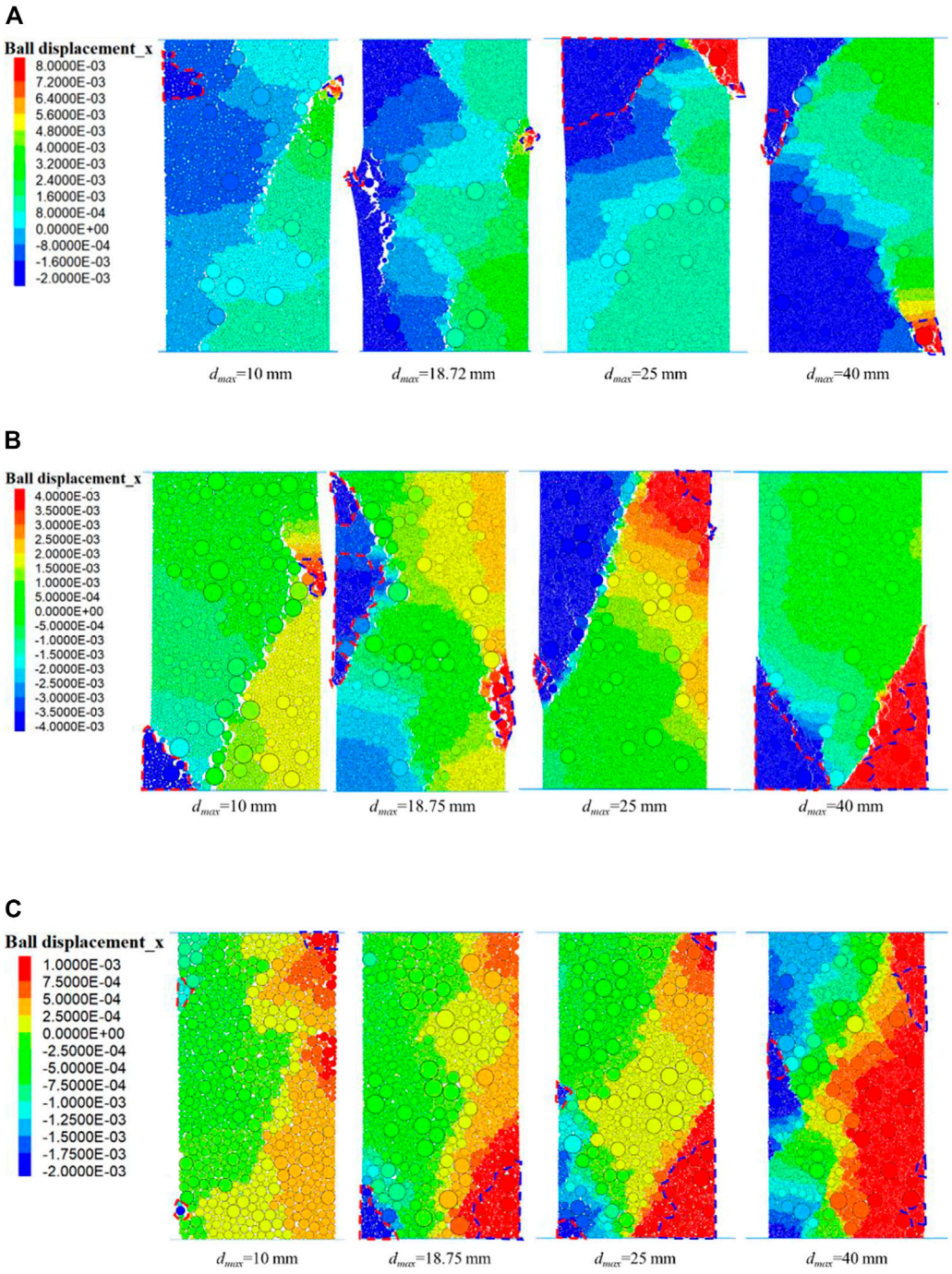

FIGURE 5
Horizontal displacement distribution of samples with different d_{max} values with **(A)** 20%; **(B)** 40%; **(C)** 90% *VBP* at the destruction stage.

apparent when *VBP* reaches to 40% as d_{max} = 10 mm, whereas the β values of samples are close to 50% with a d_{max} range of 12.5–40 mm. The negative influence on the *UCS* value of rock blocks with various d_{max} values under the high *VBP* condition (such as *VBP* = 90%) is virtually the same, and the β value is about 85%–90%. The sample with the lower d_{max} value has a considerably more pronounced detrimental impact of the rock block on the *UCS* in the low *VBP* stage (20% and 40%). Because there are more rock particles and soil-rock interfaces with the same *VBP* due to the smaller rock size, the soil integrity and UCS

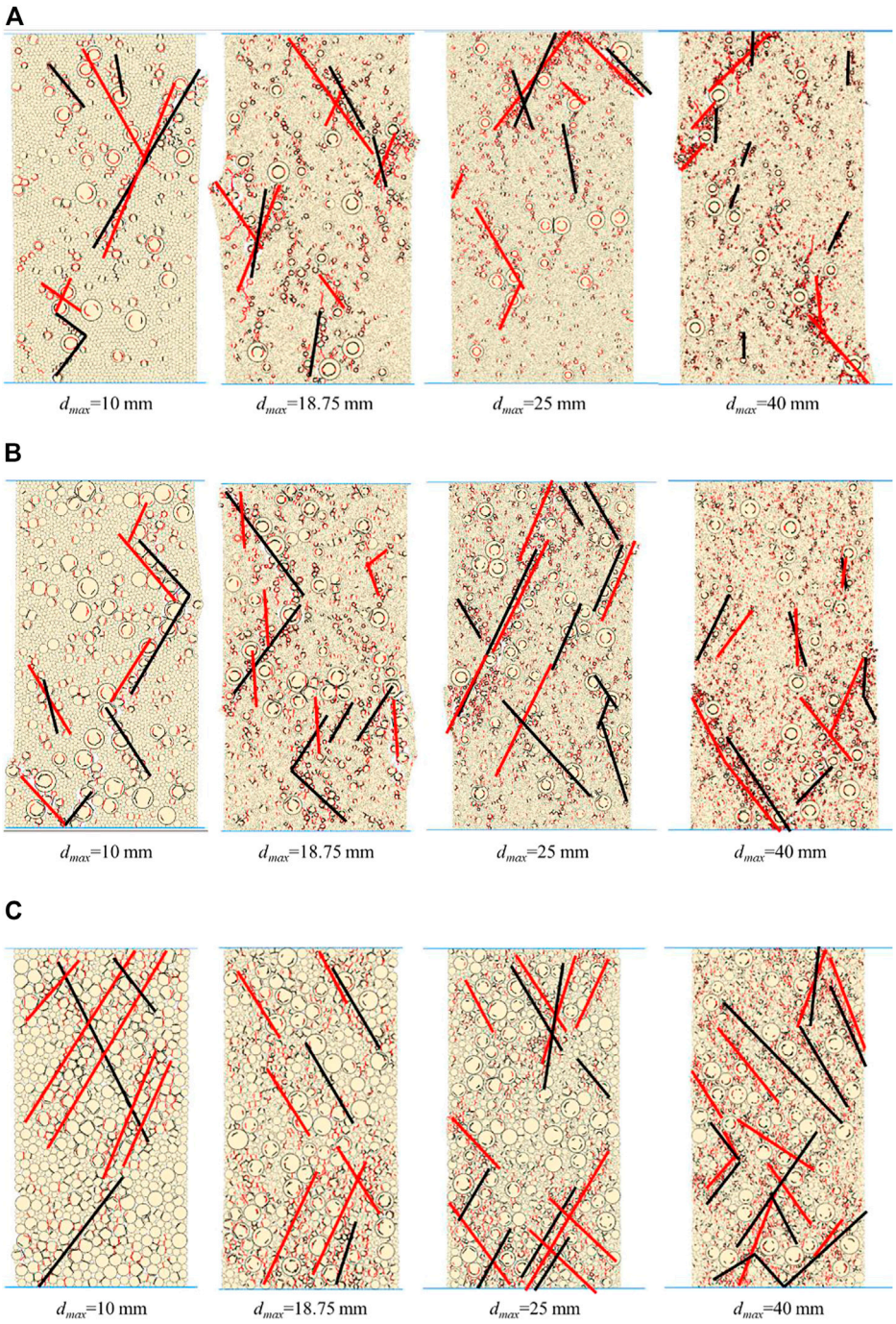

FIGURE 6
Micro-crack distribution of the sample with different d_{max} values with **(A)** 20%; **(B)** 40%; **(C)** 90% *VBP* at the destruction stage.

value are more severely damaged. The influence of size differences on the disruption of mechanical behaviors eventually diminishes as *VBP* increases.

Figure 5 depicts the horizontal displacement distribution of the S-RM samples with various d_{max} values under different *VBP*s at the destruction stage, and the destruction stage refers to the stage in which the axial stress reduces to the stress that is 0.7 times peak stress in the post-peak stage. The result demonstrates that when the d_{max} value increases from 10 to 40 mm, a boarder distribution area of blue and red colored particle displacement appears and an increase in the difference in the horizontal displacement as shown in Figure 5A. The phenomenon of soil particle detachment was

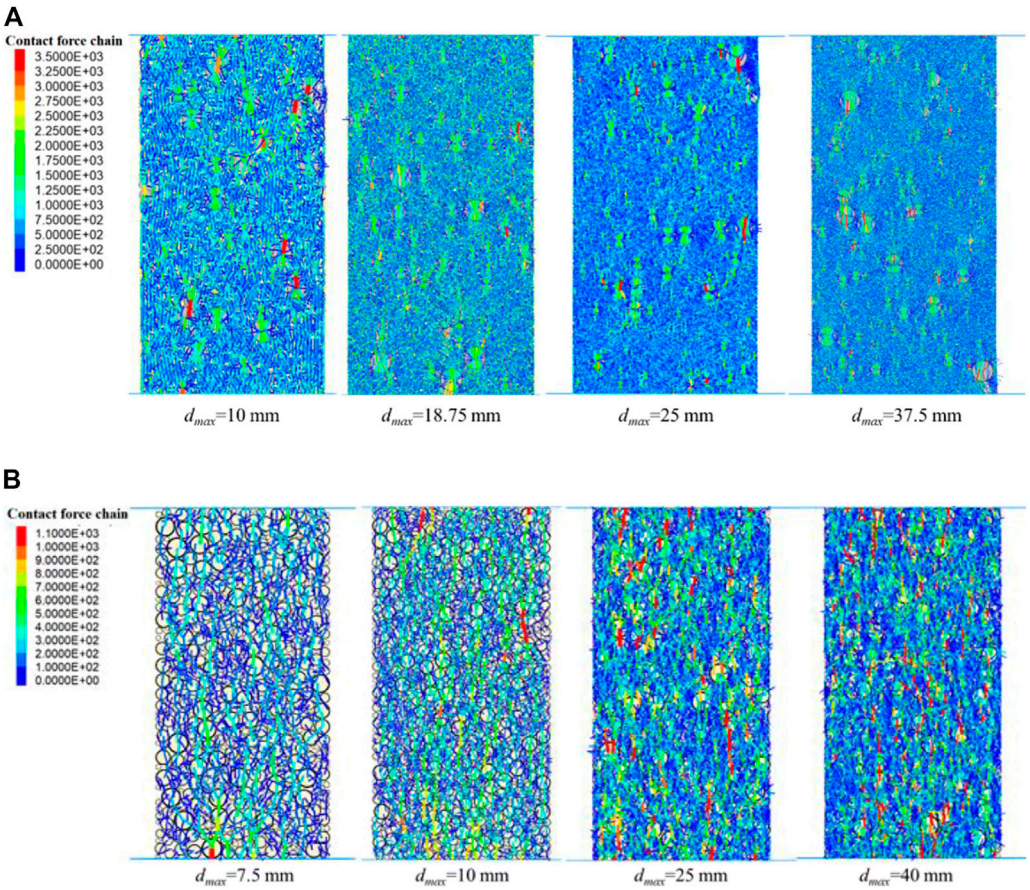

FIGURE 7
Force chain distributions of the S-RM sample with different d_{max} values with **(A)** 20%; **(B)** 90% *VBP* at the peak stress stage.

discovered as a result of the weak soil-rock contact strength, and the increase in d_{max} value causes a larger degree of anisotropy. On both sides of the sample, the evident destructions in the irregular form were discovered.

The noteworthy region in Figure 5 is shown by a blue and red dotted line that delineates the region of which the horizontal displacement more or less than 0.6 times the greatest displacement. Particularly in the sample with d_{max} = 25 mm–40 mm, the position of the rock blocks is connected to the shape of the noteworthy region. The separation of the soil-rock aggregates has become more obvious as *VBP* increases, and in Figures 5B,C, the area of the noteworthy region has grown significantly. The contact failure within the sample is caused by an increase in both the *VBP* and d_{max} values because the contact strength between the rock-rock and rock-soil is significantly lower than that between the soil particles. As a result, the local destruction within the sample usually occurs in the area around the large size rock blocks.

The shear and tension micro-crack are indicated as black and red line segments between particles in Figure 6, which shows the micro-crack distribution of the sample with various d_{max} values at the destruction stage. The results show that the distributions of the tension and shear micro-crack are comparatively dispersed in the sample with d_{max} = 10 mm. The micro-crack gradually spreads parallel to the diagonal from the top or bottom of the sample, and more micro-crack are present as the d_{max} value increases as shown in Figure 6A. In Figures 6B,C the difference in the micro-crack distribution in the samples with d_{max} = 10 mm and 40 mm is more pronounced. When *VBP* reaches 40%, the micro-cracks in the sample with d_{max} = 10 mm were primarily found close to the larger rock blocks, and did not clearly link to one another. The micro-cracks mostly begin in the contact region of the sample with the wall when the d_{max} within the specimen is 40 mm. The micro-cracks are more widely spaced out and seem to be clearly connected when *VBP* is 90%. The failure of the rock-rock and rock-soil contact models, as discussed above, is the main cause of the deformation and failure of the sample. The 'rounding rock effect' is well presented as the extension of the micro-crack occurs along the weak soil-rock interface, and the increasing unevenness of the crack as the rock block size increases. The

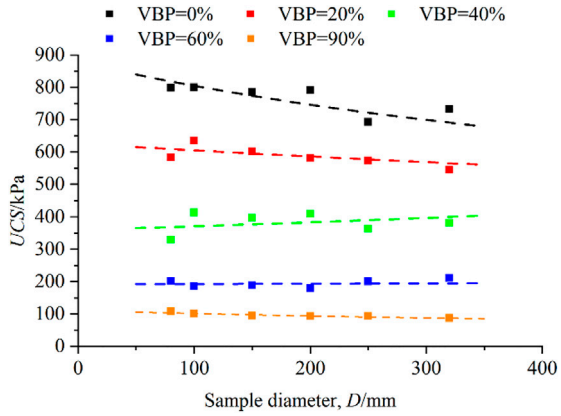

FIGURE 8
Comparisons between the simulation and calculation based on Bažant theory.

shear and tension micro-cracks can be found around the rock block particles in Figure 6C, which indicates that when the *VBP* is relatively large, the failure modes of the contact model inside the sample appear to less connected to the particle size.

The force chain distributions of the S-RM sample with various d_{max} values and *VBP*s at the peak stress stage are displayed in Figure 7. The wider cyan and red force chains with the higher contact force were identified between the rock-rock with a bigger size, while the blue force chains with low contact force are extensively dispersed between the soil-soil particles. As the d_{max} value increases, there are more strong force chains, which suggests that there is a more evident transformation of the external force between the rock blocks (Figure 7A). The anisotropy in the contact force between the particles results in the local destruction and the decrease of *UCS* value. The difference in the contact force between rock-rock and rock-soil becomes more noticeable as *VBP* increases. In Figure 7B, the red and cyan force chains that have a reasonably strong contact force and are situated close to rock blocks with a relatively big size have been linked together. The rock blocks make contact with one another to form the rock skeleton under the high *VBP* condition, and they play the dominant role in transforming and bearing the external force under this circumstance. Due to the additional external force, the sample is more likely to be destroyed because of the poor strength of the rock-rock and rock-soil contact models.

A method for determining the strength parameters of soil-rock mixture considering size effect

Researchers have also undertaken quantitative discussions regarding the size effect, and numerous theories have been put out to explain and predict the variance of the mechanical properties as the sample size increases.

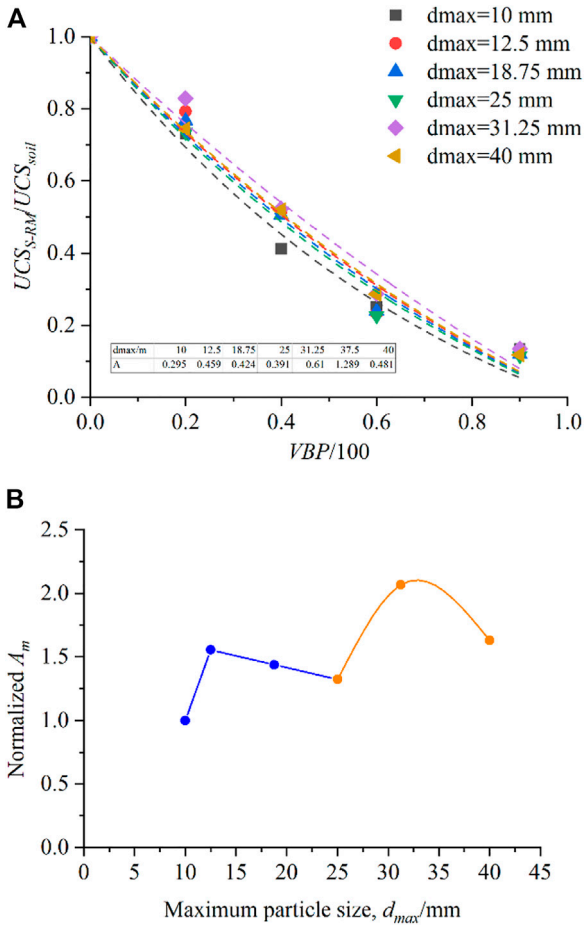

FIGURE 9
(A) Normalized *UCS*; **(B)** characteristic parameter *A* of S-RM with different d_{max} values.

Bažant theory (Bažant and Oh, 1983; Bažant, 1997) is one of the typical theories that is frequently utilized in the investigation of the quasi-brittle material size effect. Bažant (1997) indicates that the size effect was caused by the dissipation of strain energy during the macro crack growth. The unified nominal strength calculation formula function of the characteristics size *D* is shown in Eq. 5.

$$\sigma_N = \frac{Bf_t}{\sqrt{1 + \frac{D}{D_0}}} \tag{5}$$

where f_t is the tensile strength of the standard sample; *B* and D_0 are empirical constants determined by test results.

Figure 8 displays the *UCS* simulated results and the fitting curves using Bažant theory. The obvious inaccuracy is identified as the S-RM sample with a VBP range of 60%–90% and greater d_{max} values based on the disparities between the simulated and fitted values. According to the simulation results above, the *UCS*

value of the sample at *VBP* = 40% exhibits a declining trend with respect to the d_{max} value, however, it appears that at *VBP* = 90% the *UCS* value is less impacted by particle size. The peak stress and stress drop are no longer discernible, and the continuous deformation can be detected once the axial stress exceeds the yield stress, according to the axial stress-strain curves of S-RM with various d_{max} values as *VBP* = 90%. The increases in *VBP* and d_{max} lead to the ductility feature appearance of S-RM, and it is improper to use the size effect theory based on the test results of the quasi-brittle material.

Even though the connections between the sample (or particle) size and mechanical parameters have been discussed by many researchers in recent years, the study about the effect of particle size on the *UCS* value of S-RM is still few. According to the empirical formula of *UCS* with various *VBP*s presented by Kalender et al. (2014) as Eq. 2, the presence of rock blocks destroys the integrity of the soil matrix, and the occurrence of the weak soil-rock interface increases the failure possibility of the sample, resulting in a decrease in strength. The characteristic parameter *A* is utilized to describe the role in the material strength played by the soil-rock interface, and a larger value of *A* indicates a stronger strength of the interface. The form and roughness of the rock blocks as well as the *UCS* value of the soil matrix all influence the value of characteristic parameter *A*; however, the size effect has not been taken into account so far. Based on the non-linear fitting, the characteristic parameter *A* of the S-RM with various d_{max} values is derived, and the results suggest that the particle size has an impact on parameter *A* as shown in Figure 9A. Based on the compositions of the test samples mentioned above, the d_{max} value of the sample in regular-size is generally less than 10 mm. In this study, the standard d_{max} value of the S-RM sample is set to 10 mm, which is named d_{10}. The normalized A_m (relative to the A_{10} of the sample with the standard d_{max}) and d_{max} value is shown in Figure 9B, and the result shows that when the d_{max} value is less than 25 mm, the normalized A_m remains constant at around 1.5, and the size effect is evident in the sample within the d_{max} range of 25 mm–40 mm. According to Figure 4B, the relative disturbance *UCS* ratio (β) of the S-RM samples with various d_{max} values shows that the β values of the samples with a d_{max} range of 12.5 mm–25 mm under different *VBP*s appear to be similar and are in a relatively narrow variation range when compared with that of the sample with d_{max} = 10 mm. However, the β value exhibits a distinct connection with the d_{max} value when the d_{max} value is larger than 25 mm. It is suggested that the normalized A_m and d_{max} value have the following connection.

$$A_m/A_{10} = \begin{cases} 1.5 & 10 < d_{\max} < 25 \\ -1.12\,(d_{\max}/d_{10})^2 + 7.51 d_{\max}/d_{10} - 10.42 & 25 \le d_{\max} \le 40 \end{cases} \tag{6}$$

where A_m and A_{10} are characteristic parameters of the sample with a certain d_{max} value and standard d_{max} (d_{10}), and the standard d_{max} value is 10 mm in this study.

The characteristic parameter A_{10} of the sample with the d_{10} can be obtained based on the parameter value table, and the characteristic parameter A_m of the sample with a certain d_{max} value can be obtained using A_{10} and Eq. 6. The *UCS* value of S-RM with d_{max} value smaller than 40 mm under various *VBP* conditions is calculated based on characteristic parameter A_m and *UCS* of the soil matrix, and the following prediction formula is suggested.

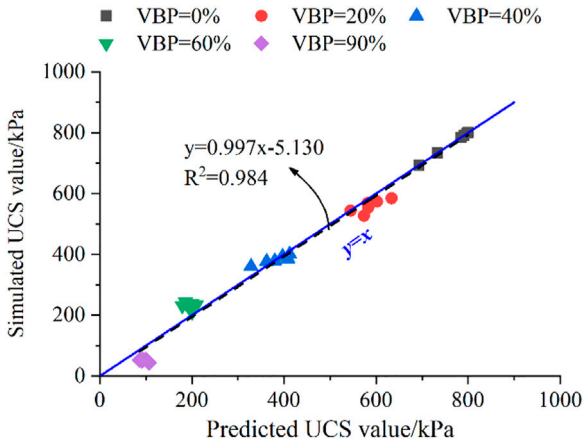

FIGURE 10
Comparison of the predicted and simulated *UCS* values.

$$\sigma_{c-SRM}/\sigma_c = \frac{A_m - A_m^{\frac{VBP}{100}}}{A_m - 1} \tag{7}$$

Figure 10 displays the comparisons between the predicted and simulated *UCS* values. The fitting functions suggested in this work may be used as a prediction reference for the *UCS* and shear strength of the engineering S-RM material taking the size effect into account since the error between the predicted and simulated values is acceptable.

A prediction method to determine the *UCS* value of the S-RM material with a d_{max} less than 10 mm, which is much smaller than the rock block size of the natural S-RM on the deposit slope, has been described in the existing work. As a result, the particle size range of the mechanical parameters in the prediction method for the shear strength of S-RM involved *UCS* value has not been consistent, of which the corresponding d_{max} value of the *UCS* and shear strength value is 10 mm and 40 mm–60 mm, respectively. Therefore, the aforementioned discussions above offer an empirical method to determine the *UCS* value of the S-RM material with a d_{max} ranging from 10 to 40 mm, which can fulfill the majority of the particle size range of the deposit slope of weathered origin. The typical large-scale apparatus used to determine the shear strength of natural S-RM has a maximum allowable d_{max} value of less than 40 mm. It is now feasible to utilize the same material with the same particle size range for all the experimental data used in the shear strength prediction formula (Eq. 1) due to the expansion of the relevant particle

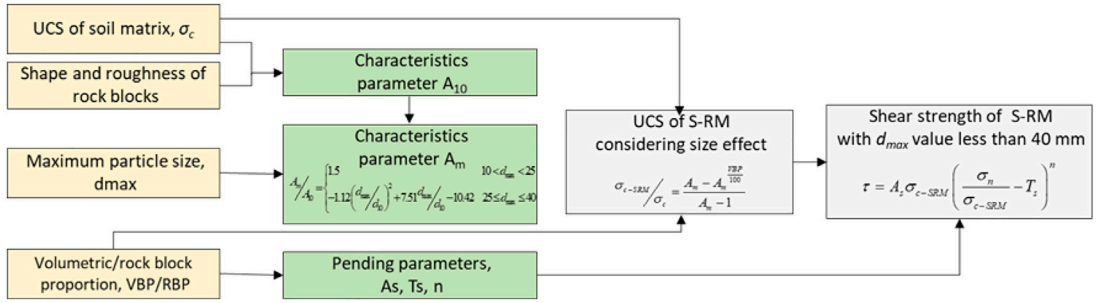

FIGURE 11
Flow chart of the shear strength determination method of S-RM considering size effect.

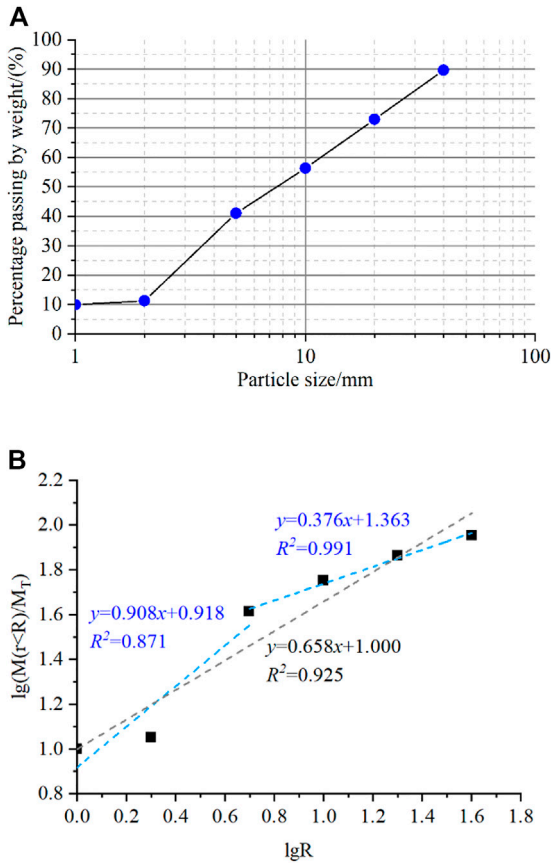

FIGURE 12
(A) Particle grain-size distribution and **(B)** fractal dimension curve of the S-RM material.

size range. The flow chart for the shear strength prediction of the S-RM with a d_{max} value smaller than 40 mm is shown in Figure 11. Based on the strength envelope, it is possible to determine the shear strength parameters of S-RM with a d_{max} value less than 40 mm can be obtained, which serves as a guide for the parameter selection during the assessment of the stability of deposit slope and the design of reinforcement engineering.

Engineering application of the determination method

In this study, a typical deposit slope located in Shiyan City, Hubei Province, is chosen as the engineering application for the shear strength determination method of S-RM to take the size effect into consideration. The study slope is a high fill deposit slope, and the S-RM in the shallow region is made up of reddish brown cohesive soil and strongly weathered maroon argillaceous siltstone rock blocks of different sizes. The size of the rock block in the S-RM material inside the slope ranges from 2 mm to 50 mm, and occasionally there are even large rock blocks with a particle size of up to 100 mm. The internally cohesive structure of the moderately weathered glutenite strata underneath is comparatively complete, and the strength of the moderately weathered layer is significantly higher than that of the shallow strongly weathered region. The results of the *in-situ* sieving test used to determine the particle size distribution of S-RM material are displayed in Figure 12. Given that the particle size of S-RM is 5 mm, the fractal dimension clearly displays the multiple fractal characteristic, meaning that the properties of the particle size distribution are very distinct in the region above and below this particle size. Therefore, the soil-rock threshold of the S-RM in this study is chosen at 5 mm, and the rock content of S-RM is around 60%.

The shear strength parameters of the S-RM in the shallow region of the deposit slope are obtained using the determination method proposed in this study. The calculation steps are as follows.

(a) The soil matrix sample was collected from the construction site, and the *UCS* value of the soil matrix was determined to be 245 kPa based on the laboratory uniaxial compressive test.

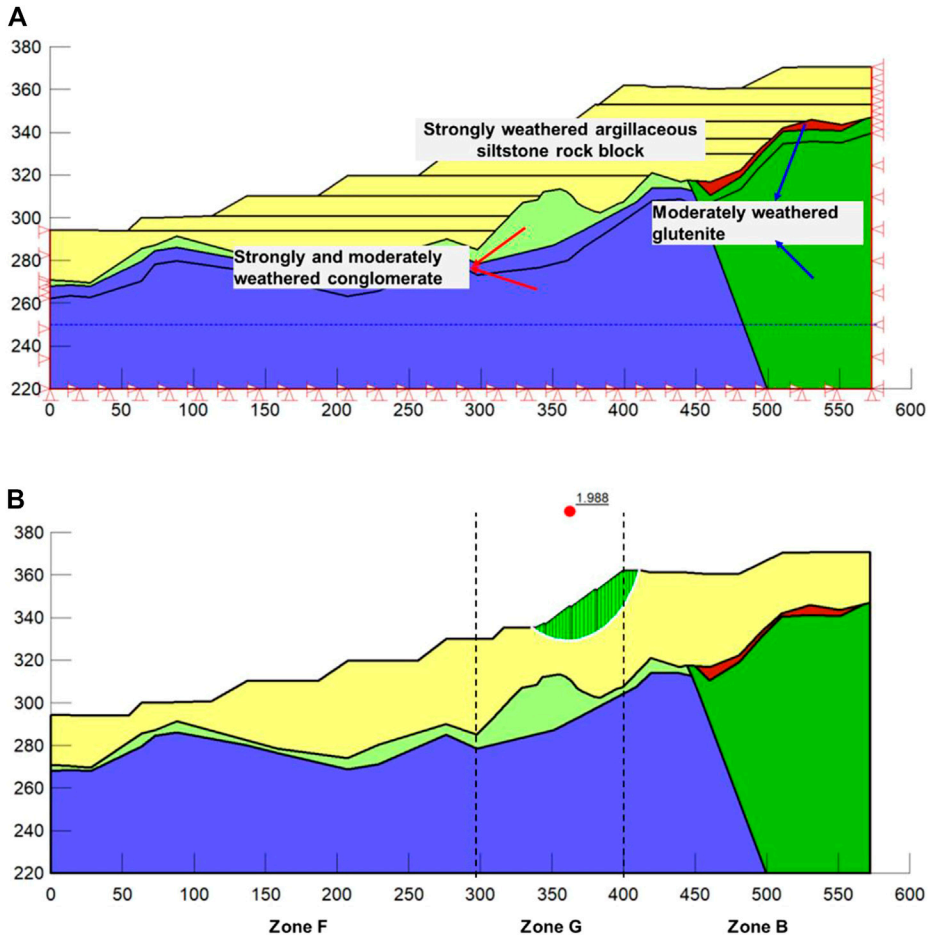

FIGURE 13
(A) Numerical model and the **(B)** potential sliding surface of the deposit slope.

The friction angle of the rock block with the sub-round form is about 27°, and the characteristic parameter A_{10} was selected based on the value selection table proposed by Kalender et al. (2014) as around 1.2.

(b) The particle size distribution as illustrated in Figure 12 indicates that the d_{max} value of the material is larger than 40 mm. However, the rock content of the particle larger than 40 mm is fewer than 10%, which is only a small part of the total. The focus of this study was on the particle size range of 10 mm–40 mm, and a 40 mm d_{max} value was chosen. The characteristic parameter A_m taking into account the size effect can be obtained using Eq. 6 as 2.304.

(c) The *UCS* value of S-RM with 60% rock content was obtained using the *UCS* value of soil matrix and characteristic parameter A_m as 122.87 kPa based on Eq. 7. The resulting test and physical property parameters might be used to calculate the remaining pending parameters in Eq. 1. The cohesion of the S-RM is 72.88 kPa and the friction angle is 17.5°.

The image data of the target slope was captured using multi-rotor UAV equipment. A typical geological profile was selected to build a numerical model of the deposit slope in a two-dimensional plane, as illustrated in Figure 13A. The high-filled deposit slope was assessed for the stability under self-weight. The surface of the slope is assigned as the free boundary for the mechanical analysis of excavation, whereas only vertical displacement is allowed on the left and right boundaries, and the bottom boundary is restrained from movements.

Figure 13B shows that potential sliding surface of the deposit slope is mostly found in Zone G and extends to a maximum depth of 20.29 m. The safety factor was calculated based on the finite element-limit equilibrium method as 1.988, and no evident plastic zone was observed. According to the Technical code for building slope engineering, when the safety factor is larger than 1.25, the slope can be considered to be in a stable state under normal condition. Because the smallest safety factor in this study meets the stability criteria, the high-filled deposit slope is in a

stable state, which is also compatible with the field monitor data. The shear strength determination method taking the size effect into consideration that is proposed in this study is expected to serve as a reference for the values of the mechanical parameters during the deposit slope engineering design and construction process.

Conclusion

In this study, a shear strength determination method was presented while taking into account how size affects the mechanical behaviors of S-RM. The uniformity of the particle size range of the material according to the required test data within the determination technique was attained with careful attention paid to fluctuations in the UCS value of S-RM with varied d_{max} values. The conclusion are summarized as follows.

1. The uniaxial compressive computer simulation tests of the S-RM sample in the same size with various d_{max} values reveal that the *UCS* value exhibits a decreasing trend as the d_{max} value increases, and the influence of the size effect on the S-RM sample in the same size decreases gradually. Based on the simulation results, a appropriated D/d_{max} value of 8 was suggested, which indicates that the particle motion inside the sample is not limited by boundaries.
2. The size effect simulation test results show that the *UCS* value decreases as the d_{max} value increases, and the disturbance caused by the rock block on the soil matrix has a connection with d_{max} of *VBP* = 20%–60%. The contact failure is more likely to occur close to the large-size rock blocks as the particle size increases, leading to rounding rock effect of the damaged surface. The distributions of the particle displacement and micro-crack are proportional to the particle size. As the d_{max} value increases, the rock blocks inside the sample begin to interact with one another and build a rock skeleton than can bear and transform the external force, especially when the *VBP* is high.
3. A modified method to estimate the *UCS* value taking the size effect into account was presented following the quantitative discussions. The relationship between the A_m and d_{max} value was proposed after an analysis of the characteristic parameter A_m within the formula under different particle size conditions. By comparing the predicted and simulated values, it has been demonstrated that the accuracy of the predicted equation. The shear strength was calculated using the modified *UCS* and shear strength estimation methods and the stability of a typical deposit slope was assessed using the determination method as the engineering application. The study results can be used as a guide for estimating the strength parameters of S-RM and assessing the deposit slope stability as well as for understanding the impact of rock size on the mechanical behaviors of the S-RM under the uniaxial compressive condition.

Data availability statement

The original contributions presented in the study are included in the article/supplementary material, further inquiries can be directed to the corresponding author.

Author contributions

YZ and LZ contributed to the conception of the study; GS proposed the methodology of the study; GS and SQ helped perform the validation of the analysis results; YZ and JC contributed significantly to the original draft preparation; GS and HX contributed to the review and editing of the manuscript. All authors have read and agreed to the published version of the manuscript.

Conflict of interest

Authors YZ, SQ, LZ, JC, and HX were employed by the company State Grid Hubei Electric Power Company Limited Economic Research Institute and author GS was employed by the company State Grid Hubei Electric Power Co. Ltd.

The authors declare that the research was conducted in the absence of any commercial or financial relationships that could be construed as a potential conflict of interest.

Publisher's note

All claims expressed in this article are solely those of the authors and do not necessarily represent those of their affiliated organizations, or those of the publisher, the editors and the reviewers. Any product that may be evaluated in this article, or claim that may be made by its manufacturer, is not guaranteed or endorsed by the publisher.

References

Bai, B., Wang, Y., Rao, D., and Bai, F. (2022). The effective thermal conductivity of unsaturated porous media deduced by pore-scale SPH simulation. *Front. Earth Sci. (Lausanne).* 10, 943853. doi:10.3389/feart.2022.943853

Bai, B., Yang, G. C., Li, T., and Yang, G. S. (2019). A thermodynamic constitutive model with temperature effect based on particle rearrangement for geomaterials. *Mech. Mater.* 139, 103180. doi:10.1016/j.mechmat.2019.103180

Bai, B., Zhou, R., Cai, G. Q., Hu, W., and Yang, G. C. (2021). Coupled thermo-hydro-mechanical mechanism in view of the soil particle rearrangement of granular thermodynamics. *Comput. Geotechnics* 137 (8), 104272. doi:10.1016/j.compgeo.2021.104272

Bažant, Z. P., and Oh, B. H. (1983). Crack band theory for fracture of concrete. *Mat. Constr.* 16 (3), 155–177. doi:10.1007/bf02486267

BaŽAnt, Z. P. (1997). Scaling of quasibrittle fracture: Asymptotic analysis. *Int. J. Fract.* 83 (1), 19–40.

Chaulagai, R., Osouli, A., Salam, S., Tutumluer, E., Beshears, S., Shoup, H., et al. (2017). Influence of maximum particle Size, fines content, and dust ratio on the behavior of base and subbase coarse aggregates. *Transp. Res. Rec.* 2655 (2655), 20–26. doi:10.3141/2655-04

Ding, X. B., Zhang, L. Y., Zhu, H. H., and Zhang, Q. (2014). Effect of model scale and particle size distribution on PFC3D simulation results. *Rock Mech. Rock Eng.* 47 (6), 2139–2156. doi:10.1007/s00603-013-0533-1

Du, W. J., Sheng, Q., Fu, X. D., Chen, J., and Zhou, Y. (2022). A TPDP-MPM-based approach to understanding the evolution mechanism of landslide-induced disaster chain. *J. Rock Mech. Geotechnical Eng.* 14 (4), 1200–1209. doi:10.1016/j.jrmge.2022.03.004

Fu, X. D., Ding, H. F., Sheng, Q., Zhang, Z., Yin, D., and Chen, F. (2022). Fractal analysis of particle distribution and scale effect in a soil–rock mixture. *Fractal Fract.* 6 (2), 120. doi:10.3390/fractalfract6020120

Fu, X. D., Du, Y. X., and Sheng, Q. (2021a). Geo-engineering descriptions and damage characteristics assessment for Xigeda formation, Yunnan Province, China. *Environ. Earth Sci.* 80 (19), 670. doi:10.1007/s12665-021-09982-z

Fu, X. D., Zhang, Z. P., Sheng, Q., Zhou, Y., Huang, J., Wu, Z., et al. (2021b). Applications of an innovative strength parameter estimation method of the soilrock mixture in evaluating the deposit slope stability under rainfall. *Front. Earth Sci. (Lausanne).* 9, 768757. doi:10.3389/feart.2021.768757

Giang, P. H. H., Van Impe, P. O., Van Impe, W. F., Menge, P., and Haegeman, W., (2007). Small-strain shear modulus of calcareous sand and its dependence on particle characteristics and gradation. *Soil Dyn. Earthq. Eng.* 100, 371–379. doi:10.1016/j.soildyn.2017.06.016

Guo, Z. Z., Chen, L. X., Gui, L., Du, J., Yin, K. L., and Minh, D. H., (2019). Landslide displacement prediction based on variational mode decomposition and WA-GWO-BP model. *Landslides* 17, 567–583. doi:10.1007/s10346-019-01314-4

Hong, C. J., Huang, M., Zhang, D. Y., Shou, P., and Zhu, Z. (2020). Characteristics of direct shear and particle breakage of pebble gravel materials. *Geofluids* 2020, 1–13. doi:10.1155/2020/8820045

Ji, T., Chen, B. C., and Zhuang, Y. Z. (2011). "Effects of sand particle size and gradation on strength of reactive powder concrete," in *Paper presented at the international conference on civil engineering and building materials (CEBM), kunming, PEOPLES R China*. <Go to ISI>://WOS:000306441600040.

Ji, X., Lu, H., Dai, C., Ye, Y., Cui, Z., and Xiong, Y. (2021). Characterization of properties of soil–rock mixture prepared by the laboratory vibration compaction method. *Sustainability* 13 (20), 11239. doi:10.3390/su132011239

Kalender, A., Sonmez, H., Medley, E., Tunusluoglu, C., and Kasapoglu, K. (2014). An approach to predicting the overall strengths of unwelded bimrocks and bimsoils. *Eng. Geol.* 183, 65–79. doi:10.1016/j.enggeo.2014.10.007

Li, C., He, C., Wang, C., and Zhao, H. F. (2008). Study of scale effect of large-scale triaxial test of coarse-grained materials. *Rock Soil Mech.* 29 (S1), 563–566. doi:10.3969/j.issn.1000-7598.2008.z1.114

Li, Y. (2013). Effects of particle shape and size distribution on the shear strength behavior of composite soils. *Bull. Eng. Geol. Environ.* 72 (3), 371–381. doi:10.1007/s10064-013-0482-7

Lin, H., Wang, H., Fan, X., Cao, P., and Zhou, K. (2019). Particle size distribution effects on deformation properties of graded aggregate base under cyclic loading. *Eur. J. Environ. Civ. Eng.* 23 (3), 269–286. doi:10.1080/19648189.2016.1276480

Lv, X. L., Xue, D. W., Ma, Y. Y., Zeng, S., and Huang, M. S. (2022). Microscopic and macroscopic numerical simulation of the progressive failure of granular materials. *Sci. Sin. -Tech.* 52, 1022–1034. doi:10.1360/sst-2021-0326

Ovalle, C., and Dano, C. (2020). Effects of particle size–strength and size–shape correlations on parallel grading scaling. *Géotechnique Lett.* 10, 191–197. doi:10.1680/jgele.19.00095

Peng, J., Wong, L., and Teh, C. (2017). Effects of grain size-to-particle size ratio on micro-cracking behavior using a bonded-particle grain-based model. *Int. J. Rock Mech. Min. Sci.* 100, 207–217. doi:10.1016/j.ijrmms.2017.10.004

Ueda, T., Matsushima, T., and Yamada, Y. (2011). Effect of particle size ratio and volume fraction on shear strength of binary granular mixture. *Granul. Matter* 13 (6), 731–742. doi:10.1007/s10035-011-0292-1

Vahidi-Nia, F., Bayesteh, H., and Khodaparast, M. (2020). Effect of initial packing density, stress level and particle size ratio on the behavior of binary granular material: A micromechanical approach. *Granul. Matter* 22 (3), 68. doi:10.1007/s10035-020-01036-8

Wang, Z. Y., Wang, P., Yin, Z. Y., and Wang, R. (2022). Micromechanical investigation of the particle size effect on the shear strength of uncrushable granular materials. *Acta Geotech.* 17, 4277–4296. doi:10.1007/s11440-022-01501-z

Wolinski, S., Hordijk, D. A., Reinhardt, H. W., and Cornelissen, H. A. (1987). Influence of aggregate size on fracture mechanics parameters of concrete. *Int. J. Cem. Compos. Lightweight Concr.* 9 (2), 95–103. doi:10.1016/0262-5075(87)90025-x

Wu, L. Q., Ye, F., and Qing, L. W. (2020). Experimental study on scale effect of mechanical properties of rockfill materials. *Chin. J. Geotechnical Eng.* 42, 141–145. doi:10.11779/CJGE2020S2025

Xu, W. J., and Hu, R. L. (2009). Conception, classification and significations of soil-rock mixture. *Hydrogeology Eng. Geol.* 36 (4), 50–56+70. doi:10.3969/j.issn.1000-3665.2009.04.012

Xu, W. J., Hu, R. L., and Tan, R. J. (2007). Some geomechanical properties of soil-rock mixtures in the Hutiao Gorge area, China. *Geotechnique* 57 (3), 255–264. doi:10.1680/geot.2007.57.3.255

Yang, Y. T., Chen, T., Wu, W. A., and Zheng, H. (2021). Modelling the stability of a soil-rock-mixture slope based on the digital image technology and strength reduction numerical manifold method. *Eng. Analysis Bound. Elem.* 126, 45–54. doi:10.1016/j.enganabound.2021.02.008

Zhang, Z. P., Fu, X. D., Sheng, Q., Zhou, Y., and Huang, J. (2021). Effect of rainfall pattern and crack on the stability of a red bed slope: A case study in yunnan province. *Adv. Civ. Eng.* 21, 1–21. doi:10.1155/2021/6658211

Zhao, Y. X., and Liu, Z. X. (2018). Study of material composition effects on the mechanical properties of soil-rock mixtures. *Adv. Civ. Eng.* 2018, 1–10. doi:10.1155/2018/3854727

Zhou, Y. Q., Sheng, Q., Li, N. N., and Fu, X. (2022). The dynamic mechanical properties of a hard rock under true triaxial damage-controlled dynamic cyclic loading with different loading rates: A case study. *Rock Mech. Rock Eng.* 55, 2471–2492. doi:10.1007/s00603-021-02756-w

Zhou, Z., Yang, H., Wang, X. C., and Liu, B. (2017). Model development and experimental verification for permeability coefficient of soil-rock mixture. *Int. J. Geomech.* 17 (4), 04016106. doi:10.1061/(asce)gm.1943-5622.0000768

frontiers | Frontiers in Materials

TYPE Original Research
PUBLISHED 28 November 2022
DOI 10.3389/fmats.2022.1082292

Check for updates

OPEN ACCESS

EDITED BY
Bing Bai,
Beijing Jiaotong University, China

REVIEWED BY
Shun Wang,
Wuhan University, China
Yin-Fu Jin,
Shenzhen University, China

*CORRESPONDENCE
Xi-Long Huang,
XilongHuang2022@my.swjtu.edu.cn

SPECIALTY SECTION
This article was submitted to Structural Materials, a section of the journal Frontiers in Materials

RECEIVED 28 October 2022
ACCEPTED 11 November 2022
PUBLISHED 28 November 2022

CITATION
Jiang J-H, Huang X-L, Shu X-R, Ning X, Qu Y and Xiong W-L (2022), Application of a damage constitutive model to pile–slope stability analysis.
Front. Mater. 9:1082292.
doi: 10.3389/fmats.2022.1082292

COPYRIGHT
© 2022 Jiang, Huang, Shu, Ning, Qu and Xiong. This is an open-access article distributed under the terms of the Creative Commons Attribution License (CC BY). The use, distribution or reproduction in other forums is permitted, provided the original author(s) and the copyright owner(s) are credited and that the original publication in this journal is cited, in accordance with accepted academic practice. No use, distribution or reproduction is permitted which does not comply with these terms.

Application of a damage constitutive model to pile–slope stability analysis

Jian-Hong Jiang[1,2], Xi-Long Huang[2]*, Xiao-Rui Shu[1], Xiao Ning[1], Yan Qu[3] and Wei-Lin Xiong[2]

[1]Shandong Provincial Communications Planning and Design Institute Group Co., Ltd., Jinan, China, [2]Department of Geotechnical Engineering, School of Civil Engineering, Southwest Jiaotong University, Chengdu, China, [3]School of Qilu Transportation, Shandong University, Jinan, China

Piles were regarded as elastic materials in the traditional numerical simulation. The elastic pile would not reflect the damage of the pile in engineering, which would misjudge the reinforcement effect of piles on slopes. The specific objective of this study was to propose a damage constitutive model to replace the traditional elastic constitutive model in the numerical analysis of pile–slope stability. In this study, the pile was simulated by a damage constitutive model, which can reflect the plastic deformation of the pile. The factors of pile position and reinforcement ratio on a slope's factor of safety (FOS) are investigated by the finite difference method using FLAC3D. The lateral displacement, bending moment, shear force, and soil pressure of balance-reinforced piles are used to study the difference between damage and elastic constitutive models. The results showed that the FOS considering the damage constitutive model could be smaller, approximately 15% less than that considering an elastic constitutive model under specific conditions. Furthermore, the difference between the two evaluation results of the internal force of the same pile can reach about 30%. It was observed that the elastic constitutive model would overestimate the reinforcement effect of the pile on the slope, which will cause potential safety hazards in engineering. This study provides a realistic damage constitutive model for the design and evaluation of slope-stabilizing piles.

KEYWORDS

damage constitutive model, piles, slope stabilization, safety factor, numerical simulation

Introduction

There are a large number of natural slopes due to the complex geographic and geomorphic conditions in China. Furthermore, many engineering slopes are caused by mining, highway, metro, railway, and hydropower projects in China (Chen et al., 2016). The landslide disaster on unstable slopes is one of the greatest challenges in geotechnical engineering (Bai et al., 2022). A considerable amount of technology has been established for slope reinforcement (Bai et al., 2021). Sun et al. (2010) indicated that the drainage tunnels significantly contribute to landslide control due to the dropping of the

underground water level. Extensive research has shown that the natural slope stability can be notably increased by various reinforcement technologies, including anchored piles, cantilever piles, pre-stressed anchor cables, rock bolts, pre-consolidation grouting, and bottom drainage holes (Rahardjo et al., 2003; Jiang et al., 2015; Bai et al., 2019; Yan et al., 2019; Zheng et al., 2019; Chen et al., 2021; Xu and Xuang, 2021). For the past 30 years, we have seen increasingly rapid advances in the pile-reinforced slope. Researchers regarded pile reinforcement as a vital technology for slope stabilization, such as the advantage of lower cost, limited land occupation, and strong adaptability in engineering (Lin et al., 2018; Qu et al., 2018; Huang et al., 2020).

Recent trends in mathematics and computer science have led to a proliferation of studies about the numerical assessment of the stability of pile-reinforced slopes. Most researchers investigated the interaction of pile–soil under the lateral load based on finite element analysis software, such as FLEX 3D (Martin and Chen, 2005), ABAQUS (Gu et al., 2014), and ANSYS (Bakri et al., 2014). Cai and Ugai (2000) used the three-dimensional elastoplastic shear strength reduction finite element method to demonstrate that the pile should be installed in the middle of the slope. One study by Jeong et al. (2003) illustrated that the evaluation of pile-reinforced slopes is more conservative by uncoupled analysis than coupled analysis. Cheng and Jeremic (2009) presented a fully coupled soil–water dynamic finite element formulation to simulate the response of piles in liquefiable soil. The seismic displacement of the pile-reinforced slope was investigated by a three-dimensional limit analysis (He et al., 2015a). The pile-stabilized slopes under surface loading were analyzed comprehensively by finite difference analyses (Sharafi and Sojoodi, 2016). Many recent studies have established that numerical simulation could replace experiments to provide an accurate solution (Henke, 2010; He et al., 2015b; Jamsawang et al., 2015).

The failure mechanism of the pile with lateral load is complicated due to the interaction of many factors. Various studies have assessed the influence of soil stiffness, pile material, pile diameter, pile position, pile spacing, loading type, and slope gradient on slope stability (Won et al., 2005; Ashour and Ardalan, 2012; He et al., 2015c; Kavitha et al., 2016). It is essential to predict an accurate interaction behavior between piles and soil, and the safety factor of pile-reinforced slopes. Recently, two failure mechanisms of the laterally loaded pile have been mentioned. The pile was regarded as elastic or rigid material at the first failure mechanism. At this assumption, a sufficiently large anti-sliding force can be generated without causing pile failure. Moreover, the behavior of soil failure could be simulated by flow and short-pile modes (Poulos, 1995). The pile failure was considered to be another failure mechanism. When the maximum tensile stress of the pile reaches its ultimate strength, the plastic deformation and cracking of the pile will lead to the loss of slope stability. The existence of pile failure cannot be ignored in pile-reinforced slope engineering. However,

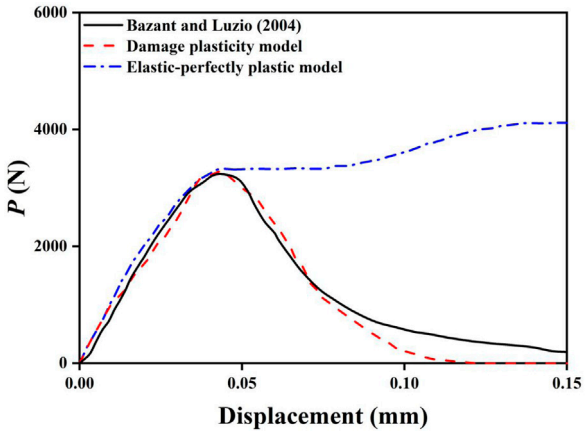

FIGURE 1
Load (P)–displacement curve from Zheng et al. (2018).

to simplify the calculation, many recent researchers regarded piles as elastic solids when the stability of a pile–slope was analyzed by numerical simulation (Won et al., 2005; Hassen et al., 2009; Lin et al., 2018). The elastic pile, without considering the failure, would overestimate the slope instability. Furthermore, the elastic constitutive model did not accurately indicate the effect of piles with different reinforcement rates on slope stability. Piles with different reinforcement rates were modeled as elastic piles with different stiffnesses in the simulation. However, the stiffness of the piles made a small contribution to the stability of the slope (Lee et al., 1995). The tensile strength is significantly varied with the reinforcement ratio. Therefore, it is more realistic and accurate to use a constitutive model that can reflect the tensile strength and failure of the pile to estimate the slope reinforced with the pile.

In recent years, there has been an increasing interest in the numerical simulation of pile damage. Comodromos et al. (2009) presented a three-dimensional nonlinear analysis to estimate the cracking influences of concrete on the response of piles under lateral loading. The study by Larsson et al. (2012) demonstrated that a concrete damage plasticity model made it possible to simulate the fracture development of laterally loaded lime–cement columns. Yapage et al. (2015) offered a constitutive model affiliating a strain-softening behavior to explain the time-dependent failure of deep cement mixed columns reinforced embankment. Zheng et al. (2019) proposed a damage plasticity model to describe the strain-softening behavior of concrete piles, which has verified that a damage plasticity model closely matched the experimental results in the three-point bending test (Figure 1). Furthermore, Dai et al. (2022) developed an advanced damaged plasticity model to simulate the bending moment degradation of slope-stabilizing piles due to concrete cracking and crushing.

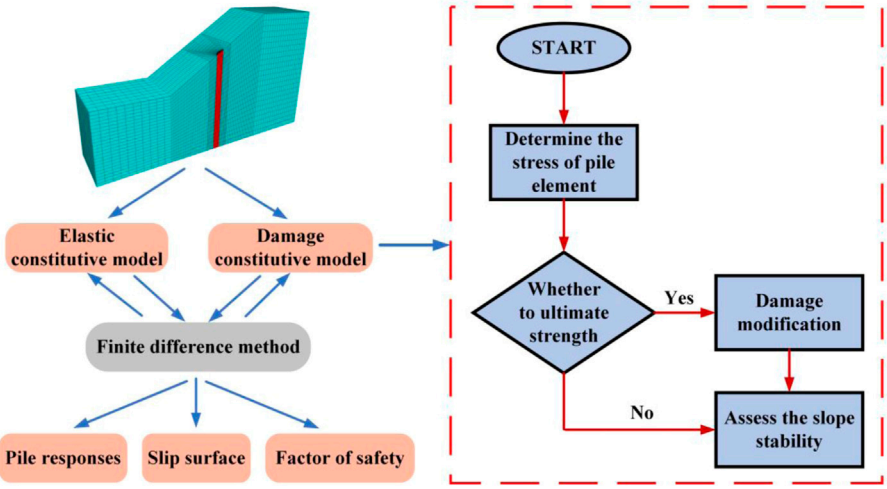

FIGURE 2
Schematic illustration of slope stability analysis.

The main aim of this study is to establish a new approach to pile–slope stability analysis considering the damage constitutive model. Figure 2 illustrates the schemata of the slope stability analysis in the current study. A finite different method, in which the FOS of a pile-reinforced slope is calculated, was performed by FLAC3D software. The pile was simulated by the elastic constitutive model and the damage constitutive model. The influences of pile position and reinforcement ratio on the slope's safety factor were explicitly investigated in this study. Additionally, the responses of the balance-reinforced pile were predicted by various constitutive models. All results obtained from the damage constitutive model were compared with that calculated by the elastic constitutive model in this study. The current study introduced a damage constitutive model instead of a traditional elastic model in the stability analysis of pile-reinforced slope. In this study, the responses of piles due to the lateral soil movement can provide a new reference for the design and implementation of reinforcing piles to increase slope stability.

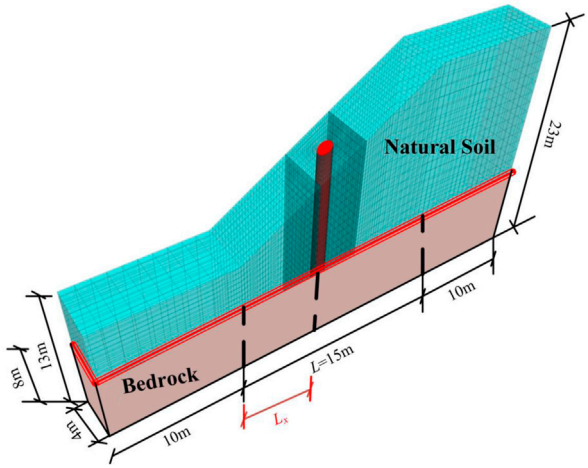

FIGURE 3
Schematic illustration of a homogeneous soil slope.

Methodology and theory

Damage constitutive simulations of piles

The damage constitutive model can reflect the fracturing and crushing of piles during horizontal loading, which is unavailable for the traditional elastic model. The reinforcement ratios of piles are represented by different tensile strengths. A reinforced concrete pile undergoes irreversible cracking when it reaches a critical state. The damage constitutive model simulates the destruction of piles in the reduction of tensile strength and shear strength. To simulate the cracking performance, both the tensile strength and the elastic modulus perpendicular to the crack are set to zero when the tensile stress of a zone exceeds the tensile strength of the concrete (Cedolin et al., 1982; Comodromos et al., 2009).

Furthermore, the shear strength of piles will be reduced due to the shear stress redistribution on cracks. The concrete interface crossed by a reinforcing bar in the pile will be subjected to a shear displacement when the landslide happens. A local increase in the crack width will occur due to the deformation of protruding asperities in the shear displacement (Maekawa and Qureshi, 1997). The lateral dilatancy leads to a pullout force that responded by reinforcing bars, which is balanced with the

TABLE 1 Mechanical parameters of soil and pile.

Material ID	v	E (MPa)	c (kPa)	φ (°)	ψ (°)	ρ (kg/m^3)
Natural soil	0.25	200	10	20	0	2,000
Bedrock	0.25	3,000	100	60	0	2,600
Pile	0.2	30,000				

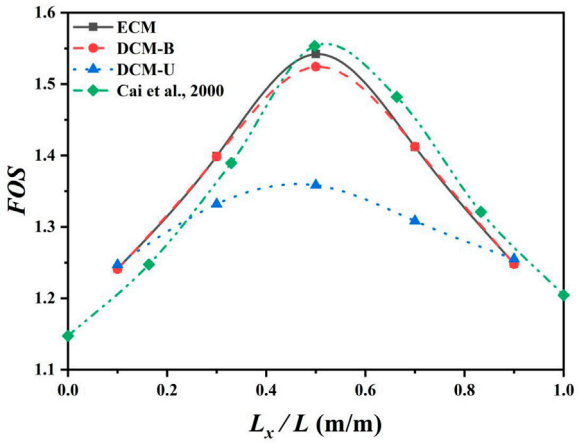

FIGURE 4
Effects of pile position on pile–soil stability considering damage constitutive simulation.

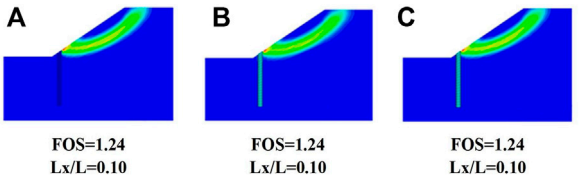

FIGURE 5
Positional variation of the slip surface at the toe of the slope for **(A)** the ECM, **(B)** DCM-U, and **(C)** DCM-B.

compressive force acting on the concrete near the bar (Murcia-Delso and Benson Shing, 2016). Based on the aforementioned phenomenon, Tassios and Vintzeleou (1987) have proposed a phenomenological model to describe the relationship between normal compressive stresses with steel stress:

$$\sigma_c = \rho\sigma_s, \tag{1}$$

where σ_c is the normal compressive stress acting on the interface, σ_s is the steel stress, and ρ is the reinforcement percentage.

Significant dilatancies are expected when cracks through reinforced piles occur due to the interlocking of the protruding aggregates (Millard and Johnson, 1984). The

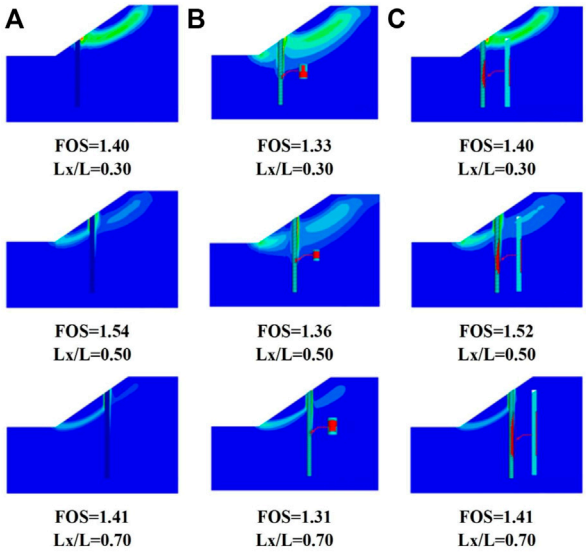

FIGURE 6
Positional variation of the slip surface near the middle of the slope for **(A)** the ECM, **(B)** DCM-U, and **(C)** DCM-B.

considerable dilatancy causes high tensile stresses in the bars. It is precisely due to this dilatancy performance that a frictional resistance from the reinforcing bar is an evident part of the total shear resistance on the cracking interface (Harries et al., 2012). To obtain the shear strength in the reinforced pile, a model established by Tassios and Vintzeleou (1987) is applied.

$$\tau_{fr,max} = \mu\sigma_{c,max}, \tag{2}$$

where $\tau_{fr,max}$ is the maximum shear stress due to friction, μ is the friction coefficient, and $\sigma_{c,max}$ is the maximum normal compressive stress acting on the interface. The $\tau_{fr,max}$ is regarded as the shear strength in the numerical analysis. The above damage constitutive model was coded into FLAC3D by the FISH programming language.

Model of a pile-reinforced slope

Figure 3 indicates a three-dimensional finite difference computational model of pile-reinforced slopes. An idealized slope with a height (H) of 10 m and a length (L) of 15 m is

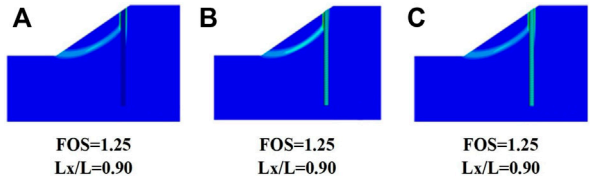

FIGURE 7
Positional variation of the slip surface at the top of the slope for **(A)** the ECM, **(B)** DCM-U, and **(C)** DCM-B.

simulated with the software FLAC3D. The bedrock is 15 m below the ground surface as a rigid base. A damage constitutive simulation models a pile with a diameter of 1 m. L_x is the horizontal distance from the slope toe to the pile. Hence, the ratio between L_x and L (L_x/L) can be represented by the installation location of the pile. Interface elements in FLAC3D are applied to assume the interface between the pile and the soil, and the stiffness (k_n) can be determined as follows (Itasca, 2006):

$$k_n = 10 \times max\left[\frac{\left(K + \frac{4}{3}G\right)}{\Delta Z_{min}}\right], \quad (3)$$

where K is the bulk moduli, G is the shear moduli, and the ΔZ_{min} is the minimum width of an adjacent zone in the normal direction. In the current study, the mechanical parameters were obtained from Cai and Ugai (2000). The mechanical parameters of the soil and the pile are summarized in Table 1.

Result and discussion

Pile-reinforced slope stability analysis

Figure 4 indicates that the FOS of the pile-reinforced slope varied along the location of the pile. Three pile models are applied in the simulations, namely, the elastic constitutive model (ECM), damage constitutive model considering a balanced-reinforced (DCM-B) pile, and under-reinforced (DCM-U) pile, respectively. Moreover, the results calculated by a finite element method under the same parameters are plotted in Figure 4, where the piles are treated as linear elastic solid material (Cai and Ugai, 2000). A comparison of the findings with those of Cai and Ugai (2000) shows that they are similar, which confirms that the damage constitutive model is valid. It can be observed that the FOSs are in a parabolic shape along the L_x/L, and the most forceful pile location is in the middle of the slope. Compared to the FOS of the ECM, the FOS calculated by the DCM-U makes an approximately 12% reduction at L_x/L = 0.5. Nevertheless, the maximum FOS of DCM-B is just 2% smaller than that of the ECM, which makes a slight reduction. Interestingly, the FOS considered by DCM-B is approximately equal to the FOS of the ECM at the whole range of L_x/L. The FOSs

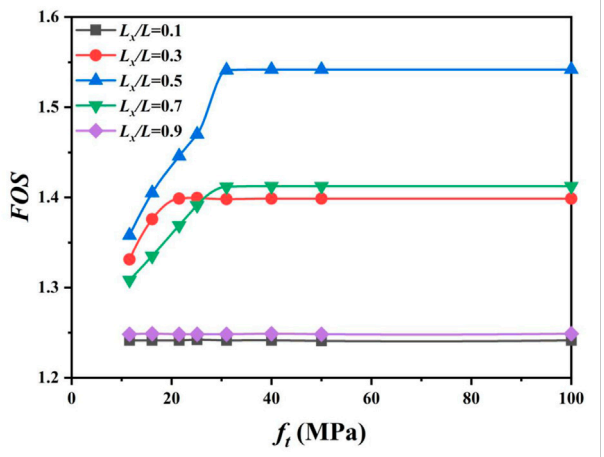

FIGURE 8
Effects of reinforcement ratio on pile–soil stability considering damage constitutive simulation.

obtained by DCM-B and DCM-U differ from those calculated by the ECM. The reason for this phenomenon is that the damage constitutive model can reflect the cracking development of the pile.

The observations are further expounded in Figures 5–7, which present the positional variation of a slip surface for elastic and damage constitutive models. The depth development of cracks on the pile is marked on the right side of the simulated pile. It can be seen in Figures 5–7 that the unstable slip surface will not pass through the pile when the pile installation location is close to the slope toe or crest. When the pile is positioned close to the middle of the slope (Figure 6), slope failure passes through the pile. Meanwhile, the different types of constitutive models reflect various responses of the piles. Cracks appear in the piles of DCM-B and DCM-U when the pile position is close to the middle of the slope, causing the reduction of the FOS. It can be seen that the level extension of cracks in the under-reinforced pile is much deeper than that in the balanced-reinforced pile. Cracks develop across the cross-section of the under-reinforced pile, while cracks are just presented on the concrete cover of the balance-reinforced pile. Hence, the FOS obtained from DCM-U is smaller than that calculated by the ECM and DCM-B. The damage constitutive model can reflect the influence of cracks on the tensile strength of the pile, which would make a more precise and realistic analysis of the slope stability. The existence of cracks on the pile is not negligible in slope engineering, which would decrease the FOS of the slope. The traditional elastic constitutive model regarded piles as a material without damage, and hence, the stability of the slope will be overestimated. The overestimated factor of slope stability is potentially dangerous in geotechnical engineering. Therefore, it is necessary to simulate piles by the damage constitutive model in pile–slope stability analysis.

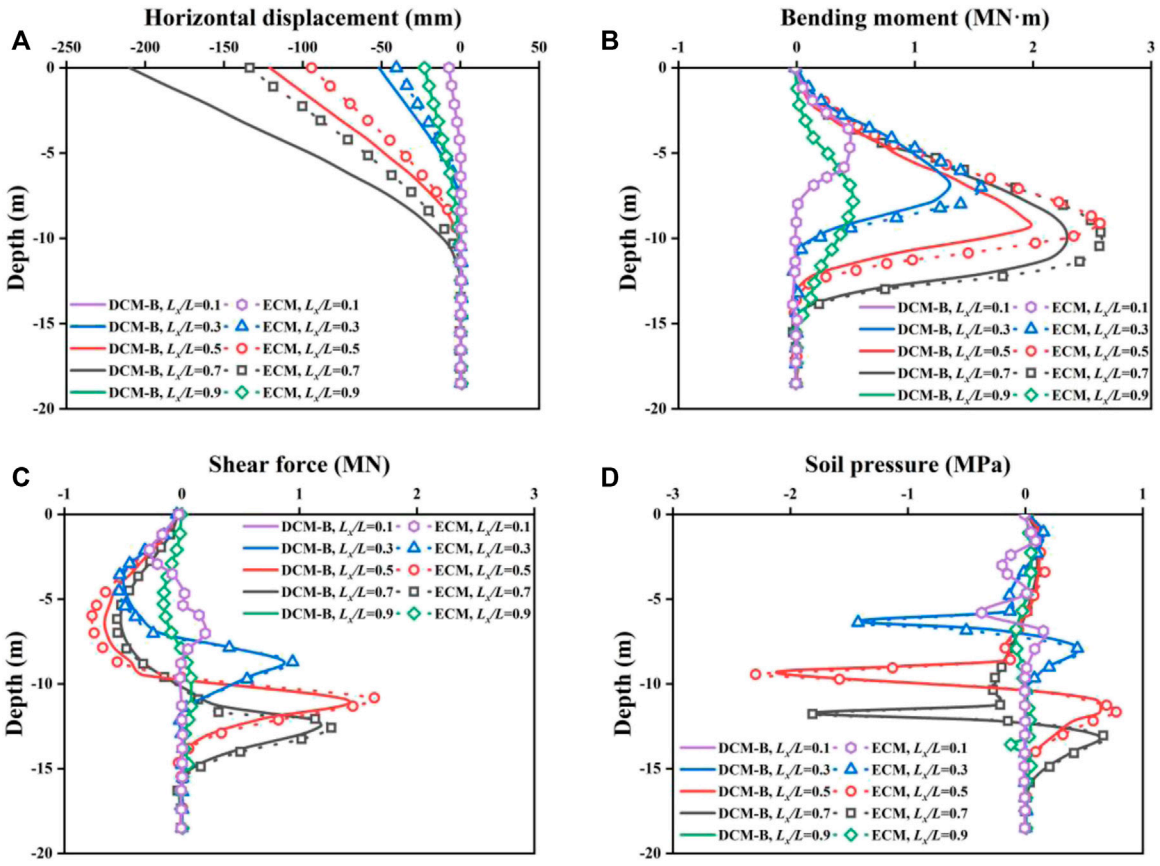

FIGURE 9
Pile behavior characteristics of **(A)** horizontal displacement, **(B)** bending moment, **(C)** shear force, and **(D)** soil pressure for elastic and damage constitutive models.

Figure 8 represents the relationship between the pile's reinforcement ratio and the FOS on the slope. The reinforcement ratio could be equivalent to the tensile strength of the pile (f_t) in this study. The five damage constitutive models with pile positions (L_x/L = 0.1, 0.3, 0.5, 0.7, and 0.9) were compared. When the pile was installed near the top or toe of the slope (L_x/L = 0.1 and 0.9), the f_t affected the FOS slightly. It can be indicated that the FOS, which is the pile position close to the middle of the slope, increases to a constant value in the whole range of f_t. The peak value of the FOS appeared when the f_t was approximately 30 MPa, which means the pile is a balance-reinforced pile. When the pile is under-reinforced, the f_t is less than that of the balance-reinforced pile, and hence, the FOS would be reduced. In addition, the over-reinforced pile made a small contribution to the FOS, which is uneconomical in engineering. This is because the tensile failure would occur on the concrete of the pile instead of the bar. The optimum reinforcement ratio of the pile could be determined by the damage constitutive model at specific slope engineering, which can avoid the appearance of the under-reinforced and over-reinforced piles.

Pile responses in slope failure

Figure 9 summarizes the distribution of pile behavior characteristics along the depth under the action of landslide, including 1) horizontal displacement, 2) bending moment, 3) shear force, and 4) soil pressure. Pile responses at the specific position were obtained from elastic (ECM) and damage constitutive simulation (DCM-B). The results observed from the ECM and DCM-B are consistent with each other only at L_x/L = 0.1 and 0.9, respectively.

It can be seen from Figure 9A that the lateral deformation is reduced to zero at a depth of approximately 13 m. The horizontal deformation of the pile top of the DCM-B at L_x/L = 0.7 is the biggest, with a value of 210 mm. The slightest lateral deformation of the pile toe is 7.2 mm at L_x/L = 0.1. The displacement of the ECM is smaller by 57% than that of the DCM-B at L_x/L = 0.7, which is an enormous difference. The pile deformation calculated by the DCM-B is more significant than the ECM. Nevertheless, the bending moments of the pile obtained from DCM-B are smaller than that from the ECM at L_x/L = 0.3, 0.5, and 0.7.

Figure 9B shows that the bending moment increases at first and then decreases along the depth. The maximum bending moments at all pile positions occur at the boundary between the natural soil and bedrock. The reason for this phenomenon is that Young's modulus (E) of natural soil (200 MPa) is relatively smaller than that of bedrock (3000 MPa), which has been shown in Table 1. The apparent distinction of E at the boundary would lead to the stress concentration of the pile, and hence, the maximum bending moment was caused. Additionally, the difference in internal forces between the DCM-B (2.0 MN·m) and the EMC (2.6 MN·m) is most significant at L_x/L = 0.5.

A similar observation can be found in Figure 9C, which plots the distribution of shear force along the depth. At L_x/L = 0.5, the maximum negative and positive shear force of DCM-B is 17% and 18%, respectively, smaller than those of the ECM. It can be observed that the distribution law of shear force with different pile positions and constitutive models is similar. With the increase of depth, the maximum negative shear force occurs first, and then the maximum positive shear force appears. The depths, where the shear force of piles located at Lx/L = 0.1, 0.3, 0.5, 0.7, and 0.9 is zero, are approximately 5.5, 7.5, 9.5, 10, and 8 m, respectively. Concurrently, the bending moment reaches the maximum value at the corresponding depth where the shear force is zero.

The variations of soil pressure along the depth are presented in Figure 9D. The maximum soil pressure of the pile at L_x/L = 0.1 (0.37 MPa) and 0.9 (0.12 MPa) is smaller than that at other positions, which indicates that the reinforced effect of the pile on the soil is slightly at the top or toe of the slope. At L_x/L = 0.5, the DCM-B results for soil pressures disagree slightly with the data observed by the ECM at 9.0-m and 11.7-m depth. It is expected that the pile is to be installed at the middle of the slope (L_x/L = 0.5), there is an apparent agreement of the simulated data for the soil pressure in the DCM-B and the ECM.

Figure 9 further explains the dissimilarity of FOS in DCM-B and ECM piles. The neglect of pile plastic failure rigidity tends to overestimate the pile capacity. The damage constitutive model can reflect the irreversible plastic deformation of the balance-reinforced pile. Therefore, compared to the elastic constitutive model, the damage model predicted larger lateral displacements and a smaller internal force in the pile at a specific condition.

Conclusion

The purpose of the current study was to propose a damage constitutive model to assess the stability of the pile-reinforced slope. The pile was simulated by the damage constitutive model to investigate the influence of the pile's installation position and reinforcement ratio on the stability of the pile-reinforced slope. It has been demonstrated that the FOS calculated by the elastic and damage constitutive models are different only when the pile was damaged. The difference in the FOS between the ECM and DCM could be more than 12% when L_x/L was equal to 0.5. The second significant finding is that the influence of the reinforcement ratio on a pile-reinforced slope could be reflected by the damage constitutive model. The balance-reinforced pile (FOS = 1.54 and L_x/L = 0.5) increased the FOS by 14% more than the under-reinforced pile (FOS = 1.36 and L_x/L = 0.5). Moreover, the horizontal displacement, bending moments, shear force, and soil pressure along the pile shaft versus the depth below the ground surface were studied. The results illustrated that the traditional elastic damage model would overestimate the internal force in a pile, which can be visibly detected in the bending moments (the maximum difference of bending moment is 30%). The advantage of the damage constitutive model is that the existence of a crack on a pile can be expressed by the reduction of tensile strength, which provides the reference for the slope engineering design.

Data availability statement

The original contributions presented in the study are included in the article/Supplementary Material; further inquiries can be directed to the corresponding author.

Author contributions

J-HJ: investigation, validation, and methodology. X-LH: post-processing data and analysis and writing—original draft. XS: writing—review and editing. XN: numerical simulation. YQ: methodology. WX: analysis.

Conflict of interest

The authors declare that the research was conducted in the absence of any commercial or financial relationships that could be construed as a potential conflict of interest.

Publisher's note

All claims expressed in this article are solely those of the authors and do not necessarily represent those of their affiliated organizations, or those of the publisher, the editors, and the reviewers. Any product that may be evaluated in this article, or claim that may be made by its manufacturer, is not guaranteed or endorsed by the publisher.

References

Ashour, M., and Ardalan, H. (2012). Analysis of pile stabilized slopes based on soil–pile interaction. *Comput. Geotechnics* 39, 85–97. doi:10.1016/j.compgeo.2011.09.001

Bai, B., Wang, Y., Rao, D., and Fan, B. (2022). The effective thermal conductivity of unsaturated porous media deduced by pore-scale SPH simulation. *Front. Earth Sci. (Lausanne).* 10. doi:10.3389/feart.2022.943853

Bai, B., Yang, G., Tao, L., and Yang, G. (2019). A thermodynamic constitutive model with temperature effect based on particle rearrangement for geomaterials. *Mech. Mater.* 139, 103180. doi:10.1016/j.mechmat.2019.103180

Bai, B., Zhou, R., Cai, G., Hu, W., and Yang, G. (2021). Coupled thermo-hydro-mechanical mechanism in view of the soil particle rearrangement of granular thermodynamics. *Comput. Geotechnics* 137 (8), 104272. doi:10.1016/j.compgeo.2021.104272

Bakri, M., Xia, Y. Y., and Wang, H. B. (2014). Numerical analysis of stabilization of slopes overlying bedrock using piles and effect of socketed length of pile on stability. *Appl. Mech. Mater.* 580, 424–431. Trans Tech Publications Ltd. doi:10.4028/www.scientific.net/amm.580-583.424

Cai, F., and Ugai, K. (2000). Numerical analysis of the stability of a slope reinforced with piles. *Soils Found.* 40 (1), 73–84. doi:10.3208/sandf.40.73

Cedolin, L. Darwin, D. Ingraffea, A. R. Pecknold, E. A. and Schnobrich, W. C. (1982). *Concrete cracking." State of the art Rep. on finite element analysis of reinforced concrete*. New York: ASCE, 204–233.

Chen, H., Zhang, G., Chang, Z., Wen, L., and Gao, W. (2021). Failure analysis of a highway cut slope with anti-slide piles. *Geofluids* 2021, 6622214. doi:10.1155/2021/6622214

Chen, Z., Wang, Z., Xi, H., Yang, Z., Zou, L., Zhou, Z., et al. (2016). Recent advances in high slope reinforcement in China: Case studies. *J. Rock Mech. Geotechnical Eng.* 8 (6), 775–788. doi:10.1016/j.jrmge.2016.11.001

Cheng, Z., and Jeremić, B. (2009). Numerical modeling and simulation of pile in liquefiable soil. *Soil Dyn. Earthq. Eng.* 29 (11-12), 1405–1416. doi:10.1016/j.soildyn.2009.02.008

Comodromos, E. M., Papadopoulou, M. C., and Rentzeperis, I. K. (2009). Effect of cracking on the response of pile test under horizontal loading. *J. Geotech. Geoenviron. Eng.* 135 (9), 1275–1284. doi:10.1061/(asce)gt.1943-5606.0000069

Dai, Z., Yang, J., Dai, R., and Zhu, Q. (2022). Three-dimensional and threefold nonlinear numerical modeling for slope-stabilizing pile. *KSCE J. Civ. Eng.* 26, 4390–4406. doi:10.1007/s12205-022-1474-6

Gu, X. J., Zhou, T. Q., and Lu, S. L. (2014). Stability analysis on anti-slide pile to reinforce slope based on ABAQUS. *Appl. Mech. Mater.* 580, 711–714. Trans Tech Publications Ltd. doi:10.4028/www.scientific.net/amm.580-583.711

Harries, K. A., Zeno, G., and Shahrooz, B. (2012). Toward an improved understanding of shear-friction behavior. *ACI Struct. J.* 109 (6), 835.

Hassen, G., Dias, D., and de Buhan, P. (2009). Multiphase constitutive model for the design of piled-embankments: Comparison with three-dimensional numerical simulations. *Int. J. Geomech.* 9 (6), 258–266. doi:10.1061/(asce)1532-3641(2009)9:6(258)

He, Y., Hazarika, H., Yasufuku, N., and Han, Z. (2015c). Evaluating the effect of slope angle on the distribution of the soil–pile pressure acting on stabilizing piles in sandy slopes. *Comput. Geotechnics* 69, 153–165. doi:10.1016/j.compgeo.2015.05.006

He, Y., Hazarika, H., Yasufuku, N., Han, Z., and Li, Y. (2015a). Three-dimensional limit analysis of seismic displacement of slope reinforced with piles. *Soil Dyn. Earthq. Eng.* 77, 446–452. doi:10.1016/j.soildyn.2015.06.015

He, Y., Hazarika, H., Yasufuku, N., Teng, J., Jiang, Z., and Han, Z. (2015b). Estimation of lateral force acting on piles to stabilize landslides. *Nat. Hazards (Dordr).* 79 (3), 1981–2003. doi:10.1007/s11069-015-1942-0

Henke, S. (2010). Influence of pile installation on adjacent structures. *Int. J. Numer. Anal. methods geomechanics* 34 (11), 1191–1210. doi:10.1002/nag.859

Huang, Y., Xu, X., and Mao, W. (2020). Numerical performance assessment of slope reinforcement using a pile-anchor structure under seismic loading. *Soil Dyn. Earthq. Eng.* 129, 105963. doi:10.1016/j.soildyn.2019.105963

Itasca (2006). *Fast Lagrangian analysis of continua in 3 dimensions*. Minneapolis, USA: User's Manual, Itasca Consulting Group. Version 3.1.

Jamsawang, P., Bergado, D. T., and Voottipruex, P. (2015). "Full-scale tests on stiffened deep cement mixing piles including three-dimensional finite element simulation," in *Ground improvement case histories* (Oxford: Butterworth-Heinemann), 31–77.

Jeong, S., Kim, B., Won, J., and Lee, J. (2003). Uncoupled analysis of stabilizing piles in weathered slopes. *Comput. Geotechnics* 30 (8), 671–682. doi:10.1016/j.compgeo.2003.07.002

Jiang, Q., Qi, Z., Wei, W., and Zhou, C. (2015). Stability assessment of a high rock slope by strength reduction finite element method. *Bull. Eng. Geol. Environ.* 74 (4), 1153–1162. doi:10.1007/s10064-014-0698-1

Kavitha, P. E., Beena, K. S., and Narayanan, K. P. (2016). A review on soil–structure interaction analysis of laterally loaded piles. *Innov. Infrastruct. Solut.* 1 (1), 14–15. doi:10.1007/s41062-016-0015-x

Larsson, S., Malm, R., Charbit, B., and Ansell, A. (2012). Finite element modelling of laterally loaded lime–cement columns using a damage plasticity model. *Comput. Geotechnics* 44, 48–57. doi:10.1016/j.compgeo.2012.03.004

Lee, C. Y., Hull, T. S., and Poulos, H. G. (1995). Simplified pile-slope stability analysis. *Comput. Geotechnics* 17 (1), 1–16. doi:10.1016/0266-352x(95)91300-s

Lin, Y. L., Cheng, X. M., Yang, G. L., and Li, Y. (2018). Seismic response of a sheet-pile wall with anchoring frame beam by numerical simulation and shaking table test. *Soil Dyn. Earthq. Eng.* 115, 352–364. doi:10.1016/j.soildyn.2018.07.028

Maekawa, K., and Qureshi, J. (1997). Stress transfer across interfaces in reinforced concrete due to aggregate interlock and dowel action. *Dob. Gakkai Ronbunshu* 1997 (557), 159–172. doi:10.2208/jscej.1997.557_159

Martin, G. R., and Chen, C. Y. (2005). Response of piles due to lateral slope movement. *Comput. Struct.* 83 (8-9), 588–598. doi:10.1016/j.compstruc.2004.11.006

Millard, S. G., and Johnson, R. P. (1984). Shear transfer across cracks in reinforced concrete due to aggregate interlock and to dowel action. *Mag. Concr. Res.* 36 (126), 9–21. doi:10.1680/macr.1984.36.126.9

Murcia-Delso, J., and Benson Shing, P. (2016). Elastoplastic dilatant interface model for cyclic bond-slip behavior of reinforcing bars. *J. Eng. Mech.* 142 (2), 04015082. doi:10.1061/(asce)em.1943-7889.0000994

Poulos, H. G. (1995). Design of reinforcing piles to increase slope stability. *Can. Geotech. J.* 32 (5), 808–818. doi:10.1139/t95-078

Qu, H. L., Luo, H., Hu, H. G., Jia, H. Y., and Zhang, D. Y. (2018). Dynamic response of anchored sheet pile wall under ground motion: analytical model with experimental validation. *Soil Dyn. Earthq. Eng.* 115, 896–906. doi:10.1016/j.soildyn.2017.09.015

Rahardjo, H., Hritzuk, K. J., Leong, E. C., and Rezaur, R. B. (2003). Effectiveness of horizontal drains for slope stability. *Eng. Geol.* 69 (3-4), 295–308. doi:10.1016/s0013-7952(02)00288-0

Sharafi, H., and Sojoudi, Y. (2016). Experimental and numerical study of pile-stabilized slopes under surface load conditions. *Int. J. Civ. Eng.* 14 (4), 221–232. doi:10.1007/s40999-016-0017-2

Sun, H. Y., Wong, L. N. Y., Shang, Y. Q., Shen, Y. J., and Lü, Q. (2010). Evaluation of drainage tunnel effectiveness in landslide control. *Landslides* 7 (4), 445–454. doi:10.1007/s10346-010-0210-3

Tassios, T. P., and Vintzêleou, E. N. (1987). Concrete-to-concrete friction. *J. Struct. Eng. (N. Y. N. Y).* 113 (4), 832–849. doi:10.1061/(asce)0733-9445(1987)113:4(832)

Won, J., You, K., Jeong, S., and Kim, S. (2005). Coupled effects in stability analysis of pile–slope systems. *Comput. Geotechnics* 32 (4), 304–315. doi:10.1016/j.compgeo.2005.02.006

Xu, X., and Huang, Y. (2021). Parametric study of structural parameters affecting seismic stability in slopes reinforced by pile-anchor structures. *Soil Dyn. Earthq. Eng.* 147, 106789. doi:10.1016/j.soildyn.2021.106789

Yan, M., Xia, Y., Liu, T., and Bowa, V. M. (2019). Limit analysis under seismic conditions of a slope reinforced with prestressed anchor cables. *Comput. Geotechnics* 108, 226–233. doi:10.1016/j.compgeo.2018.12.027

Yapage, N. N. S., Liyanapathirana, D. S., Poulos, H. G., Kelly, R. B., and Leo, C. J. (2015). Numerical modeling of geotextile-reinforced embankments over deep cement mixed columns incorporating strain-softening behavior of columns. *Int. J. Geomech.* 15 (2), 04014047. doi:10.1061/(asce)gm.1943-5622.0000341

Zheng, G., Yang, X., Zhou, H., and Chai, J. (2018). Numerical modeling of progressive failure of rigid piles under embankment load. *Can. Geotech. J.* 56 (1), 23–34. doi:10.1139/cgj-2017-0613

Zheng, Y., Chen, C., Liu, T., Song, D., and Meng, F. (2019). Stability analysis of anti-dip bedding rock slopes locally reinforced by rock bolts. *Eng. Geol.* 251, 228–240. doi:10.1016/j.enggeo.2019.02.002

frontiers | Frontiers in Materials

TYPE Original Research
PUBLISHED 01 December 2022
DOI 10.3389/fmats.2022.1084906

Check for updates

OPEN ACCESS

EDITED BY
Bing Bai,
Beijing Jiaotong University, China

REVIEWED BY
Yong Yuan,
China University of Mining and Technology, China
Yu Wang,
University of Science and Technology Beijing, China

*CORRESPONDENCE
Zhangjun Dai,
zjdai@whrsm.ac.cn

SPECIALTY SECTION
This article was submitted to Structural Materials,
a section of the journal
Frontiers in Materials

RECEIVED 31 October 2022
ACCEPTED 21 November 2022
PUBLISHED 01 December 2022

CITATION
Dai Z, Wang Y, Zhou Z, Li J, Yu F and Chen S (2022), Analysis of the deterioration process of the dolomite with the interlayer in different directions during wetting.
Front. Mater. 9:1084906.
doi: 10.3389/fmats.2022.1084906

COPYRIGHT
© 2022 Dai, Wang, Zhou, Li, Yu and Chen. This is an open-access article distributed under the terms of the Creative Commons Attribution License (CC BY). The use, distribution or reproduction in other forums is permitted, provided the original author(s) and the copyright owner(s) are credited and that the original publication in this journal is cited, in accordance with accepted academic practice. No use, distribution or reproduction is permitted which does not comply with these terms.

Analysis of the deterioration process of the dolomite with the interlayer in different directions during wetting

Zhangjun Dai[1]*, Yinhui Wang[1,2], Zhe Zhou[1,2], Jian Li[1], Fei Yu[1] and Shanxiong Chen[1]

[1]State Key Laboratory of Geomechanics and Geotechnical Engineering, Institute of Rock and Soil Mechanics, Chinese Academy of Sciences, Wuhan, China, [2]University of Chinese Academy of Sciences, Beijing, China

Taking the dolomite with anhydrite interlayer at the bottom of Huangcaoshan Tunnel in Shanghai-Wuhan-Chengdu high-speed railway as the research object, the wetting deterioration and uniaxial compression tests were performed to study the influence of different interlayer orientations on the hygroscopic deterioration characteristics of rock and to analyze the process of rock deterioration. The wetting cracking and deformation characteristics of dolomite with interlayer in different directions were analyzed respectively from the time effect of rock micro-expansion and the change of ultrasonic longitudinal wave velocity, and the uniaxial compression evolution process of samples with different moisture absorption conditions and interlayer directions was analyzed respectively from the aspects of crack volume strain and energy dissipation. The results show that the direction of interlayer had a significant effect on the wetting and deterioration of the rock. The sample with vertical interlayer cracked obviously during wetting, resulting in volume expansion along the axial and radial directions of the sample; However, the sample with horizontal interlayer had almost only axial volume expansion, and the expansion rate was small. After the rock was wet and deteriorated, the propagation velocity of ultrasonic longitudinal wave in the rock decreased, and the decrease amplitude in the sample with vertical interlayer was greater than that in the sample with horizontal interlayer. After rock wetting, its uniaxial compressive strength, crack initiation level, expansion level, and the threshold value of elastic strain energy density for failure decreased, while the radial peak strain, the energy conversion rate of dissipation increased, and the plastic characteristics of the sample were enhanced, and the sample with vertical interlayer changed significantly compared with the sample with horizontal interlayer.

KEYWORDS

deterioration process, dolomite, anhydrite, interlayer, wetting, uniaxial compression

1 Introduction

Water rock interaction exists widely in various practical geotechnical engineering. Under the action of water, the rock will often be softened, cracked, expanded, disintegrated and other deterioration phenomena (Zhao et al., 2021; Zhou K. et al., 2022; Feng et al., 2022; Li et al., 2022), and this deterioration of rock in water has a great impact on the safety of various engineering construction (Bai et al., 2021; Du et al., 2022; Fu et al., 2022). Therefore, the research on the law of rock wetting deterioration has always been the focus of researchers (Jiang et al., 2015; Hua et al., 2019).

In terms of the cracking, disintegration and expansion effect of rocks under the action of water and rock. Zeng et al. (2019) took the completely disintegrated carbonaceous mudstone as the research object, and used the image processing technique to analyze the crack evolution process and geometric characteristics of the sample under the action of dry-wet cycle. Chai et al. (2015) based on the comparative test of the slaking resistance of mudstone in coal measures in different diagenetic stages, used XRD (X-ray Diffraction) and mercury intrusion tests to find that the difference in the slaking resistance of mudstone was mainly related to the mineral composition, rock pore and crack structure. Yang (2017), Diao et al. (2017) studied the hygroscopic expansion characteristics and water migration laws of mudstone under different temperature and humidity conditions. He et al. (2019) carried out indoor expansion characteristics tests on red-bed soft rocks of different lithology in a tunnel area, and found that the logarithm of expansion force was linear with expansion strain, the expansion force was positively correlated with dry unit weight and water absorption, and negatively correlated with initial moisture content. Ma (2015) studied the deformation law, development process, development stage and micro expansion mechanism of the micro expansion deformation of low clay mineral mudstone.

In terms of softening of the mechanical properties of rocks under the action of water and rock, Zhou et al. (2005) conducted mechanical tests on different types of rocks such as sandstone, mudstone and carbonaceous mudstone with different immersion times, and found that their compressive strength, tensile strength and shear strength decreased exponentially with the saturation time. Cai et al. (2021) conducted direct shear tests on phyllite under different immersion conditions and found that the cohesion was most affected by immersion conditions, the peak stress was second, and the internal friction angle was the smallest. Jiang et al. (2022) established the damage constitutive model of sandstone under the water rock interaction through the experimental analysis, combined with the deduction of statistical strength theory and damage mechanics. Uniaxial compression characteristics, as one of the indispensable indexes to measure the basic physical and mechanical properties of rocks, are widely used in various engineering practices and scientific research work because of its relatively simple and clear test principles and easily realized test equipment. He et al. (2022) carried out uniaxial compression test on sandstone, and found that with the increase of moisture content, the nonlinear characteristics of the rock stress-strain curve at the initial stage and the drop phenomenon after the strength peak became more obvious, and the sample changed from splitting failure to shear failure. Song et al. (2021) established a sandstone deterioration model under dry wet cyclic loading through uniaxial compression test and acoustic emission testing technology. Zhang et al. (2020) compared the difference of stress threshold under different calculation methods based on the uniaxial compression test of siliceous siltstone, and provided an optimization method for obtaining the stress threshold. Zhang et al. (2021) analyzed the influence of the crack dip angle on the crack initiation stress, peak strength, stress-strain curve characteristics and failure mode of rock during uniaxial compression. Hou et al. (2019) explored the anisotropy law in the process of rock energy conversion through energy analysis of the uniaxial compression process of layered marble. Tang et al. (2022) studied the influence of loading rate on energy evolution characteristics during uniaxial compression of rocks.

Therefore, researchers have made a lot of achievements in the study of rock wetting deterioration effect. However, the previous studies mostly focused on the deterioration effect of relatively homogeneous soft rock, while the research on the wetting deterioration effect of hard rock containing expansive materials in non-expansive rock, especially on the change of rock uniaxial compression characteristics before and after deterioration, was less. For this reason, this study selected dolomite with anhydrite interlayer at the tunnel bottom in the abnormal deformation section of high-speed railway as the research object, conducted wetting deterioration test on it, obtained the change characteristics of free expansion rate with time, and quantitatively evaluated its deterioration based on the measured changes of acoustic velocity before and after deterioration. Finally, based on the uniaxial compression test, the uniaxial compression process was analyzed from the perspective of crack volume strain and energy dissipation, and the effects of different interlayer directions and wetting conditions on the compression process and mechanical characteristics were compared. This study revealed the mechanism of moisture absorption expansion and deterioration of interlayered dolomite, and provided a scientific basis for the analysis of abnormal deformation of subgrade and track, especially uplift deformation of high-speed railway and other projects. It provided important reference for railway engineering construction and geological disaster prevention.

2 Materials

2.1 Engineering geological characteristics

The sampling site was located in Huangcaoshan Tunnel, Changshou County, Chongqing, China. This tunnel was a high-

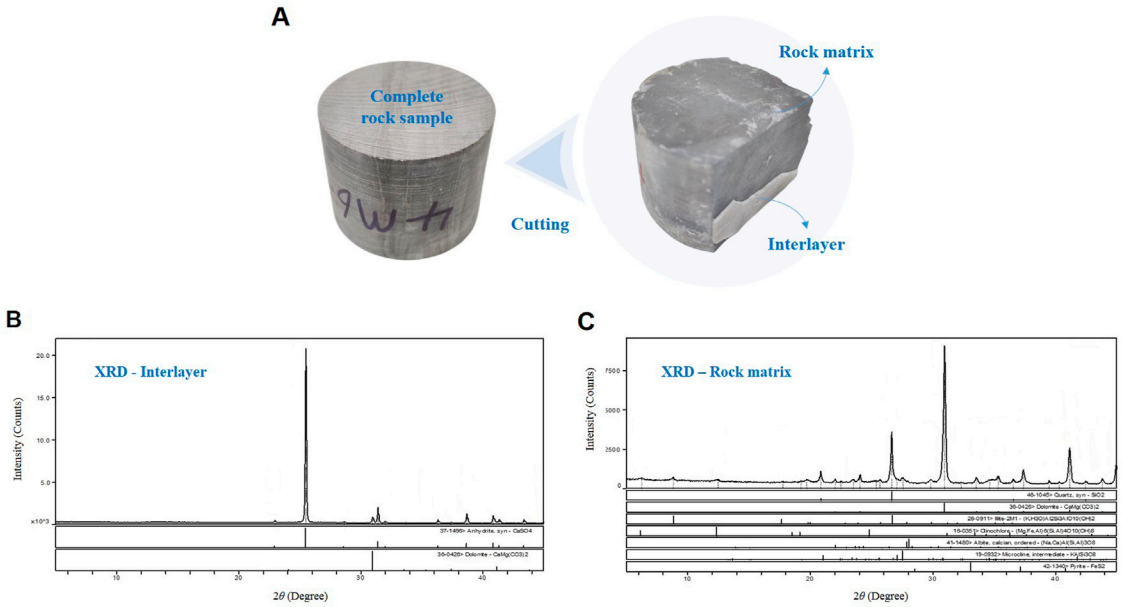

FIGURE 1
XRD pattern for the dolomite with the interlayer **(A)** Schematic diagram of rock matrix and interlayer **(B)** XRD pattern for interlayer **(C)** XRD pattern for rock matrix.

speed railway tunnel, and the stratum it passed through was located at the top of a box anticline. The rock stratum at the tunnel bottom was Leikoupo Formation of Middle Triassic (T_2l), mainly composed of gray and light gray dolomite and limestone, medium-thick layered, with good water permeability. There were thin layers of gypsum and anhydrite in the rock stratum. The rock samples used in this study were mainly dolomite. The rock was relatively complete with developed cracks. Some rock samples had no complete structure and were scattered. The average density of rock samples was 2.83 g/cm^3, the moisture content ranges from 0.03% to 0.29%, and the average moisture content was 0.20%.

2.2 Mineral composition

The rock sample contains interlayers. Samples were taken from the rock matrix and interlayers respectively. After rolling, it should pass 0.05 mm sieve, and then it was dried for preparation. The mineral composition was analyzed by X-ray diffraction. The analysis results were shown in Figure 1. Anhydrite occurred in dolomite in the form of thin interlayer, visible to the naked eye, with the thickness between 0.1 and 2.0 mm, and most of them were less than 0.5 mm. The rock was mainly composed of dolomite, containing a certain amount of clay minerals (illite, chlorite, *etc.*) and siliceous (quartz) cements, and anhydrite, an expansive mineral, also accounted for a certain proportion in the rock. Among them, in the interlayer, anhydrite accounted for 93.1% and dolomite accounted for 6.9%. The rock matrix consisted of 73.9% dolomite, 13.8% quartz, 8.0% clay minerals, and a small amount of feldspar and pyrite.

2.3 Microstructure

The microstructure of different parts of the sample was analyzed by scanning electron microscope. Figure 2 shows the rock SEM (Scanning Electron Microscope) microstructure. It showed that dolomite, anhydrite, illite and other mineral particles could be seen in the rock. Most dolomite crystals were in the form of semi idiomorphic to idiomorphic inlaid contact, with flat boundaries, and the crystals were mostly connected by crystal planes (Figure 2A). The anhydrite crystal structure was compact fiber collection, plate or sheet stacking, and its fibrous crystal features were obvious. The crystals were closely arranged, orderly, multi-layer overlapping, three-dimensional, and the crystal surface was smooth and shiny, with occasional bumps and depressions (Figure 2B). The results also showed significant flocculent clay mineral distribution, some of which had obvious microcracks. The clay particles were curved and curly, and most of them were in the form of face to face overlapping and

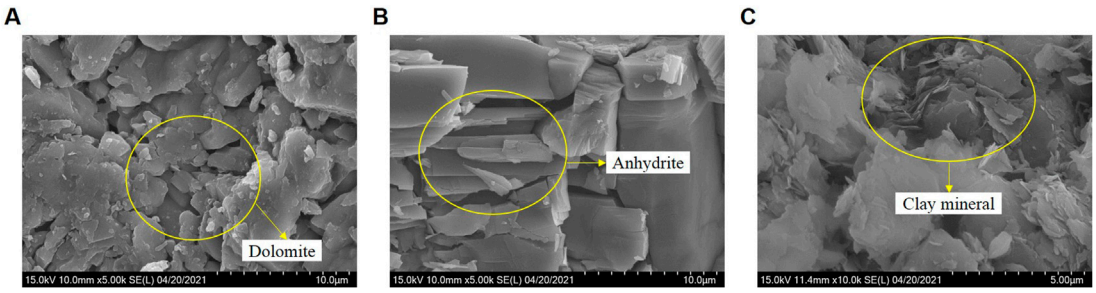

FIGURE 2
SEM results **(A)** Dolomite **(B)** Anhydrite **(C)** Clay mineral.

edge to face overlapping, thus forming a relatively dense form (Figure 2C).

From the XRD and SEM test results, it could be seen that the rock had the potential of expansion and wetting deterioration. It provided the material and structural basis for the interlayer effect and crack expansion effect of rock.

3 Deterioration characteristics of rocks in different interlayer directions after wetting

The free expansion rate is the ratio of the increment of rock expansion to the initial size of the sample under no load conditions. The obtained rock was polished and made into the sample, and then put it into a self-developed dilatometer for three-way expansion rate test. After water injection, observed the three-dimensional deformation of the sample, and monitored the rock cracking characteristics and expansion time history change law.

Many researchers have found that there is a positive correlation between the longitudinal wave velocity and the compactness of the rock's internal structure (Anderson et al., 1974; King et al., 1995; Jia et al., 2019). The denser and more uniform the structure, the higher the wave velocity value. On the contrary, if the sample is looser and the internal voids are more, the measured wave velocity will be lower. Therefore, in this study, the corresponding samples were taken for rock acoustic velocity test to explore the change of longitudinal wave velocity of rock under the initial conditions of samples and after immersion and air drying.

3.1 Sample preparation

The test samples were taken from the tunnel bottom in the abnormal deformation section of the high-speed railway Huangcaoshan Tunnel. The samples were taken from the rock stratum by means of drilling and sampling, and the core drilling and cutting processing were carried out in the laboratory. In order to reduce the dispersion of the samples, the original rocks of the test samples were taken from the same location at the tunnel bottom. Limited to the on-site drilling conditions and considering as much as possible the interlayers of the samples, the rock was processed into cylinder samples with the diameter of 50 mm and the height of 40 mm, and their two ends and sides were carefully polished to make the unevenness of both ends less than 0.05 mm.

3.2 Wetting deterioration test

In order to facilitate the subsequent test and realize the uniaxial compression of the sample along the interlayer direction after wetting and deterioration, a group of vertical interlayer samples (JZ-1, JZ-2, JZ-3) was selected for the free expansion rate test, and another group of horizontal interlayer samples (JH-1, JH-2, JH-3) was taken as the control group. The schematic diagram of core drilling sampling and finished samples are shown in Figure 3. The acoustic longitudinal wave velocity of rock was tested under the initial conditions and after the natural conditions were dried until the sample quality no longer changes after immersion, and the acoustic wave velocity changes before and after rock wetting and deterioration were analyzed.

The self-developed three-way expansion rate instrument was used to conduct the three-way free expansion rate test of rock, as shown in Figure 4. Holes were reserved in the center of the plexiglass on four sides, and dial indicators were installed to monitor the radial deformation of the sample. A dial indicator was equipped on the top of the instrument to monitor the axial deformation of the sample.

Rock acoustic velocity test adopted ultrasonic pulse penetration method to conduct longitudinal wave test on samples. The test instrument was RSM-SY6 intelligent acoustic detector produced by Institute of Rock and Soil

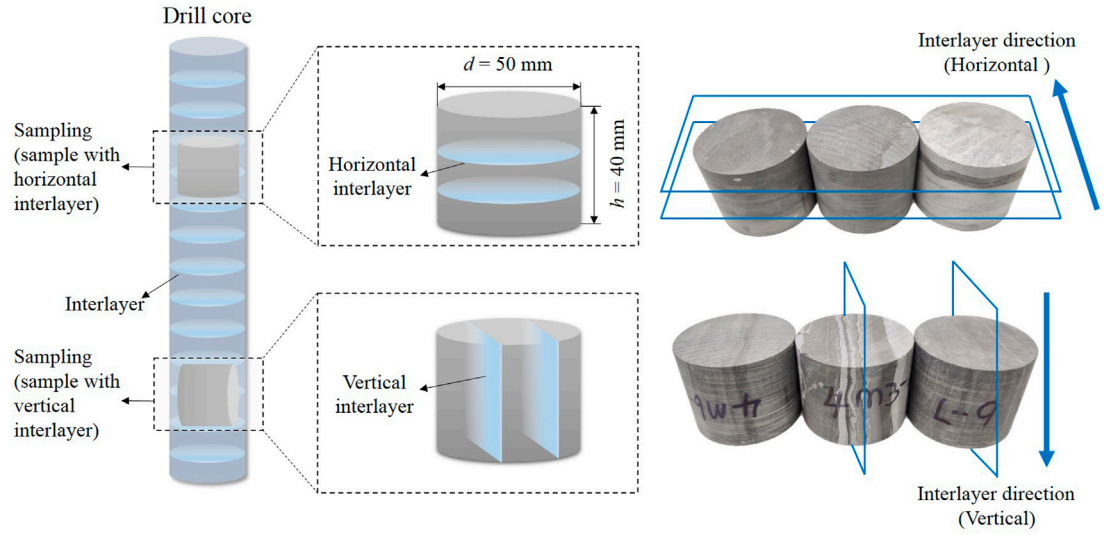

FIGURE 3
Sampling diagram and dolomite sample with interlayer in different directions.

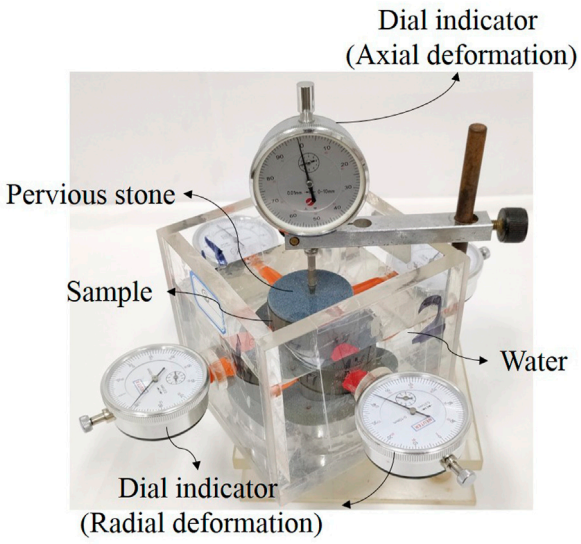

FIGURE 4
Test device for three-way expansion rate of rock.

Mechanics, Chinese Academy of Sciences. The low pass frequency of longitudinal wave transducer was 60 kHz, the high pass frequency was 0.1 kHz, and the sampling interval was 0.1 μs. During the test, ultrasonic flaw detection couplant was used to couple the longitudinal wave transducer with the sample, and a certain pressure was applied to make the transducer closely fit with the end face of the sample, and longitudinal wave velocity was tested one by one.

3.3 Analysis of deterioration characteristics of rock after wetting

The final axial and average radial expansion rates of each sample are shown in Table 1. Each sample of the vertical interlayer had obviously cracked after immersion, as shown in Figure 5. The main cracks developed along the direction of the interlayer, accompanied by a small number of secondary cracks with a certain angle to the vertical direction. After the test, the sample was looser than the original sample, which was also consistent with the results of longitudinal wave velocity test of rock. Although the horizontal interlayer sample had axial and radial expansion, the expansion amount was obviously smaller than that of the vertical interlayer sample, and the sample had no obvious cracking.

Figure 6 shows the change curves of the axial and average radial expansion rates with time for the typical JZ-3 sample with vertical interlayer and JH-2 sample with horizontal interlayer respectively. The sample with vertical interlayer reached stability after 58 h, and the whole process of immersion expansion and deformation of the sample in axial and radial directions could be divided into four stages, starting stage, rapid growth stage, decelerating growth stage and gradually stabilizing stage. The final average radial expansion rate of the sample was 0.728%, the axial expansion rate was 0.470%, and the average radial expansion rate was 54.9% greater than the axial expansion rate. However, the sample with horizontal interlayer reached stability after 86 h, and its axial and radial expansion rate curves were all in a stepwise rising shape, that was, after the initial rapid growth stage, the sample entered a deceleration or gradually stable stage, but after a period of time, it would continue to enter

TABLE 1 Test results of expansion rate and longitudinal wave velocity.

Sample no.	Density of undisturbed sample (kg/m^3)	Axial expansion rate (%)	Average radial expansion rate (%)	Longitudinal wave velocity (m/s)		Decrease rate of longitudinal wave velocity (%)
				Before immersion	After immersion	
JZ-1	2,704.4	0.383	0.424	4,761.9	4,210.5	11.6
JZ-2	2,685.8	0.415	0.632	4,522.3	3,860.2	14.6
JZ-3	2,671.5	0.470	0.728	4,210.5	3,508.8	16.7
JH-1	2,691.5	0.186	0.062	4,601.7	4,426.8	3.8
JH-2	2,673.1	0.234	0.090	4,296.8	4,101.5	4.5
JH-3	2,701.6	0.172	0.055	4,698.2	4,536.3	3.4

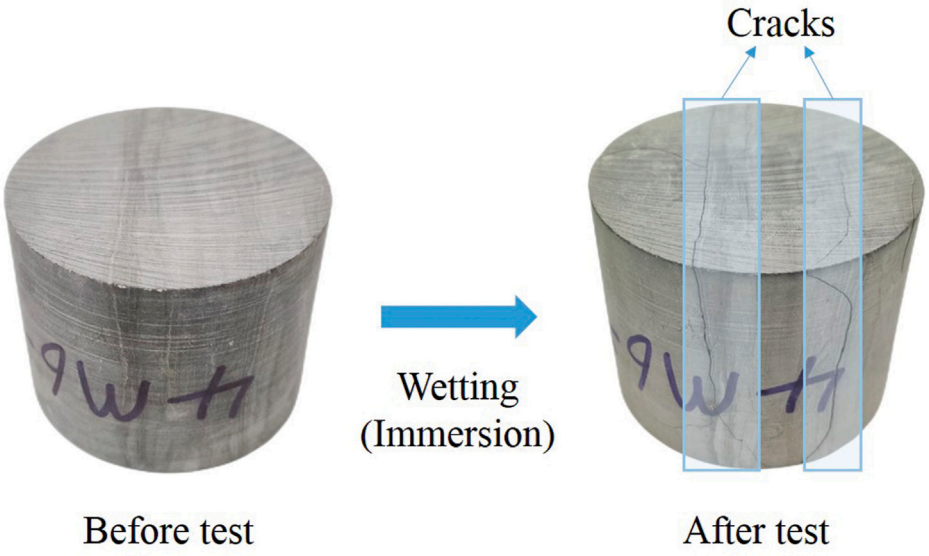

FIGURE 5
Comparison of samples with vertical interlayer before and after wetting and deterioration.

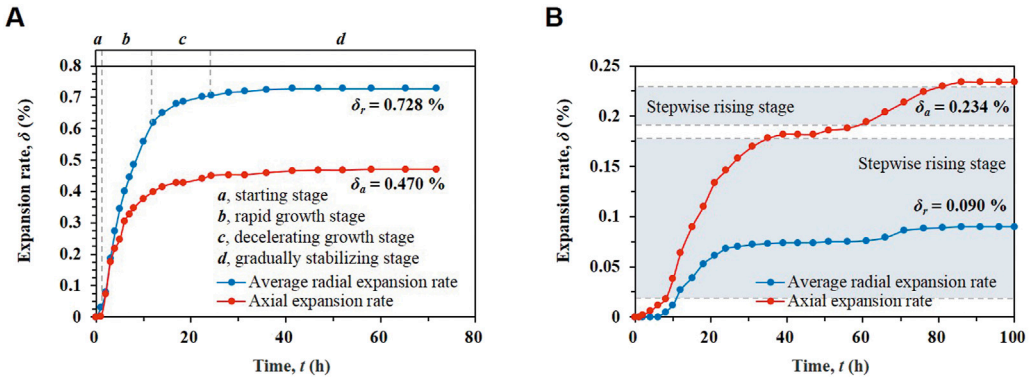

FIGURE 6
Three-way expansion rate time history curve **(A)** sample with vertical interlayer **(B)** sample with horizontal interlayer.

the next rapid growth stage until gradually stable. The final average radial expansion rate of the sample was 0.090%, and the axial expansion rate was 0.234%.

It could be seen from the three-way expansion rate test results that for the sample with vertical interlayer, the axial expansion rate of rock generally lagged behind the radial expansion rate. The rock first cracked along the interlayer plane to form a main crack, and the interlayer direction of the sample was not completely vertical under natural conditions, so the axial volume expansion component would be generated during the cracking along the interlayer direction, this was also the reason why the final axial expansion rate did not have a high multiple gap with the radial expansion rate. However, for the sample with horizontal interlayer, due to its own gravity, the interlayer gap was relatively tight, and it was difficult for water to enter into the rock and react with anhydrite to cause expansion cracking. Its expansion speed was slower than that of the sample with vertical interlayer, and it developed in a gradual and progressive manner.

The test results of rock longitudinal wave velocity showed that the rock longitudinal wave velocity decreased to varying degrees after the samples were immersed in water and deteriorated. The longitudinal wave velocity of the sample with vertical interlayer decreased more than that of the sample with horizontal interlayer. The longitudinal wave velocity of samples with vertical interlayer JZ-1, JZ-2 and JZ-3 decreased by 11.6%, 14.6% and 16.7% respectively, while that of samples with horizontal interlayer JH-1, JH-2 and JH-3 decreased by 3.8%, 4.5% and 3.4% respectively. The speed of longitudinal wave propagation was positively related to the compactness of rock. The denser the rock was, the faster the longitudinal wave propagation in the rock was. After the sample was deteriorated by immersion, its internal cracks developed. When the ultrasonic wave propagated along the test direction, it would diffract because it passed through discontinuities such as pores and cracks in the rock. If the number of times of diffraction was more, the actual distance in the acoustic wave propagation process was longer, which led to the lower transmission speed of the acoustic wave in the rock.

4 Analysis of rock compression evolution process

4.1 Sample selection

In order to study the influence of wetting deterioration of layered rock and interlayer effect on rock cracking and expansion, we continued to take the above JZ-1, JZ-2 and JZ-3 samples after air drying and record them as Group A, JH-1, JH-2 and JH-3 samples after air drying and record them as Group B, and took three undisturbed samples containing vertical and horizontal interlayer and record them as Group C and Group D respectively for rock uniaxial compression test.

4.2 Test equipment and process

The test was carried out on the RMT-150C multi-function rock testing machine in the Institute of Rock and Soil Mechanics, Chinese Academy of Sciences. This testing machine can complete a variety of rock mechanics tests such as uniaxial compression, uniaxial indirect tension, triaxial compression and shear, and its maximum vertical output is 1,000 kN. Before the test, a layer of Vaseline should be evenly coated on the upper and lower end faces of the sample to reduce the end effect of rock under uniaxial compression. The loading mode of the testing machine was set as axial displacement control, and the loading rate was set as 0.002 mm/s. During the test, radial and axial strain displacement sensors were used to monitor the deformation of rock (Figure 7).

4.3 Crack volume strain characteristics

Martin and Chandler (1994) put forward the calculation method of crack volume strain in the process of uniaxial compression of rock, and believed that the volume strain of rock was composed of elastic volume strain and crack volume strain. The calculation of crack volume strain could be obtained by subtracting the elastic volume strain from the total volume strain. According to crack volume strain curve, total volume strain curve and stress-strain curve, the whole compression process of rock was divided into five stages, crack closure stage, elastic stage, stable crack expansion stage, unstable crack expansion stage and post peak deformation stage.

The volume strain of rock ε_v could be calculated from the axial strain ε_1 and radial strain ε_3 measured by the strain displacement sensor according to Eq. (1).

$$\varepsilon_v = \varepsilon_1 + 2\varepsilon_3 \tag{1}$$

The rock elastic modulus E and Poisson's ratio ν could be calculated from the rock stress-strain curve. Since the three principal stresses σ_1, σ_2, σ_3, $\sigma_2 = \sigma_3 = 0$, the elastic volumetric strain ε_v^e of the rock was

$$\varepsilon_v^e = \frac{1-2\nu}{E}\sigma_1 \tag{2}$$

According to the crack strain model, the crack volume strain ε_v^c was

$$\varepsilon_v^c = \varepsilon_v - \varepsilon_v^e \tag{3}$$

The typical samples of each group were taken respectively. The crack volume strain curve and total volume strain curve were shown in Figure 8. The characteristic parameters of the test process were shown in Table 2.

The uniaxial compressive strength of each sample decreased after immersion, while the deformation of the sample increased along the radial direction, and the plastic characteristics were

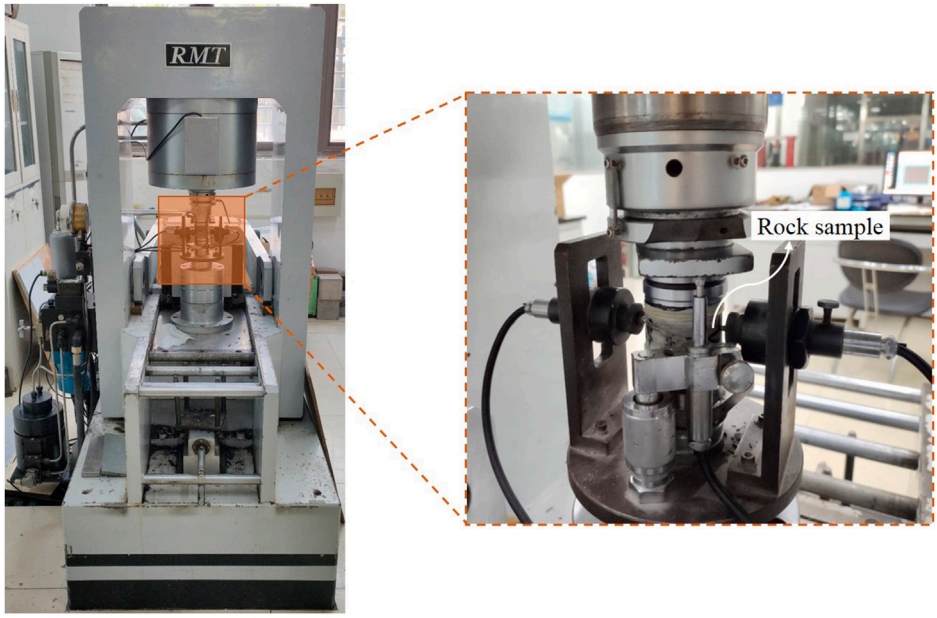

FIGURE 7
Uniaxial compression test of rock.

enhanced. The average uniaxial compressive strength of the sample with horizontal interlayer before and after immersion decreased from 170.22 MPa to 154.3 MPa, with a decrease rate of 9.35%. The average uniaxial compressive strength of the sample with vertical interlayer before and after immersion decreased from 104.45 MPa to 86.44 MPa, with a decrease rate of 17.24%. The average radial peak strain of the sample with horizontal interlayer before and after immersion increased from 0.10% to 0.12%, with an increase ratio of 20%. The average radial peak strain of the sample with vertical interlayer before and after immersion increased from 0.14% to 0.17%, with an increase ratio of 21.43%. It could be seen that the wetting effect had obvious deterioration effect on intercalated dolomite, which made the mechanical properties of rock decline, the deformation increased during the test, and the bearing failure changed to plastic failure. The direction of interlayer also had an important influence on the compressive strength and peak strain of rock. The compressive strength of the sample with vertical interlayer was obviously smaller than that of the sample with horizontal interlayer, and the peak radial strain was larger. Therefore, after wetting and deterioration, the rock had the weakest compressive property and the most obvious cracking expansion capacity under the force along the interlayer.

The whole loading process of rock could be divided into five stages by the four stress thresholds of crack closure stress σ_{cc}, crack initiation stress σ_{ci}, expansion stress σ_{cd} and peak stress σ_f: crack closure stage, elastic deformation stage, stable crack growth stage, unstable crack growth stage and post failure peak stage.

When the rock was initially compressed, the internal primary cracks and pores were compacted, and the crack volume decreased until the crack closure stress was reached. The calculated crack volume strain was zero. In this crack closure stage (stage I), the axial and radial stress-strain curves of rock were generally concave, that was, the relationship between stress and strain was nonlinear. With the continuous loading, the rock entered the elastic deformation stage (stage II), and the calculated crack volume strain basically maintained at the zero growth level; The axial and radial strains increased linearly with the increase of stress, and the total volume strain also increased in a linear manner, and the rock continued to be compressed. When the rock stress exceeded the crack initiation stress, the cracks in the rock began to continue to develop, thus entering the stable crack growth stage (stage III), at which time the calculated crack volume strain increased from zero; The axial and radial strains and the total volume strain began to break away from the linear deformation. As the rock compression reached the limit and began to expand, the rock began to enter the unstable crack growth stage (stage IV). The stress corresponding to the reverse bending point of the volume strain curve was the expansion stress. Many researchers generally believed that the expansion stress was an indicator to determine the long-term strength of the rock (Bai et al., 2019; Bai et al., 2022; Zhou Y. Q. et al., 2022).

The ratio of crack initiation stress to peak stress σ_{ci}/σ_f was taken as the crack initiation level; The ratio of expansion stress to peak stress σ_{cd}/σ_f was taken as the expansion level. The calculation results of each sample are shown in Table 2.

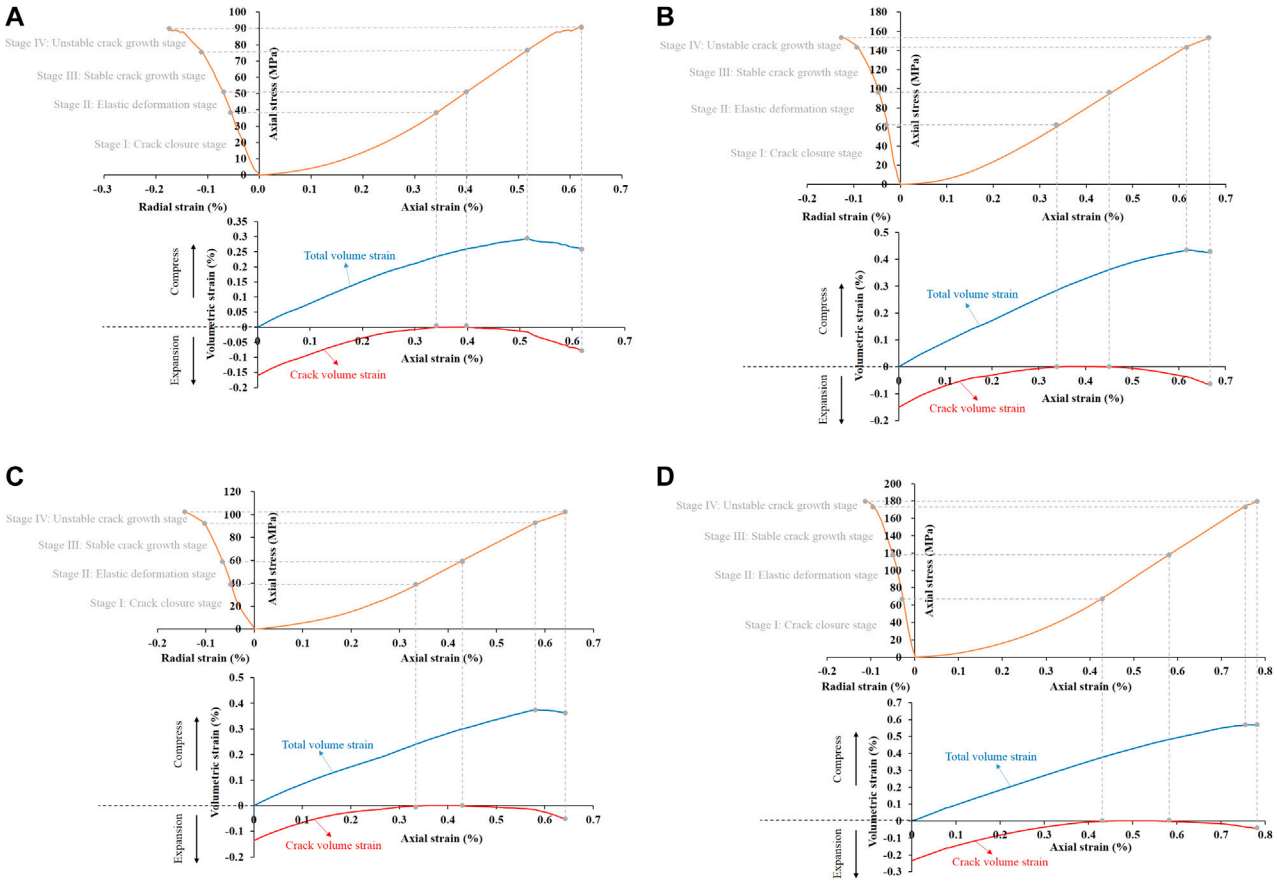

FIGURE 8
Stress-strain, total volume strain and crack volume strain curve of sample in uniaxial compression process **(A)** Sample with vertical interlayer after immersion **(B)** Sample with horizontal interlayer after immersion **(C)** Undisturbed sample with vertical interlayer **(D)** Undisturbed sample with horizontal interlayer.

The crack initiation level reflected the degree of defects existing in the rock, such as the difference in the internal structure of the rock and the dispersion of microcracks, grain boundaries and lattice defects (Wang et al., 2014; Hou et al., 2019). The larger the value was, the less fully developed the micro cracks in the rock were, and the more homogeneous the structure was. In addition, the crack initiation level and expansion level also reflected the relative difficulty of the initiation and development of different rock cracks in their stress deterioration stage to a certain extent.

After water immersion and air drying, the crack initiation level and expansion level of the samples with vertical interlayer (Group A) were the minimum, 0.560 and 0.837 respectively; The undisturbed samples with horizontal interlayer (Group D) were the largest, 0.616 and 0.978 respectively. However, the two values of the original sample containing vertical interlayer (Group C) and the sample containing horizontal interlayer after wetting and air drying (Group B) were between the two. The effect of sample wetting deterioration and the direction of interlayer had significant effects on the crack initiation level and expansion level of the sample under uniaxial compression. After wetting and deterioration, the external force required for rock cracking and expansion due to the force along the interlayer direction was the minimum, and the plastic stage of the sample was relatively long, with low brittleness, showing large plastic deformation, fully showing the effect of cracking and expansion. For the sample without wetting and deterioration, when the rock entered the plastic state during loading, it reached the peak stress in a short time, showing obvious brittle failure, relatively weak crack expansion effect, and the sample with the interlayer direction perpendicular to the stress direction showed more obvious brittle characteristics than the sample with the interlayer direction parallel to the stress direction.

TABLE 2 Characteristic parameters of compression process.

Sample no.		σ_{ci} (MPa)	σ_{cd} (MPa)	σ_f (MPa)	Axial peak strain (%)	Radial peak strain (%)	Crack initiation level	Expansion level	Average crack initiation level	Average expansion level
Group A	JZ-1	51.327	76.404	90.481	0.616	0.178	0.567	0.844	0.560	0.837
	JZ-2	46.685	69.402	83.516	0.585	0.163	0.559	0.831		
	JZ-3	47.185	71.332	85.325	0.591	0.169	0.553	0.836		
Group B	JH-1	90.604	144.018	152.676	0.665	0.120	0.593	0.943	0.597	0.946
	JH-2	92.155	146.182	154.363	0.671	0.122	0.597	0.947		
	JH-3	93.536	147.942	155.893	0.675	0.122	0.600	0.949		
Group C	Z-1	67.278	104.089	113.263	0.643	0.141	0.594	0.919	0.589	0.914
	Z-2	59.771	92.631	101.390	0.641	0.139	0.590	0.914		
	Z-3	57.538	89.613	98.693	0.637	0.136	0.583	0.908		
Group D	H-1	110.018	175.696	178.314	0.777	0.106	0.617	0.985	0.616	0.978
	H-2	108.250	170.830	174.316	0.747	0.110	0.621	0.980		
	H-3	96.556	153.131	158.030	0.690	0.089	0.611	0.969		

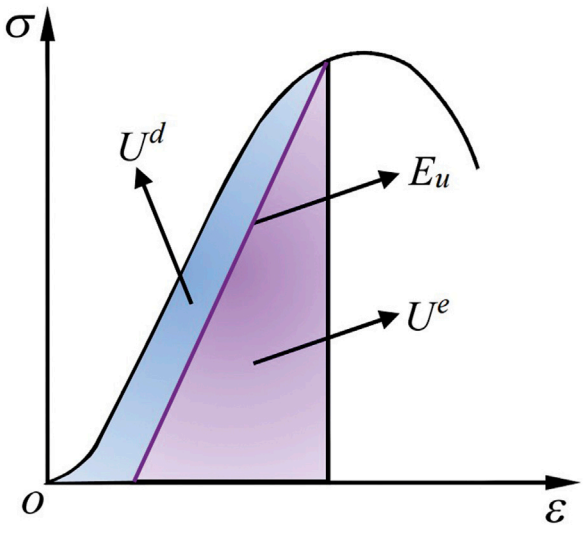

FIGURE 9
Schematic diagram of energy relationship in unit volume rock.

4.4 Energy dissipation characteristics

The process of rock uniaxial compression was analyzed from the aspect of energy dissipation. The energy change of rock in the process of uniaxial compression included the input of strain energy generated by external force work, the storage of releasable elastic strain energy and the irreversible loss of dissipated energy (Xie et al., 2005). Assuming that in a closed system, rocks were deformed by external forces, it could be concluded from the first law of thermodynamics that:

$$U = U^e + U^d \tag{4}$$

Where, U is the total strain energy per unit volume of rock generated by external force work, U^e is the elastic strain energy per unit volume of rock that can be released, and U^d is the dissipated energy per unit volume of rock.

Figure 9 shows the relationship among U, U^e and U^d in the stress-strain curve of rock under uniaxial compression. The total strain energy per unit volume of rock generated by external work U was the area enclosed by the stress-strain curve and the coordinate axis, which could be obtained by integrating the corresponding stress-strain curve; The released elastic strain energy per unit volume of rock U^e was the area of the shaded part in Figure 9, that was, the area enclosed by the unloading elastic modulus E_u and the coordinate axis. According to the test results (Xie et al., 2005; You et al., 2001; Liang et al., 2015), the unloading elastic modulus E_u could be approximately taken as the initial elastic modulus E_0; The dissipated energy per unit volume of rock U^e was the area enclosed by the stress-strain curve and unloading elastic modulus E_u. The dissipated energy was mainly accompanied by the internal damage and plastic deformation of rock.

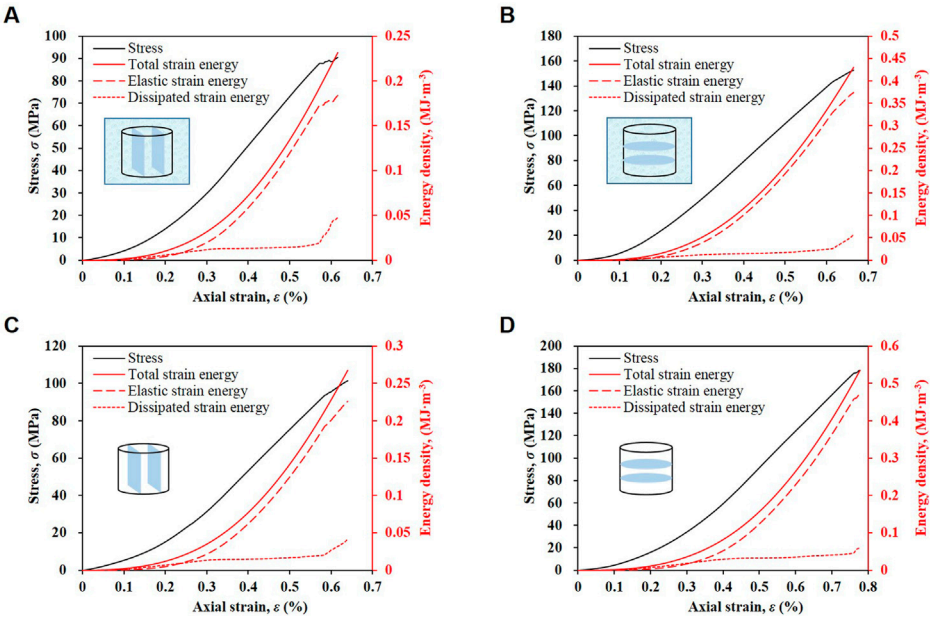

FIGURE 10
Relation curves between strain energy density and axial strain of rock samples under different initial conditions **(A)** Sample with vertical interlayer after immersion **(B)** Sample with horizontal interlayer after immersion **(C)** Undisturbed sample with vertical interlayer **(D)** Undisturbed sample with horizontal interlayer.

According to the above analysis, the total strain energy per unit volume of rock generated by external force work U, the released elastic strain energy per unit volume of rock U^e and the dissipated energy per unit volume of rock U^d could be calculated by Equations (5–7) respectively:

$$U = \frac{1}{2}\sum_{i=1}^{n}\left(\sigma_{h(i)} + \sigma_{h(i-1)}\right)\left(\varepsilon_{h(i)} - \varepsilon_{h(i-1)}\right) \tag{5}$$

$$U^e = \frac{\sigma_{h(i)}^2}{2E_0} \tag{6}$$

$$U^d = U - U^e = \frac{1}{2}\sum_{i=1}^{n}\left(\sigma_{h(i)} + \sigma_{h(i-1)}\right)\left(\varepsilon_{h(i)} - \varepsilon_{h(i-1)}\right) - U^e = \frac{\sigma_{h(i)}^2}{2E_0} \tag{7}$$

Where, $\sigma_{h(i)}$ and $\varepsilon_{h(i)}$ are the stress and axial strain values at the point $h(i)$ on the stress-strain curve respectively; $\sigma_{h(i\text{-}1)}$ and $\varepsilon_{h(i\text{-}1)}$ are the stress and axial strain values at the point h (i-1) on the stress-strain curve respectively.

It can be seen from Figure 10 that the total strain energy of each sample increased with a concave tendency. The elastic strain energy first showed a concave growth, and then became irregular growth or small amplitude oscillation after reaching a certain value. The dissipative strain energy first showed a convex growth, that was, the initial growth was fast, then slowed down, and then started to increase significantly at a certain value. The variation characteristics of rock energy curve could reflect the crack development and energy evolution during rock compression. In the initial compaction stage, the primary cracks closed and consumed more energy, and the dissipated strain energy in this stage was roughly equal to the elastic strain energy. When the sample entered the elastic deformation stage, at this time, the crack volume strain was almost zero, and there was basically no damage in the rock. Therefore, almost all the energy input due to the work done by the external force was converted into elastic strain energy and stored in the rock. The elastic strain energy curve was basically parallel to the total strain energy curve, while the curve of the dissipative strain energy was approximately horizontal due to no growth. In the stable crack growth stage, the dissipative strain energy started to increase slightly, which indicated that the sample began to regenerate damage cracks and produced irreversible plastic deformation. After the sample entered the unstable crack growth stage, its internal cracks were rapidly generated, developed and connected. The total volume strain changed from compression to expansion, and the dissipated strain energy increased significantly. Although the elastic strain energy was still accumulating inside the rock, its growth rate slowed down until it reached a limit, and the elastic strain energy was rapidly released to finally destroyed the rock as a whole (Xie et al., 2005).

Table 3 shows the results of energy characteristic values obtained from rock uniaxial compression tests under different initial conditions. The ratio of the dissipative strain energy density and the elastic strain energy density to the total strain energy density was taken as the dissipative energy conversion rate and the elastic energy conversion rate, respectively. The energy conversion rate had an

TABLE 3 Characteristic parameters of compression energy.

Sample no.		Total strain energy (kJ/m^3)	Elastic strain energy (kJ/m^3)	Dissipated strain energy (kJ/m^3)	Dissipated energy conversion rate (%)	Elastic energy conversion rate (%)	Average energy dissipation conversion rate (%)	Average elastic energy conversion rate (%)
Group A	JZ-1	231.42	183.73	47.69	20.61	79.39	23.58	76.42
	JZ-2	210.03	156.77	53.26	25.36	74.64		
	JZ-3	215.56	162.17	53.39	24.77	75.23		
Group B	JH-1	430.87	374.01	56.86	13.20	86.80	12.80	87.20
	JH-2	437.96	381.86	56.10	12.81	87.19		
	JH-3	442.12	387.39	54.73	12.38	87.62		
Group C	Z-1	299.56	257.23	42.33	14.13	85.87	15.57	84.43
	Z-2	267.38	226.28	41.10	15.37	84.63		
	Z-3	258.63	214.12	44.51	17.21	82.79		
Group D	H-1	535.85	472.93	62.93	11.74	88.26	11.87	88.13
	H-2	523.67	461.56	62.11	11.86	88.14		
	H-3	455.86	401.11	54.75	12.01	87.99		

important influence on the characteristics of the rock compression evolution process (Zhang et al., 2019). The results show that the undisturbed rock with horizontal interlayer without water immersion needed the most external input energy in the process of vertical compression failure, and was the most difficult to be damaged. In the process of compression, the external force work was mainly converted into elastic strain energy and stored in the rock. When the peak stress was reached, the average elastic energy conversion rate was 88.13%. However, the proportion of energy dissipated by plastic deformation such as crack generation and development and friction between cracks was very small, which indicated that the whole compression process showed obvious brittleness, and the cracking expansion was concentrated at the moment of rock failure. However, after immersion, the threshold value of elastic strain energy density required for failure of rock with horizontal interlayer decreased, and the conversion rate of dissipated energy and the plasticity increased during compression. The average value of external input energy required for failure of undisturbed samples with vertical interlayer without water immersion was only 54.48% of that of undisturbed samples with horizontal interlayer under the same conditions, which fully indicated that the angle between the direction of rock stress and the direction of interlayer determined the degree of rock failure. For the sample with vertical interlayer, the average value of external input energy required for failure after immersion had decreased by 20.42%, and the average value of energy conversion rate of dissipation had also significantly increased from 15.57% to 23.58%, which indicated that the rock had undergone relatively sufficient wetting and deterioration during immersion, resulting in the continuous development and expansion of cracks and the enhancement of plastic characteristics of the rock during compression under force.

5 Conclusion

1) The rock sample had obvious interlayer structure and its mineral composition contained anhydrite, an expansive material and hydrophilic clay mineral, which made the sample had the deterioration potential of cracking and expansion after immersion.
2) The three-way expansion rate test of rock showed that the sample with vertical interlayer showed the deterioration characteristics of micro expansion and cracking along the direction of interlayer after wetting, and its expansion process included four stages: starting stage, rapid growth stage, decelerating growth stage and gradually stabilizing stage. However, the axial and radial expansion rates of samples with horizontal interlayer were obviously lower than those with vertical interlayer after immersion, and the expansion process presented a hierarchical and progressive development.
3) Before and after immersion, the longitudinal wave velocity of the ultrasonic wave passing through the sample decreased, but the decrease amplitude of the sample with vertical interlayer was obviously larger than that of the sample with horizontal interlayer, and the average decrease rate was 14.3% and 3.9% respectively. It reflected that the development of internal cracks occurred in all samples after immersion, and the wetting deterioration effect of samples with vertical interlayer was more significant than that of samples with horizontal interlayer.
4) The crack volume strain method was used to analyze the evolution process of rock under uniaxial compression. The test results showed that the uniaxial compressive strength, crack initiation level, and expansion level of the sample had

decreased after wetting and deterioration, while the radial peak strain of the sample had increased, and the change amplitude of the sample with vertical interlayer was greater than that of the sample with horizontal interlayer before and after wetting, and the cracking expansion and plasticity were more obvious.

5) In terms of energy conversion in uniaxial compression process, the threshold value of the elastic strain energy density required for the sample to reach failure decreased after wetting, and the threshold value of the sample with vertical interlayer was smaller than that of the sample with horizontal interlayer before and after immersion. The dissipative energy conversion rate to reflect the plastic deformation such as crack generation, expansion and friction between cracks of the undisturbed sample with vertical interlayer was significantly higher than that of the undisturbed sample with horizontal interlayer, and the growth rate was greater after wetting. The average dissipative energy conversion rate of the sample with vertical interlayer increased from 15.57% to 23.58%, and the average dissipative energy conversion rate of the sample with horizontal interlayer increased from 11.87% to 12.80%.

Data availability statement

The original contributions presented in the study are included in the article/supplementary material, further inquiries can be directed to the corresponding author.

Author contributions

ZD: Writing—review and editing, Supervision, Validation, Funding acquisition. YW: Data curation, Methodology, Writing—original draft. ZZ: Data curation, Investigation. JL: Validation. FY: Methodology, Investigation. SC: Project administration, Supervision.

Funding

The work reported in this paper was financially supported by the National Natural Science Foundation of China (No. 42172308), the Youth Innovation Promotion Association CAS (No. 2022331) and the Key Research and Development Program of Hubei Province (No. 2022BAA036).

Acknowledgments

We would like to acknowledge the reviewers and the editors for their comments and suggestions.

Conflict of interest

The authors declare that the research was conducted in the absence of any commercial or financial relationships that could be construed as a potential conflict of interest.

Publisher's note

All claims expressed in this article are solely those of the authors and do not necessarily represent those of their affiliated organizations, or those of the publisher, the editors and the reviewers. Any product that may be evaluated in this article, or claim that may be made by its manufacturer, is not guaranteed or endorsed by the publisher.

References

Anderson, D. L., Minster, B., and Cole, D. (1974). The effect of oriented cracks on seismic velocities. *J. Geophys. Res.* 79 (26), 4011–4015. doi:10.1029/JB079i026p04011

Bai, B., Wang, Y., Rao, D., and Bai, F. (2022). The effective thermal conductivity of unsaturated porous media deduced by pore-scale SPH simulation. *Front. Earth Sci. (Lausanne).* 10, 943853. doi:10.3389/feart.2022.943853

Bai, B., Yang, G., Li, T., and Yang, G. (2019). A thermodynamic constitutive model with temperature effect based on particle rearrangement for geomaterials. *Mech. Mater.* 139, 103180. doi:10.1016/j.mechmat.2019.103180

Bai, B., Zhou, R., Cai, G., Hu, W., and Yang, G. (2021). Coupled thermo-hydro-mechanical mechanism in view of the soil particle rearrangement of granular thermodynamics. *Comput. Geotechnics* 137 (8), 104272. doi:10.1016/j.compgeo.2021.104272

Cai, G., Cheng, Y., Zhong, C., Jia, J., Zhao, D., and Feng, W. (2021). Experimental on softening effect of phyllite in saturated water. *Sci. Technol. Eng.* 21 (8), 3032–3038.

Chai, Z., Zhang, Y., and Zhang, X. (2015). Experimental investigations on correlation with slake durability and mineral composition of mudstone. *J. China Coal Soc.* 40 (5), 1188–1193. doi:10.13225/j.cnki.jccs.2014.0897

Diao, X., Yang, S., and Mao, X. (2017). Experimental study on water absorption and expansion characteristics of mudstone under conditions of different temperature and humidity. *J. East China Jiaot. Univ.* 34 (3), 14–18. doi:10.16749/j.cnki.jecjtu.2017.03.003

Du, W., Sheng, Q., Fu, X., Chen, J., and Zhou, Y. (2022). A TPDP-MPM-based approach to understanding the evolution mechanism of landslide-induced disaster chain. *J. Rock Mech. Geotechnical Eng.* 14 (4), 1200–1209. doi:10.1016/j.jrmge.2022.03.004

Feng, Z., Xu, Q., Luo, X., Huang, R., Liao, X., and Tang, Q. (2022). Microstructure, deformation characteristics and energy analysis of mudstone under water absorption process. *Energies* 15 (20), 7511. doi:10.3390/en15207511

Fu, X., D, H., Sheng, Q., Zhang, Z., Yin, D., and Chen, F. (2022). Fractal analysis of particle distribution and scale effect in a soil-rock mixture. *Fractal Fract.* 6 (2), 120. doi:10.3390/fractalfract6020120

He, M., Wei, L., Jia, Y., Huang, A., Wang, J., and Huang, X. (2019). Experimental study on expansive mechanical characteristics of red-bed soft rock. *Water Resour. Hydropower Eng.* 50 (4), 171–178. doi:10.13928/j.cnki.wrahe.2019.04.024

He, Q., Sun, L., Song, J., Ding, B., and Wang, Z. (2022). Association between sleep duration and hypertension among adults in southwest China. *Glob. Heart* 45 (5), 10–1217. doi:10.5334/gh.1100

Hou, Z., Wang, Y., Liu, D., and Li, C. (2019). Investigation of the anisotropic mechanical behaviors and energy evolution during uniaxial deformation of interbedded marble. *J. Min. Saf. Eng.* 36 (4), 794–804. doi:10.13545/j.cnki.jmse.2019.04.019

Hua, W., Li, J., Dong, S., and Pan, X. (2019). Experimental study on mixed mode fracture behavior of sandstone under water-rock interactions. *Processes* 7 (2), 70. doi:10.3390/pr7020070

Jia, H., Wang, E., Song, D., Wang, X., and Ali, M. (2019). Precursory changes in wave velocity for coal and rock samples under cyclic loading. *Results Phys.* 12, 432–434. doi:10.1016/j.rinp.2018.11.096

Jiang, J., Hou, Z., Hou, K., Lu, Y., Sun, H., and Niu, X. (2022). The damage constitutive model of sandstone under water-rock coupling. *Geofluids* 2022, 1–12. doi:10.1155/2022/1731254

Jiang, J., Xiang, W., Rohn, J., Zeng, W., and Schleier, M. (2015). Research on water-rock (soil) interaction by dynamic tracing method for Huangtupo landslide, Three Gorges Reservoir, PR China. *Environ. Earth Sci.* 74 (1), 557–571. doi:10.1007/s12665-015-4068-5

King, M. S., Chaudhry, N. A., and Shakeel, A. (1995). Experimental ultrasonic velocities and permeability for sandstones with aligned cracks. *Int. J. Rock Mech. Min. Sci. Geomechanics Abstr.* 32 (2), 155–163. doi:10.1016/0148-9062(94)00033-Y

Li, S., Huang, Z., Liang, Q., Liu, J., Luo, S., and Zhou, W. (2022). Evolution mechanism of mesocrack and macrocrack propagation in carbonaceous mudstone under the action of dry-wet cycles. *Geofluids* 2022, 1–8. doi:10.1155/2022/6768370

Liang, C., Wu, S., Li, X., and Xin, P. (2015). Effects of strain rate on fracture characteristics and mesoscopic failure mechanisms of granite. *Int. J. Rock Mech. Min. Sci. (1997).* 76, 146–154. doi:10.1016/j.ijrmms.2015.03.010

Ma, L. (2015). *Research on low clay mineral mudstone expansion mechanism and influence for high-speed railway subgrade*. dissertation (Lanzhou: Lanzhou Jiaotong University).

Martin, C. D., and Chandler, N. A. (1994). The progressive fracture of Lac du Bonnet granite. *Int. J. Rock Mech. Min. Sci. Geomechanics Abstr.* 31 (6), 643–659. doi:10.1016/0148-9062(94)90005-1

Song, Y., Chen, J., Zhang, L., Ren, J., Che, Y., and Yang, H. (2021). Damage and degradation characteristics of loaded sandstone under drying-wetting cycles. *J. Yangtze River Sci. Res. Inst.* 38 (9), 133–140. doi:10.11988/ckyyb.20200679

Tang, Y., Hao, T., Li, F., Zhao, L., and Liu, J. (2022). Energy evolution and infrared radiation characterization of coal rocks considering strain rate effect. *Chin. J. Rock Mech. Eng.* 41 (6), 1126–1135. doi:10.13722/j.cnki.jrme.2021.0952

Wang, Y., Li, X., Wu, Y., Ben, Y., Li, S., He, J., et al. (2014). Research on relationship between crack initiation stress level and brittleness indices for brittle rocks. *Chin. J. Rock Mech. Eng.* 33 (2), 264–275. doi:10.13722/j.cnki.jrme.2014.02.003

Xie, H., Ju, Y., and Li, L. (2005). Criteria for strength and structual failure of rocks based on energy dissipation and energy release principles. *Chin. J. Rock Mech. Eng.* 24 (17), 3003–3010.

Yang, S. (2017). *Study on Hygroscopic properties of expansive rock under high temperature and high humidity environment*. master's thesis (Nanchang: East China Jiaotong University).

You, M., Su, C., and Xu, T. (2001). Loading or unloading process in axial direction and Young's modulus of rock specimen. *Chin. J. Geotechnical Eng.* 23 (5), 588–592.

Zeng, L., Liu, J., Gao, Q., and Bian, H. (2019). Evolution characteristics of the cracks in the completely disintegrated carbonaceous mudstone subjected to cyclic wetting and drying. *Adv. Civ. Eng.* 2019, 1–10. doi:10.1155/2019/1279695

Zhang, J., Xi, X., Guo, Q., and Wu, X. (2021). Meso multi-phase particle flow simulation of granite failure with preexisting crack. *J. Huazhong Univ. Sci. Tech. Nat. Sci. Ed.* 49 (4), 79–85. doi:10.13245/j.hust.210413

Zhang, X., Lü, G., Zhang, Q., Liu, Q., Li, W., and Xu, J. (2020). Uniaxial compression test for three stress thresholds of siliceous siltstone. *J. Eng. Geol.* 28 (3), 441–449. doi:10.13544/j.cnki.jeg.2019-085

Zhang, Z., Xie, H., Zhang, R., Zhang, Z., Gao, M., Jia, Z., et al. (2019). Deformation damage and energy evolution characteristics of coal at different depths. *Rock Mech. Rock Eng.* 52 (5), 1491–1503. doi:10.1007/s00603-018-1555-5

Zhao, Z., Liu, H., Lyu, X., Wang, L., Tian, Z., and Sun, J. (2021). Experimental study on the damage and deterioration behaviour of deep soft rock under water-rock interaction. *Geofluids* 2021, 1–11. doi:10.1155/2021/8811110

Zhou, C., Deng, Y., Tan, X., Liu, Z., Shang, W., and Zhan, S. (2005). Experimental research on the softening of mechanical properties of saturated soft rocks and application. *Chin. J. Rock Mech. Eng.* 24 (1), 33–38.

Zhou, K., Dou, L., Gong, S., Chai, Y., Li, J., Ma, X., et al. (2022a). Mechanical behavior of sandstones under water-rock interactions. *Geomechanics Eng.* 29 (6), 627–643. doi:10.12989/gae.2022.29.6.627

Zhou, Y. Q., Sheng, Q., Li, N. N., and Fu, X. D. (2022b). The dynamic mechanical properties of a hard rock under true triaxial damage-controlled dynamic cyclic loading with different loading rates: A case study. *Rock Mech. Rock Eng.* 55 (4), 2471–2492. doi:10.1007/s00603-021-02756-w

frontiers | Frontiers in Materials

TYPE Original Research
PUBLISHED 01 December 2022
DOI 10.3389/fmats.2022.1080547

Check for updates

OPEN ACCESS

EDITED BY
Xianze Cui,
China Three Gorges University, China

REVIEWED BY
Rui Rui,
Wuhan University of Technology, China
Xingxin Chen,
Huaqiao University, China

*CORRESPONDENCE
Shixuan Yi,
yishixuan@dtsjy.com

SPECIALTY SECTION
This article was submitted to Structural Materials, a section of the journal Frontiers in Materials

RECEIVED 26 October 2022
ACCEPTED 15 November 2022
PUBLISHED 01 December 2022

CITATION
Yi S (2022), Parametric study of passive piles subjected to adjacent surcharge load in extensively deep soft soil. *Front. Mater.* 9:1080547. doi: 10.3389/fmats.2022.1080547

COPYRIGHT
© 2022 Yi. This is an open-access article distributed under the terms of the Creative Commons Attribution License (CC BY). The use, distribution or reproduction in other forums is permitted, provided the original author(s) and the copyright owner(s) are credited and that the original publication in this journal is cited, in accordance with accepted academic practice. No use, distribution or reproduction is permitted which does not comply with these terms.

Parametric study of passive piles subjected to adjacent surcharge load in extensively deep soft soil

Shixuan Yi*

Structural Engineer, Guangzhou Metro Design & Research Institute Co., Ltd., Guangzhou, China

This study applied the three-dimensional finite different method (FDM) to model a single pile subjected to passive loading due to a new embankment in extensively soft soil. Four important parameters (pile bending stiffness, distance between the long edge of the loading area and the pile (*D*), embankment height, and cushion thickness) were investigated to evaluate their effects on the deformations and stresses on the passive pile. The displacement of the pile shaft, vertical displacement of the foundation soil, excess pore water pressure (EPWP), and lateral earth pressure were analyzed. The numerical results showed that the lateral displacement of the pile was significantly affected by the four parameters. The maximum lateral displacement decreased dramatically for the high-stiffness pile. A cushion thickness of <1 m slightly increased the lateral displacement of the pile. Increased *D* value and decreased embankment height significantly reduced the lateral displacement of the pile. The vertical displacement of the loading area was unaffected by pile stiffness. The distribution shape of the vertical displacement was close to symmetrical with increasing *D* value. The embankment height and cushion thickness significantly affected the vertical displacement. Due to the low permeability of the foundation soil and short construction time, the EPWP was not fully dissipated with varying pile stiffness and *D* values. A decreased pile stiffness increased the lateral earth pressure at the pile, while increasing embankment height and cushion thickness increased the lateral earth pressure.

KEYWORDS

passive pile, surcharge load, bending stiffness, embankment height, cushion thickness

Introduction

Pile foundations unavoidably experience lateral soil movement due to nearby excavation, surcharge load, tunneling, and moving slopes, which differs from the vertical (e.g., superstructure) and horizontal (e.g., wind) loads acting on the pile head. Piles experiencing these forces are referred to as passive piles, the design of which generally consider pile-soil relative stiffness, rotational constraints, and possible dragging (Guo, 2003). Guo et al. (2017) reported that soil movement and profile were critical for passive pile design. Particularly, the failure of passive piles was generally governed by lateral deformation rather than the bearing capacity. The impact of lateral displacement is

complex due to the complexity of pile-soil interactions. Many studies have investigated the deformations and stresses of passive piles under different situations.

Field tests (Ong, 2018), model tests (Sabbagh et al., 2019; Al-abboodi et al., 2020; Karkush and Jaffar, 2020), theoretical studies (Zhang et al., 2020a; Bellezza, 2020; Bai et al., 2021; Ramalakshmi, 2021), and numerical analyses (Karim, 2013; Karim et al., 2014; Abo-Youssef et al., 2021; Li et al., 2021; Bai et al., 2022a) on passive piles have provided valuable results. Karkush et al. (2020) conducted model tests to study single piles adjacent to embankment construction and found that the vertical load acting on top of the passive pile increased the soil resistance. Zhang et al. (2020b) proposed a load transfer model for analyzing the pile-soil interaction and provided a semi-analytical solution. Al-abboodi and Sabbagh (2019) used Plaxis3D to investigate the group piles under soil movement in sand layers and identified a discrepancy between the predicted and test results. However, the study did not properly consider the relative lateral displacement between pile and soil and the density variation of sand. Cole (2003) reported that passive characteristics were often neglected in the design. The prediction methods lacked validation by field test data. Therefore, field tests are essential to investigate passive piles behavior. Yi and Liu (2022) performed field tests to study the effects of embankment load on the behaviors of the adjacent pile. Lateral deformation of the pile, lateral earth pressure, and excess water pressure were measured and analyzed during the construction of a 4 m thick embankment.

However, it is impractical to perform intensive field tests with changing parameters due to limited time, high cost, and poor repeatability (Bai et al., 2022b; Gu et al., 2022b; Shan et al., 2022; Yuan et al., 2022). Numerical methods allow comparative analyses by varying the parameters, which is a popular approach to overcoming the disadvantages of field tests. Yang et al. (2017) used 2D FEM models to conduct a parametric study. The results showed that the displacement in pile top under fast loading was about 1.4 times that under staged loading. Li et al. (2019) performed a series of field tests and established a 3D FEM model to analyze the behavior of piles subjected to surcharge loading. They found that the earth pressure facing the loading region was larger than that opposite the loading region. Zhang and Sun (2020) analyzed the deformation and migration law of soft soil for the pile under backfill surcharge using 3D FEM models. The results showed that the distance should be >120 m to reduce the impact of external load on the pile. Gu et al. (2022a) reported the results of a comprehensive investigation of a passive pile constructed in extensively deep soft soil using the three-dimensional finite difference method. They reported a much smaller horizontal resistance of the foundation soil compared to the proposed value based on the design code in the situation of large lateral deformations and high surcharge load.

The present study used the three-dimensional finite different method (FDM) to conduct a parametric study of passive piles subjected to adjacent surcharge load. The FDM model was established based on the numerical model proposed by Gu et al. (2022a), which was validated by the field measurements provided by Yi and Liu (2022). A series of 3D FDM models was developed to investigate the effect of four important factors (pile bending stiffness, distance between the long edge of the loading area and the pile, embankment height, and cushion thickness) on the behavior of a single steel pipe pile installed in extensively soft soil and subjected to adjacent surcharge loading.

Numerical simulation

The three-dimensional fast Lagrangian analysis of continuum FLAC3D (Itasca, 2018) was applied to study the behavior of a single pile installed in extensively soft soil under surcharge loading. The details of the field test and numerical model validated by the field test were described by Yi and Liu (2022) and Gu et al. (2022a), respectively. Briefly, the field test and numerical model applied in the present parametric study were as follows. Table 1 summarizes the parameter of the FDM models used to investigate the influence of the four important factors (pile bending stiffness, distance between the long edge of the loading area and pile, embankment height, and cushion thickness) on the behavior of passive pile. The successive values of four factors in the prototype FDM corresponding to the field test were 1.61 GPa, 1m, 4.8m, and 1.0 m. When one of the factors varied during the parametric study, the other factors were the same as in the prototype.

Figure 1 shows a photograph and general layout of the field test. A hollow cylindrical steel pipe pile with a 630 mm outer diameter and 35 m length (welded in three parts during piling) was manufactured to investigate the pile-soil interaction. The pile was 1 m away from the edge of the loading area (D value = 1 m in the real field test). Six inclinometer tubes 70 mm in outer diameter and 30 m in length were prepared to monitor the soil and pile deformation. Earth pressure cells and piezometers were also used to measure the earth pressure and pore water pressure (PWP), respectively. A 4-m high embankment was constructed in five lifts (each lift was 0.8 m thick and maintained for 3 days until the next lift) to simulate surcharge loading. The embankment fill length, width, and slope gradient were 24 m, 16 m, and 1:1.5, respectively. After all the instruments and structures were installed, the embankment was constructed (Bai et al., 2022b). The laws of lateral displacement of the pile, vertical displacement, excess pore water pressure (EPWP), and lateral earth pressure on the pile were investigated according to the parametric change in FDM. The monitored positions in the FDM are shown in Figure 1B.

Figure 2 shows the profile and plan view of the numerical model in FDM that was calibrated against the real field test. The model was 46 m wide, 50 m deep, and 162.63 long. A zone-type element was used to simulate the foundation soil and surcharge loading (modeled as elastic materials). The gravel, sandy silt, and

TABLE 1 Summary of FDM model parameters.

Pile stiffness (GPa)		*D* (m)		Embankment height (m)		Cushion thickness (m)	
Model 1	0.04	Model 7	1	Model 13	0.8	Model 19	0
Model 2	0.40	Model 8	5	Model 14	1.6	Model 20	0.5
Model 3	0.81	Model 9	9	Model 15	2.4	Model 21	1.0
Model 4	1.61	Model 10	13	Model 16	3.2	Model 22	1.5
Model 5	8.06	Model 11	17	Model 17	4.0	Model 23	2.0
Model 6	16.11	Model 12	21	Model 18	4.8	-	-

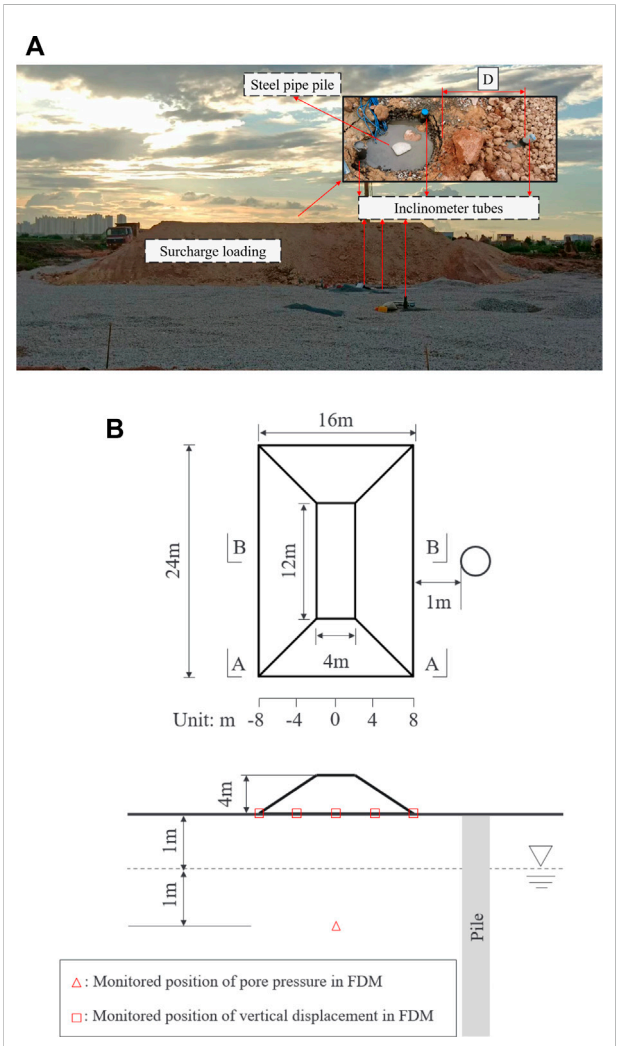

FIGURE 1
Schematic diagram of the real field test: **(A)** construction photograph; **(B)** general layout.

silty sand all used the Mohr-Coulomb constitutive model, while the Drucker-Prager constitutive model was used to model the sea-land sedimentary silt and mud. The pile-type and shell-type elements modeled as elastic materials were used to simulate the inclinometer tubes and steel pipe pile, respectively. The numerical model divided the 37 m of soft soil into six layers to capture the actual soil properties. The bottom and side surfaces of the foundation soil were fixed by normal velocity in the FDM to simulate the actual boundary conditions in the field. The zone-, pile- and shell-type elements were generated first, and their properties were assigned according to Table 1. The initial force balance of the model under gravity was conducted. Underground water was then introduced by setting the water table at 1 m below the ground surface. The PWP at the bottom surface of the first layer was then set to zero in the numerical model. Next, the fluid command was activated, and fluid balance was conducted after the fluid properties were assigned. The fluid density, modulus, and porosity were 1000 kg/m^3, 2.18e9 Pa, and 0.60, respectively. The permeability of the second, third, fourth, and fifth soil layers were 1e^{-10}, 1e^{-8}, 1e^{-2}, and1e^{-2} m/s, respectively. Surcharge loading was then carried out by activating the elastic fill layer in stages. The information was recorded by writing the *fish function* and *history command*.

Results and discussion

Based on the literature review and test results, the following four critical factors were identified for a parametric study of the behavior of a single pile subjected to surcharge loading in extensively soft soil: 1) pile bending stiffness, 2) distance between the long edge of the loading area and the pile (*D*), 3) embankment height, and 4) cushion thickness.

Effect of pile stiffness

Figure 3 shows the variations in the lateral displacement of the pile at depths for different bending stiffness after the fifth loading. The lateral displacement at the ground surface increased with increasing bending stiffness. The displacement of the pile shaft decreased along the pile depth regardless of the bending stiffness. The maximum lateral displacements were 189.40,

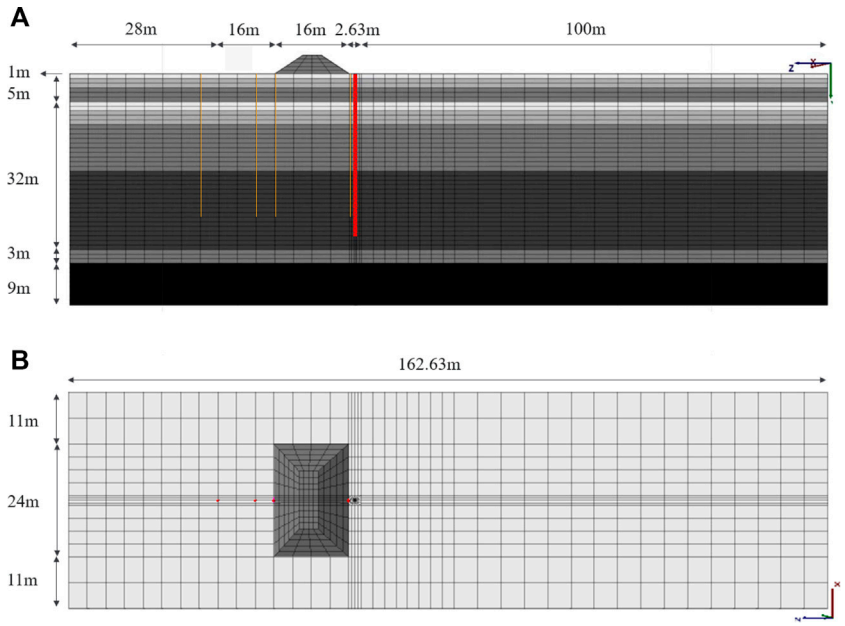

FIGURE 2
3D FDM model of the real field test: **(A)** profile view; **(B)** plan view.

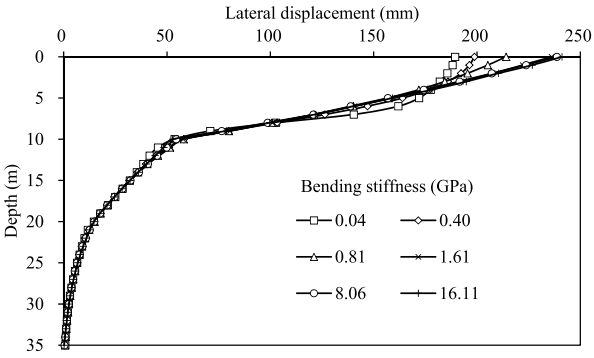

FIGURE 3
Lateral displacements of pile shafts with different bending stiffnesses after the fifth loading.

198.74, 214.05, 236.11, 238.61, and 241.12 mm for bending stiffnesses of 0.04, 0.4, 0.81, 1.61, 8.06, and 16.11 GPa, respectively, and all appeared at the top of the pile. The decrease in pile bending stiffness significantly decreased the maximum lateral displacement of the pile compared to the real field test model in the FDM (i.e., a bending stiffness of 1.61 GPa), while only a slight increase in maximum lateral displacement was observed with increased bending stiffness. The vertical movement of the soil mainly appeared in the central loading area, as shown in Figure 4, and the distance had already existed between the loading area and the pile; thus, the soil movement pushing the pile was approximately 3 m below the ground surface combined with displacement vector of the foundation soil in the FDM. Therefore, the high-stiffness pile pushed by soil movement increased the maximum displacement, while the low-stiffness pile was the opposite due to gravel with relatively high performance in the first layer. However, the lateral displacement of the pile was almost unchanged at depths >8 m.

Figure 4 shows the variation in the final vertical displacement of the foundation soil at the ground surface in the loading area for different pile bending stiffnesses. The A-A section (short edge of the loading area) and the B-B section (center of the loading area) were monitored and shown in Figure 1. As shown in Figure 4A, the settlement (i.e., positive values) developed in the middle zone of the A-A section, with a distribution length of 12 m. In contrast, the corner of the A-A section developed an uplift (i.e., negative values) of 4 m in width. The distribution of vertical displacement was basically symmetrical in the A-A section due to its position away from the pile compared to the B-B section. Contrarily, the distribution of vertical displacement in the B-B section was not symmetrical due to its close proximity to the pile. The maximum settlement values in the A-A section were 108.68, 108.21, 107.78, 111.46, 110.72, and 110.26 mm for bending stiffnesses of 0.04, 0.4, 0.81, 1.61, 8.06, and 16.11 GPa, respectively. The maximum average uplift values were 74.50, 73.84, 74.08, 78.40, 78.48, and 78.17 mm bending stiffnesses of 0.04, 0.4, 0.81, 1.61, 8.06, and 16.11 GPa, respectively. As shown in Figure 4B, only positive values (i.e., settlement) were observed in the B-B section and were

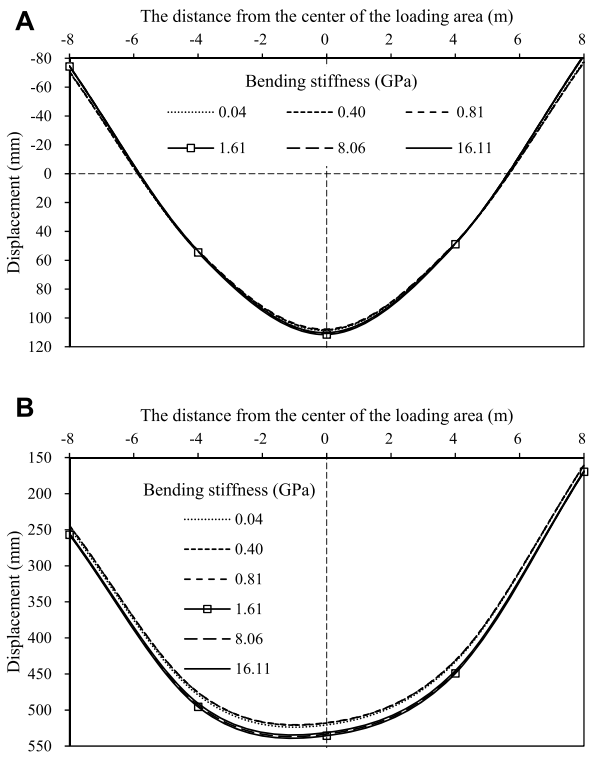

FIGURE 4
Foundation soil final vertical displacement in the bottom surface of the loading area at different pile bending stiffnesses at the **(A)** A-A and **(B)** B-B sections.

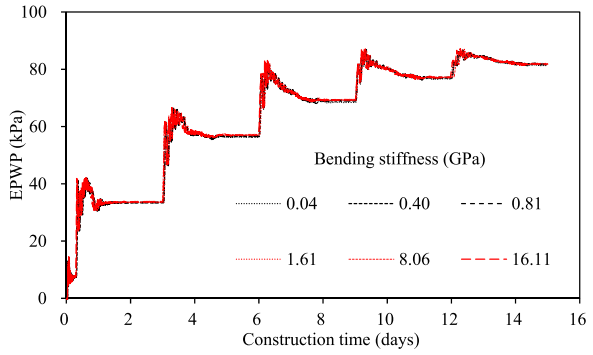

FIGURE 5
Variation in EPWP with construction time for different bending stiffnesses.

generally larger than those in the A-A section. The maximum settlement values in the B-B section were 520.65, 517.93, 517.51, 535.50, 533.28, and 531.21 mm for bending stiffnesses of 0.04, 0.4, 0.81, 1.61, 8.06, and 16.11 GPa, respectively. The vertical displacement for the low-stiffness pile in the B-B section was slightly larger than that of the high-stiffness pile, with a

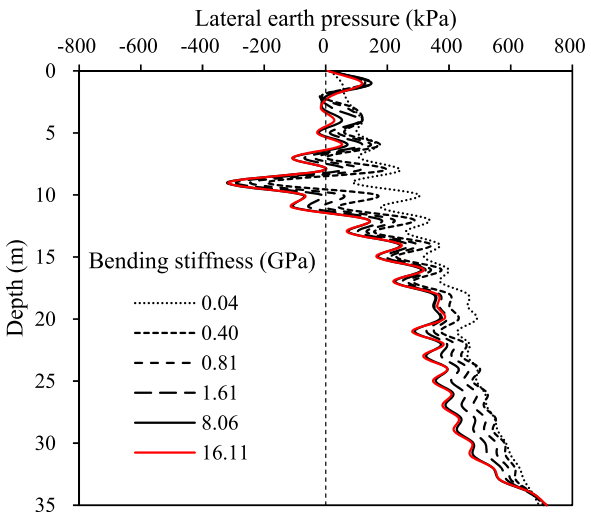

FIGURE 6
Distribution of lateral earth pressure with depth at different bending stiffnesses after the fifth loading.

maximum variation of about 3.4% for a bending stiffness increase from 0.81 to 1.61 GPa. Therefore, the pile bending stiffness slightly impacted the final vertical displacement of the foundation soil at the ground surface in the loading area.

Figure 5 shows the excess pore water pressure (EPWP) *versus* the construction time for different bending stiffness. The monitored position of PWP was 1 m below the water table, as shown in Figure 1B). The EPWPs increased rapidly after the placement of each new lift and then slowly dissipated with time. The EPWP may not completely dissipate due to the extremely low permeability of the foundation soil and the limitation of construction time. Therefore, the EPWP continuously accumulated after each new lift was placed. The tendencies and values of EPWP at different bending stiffness were similar. Using a bending stiffness of 11.61 GPa as an example, the EPWP increments were approximately 33.9, 23.2, 12.2, 8.0, and 4.5 kPa after each lift loading, respectively. The EPWP increment decreased significantly and was nonlinear with increased surcharge loading. The results showed that the EPWP was nearly not dependent on the bending stiffness.

Figure 6 shows the variation in the lateral earth pressure with depth for different bending stiffness after the fifth loading. The lateral earth pressure acting at the pile was selected from the horizontal stress of the adjacent foundation soil zone in the numerical model. Lateral earth pressures at depths >2 m depth were almost unchanged for different bending stiffness, except for a bending stiffness of 0.04 GPa. The lateral earth pressure <2 m of ground surface decreased with increasing bending stiffness. The increment of lateral earth pressure <2 m of the ground surface reduced with increasing bending stiffness. Particularly, the lateral earth pressure changed slightly as the bending stiffness increased

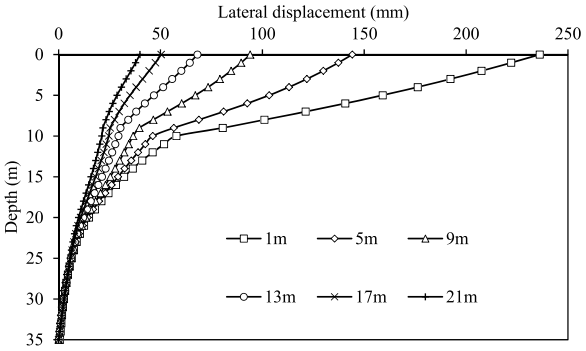

FIGURE 7
Lateral displacement of the pile shaft for different *D* values after the fifth loading.

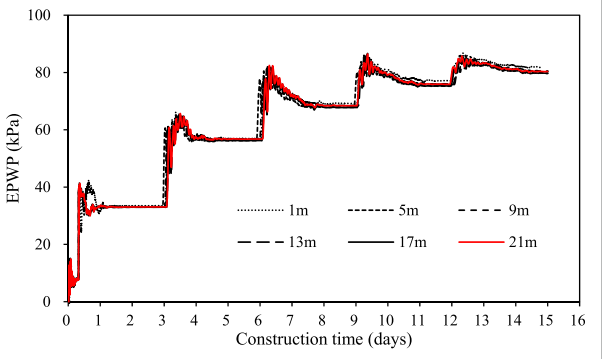

FIGURE 9
Variation in EPWP with construction time for different *D* values.

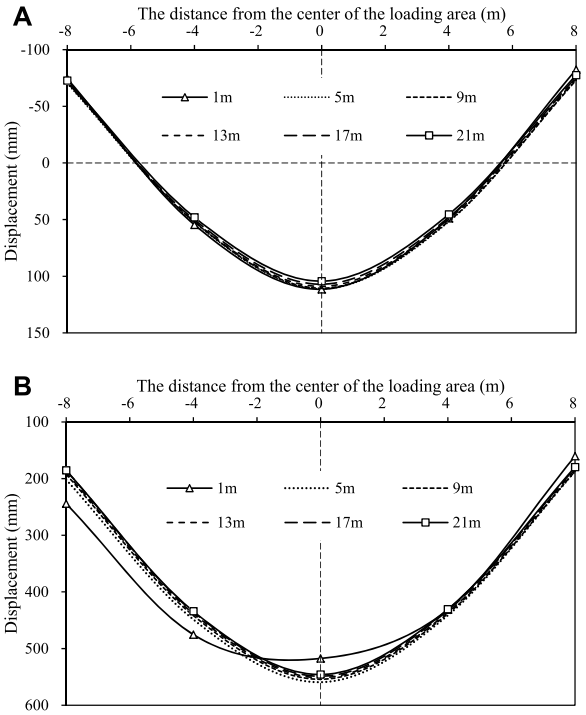

FIGURE 8
Foundation soil final vertical displacement in the bottom surface of the loading area for different *D* values at the **(A)** A-A and **(B)** B-B sections.

from 8.06 to 16.11 GPa. The lateral earth pressure values for the bending stiffness of 0.04 GPa were positive for different depths and typically increased with increased depth at the end of the fifth lift loading. The lateral earth pressure values for all bending stiffnesses were negative at a depth of 9 m, except for the bending stiffness of 0.04 GPa. The suction effect may explain the negative earth pressure, mainly in piles with relatively high bending stiffnesses.

Effect of D

The foundation soil directly contacted and pushed the passive pile under the surcharge load. The distance between the long edge of the loading area and the pile (*D* = 1, 5, 9, 13, 17, and 21 m) was important and selected as the critical factor in investigating its influence on the passive pile. Figure 7 shows the variations in lateral displacement with depth for different *D* values after the fifth loading. The lateral displacements of the pile for different *D* values decreased with increasing depth, with the fastest lateral displacement reduction rate observed at depths >10 m. The lateral displacement reduction rate of the pile was relatively slow at depts of 10–20 m; moreover, the lateral displacement of the pile did not change significantly with increasing *D* value for depths >20 m. Both the lateral displacement of the pile and its reduction rate decreased with increasing *D* value. The maximum lateral displacements of the pile were at the ground surface regardless of the *D* value, at 236.11, 144.13, 94.01, 68.10, 50.32, and 39.88 mm for *D* values of 1, 5, 9, 13, 17, and 21 m, respectively.

Figure 8 shows the variations in the final vertical displacement of the foundation soil at the ground surface in the loading area for different *D* values. The shapes of settlement (i.e., positive values) and uplift (i.e., negative values) in Figure 8 are similar to those in Figure 4. The maximum settlement values in the A-A section were 111.46, 111.09, 110.54, 108.95, 107.03, and 104.30 mm for *D* values of 1, 5, 9, 13, 17, and 21 m, respectively. The maximum average uplift values were 78.40, 71.82, 72.25, 72.54, 73.50, and 75.16 mm for *D* values of 1, 5, 9, 13, 17, and 21 m, respectively. The maximum settlement values in the B-B section were 517.51, 559.34, 554.20, 551.29, 548.81,

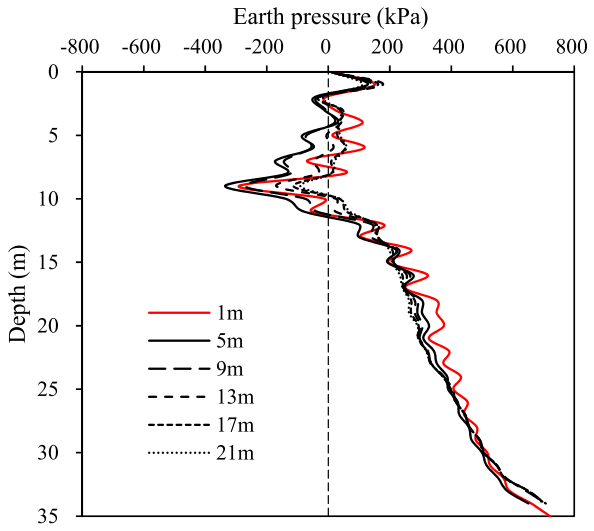

FIGURE 10
Distribution of earth pressure with depth for different *D* values after the fifth loading.

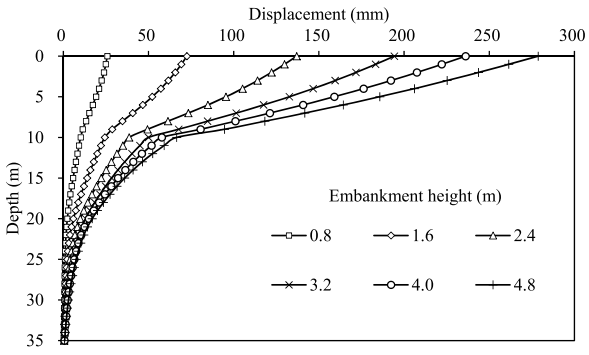

FIGURE 11
Lateral displacement of the pile shaft for different embankment heights.

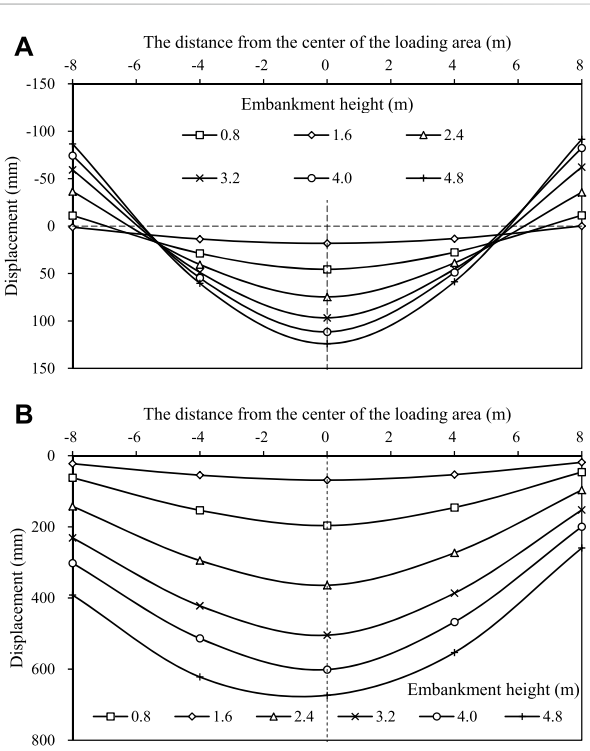

FIGURE 12
Foundation soil final vertical displacement in the embankment's bottom surface under different embankment heights at the **(A)** A-A and **(B)** B-B sections.

and 545.76 mm for *D* values of 1, 5, 9, 13, 17, and 21 m, respectively. The maximum settlement value in the A-A section decreased slightly with increased *D* value, except in the uplift zone. The maximum settlement value in the B-B section decreased slightly with increased *D* values except for the *D* value at 1 m. The vertical displacement shape for both sections tended to be symmetrical with increasing *D* value due to the gradually increasing distance of the loading area from the pile.

Figure 9 shows the EPWP *versus* the construction time for different *D* values. The change in EPWP for different *D* values was slight, at approximately 33, 57, 69, 76, and 80 kPa at the end of each lift for different *D* values. The changes in EPWP were approximately 33, 24, 12, 7, and 4 kPa after each lift loading, respectively. The EPWP decreased with increasing surcharge loading. The EPWP increased significantly after each new lift loading and then dissipated to a value within the maintenance time of 3 days due to the closing of the water table. The value of the EPWP accumulated after each new lift loading due to the extremely low permeability and limitation of construction time. The results showed that the distance between the long edge of the loading area and pile *D* slightly affected the EPWP generation and dissipation.

Figure 10 shows the variation in lateral earth pressure with depth at different *D* values after the fifth loading. Lateral earth pressures at 2–15 m depth increased with increasing *D* values except for the *D* value at 1 m. At depths of 15–25 m, the pressures decreased slightly with increasing *D* values. The lateral earth pressure was almost unchanged at different *D* values for other depths. Due to the existing pile, the lateral earth pressure changed irregularly when the loading area was close to the pile; i.e., a *D* value of 1 m. The lateral earth pressure for all *D* values was negative at a depth of approximately 9 m depth to the suction effect. Therefore, the *D* value significantly affected the lateral earth pressure on the pile.

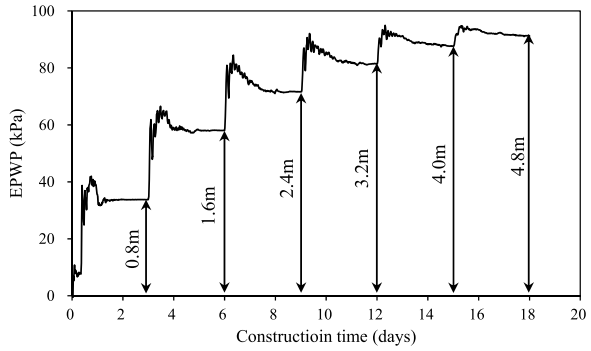

FIGURE 13
Variation in EPWP with construction time for different embankment heights.

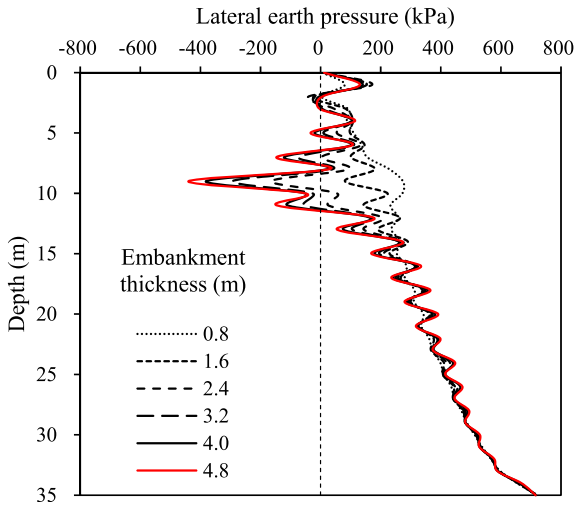

FIGURE 14
Distribution of earth pressure with depth at different embankment heights at the end of loading.

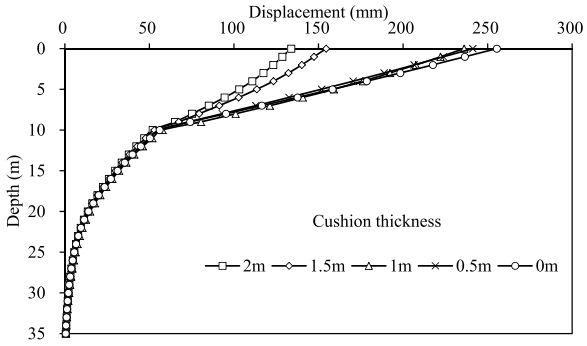

FIGURE 15
Lateral displacement of the pile shaft for different cushion thicknesses at the end of loading.

Effect of embankment height

Figure 11 shows the lateral displacement of the pile according to depth and embankment height. Each load (maintained for 3 days) equaled an embankment height of 0.8 m on the loading area until the total height reached the desired embankment height. The embankment height significantly affected the lateral displacement of the pile, especially at ground level. The maximum lateral displacement values for embankment heights of 0.8, 1.6, 2.4, 3.2, 4.0, and 4.8 m were 25.82, 72.47, 136.96, 194.27, 236.11, and 278.72 mm, respectively. The maximum lateral displacement was at the top of the pile. The lateral displacement and its increment increased and decreased with the increasing embankment height, respectively. The lateral displacement decreased with increasing depth, with the fastest reduction at depths of >10 m depth.

Figure 12 shows the variation in the final vertical displacement of the foundation soil at ground level in the loading area for different embankment heights. As shown in Figure 12A, the settlement (i.e., positive value) and uplift (i.e., negative value) in the A-A section increased with increasing embankment height. For example, the maximum settlement value in the A-A section increased from 18.17 to 123.98 mm as the embankment height increased from 0.8 to 4.8 m, and from 11.30 to 89.13 mm as the embankment height increased from 0.8 to 4.8 m. As shown in Figure 12B, all displacement values in the B-B section were positive (i.e., settlement). The settlement increased with increasing embankment height. The maximum settlement value in the B-B section increased from 68.73 to 673.72 mm as the embankment height increased from 0.8 to 4.8 m. Therefore, the vertical displacement in the loading area was sensitive to the embankment height.

Figure 13 shows the variation in EPWP with construction time for different embankment heights. The EPWP increased increasing embankment height. The EPWP values after the construction of embankment heights of 0.8, 1.6, 2.4, 3.2, 4.0, and 4.8 m were 33.78, 58.03, 72.18, 81.29, 87.71, and 91.30 kPa, respectively. Due to the position closing the water table and low permeability, the EPWP dissipated. Therefore, the EPWP depended on the embankment height.

Figure 14 shows the variation in lateral earth pressure with depth at different embankment heights at the end of loading. The lateral earth pressures at depths of 2–15 m increased with increasing embankment height, while depths <15 m changed slightly with changing embankment height. The biggest change was at a depth of 9 m due to stress concentration. The lateral earth pressure values for all embankment heights

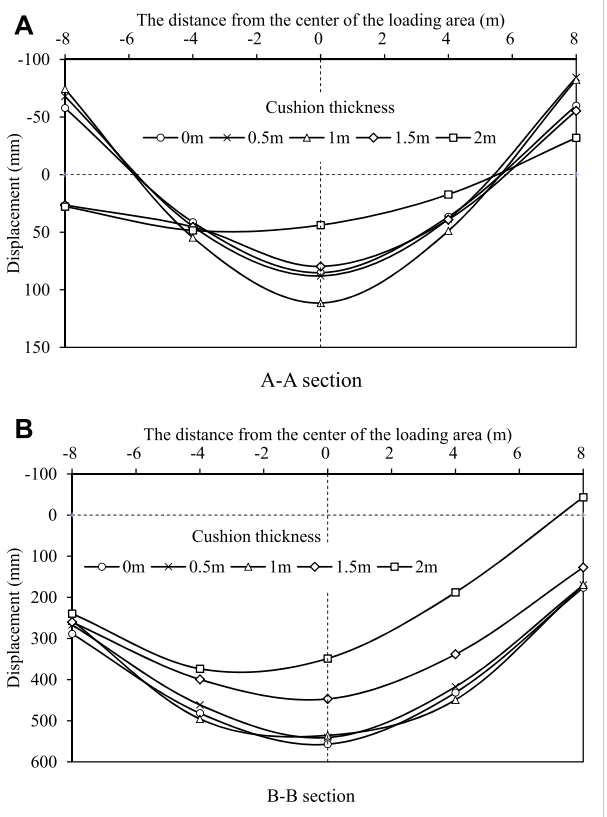

FIGURE 16
Foundation soil final vertical displacement in the embankment's bottom surface under different embankment heights at the **(A)** A-A and **(B)** B-B sections.

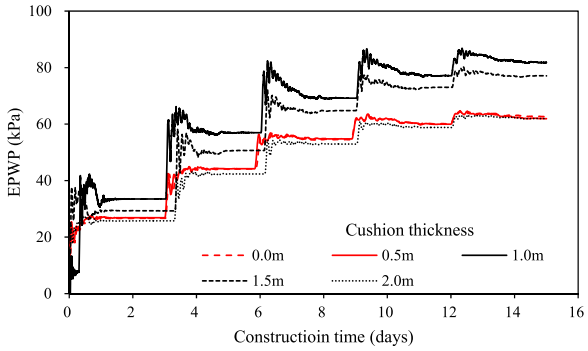

FIGURE 17
Variation in EPWP with construction time for different cushion thicknesses.

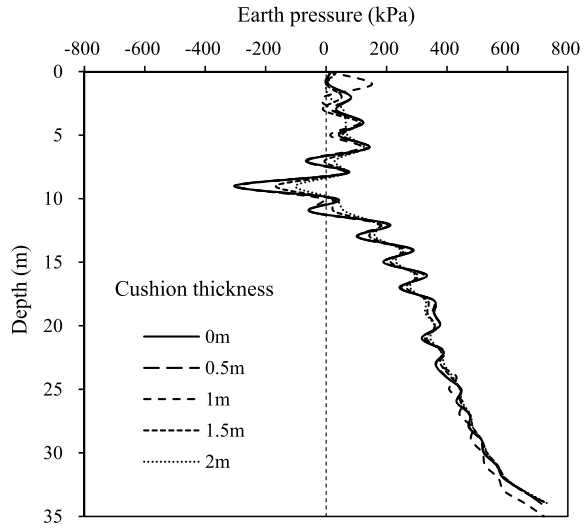

FIGURE 18
Distribution of earth pressure with depth for different cushion thicknesses at the end of loading.

were negative values at a depth of approximately 9 m due to the suction effect. Therefore, the embankment height significantly impacted the lateral earth pressure on the pile.

Effect of cushion thickness

In the real field test, a 1 m thick gravel cushion was placed on the ground surface as the first layer. This section discusses the effect of the replacement method on improving the foundation; i.e., the influence of the thickness of the soil replacement cushion. Figure 15 shows the lateral displacement of the pile shaft for different cushion thicknesses. The lateral displacement of the pile increased with increasing cushion thickness. The lateral displacements at the top of the pile for cushion thicknesses of 0, 0.5, 1.0, 1.5, and 2.0 m were 255.40, 241.21, 236.11, 154.48, and 133.80 mm, respectively. The lateral displacement of the pile decreased significantly with increasing cushion thickness from 1 to 1.5 m. The lateral displacement showed a relatively large decrease with increasing cushion thickness from 1.5 m to 2.0 m. However, the lateral displacement reduction was slight for increasing cushion thickness from 0 to 1 m. These findings demonstrated an effective cushion thickness of 1.5 m based on the measurements of lateral displacement.

Figure 16 shows the variation in the final vertical displacement of the foundation soil at the ground surface in the loading area for different embankment heights. As shown in Figure 16A, the settlement and uplift values increased with increased cushion thickness from 0 to 1 m and decreased with an increased cushion thickness from 1 to 2 m. As shown in Figure 16B), the settlement value decreased with increased cushion thickness from 1 to 2 m and was stable with increased cushion thickness from 0 to 1 m. The vertical displacement was negative in section B-B at a cushion

thickness of 2 m. Thus, cushion thickness improved the vertical displacement of the loading area.

Figure 17 shows the variation in EPWP with construction time for different cushion thicknesses. All EPWP increased significantly after each lift loading and dissipated due to low permeability and the limitation of construction time. The increase in cushion thickness from 1 to 2 m resulted in decreased EPWPs; moreover, a decrease in cushion thickness from 1 to 0 m also decreased the EPWP. However, the change in EPWP was slight when the cushion thickness decreased from 0.5 to 0 m, which can be attributed to a change in drainage capacity with increasing cushion thickness. The thin cushion did not carry the load at a shallow depth (i.e., 2 m from the ground surface).

Figure 18 shows the variation in lateral earth pressure with depth for different cushion thicknesses at the end of loading. The lateral earth pressure at a depth of 6–12 m decreased with increasing cushion thickness, while its value at <12 m depth slightly changed changes in cushion thickness. However, a slight decrease in lateral earth pressure at a depth of 6–12 m depth was observed when the cushion thickness decreased from 1 to 0 m. The biggest change was observed at a depth of 9 m due to the stress concentration. The lateral earth pressure values for all cushion thicknesses were negative at depths of approximately 9 m depth due to the suction effect. Therefore, the cushion thickness slightly affected the lateral earth pressure on the pile at cushion thicknesses <1 m.

Conclusion

This study investigated four essential factors (pile bending stiffness, distance between the long edge of the loading area and pile *D*, embankment height, and cushion thickness) in a series of three-dimensional finite element method (FEM) models to assess their effects on the characteristic of a single pile installed in extensively soft soil and subjected to passive loading due to the adjacent surcharge load. Based on the results obtained from the numerical models, the following conclusions can be drawn:

1) Compared to the real field test modeled in FDM, decreased and increased bending stiffness significantly reduced and slightly increased the pile's maximum lateral displacement, respectively. The effect of cushion thickness on lateral displacement was contrary to the bending stiffness. Increased *D* value and decreased embankment height remarkably decreased the pile's lateral displacement.
2) Variation in pile bending stiffness did not affect the vertical displacement at the ground surface in the loading area. Increased *D* values made the distribution shape of the vertical displacement closer to symmetrical. The embankment height and cushion thickness significantly affected the vertical displacement.
3) Due to the low permeability of the foundation soil and the limitation of the construction time, variation in pile bending stiffness and *D* value hardly affected EPWP dissipation and generation. Increased embankment height increased the EPWP.
4) Pile bending stiffness significantly affected the lateral earth pressure, with increasing stiffness decreasing the pressure. Decreased *D* values up to 1 m increased the lateral earth pressure. The embankment height significantly affected the lateral earth pressure. A cushion thickness of <1 m did not affect the lateral earth pressure.

Data availability statement

The raw data supporting the conclusion of this article will be made available by the author without undue reservation.

Author contributions

SY was the first author and was responsible for the analysis and writing.

Funding

This research was funded by the National Natural Science Foundation of China (grant no. 51908150). The above support was appreciated.

Conflict of Interest

SY was employed by Guangzhou Metro Design & Research Institute Co., Ltd.

The author declare that the research was conducted in the absence of any commercial or financial relationships that could be construed as a potential conflict of interest.

Publisher's note

All claims expressed in this article are solely those of the authors and do not necessarily represent those of their affiliated organizations, or those of the publisher, the editors, and the reviewers. Any product that may be evaluated in this article, or claim that may be made by its manufacturer, is not guaranteed or endorsed by the publisher.

References

Abo-Youssef, A., Morsy, M. S., ElAshaal, A., and ElMossallamy, Y. M. (2021). Numerical modelling of passive loaded pile group in multilayered soil. *Innov. Infrastruct. Solut.* 1 (6), 101–113. doi:10.1007/s41062-021-00464-6

Al-abboodi, I., Sabbagh, T. T., and Al-salih, O. (2020). Response of passively loaded pile groups-an experimental study. *Geomechanics Eng.* 333 (20), 333–343.

Al-abboodi, I., and Sabbagh, T. T. (2019). Numerical modelling of passively loaded pile groups. *Geotech. Geol. Eng. (Dordr).* 2747 (37), 2747–2761. doi:10.1007/s10706-018-00791-z

Bai, B., Fan, B., Li, X., Nie, Q., Jia, X., and Wu, H. (2022a). The remediation efficiency of heavy metal pollutants in water by industrial red mud particle waste. *Environ. Technol. Innovation* 28, 102944. doi:10.1016/j.eti.2022.102944

Bai, B., Wang, Y., Rao, D., and Fan, B. (2022b). The effective thermal conductivity of unsaturated porous media deduced by pore-scale SPH simulation. *Front. Earth Sci. (Lausanne)* 10. doi:10.3389/feart.2022.943853

Bai, B., Zhou, R., Cai, G., Hu, W., and Yang, G. (2021). Coupled thermo-hydro-mechanical mechanism in view of the soil particle rearrangement of granular thermodynamics. *Comput. Geotech.* 137 (8), 104272. doi:10.1016/j.compgeo.2021.104272

Basack, S., Indraratna, B., and Rujikiatkamjorn, C. (2016). Modeling the performance of stone column–reinforced soft ground under static and cyclic loads. *J. Geotech. Geoenviron. Eng.* 142, 04015067. doi:10.1061/(asce)gt.1943-5606.0001378

Bellezza, I. (2020). Closed-form expressions for a rigid passive pile in a two-layered soil. *Géotechnique Lett.* 242 (10), 242–249. doi:10.1680/jgele.19.00250

Cole, R. T. (2003). *Full-scale effects of passive earth pressure on the lateral resistance of pile caps*. USA: Brigham Young University.

Deb, K., Dhar, A., and Purohit, S. (2016). "A simulation-optimization model for Stone column-supported embankment stability considering rainfall effect," in AIP Conference Proceedings, 01 February 2016.

Fattah, M. Y., Zabar, B. S., and Hassan, H. A. (2016). Experimental analysis of embankment on ordinary and encased stone columns. *Int. J. Geomech.* 16, 04015102. doi:10.1061/(asce)gm.1943-5622.0000579

Gu, M., Cai, X., Fu, Q., Li, H., Wang, X., and Mao, B. (2022a). Numerical analysis of passive piles under surcharge load in extensively deep soft soil. *Buildings* 12, 1988. doi:10.3390/buildings12111988

Gu, M., Mo, H., Qiu, J., Yuan, J., and Xia, Q. (2022b). Behavior of floating stone columns reinforced with geogrid encasement in model tests. *Front. Mat.* 9, 980851. doi:10.3389/fmats.2022.980851

Guo, W. (2003). "A simplified approach for piles due to soil movement," in Proceedings of the 12th Panamerican Conference on Soil Mechanics and Geotechnical Engineering, Germany, 2003.

Guo, W. D., Qin, H., and Ghee, E. (2017). Modeling single piles subjected to evolving soil movement. *Int. J. Geomech.* 17, 04016111. doi:10.1061/(asce)gm.1943-5622.0000803

Itasca (2018). *FLAC3D 6.0 document*. Minneapolis, MN: Itasca Consulting Group.

Kadhim, S., Parsons, R. L., and Han, J. (2015). Stability analysis of embankments supported by geosynthetic encased stone columns. *IFCEE* 2318, 2318–2327.

Kalantari, B., and Tavan, Y. (2019). 2d fem analysis of stone column-supported embankment and studying the effects of various parameters on its stability using cam-clay model. *Comput. Geotechnics* 68, GT4. doi:10.1016/j.compgeo.2015.03.014

Karim, M., Lo, S.-C., and Gnanendran, C. (2014). Behaviour of piles subjected to passive loading due to embankment construction. *Can. Geotech. J.* 303 (51), 303–310. doi:10.1139/cgj-2012-0468

Karim, M. R. (2013). Behaviour of piles subjected to passive subsoil movement due to embankment construction–A simplified 3D analysis. *Comput. Geotechnics* 1 (53), 1–8. doi:10.1016/j.compgeo.2013.04.004

Karkush, M., Aljorany, A., and Jaffar, G. (2020). Behavior of passive single pipe pile in sandy soil. *IOP Conf. Ser. Mater. Sci. Eng.* 737, 012106. doi:10.1088/1757-899X/737/1/012106

Karkush, M. O., and Jaffar, G. S. (2020). Simulation the behavior of passive rigid pile in sandy soil. *J. Eng. Technol. Sci.* 449 (52), 449–467. doi:10.5614/j.eng.technol.sci.2020.52.4.1

Li, H.-q., Wei, L.-m., Feng, S.-y., and Chen, Z. (2019). Behavior of piles subjected to surcharge loading in deep soft soils: Field tests. *Geotech. Geol. Eng. (Dordr).* 4019 (37), 4019–4029. doi:10.1007/s10706-019-00890-5

Li, H., Liu, S., Yan, X., Gu, W., and Tong, L. (2021). Effect of loading sequence on lateral soil-pile interaction due to excavation. *Comput. Geotechnics* 104134 (134), 104134. doi:10.1016/j.compgeo.2021.104134

Malarvizhi, S., and Ilamparuthi, K. (2007). Comparative study on the behavior of encased stone column and conventional stone column. *Soils Found.* 873 (47), 873–885. doi:10.3208/sandf.47.873

Ong, D. (2018). Detrimental effects of lateral soil movements on pile behaviour. *Geotech. Eng.* 85 (49), 85–95.

Qin, H., and Guo, W. D. (2016). Response of piles subjected to progressive soil movement. *Geotechnical Test. J.* 39, 1. doi:10.1520/GTJ20140148

Ramalakshmi, M. (2021). Force-displacement response of bridge abutments under passive push. *Mater. Today Proc.* 883 (43), 883–887. doi:10.1016/j.matpr.2020.07.202

Sabbagh, T. T., Al-Salih, O., and Al-Abboodi, I. (2019). Experimental investigation of batter pile groups behaviour subjected to lateral soil movement in sand. *Int. J. Geotechnical Eng.* 14, 705–716. doi:10.1080/19386362.2019.1585596

Şahinkaya, F., Vekli, M., and Çadır, C. C. (2017). Numerical analysis under seismic loads of soils improvement with floating stone columns. *Nat. Hazards (Dordr).* 891 (88), 891–917. doi:10.1007/s11069-017-2897-0

Shan, Y., Zhao, J., Tong, H., Yuan, J., Lei, D., and Li, Y. (2022). Effects of activated carbon on liquefaction resistance of calcareous sand treated with microbially induced calcium carbonate precipitation. *SOIL Dyn. Earthq. Eng.* 161, 107419. doi:10.1016/j.soildyn.2022.107419

Yang, M., Shangguan, S., Li, W., and Zhu, B. (2017). Numerical study of consolidation effect on the response of passive piles adjacent to surcharge load. *Int. J. Geomech.* 17, 04017093. doi:10.1061/(asce)gm.1943-5622.0000991

Yi, S., and Liu, J. (2022). Field investigation of steel pipe pile under lateral loading in extensively soft soil. *Front. Mat.* 9, 480. doi:10.3389/fmats.2022.971485

Yuan, J., Lei, D., Shan, Y., Tong, H., Fang, X., and Zhao, J. (2022). Direct shear creep characteristics of sand treated with microbial induced calcite precipitation. *Int. J. Civ. Eng.* 20, 763–777. doi:10.1007/s40999-021-00696-8

Zhang, H., Shi, M., and Guo, Y. (2020a). Semianalytical solutions for abutment piles under combined active and passive loading. *Int. J. Geomech.* 20, 04020171. doi:10.1061/(asce)gm.1943-5622.0001804

Zhang, H., Shi, M., Yang, L., and Guo, Y. (2020b). A semianalytical solution for passively loaded piles adjacent to surcharge load. *Adv. Civ. Eng.* 1 (2020), 1–19. doi:10.1155/2020/2398389

Zhang, H., and Sun, K. (2020). Influence of surcharge load on the adjacent pile foundation in coastal floodplain. *Insight-Civil Eng.* doi:10.18282/ice.v3i1.312

frontiers | Frontiers in Materials

TYPE Original Research
PUBLISHED 04 January 2023
DOI 10.3389/fmats.2022.1112425

Check for updates

OPEN ACCESS

EDITED BY
Bing Bai,
Beijing Jiaotong University, China

REVIEWED BY
Yang Lu,
Sichuan University, China
Wen Nie,
Jiangxi University of Science and Technology, China

*CORRESPONDENCE
Jia Zhengpeng,
553411469@qq.com

SPECIALTY SECTION
This article was submitted to Structural Materials, a section of the journal Frontiers in Materials

RECEIVED 30 November 2022
ACCEPTED 15 December 2022
PUBLISHED 04 January 2023

CITATION
Chunyu L, Zhengpeng J, Zhi L, Kefeng X and Bohan W (2023), Analyses on face stability of shallow tunnel considering different constitutive models. *Front. Mater.* 9:1112425. doi: 10.3389/fmats.2022.1112425

COPYRIGHT
© 2023 Chunyu, Zhengpeng, Zhi, Kefeng and Bohan. This is an open-access article distributed under the terms of the Creative Commons Attribution License (CC BY). The use, distribution or reproduction in other forums is permitted, provided the original author(s) and the copyright owner(s) are credited and that the original publication in this journal is cited, in accordance with accepted academic practice. No use, distribution or reproduction is permitted which does not comply with these terms.

Analyses on face stability of shallow tunnel considering different constitutive models

Luo Chunyu[1], Jia Zhengpeng[2]*, Li Zhi[3], Xiao Kefeng[3] and Wu Bohan[2]

[1]Road Tunnel Branch of Sichuan Highway Bridge Construction Group Co., Ltd., Chengdu, Sichuan, China, [2]Civil Engineering, The Southwest Jiaotong University, Chengdu, Sichuan, China, [3]Faculty of Geosciences and Environmental Engineering, The Southwest Jiaotong University, Chengdu, Sichuan, China

Based on the finite element limit analysis method, the stability of the face in case of active failure under three constitutive models, the Mohr-Coulomb model (MC), the modified Cambridge model (MCC) and the Drucker-Prager model (DP), were analyzed. The ultimate support pressure of the face and the influence of factors such as different burial depth ratios (*C/D*), cohesion (*c*) and friction angle (φ) in the MC model are also discussed. The results show that the safety factor obtained by the MCC model under the same support pressure is always smaller than that of the MC model, and the difference is the largest when there is no support pressure. As the support pressure increases, it will gradually approach the MC model. When the support pressure is small, the safety factor obtained by the DP model is larger than the MC model, but when the support pressure is large, it is smaller than the MC model, and the final difference tends to be stable. It is necessary to select an appropriate constitutive model according to different rock masses in practical engineering. The self-stabilizing performance of the face is not affected by *C/D*, and the ultimate support pressure will increase with the increase of *C/D*, decrease linearly with the increase of cohesion, and decrease with the increase of friction angle. When the friction angle is small, the ultimate support pressure is greatly affected by *C/D*, and when the friction angle is large, it is hardly affected by *C/D*.

KEYWORDS

railway tunnel, constitutive model, numerical calculation, stable tunnel face, ultimate support pressure

1 Introduction

The development of underground space in cities has become a trend with the rapid growth of urban rail transportation in China. The current shield construction technology is one of the leading engineering methods for urban underground tunnel construction (Sui et al., 2021) the shield excavation process, the support on the tunnel face is the guarantee to maintain the stability of the tunnel. When the support pressure is too small, the tunnel will collapse, and when the support pressure is too enormous the ground

surface will bulge (Zamora Hernández et al., 2019). Therefore, how to solve the ultimate support pressure more accurately has become a sensitive research topic for most scholars.

In the early days, the stability of the tunnel face after tunnel excavation was studied by empirical formulas and simple qualitative or quantitative analysis (Broms and Bennermark, 1967). However, these methods were relatively crude in the calculation. Subsequently, the limit equilibrium method and the limit analysis method were rapidly developed for geotechnical applications (He et al., 2019a; He et al., 2019b; He et al., 2021; He et al., 2022) and were also widely used in the stability analysis of tunnel faces and could be used to find out the ultimate support pressure of tunnel faces (Chen, 1975; Davis et al., 1980; Comejo, 1989; Leca and Dormieus, 1990; Mollon et al., 2010; Han et al., 2016; Lu et al., 2017). However, these two methods have many assumptions that make it difficult to solve complex problems. The emergence of finite element methods have brought new solvers to geotechnical issues (Sloan and Assadi, 1991; Wilson et al., 2011; Zheng et al., 2012; He et al., 2019c; Shiau Al-Asadi, 2020), and with the development of computer and numerical computation technology, various numerical simulation software has become more and more widely used, and not only finite element numerical software such as ABAQUS, ANSYS, FLAC 3D and OPTUM G2 have been used for stability analysis of tunnel faces (Do et al., 2014; Li and Li, 2019; Zamora Hernández et al., 2019; Huang et al., 2020; Zheng et al., 2022), but many discrete element numerical software is also maturing and being used in the study of geotechnical properties (Bai et al., 2022).

The Mohr-Coulomb constitutive model (MC model) is mainly used in the above tunnel face stability analysis (Ji et al., 2021; Feng et al., 2022), which is popular among scholars and engineers because of its simple and practical features, and as research progresses, more and more Constitutive models are proposed and gradually used in the stability analysis of tunnel faces (Bai et al., 2019; Bai et al., 2021). The Mohr-Coulomb model considers that the compression modulus and rebound modulus of the soil are the same, and there are some cases where the Mohr-Coulomb model is not applicable, and it is necessary to select a suitable constitutive model according to different tunneling conditions. Zhao et al. (2015) used the HSS model to simulate the shield supported mechanized excavation of the Western Scheldt tunnel in the Netherlands. Keawsawasvong and Ukritchon, (2020) used the Hoek-Brown model to develop a new design equation for stability analyses of shallow unlined circular tunnels in rock masses. Liu et al. (2020) used the DP model to present a semi-analytical solution as well as finite element numerical simulations for the tunnel excavation problem. Fang et al. (2022) used a number of constitutive models to account for initial soil anisotropy and non-coaxial plasticity, which were confirmed in a field investigation through the Tsinghua Park Tunnel of the Beijing-Zhang High Speed Railway in China.

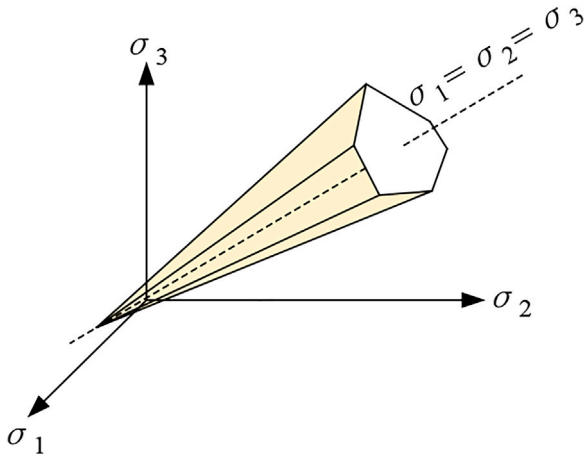

FIGURE 1
MC yield surface in principal stress space.

Therefore, this paper discusses the stability of the tunnel face under active failure calculated with three constitutive models and solves for the ultimate support pressure, and discusses the effects of parameters such as burial depth ratio C/D and cohesion c, friction angle φ.

2 Constitutive model

2.1 Mohr-coulomb model (MC)

The MC model is very widely used in geotechnical analysis nowadays. It is not only a relatively simple model, but more importantly is that all of its parameters have direct physical meaning and can be measured by conventional tests such as direct shear and triaxial tests. The principal stresses σ_1 and σ_3 are used to represent the yield surface (as shown in Figure 1) as a function of

$$F = (\sigma_1 - \sigma_3) + (\sigma_1 + \sigma_3)\sin\varphi - 2c\cos\varphi \tag{1}$$

In order to avoid explicit calculation of principal stresses, Nayak and Zienkiewicz (Nayak and Zienkiewicz, 1972) proposed to use the following variables based on the stress tensor principle:

$$F = \sigma_m \sin\varphi + \bar{\sigma}K(\theta) - c\cos\varphi \tag{2}$$

which

$$\sigma_m = \frac{1}{3}\left(\sigma_x + \sigma_y + \sigma_z\right) \tag{3}$$

$$\bar{\sigma} = \sqrt{\frac{1}{2}\left(s_x^2 + s_y^2 + s_z^2\right) + \tau_{xy}^2 + \tau_{xz}^2 + \tau_{yz}^2} \tag{4}$$

$$\theta = \frac{1}{3}\sin^{-1}\left(-\frac{3\sqrt{3}}{2}\frac{J_3}{\bar{\sigma}^3}\right) \tag{5}$$

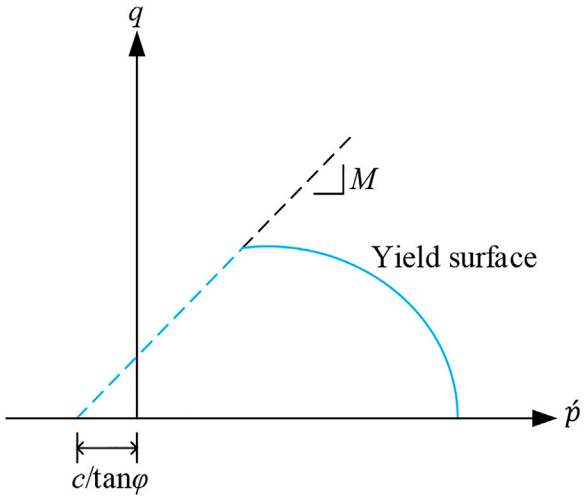

FIGURE 2
MCC yield surface in the q-$\boldsymbol{p}$ plane.

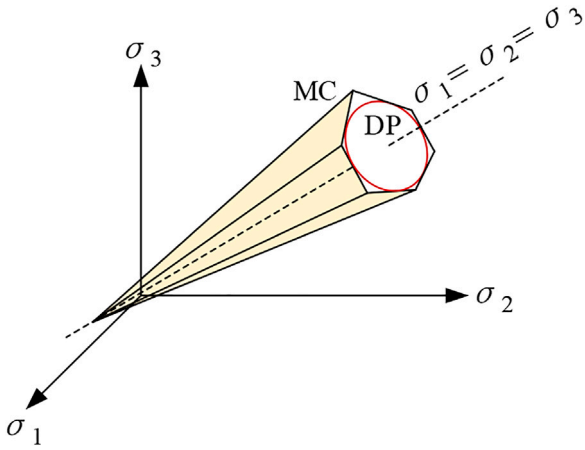

FIGURE 3
MC and DP yield surfaces in principal stress space.

$$J_3 = s_x s_y s_z + 2\tau_{xy}\tau_{xz}\tau_{yz} + s_x\tau_{yz}^2 + s_y\tau_{xz}^2 + s_z\tau_{xy}^2 \quad (6)$$

$$s_x = \sigma_x - \sigma_m \quad (7)$$

$$s_y = \sigma_y - \sigma_m \quad (8)$$

$$s_z = \sigma_z - \sigma_m \quad (9)$$

The MC model is controlled by the elastic modulus E and Poisson's ratio υ for elastic deformation, and the cohesion c, friction angle φ and shear expansion angle ψ for plastic deformation.

2.2 Modified cam-clay model (MCC)

The Cambridge model was constructed by Roscoe and Burland (Roscoe and Burland, 1968); in 1968 and was later modified and refined for the analysis of elastic-plastic deformation of clay soils (both consolidated and superconsolidated). A slightly extended version of this model was implemented according to the scheme proposed by Krabbenhoft (Krabbenhoft and Lyamin, 2012), and the yield surface (as shown in Figure 2) functioned as:

$$F = q^2 - Mp'^2\left(p_c - p'\right) \quad (10)$$

which

$$p' = \frac{1}{3}\left(\sigma_x' + \sigma_y' + \sigma_z'\right) \quad (11)$$

$$q = \sqrt{\frac{1}{2}\left(\sigma_x - \sigma_y\right)^2 + \frac{1}{2}\left(\sigma_y - \sigma_z\right)^2 + \frac{1}{2}\left(\sigma_z - \sigma_x\right)^2 + 3\tau_{xy}^2 + 3\tau_{yz}^2 + 3\tau_{zx}^2} \quad (12)$$

$$M = \frac{3\sin\varphi}{\sqrt{3}\cos\theta + \sin\theta\sin\varphi} \quad (13)$$

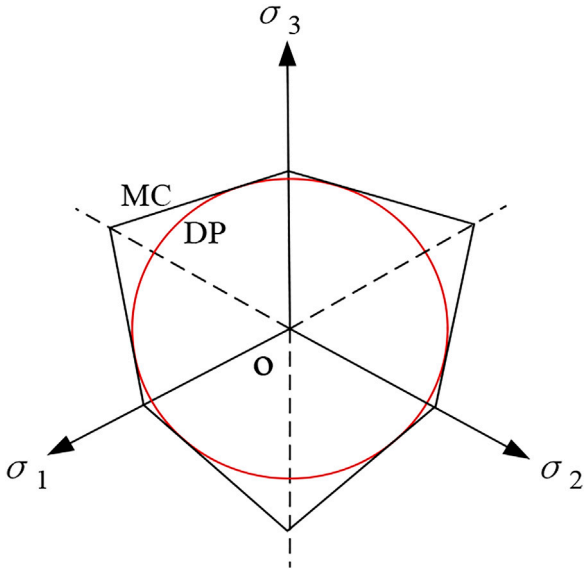

FIGURE 4
MC and DP yield surfaces in the π plane.

$$\theta = \tan^{-1}\left[\frac{1}{\sqrt{3}}\left(2\frac{\sigma_2 - \sigma_3}{\sigma_1 - \sigma_3} - 1\right)\right] \quad (14)$$

Where the superscripts of the variables indicate the effective stress and p_c is the prior consolidation pressure. The MCC model is controlled by the parameters of compression index λ, resilience index κ, initial pore ratio e_0, cohesion c and friction angle φ, all of which can be obtained experimentally.

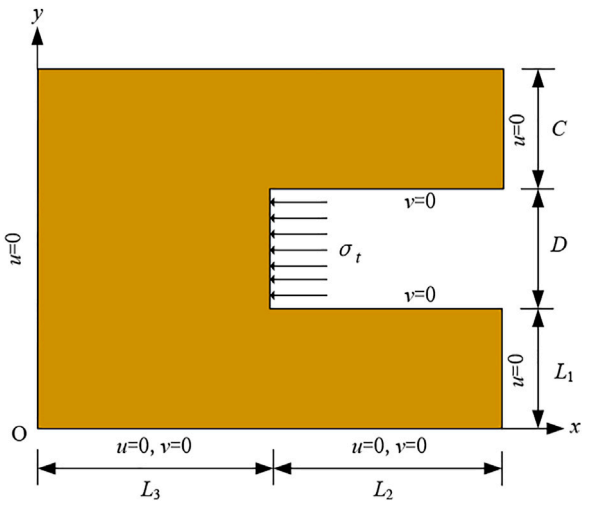

FIGURE 5
Stability analysis model of tunnel face.

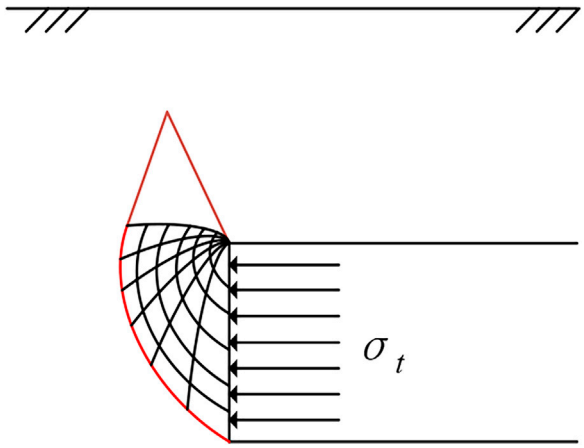

FIGURE 6
Failure model of shallow tunnel face.

2.3 Drucker-Prager model (DP)

Drucker-Prager modified the Mises criterion to propose a new yielding criterion for the damage analysis of rocks with the yield surface shown in Figure 3. The projection in the π-plane is the inner tangent circle of the MC yield surface projection shown in Figure 4, and the yield function is expressed as

$$F = Mp + q - k \tag{15}$$

which

$$p = \frac{1}{3}\left(\sigma_x + \sigma_y + \sigma_z\right) \tag{16}$$

$$q = \sqrt{\frac{1}{2}\left(\sigma_x - \sigma_y\right)^2 + \frac{1}{2}\left(\sigma_y - \sigma_z\right)^2 + \frac{1}{2}\left(\sigma_z - \sigma_x\right)^2 + 3\tau_{xy}^2 + 3\tau_{yz}^2 + 3\tau_{zx}^2} \tag{17}$$

Where the parameters M and k are constants related to the soil friction angle φ and cohesion c respectively. To ensure that the soil material parameters match the numerical calculations and to consider the associated flow rule, the DP model and MC model parameters can be equivalently transformed by the following equation.

$$M = \frac{3\sin\varphi}{\sqrt{\sin^2\varphi}}, k = \frac{3c\cos\varphi}{\sqrt{\sin^2\varphi}} \tag{18}$$

3 Ultimate support pressure analysis at the tunnel face

In this paper, the stability of the tunnel face is analyzed by three methods: finite element limit analysis, finite difference method and limit analysis upper limit method, and the ultimate support pressure on the tunnel face is obtained.

Based on the OPTUM G2 (Finite Element Limit Analysis) and FLAC (Finite Difference Method) platforms. To simplify the analysis, the median plane of the 3D tunnel is intercepted, and a two-dimensional analysis is carried out considering the plane strain problem, as shown in Figure 5. The tunnel diameter D is 8 m. In order to ignore the influence of boundary conditions as far as possible, the length of the tunnel extension below L_1 = 8 m, the longitudinal length of the tunnel L_2 = 16 m, and the length of the model extension in the horizontal direction L_3 = 16 m. The entire bottom boundary of the model is fully constrained, and the left and right boundaries of the model and the upper and lower boundaries inside the tunnel are constrained normally to each other.

Meanwhile, this paper adopts the multi-block damage model of the tunnel face proposed by Yang Feng (Yang et al., 2010), as shown in Figure 6; the red line in the figure indicates the damaged surface, based on the theory of limit analysis upper limit method, construct the constraint and objective function and use the non-linear solver fmincon in MATLAB to program the ultimate support pressure of the tunnel face can be found, the specific solution process and calculation formulae are shown in the literature (Nayak and Zienkiewicz, 1972).

Where the soils have a weight of 20 kN/m^3 and a cohesive force of 10 kPa, calculations were carried out using the Mohr-Coulomb yielding constitutive model. The variation of the ultimate support pressure with friction angle at the tunnel face for two working conditions (C/D = 1, C/D = 2) was explored using the three methods mentioned above, and the results are shown in Figures 7, 8.

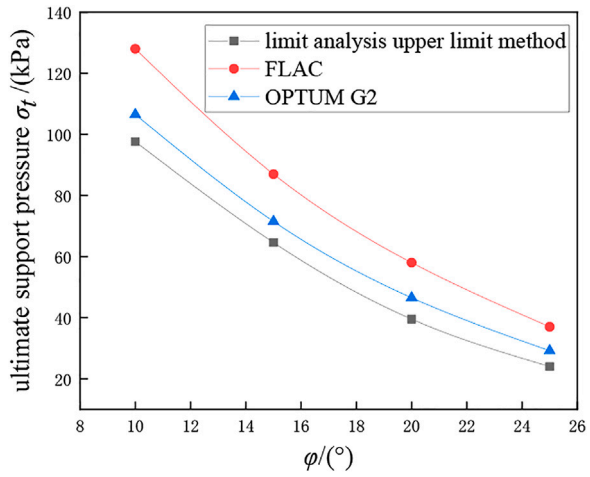

FIGURE 7
When C/D = 1 in MC model, the ultimate support pressure varies with friction.

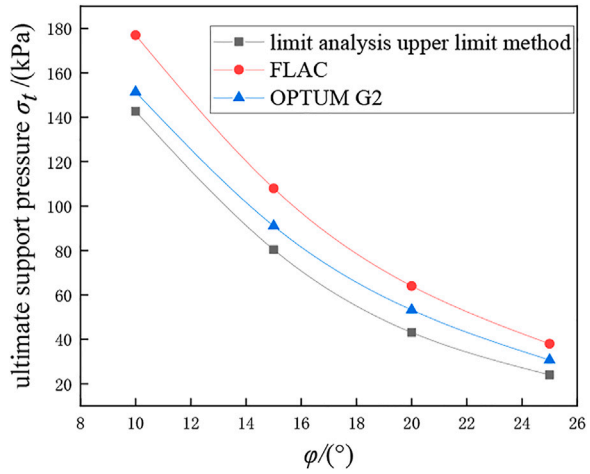

FIGURE 8
When C/D = 2 in MC model, the ultimate support pressure varies with friction.

During the analysis, the simulation of the working conditions at different C/D was controlled only by changing the thickness C of the overburden layer, while other values were kept constant. It can be seen from Figures 7, 8 that the ultimate support pressure at the tunnel face decreases as the friction angle increases, and the larger the C/D, the greater the ultimate support pressure required. All three calculation methods show the same variation pattern, and the results are close to each other, with the limit analysis upper limit method being more dangerous, FLAC (finite difference method) being more conservative, and OPTUM G2 (finite element limit analysis method) being in between and the tunnel face damage pattern (shown in Figure 9) is consistent with the damage pattern used in the limit analysis upper limit method (shown in Figure 6) hence this method is used consistently in the subsequent discussions of the constitutive model analysis.

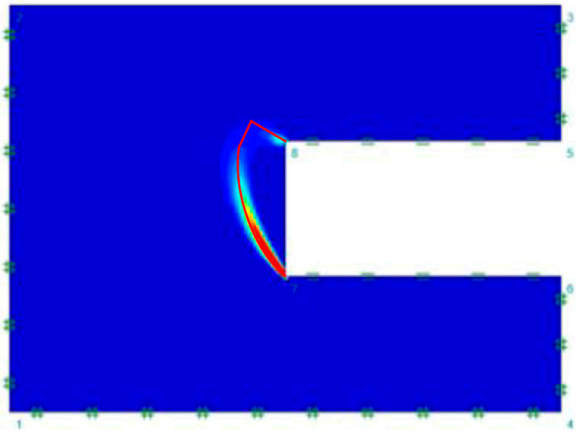

FIGURE 9
C/D = 1 finite element limit analysis calculation of the failure mode of the tunnel face.

4 Analysis of different constitution models

4.1 Model building

In order to analyze the effect of different constitutive models on the ultimate support pressure at the tunnel face, the three constitutive models mentioned in Section 1 were used for the analysis: i) the ideal elastoplastic constitutive Mohr-Coulomb model (MC); ii) the Modified Cambridge model (MCC), which reflects the elastic-plastic damage of soft soils well; and iii) the Drucker-Prager model (DP), which reflects the elastic-plastic damage of rocks. The calculation method was selected from the finite element limit analysis method used in the previous section.

Refer to Figure 5 for a geometric model of the tunnel with geometric parameters taken from the literature (Yuan et al., 2021), where the diameter of the tunnel D is 9 m, the extension length below L_1 = 9 m, the longitudinal length L_2 = 18 m, and the horizontal extension length L_3 = 18 m.

4.2 Soil parameters

The soil parameters in the tunnel model were taken from the literature (Yuan et al., 2021) and the values of the soil

TABLE 1 The calculation parameters of MC model.

E/MPa	υ	*c*/kPa	φ/(°)	Ψ/(°)
50	0.2	10	20	20

TABLE 2 The calculation parameters of MCCmodel.

c/kPa	φ/(°)	λ	*k*	e_0
10	20	0.1	0.016	0.66

TABLE 3 The calculation parameters of DP model.

E/MPa	υ	*M*	*k*/kPa
50	0.2	0.5812	15.97

parameters for the three constitutive models are shown in Tables 1–Tables 3. where the natural weight of the soil γ = 18 kN/m^3 and the associated flow rule was used for the calculation.

5 Analysis of results

Based on the finite element limit analysis and strength reduction method, this paper analyses the stability of the tunnel face under three different constitutive models and discusses the effect of varying burial depth ratios *C*/*D* on the ultimate support pressure.

5.1 Analysis of the results of different constitution models

Considering two working conditions with *C*/*D* is 1 and 1.5, calculate the variation of safety factor with support pressure at the tunnel face under three constitutive models (see Figure 10).

It can be seen from Figure 10 that the factor of safety increases with the increase in support pressure regardless of the working conditions or the constitutive model (only active damage is considered). For the same support pressure, the safety factor obtained with the MC model is always slightly higher than that of the MCC model; when the safety factor is less than 1, the safety factor obtained with the DP model is greater than that of the MC and MCC models for the same support pressure, but when the required safety factor is greater than 1, the safety factor calculated with the DP model is less than that of the MC model (this is consistent with the fact that the yield surface of the DP model is tangent to the yield surface of the MC model). The

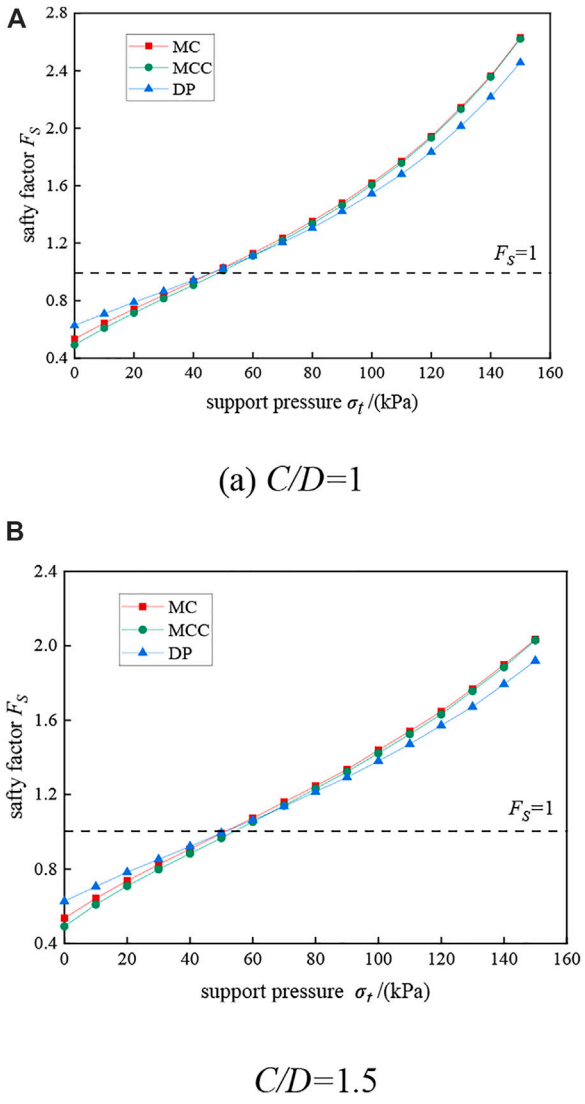

FIGURE 10
The safety factor varies with support pressure under different constitutive conditions. **(A)** C/D = 1, **(B)** C/D = 1.5.

ultimate support pressures (safety factor equal to 1) obtained with the MC and DP models are almost identical, while the ultimate support pressures obtained with the MCC model are relatively large.

To reflect the influence of different constitutive models on the stability of the tunnel face more intuitively, the percentage difference in the safety factor under different constitutive models (compared with the MC model) is discussed, and the burial depth ratio *C*/*D* is taken as 1 for calculation, and the results are shown in Figure 11.

The positive sign in Figure 11 indicates that the result is larger than that calculated by the MC model, and the negative sign indicates that it is smaller. It can be seen that the safety

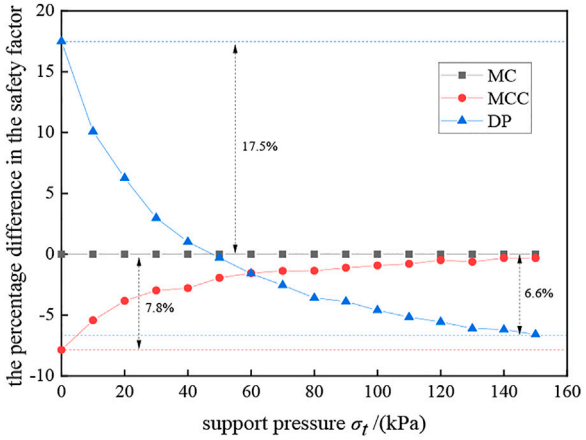

FIGURE 11
Percentage of safety factor gap when C/D = 1.

coefficient calculated by the MCC model is smaller than that of the MC model under the same support pressure, and the difference is the largest when the support pressure is not considered, which is 7.8% smaller than that of the MC. The coefficient of safety at the intersection of the DP model and the MC model is 1, indicating that the ultimate support pressure under the MC model and the DP model is the same. When the support pressure is small, the coefficient of safety obtained under the DP model is larger than that under the MC model, and the difference is the largest when the support pressure is not considered, with a value of 17.5%. The difference tends to stabilize and gradually converges to 6.6% in this paper.

5.2 Analysis of C/D results for different burial depth ratios

In the discussion of the previous section, it was found that the burial depth ratio C/D has a greater effect on the ultimate support pressure, so the effect of the C/D ratio on the stability of the tunnel face and the ultimate support pressure under active failure was further investigated, and the results are shown in Figure 12.

When the support pressure is zero, the coefficient of safety obtained from different C/D is almost the same, indicating that the self-stabilizing performance of the tunnel face is almost independent of C/D. As the support pressure increases, the smaller the C/D the greater the coefficient of safety, and the greater the coefficient of safety is influenced by the support pressure (the slope of the curve in the graph). And the greater the C/D, the greater the ultimate support pressure obtained and the more dangerous the tunnel face is.

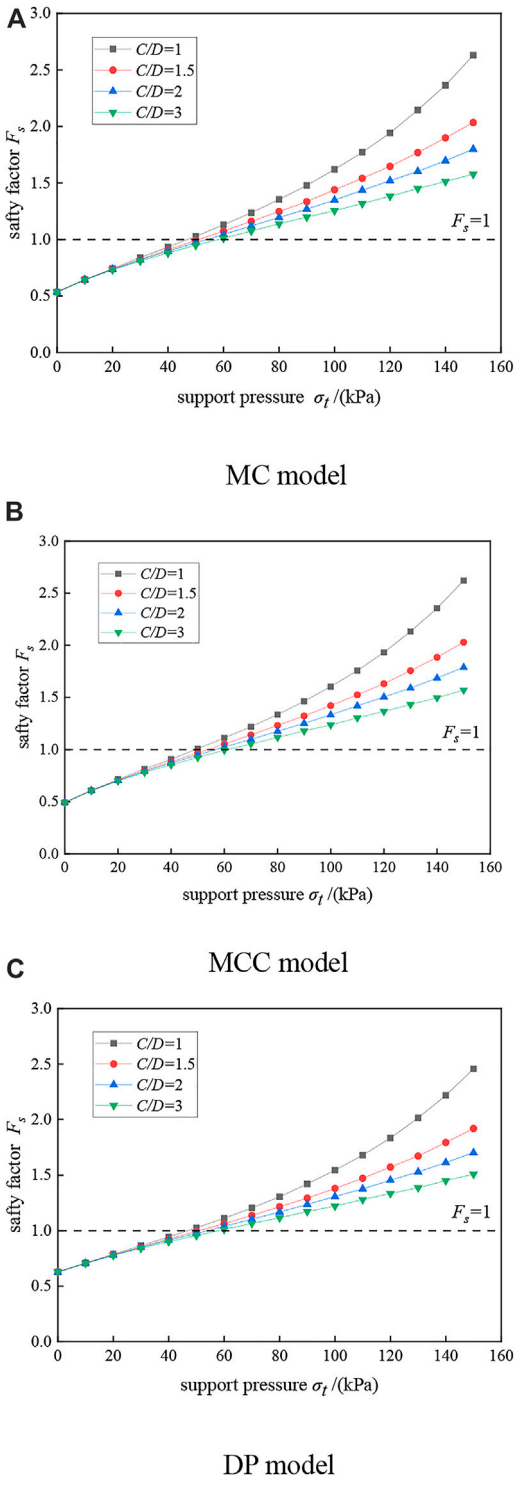

FIGURE 12
Variation of safety factor with support pressure under different C/D. **(A)** MC model, **(B)** MCC model, **(C)** DP model.

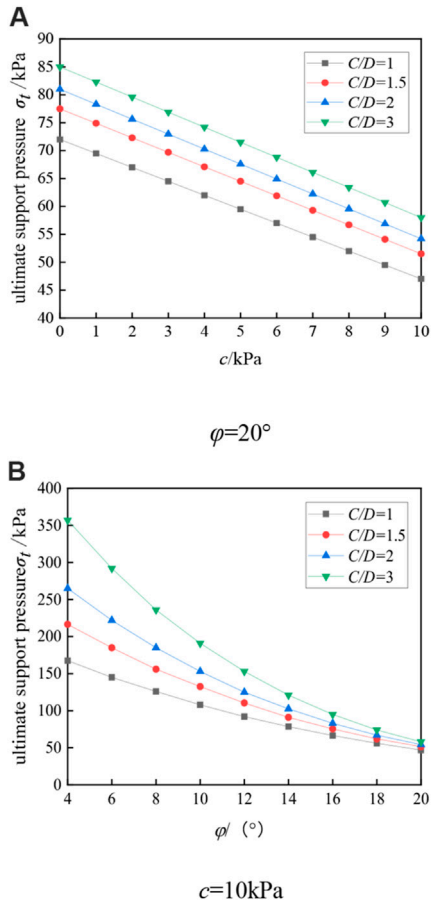

FIGURE 13
Influence of MC model parameters on ultimate support pressure under different *C/D* conditions. **(A)** φ=20°, **(B)** c=10 kPa.

6 Analysis of MC model strength parameters

The MC model was selected in order to analyze the influence of the strength parameters of the soil on the ultimate support pressure at the tunnel face further. The tunnel geometry model constructed in Section 3.1 was used to explore the influence of the friction angle *c* and cohesion *φ* on the ultimate support pressure at the tunnel face in the MC model based on the finite element limit analysis method, and the influence of four different *C/D* working conditions was also analyzed, and the calculation results are shown in Figure 13.

It can be seen that the ultimate support pressure at the tunnel face decreases with the increase of cohesion, and presents a linear relationship, the larger the *C/D*, the greater the ultimate support pressure, and the ultimate support pressure-viscosity curve under different *C/D* conditions is approximately parallel; the ultimate support pressure also decreases with the increase of friction angle, presenting a non-linear relationship, and finally tends to a stable value. When the friction angle is small, it is influenced by *C/D*, however, when the friction angle is large, it is almost independent of *C/D*, and the ultimate support pressure under different *C/D* is close to the same.

7 Conclusion

This paper adopts the finite element limit analysis method to establish a two-dimensional tunnel face model, analyses the stability of the tunnel face under three different constitutive models, and solves for the ultimate support pressure, taking into account the effects of parameters such as burial depth ratio, cohesion and friction angle in the MC model. And leading to the following conclusions:

(1) Compared to the MC model, the safety factor obtained by the MCC model for the same support pressure is always smaller than that of the MC model, with a maximum difference of 7.8% when there is no support pressure, but gradually converges to that of the MC model as the support pressure increases. This shows that the MCC model is more conservative than the MC model.
(2) Compared to the MC model, the DP model gives a greater safety factor than the MC model when the support pressure is small and 17.5% greater than the MC model when there is no support pressure; however, when the support pressure is large, the safety factor is less than the MC model and the final difference leveled off at 6.6%.
(3) The larger the *C/D*, the greater the required ultimate support pressure of the tunnel face. When the support pressure is not considered, the safety coefficients under different *C/D* calculations are the same, which means that the self-stabilizing performance of the tunnel face is almost independent of *C/D*. When the support pressure is greater, the smaller the C/D is the greater the influence.
(4) The ultimate support pressure at the tunnel face decreases linearly with the increase of cohesion, and the curves of the ultimate support pressure with cohesion are approximately parallel to each other at different burial depth ratios *C/D*. The larger the friction angle is, the higher the friction angle is, the ultimate support pressure at the tunnel face decreases non-linearly with the friction angle and finally tends to a stable value. When the friction angle is small, the ultimate support pressure is more influenced by *C/D*, and when the friction angle is large, it is less influenced by *C/D*. At this time, the ultimate support pressure under different *C/D* is almost the same.

Data availability statement

The datasets presented in this study can be found in online repositories. The names of the repository/repositories and accession number(s) can be found in the article/supplementary material.

Author contributions

LC: Investigation, Software, Validation, Data curation, Funding acquisition, Supervision, Writing—original JZ: draft, Conceptualization, Methodology, Resources, Visualization, Writing—original draft. LZ: Supervision, Conceptualization, Writing—review and editing. XK: Funding acquisition, Data curation, Writing—review and editing. WB: Data curation, Writing—review and editing.

Funding

This study was supported by the Natural Science Foundation of Sichuan Province (2022NSFSC0407) and the Sichuan Science and Technology Funding Scheme: Seismic Instability Mechanism and Stability Evaluation of Mixed Earth and Rock Slopes in Deep Canyon Areas on the Southeast Rim of the Qinghai-Tibet Plateau (2021YFH0037).

Conflicts of interest

Authors LC was employed by the company Road Tunnel Branch of Sichuan Highway Bridge Construction Group Co., Ltd.

The remaining authors declare that the research was conducted in the absence of any commercial or financial relationships that could be construed as a potential conflict of interest.

Publisher's note

All claims expressed in this article are solely those of the authors and do not necessarily represent those of their affiliated organizations, or those of the publisher, the editors and the reviewers. Any product that may be evaluated in this article, or claim that may be made by its manufacturer, is not guaranteed or endorsed by the publisher.

References

Bai, B., Wang, Y., Rao, D., and Fan, B. (2022). The effective thermal conductivity of unsaturated porous media deduced by pore-scale SPH simulation. *Front. Earth Sci.* 10, 943853. doi:10.3389/feart.2022.943853

Bai, B., Yang, G., Tao, L., and Yang, G. (2019). A thermodynamic constitutive model with temperature effect based on particle rearrangement for geomaterials. *Mech. Mater.* 139, 103180. doi:10.1016/j.mechmat.2019.103180

Bai, B., Zhou, R., Cai, G., Hu, W., and Yang, G. (2021). Coupled thermo-hydro-mechanical mechanism in view of the soil particle rearrangement of granular thermodynamics. *Comput. Geotechnics* 137 (8), 104272. doi:10.1016/j.compgeo.2021.104272

Broms, B. B., and Bennermark, H. (1967). Stability of clay at vertical opening. *J. Soil Mech. Found. Div. ASCE* 96 (1), 71–94. doi:10.1061/jsfeaq.0000946

Chen, W. F. (1975). *Limit analysis and soil plasticity[M]*. Amsterdam: Elsevier.

Comejo, L. (1989). Instability at the face: Its repercussions for tunneling technology [J]. *Tunn. tunnlgV21* 26(5), 69–74.

Davis, E. H., Gunn, M. J., Mair, R. J., and Seneviratine, H. N. (1980). The stability of shallow tunnels and underground openings in cohesive material. *Géotechnique* 30, 397–416. doi:10.1680/geot.1980.30.4.397

Do, N., Dias, D., Oreste, P., and Djeran-Maigre, I. (2014). Three-dimensional numerical simulation of a mechanized twin tunnels in soft ground. *Tunn. Undergr. Space Technol.* 42, 40–51. doi:10.1016/j.tust.2014.02.001

Fang, Y., Cui, J., Wanatowski, D., Nikitas, N., Yuan, R., and He, Y. (2022). Subsurface settlements of shield tunneling predicted by 2D and 3D constitutive models considering non-coaxiality and soil anisotropy: A case study. *Can. geotechnical J.* 59 (3), 424–440. doi:10.1139/cgj-2020-0620

Feng, X., Wang, P., Liu, S., Wei, H., Miao, Y., and Bu, S. (2022). Mechanism and law analysis on ground settlement caused by shield excavation of small-radius curved tunnel. *Rock Mech. rock Eng.* 55 (6), 3473–3488. doi:10.1007/s00603-022-02819-6

Han, K., Zhang, C., and Zhang, D. (2016). Upper-bound solutions for the face stability of a shield tunnel in multilayered cohesive–frictional soils. *Comput. geotechnics* 79, 1–9. doi:10.1016/j.compgeo.2016.05.018

He, Y., Liu, Y., Hazarika, H., and Yuan, R. (2019a). Stability analysis of seismic slopes with tensile strength cut-off. *Comput. geotechnics* 112, 245–256. doi:10.1016/j.compgeo.2019.04.029

He, Y., Liu, Y., Zhang, Y., and Yuan, R. (2019b). Stability assessment of three-dimensional slopes with cracks. *Eng. Geol.* 252, 136–144. doi:10.1016/j.enggeo.2019.03.001

He, Y., Wang, X., Yuan, R., Liu, K. W., and Zhuang, P. Z. (2019c). On the computational precision of finite element algorithms in slope stability problems. *J]. Math. problems Eng.* 2019, 1–15. doi:10.1155/2019/9391657

He, Y., Yu, J., Yuan, R., Wang, W., and Nikitas, N. (2022). Stability and failure mechanisms in three-dimensional cracked slope: Static and dynamic analysis. *Comput. geotechnics* 144, 104626. doi:10.1016/j.compgeo.2021.104626

He, Y., Yu, J., Yuan, R., and Yong, F. (2021). Stability analysis of the soil slope with cracks considering the upper slope inclination[J]. *China J. Highw. Transp.* 34 (05), 45–54. (In Chinese). doi:10.19721/j.cnki.1001-7372.2021.05.005

Huang, Z., Zhang, C., Fu, H., Deng, H., Ma, S., and Fu, J. (2020). Numerical study on the disturbance effect of short-distance parallel shield tunnelling undercrossing existing tunnels. *Adv. Civ. Eng.* 2020, 1–14. doi:10.1155/2020/8810658

Ji, J., Zhang, Z., Wu, Z., Xia, J., Wu, Y., and Lu, Q. (2021). An efficient probabilistic design approach for tunnel face stability by inverse reliability analysis. *Geosci. Front.* 12 (5), 101210. doi:10.1016/j.gsf.2021.101210

Keawsawasvong, S., and Ukritchon, B. (2020). Design equation for stability of shallow unlined circular tunnels in Hoek-Brown rock masses. *Bull. Eng. Geol. Environ.* 79 (8), 4167–4190. doi:10.1007/s10064-020-01798-8

Krabbenhoft, K., and Lyamin, A. V. (2012). Computational Cam clay plasticity using second-order cone programming. *Comput. Methods Appl. Mech. Eng.* 209, 239–249. doi:10.1016/j.cma.2011.11.006

Leca, E., and Dormieus, L. (1990). Upper and lower bound solutions for the face stability of shallow circular tunnels in frictional material. *Géotechnique* 40, 581–606. doi:10.1680/geot.1990.40.4.581

Li, B., and Li, H. (2019). Prediction of tunnel face stability using a naive bayes classifier. *Appl. Sci.* 9 (19), 4139. doi:10.3390/app9194139

Liu, K., Chen, S., and Xiaoqiang, G. (2020). Analytical and numerical analyses of tunnel excavation problem using an extended drucker–prager model. *Rock Mech. rock Eng.* 53 (4), 1777–1790. doi:10.1007/s00603-019-01992-5

Lu, X., Zhou, Y., Huang, M., and Li, F. (2017). Computation of the minimum limit support pressure for the shield tunnel face stability under seepage condition. *Int. J. Civ. Eng.* 15 (6), 849–863. doi:10.1007/s40999-016-0116-0

Mollon, G., Dias, D., and Soubra, A. (2010). Face stability analysis of circular tunnels driven by a pressurized shield. *J. geotechnical geoenvironmental Eng.* 136 (1), 215–229. doi:10.1061/(asce)gt.1943-5606.0000194

Nayak, G. C., and Zienkiewicz, O. C. (1972). Convenient form of stress invariants for plasticity. *J. Struct. Div. ASCE* 98 (98), 949–954. doi:10.1061/jsdeag.0003219

Roscoe, K. H., and Burland, B. (1968). *On the generalised stress-strain behaviour of an ideal wet clay[C]. HEYMAN, LECKIE. Engineering Plasticity*. Cambridge: Cambridge University Press, 535–609.

Shiau, J., and Al-Asadi, F. (2020). Two-dimensional tunnel heading stability factors F, F and F. *Tunn. Undergr. space Technol.* 97, 103293. doi:10.1016/j.tust.2020.103293

Sloan, S. W., and Assadi, A. (1991). Undrained stability of a square tunnel in a soil whose strength increases linearly with depth. *Comput. Geotechnics* 12 (4), 321–346. doi:10.1016/0266-352x(91)90028-e

Sui, H., Ma, C., Dai, C., and Yang, T. (2021). Study on stability of shield tunnel excavation face in soil-rock composite stratum. *Math. problems Eng.* 2021, 1–19. doi:10.1155/2021/5579103

Wilson, D. W., Abbo, A. J., Sloan, S. W., and Lyamin, A. V. (2011). Undrained stability of a circular tunnel where the shear strength increases linearly with depth. *Can. Geotechnical J.* 48 (9), 1328–1342. doi:10.1139/t11-041

Yang, F., Yang, J., and Zhao, L. (2010). Collapse mechanism and support pressure for shallow tunnel face [J]. *Chin. J. Geotechnical Eng.* 32 (2), 279–284. (In Chinese). doi:10.16285/j.rsm.2015.01.035

Yuan, R., Xiong, W., and He, Y. (2021). Analysis on the law of ground settlement in shallow tunnel excavation in camposite layered strata[J]. *J. Southwest Jiaot. Univ.* 40 (9), 1000–1005. In Chinese. doi:10.3969/j.issn.0258-2724.20210473

Zamora Hernández, Y., Durand Farfán, A., and Pacheco De Assis, A. (2019). Three-dimensional analysis of excavation face stability of shallow tunnels. *Tunn. Undergr. space Technol.* 92, 103062. doi:10.1016/j.tust.2019.103062

Zhao, C., Lavasan, A. A., Barciaga, T., Zarev, V., Datcheva, M., and Schanz, T. (2015). Model validation and calibration via back analysis for mechanized tunnel simulations – the Western Scheldt tunnel case. *Comput. geotechnics* 69, 601–614. doi:10.1016/j.compgeo.2015.07.003

Zheng, G., Fan, Q., Zhang, T., and Zhang, Q. (2022). Numerical study of the Soil-Tunnel and Tunnel-Tunnel interactions of EPBM overlapping tunnels constructed in soft ground. *Tunn. Undergr. space Technol.* 124, 104490. doi:10.1016/j.tust.2022.104490

Zheng, Y., Zhu, H., and Fang, Z. (2012). *The stability analysis and design theory of surrounding rock of underground engineering [M]*. Beijing: China Communications Press, 305–311.

frontiers | Frontiers in Materials

TYPE Original Research
PUBLISHED 06 January 2023
DOI 10.3389/fmats.2022.1104566

Check for updates

OPEN ACCESS

EDITED BY
Xianze Cui,
China Three Gorges University, China

REVIEWED BY
Qian Yin,
China University of Mining and Technology, China
Yongting Duan,
Northeastern University, China

*CORRESPONDENCE
Yu Wang,
wyzhou@ustb.edu.cn

SPECIALTY SECTION
This article was submitted to Structural Materials, a section of the journal Frontiers in Materials

RECEIVED 21 November 2022
ACCEPTED 21 December 2022
PUBLISHED 06 January 2023

CITATION
Li X, Wu J, Yang H and Wang Y (2023), On the effect of water content on fatigue mechanical behaviors of mud-shale under stress disturbance conditions.
Front. Mater. 9:1104566.
doi: 10.3389/fmats.2022.1104566

COPYRIGHT
© 2023 Li, Wu, Yang and Wang. This is an open-access article distributed under the terms of the Creative Commons Attribution License (CC BY). The use, distribution or reproduction in other forums is permitted, provided the original author(s) and the copyright owner(s) are credited and that the original publication in this journal is cited, in accordance with accepted academic practice. No use, distribution or reproduction is permitted which does not comply with these terms.

On the effect of water content on fatigue mechanical behaviors of mud-shale under stress disturbance conditions

Xuguang Li[1], Jihuan Wu[1], Haonan Yang[2] and Yu Wang[2]*

[1]Shenyang Center of Geological Survey, China Geological Survey, Liaoning Shenyang, Shenyang, China, [2]Department of Civil Engineering, School of Civil and Resource Engineering, University of Science and Technology Beijing, Beijing, China

This paper aims to reveal the fatigue damage and instability behaviors of mud-shale under multistage increasing-amplitude fatigue loading. The fatigue loading tests combined with real-time acoustic emission (AE) monitoring technique were employed to investigate the influence of water content on the deformation, damage, and fracture characteristics. Testing results show that rock fatigue life decreases with the increase of water content, and the hysteresis curve changes regularly with time. The failure process can be divided into three stages: initial stage, stable development stage and acceleration stage. The acoustic emission output activities were also influenced by the water content. The acoustic emission ring count and acoustic emission energy both decrease with increasing water ratio and the accumulative count and energy are the least for a sample having high water ratio. The acoustic emission activity shows a sudden increase trend at the amplitude-increasing moment, indicating the occurrence of strong damage within rock sample. The damage propagation within a cyclic loading stage is relatively small compared to the stress-increasing moment. The results are helpful to understand the fatigue mechanical responses of water-sensitive soft rock, as well as the slope stability of the open-pit mine. The research results have important theoretical and practical significance for promoting slope treatment and disaster prevention.

KEYWORDS

cyclic loads, mud-shale, fatigue deformation, acoustic emission, instability precursor

Introduction

Soft rock is extensively distributed in nature, which has an important influence on the stability of slope engineering. The slope stability of soft rock has been paid more and more attention and studied by more and more scholars. In the field of geotechnical engineering, soft rock has unique physical and mechanical properties, exhibits obvious rheological characteristics under the action of external factors, and has obvious time effect (Guo et al., 2012; Li et al., 2012; Cerfontaine and Collin 2018; Hashemnejad et al., 2021; Bai et al., 2022b; Wang et al., 2022a; Wang et al., 2022b; Wang et al., 2022c) Therefore, soft rock has always been a key and difficult problem in the study. In many soft rock open pit slopes, the rock mass is usually subjected to continuous and repeated stress disturbance, which will affect the stability of the slope and cause slope instability accidents and disasters. In practical engineering, cyclic loading and unloading are closer to the actual engineering situation. Exploring the influence of cyclic loading on rock structural deterioration and instability is of importance to ensure the long-term stability of mining slopes.

Plenty of attempts have been performed to reveal the mechanical response of rock subjected to cyclic loads. The effect of stress frequency, stress amplitude, stress level on rock strength (Singh 1988; Singh, 1989), deformation (Voznesenskii et al., 2016; Fan et al., 2019; Bai et al., 2021), hysteresis ratio (Song et al., 2012; Chen et al., 2017; Guo et al., 2018), energy dissipation (Peng et al., 2020; Song et al., 2020) and failure modes (Liu et al., 2018; Vaneghi et al., 2018; Wang et al., 2023) were investigated in the laboratory. Among the factors affecting rock fatigue mechanical behavior, stress amplitude and loading frequency have always been the focus of research. Bagde and Petros, (2005) carried out cyclic loading tests on complete sandstone samples from a coal mine and found that loading frequency and stress amplitude had a great influence on rock dynamic behavior. Liu et al. (2012) conducted a triaxial cycle test on sandstone and found that dynamic frequency has a great influence on dynamic deformation, dynamic stiffness and failure mode. Roberts et al. (2015) studied the creep and expansion behavior of salt rock under fatigue load and revealed the deformation characteristics of salt rock. Momeni et al. (2015) carried out cyclic loading tests on granite samples and found that maximum stress level and frequency have greater influence on fatigue behavior than amplitude. They also found that rock fatigue life increases with increasing frequency and decreasing maximum stress level. Taheri et al. (2017) conducted a cyclic loading test on lignite and found that the cyclic loading and cumulative irreversible axial strain had little effect on the mechanical properties of lignite. Meng et al. (2020) revealed the effect of loading frequency on fracture and acoustic emission modes rock with pre-flaws, and found that rock bridges are prone to fracture at lower dynamic frequencies. Zheng et al. (2020) revealed the dynamic and damage properties of artificial jointed rock samples under triaxial cyclic loads with different dynamic frequency, they found that the loading frequency impacts the irreversible strain, and the axial, radial and volumetric strain exhibit different evolution pattern.

Although the influences of fatigue loading parameters on rock damage and fracture have been widely studied, most of the studies are focusing on intact and pre-flawed hard rock, such as granite, marble, basalt, limestone, diorite, and also the block-in-matrix-rocks (Al-Shayea 2004; Zhou et al., 2015; Xu et al., 2021; Wang et al., 2022d; Wang et al., 2023). Investigations on the fatigue mechanical behaviors of water-sensitive rock, e.g., mud-shale in this work, exposed to cyclic loads are relatively less, especially the influence of water content on the deformation and damage evolution are rarely reported. As a result, this work emphatically investigates the influence of water content on mechanical responses of mud-shale, which is a kind of typical soft work, to reveal the damage and fracture characteristics. This study can give new insight into the fracture and instability of water-sensitive mud-shale and the associated long-term stability predication to soft rock engineering.

Methods

Tested mud-shale description

The tested rock material was obtained from the west open-pit mining area, which is located in the southwest of Fushun city, Liaoning Province. The Fushun west open pit was built in the early 20th century, is a mining with hundreds of years history of open-pit mine, since last century west open pit mining, formed the things is about 6.6 km long, north and south is about 2.2 km wide, vertical excavation depth of about 400–500 m, large volume of 1.7 billion cubic meters of mine, and known as the largest open pit in Asia, as shown in Figure 1. The coal and oil shale are the two main minerals mined in the West open-pit mine, and Fushun, and the term of "coal capital", was born from this mine. The tested mud shale is widely distributed in the north boundary of the West open pit slope, field drilling reveals the thickness distribution of the mud shale, as shown in Figure 2.

The sample used in this study is a cylinder with a diameter of 50 mm and a height of 100 mm. Considering the test accuracy, all the rock samples in this test are refined and cut and ground with high precision, so as to ensure that the external dimensions of the rock samples are within the corresponding measurement accuracy requirements and meet the requirements of international rock mechanics: 1) The non-parallelism error of the two end faces should not exceed 0.05 mm; 2) The roughness error of the end face shall not exceed 0.02 mm; 3) The maximum deviation of the vertical axis of the end face shall not exceed 0.25. A non-destructive immersion test device is used to prepare mud-shale with different water content, and the water ratio is 0%, 2.11%, 2.56%, 4.36%, and 6.25%,

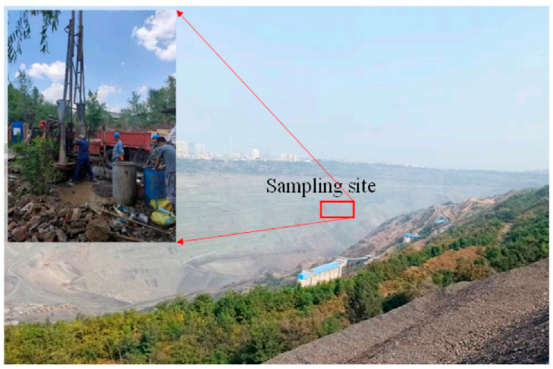

FIGURE 1
The overview of the Fushun west open pit slope and the sampling site.

FIGURE 2
Drilling core of the mud-shale at a depth of 80–90 m.

TABLE 1 Description of the basic physical state and loading conditions for the samples.

Sample id	Length × width (mm × mm)	Mass g)	Water content (%)	Mass loss ratio (%)
UFW1	99.81 × 49.95	408.02	0	0
UFW2	99.58 × 49.88	407.83	0	0.07
UFW3	99.79 × 50.02	393.65	2.11	0.09
UFW4	99.66 × 49.77	392.92	2.11	0.08
UFW5	99.95 × 49.79	398.31	2.56	0.15
UFW6	99.73 × 49.98	398.56	2.56	0.13
UFW7	100.01 × 49.88	397.14	4.36	0.23
UFW8	100.02 × 50.01	396.66	4.36	0.26
UFW9	100.02 × 49.94	397.32	6.25	0.38
UFW10	99.95 × 50.02	396.68	6.25	0.42

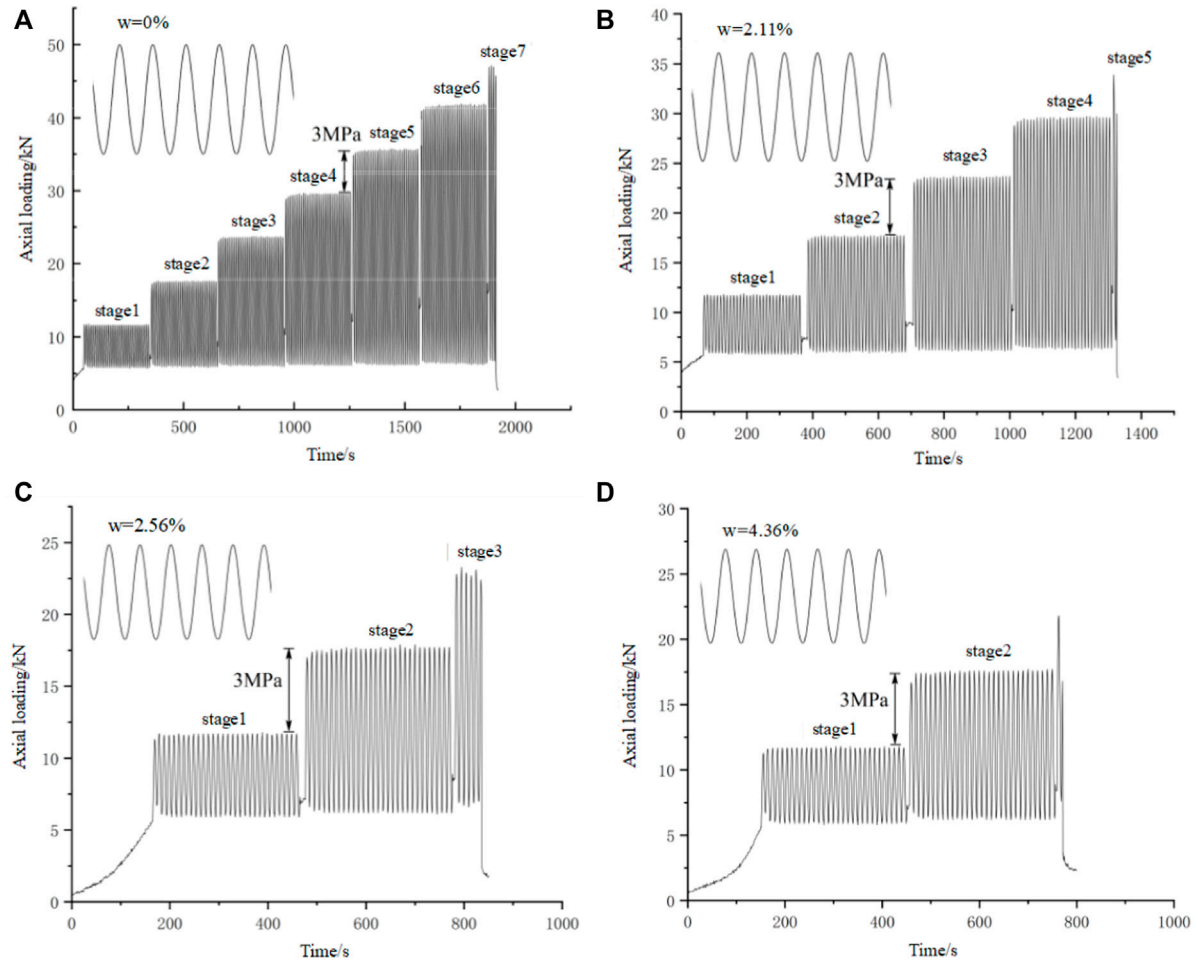

FIGURE 3
Specific stress path with different dynamic frequency for the tested mud shale samples. **(A-D)** The water content is 0%, 2.21%, 2.56%, and 4.36%, respectively).

respectively. The mass loss of the mud-shale is also shown in Table 1, it is shown that the loss ratio increases with the increase of water ratio. During the test, it is observed that rock surface material peeling off gradually, and with the infiltration of water, the presence of water on the mud shale pore fissure have softening effect, causing damage to the internal structure of the rock.

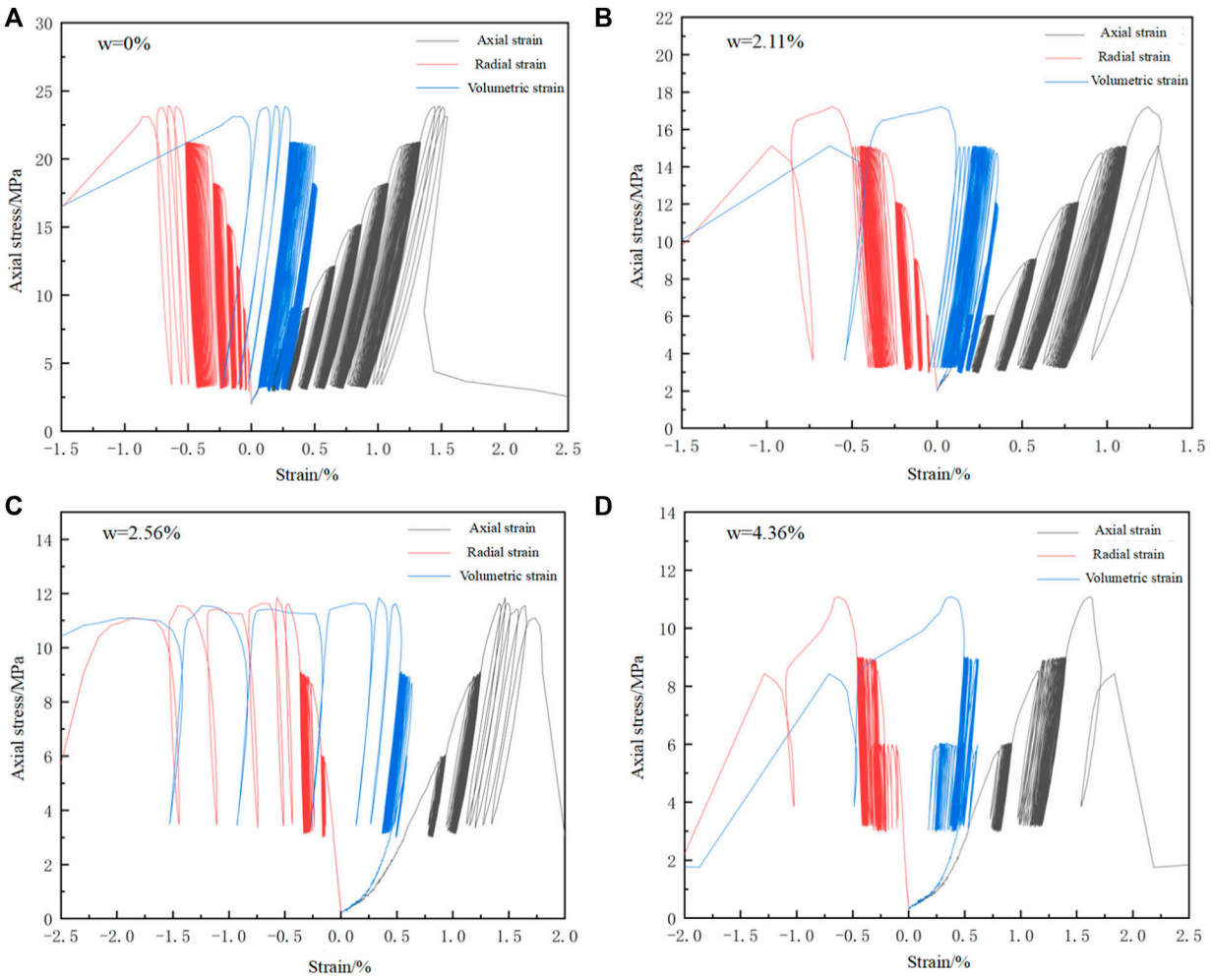

FIGURE 4
Typical axial, radial and volumetric stress strain curves **(A–D)** The water content is 0%, 2.21%, 2.56%, and 4.36%, respectively).

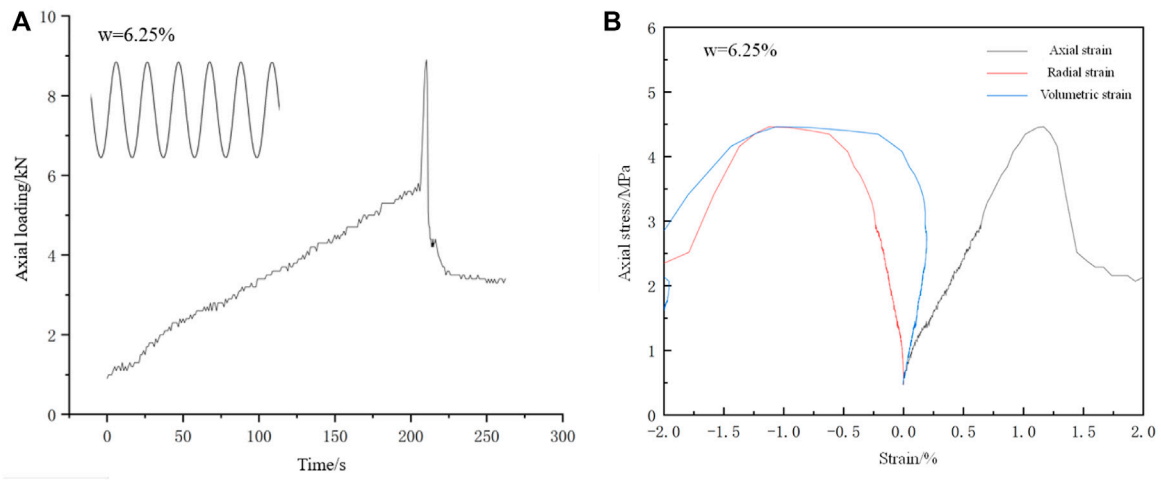

FIGURE 5
The loading path and complete stress strain responses with moisture content of w = 6.25%. **(A)** The loading path; **(B)** The axial, radial and volumetric stress strain curves.

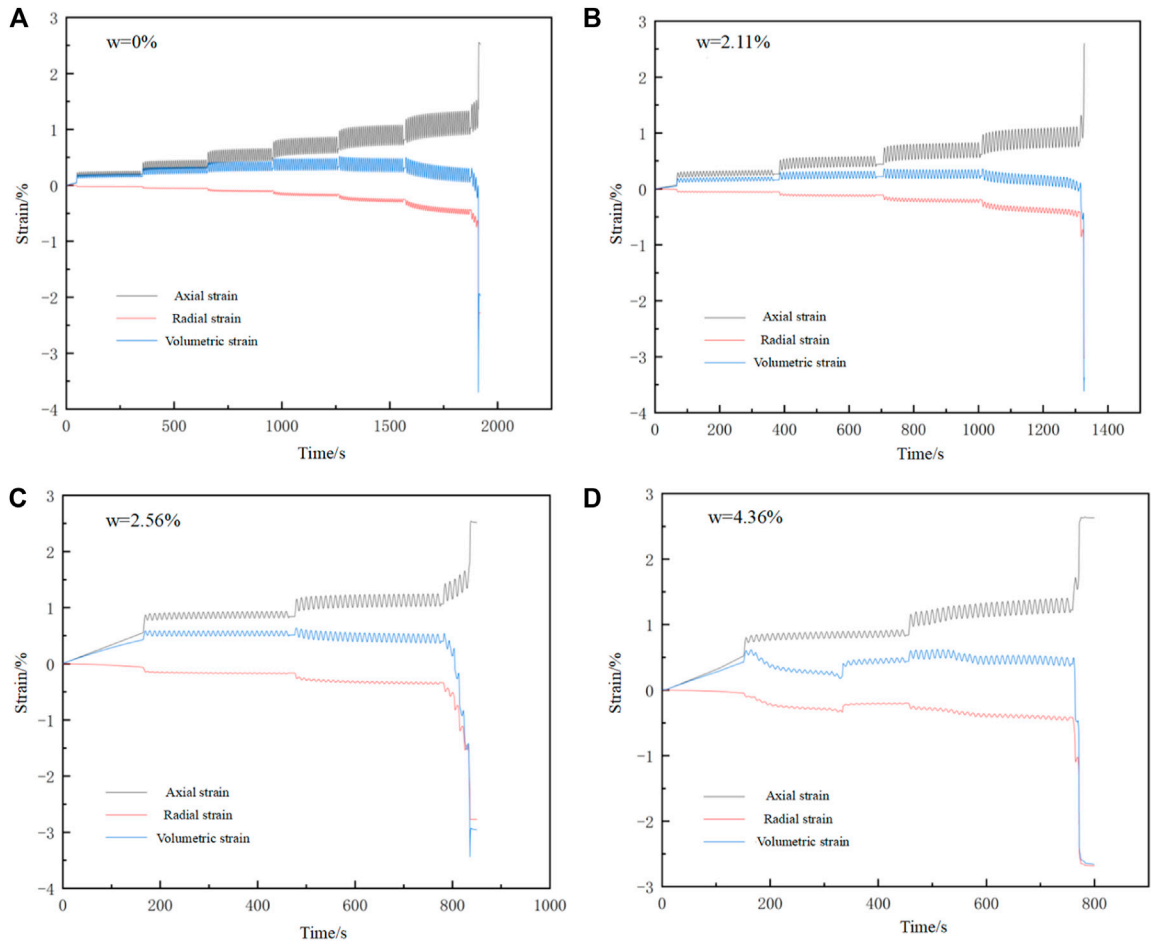

FIGURE 6
Deformation evolution characteristics **(A-D)** Plots of the axial, radial and volumetric strain for rock with water content of 0%, 2.21%, 2.56%, and 4.36%, respectively).

Experimental device and method

In order to study the strength characteristics, deformation evolution, and damage development of mud-shale under fatigue loads, a specially designed multi-stage cyclic loading and unloading compression test is designed. The stress-strain relationship curves and acoustic emission characteristics of mud-shale under different loading conditions were obtained by using the GCTS RTR 2000 rock mechanics testing machine. The detailed testing scheme is listed in Table 1. In order to study the water content on rock damage and instability, multi-stage uniaxial cyclic loading testing with a stress-control mode was employed in this work. The disturbed stress is applied with sinusoidal wave and the loading frequency is 0.1 Hz for all the tested rock, the stress amplitude of each cyclic loading stage was increased by 3.0 MPa, 30 cycles were applied at each stage.

Apart from the stress strain tests during the cyclic loading process, real-time acoustic emission technique was also employed to record the fracturing signals in order to record rock deformation, crack propagation, and the failure process. The AE monitoring can provide effective precursor information to predict the fracture and instability of rock mass under stress disturbance. The PAC AE monitoring system was used during the experiment. The maximum sampling rate was 1MSPS, the resolution was 18 bits, and the sampling filter frequency was 125–750 kHz. A kind of nano-30 AE sensor made from the PAC, United States of America, with its diameter of 6 mm × 6 mm and a resonance frequency of 300 kHz, was employed to record AE activities. The AE sampling interval was 50 μs, the sampling threshold was set to be 42 dB, and the sampling frequency range was 10^2~10^4 Hz.

Results

Fatigue stress strain descriptions

It can be seen from the specially designed loading path that the samples after different water treatment go through different fatigue loading stages and eventually fail. For each stage, a total of 30 cycles of loading and unloading are carried out in each fatigue loading stage. The samples having different water content fail at the seventh, fifth, third and third stages respectively. Therefore, the number of loading cycles experienced by the samples is also different, and the fatigue life is different. The total number of loading cycles of the typical samples with different water content are 154, 121, 65, 61, and 1, respectively, as shown in Figure 3. It can be seen that with the increase of water

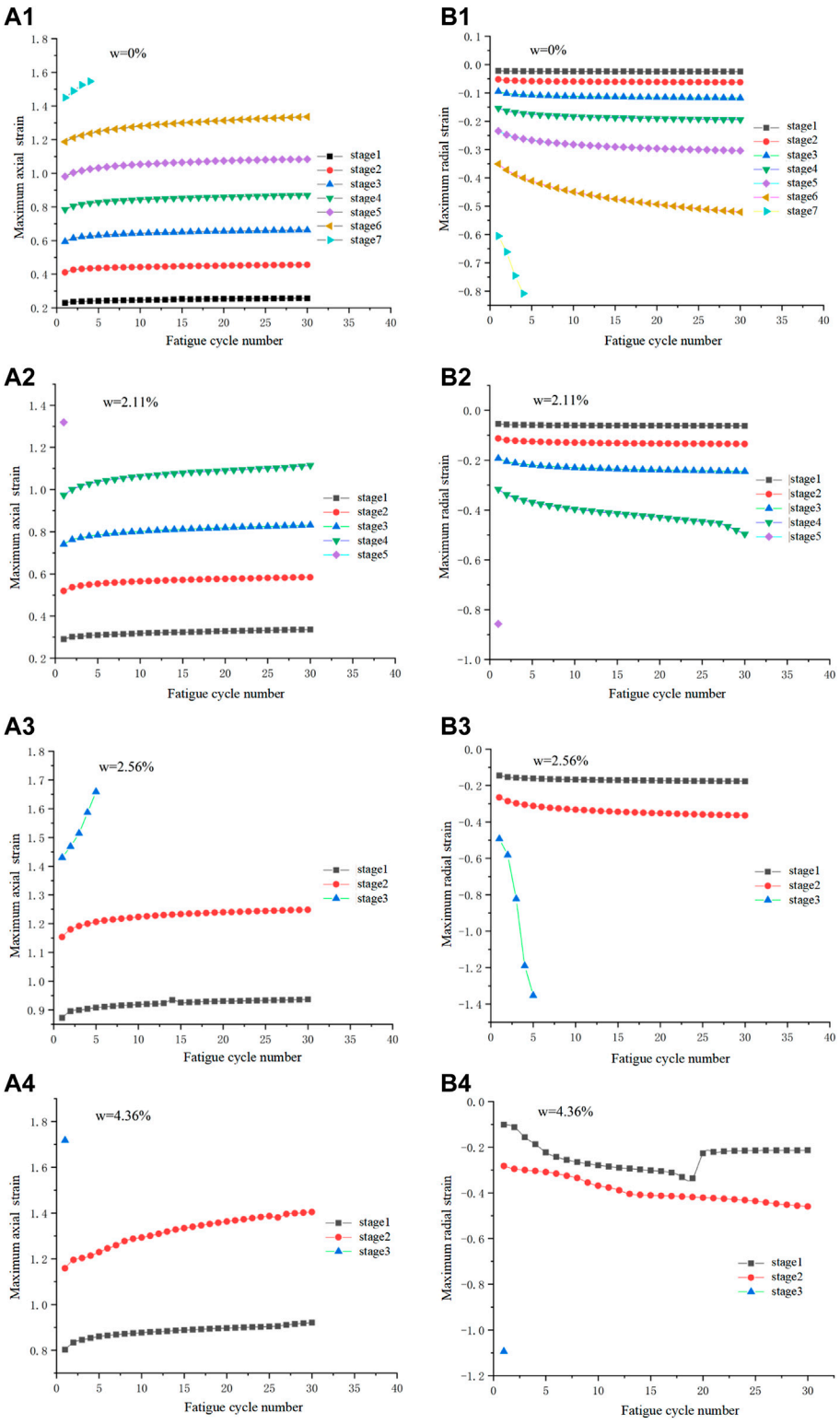

FIGURE 7
Depict of maximum axial and radial strain with cyclic number at various cyclic loading stage **(A1-A4)** Plots of the maximum axial strain against cycle number for rock with water content of 0%, 2.21%, 2.56%, and 4.36%, respectively; **(B1-B4)** Plots of the maximum radial strain against cycle number for rock with water content of 0%, 2.21%, 2.56%, and 4.36%, respectively).

content, the number of loading cycles gradually decreases, and the fatigue life decreases accordingly. The results show that water content has obvious effect on the strength, deformation and fracture characteristics of shales, and the interaction between water and shales can change the internal structure of the rock and soften it. Therefore, it is not difficult to explain the test results that fatigue life

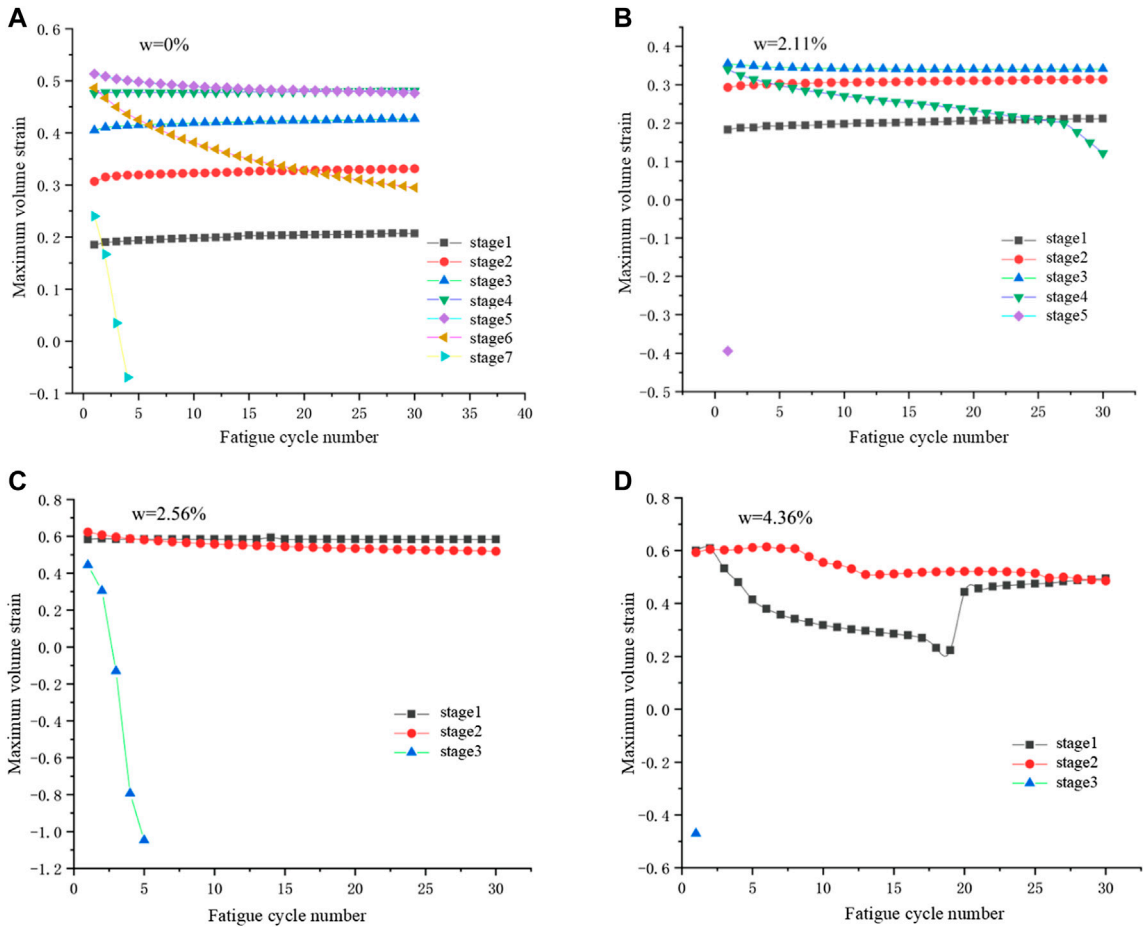

FIGURE 8
The aximum volumetric strain *versus* cyclic number at various cyclic loading stage **(A–D)**: The rock with water content of 0%, 2.21%, 2.56%, and 4.36%, respectively).

decreases with the increase of water content. In order to further reveal the influence of water content on rock deformation and damage pattern, the stress-strain curves are also plotted, as shown in Figure 4.

As can be seen from the stress-strain curve under cyclic loading, with the increase of testing time, the loading curve and unloading curve no longer overlaps. The curve in the loading stage is above the curve in the unloading stage, and the stress and strain are not synchronized, which is due to the plastic deformation inside the rock sample, resulting in the formation of hysteresis loops. The hysteresis curve varies with loading time. For each fatigue loading stage before failure, the hysteresis curve is sparse and then becomes intensive. The sparse shape of hysteresis curve is due to the large plastic deformation caused by the increase of stress amplitude, and then the formed cracks are gradually closed, and the hysteresis curve becomes dense. In each stage before the failure stage, the hysteresis curve shows a sparse to dense trend. However, the last failure stage of fatigue loading is different from the stage before failure, showing that the hysteretic curve of the sample is very sparse until failure occurs. The morphological characteristics of hysteresis curve in the loading process reflect the changes of the deterioration of meso-structure inside rock, which is closely related to the initiation and propagation behavior of cracks. The testing results also reveal that the fatigue damage of the tested rock is maximum at the beginning of each stage, that is, the moment when the stress amplitude increases.

When the moisture content is 6.25%, the rock strength decreases greatly and the damage occurs after only one cycle of loading and unloading. Figure 5 shows its loading curve, it can be seen from Fgi.5 b that the curve morphology is similar to the failure curve under uniaxial compression. Therefore, its loading path and stress-strain curve are listed separately. When the water content is 6.25%, the rock strength is very low.

In order to further study the influence of water content on its mechanical properties, according to the results of each group of tests, the test results were integrated to obtain the peak stress of shale after different water content treatments. It can be seen that under the same loading conditions, the peak stress after water treatment are 23.9 MPa, 17.3 MPa, 11.85 MPa, 11.1 MPa, 4.5 MPa, respectively. The order of peak stress is σ_{max} (w = 0%) > σ_{max} (w = 2.11%) > σ_{max} (w = 2.56%) > σ_{max} (w = 4.36%) > σ_{max} (w = 6.25%), and the value decreases successively. The peak stress loss rate can be calculated by the peak stress, and the loss rates were 27%, 47.25%, 59.07%, and 81.01%, respectively. As can be seen from Figure 5, the peak stress loss rates of rock samples gradually increased with the increase of water content. When the water content is 6.25%, the peak stress loss rate of rock sample reaches to 80.01%, indicating that

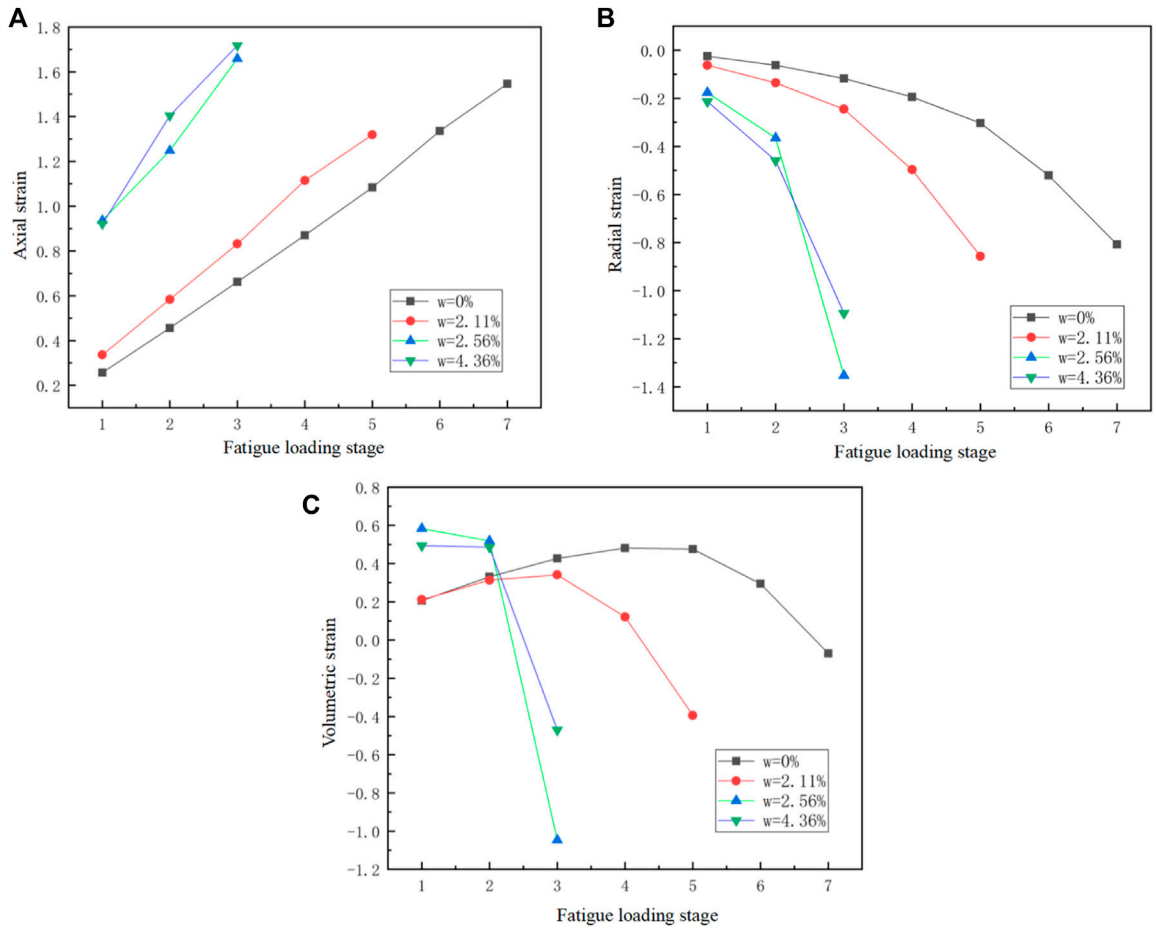

FIGURE 9
Plots of the relationship between the maximum axial strain **(A)**, maximum radial strain **(B)**, and the volumetric strain **(C)** against fatigue loading stage.

water treatment has a significant reduction effect on the mud-shale samples, the water-sensitive property of this rock is strong.

To summarize, the stress-strain curves of different water content are very different, and the peak strength of the rock sample with water content 6.25% is about 19% of that of the rock sample without water treatment. With the increase of water content, mud shale absorbs water and expands easily, and the rock mass structure changes gradually. From the microscopic perspective, the clay-like minerals near the mesenchymal surface of rock, such as chlorite and illite, interact with water, and water molecules enter the pores, resulting in the expansion of clay minerals and resulting in swelling stress. At the same time, in the process of immersion, the wetting angle decreases, and the surface tension of particles in the rock also decreases. The combined effect of several factors reduces the internal bonding force of the rock, showing that the rock softens and decreases its strength on the macro level.

Fatigue deformation analysis

The deformation of rock increases with the increase of loading period, and the increase rate is affected by loading stage and water content. The relationship between the axial, radial and volumetric strains and the testing time is shown by the deformation curve of the rock during the whole test time. As shown in Figure 6, the axial, radial and volumetric strains are small when the number of loading cycles is small. However, after a certain number of loading cycles, the incremental rate of axial, lateral and volumetric strains change obviously until failure. It can be seen that in the several stages before failure, the deformation amount of the fatigue cycle increases steadily in each stage; however, when the applied amplitude changes, that is, when the loading stage changes, the deformation increases substantially.

At the last loading stage, the deformation growth rate reaches the maximum, and the specimen deformation becomes large until failure. During the whole process of failure, the rate of change gradually increases. For rock samples with water content of 2.56%, 4.36%, and 6.25%, the volumetric strain in the first cycle at the time of failure increases significantly compared with the sample with water ratio of 0% and 2.11%. The sample having relative high water content results in relatively large volumetric expansion, indicating that water affects the structure of the sample, ot has obvious softening effect on the rock mass, and the plasticity of the sample is enhanced.

The deformation characteristics of the sample can be described more intuitively by drawing the relation curve between deformation and fatigue cycles, as shown in Figure 7. It can be seen that as the number of fatigue cycles increases, the axial and lateral growth rates increase. In the last stage of fatigue loading, the axial and transverse

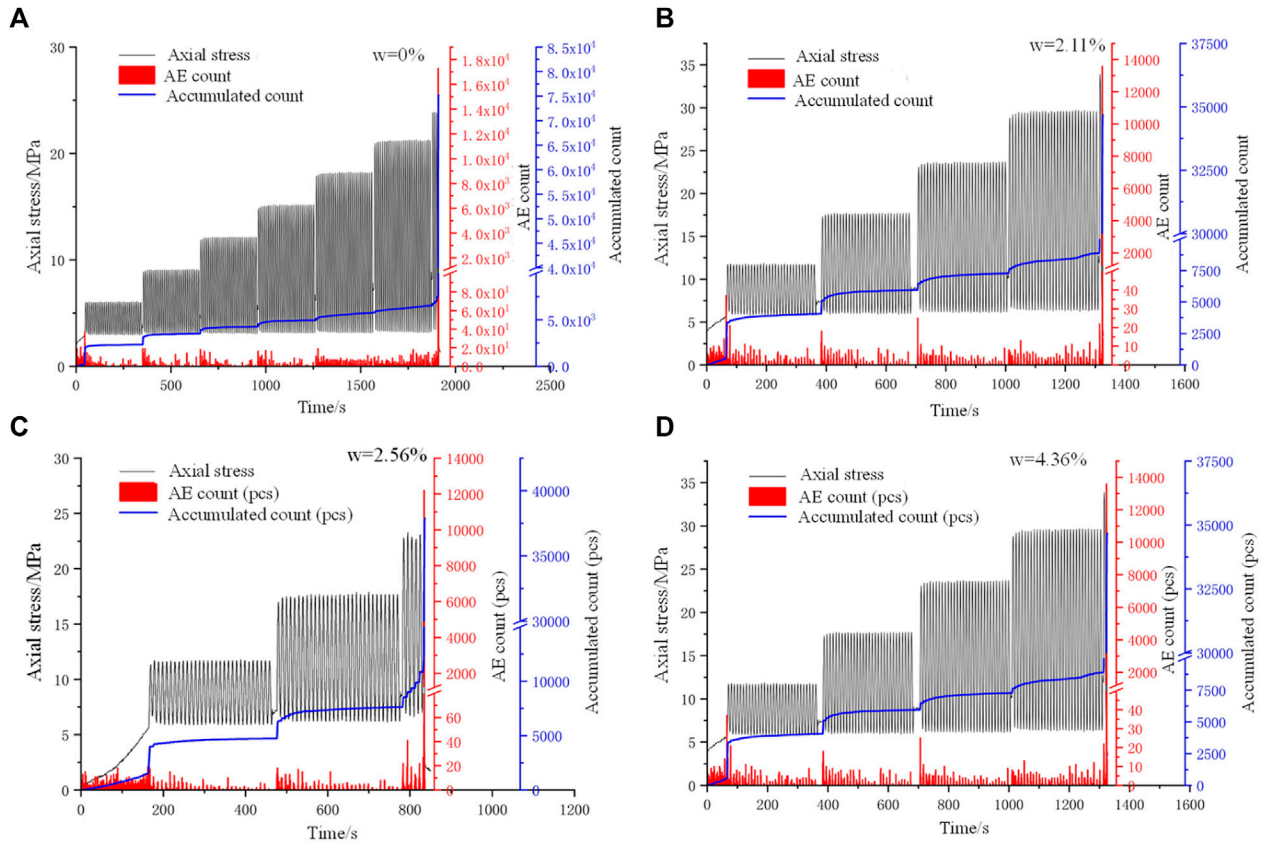

FIGURE 10
The AE ring count and AE accumulative ring count distribution *versus* experimental time. **(A-D)** The tested rock samples with water content of 0%, 2.21%, 2.56%, and 4.36%, respectively).

strains increase sharply with the increase of loading cycles. In the loading process, when the loading phase changes, the deformation increases greatly with the sudden increase of stress. The essence of the rapid increase of specimen deformation is that the sudden increase of stress causes great damage to the rock. In the same stage of initial loading, the deformation gradually tends to be stable. This is because the loading stress is small and the amplitude change is small, and the rock is in the adaptation and adjustment stage of cyclic loading. The essence of specimen deformation is the result of stress adjustment of each component inside the material. At the final failure stage, the deformation of the specimen increases sharply.

To better describe the influence of axial deformation (ε_a) and radial deformation (ε_r) on the volumetric strain (εv), the volumetric strain (εv) of the sample was calculated according to the formula ($\varepsilon_v = \varepsilon_a + 2\varepsilon_r$). The volumetric strain reflects the combined effect of axial and radial deformation on specimen deformation, as shown in Figure 8.

As can be seen from the relationship diagram between loading stage and strain in Figure 9, the axial strain of rock approximately changes linearly with the fatigue loading stage. The change rate of axial cumulative strain at each stage of the loading process basically remains unchanged, which is related to the loading conditions of the sample. The changing rate of the radial cumulative strain increases gradually. As can be seen from the volumetric strain, the maximum volumetric strain experienced compression-dominant stage to the expansion-dominant stage before failure. This phenomenon is more significant for the rock samples with water content of 0% and 2.11%.

AE activity analysis

The stress-strain curves reflect the macroscopic fracture evolution characteristics of rock samples. The acoustic emission activities recorded during the deformation of samples provides effective information for understanding the meso-fracture process of rocks. Figure 10 shows the relationship between the number of AE rings, axial stress and the experimental time. It can be seen from the change of acoustic emission ringing number during the whole loading process that the acoustic emission ringing number increases obviously at the beginning of each fatigue loading stage due to the sudden increase of axial stress. The sudden increase of axial stress leads to crack propagation in the rock sample. In the fatigue loading stage, the acoustic emission ringing number increases rapidly in the first several cyclic loading stages. However, the acoustic emission ringing counts increased faster in the last few loading stages. The occurrence and increase of AE ringing count are caused by the damage of the meso-structure inside the rock sample. The AE ring count gradually increases with the increase of the number of loading cycles. The

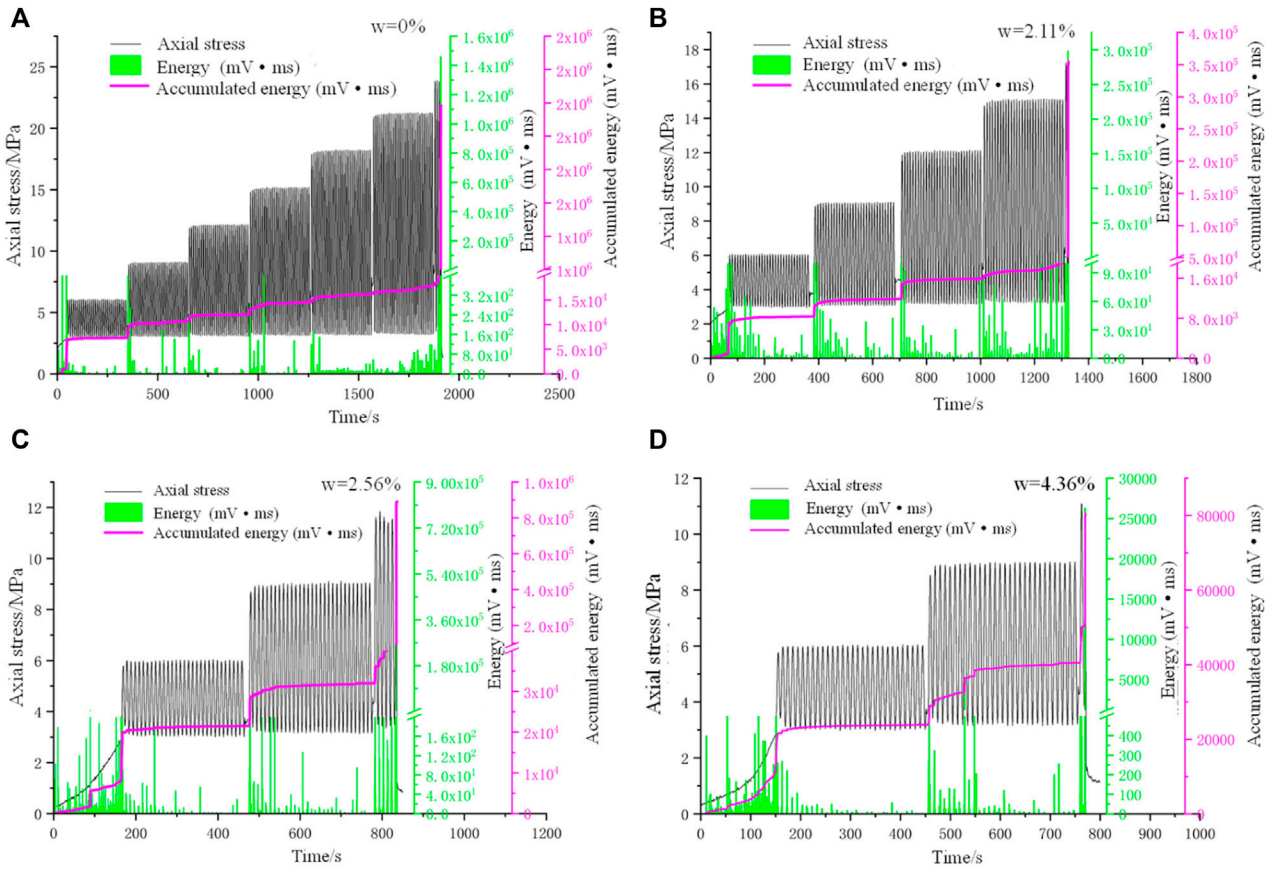

FIGURE 11
Plots of the AE energy and accumulative energy distribution against experimental time. **(A-D)** The tested rock samples with water content of 0%, 2.21%, 2.56%, and 4.36%, respectively).

progressive increase of the AE cumulative ringing count also indicates a sudden increase in AE ringing count at the beginning of each fatigue loading stage. As can be seen from the curve of AE cumulative ringing count, its value is increasing, indicating that the cumulative damage, crack initiation, propagation and coalescence behaviors of rock samples.

By comparing the AE ringing count curves for samples with different water ratio, it can be found that the cumulative acoustic emission ringing count decreases with the increase of water ratio. Especially for the sample having a water ratio of 4.36%, the ringing count is significantly reduced compared with the samples having other water content. At the first few stages before the sample failure, the AE ringing count activities present sporadic distribution, and the value is very small, and the AE phenomenon is very weak.

In order to further reveal the influence of water content on AE output, the relationships between the energy/cumulative energy count, and fatigue loading stage are plotted in Figure 11. For the AE non-destructive testing, the energy of AE signal is a parameter related to the amplitude and amplitude distribution of the signal. It is defined from the signal waveform, rather than the actual physical energy released by the AE source. However, AE energy is still of great significance for measuring and evaluating the fracture and damage degree of materials. It can be seen from the curves that at the beginning of each loading stage, the energy count has a sudden increase, and the cumulative energy count jumps up in each stage, showing obvious energy growth. This is due to the sudden increase of stress at the following fatigue loading stage, the occurrence structural failures, and the release of a large number of stress waves, leading to the rapid growth of the AE energy accumulation curve. Throughout the whole failure process, the AE energy count increases with the increase of loading stage. The cumulative AE energy counts changed in two stages, first increasing stably and then increasing rapidly. The stable stage is the steady damage of the internal structure and the gradual expansion of cracks, while the sudden increase stage is the process of the final crack penetration. In addition, through comparing the different curves, the energy release is larger for a sample having low water content than those having high water content.

Discussions

The damage and failure mechanism of soft rock has been studied by many scholars, and it is widely believed that there are a large number of defects in soft rock, such as joints, cracks and pores, which affect the propagation path and related failure modes (Jiang et al., 2016; Liu et al., 2018; Bai et al., 2022a). At present, plenty of studies have been performed on soft rock, and the mechanical properties, energy loss, and deformation characteristics of soft rock under cyclic loading have attracted extensive attention. However, almost all of the research is about the natural dry conditions. It should be noted that the

engineering soft rocks are frequently encountered with precipitation and groundwater seepage, especially is affected by seasonal changes. Its strength and other mechanical properties can change significantly, which impacts the stability of open pit slope. In this work, we consider the actual engineering state of mud-shale, rock samples with different water contents were produced. Cyclic loading and unloading tests were carried out on mud shale under different water ratio. Through the analysis of stress-strain and acoustic emission data, the evolution law of deformation and failure of mud shale under different water ratio was revealed. The effect of water content on damage mechanics and acoustic emission characteristics of shale is deeply explored.

In this study, it is found that water will cause the changes in the internal structure of mud-shale, which has a softening effect on it. With the increase of water content, the mass loss rate shows the characteristics of gentle at first and then rising sharply. In addition, different from previous studies, the cyclic mechanical properties of soft rock are discussed in more detail in this study. It is found that rock strength loss rate decreases gradually with the gradual increase of water content. The axial, radial and volumetric deformation show different trends. According to the volumetric strain, the sample will undergo dilatation before failure. In addition, the samples with low water content produced more ringing/energy counts than those with relatively high water content. It should be noted that soft rock has obvious rheological characteristics, and its creep deformation will seriously affect the stability of slope. In the further studies, deep investigations should be carried out to study creep and damage characteristics of mud shale and establish damage constitutive model. In addition, the influence of complicated fatigue loading paths, e.g., frequency, amplitude, waveform type, on the damage and instability of mud-shale need to be clariid in the next studies.

Conclusion

In this work, macroscopic mechanical tests combined with acoustic emission monitoring was performed on mud shale to reveal the influence of water content on the stress strain responses, deformation, and AE activities. Based on the above analysis, some key conclusions can be drawn as below:

1) With the gradual increase of water content, the number of loading cycles gradually decreases and the fatigue life decreases, indicating that the water ratio has an impact on the strength, deformation and fracture characteristics of shale.
2) The morphology of hysteresis curve changes with loading time. The hysteresis curve is sparse and becomes intensive in each fatigue loading stage before failure, while it is sparse in the final failure stage. At the same loading frequency, the axial strain changes approximately linearly with the fatigue loading stage, while the radial cumulative strain increases gradually. The maximum volume strain first increases steadily, then decreases steadily, and finally decreases sharply to a negative value. Accordingly, the failure process of the sample can be divided into three stages: initial stage, stable development stage and acceleration stage.
3) With the increase of water ratio, the cumulative AE ringing count and AE energy increase accordingly. In the first few stages before failure, the ringing count of AE presents sporadic distribution, and the value is very small, and the AE phenomenon is very weak. However, in the last several stages, the AE ringing count is more active. There is a good correspondence between the whole process of AE energy and ringing count. Especially, the change of AE energy is consistent with ring count, indicating that ringing count and energy are basically proportional to each other in an AE signal event.

Data availability statement

The raw data supporting the conclusions of this article will be made available by the authors, without undue reservation.

Author contributions

XL, review and editing; JW, methodology, conceptualization; HY, experiments, data analysis; YW, supervision, funding acquisition, project administration.

Funding

Geological Survey Project of CGS (DD20221730), and National Natural Science Foundation of China (52174069).

Conflict of interest

The authors declare that the research was conducted in the absence of any commercial or financial relationships that could be construed as a potential conflict of interest.

Publisher's note

All claims expressed in this article are solely those of the authors and do not necessarily represent those of their affiliated organizations, or those of the publisher, the editors and the reviewers. Any product that may be evaluated in this article, or claim that may be made by its manufacturer, is not guaranteed or endorsed by the publisher.

References

Al-Shayea, N. A. (2004). Effects of testing methods and conditions on the elastic properties of limestone rock. *Eng. Geol.* 74 (1-2), 139–156. doi:10.1016/j.enggeo.2004.03.007

Bagde, M. N., and Petroš, V. (2005). Fatigue properties of intact sandstone samples subjected to dynamic uniaxial cyclical loading. *Int. J. Rock Mech. Min. Sci.* 42, 237–250. doi:10.1016/j.ijrmms.2004.08.008

Bai, B., Bai, F., Li, X., Nie, Q., Jia, X., and Wu, H. (2022a). The remediation efficiency of heavy metal pollutants in water by industrial red mud particle waste. *Environ. Technol. Innovation* 28, 102944. doi:10.1016/j.eti.2022.102944

Bai, B., Wang, Y., Rao, D., and Bai, F. (2022b). The effective thermal conductivity of unsaturated porous media deduced by pore-scale SPH simulation. *Front. Earth Sci.* 10, 943853. doi:10.3389/feart.2022.943853

Bai, B., Zhou, R., Cai, G., Hu, W., and Yang, G. (2021). Coupled thermo-hydro-mechanical mechanism in view of the soil particle rearrangement of granular thermodynamics. *Comput. Geotechnics* 137, 104272. doi:10.1016/j.compgeo.2021.104272

Cerfontaine, B., and Collin, F. (2018). Cyclic and fatigue behaviour of rock materials: Review, interpretation and research perspectives. *Rock Mech. Rock Eng.* 51 (2), 391–414. doi:10.1007/s00603-017-1337-5

Chen, X., Huang, Y., Chen, C., Lu, J., and Fan, X. (2017). Experimental study and analytical modeling on hysteresis behavior of plain concrete in uniaxial cyclic tension. *Int. J. Fatigue* 96, 261–269. doi:10.1016/j.ijfatigue.2016.12.002

Fan, J., Jiang, D., Liu, W., Wu, F., Chen, J., and Daemen, J. (2019). Discontinuous fatigue of salt rock with low-stress intervals. *Int. J. Rock Mech. Min. Sci.* 115, 77–86. doi:10.1016/j.ijrmms.2019.01.013

Guo, H., Ji, M., Zhang, Y., and Zhang, M. (2018). Study of mechanical property of rock under uniaxial cyclic loading and unloading. *Adv. Civ. Eng.* 2018, 1–6. doi:10.1155/2018/1670180

Guo, Z. B., Li, E. Q., Liu, J. W., and Wang, J. (2012). Study on deformation mechanism of deep soft rock roadway in daqiang coal mine of tiefa coal industry. *Adv. Mater. Res.* 542, 34–41. doi:10.4028/www.scientific.net/AMR.542-543.34

Hashemnejad, A., Aghda, S. M. F., and Talkhablou, M. (2021). Introducing a new classification of soft rocks based on the main geological and engineering aspects. *Bull. Eng. Geol. Environ.* 80 (6), 4235–4254. doi:10.1007/s10064-021-02192-8

Jiang, D., Fan, J., Chen, J., Li, L., and Cui, Y. (2016). A mechanism of fatigue in salt under discontinuous cycle loading. *Int. J. Rock Mech. Min. Sci.* 86, 255–260. doi:10.1016/j.ijrmms.2016.05.004

Li, Z. J., Li, S. B., and Zhao, X. L. (2012). Floor heave controlling technology of deep soft rock roadway. *Appl. Mech. Mater.* 170, 68–71. doi:10.4028/www.scientific.net/AMM.170-173.68

Liu, E., Huang, R., and He, S. (2012). Effects of frequency on the dynamic properties of intact rock samples subjected to cyclic loading under confining pressure conditions. *Rock Mech. rock Eng.* 45 (1), 89–102. doi:10.1007/s00603-011-0185-y

Liu, Y., Dai, F., Dong, L., Xu, N., and Feng, P. (2018). Experimental investigation on the fatigue mechanical properties of intermittently jointed rock models under cyclic uniaxial compression with different loading parameters. *Rock Mech. Rock Eng.* 51 (1), 47–68. doi:10.1007/s00603-017-1327-7

Meng, H. J., Wang, Y., Zhang, B., and Gao, S. H. (2020). Investigation on the effect of dynamic frequency on fracture evolution in preflawed rock under multistage cyclic loads: Insight from acoustic emission monitoring. *Geofluids* 2020, 1–15. doi:10.1155/2020/8891395

Momeni, A., Karakus, M., Khanlari, G. R., and Heidari, M. (2015). Effects of cyclic loading on the mechanical properties of a granite. *Int. J. Rock Mech. Min. Sci.* 77, 89–96. doi:10.1016/j.ijrmms.2015.03.029

Peng, K., Zhou, J., Zou, Q., and Song, X. (2020). Effect of loading frequency on the deformation behaviours of sandstones subjected to cyclic loads and its underlying mechanism. *Int. J. Fatigue* 131, 105349. doi:10.1016/j.ijfatigue.2019.105349

Roberts, L. A., Buchholz, S. A., Mellegard, K. D., and Düsterloh, U. (2015). Cyclic loading effects on the creep and dilation of salt rock. *Rock Mech. Rock Eng.* 48 (6), 2581–2590. doi:10.1007/s00603-015-0845-4

Singh, S. K. (1989). Fatigue and strain hardening behaviour of graywacke from the flagstaff formation, New South Wales. *Eng. Geol.* 26, 171–179. doi:10.1016/0013-7952(89)90005-7

Singh, S. K. (1988). Relationship among fatigue strength, mean grain size and compressive strength of a rock. *Rock Mech. Rock Eng.* 21, 271–276. doi:10.1007/bf01020280

Song, D., Wang, E., and Liu, J. (2012). Relationship between EMR and dissipated energy of coal rock mass during cyclic loading process. *Saf. Sci.* 50 (4), 751–760. doi:10.1016/j.ssci.2011.08.039

Song, S., Liu, X., Tan, Y., Fan, D., Ma, Q., and Wang, H. (2020). Study on failure modes and energy evolution of coal-rock combination under cyclic loading. *Shock Vib.* 2020, 1–16. doi:10.1155/2020/5731721

Taheri, A., Squires, J., Meng, Z., and Zhang, Z. (2017). Mechanical properties of Brown coal under different loading conditions. *Int. J. Geomechanics* 17 (11), 06017020. doi:10.1061/(asce)gm.1943-5622.0000993

Vaneghi, R. G., Ferdosi, B., Okoth, A. D., and Kuek, B. (2018). Strength degradation of sandstone and granodiorite under uniaxial cyclic loading. *J. Rock Mech. Geotechnical Eng.* 10 (1), 117–126. doi:10.1016/j.jrmge.2017.09.005

Voznesenskii, A., Kutkin, Y., Krasilov, M., and Komissarov, A. (2016). The influence of the stress state type and scale factor on the relationship between the acoustic quality factor and the residual strength of gypsum rocks in fatigue tests. *Int. J. Fatigue* 84, 53–58. doi:10.1016/j.ijfatigue.2015.11.016

Wang, Y., Mao, T., Xia, Y., Li, X., and Yi, X. (2022b). Macro-meso fatigue failure of bimrocks with various block content subjected to multistage fatigue triaxial loads. *Int. J. Fatigue* 163, 107014. doi:10.1016/j.ijfatigue.2022.107014

Wang, Y., Su, Y., Xia, Y., Wang, H., and Yi, X. (2022a). On the effect of confining pressure on fatigue failure of block-in-matrix soils exposed to multistage cyclic triaxial loads. *Fatigue & Fract. Eng. Mater. Struct.* 45 (9), 2481–2498. doi:10.1111/ffe.13760

Wang, Y., Tan, P. F., Han, J., and Li, Peng. (2023). Energy-driven fracture and instability of deeply buried rock under triaxial alternative fatigue loads and multistage unloading conditions: Prior fatigue damage effect. *Int. J. Fatigue* 168, 107410. doi:10.1016/j.ijfatigue.2022.107410

Wang, Y., Yi, X. F., Li, P., Cai, M. F., and Sun, T. (2022c). Macro-meso damage cracking and volumetric dilatancy of fault block-in-matrix rocks induced by freeze–thaw-multistage constant amplitude cyclic (F-T-MSCAC) loads. *Fatigue & Fract. Eng. Mater. Struct.* 45 (10), 2990–3008. doi:10.1111/ffe.13798

Wang, Y., Zhu, C., He, M., Wang, X., and Le, H. (2022d). Macro-meso dynamic fracture behaviors of xinjiang marble exposed to freeze thaw and frequent impact disturbance loads: A lab-scale testing. *Geomechanics Geophys. Geo-Energy Geo-Resources* 8 (5), 154–218. doi:10.1007/s40948-022-00472-5

Xu, J., Sun, H., Cui, Y., Fei, D., Lan, H., Yan, C., et al. (2021). Study on dynamic characteristics of diorite under dry–wet cycle. *Rock Mech. Rock Eng.* 54 (12), 6339–6349. doi:10.1007/s00603-021-02593-x

Zheng, Q., Liu, E., Sun, P., Liu, M., and Yu, D. (2020). Dynamic and damage properties of artificial jointed rock samples subjected to cyclic triaxial loading at various frequencies. *Int. J. Rock Mech. Min. Sci.* 128, 104243. doi:10.1016/j.ijrmms.2020.104243

Zhou, S. W., Xia, C. C., Hu, Y. S., Zhou, Y., and Zhang, P. Y. (2015). Damage modeling of basaltic rock subjected to cyclic temperature and uniaxial stress. *Int. J. Rock Mech. Min. Sci.* 77, 163–173. doi:10.1016/j.ijrmms.2015.03.038

frontiers | Frontiers in Materials

TYPE Original Research
PUBLISHED 07 February 2023
DOI 10.3389/fmats.2023.1135276

Check for updates

OPEN ACCESS

EDITED BY
Bing Bai,
Beijing Jiaotong University, China

REVIEWED BY
Zhengzheng Cao,
Henan Polytechnic University, China
Teng Teng,
China University of Mining and Technology, Beijing, China

*CORRESPONDENCE
Jun Huang,
hgvyoe@xsyu.edu.cn
Naifei Liu,
liunaifei@xauat.edu.cn

SPECIALTY SECTION
This article was submitted to Structural Materials, a section of the journal Frontiers in Materials

RECEIVED 31 December 2022
ACCEPTED 18 January 2023
PUBLISHED 07 February 2023

CITATION
Huang J, Liu N, Ma Z, Lu L and Dang K (2023), The construction stability of large section tunnel considering the deterioration of clay mechanical properties. *Front. Mater.* 10:1135276. doi: 10.3389/fmats.2023.1135276

COPYRIGHT
© 2023 Huang, Liu, Ma, Lu and Dang. This is an open-access article distributed under the terms of the Creative Commons Attribution License (CC BY). The use, distribution or reproduction in other forums is permitted, provided the original author(s) and the copyright owner(s) are credited and that the original publication in this journal is cited, in accordance with accepted academic practice. No use, distribution or reproduction is permitted which does not comply with these terms.

The construction stability of large section tunnel considering the deterioration of clay mechanical properties

Jun Huang[1,2]*, Naifei Liu[2]*, Zongyuan Ma[3], Liang Lu[4] and Kangning Dang[5]

[1]School of Earth Sciences and Engineering, Xi'an Shi-you University, Xi'an, China, [2]Shaanxi Key Laboratory of Geotechnical and Underground Space Engineering, Xi'an University of Architecture and Technology, Xi'an, China, [3]Guizhou communications polytechnic, Guiyang, China, [4]Gansu Institute of Architectural Design and Research Co, LTD, Lanzhou, China, [5]Hanjiang-to-Weihe river valley water diversion project construction Co, LTD, Xi'an, China

The stability of large-section clay tunnels is closely related to the mechanical behavior of the surrounding rock. The mechanical behavior of the surrounding rock is characterized by the coupled response of the physico-mechanical properties of the clay material and the tunnel construction conditions. Therefore, this paper proposes a numerical experimental study based on the response surface method to quantitatively link the stability of large-section clay tunnels with construction factors. It will provide a basis for quantitatively guiding the tunnel construction plan adjustment to ensure its stability. Firstly, the tunnel stability reserve is evaluated by considering the deterioration of physico-mechanical properties of clay surrounding rocks, and the relationship between the tunnel stability index and construction factors is established according to Taylor's theorem. Secondly, the response surface method and the steepest ascent method are used to find the optimal fitting relationship between the tunnel stability reserve factor and tunnel construction factors. Finally, the analysis of a tunnel application shows that (a) the stability evaluation considering the deterioration of physical and mechanical properties of clay is well representative; (b) the "curved" region of the response of the tunnel stability reserve factor can be effectively determined by the steepest slope method; (c) for the "curved" region, a second-order response surface is more appropriate. This research will reveal the coupling relationship between tunnel stability, physico-mechanical properties of clay, and tunnel construction conditions, which will contribute to the development of intelligent tunnel construction.

KEYWORDS

physico-mechanical properties of clay, stability evaluation, construction factors, numerical experiment, response surface method

1 Introduction

With the continuous development of underground space development and utilization, the large-section tunnel stability evaluation must face more complex situations and difficulties. Large cross-section clay tunnels make studying surrounding rock stability a more severe and complex challenge. Moreover, large-section excavation will cause more complex stress concentrations and deformation localization in the surrounding rock. The larger scale of underground construction, shorter construction cycles, and higher degree of construction

automation and intelligence require experts and engineers to quickly, accurately, and systematically evaluate the stability of the surrounding rock and make decisions on countermeasures. All these directions and trends depend on the improvement and development of the evaluation system of the fundamental theories and methods for the large-section tunnels' stability.

Theories and methods of stability analysis of large-section clay tunnels are also based on the stability of ordinary tunnels (Höfle et al., 2008; Lü et al., 2020; Song et al., 2021; Xue et al., 2023b). The tunnel stability problem is derived from the difficulties encountered in the construction of underground projects (Huang et al., 2019; Liu et al., 2020; Kumar and Sahoo, 2021; Zhang et al., 2022b). The research work on it is also one of the essential manifestations of the close connection between theory and reality (Lee et al., 2006; Wilson et al., 2011; Tyagi et al., 2018; Rahaman and Kumar, 2020; Li et al., 2021). Those problems have been analyzed and summarized by researchers and engineers, e.g., the classification and failure mechanism of the surrounding rock by observing and monitoring the mechanical indicators and anomaly phenomena of the surrounding rock during the tunnel construction process. The calculation formulas of the surrounding rock pressure and the stress-strain relationship of the surrounding rock are established *via* some idealized assumptions (Bai et al., 2019; Zhong and Yang, 2020; Hou et al., 2022; Man et al., 2022; Xue et al., 2023a). The changes in the mechanical state inside the surrounding rock during the construction process of the tunnel and underground engineering are very complicated to be recognized. A series of indoor experimental studies, including the centrifuge tunnel model through similar models in the chamber, are processed (Juneja et al., 2010; Alavi Gharahbagh et al., 2014; Song and Marshall, 2020; Bai et al., 2021a; Li et al., 2021). The researchers also used numerical models of tunnels through finite elements, discrete elements, and et al. to carry out stability analysis related to the mechanical state of the surrounding rock and the most likely failure form (Zhang et al., 2011; Roateşi, 2014; Ukritchon et al., 2017; Lü et al., 2018; Liu et al., 2022b; Hou et al., 2022; Xue et al., 2023b). The advantages of numerical analysis are becoming more and more evident as technology advances, especially in terms of geometry, boundary conditions, and visualization of results, making it a powerful tool.

All research and practice are aimed at better ensuring the stability of the construction solution to support the tunnel surrounding rock (Dias, 2011; Pan and Dias, 2017; Park et al., 2017; Zare Naghadehi et al., 2019; Bai et al., 2021b; Zhang et al., 2022a). Thus, researchers have conducted various studies on the mechanical state, deformation state, and stability of the surrounding rock through theoretical, experimental, numerical, and field monitoring methods to study the tunnel burial depth, hole diameter, excavation plan, and support plan (Tyagi et al., 2018; Antão et al., 2021; Kumar and Sahoo, 2021; Shiau and Al-Asadi, 2022). These research results have greatly enriched and improved the knowledge of tunnel construction theory and practice.

Tunnel stability research work has made significant progress after years of development. The underground projects, including tunnels, are faced with the difficulties posed by construction in high-risk environments where geological engineering problems are frequent at the early stage of tunnel construction (Rojat et al., 2015; Weng et al., 2020; Yertutanol et al., 2020; Xue et al., 2022). Traffic tunnels are also trending toward larger cross-sections, and the requirement for faster and better construction periods and the engineers need to pay more attention to the role of construction solutions in securing tunnel stability. Artificial intelligence, construction intelligence, and automation will also bring new changes to tunnel construction (Mahmoodzadeh et al., 2020; Higgins and Stathopoulos, 2021; Liu et al., 2022a; Ayawah et al., 2022; Baghbani et al., 2022; Soranzo et al., 2022). Following these trends, such as rapid decision-making mechanisms for construction solutions, cannot be separated from the development of methods for analyzing tunnel stability foundations.

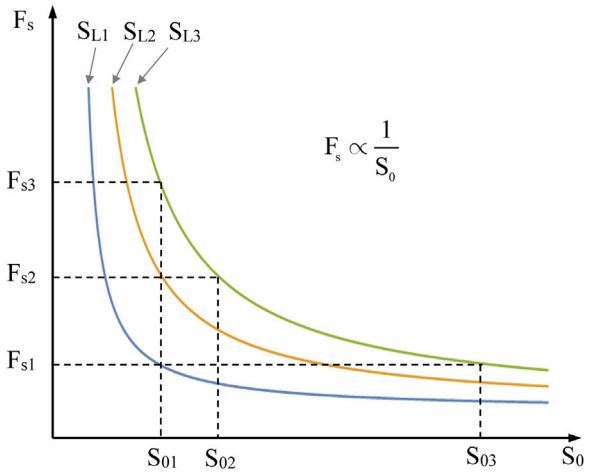

FIGURE 1
Diagram of the deterioration of clay mechanical properties.

Research work in these areas has contributed significantly to developing tunnel stability theory, methods and practice. However, the current research results are difficult to play a more significant role in construction automation, intelligence, and rapid decision-making. Therefore, with the advantage of numerical analysis tools, this paper proposes a numerical experimental study based on response surface design for quantitative linkage between stability and construction factors at the face of large-section clay tunnels. It should be provided a systematic direction for developing decision-making methods, and the techniques and ideas used will contribute to the realization of tunnel construction intelligence and automation.

2 Stability evaluation *via* the deterioration of clay mechanical properties

2.1 The stability index of clay surrounding rocks

The stability evaluation index for large-section clay tunnels is quantitative, and it can estimate the variability between the mechanical state of the surrounding rock after tunnel excavation and its limit state.

(1) The stability reserve factor for the large cross-section clay tunnel

Firstly, the actual mechanical state of the surrounding rock at one point after tunnel excavation is S_0 and the limit state at that point is S_L, by analogy with the slope safety factor, the calculated expression for the tunnel stability reserve factor F_s is given as follows.

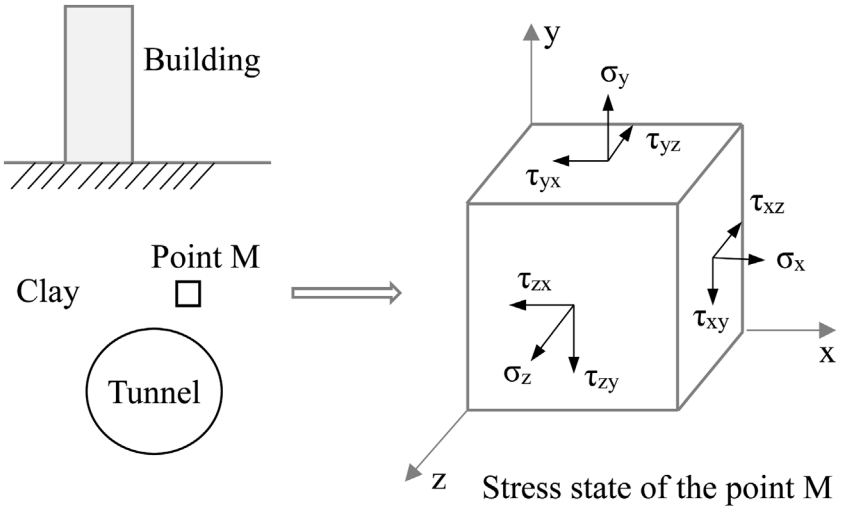

FIGURE 2
Stress state at a point in the clay tunnel surrounding rocks.

$$F_s = \frac{S_L}{S_0} \tag{1}$$

The tunnel stability reserve factor can be applied to different geological conditions, environmental conditions, additional loading factors, et al., it only depends on the actual mechanical state and the limit state of the surrounding rock and does not depend on the constitutive model. Therefore, it is well suited for the stability evaluation of a large cross-section clay tunnel.

Figure 1 gives the correlation between the tunnel stability reserve factor based on Eq. 1 and the actual mechanical state of the surrounding rock. The ultimate state of the surrounding rock is closely related to the physico-mechanical properties of the clay. The process of deterioration of the physico-mechanical properties of the clay is specifically characterized as a change in the limit state of the surrounding rock. When the physico-mechanical properties of the surrounding rock remain unchanged, then the actual mechanical state of the surrounding rock can be adjusted to meet a given tunnel stability reserve factor.

(2) Mechanical state of the surrounding rock in a large-section clay tunnel.

A tunnel is excavated in a clay stratum, and the stress state and strain state of a point in the surrounding rock is the response of the internal forces and deformation of the surrounding rock under the generalized load. Therefore, the mechanical state of the surrounding rock can be characterized by its stress state and strain state.

The stress state and strain state of a point, $M(x, y, z)$, in the surrounding rock of a clay tunnel can be expressed by the stress component and strain component of the element at that point (shown in Figure 2).

$$\boldsymbol{\sigma} = \begin{pmatrix} \sigma_x & \tau_{xy} & \tau_{xz} \\ \tau_{yx} & \sigma_y & \tau_{yz} \\ \tau_{zx} & \tau_{zy} & \tau_z \end{pmatrix}, \quad \boldsymbol{\varepsilon}^{\mathrm{T}} = \begin{pmatrix} \varepsilon_x & \varepsilon_y & \varepsilon_z & \gamma_x & \gamma_y & \gamma_z \end{pmatrix} \tag{2}$$

The following equation can express the relationship between the mechanical state of a point in the surrounding rock and its stress state and strain state.

$$\mathbf{S} = s\ (\boldsymbol{\sigma}, \boldsymbol{\varepsilon}) \tag{3}$$

S is the mechanical state tensor of a point in the surrounding rock after tunnel excavation. If the constitutive model is determined, the stress and strain state is the relevant variables. Then the mechanical state function of surrounding rocks can be expressed by one of the stress or strain states (for example, Eq. 4).

$$\mathbf{S} = s\ (\boldsymbol{\sigma}) \quad \text{or} \quad \mathbf{S} = s\ (\boldsymbol{\varepsilon}) \tag{4}$$

For the clay tunnel surrounding rocks, failure of surrounding rock is caused by shear stress reaching the shear strength of clay. The stress state of a point in the clay surrounding rock can be replaced by the shear stress in Eq. 3, and the strain state is retained. The mechanical state function of the surrounding rock can be expressed by the following.

$$S = s(\tau, \varepsilon) \tag{5}$$

Therefore, the actual mechanical state of a point in the surrounding rock under the unloading effect of tunnel excavation can be expressed as follows.

$$S_0 = s\ (\tau_0, \varepsilon_0) \tag{6}$$

Where τ_0 is the actual shear stress state at a point, and ε_0 is the actual strain state at the same point.

(3) The limit state of the surrounding rock in a large cross-section clay tunnel

The failure of the tunnel due to insufficient strength surrounding rock can be regarded as the mechanical state of the surrounding rock exceeding the limit state of bearing capacity. The failure of the tunnel due to excessive deformation of the surrounding rock can be regarded as the mechanical state of the surrounding rock exceeding the serviceability limit state. The tunnel limit state S_L has three situations of expression shown as follows.

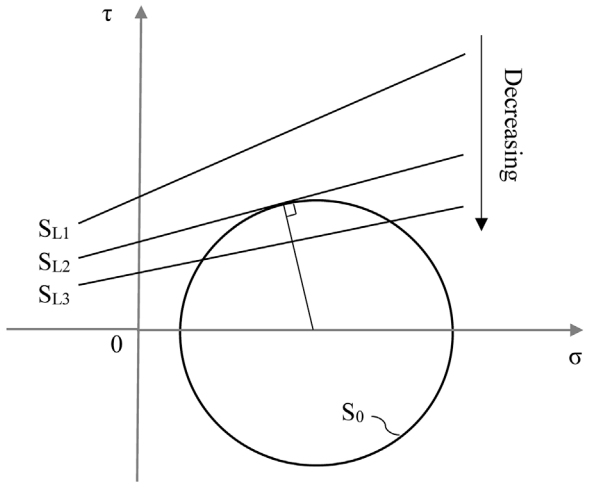

FIGURE 3
Calculation method of the deterioration of clay mechanical properties based on Mohr circle.

(a) The stress state at a point in the surrounding rock reaches the limit, $S_L = s(\sigma_L)$;
(b) The strain state of the surrounding rock reaches the limit at a certain point, $S_L = s(\varepsilon_L)$;
(c) The stress and strain state at a point of the surrounding rock reaches the limit simultaneously, $S_L = s(\sigma_L, \varepsilon_L)$.

According to Eq. 1: when $F_s > 1$ representing the surrounding rock in a stable state, the larger F_s, the more stability reserves of the tunnel; when $F_s = 1$ representing the surrounding rock in limit equilibrium, according to the stress-strain analysis can be seen at this time the surrounding rock in a state of yield; when $F_s < 1$ represents the surrounding rock in a failure state.

Although Eq. 1 is a general expression, difficulties are encountered in the calculation process. The theoretical calculation of the mechanical state of the surrounding rock caused by tunnel excavation is relatively tricky. The shear strength can be simply determined by Coulomb's law. Therefore, this paper uses the strength reduction method (Meng et al., 2019; Nie et al., 2019; Abra and Mahdi, 2022) and the strength-deformation parameter deterioration method (Huang et al., 2023) to calculate the tunnel stability reserve factor. The principle of the calculation of the tunnel stability reserve factor is simply represented by a Mohr circle and the strength envelope in Figure 3.

2.2 Factor analysis for the stability of tunnel construction

The factors of the stability of a large-section clay tunnel can be divided into internal and external factors. The tunnel stability reserve factor can be determined by Eq. 1. The mechanical conditions and the surrounding rock's limit state also affect the tunnel stability. Equation 1 can be expressed by the following implicit function.

The complete set of influence factors of tunnel stability is U, and the groups of intrinsic and extrinsic factors are U_i and U_e, respectively ($U = U_i \cup U_e$). Suppose $t_i \in U_i$ and $t_e \in U_e$, then the binary implicit function of the tunnel stability reserve factor can be expressed as follows.

$$F_s = F(t_i, t_e) \tag{7}$$

The internal and external variables in Eq. 7 contain at least one factor. The equation is not strictly a binary function.

(1) Internal factors affecting the stability of a large-section clay tunnel

The physical and mechanical properties of the surrounding rock (mainly including strength parameters, deformation parameters, weight, water content, et al.) are inherent and are internal factors affecting the stability of the tunnel. When the surrounding rock is clay, its physical and mechanical properties should conform to Coulomb's law. And the shear strength of the surrounding rock can be determined by the strength parameters (Strength parameters are a collective term for the mechanical properties that affect the shear strength of clays) i.e., cohesion and angle of internal friction. The deformation of clay is determined by Young's modulus and Poisson's ratio *via* the generalized Hooke's law. The deformation of the surrounding rock can be referred to as deformation parameters. The strength parameter and deformation parameter are the characterization of the inherent properties of materials.

Taking the limit state of the surrounding rock and the limit state of regular condition into account, the general expressions of the limit state of the surrounding rock at one point concerning the strength parameter and the deformation parameter are shown below.

$$S_L = s_l(c, \varphi, E, \nu) \tag{8}$$

Where c is the cohesion; φ is the angle of internal friction; E is Young's modulus; and ν is Poisson's ratio. c and φ are collectively referred to as the strength parameters; E and ν are collectively referred to as deformation parameters.

The above equations are supported by strength theory, and the constitutive relationship verifies their rationality. The clay's bulk weight and water content may also be critical internal factors. To make the analysis more focused, their effects on strength and deformation are not considered here.

(2) External factors affecting the stability of a large cross-section clay tunnel

Tunnel excavation causes stress concentration or strain localization in the stratum in static equilibrium due to changes in structural form, boundary conditions, loading effects, et al. Moreover, the mechanical response (also called mechanical state) of the surrounding rock is the external condition and also is the key factor of the stability state of the surrounding rock. Therefore, the external factors affecting the stability of the tunnel are also the external conditions affecting the mechanical state of the surrounding rock, such as the action of additional loads on the surrounding rock, boundary conditions, the form of tunnel support, geometry, et al. These external conditions are closely related to the tunnel structure design plans, excavation plans, and support plans, which are collectively referred to as construction factors.

For a more focused subsequent analysis and to make the expressions more concise, the construction factors are here divided into three categories. For large cross-section clay tunnels, it is assumed that the set of factors related to the structural design scheme (e.g.,

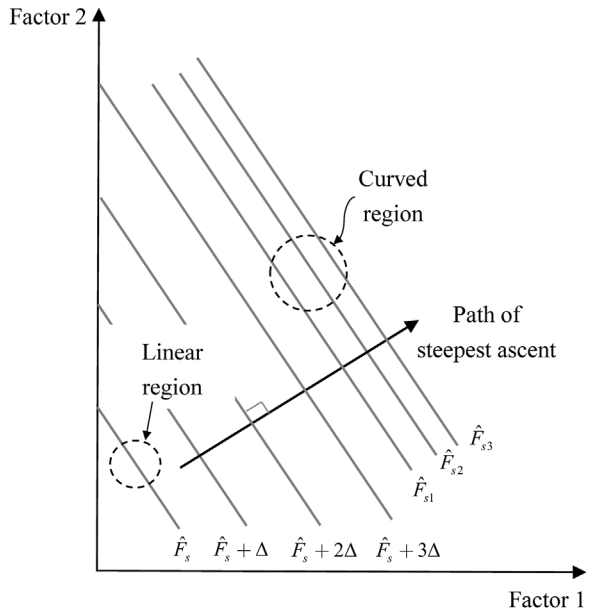

FIGURE 4
Schematic diagram of the steepest ascent path in the "curved" response region.

burial depth, hole diameter, section shape, et al.) is A, which satisfies $\alpha \in A$; the set of factors related to the excavation scheme (e.g., excavation sequence, additional load, construction precipitation, et al.) is B, which satisfies $\beta \in B$; the set of factors related to the support scheme (e.g., support form, support pressure, support distance, et al.) is C, which satisfies $\eta \in C$. The actual stress state of a point can be expressed as follows concerning Lame's formula.

$$\tau_0 = \tau_0(\alpha, \beta, \eta) \tag{9}$$

The actual strain state at this point can be expressed as follows.

(a) When the stress-strain relationship is linear elastic

$$\varepsilon_0 = \varepsilon_0(E, \nu, \alpha, \beta, \eta) \tag{10}$$

(b) When the stress-strain relationship is non-linearly elastic

$$\varepsilon_0 = \varepsilon_0(c, \varphi, E, \nu, \alpha, \beta, \eta) \tag{11}$$

Regardless of the stress-strain relationship, Eq. 6 can be further expressed as:

$$S_0 = s_0\, c, \varphi, E, \nu, \alpha, \beta, \eta \tag{12}$$

The joint analysis of Eq. 7 with Eqs. 8–12 leads to an implicit function in which more explicit variables can express the tunnel stability reserve factor.

$$F_s = f(c, \varphi, E, \nu, \alpha, \beta, \eta) \tag{13}$$

When the surrounding rock material is the same, the stability state of the tunnel (which can also be considered as the actual mechanical state of the surrounding rock) must be different for different structural design plans, excavation plans, or support plans. Thus the tunnel stability index (i.e., the tunnel stability reserve factor) must be different. The engineers can estimate the current state characteristics of the tunnel *via* the quantitative evaluation of tunnel stability during the actual tunnel construction process. The stability evaluation guides the design, adjustment, or optimization of the construction can be planned to ensure the safety and stability of the tunnel, which is the most crucial goal pursued by engineers. Therefore, it is essential to determine the relationship between tunnel stability indicators and these main construction factors.

2.3 General formula of the clay tunnel stability index and construction factors

Large cross-sectional clay tunnels with little change in the distribution of the surrounding rock material can be regarded as interval sections of the same material. The tunnel stability reserve factor is closely related to the construction factors. At this point, Eq. 13 can be simplified to the following function.

$$F_s = f(\alpha, \beta, \eta) \tag{14}$$

Equation 14 reflects that we can use the tunnel stability reserve factor as a stability index while constructing the large cross-section clay tunnel. In developing a specific construction plan, this indicator can be used as a quantitative basis for the optimization and adjustment of the construction plan, and engineers can make construction decisions to optimize the safety and stability of the tunnel. The premise of all this is to determine the response of the tunnel stability reserve factor to these construction factors. α, β, and η represent one or more factors of a particular type. Therefore, to keep the discussion simple and general, α, β, η are still used here as a single variable for the analysis.

Any construction scenario for any large cross-sectional clay tunnels can be represented by a set of construction factors $(\alpha_i, \beta_j, \eta_k)$ within the definition domain U. The tunnel stability reserve factor F_s for that set of construction scenarios can be defined as:

$$F_s = f(\alpha_i, \beta_j, \eta_k) \tag{15}$$

According to the assumption of homogeneity of the surrounding rock material and physical-mechanical continuity, a higher-order partial derivative of F_s exists in the definition domain U. If the initial construction solution is denoted as $(\alpha_0, \beta_0, \eta_0)$, then the initial tunnel stability reserve factor can be denoted as $F_{s0} = f(\alpha_0, \beta_0, \eta_0)$. The tunnel stability reserve factor F_s can be denoted as the following equation according to Taylor's theorem.

$$F_s = F_{s0} + \sum_{t=1}^{n} \frac{1}{t!}\left(\Delta\alpha\frac{\partial}{\partial\alpha} + \Delta\beta\frac{\partial}{\partial\beta} + \Delta\eta\frac{\partial}{\partial\eta}\right)^t f(\alpha_0, \beta_0, \eta_0) + R_n \tag{16}$$

Is the Lagrange residual term that can be used to estimate the error if there exists $\xi \in (0, 1)$.

$$R_n = \frac{1}{(n+1!)}\left(\Delta t\frac{\partial}{\partial t} + \Delta\sigma_t\frac{\partial}{\partial\sigma_t} + \Delta\sigma_s\frac{\partial}{\partial\sigma_{s0}}\right)^{n+1} F(\alpha_r, \beta_r, \eta_r) \tag{17}$$

Where,

$$\begin{cases} \Delta\alpha = \alpha - \alpha_0 \\ \Delta\beta = \beta - \beta_0 \\ \Delta\eta = \eta - \eta_0 \end{cases}, \begin{cases} \alpha_r = \sigma + \xi\Delta\alpha \\ \beta_r = \beta + \xi\Delta\beta \\ \eta_r = \eta + \xi\Delta\eta \end{cases} \tag{18}$$

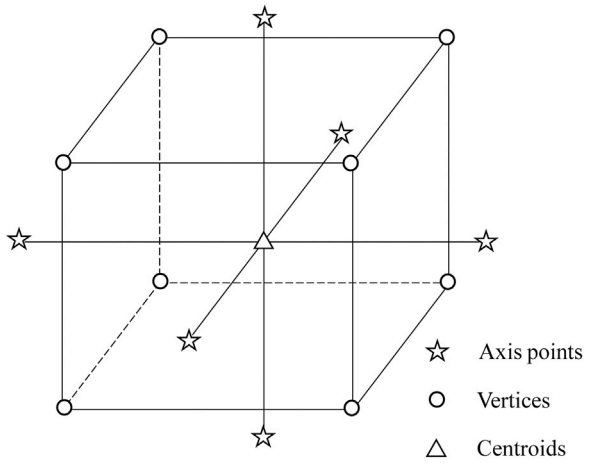

FIGURE 5
The "cube" experimental point of the central composite design.

Generally, as n increases, the higher the accuracy of the formula, but this will cause a rapid increase in the calculation and analysis of the computational effort, making its specific application difficult to promote; numerical analysis also shows that not higher-order Taylor formula will be able to achieve better accuracy, such as the Runger phenomenon. For the entire definition domain, complex functions are difficult to describe accurately with a simple Taylor formula. The first-order or second-order Taylor formula can follow the accuracy requirements in a relatively small sub-domain. The better fitting formula between the tunnel stability reserve factor and the many construction factors can be processed based on the above analysis. Equation 16 has a more apparent guiding meaning and practical value, which is further described as follows.

The initial construction scenario characterized by the main construction factors is $(\alpha_0, \beta_0, \eta_0)$, and the corresponding tunnel stability reserve factor F_{s0} is characterized by the main construction factors, when the location of the large section tunnel is determined (i.e., the stratum is determined), the initial construction scenario. The stability of the tunnel under the initial construction scenario is thus quantitatively evaluated.

(a) If $F_{s0} \le 1$, then it indicates that the tunnel is difficult to maintain stability under the initial construction scenario.
(b) If $F_{s0} > 1$, then the tunnel will remain stable under the initial construction scenario.

To ensure a stable and safe tunnel construction, this faced two kinds of construction plan adjustments.

(a) When $F_{s0} \le 1$, the engineer needs to adjust the construction plan that $(\alpha_0, \beta_0, \eta_0) \rightarrow (\alpha_i, \beta_j, \eta_k)$, so that the new construction plan at least meets $F_s > 1$.
(b) When $F_{s0} > 1$, but $F_{s0} < F_{st}$, then the engineer also needs to adjust the construction plan, i.e. $(\alpha_0, \beta_0, \eta_0) \rightarrow (\alpha_i, \beta_j, \eta_k)$, so that $f(\alpha_i, \beta_j, \eta_k) = F_{st}$, F_{st} is the target value.
(c) When $F_s > 1$, but $F_{s0} > F_{st}$, engineers need to consider the balance between stability reserve and cost control to adjust the construction plan, i.e. $(\alpha_0, \beta_0, \eta_0) \rightarrow (\alpha_i, \beta_j, \eta_k)$, so that $f(\alpha_i, \beta_j, \eta_k) = F_{st}$

Although we obtained the multivariate Taylor formula for tunnel stability index and construction factors, the procedure is still unknown. It is necessary to find their exact or approximate relationship equations.

3 Response surface method for construction stability

It is difficult to obtain the exact expression and solve for all partial derivatives in Eq. 16 directly. In this study, we tried to fit the relational equation and to ensure the accuracy of the fitted expressions. The valid data requires efficient and reliable experimental design or field monitoring techniques, the experimental design is relatively more economical and reliable and has less chance of error. The experimental method cannot be separated from the experimental model. Experimental models can be divided into numerical, similar, and *in situ* models. In contrast, numerical experiments have been applied and shown to be superior in many engineering practices, so this paper also relies on the experimental design of the numerical tunnel model to obtain its fitted relationship.

For large-section tunnels, the design of the construction plan is closely related to the selection of construction factors. These factors are both independent of each other and interact with each other. The response surface method (RSM) can be better applied to the experimental study of the relationship between the stability index and multiple factors of tunnel construction because its process optimization not only considers the interaction between the factors better but also allows for a more approximate relationship. This optimization process is also very compatible with the idea of construction plan optimization. This paper considers the tunnel stability reserve factors as the response parameter, and the set of construction factors corresponding to any construction scheme is (α, β, η).

3.1 First-order response surface analysis of tunnel stability

Suppose the variables $(x_1, x_2, \cdots, x_n)$ corresponding to any group of construction factors (α, β, η) are fitted, then the first-order response model of tunnel stability reserve factor F_s is shown in the following equation.

$$\hat{F}_s = \omega_0 + \sum_{i=1}^{n} \omega_i x_i + \delta \tag{19}$$

3.1.1 Determining the range of variation in each factor and coding the transformation

The range of these variables in the construction factors varies, and the settings may differ considerably. All variables can be linearly transformed (also called coding transformation). The region of these factors is transformed into a "cube" with the center as the origin, and the coding can solve the design problems caused by the different scales. The coding transformation method is described below.

Let the ith variable x_i change interval be $[z_i^l, z_i^u]$, z_i^l and z_i^u be the lower and upper bounds of the interval, $i = 1, 2, 3\cdots, n$, respectively; and note that the midpoint and half-length of the interval are z_{ci} and

TABLE 1 Number of experimental points of the CCD (Number of factors <6).

Number of factors	Number of factorial points	Number of axial points	Number of center points	Total number	λ (rotatability)
2	4	4	5	13	1.414
3	8	6	6	20	1.682
4	16	8	6	30	2.000
5	16	10	7	33	2.378
5	32	10	10	52	2.378

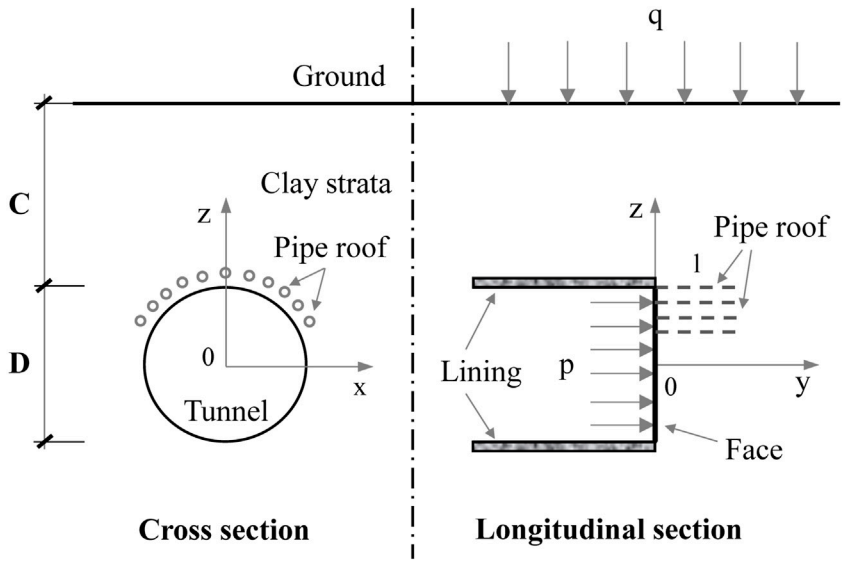

FIGURE 6
Tunnel configuration and construction factors.

κ_i, respectively, the latter also known as the radius of transformation of the factors, which can be expressed as follows

$$z_{ci} = \frac{z_i^l + z_i^u}{2}, \quad \kappa_i = \frac{z_i^u - z_i^l}{2} \tag{20}$$

All variables $(x_1, x_2, \cdots, x_n)$ of the construction factors are linearly transformed as follows.

$$\chi_i = \frac{x_i - z_{ci}}{\kappa_i} \tag{21}$$

χ_i is the canonical variable for the ith variable, satisfying $\chi_i \in [-1, 1]$. This transforms the factorial region, which is shaped like a 'rectangle', into a 'cube' region with the center at the origin.

3.1.2 Experimental arrangement

After coding transformation in the factors, the number of their levels can now be considered as the upper and lower two levels (i.e. −1 and 1). The full factorial experiment can be used directly; if there are more than three construction factors and no more than seven, the two-level orthogonal table $(L_8(2^7))$ can be chosen for the experiment. Suppose it is necessary to estimate the experimental error of the first-order model and test the suitability of the first-order model. In that case, it is necessary to repeat the observed values at the center point.

3.1.3 The steepest ascent method

The "curved" response region of the tunnel stability reserve factor is found by the steepest ascent method.

(a) When the fit of the first-order response model in the defined domain is not significant, it directly reflects the curvature of the response in that interval. The steepest ascent method allows a better search for the region where the curved is most pronounced.
(b) When the fit of the first-order response model in the defined domain is significant, it indicates that the first-order response model can be used in the interval. It is necessary to determine the "curved" part by the steepest ascent method and to design and calculate the second-order response experiment for the curved region. Figure 4 shows the calculation principle of the steepest ascent method and its path.

3.2 Second-order response surface analysis of tunnel stability

The region corresponding to these construction factors is designed and calculated by the second-order model when the response surface of the tunnel stability reserve factor is close to or "curved". In this case,

TABLE 2 Physico-mechanical parameters of surrounding rocks and initial support.

Material	γ (kN/m^3)	E (GPa)	c (kPa)	φ (°)	ν	f_t (MPa)
Clay	18.6	0.03	62.0	25	0.3	-
Bolt	78.5	210.0	-	-	-	240.0
Pipe roof	23	210.0	-	-	0.15	240.0

TABLE 3 Response of experimental design and stability factor of safety in the initial region U_1.

Serial No.	Normative variables			Actual Variables			Response
	ζ_1	ζ_2	ζ_3	l (m)	p (kPa)	q (kN/m)	F_s
1	1	1	−1	20	30	0	2.18
2	1	1	1	20	30	60	1.54
3	−1	−1	1	0	0	60	0.75
4	1	−1	−1	20	0	0	2.12
5	−1	1	1	0	30	60	0.81
6	1	−1	1	20	0	60	1.67
7	−1	1	−1	0	30	0	1.02
8	−1	−1	−1	0	0	0	0.89
9	0	0	0	10	15	30	1.36

there is a non-linear relationship between the stability reserve factor and these factors. In most cases, a second-order model is appropriate, as shown below.

$$\hat{F}_s = \omega_0 + \sum_{i-1}^{n} \omega_i x_i + \sum_{i-1}^{n} \omega_{ii} x_i^2 + \sum_{i<j} \omega_{ij} x_i x_j + \delta \tag{22}$$

Additional experimental points are usually required in this region U_2 to achieve a better approximation. The estimation and optimization of the second-order response model also depend on a reliable experimental design scheme. Although there are other design methods, this paper uses the central composite design (CCD) as an example. Since the central composite design is robust to the assumption of strict linear effects, it also makes the RSM robust. The central composite design is a full or partial factorial design (usually with factors greater than five) with the addition of axis points n_a and center points n_c. The factor points are situated in the cube's vertices, the centroids are located at the cube's center, if the experimental design is represented as a 'cube', and the axis points are located on the cube's axes in Figure 5.

The construction factors are coded and converted using Eq. 21. For CCD, each construction factor is now at three levels (i.e., high, medium, and low levels) of −1, 0, and 1. The distance of the axis point from the center point is assumed to be coded as λ. According to the center combination design, to satisfy the rotatability condition, the number of center points n_c needs to be appropriately selected to ensure that it is the predicted value with consistent uniform progress throughout the test area. Table 1 lists the number of experimental points of CCD with no more than five factors.

The number of experimental points in the CCD is more obviously influenced by some factors (as shown in Table 1). The distance λ of the axis point from the center point needs to be determined according to the rotatability, which can generally be calculated using the following equation.

$$\lambda = 2^{\frac{N_f}{4}} \tag{23}$$

N_f is the number of factors in the CCD.

4 Example application of the construction stability of a large-section tunnel

4.1 Project example overview

A new tunnel somewhere on the Lanzhou Metro Line No. 3 multiplex is used as the study object. The tunnel is 970 m long and will cross the existing high-speed railway line at DK297 + 350 DK298 + 320. The tunnel axis is approximately 90° orthogonal to the high-speed railway line axis, and the minimum distance between the tunnel vault and the high-speed railway line is only 12 m. The new tunnel is mainly in the loess stratum. The tunnel in this scope is constructed by the shield method with a whole cross-section, and the excavation area is about 180 m^2, which is typical of a large cross-section shield tunnel.

The tunnel construction adopts the joint overrun support of a dense row of large pipe roofs and reinforcement bolts to ensure the stability of the tunnel construction and the minimum impact on the high-speed railway line. The row of large pipe roofs is constructed within a 150° angle and a 25 mm diameter reinforcement cage is inserted and filled with cement mortar to increase the stiffness (10 m

in length, 180 mm in diameter, 10 mm in wall thickness, and 22 mm in diameter, 8 m in length and 1.2 m in spacing, in the plum-shaped arrangement).

The construction factors affecting tunnel stability in this paper mainly include the length of the pipe roof, the support pressure on the face, and the additional load on the ground. These construction schemes involve more complex conditions and are not convenient to use directly, a simplified approach is adopted in this paper to deal with them. For example, the length of the pipe roof is expressed as distance l from the face, the support pressure on the face is described as p, and the additional load on the ground is denoted as q, as shown in Figure 6.

TABLE 4 Experimental design and response of CCD within region U_2.

Serial No.	Actual Variables			Response
	l (m)	p (kPa)	q (kN/m)	F_s
1	26.0	15.35	27.15	1.65
2	22.0	15.41	28.12	1.82
3	22.0	15.41	23.33	1.8
4	22.0	15.50	25.73	1.98
5	18.0	15.35	27.15	1.75
6	22.0	15.41	25.73	2.24
7	28.7	15.41	25.73	1.75
8	26.0	15.46	24.30	1.71
9	18.0	15.46	24.30	1.69
10	22.0	15.41	25.73	2.25
11	22.0	15.41	25.73	2.23
12	22.0	15.41	25.73	2.19
13	18.0	15.35	24.30	1.77
14	26.0	15.35	24.30	1.7
15	15.3	15.41	25.73	1.65
16	26.0	15.46	27.15	1.68
17	22.0	15.41	25.73	2.2
18	18.0	15.46	27.15	1.68
19	22.0	15.41	25.73	2.21
20	22.0	15.31	25.73	1.89

4.2 Numerical experimental design and analysis

The surrounding rock is a homogeneous clay layer and follows the ideal elastic-plastic constituted relationship. The numerical model is long enough in the axial direction, and the face is not less than five times the diameter of the hole from the left to the right boundaries to weaken the influence of the distal boundary on the analysis. The bottom of the tunnel arch is much larger than three times the tunnel's diameter from the bottom edge. The other geometric dimensions of the numerical model (the diameter $C = 20$ m and the buried depth $D = 14$ m) and the initial clay physical and mechanical parameters are shown in Figure 6; Table 2.

The ideal tunnel model and the initial construction parameters are kept unchanged. The influence of the three construction factors (the length of the pipe roof l, the face support pressure, and the additional load on the ground as shown in Figure 6) on the stability of the face is analyzed. The region U_1, $U_1 = \{(l, p, q) | l \in (0, 20), p \in (30, 100), q \in (0, 60)\}$ is taken into account, where the unit of l is m, the unit of p is kPa, and the unit of q is kN/m.

The response surface method is used for numerical experimental design and function fitting. The finite element strength reduction method solves the tunnel stability reserve factor F_s. The finite element failure criteria are based on the unified use of the plastic zone penetration as the tunnel instability characteristics to avoid errors in the results. The different center point data acquisition is mainly achieved through variable grid size.

The full factorial experiments fitting the first-order response model were first arranged, and the obtained tunnel stability reserve factors are listed in Table 3. Note also that the tunnel stability reserve factor is calculated by the strength reduction method.

The resulting fit yields a first-order response model as:

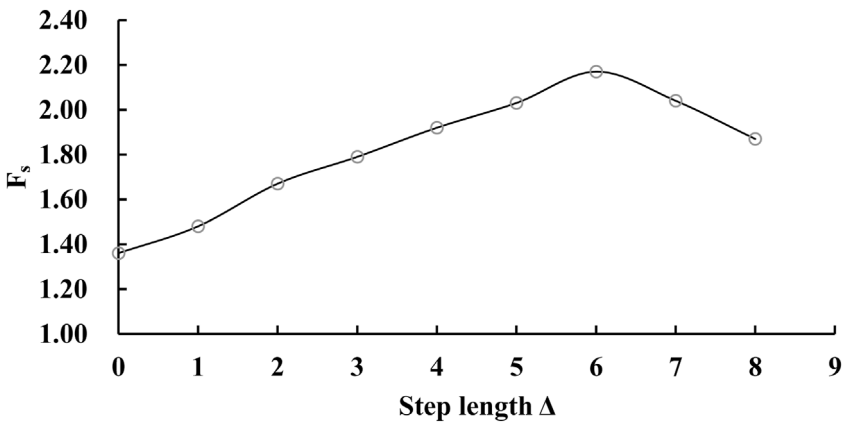

FIGURE 7
The variation pattern of the tunnel stability reserve factor with step length along the steepest ascent path.

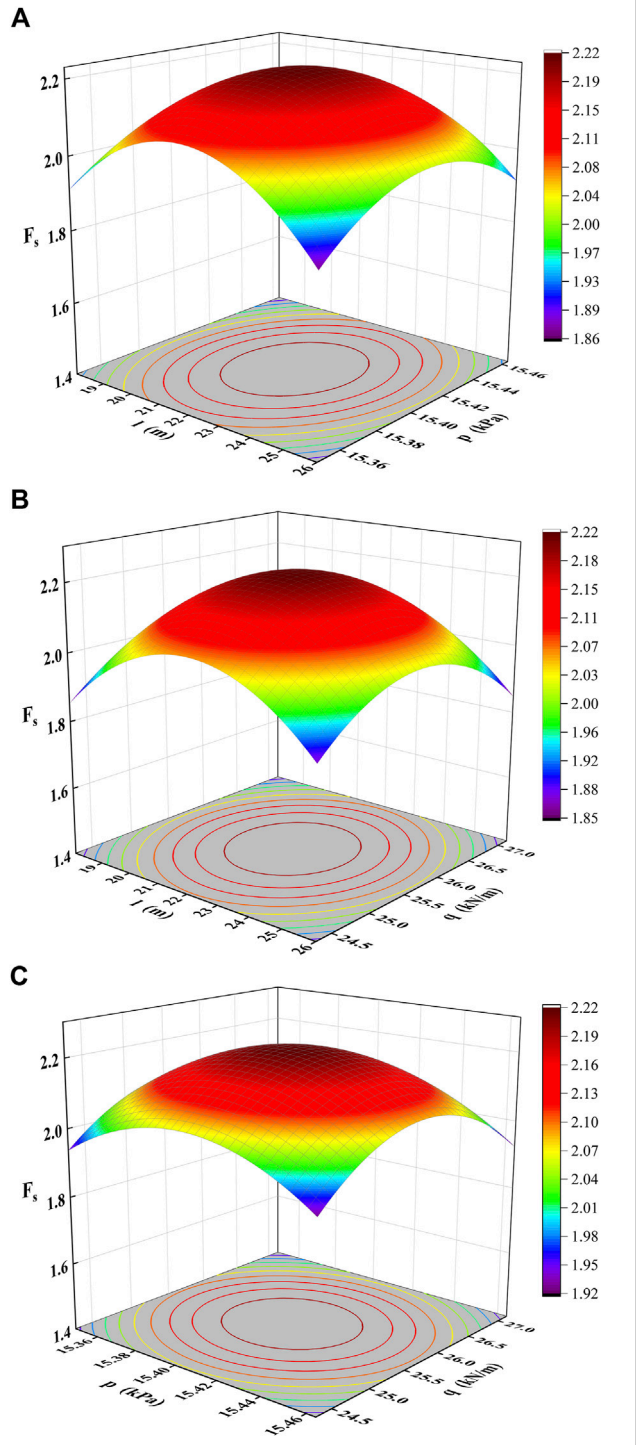

FIGURE 8
Response surface of the tunnel stability reserve factor in the region U_2. **(A)** Response surface corresponding to support length l and support pressure p. **(B)** Response surface corresponding to support length l and ground surcharge load q. **(C)** Response surface corresponding to support pressure p and ground surcharge load q.

$$F_s = 1.031 + 0.0505l + 0.001p - 0.006q \tag{24}$$

The fitted first-order response model, represented by the canonical variables, is

$$F_s = 1.37 + 0.505\zeta_1 + 0.015\zeta_2 - 0.18\zeta_3 \tag{25}$$

Analysis of variance (ANOVA, $R^2 = 96.3\%$) shows that the first-order response model fits significantly in region U_1. The ratio of the main effects of the pipe roof overrun support length, and support pressure on the face. The additional ground load will be further analyzed in the "curved" region U_2 using the steepest ascent method as follows:

$$b_l: b_p: b_q = 1: 0.029: (-0.356) \tag{26}$$

The steepest ascent method is conducted by a path of integer multiples of the step length Δ with the center point as the initial point, i.e., $\bar{l} = 10.0$m, $\bar{p} = 15.0$kPa, $\bar{q} = 30$ kN/m.

Figure 7 shows the stability factor of safety for the face at each step along the steepest ascent path. The rate of increase in response is observed to be faster up to step 4. The rate of growth in the stability factor of safety remains essentially the same for each subsequent step. There is a significant "curved" after step 4, which requires a central composite design in the corresponding region U_2. The region U_2 for further fitting of the second-order response is

$$U_2 = \{(l, p, q) | l \in (18, 26), p \in (15.348, 15.464), q \in (24.30, 27.15)\} \tag{27}$$

Second-order response model for the tunnel stability reserve factor in region U_2.

$$\begin{aligned} F_s = &-9.343 \times 10^3 - 1.079l + 1.209 \times 10^3 p + 3.419q + 1.08\times 10^{-1} l \cdot p \\ &- 1.1 \times 10^{-3} l \cdot q + 4.785 \times 10^{-2} p \cdot q - 1.263 \times 10^{-2} l^2 \\ &- 3.936 \times 10 p^2 - 8.039 \times 10^{-2} q^2 \end{aligned} \tag{28}$$

The results of model fit *via* the analysis of variance (ANOVA, $R^2 = 96.0\%$) show that the second-order model (Eq. 28) is a suitable approximation to the entire surface and a more accurate fit of the function $F_s = F(l, p, q)$ for the stability of the palm surface in the region U_2.

Table 4 presents the results of the tunnel stability reserve factor of experimental points by CCD, and is used for second-order response fitting. The best-fitting expression can be obtained by effective tracing analysis of construction factors on these response surfaces (shown in Figure 8). The best-fitted model can be obtained in this numerical test, i.e., Eq. 28, which also reflects the strength of the interaction effect from the shape of contour lines in Figure 8. The interaction between the support pressure of the face and the additional load on the ground is more significant, which is consistent with the characteristics of their regression coefficients in Eq. 28. The contour line in Figure 8C is closer to the elliptical type, so the interaction between the support pressure of the face and the additional surface load is more significant. The response surfaces from Figure 8A ~ (c) are a reasonable verification of the consistency and validity of Eq. 28 to the numerical tests. The corresponding construction plan can be determined more quantitatively according to this method in the early design and construction evaluation periods, thus ensuring the tunnel's stability and safety.

5 Conclusion

In this paper, experimental schemes are designed based on the response surface method through numerical model tests of the large-

section clay tunnel and revealing the quantitative relationship equations between tunnel stability index and construction factors. The main conclusions based on the theoretical analysis, experimental design, and example applications are listed below.

(1) The physico-mechanical properties of the surrounding rock are regarded as internal factors and construction factors as external factors. Considering the deterioration of the physical and mechanical properties of clay, the tunnel stability reserve can be simply evaluated. The relationship between the tunnel stability index and the construction factors is constructed as a function *via* Taylor's formula.
(2) An experimental design of multivariate response between the tunnel stability reserve factor and some construction factors is processed by the response surface method. It explicitly gives the analysis methods and procedures for the first-order and second-order response surfaces of tunnel stability. The implicit function expressions are fitted to reveal the multivariate second-order response relationship between them.
(3) This numerical experimental design method can be well applied to study the construction stability of large-section clay tunnels. It may provide a research method with better theoretical and practical values to engineering practice. The research could provide a basis for guiding the construction scheme and provide some technical support for the development of intelligent and automatic tunnel construction.

Data availability statement

The original contributions presented in the study are included in the article/supplementary material, further inquiries can be directed to the corresponding authors.

Author contributions

JH was in charge of conceptualization, funding acquisition, writing of the original draft, and editing. NL was in charge of data resources and analysis. ZM was in charge of the development of the mathematical model of the research and overall supervision of the whole research investigation. LL was in charge of the experimental design. KD was in charge of the post-processing data.

Funding

This work was supported by the Science and technology innovation fund project of Hanjiang-to-Weihe river valley water diversion project construction Co., LTD (No. 2020302), Open Research Fund Program of State Key Laboratory of Eco-hydraulics in Northwest Arid Region (No. 2018KFKT-16), Open Research Fund Program of Shaanxi Key Laboratory of Geotechnical and Underground Space Engineering (No. YT202009), the Shaanxi Natural Science Foundation (No. 2022JM-190). The authors declare that this study received funding from Hanjiang-to-Weihe river valley water diversion project construction Co. LTD. The funder had the following involvement in the study: the funder participated in the data processing.

Acknowledgments

The authors would like to thank Shaanxi Key Laboratory of Petroleum Accumulation Geology for providing high-performance computing devices. Xingwang NL provided invaluable assistance in the conduct of the deformation surveys.

Conflict of interest

LL was employed by Gansu Institute of Architectural Design and Research Corporation Limited: KD was employed by Hanjiang-to-Weihe River Valley Water Diversion Project Construction Corporation Limited.

The remaining authors declare that the research was conducted in the absence of any commercial or financial relationships that could be construed as a potential conflict of interest.

Publisher's note

All claims expressed in this article are solely those of the authors and do not necessarily represent those of their affiliated organizations, or those of the publisher, the editors and the reviewers. Any product that may be evaluated in this article, or claim that may be made by its manufacturer, is not guaranteed or endorsed by the publisher.

References

Abra, O., and Mahdi, B. F. (2022). Strength reduction design method for reinforced concrete structures: Generalization. *Eng. Struct.* 258, 114134. doi:10.1016/j.engstruct.2022.114134

Alavi Gharahbagh, E., Rostami, J., and Talebi, K. (2014). Experimental study of the effect of conditioning on abrasive wear and torque requirement of full face tunneling machines. *Tunn. Undergr. Space Technol.* 41, 127–136. doi:10.1016/j.tust.2013.12.003

Antão, A. N., Vicente da Silva, M., Monteiro, N., and Deusdado, N. (2021). Upper and lower bounds for three-dimensional undrained stability of shallow tunnels. *Transp. Geotech.* 27, 100491. doi:10.1016/j.trgeo.2020.100491

Ayawah, P. E. A., Sylvanus, S. N., Azure, J. W. A., Kaba, A. G. A., Anani, A., Bansah, S., et al. (2022). A review and case study of Artificial intelligence and Machine learning methods used for ground condition prediction ahead of tunnel boring Machines. *Tunn. Undergr. Space Technol.* 125, 104497. doi:10.1016/j.tust.2022.104497

Baghbani, A., Choudhury, T., Costa, S., and Reiner, J. (2022). Application of artificial intelligence in geotechnical engineering: A state-of-the-art review. *Earth-Science Rev.* 228, 103991. doi:10.1016/j.earscirev.2022.103991

Bai, B., Nie, Q., Zhang, Y., Wang, X., and Hu, W. (2021a). Cotransport of heavy metals and SiO2 particles at different temperatures by seepage. *J. Hydrology* 597, 125771. doi:10.1016/j.jhydrol.2020.125771

Bai, B., Yang, G., Li, T., and Yang, G. (2019). A thermodynamic constitutive model with temperature effect based on particle rearrangement for geomaterials. *Mech. Mater.* 139, 103180. doi:10.1016/j.mechmat.2019.103180

Bai, B., Zhou, R., Cai, G., Hu, W., and Yang, G. (2021b). Coupled thermo-hydro-mechanical mechanism in view of the soil particle rearrangement of granular thermodynamics. *Comput. Geotechnics* 137, 104272. doi:10.1016/j.compgeo.2021.104272

Dias, D. (2011). Convergence-confinement approach for designing tunnel face reinforcement by horizontal bolting. *Tunn. Undergr. Space Technol.* 26 (4), 517–523. doi:10.1016/j.tust.2011.03.004

Higgins, S., and Stathopoulos, T. (2021). Application of artificial intelligence to urban wind energy. *Build. Environ.* 197, 107848. doi:10.1016/j.buildenv.2021.107848

Höfle, R., Fillibeck, J., and Vogt, N. (2008). Time dependent deformations during tunnelling and stability of tunnel faces in fine-grained soils under groundwater. *Acta Geotech.* 3 (4), 309–316. doi:10.1007/s11440-008-0075-y

Hou, C., Pan, Q., Xu, T., Huang, F., and Yang, X. (2022). Three-dimensional tunnel face stability considering slurry pressure transfer mechanisms. *Tunn. Undergr. Space Technol.* 125, 104524. doi:10.1016/j.tust.2022.104524

Huang, J., Liu, X., Ma, Z., Lv, G., and Dang, K. (2023). The stability evaluation of clay tunnels via the non-linear deterioration of physical and mechanical properties of surrounding rocks. *Front. Earth Sci.* 10. doi:10.3389/feart.2022.1112410

Huang, M., Wang, H., Yu, J., and Tang, Z. (2019). Undrained stability analysis of a plane strain circular tunnel using streamline velocity fields. *Int. J. Geomechanics* 19 (5), 06019006. doi:10.1061/(ASCE)GM.1943-5622.0001395

Juneja, A., Hegde, A., Lee, F. H., and Yeo, C. H. (2010). Centrifuge modelling of tunnel face reinforcement using forepoling. *Tunn. Undergr. Space Technol.* 25 (4), 377–381. doi:10.1016/j.tust.2010.01.013

Kumar, B., and Sahoo, J. P. (2021). Stability of unsupported circular tunnels in anisotropic normally and over consolidated saturated clay. *Comput. Geotechnics* 135, 104148. doi:10.1016/j.compgeo.2021.104148

Lee, C. J., Wu, B. R., Chen, H. T., and Chiang, K. H. (2006). Tunnel stability and arching effects during tunneling in soft clayey soil. *Tunn. Undergr. Space Technol.* 21 (2), 119–132. doi:10.1016/j.tust.2005.06.003

Li, L. P., Shang, C. S., Chu, K. W., Zhou, Z. Q., Song, S. G., Liu, Z. H., et al. (2021). Large-scale geo-mechanical model tests for stability assessment of super-large cross-section tunnel. *Tunn. Undergr. Space Technol.* 109, 103756. doi:10.1016/j.tust.2020.103756

Liu, N. F., Li, N., Li, G. F., Song, Z. P., and Wang, S. J. (2022a). Method for evaluating the equivalent thermal conductivity of a freezing rock mass containing systematic fractures. *Rock Mech. Rock Eng.* 55 (12), 7333–7355. doi:10.1007/s00603-022-03038-9

Liu, N. F., Li, N., Wang, S. J., Li, G. F., and Song, Z. P. (2022b). A fully coupled thermo-hydro-mechanical model for fractured rock masses in cold regions. *Cold Regions Sci. Technol.* 205, 103707. doi:10.1016/j.coldregions.2022.103707

Liu, N. F., Li, N., Xu, C. B., Li, G. F., Song, Z. P., and Yang, M. (2020). Mechanism of secondary lining cracking and its simulation for the dugongling tunnel. *Rock Mech. Rock Eng.* 53 (9), 4539–4558. doi:10.1007/s00603-020-02183-3

Lü, X., Zeng, S., Zhao, Y., Huang, M., Ma, S., and Zhang, Z. (2020). Physical model tests and discrete element simulation of shield tunnel face stability in anisotropic granular media. *Acta Geotech.* 15 (10), 3017–3026. doi:10.1007/s11440-020-01041-4

Lü, X., Zhou, Y., Huang, M., and Zeng, S. (2018). Experimental study of the face stability of shield tunnel in sands under seepage condition. *Tunn. Undergr. Space Technol.* 74, 195–205. doi:10.1016/j.tust.2018.01.015

Mahmoodzadeh, A., Mohammadi, M., Daraei, A., Faraj, R. H., Mohammed Dler Omer, R., and Sherwani, H. A. F. (2020). Decision-making in tunneling using artificial intelligence tools. *Tunn. Undergr. Space Technol.* 103, 103514. doi:10.1016/j.tust.2020.103514

Man, J., Huang, H., Ai, Z., and Chen, J. (2022). Analytical model for tunnel face stability in longitudinally inclined layered rock masses with weak interlayer. *Comput. Geotechnics* 143, 104608. doi:10.1016/j.compgeo.2021.104608

Meng, Q. X., Wang, H. L., Xu, W. Y., Cai, M., Xu, J., and Zhang, Q. (2019). Multiscale strength reduction method for heterogeneous slope using hierarchical FEM/DEM modeling. *Comput. Geotechnics* 115, 103164. doi:10.1016/j.compgeo.2019.103164

Nie, Z., Zhang, Z., and Zheng, H. (2019). Slope stability analysis using convergent strength reduction method. *Eng. Analysis Bound. Elem.* 108, 402–410. doi:10.1016/j.enganabound.2019.09.003

Pan, Q., and Dias, D. (2017). Safety factor assessment of a tunnel face reinforced by horizontal dowels. *Eng. Struct.* 142, 56–66. doi:10.1016/j.engstruct.2017.03.056

Park, J., Lee, K.-H., Kim, B.-K., Choi, H., and Lee, I.-M. (2017). Predicting anomalous zone ahead of tunnel face utilizing electrical resistivity: II. Field tests. *Tunn. Undergr. Space Technol.* 68, 1–10. doi:10.1016/j.tust.2017.05.017

Rahaman, O., and Kumar, J. (2020). Stability analysis of twin horse-shoe shaped tunnels in rock mass. *Tunn. Undergr. Space Technol.* 98, 103354. doi:10.1016/j.tust.2020.103354

Roateşi, S. (2014). Analytical and numerical approach for tunnel face advance in a viscoplastic rock mass. *Int. J. Rock Mech. Min. Sci.* 70, 123–132. doi:10.1016/j.ijrmms.2014.04.007

Rojat, F., Labiouse, V., and Mestat, P. (2015). Improved analytical solutions for the response of underground excavations in rock masses satisfying the generalized Hoek–Brown failure criterion. *Int. J. Rock Mech. Min. Sci.* 79, 193–204. doi:10.1016/j.ijrmms.2015.08.002

Shiau, J., and Al-Asadi, F. (2022). Stability factors F_c, F_s, and F_γ for twin tunnels in three dimensions. *Int. J. Geomechanics* 22 (3), 04021290. doi:10.1061/(ASCE)GM.1943-5622.0002264

Song, D., Liu, X., Chen, Z., Chen, J., and Cai, J. (2021). Influence of tunnel excavation on the stability of a bedded rock slope: A case study on the mountainous area in southern anhui, China. *KSCE J. Civ. Eng.* 25 (1), 114–123. doi:10.1007/s12205-020-0831-6

Song, G., and Marshall, A. M. (2020). Centrifuge modelling of tunnelling induced ground displacements: Pressure and displacement control tunnels. *Tunn. Undergr. Space Technol.* 103, 103461. doi:10.1016/j.tust.2020.103461

Soranzo, E., Guardiani, C., and Wu, W. (2022). The application of reinforcement learning to NATM tunnel design. *Undergr. Space* 7 (6), 990–1002. doi:10.1016/j.undsp.2022.01.005

Tyagi, A., Liu, Y., Pan, Y.-T., Ridhwan, K. B. M., and Lee, F.-H. (2018). Stability of tunnels in cement-admixed soft soils with spatial variability. *J. Geotechnical Geoenvironmental Eng.* 144 (12), 06018012. doi:10.1061/(ASCE)GT.1943-5606.0001988

Ukritchon, B., Yingchaloenkitkhajorn, K., and Keawsawasvong, S. (2017). Three-dimensional undrained tunnel face stability in clay with a linearly increasing shear strength with depth. *Comput. Geotechnics* 88, 146–151. doi:10.1016/j.compgeo.2017.03.013

Weng, X., Sun, Y., Yan, B., Niu, H., Lin, R., and Zhou, S. (2020). Centrifuge testing and numerical modeling of tunnel face stability considering longitudinal slope angle and steady state seepage in soft clay. *Tunn. Undergr. Space Technol.* 101, 103406. doi:10.1016/j.tust.2020.103406

Wilson, D. W., Abbo, A. J., Sloan, S. W., and Lyamin, A. V. (2011). Undrained stability of a circular tunnel where the shear strength increases linearly with depth. *Can. Geotechnical J.* 48 (9), 1328–1342. doi:10.1139/t11-041

Xue, Y., Liu, J., Ranjith, P. G., Gao, F., Xie, H., and Wang, J. (2022). Changes in microstructure and mechanical properties of low-permeability coal induced by pulsating nitrogen fatigue fracturing tests. *Rock Mech. Rock Eng.* 55, 7469–7488. doi:10.1007/s00603-022-03031-2

Xue, Y., Ranjith, P. G., Chen, Y., Cai, C., Gao, F., and Liu, X. (2023a). Nonlinear mechanical characteristics and damage constitutive model of coal under CO2 adsorption during geological sequestration. *Fuel* 331, 125690. doi:10.1016/j.fuel.2022.125690

Xue, Y., Ranjith, P. G., Gao, F., Zhang, Z., and Wang, S. (2023b). Experimental investigations on effects of gas pressure on mechanical behaviors and failure characteristic of coals. *J. Rock Mech. Geotechnical Eng.* doi:10.1016/j.jrmge.2022.05.013

Yertutanol, K., Akgün, H., and Sopacı, E. (2020). Displacement monitoring, displacement verification and stability assessment of the critical sections of the Konak tunnel, İzmir, TTurkey *Tunn. Undergr. Space Technol.* 101, 103357. doi:10.1016/j.tust.2020.103357

Zare Naghadehi, M., Thewes, M., and Alimardani Lavasan, A. (2019). Face stability analysis of mechanized shield tunneling: An objective systems approach to the problem. *Eng. Geol.* 262, 105307. doi:10.1016/j.enggeo.2019.105307

Zhang, Y., Fan, S., Yang, D., and Zhou, F. (2022a). Investigation about variation law of frost heave force of seasonal cold region tunnels: A case study. *Front. Earth Sci.* 9, 806843. doi:10.3389/feart.2021.806843

Zhang, Y., Song, Z., and Weng, X. (2022b). A constitutive model for loess considering the characteristics of structurality and anisotropy. *Soil Mech. Found. Eng.* 59 (1), 32–43. doi:10.1007/s11204-022-09781-z

Zhang, Z. X., Hu, X. Y., and Scott, K. D. (2011). A discrete numerical approach for modeling face stability in slurry shield tunnelling in soft soils. *Comput. Geotechnics* 38 (1), 94–104. doi:10.1016/j.compgeo.2010.10.011

Zhong, J., and Yang, X. (2020). Kinematic analysis of the three-dimensional stability for tunnel faces by pseudodynamic approach. *Comput. Geotechnics* 128, 103802. doi:10.1016/j.compgeo.2020.103802

frontiers | Frontiers in Materials

TYPE Original Research
PUBLISHED 16 February 2023
DOI 10.3389/fmats.2023.1137324

Check for updates

OPEN ACCESS

EDITED BY
Bing Bai,
Beijing Jiaotong University, China

REVIEWED BY
Qingke Nie,
Hebei Research Institute of Construction and Geotechnical Investigation Co. Ltd., China
Yang Gaosheng,
Shanxi Agricultural University, China

*CORRESPONDENCE
Jian Chen,
672445389@qq.com

SPECIALTY SECTION
This article was submitted to Structural Materials, a section of the journal Frontiers in Materials

RECEIVED 04 January 2023
ACCEPTED 06 February 2023
PUBLISHED 16 February 2023

CITATION
Yuan J, Gan Y, Chen J, Tan S and Zhao J (2023), Experimental research on consolidation creep characteristics and microstructure evolution of soft soil. *Front. Mater.* 10:1137324. doi: 10.3389/fmats.2023.1137324

COPYRIGHT
© 2023 Yuan, Gan, Chen, Tan and Zhao. This is an open-access article distributed under the terms of the Creative Commons Attribution License (CC BY). The use, distribution or reproduction in other forums is permitted, provided the original author(s) and the copyright owner(s) are credited and that the original publication in this journal is cited, in accordance with accepted academic practice. No use, distribution or reproduction is permitted which does not comply with these terms.

Experimental research on consolidation creep characteristics and microstructure evolution of soft soil

Jie Yuan, Yuexin Gan, Jian Chen*, Songming Tan and Jitong Zhao

The School of Civil Engineering, Guangzhou University, Guangzhou, China

The influence of creep deformation of soft soil on engineering construction can't be ignored. In order to deeply understand the macroscopic mechanical properties and the evolution mechanism of soft soil in microscope during consolidation creep, one-dimensional consolidation creep tests and SEM tests of Nansha soft soil were carried out in this paper. Then the image processing was performed by Image J software to obtain the consolidation creep characteristics, microscopic parameters of particles and pores under different loading pressures. The results of experiment and image processing show that 1) The creep process of Nansha soft soil is divided into the initial instantaneous deformation phase, the attenuation creep phase and the stable creep phase. The creep deformation increases with the consolidation creep stress during the three phases. 2) During the creep process, the distance between particles decreases and some particles are gradually broken, the quantity of particles and pores increases but the volume of them decreases. At the same time, the shape of particles and pores changes from nearly round and strip to nearly oval. 3) The consolidation creep stress determines the particles distance and the degree of fragmentation. And this trend is more obvious with the increase of the consolidation creep stress.

KEYWORDS

soft soil, soil creep, consolidation creep test, microstructure, SEM

1 Introduction

Soft soil shows a significant creep characteristic. Soft soil creep may cause land subsidence (Mesri and Choi, 1985; Yin et al., 2017) and slope instability (Tan et al., 2022). Creep tests are necessary means to understand the creep properties of soil qualitatively, establish the creep constitutive model and determine the model parameters. Creep tests mainly includes macroscopic and microscopic aspects.

In recent years, macroscopic creep tests of soft soil, such as one-dimensional (1D) consolidation, direct shear and triaxial shear test, have made progress in creep behavior and creep constitutive model. Some scholars have studied the creep behavior of soft clay under different stresses and strains by using triaxial creep tests (Wang and Wong, 2016; Huang et al., 2019; Nishimura, 2020), and established elastic-viscoplastic constitutive models (Zhu and Yu, 2015; Yan et al., 2019). Tran et al. (2018) researched the behavior of soil strength reduction using triaxial creep tests and predicted the time of creep failure. Furthermore, the influence of soft soil structure on creep behavior through consolidation creep tests was explored by scholars, then many corresponding constitutive models were proposed. For example, Mataic et al. (2016) investigated the creep characteristics of soft clay during

consolidation, considering the influence of clay structure and sample quality. Zhu et al. (2016) focuses on the quantitative description of the evolution of creep coefficient with both soil density and soil structure under compression. Yin et al. (2017); Yin and Karstunen, (2011) established implicit and explicit creep models based on stress and creep structures respectively under 1D condition. Li et al. (2018) studied the non-linear creep characteristics of soft soil by consolidation creep experiments on Tianjin Marine soft soil, and established a three-dimensional non-linear viscoelastic creep constitutive model reflecting the effect of time. Zou et al. (2019) proposed an elastic-viscoplastic constitutive model based on the isometric concept and Nishihara model to simulate the 1D compression behavior of Ningbo Marine soft clay. Bai et al. (2019) developed a thermo-hydro-mechanical constitutive model for consolidated soil based on the tenet of particle irreversible rearrangement. In addition, interparticle interactions were studied (Bai et al., 2021). In general, the creep properties of soft soil are studied on the macroscopic level based on mechanical tests, then the creep phenomena are integrated under various conditions and the creep equations are established through mathematical and mechanical analysis. However, some analyses of macroscopic phenomena show some deficiencies in understanding the mechanism of soil creep. Consequently, researchers tried to deduced the overall creep mechanism through the change and the characters of the soil structure in microscope.

At the microscopic level, there are some popular methods being used to explore the microstructure of the soil, such as optical microscopy, scanning electron microscope (SEM), environmental scanning electron microscopy (ESEM) (Sun et al., 2019), Mercury intrusion porosimetry (MIP), and computed tomography (CT) scanning (Kaczmarek et al., 2017). Based on these microscopic test means, the main microstructure forms and creep mechanism of soil can be described qualitatively. For example, Osipov and Sokolov (1978) introduced the results of microstructure changes, shear stress, thixotropic phenomena, and swelling of clays during compaction under different stress states through electron microscopy analysis. Gylland et al. (2013) used laboratory and small-scale field experiments to analyze the shear band structure and evolution process of thin sections of clay from initiation to maturation under light microscope and SEM. Zhao et al. (2020, 2022) studied the influence of stress on the microstructure evolution of kaolin based on the analysis of triaxial creep results and SEM. Lei et al. (2016, 2020) researched the microstructure changes of natural soft clays under accelerated creep conditions through dynamic and static triaxial tests, SEM and MIP. At the same time, the development of algorithm makes great progress in digital image processing technology, and makes the quantitative analysis of soil structure develop greatly. Through image processing software, some microscopic parameters with definite physical meaning can be used to quantitatively analyze the evolution mechanism of soil microstructure (Liu and Zhang, 2011; Xie et al., 2018; Nian et al., 2020; Dai et al., 2021; Li et al., 2022). However, these studies were explored only at the microscopic scale, and the macroscopic and microscopic experimental phenomena were not well connected.

In this paper, in order to deeply investigate the creep deformation mechanism of soft soil, the creep characteristics of soft soil at the macroscopic and microscopic levels were comprehensively researched. Firstly, consolidation creep tests of Nansha soft soil were carried out to analyze the creep characteristics of soft soil under different axial stresses at the macro level. Then, the undisturbed samples and the consolidated samples were all tested by SEM to obtain the images of microstructure during the soft soil creep. And then the parameters of microstructure such as, pore size, particle size, were obtained by Image J processing on the microstructure images. Based on the results of macroscopic and microscopic creep test, the creep deformation mechanism of Nansha soft soil was analyzed qualitatively and quantitatively.

TABLE 1 Basic physical and mechanical properties.

Properties	Value	Properties	Value
Cu	6	ω_P (%)	35.19
Cc	1.55	I_L	0.70
G_s	2.71	I_P	28.64
ω_0 (%)	53.84	$\bar{e}$	1.526
ρ_0 (g/cm^3)	1.77	P_c	1.53
ρ_d (g/cm^3)	1.43	c (kPa)	12.36
ω_L (%)	63.83	φ (°)	1.52

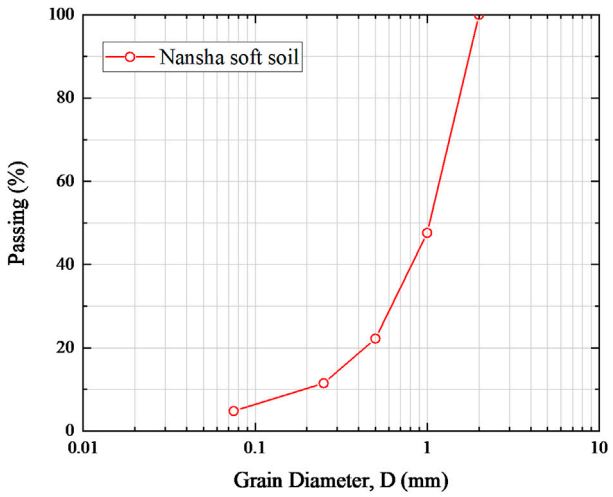

FIGURE 1
Particle size distribution of the sample.

2 Experimental method and scheme

2.1 Materials

Nansha soft soil is mainly composed of quaternary marine sediments such as silt and silty clay, which shows a significant creep characteristic. Therefore, Nansha soft soil was chosen to prepare samples in this experiment. The particle size distribution, basic physical and mechanical indexes of the soil were tested according to ASTM-D2487-11. The results are shown in Table 1 and Figure 1.

TABLE 2 One dimensional consolidation creep test scheme.

Test number	Axial stress (kPa)	Test number	Axial stress (kPa)
OCC1	25	OCC4	200
OCC2	50	OCC5	300
OCC3	100	OCC6	400

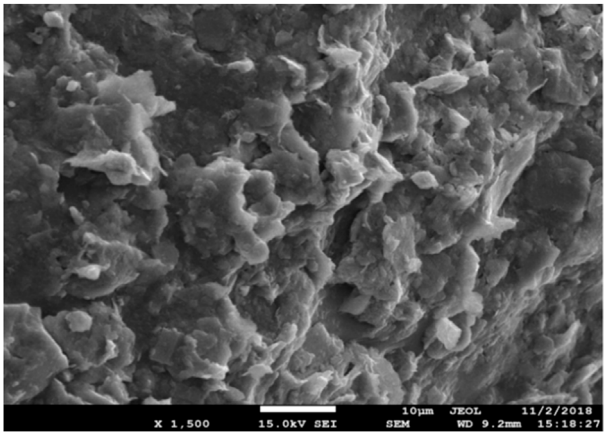

FIGURE 2
SEM image.

2.2 Method and scheme

For the classical consolidation instrument, the height of the samples is 2 cm. Since the deformation is small after the soft soil enters the creep phase, which cannot be clearly shown in the stress-strain curve. Therefore, the conventional direct shear instrument was modified in this experiment to observe the deformation more obviously. Firstly, the shear box was replaced by the consolidation box, and the pressure system was replaced by the vertical loading system of the direct shear instrument. Then, the dial indicator was assembled to measure the vertical deformation. Finally, the height of the samples was increased from 2cm to 8 cm. The samples were immediately sealed by field sampling with the special ring knife. The height of ring knife is 8 cm and the diameter is 6.18 cm. The samples were loaded separately to completely depict the creep curve of each loading grade. The loading scheme is shown in Table 2. The sample box was wrapped with film to avoid water evaporation, and the temperature and humidity were kept constant during the creep test (temperature: 25°C, humidity: 88% ± 1%). When the deformation was less than 0.005 mm within 24 h, the soil was in the stable creep phase.

In order to analyze the microstructure changes of soft soil, the SEM test was performed on the undisturbed samples and the consolidated samples. Firstly, the middle part of the sample was cut into long strip by thin steel wire. The length of strip is 2.0 cm, the width is 1.5 cm, and the height is 2.0 cm. The samples were dried by freeze-drying method to ensure the soil structure is not disturbed as much as possible. The samples were immersed in the special container containing liquid nitrogen at −193°C for 3 min by using isopentane as the transition refrigerant. After frozen, the samples were put into the pre-cooled vacuum freeze-dryer at −50°C for 24 h. Then, the samples were carefully broken apart to obtain undisturbed structural planes as the SEM shooting faces. In order to avoid the discharge phenomenon caused by the electron beam bombardment, the samples were plated a golden film by the vacuum sputtering coating machine. At last, the areas with relatively uniform soil particles and pores were scanned so that the scanned areas are representative, as shown in Figure 2.

In image processing, the soil particles and pores were divided into two substances, and the criterion for the division was the different gray value ranges of the two substances. The grayscale range of SEM images was 0–255. There was a grayscale threshold between two substances, where grayscale greater than this threshold was marked as 255 and appears as white. And grayscale less than this threshold was marked as 0 and appears as black, as shown in Figure 3A. The threshold values were different for different SEM images, and the respective threshold value was adjusted for each image by referring to the corresponding literature and experience. By threshold segmentation, the pore edges can be outlined, as shown in Figure 3B. Finally, the irregularly shaped pores were transformed into ellipses by elliptical segmentation, as shown in Figure 3C.

Considering the complexity of soil structure, in this paper some parameters were defined to quantify the structure of particles and pores as showed in Table 3.

3 Experimental results and discussion

3.1 Experimental results

3.1.1 One dimensional compression creep tests

The results of the creep test are shown in Figure 4. When the stress was applied, the samples showed a large instant strain, which was the main deformation in the whole test, and the strain increased almost in a vertical line trend. Then, the deformation increased with the increase of the stress. As time goes on, the growth rate of the strain slowed down and the slope of the stress-strain curve decreaseed continuously. At this time, the amount of soil deformation per unit time is not equal, the deformation per unit time will be smaller. This phase was called the attenuation creep phase. When the growth rate of the strain decreased to a certain degree and the curve tends to be horizontal, it can be assumed that the soil deformation per unit time was almost equal, this phase was called the stable creep phase.

Figure 5 shows the logarithmic curve of pore ratio *versus* loading time. It can be clearly seen that the slope of the curve changes significantly at t = 10 min. The phase before t = 10 min is the instantaneous deformation phase, the free water was rapidly extruded because of the creep stress, subsequently, the particles were crowded and the pores are compressed. Therefore, the pore ratio decreased faster and the curve was an oblique line. After t = 10 min, the decrease rate of pore ratio slowed down, and the curve tended to be horizontal with the development of time. At this time, the distance between particles decreased continuously and the frictional resistance between particles increased. This microstructural change was represented by an increasing deformation and decreasing pore ratio of the samples.

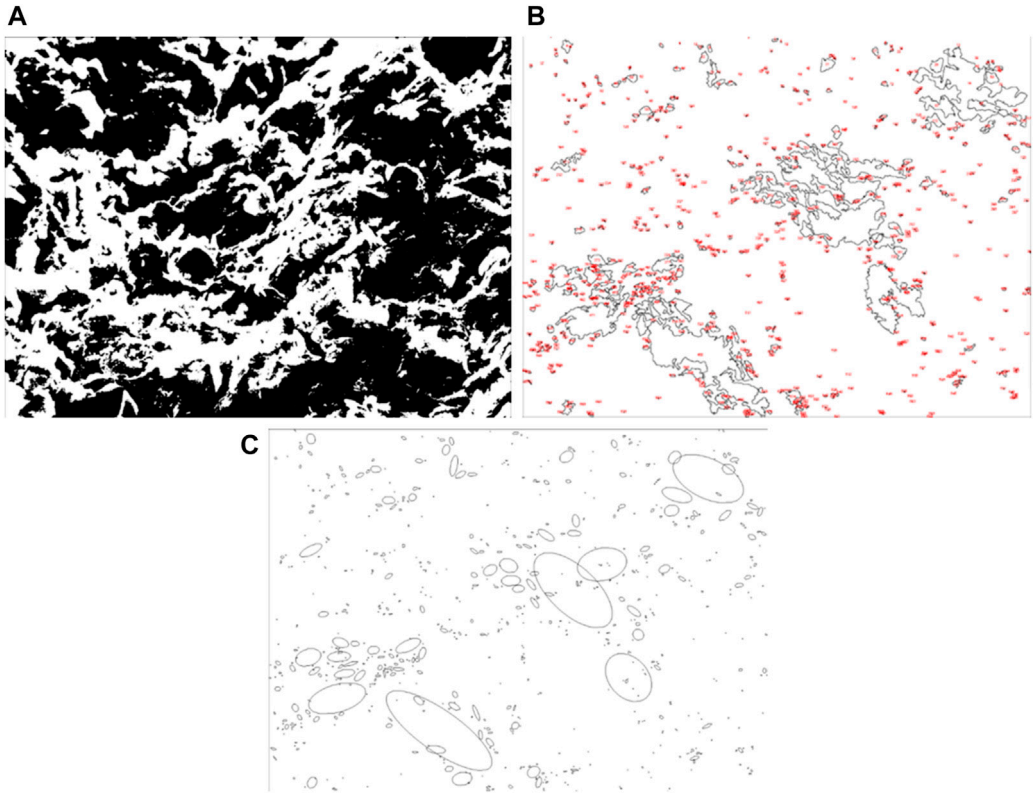

FIGURE 3
(A) Adjustment of the threshold. **(B)** The identified pores. **(C)** Ellipse segmentation.

TABLE 3 Quantitative analysis parameters.

Definition	Expression	Note
quantity	n	The quantity of particles or pores
Abundance	$C = \frac{L_s}{L_l}$	L_s is the short axis length of particle or pore
		L_l is the long axis length of particle or pore
Equivalent diameter	$\bar{D} = \sqrt{\frac{4A}{\pi}}$	A is the area of the particle or pore
Shape complexity	$e = \frac{S^2}{A}$	S is the perimeter of the particle or pore

3.1.2 Microscopic image and processing

The image processing results are shown in Figure 6. In Figure 6A, the quantities of particles and pores were all larger than the undisturbed samples', and the quantities also increased with the increase of the creep stress. Then, the equivalent diameters of particles and pores were divided into different intervals (<1 μm, 1–2 μm, 2–5 μm, >5 μm), as shown in Figure 6B and Figure 6C . It can be seen that, the proportion of particles and pores larger than 5 μm decreased with the increasing creep stress. With the increase of creep stress, the proportion of particle size in 2–5 μm increased, but the proportion of pores size in 2–5 μm decreased. At the same time, the proportion of particles and pores size in 1–2 μm and smaller than 1 μm increased with the increase of the stress. This indicated that the large particles and pores gradually broke down into small particles and pores during the creep process, and this phenomenon was more obvious with the increasing creep stress.

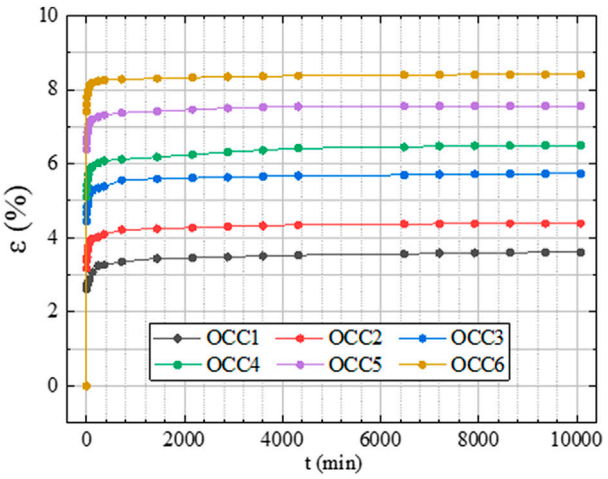

FIGURE 4
Axial stain-time curve.

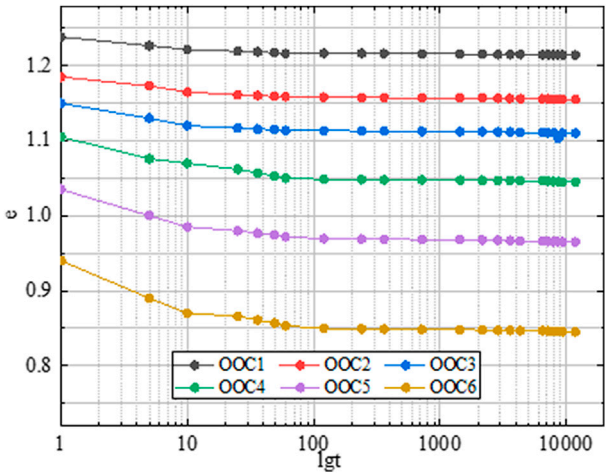

FIGURE 5
Logarithmic curve of pore ratio and time.

The complexity e) and the abundance C) are shown in Figure 7. In Figure 7A, the complexity both decreased with the increase of the creep stress. The abundance of particles and pores was divided into different intervals (0–0.2, 0.2–0.4, 0.4–0.6, 0.6–0.8, 0.8–1.0) in Figures 7B, C, where the abundance in 0–0.2 represents the particles were nearly elongated, the abundance in 0.2–0.8 was nearly elliptical, and the abundance in 0.8–1.0 was nearly circular. For the abundance of particles in Figure 7B, the proportion of the abundance in 0.4–0.6 decreased and then increases. At the same time, the proportion of the abundance in 0.6–1.0 decreased with the increasing of creep stress. This indicated that the shape of the particles changed to flatter with the increase of the creep stress. For the abundance of pores in Figure 7C, the abundance of the undisturbed samples was mainly concentrated the abundance in 0.4–0.8. However, the proportion of the abundance in 0.4–0.6 increased and then decreased with the increasing creep stress, the proportion of the abundance in 0.6–0.8 decreased greatly, and the proportion of the abundance in 0–0.4 increased. This indicated that the shape of the pores became narrower with the increase of the creep stress.

3.2 Discussion of deformation mechanism

The above phenomena can be explained by the changes in the internal structure of the soil during the creep process, as shown in Figure 8. In the process of "a," the spacing of the particles was slightly reduced, and the particles were still arranged in a similar rhombic structure without much change in the form of

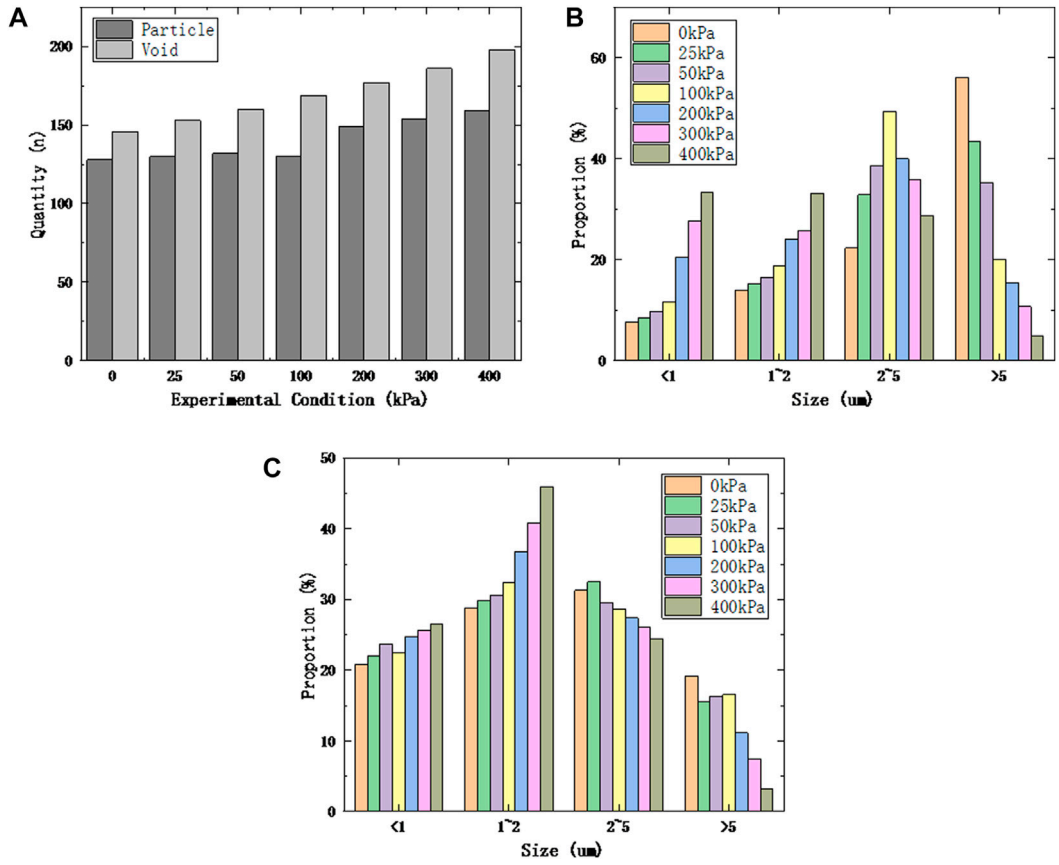

FIGURE 6
(A) The quantity of particles and pores. **(B)** The diameter distribution of particles. **(C)** The diameter distribution of pores.

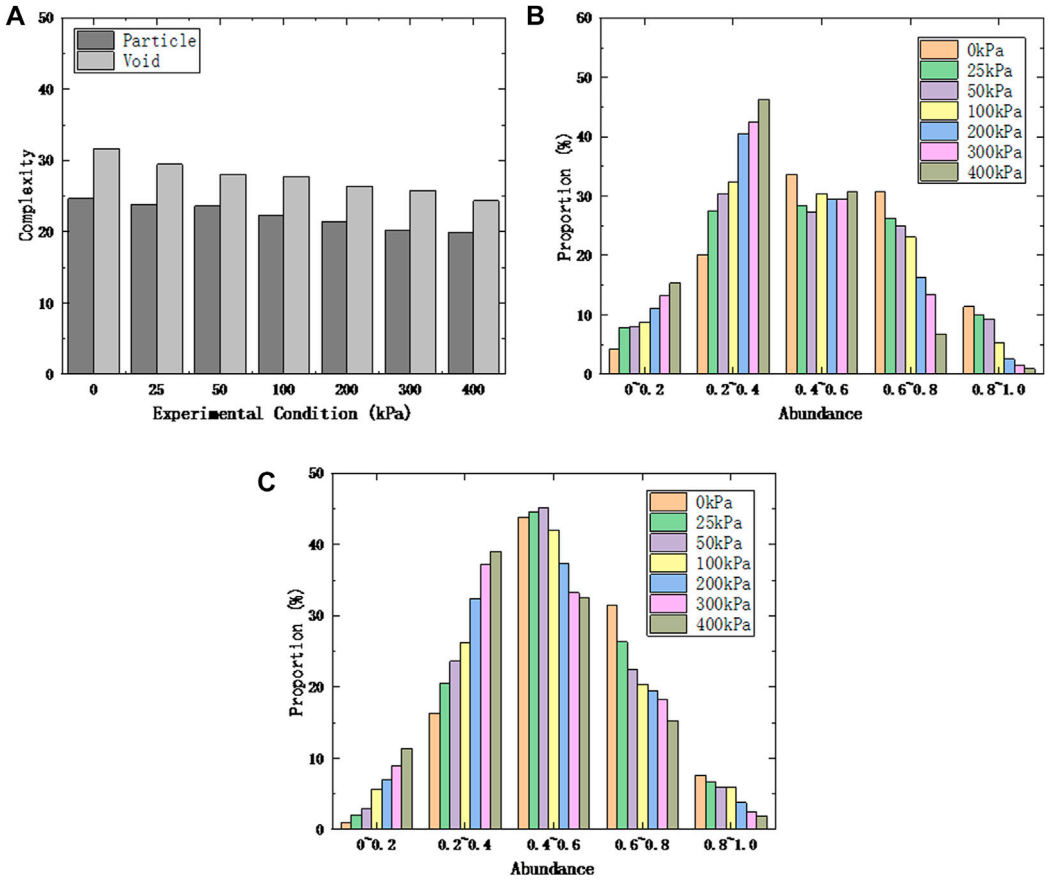

FIGURE 7
(A) The complexity of particles and pores. **(B)** The abundance of particles. **(C)** The abundance of pores.

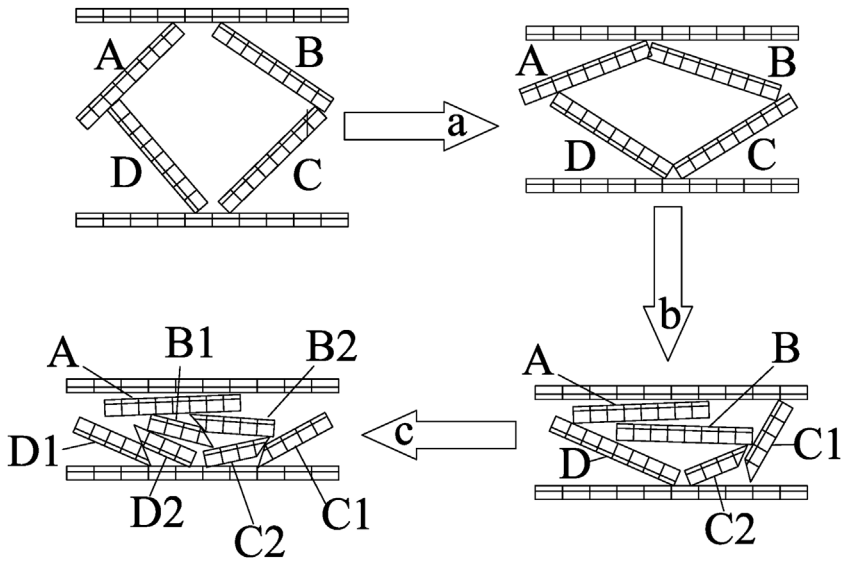

FIGURE 8
Deformation process of soil skeleton.

microstructure, but the volume of the pores decreased. At the same time, the distance between particles was reduced by a small amount. This reduction was small because of the small creep stress (25 kPa, 50 kPa). Therefore, the total deformation of the samples in Figure 4 was small, and so was the decrease of the pore ratio in Figure 5. For the same reason, the quantity of particles and pores with large diameter (>5 μm) decreased less, the complexity and abundance of particles and pores did not change significantly.

In the process of "b," the pores were further compressed and the distance of the particles was further reduced. At the same time, particle B produced a significant movement and particle C broke into particle C1 and particle C2 due to higher creep stress (100 kPa, 200 kPa). Therefore, the total deformation of the samples increased as shown in Figure 4, and the pore ratio decreased further as shown in Figure 5. For the same reason, more small pores were generated among the broken particles (Figure 6B), and this led the quantity of particles and pores with large diameter (>5 μm) to decrease greatly. At the same time, the quantity of particles and pores with medium diameter (2–5 μm) increased greatly, the quantity of particles and pores with small diameter (<1 μm, 1–2 μm) increased slightly.

In the process of "c," the creep stress was so high (300 kPa, 400 kPa) that the particles broke seriously and the distance of the particles decreased greatly. Therefore, the total deformation in Figure 4 increased further, and the pore ratio in Figure 5 decreased further. For the same reason, the quantity of particles and pores with large diameter (>5 μm) accounted for a small proportion. At the same time, the quantity of particles and pores with medium diameter (2–5 μm) decreased, but the quantity of particles and pores with small diameter (<1 μm, 1–2 μm) increased greatly.

4 Conclusion

Based on the compression creep tests, SEM tests and Image J processing this paper analyzed the creep characteristics and deformation mechanism of Nansha soft soil were analyzed in this paper. Three conclusions are drawn as following:

(1) In creep tests, the creep process was divided into three stages, the initial instantaneous deformation phase in which the pores were squeezed and reduced, the attenuation creep phase in which the particles were broken and squeezed, and the stable creep phase in which a large number of broken particles were squeezed and slipped. Furthermore, the creep deformation increased with the creep stress during the three phases.

(2) During creep process, the quantity of particles and pores increased but their volume decreased due to the decrease in the distance between particles and the gradual breaking of particles. At the same time, the shape of particles and pores changed from close to round and bar shape to close to oval shape.

(3) The above phenomenon can be explained by a sketch of the changes in the internal structure of the soil during creep. The creep rate of soft soil was related to the crowding of pore and the fragmentation of particle determined by the magnitude of creep stress. And this phenomenon was more obvious with the increase of the creep stress.

Data availability statement

The raw data supporting the conclusion of this article will be made available by the authors, without undue reservation.

Author contributions

JZ, experimental method design. ST, data collection and collation. YG, original Draft. JC, review and revision. JY, administrative and technical support.

Conflict of interest

The authors declare that the research was conducted in the absence of any commercial or financial relationships that could be construed as a potential conflict of interest.

Publisher's note

All claims expressed in this article are solely those of the authors and do not necessarily represent those of their affiliated organizations, or those of the publisher, the editors and the reviewers. Any product that may be evaluated in this article, or claim that may be made by its manufacturer, is not guaranteed or endorsed by the publisher.

References

Bai, B., Jiang, S., Liu, L., Li, X., and Wu, H. (2021). The transport of silica powders and lead ions under unsteady flow and variable injection concentrations. *Powder Technol.* 387, 22–30. doi:10.1016/j.powtec.2021.04.014

Bai, B., Yang, G., Li, T., and Yang, G. (2019). A thermodynamic constitutive model with temperature effect based on particle rearrangement for geomaterials. *Mech. Mater.* 139, 103180. doi:10.1016/j.mechmat.2019.103180

Dai, C.-X., Zhang, Q.-F., He, S.-H., Zhang, A., Shan, H.-F., and Xia, T.-D. (2021). Variation in micro-pores during dynamic consolidation and compression of soft marine soil. *J. Mar. Sci. Eng.* 9 (7), 750. doi:10.3390/jmse9070750

Gylland, A. S., Rueslåtten, H., Jostad, H. P., and Nordal, S. (2013). Microstructural observations of shear zones in sensitive clay. *Eng. Geol.* 163, 75–88. doi:10.1016/j.enggeo.2013.06.001

Huang, W., Wen, K., Li, D., Deng, X., Li, L., Jiang, H., et al. (2019). Experiment study of lateral unloading stress path and excess pore water pressure on creep behavior of soft soil. *Adv. Civ. Eng.* 2019, 1–9. doi:10.1155/2019/9898031

Kaczmarek, Ł. D., Dobak, P. J., and Kiełbasiński, K. (2017). Preliminary investigations of creep strain of neogene clay from warsaw in drained triaxial tests assisted by computed microtomography. *Studia Geotechnica Mech.* 39 (2), 35–49. doi:10.1515/sgem-2017-0014

Lei, H., Lu, H., Wang, X., Ren, Q., and Li, B. (2016). Changes in soil micro-structure for natural soft clay under accelerated creep condition. *Mar. Georesources Geotechnol.* 34 (4), 365–375. doi:10.1080/1064119X.2015.1010669

Lei, H., Xu, Y., Jiang, M., and Jiang, Y. (2020). Deformation and fabric of soft marine clay at various cyclic load stages. *Ocean. Eng.* 195, 106757. doi:10.1016/j.oceaneng.2019.106757

Li, K., Liu, R., Qiu, C., and Tan, R. (2018). "Consolidated drained creep model of soft clay in Tianjin coastal areas," in *Proceedings of GeoShanghai 2018 international conference: Fundamentals of soil behaviours*. Editors A. Zhou, J. Tao, X. Gu, and L. Hu (Springer Singapore), 157–165. doi:10.1007/978-981-13-0125-4_17

Li, Z., Wang, J., Yang, S., Liu, S., and Li, Y. (2022). Characteristics of microstructural changes of malan loess in yan'an area during creep test. *Water* 14 (3), 438. doi:10.3390/w14030438

Liu, X. X., and Zhang, J. R. (2011). Fractal approach on quantitative analysis of micro pore structure of isotropic consolidated clay. *Adv. Mater. Res.* 250–253, 1846–1851. doi:10.4028/www.scientific.net/AMR.250-253.1846

Mataic, I., Wang, D., and Korkiala-Tanttu, L. (2016). Effect of destructuration on the compressibility of perniö clay in incremental loading oedometer tests. *Int. J. Geomechanics* 16 (1), 04015016. doi:10.1061/(ASCE)GM.1943-5622.0000486

Mesri, G., and Choi, Y. K. (1985). Settlement analysis of embankments on soft clays. *J. Geotechnical Eng.* 111111 (4), 441–464. doi:10.1061/(asce)0733-9410(1985)111:4(441)

Nian, T., Jiao, H., Fan, N., and Guo, X. (2020). Microstructure analysis on the dynamic behavior of marine clay in the South China Sea. *Mar. Georesources Geotechnol.* 38 (3), 349–362. doi:10.1080/1064119X.2019.1573864

Nishimura, T. (2020). "Shear strength of an unsaturated silty soil subjected to creep deformation," in *Geotechnics for sustainable infrastructure development*. Editors P. Duc Long and N. T. Dung (Springer), 977–984. doi:10.1007/978-981-15-2184-3_128

Osipov, V. I., and Sokolov, V. N. (1978). A study of the nature of the strength and deformation properties of clay soils with the help of the scanning electron microscope. *Bull. Int. Assoc. Eng. Geol.* 17 (1), 91–94. doi:10.1007/BF02634697

Sun, H., Mašín, D., Najser, J., Neděla, V., and Navrátilová, E. (2019). Bentonite microstructure and saturation evolution in wetting–drying cycles evaluated using ESEM, MIP and WRC measurements. *Géotechnique* 69 (8), 713–726. doi:10.1680/jgeot.17.P.253

Tan, Q., Huang, M., Tang, H., Zou, Z., Li, C., Huang, L., et al. (2022). Insight into the anisotropic deformation of landslide sliding zone soil containing directional cracks based on *in situ* triaxial creep test and numerical simulation. *Eng. Geol.* 311, 106898. doi:10.1016/j.enggeo.2022.106898

Tran, T. T. T., Hazarika, H., Indrawan, I. G. B., and Karnawati, D. (2018). Prediction of time to soil failure based on creep strength reduction approach. *Geotechnical Geol. Eng.* 36 (4), 2749–2760. doi:10.1007/s10706-018-0496-9

Wang, Z., and Wong, R. C. K. (2016). Strain-dependent and stress-dependent creep model for a till subject to triaxial compression. *Int. J. Geomechanics* 16 (3), 04015084. doi:10.1061/(ASCE)GM.1943-5622.0000583

Xie, X., Qi, S., Zhao, F., and Wang, D. (2018). Creep behavior and the microstructural evolution of loess-like soil from Xi'an area, China. *Eng. Geol.* 236, 43–59. doi:10.1016/j.enggeo.2017.11.003

Yan, Z., Li, G., Zhang, J., and Zhang, R. (2019). Study on the creep behaviors of interactive marine-terrestrial deposit soils. *Adv. Civ. Eng.* 2019, 1–14. doi:10.1155/2019/6042893

Yin, Z.-Y., and Karstunen, M. (2011). Modelling strain-rate-dependency of natural soft clays combined with anisotropy and destructuration. *Acta Mech. Solida Sin.* 24 (3), 216–230. doi:10.1016/S0894-9166(11)60023-2

Yin, Z.-Y., Zhu, Q.-Y., and Zhang, D.-M. (2017). Comparison of two creep degradation modeling approaches for soft structured soils. *Acta Geotech.* 12 (6), 1395–1413. doi:10.1007/s11440-017-0556-y

Zhao, D., Gao, Q.-F., Hattab, M., Hicher, P.-Y., and Yin, Z.-Y. (2020). Microstructural evolution of remolded clay related to creep. *Transp. Geotech.* 24, 100367. doi:10.1016/j.trgeo.2020.100367

Zhao, D., Hattab, M., Hicher, P.-Y., and Yin, Z.-Y. (2022). Effect of stress level on the microstructural evolution of clay under creep. *J. Eng. Mech.* 148 (2), 04021148. doi:10.1061/(ASCE)EM.1943-7889.0002070

Zhu, Q.-Y., Yin, Z.-Y., Hicher, P.-Y., and Shen, S.-L. (2016). Nonlinearity of one-dimensional creep characteristics of soft clays. *Acta Geotech.* 11 (4), 887–900. doi:10.1007/s11440-015-0411-y

Zhu, Y.-B., and Yu, H.-M. (2015). Unsaturated creep behaviors of weak intercalated soils in soft rock of Badong formation. *J. Mt. Sci.* 12 (6), 1460–1470. doi:10.1007/s11629-014-3298-4

Zou, S.-F., Xie, X.-Y., Li, J.-Z., Wang, Z.-J., and Wang, H.-Y. (2019). Rheological characteristics and one-dimensional isotache modelling of marine soft clays. *Mar. Georesources Geotechnol.* 37 (6), 660–670. doi:10.1080/1064119X.2018.1473903

frontiers | Frontiers in Materials

TYPE Original Research
PUBLISHED 14 March 2023
DOI 10.3389/fmats.2023.1137728

Check for updates

OPEN ACCESS

EDITED BY
Bing Bai,
Beijing Jiaotong University, China

REVIEWED BY
Haiqing Zhang,
Hebei University, China
Chen Peipei,
Beijing University of Civil Engineering and Architecture, China

*CORRESPONDENCE
Jian Chen,
672445389@qq.com

SPECIALTY SECTION
This article was submitted to Structural Materials, a section of the journal Frontiers in Materials

RECEIVED 04 January 2023
ACCEPTED 28 February 2023
PUBLISHED 14 March 2023

CITATION
Yuan J, Wang TJ, Chen J and Huang jA (2023), Microscopic mechanism study of the creep properties of soil based on the energy scale method.
Front. Mater. 10:1137728.
doi: 10.3389/fmats.2023.1137728

COPYRIGHT
© 2023 Yuan, Wang, Chen and Huang. This is an open-access article distributed under the terms of the Creative Commons Attribution License (CC BY). The use, distribution or reproduction in other forums is permitted, provided the original author(s) and the copyright owner(s) are credited and that the original publication in this journal is cited, in accordance with accepted academic practice. No use, distribution or reproduction is permitted which does not comply with these terms.

Microscopic mechanism study of the creep properties of soil based on the energy scale method

Jie Yuan, Tao Jin Wang, Jian Chen* and jian An Huang

Guangzhou University, Guangzhou, Guangdong Province, China

The study of the creep properties of soils is of great importance for the management of future settlements and the safe use of buildings. However, starting from the micro level is an effective way to explore the creep mechanism of soft soil. In this paper, the influence of the mineral composition and the mineral content on the structure and creep properties of soft soil was analyzed at the microscopic level and the energy scale method was proposed. Then, the energy scale method was used to analyze and discuss the results of the direct shear creep test. The discussion showed that 1) the average viscosity coefficient of kaolin was greater than that of bentonite, which decreased with an increase of kaolin and bentonite; 2) the thickness of adsorbed water or the double electric layer (DEL) on the particle surface was positively correlated with the soft soil creep; and 3) λ was positively correlated with the adsorbed water content and negatively correlated with the average viscosity coefficient of the soft soil. λ characterized the adsorption capacity of the particles at the micro level; hence, the energy scale method can explain the mechanism of the soft soil creep at the microscopic level and also quantitatively describe the influencing law of the basic characteristics of the particles on the properties of the soft soil creep.

KEYWORDS

creep, energy scale method, coefficient of viscosity, direct shear creep test, adsorbed water

1 Introduction

Soft soils are widely distributed all over the world and are characterized by a large porosity, high water content, high compressibility, low shear strength, and bearing capacity (Xiang et al., 2021; Naeini and Mohammadi, 2022). Generally, soft soils show an evident creep phenomenon, for example, even though the main consolidation has been completed, soft soil foundations still experience deformation for a long time (Tsugawa et al., 2019). The deformation of soft soil by the creep also leads to an uneven settlement of buildings, and the Leaning Tower of Pisa is an example of this. In order to reduce the engineering hazard caused by the creep of soft soil, scholars have conducted a lot of research on the creep in soft soils.

The process of analyzing the mechanism of the soil creep phenomenon through laboratory tests has always been welcomed by scholars. First, scholars found that test conditions had an impact on the creep behavior of soft soil. For example, Wei et al. (2014) conducted a triaxial consolidation undrained shear creep test and concluded that the increase of pore water pressure makes the creep properties of silt soft soil more significant. Huang et al. (2020) conducted the lateral unloading creep test under a different excess pore water pressure, and the results showed that the higher the excess pore water pressure, the more evident the creep of soft soils. Evidently, the nature of soft soil

itself, such as the mineral composition and structural characteristics, has a more fundamental impact on its creep properties (Yuan et al., 2022). Liu et al. (2018) concluded that clay minerals, especially montmorillonite, play an important role in the creep of clay rocks through the triaxial creep test. Ni and Huang (2020) found that the influence of the mineral composition on the creep properties was much more significant than that of the other factors observed through zeta potential analysis of kaolinite, montmorillonite, and illite. Brezzi et al. (2018) used cohesive materials for collapse testing, aiming to assess how the composition of cohesive mixtures affects flow properties. Further research showed that adsorbed water on the surface of particles was an important factor in the creep properties of soft clay soils, for example, there is a correlation between the coefficient of viscosity of soft soils and the thickness of adsorbed water (Zhang and Wang, 2011; Xiao et al., 2014; Yang, 2017). In addition to the external environment, the mineral composition of particles has the most evident effect on the water adsorption state on the surface of particles (Wu, 2015; Bai et al., 2021a). For example, Gu and Fang (2009b) proposed the concept of "creep substances" and experimentally analyzed the relationship between creep properties and creep substances such as organic matter (Gu and Fang, 2009a) and clay minerals. Fang (2014) suggested that creep substances on the surface of soil particles charged them and then adsorbed water molecules to form adsorbed water; so, soil particles were connected by adsorbed water to show the overall creep properties. Tang (2021) performed isothermal adsorption tests on artificial mixed clay, and the results showed that the adsorbed water content of the mixed clay increased linearly with the increase of the montmorillonite content, and the mineral composition of the clay (montmorillonite) was the most basic influencing factor. The aforementioned research studies were mainly about the creep properties of soils from the macro scope, but the variation of the microstructure of particles is the true reflection of macro-mechanical behavior. Therefore, in order to study the intrinsic mechanism of the soft soil creep, the laws of the macroscopic creep properties and microstructural changes in soft soils have received increasing attention (Zhu et al., 2017; Zhu et al., 2019). Micromechanical studies of the soil creep have been carried out as early as the 20th century. For example, based on the rate process theory, Kuhn and Mitchell (1993) derived an expression for the ratio of the creep velocity of two contacting particles to the tangential contact force component and the normal contact force component, and introduced it into the discrete element model (DEM). Numerical simulations show that the variation of the creep velocity is related to the variation of the contact forces in tangential and normal directions. Thereafter, Gao et al. (2023) performed a numerical simulation of the biaxial shear creep in sandy soils using the discrete element method and analyzed the contribution of three contact motion modes, contact deformation (normal and tangential), Type4 rolling, and rigid-body motion, for the deformation of the specimen, where contact deformation mainly contributed to the overall volume change in terms of the overall volume strain. The studies of these scholars have shown that there is a correlation between the micro-level parameters of the soil and the macro-mechanical properties (Bai et al., 2021b), and the DEM method helps in exploring the response law between the micro-contact forms of particles and the macro-mechanical phenomena. However, due to the multi-hybrid nature of the mineral composition in soft soils, the parameter calibration of the DEM method is tedious and complicated, and the DEM method is not used in this paper for the characterization of particle microscopic contact forms.

The method of the experimental test to analyze the mechanism of the creep phenomenon in soft soil can be designed in advance to study the factor and analyze the response law of that factor and creep behavior in a targeted manner. Experimental analyses play a great role in the study of the creep mechanism from the external conditions to soft soil's factors. However, experimental studies focus on macro-level analyses and cannot truly reflect the intrinsic mechanism of the soft soil creep. For this reason, some scholars have used the discrete element method to characterize the microscopic contact morphology of particles in terms of their tangential and normal forces and then analyze the relationship between the microscopic contact morphology of the particles and creep behavior. However, due to the complexity of the soft soil composition, the calibration of discrete element parameters is often complicated; so, a new idea is adopted in this paper, where the ratio of circumferential and normal forces is directly used to characterize the microscopic contact morphology of particles.

It can be seen that the research results on the mechanism of the soft soil creep are relatively abundant but most of them consider the influence of each factor on the creep properties of soft soil in a single and scattered manner. The mineral composition and content, and binding water are coupled together to influence the macro creep properties of soil. The thickness of the adsorbed water film depends mainly on the soil composition and content, while the creep properties of clay are inseparable from adsorbed water. Therefore, in order to explore the coupling mechanism of multiple factors on soil creep, this paper adopted the energy scale method for the characterization of microscopic contact characteristics of soft soil particles based on the three factors of mineral composition, mineral content, and adsorbed water content. Then, we used the coefficient of viscosity as a parameter to quantify the macroscopic creep characteristics of soft soil. Finally, the quantitative relationship between the microscopic characteristics of particles and macroscopic creep characteristics was established to provide a multifactor coupling mechanism for future research on the soft soil creep. This paper will provide a useful reference for future research on the mechanism of multifactor coupling of the soft soil creep.

2 Energy scale method

Soft soils contain many clay particles; the clay particles always have a small specific surface area (SSA) and larger negative surface charges. The negative charges adsorb polar water molecules and cations to form an ionic liquid layer on the surface of the particles. This ionic liquid layer has a certain viscosity and is known as the diffused double electric layer (DEL, as shown in Figure 1). In the DEL, several water molecules are directly attached to the particle surface and considered immobile. These water molecules have solid shear resistance properties and are referred to as strongly adsorbed water. Compared with the small clay particles, the thickness of the DEL or adsorbed water is really considerable. So, the contact between clay particles in soft soils is more of the contact of the DEL or adsorbed water rather than the particles (as shown in Figure 2). As is commonly known, the consolidation and shear

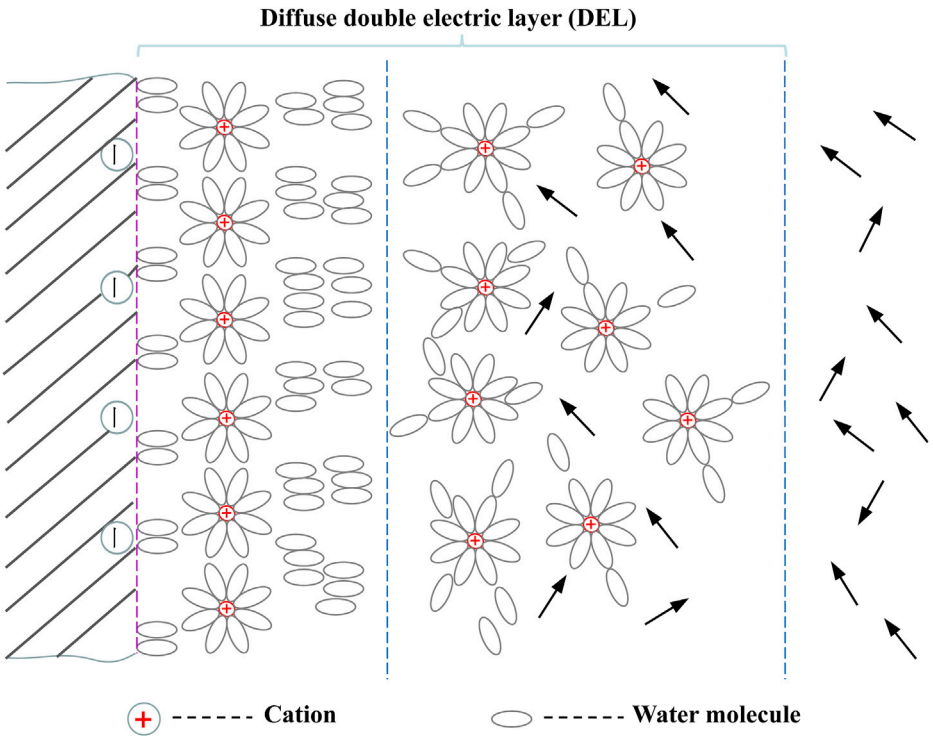

FIGURE 1
Schematic diagram of the double electric layer.

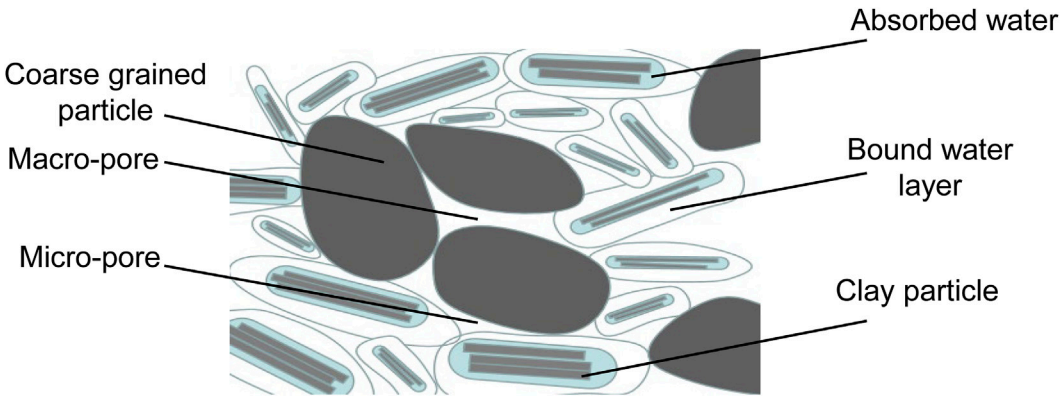

FIGURE 2
Schematic view of the clay–water system.

deformation of soil are the position rearrangement of the particles by sliding and rolling at the microscopic level. For clay particles, the position rearrangement of the particles shows a characteristic of viscosity and time continuity because of the solid shear resistance properties of the DEL and adsorbed water. In the macro scope, the aforementioned phenomenon is manifested as the creep phenomenon of clay. For non-clay minerals, the particles are generally big, the surface charges are few, and the thickness of the adsorbed water layer or the DEL on the surface of the particles is very small compared to the particle size. So, the contact between non-clay minerals particles is more of a direct contact between mineral crystals. As a result, the rolling effect between the particles is more evident, but the viscous effect between the particles is less evident; so, the creep phenomenon is not evident in non-clay soils when compared with that of clay soils.

Evidently, the creep phenomenon of the soil is significantly related to the relative thickness of the DEL or adsorbed water layer. The thickness of adsorbed water and the DEL is directly related to

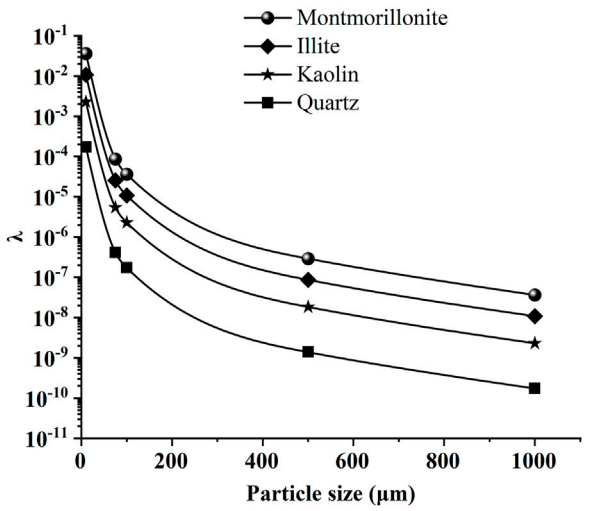

FIGURE 3
Relationship curve of the particle size and λ of the four components.

the surface charge, while the mineral composition of the particles determines the surface charge. In other words, the mineral composition of the particles determines the viscosity and time continuity characteristics of the movement between particles at the microscopic level. This means that the mechanisms of the mineral composition, clay particle content, and water content on the creep characteristics of soft soils at the macroscopic level can be explored by the aforementioned explanation at the microscopic level. Therefore, in this paper, the microscopic forces of particles are used to quantitatively measure the adsorption capacity of the particle surface to polar water and ions. These microscopic forces are also a visual display of the particle surface energy. So, this method is called the energy scale method. Then, the energy scale method reveals the intrinsic mechanism of the macroscopic creep in soft soils at the microscopic level. The energy scale method can be expressed as follows:

$$\lambda = \alpha \times \frac{F_e}{W} = \frac{6\varepsilon_0}{g} \times \frac{\alpha {\phi_0}^2}{(\mathrm{d}+H)^2 \rho d}, \quad (1)$$

where λ is the ratio of the microcoulomb force to gravity, α is the composition content, F_e is the Coulomb force, W is the gravity, ϕ_0 is the particle surface potential, ε_0 is the vacuum capacitance, g is the gravitational acceleration, d is the particle diameter, H is the mean spacing of particles, and ρ is the mass density of particles.

Taking the common clay minerals such as montmorillonite, kaolin, illite, and quartz as representatives, λ can be obtained by Equation 1 according to Huang (2018), as shown in Figure 3.

As seen in Figure 3, λ values of the three clay mineral particles are much larger than that of quartz (tens of times different), so only λ of clay mineral particles in soft soils is considered in this paper. Among clay mineral particles, the microgravity ratio of montmorillonite is the largest, followed by those of illite and kaolin, and λ of all three particles decreases with the increase of the particle size. The surface charge of the three particles, montmorillonite, illite, and kaolin, decreased in order, and the adsorption effect of water on the surface also decreased, so λ of the three minerals decreased in order. Related studies show that the creep effect of these three minerals also decreases sequentially, which indicates that the energy scale method proposed in this paper can characterize the influence law of the mineral composition in the soil creep phenomenon.

3 Soil creep tests and analyses

3.1 Test of creep properties of soil

3.1.1 Experimental materials and apparatus

This experiment mainly analyzes the creep behavior of soft soil through the direct shear creep test. There are mainly three kinds of soft soil samples in the laboratory test: the undisturbed natural soil sample, the remodeled natural soil sample, and the artificial remodeled soil. Among them, the composition of natural soil is relatively complicated, and at the same time, the sampling and preparation processes are time consuming. An artificial soil mineral powder is often used to prepare soil samples in the laboratory because of its clear mineral composition and high purity. So, the commercial powders of soil minerals such as kaolin, bentonite, quartz, and feldspar were used in this experiment. Bentonite mainly contains montmorillonite; the content of montmorillonite was tested by the X-ray diffractometer test (Germany Bruker D8 ADVANCE, Cu(monochrome)), and the results are shown in Table 1.

The diameter of these four mineral powders was tested by using the laser particle sizer; the tested result, the plastic limit (W_P), the liquid limit (W_L), and the plastic index are all shown in Table 2.

The common direct shear creep apparatus is widely used because of its easy operation and low cost. However, this instrument could not guarantee the humidity of the sample in the test process, and the accuracy of the instrument could not meet the tiny deformation of the creep. So, in this paper, an improved direct shear creep apparatus was used. In the improved direct shear creep apparatus, a moisturizing device was added to maintain humidity; in addition to this device, a percentage meter and a micrometer were also added to measure the creep displacement, which increased the measurement accuracy of creep displacement from 10 μm to 1 μm, as shown in Figure 4.

TABLE 1 Compositional information on bentonite tested using an X-ray diffractometer.

Mineral composition	Quartz (%)	Cristobalite (%)	Montmorillonite (%)	Clinoptilolite (%)	Sodalite (%)
Content	0.80	3.90	91.70	1.70	2.00

TABLE 2 Information on these four soil minerals.

Mineral composition	Bentonite	Kaolin	Quartz	Feldspar
Particle size (μm)	2.5	2.5	1.25	2.5
W_P (μm)	42.2	28.2	—	—
W_L (μm)	97.7	41.1	—	—
I_P (μm)	55.5	12.9	—	—

FIGURE 4
Physical picture of the improved direct shear creep apparatus.

3.1.2 Experimental scheme and method

The energy scale method mainly tries to explain the influence of the mineral composition and the mineral content on the creep characteristics of soft soil from the micro level. Therefore, the samples of the soft soil in this test were designed from two aspects of the mineral composition and the mineral content. Therefore, two groups of samples were designed; the first group was mainly composed of quartz and feldspar, which gradually increased the content of kaolin, while the second group also used quartz and feldspar as a matrix and gradually increased the content of bentonite.

TABLE 3 Parameters of different groups of specimens.

No.	Composition (%)			
	Kaolin	Bentonite	Quartz	Feldspar
1–1	10	—	72	18
1–2	15	—	68	17
1–3	20	—	64	16
1–4	25	—	60	15
2–1	—	10	72	18
2–2	—	15	68	17
2–3	—	20	64	16
2–4	—	25	60	15

During the sample preparation process, kaolin, bentonite, quartz, and feldspar were homogeneously mixed, according to the designed proportions in Table 3. The matrix materials were wetted and packaged overnight and then molded in samples with a diameter of 6.18 cm and a height of 4 cm, according to the design requirements. Then, the samples were saturated by vacuum evacuation, and the soil samples were soaked in water for 3 days after 3 h of vacuum evacuation. Finally, the samples were subjected to the direct shear creep test, and the shear load was loaded on seven levels, and the load of each level is shown in Table 4. During the test, the environment temperature was kept at (25 ± 1)°C and the relative humidity was kept at (88 ± 5)%.

3.2 Test results

When the soft soil creep shear test is completed according to the aforementioned test scheme and test requirements, the curve of the shear rate (γ) of each soil sample with time is obtained, as shown in Figure 5.

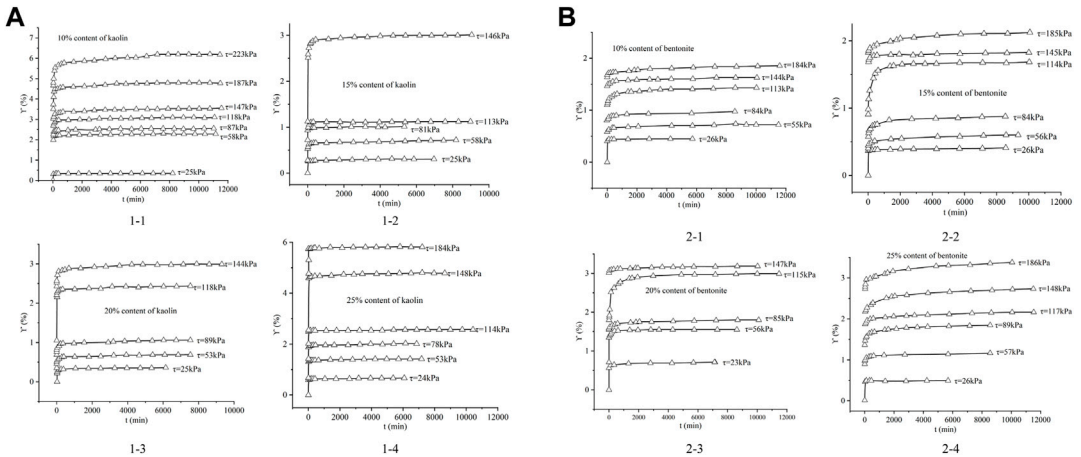

FIGURE 5
Curve of the shear rate (γ) with the time of each sample: **(A)** kaolin and **(B)** bentonite.

TABLE 4 Direct shear test scheme for different groups of specimens.

No.	P (kPa)	Horizontal shear stress magnitude and number of steps (kPa)						
		1	2	3	4	5	6	7
1–1	400	25	58	87	118	147	187	223
1–2		25	58	81	113	146		
1–3		25	53	89	118	144		
1–4		24	53	78	114	148	184	
2–1		26	55	84	113	144	184	
2–2		26	56	84	114	145	185	
2–3		23	56	85	115	147		
2–4		26	57	89	117	148	186	

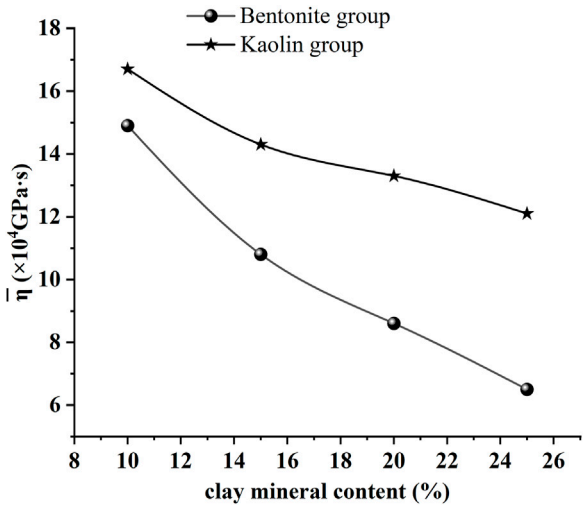

FIGURE 6
Average viscosity coefficient of different specimens.

TABLE 5 Content of adsorbed water of each sample ($W_g \approx 0.885W_P$; $W_a \approx W_L$).

No.	1–1	1–2	1–3	1–4	2–1	2–2	2–3	2–4
W_g (%)	14.2	14.6	14.9	15.3	15.7	16.2	16.5	16.9
W_a (%)	26.3	27.9	28.9	30.3	28.6	33	37.7	42.6

In Figure 5, after a relatively large change, the shear rate of each sample decreased with the time, consuming and gradually tending to the isokinetic creep phase. The cure of the isokinetic creep phase could also be expressed by the viscosity coefficient of soil, which is an important factor for the soil creep. The viscosity coefficient is written as $\eta = \tau/\Upsilon$, where η is the coefficient of viscosity (PaS), τ is the shear stress, and Υ is the shear rate. At this time, according to the shear creep curve in Figure 5, the average viscosity coefficient ($\bar{\eta}$) of each specimen was calculated and is shown in Figure 6.

From Figure 6, it can be seen that the average viscosity coefficient of each specimen decreased with the increase of the kaolin and bentonite content, and the average viscosity coefficient of kaolin was greater than that of bentonite even though they shared the same content. Compared with the kaolin group specimens, the bentonite group specimens decreased faster with the increase of the clay mineral content.

3.3 Analysis and discussion

The phenomena in Figure 6 can be interpreted at the microscopic level. As described previously, the deformation of soft soil is mostly due to the rearrangement of particles under load. Therefore, the creep deformation process is the process of a mutual staggered displacement between particles, in which the force is transferred between particles through interfacial contact. For clay particles, the contact between the particles is mainly adsorbed water or the DEL because the particles are small and the thickness of adsorbed water or the DEL is relatively large. Adsorbed water and the DEL both have a certain viscosity; when the two contacting particles have a mutual displacement, the viscous effect between adsorbed water or the DEL is observed. As a result, on a macroscopic scale, soft soils exhibit certain creep phenomena. Some scholars believe that there is a relationship between the amount of adsorbed water on the particle surface and the plastic limit of the soil. According to Yuan (2014), the maximum strongly adsorbed water content (W_g) and the maximum adsorbed water content (W_a) of each sample in this test were calculated, as shown in Figure 5.

The surface charges on bentonite are larger than those of kaolin, so the adsorbed water content of bentonite is larger than that of kaolin (Table 5), and the viscosity effect of bentonite is more evident than that of kaolin. So, the viscosity coefficient of specimens containing bentonite is smaller than that of kaolin with the same content, as shown in Figure 6. Meanwhile, with the increase of the kaolin and bentonite content, the contact of adsorbed water or the DEL is increasing, so, the coefficient of viscosity decreases (Figure 6); the creep phenomenon is more significant. When adsorbed water on the surface of the particles is relatively less, the contact between the

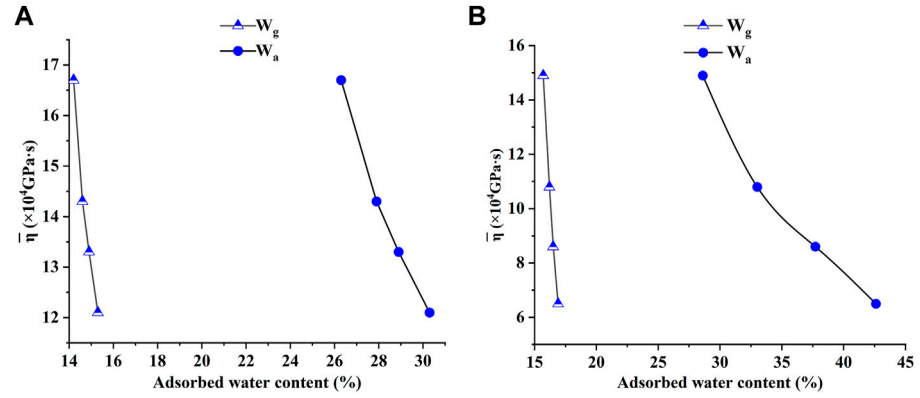

FIGURE 7
Curve of the average viscosity coefficient of samples with the adsorbed water content. **(A)** Kaolin; **(B)** bentonite.

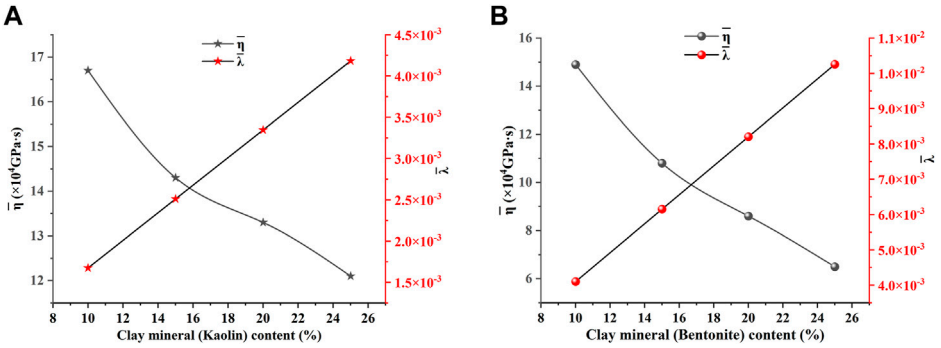

FIGURE 8
Relationship curves between λ and the average viscosity coefficient. **(A)** Kaolin; **(B)** bentonite.

particles may be the direct contact between mineral crystals. Since mineral crystals have great strength, the particles show a more evident friction effect; so, the viscosity coefficient of the soil is significant, as shown in Figure 7.

The thickness of adsorbed water can explain the creep mechanism of soft soil to a certain extent. However, the adsorption energy of particles for water is mainly determined by the surface charges of particles. For clay particles, they have more surface charge and a larger specific surface area, and it is easier for clay particles to form a sizable volume of the adsorbed water layer or the double electric layer when interacting with water. For non-clay particles, the charge on the surface of these types of particles is smaller. At the same time, non-clay particles tend to have a larger particle size and smaller specific surface area, so their ability to adsorb water is weak, and the thickness of adsorbed water or the DEL is relatively thin. The electric field force on the particle surface is a direct factor in attracting ions and polar water molecules, while the gravity of the particles characterizes the scale effect of the particle. So, the energy scale method in this paper uses these two forces, which can quantitatively measure and explain the role of the particle mineral composition in the soft soil creep. Through the energy scale method, λ of each sample was calculated by Equation (1), and the relationship between the obtained λ and the average coefficient of viscosity is plotted in Figure 8.

In Figure 8, it can be found that λ values of bentonite and kaolin group specimens all show a certain negative correlation with the clay mineral content. At the same time, λ values of the bentonite group specimens are all larger than those of the corresponding kaolin group specimens. With the increase of the clay mineral content, λ of the two groups of specimens also increased, and the increase of bentonite group specimens was larger than that of kaolin group specimens. It is not difficult to find that these phenomena are basically the same as those in Figure 6, which shows that the ratio of the microcoulomb force to the gravity of the particles obtained by the energy scale method can explain the mechanism of the soft soil creep at the microscopic level. At the same time, the ratio of the microcoulomb force to the gravity energy scale method can also quantitatively describe the influence law of the basic characteristics of the particles on the properties of the soft soil creep.

4 Conclusion

In this paper, the influence of the mineral composition, the mineral content, and adsorbed water on the soft soil creep properties

was analyzed at the microscope level and the energy scale method was adopted. Then, the energy scale method was used to analyze and discuss the results of the direct shear creep test. Finally, the following three conclusions were drawn:

(1) The average viscosity coefficient of kaolin was bigger than bentonite even though they shared the same content, and they both decreased with the increase of the kaolin and bentonite contents. Compared with the kaolin group specimens, the bentonite group specimens decreased faster with the increase of the clay mineral content.
(2) The thickness of adsorbed water or the DEL on the particle surface is positively correlated with the soft soil creep. The creep deformation of soft soil is mainly the contact deformation between particles of adsorbed water or the DEL. When the content of adsorbed water or the DEL increases, the coefficient of viscosity decreases and the creep phenomenon is more evident. Also, the creep phenomenon of bentonite is more evident than that of kaolin because adsorbed water of bentonite is more evident.
(3) The ratio of the microcoulomb force to gravity is positively correlated with the adsorbed water content on the particle surface and negatively correlated with the average viscosity coefficient of soft soil. The ratio of the microcoulomb force to gravity characterizes the adsorption capacity of particles to polar water and ions at the micro level, so the energy scale method can explain the mechanism of the soft soil creep at the microscopic level and also quantitatively describe the influence law of the basic characteristics of the particles on the properties of the soft soil creep.

Data availability statement

The original contributions presented in the study are included in the article/Supplementary Materials; further inquiries can be directed to the corresponding author.

Author contributions

JY: conceptualization, methodology, investigation, data curation, visualization, and funding acquisition; TW: writing—original draft and supervision; JC: writing—review and editing; JH: resources.

Conflict of interest

The authors declare that the research was conducted in the absence of any commercial or financial relationships that could be construed as a potential conflict of interest.

Publisher's note

All claims expressed in this article are solely those of the authors and do not necessarily represent those of their affiliated organizations, or those of the publisher, the editors, and the reviewers. Any product that may be evaluated in this article, or claim that may be made by its manufacturer, is not guaranteed or endorsed by the publisher.

References

Bai, B., Jiang, S., Liu, L., Li, X., and Wu, H. (2021a). The transport of silica powders and lead ions under unsteady flow and variable injection concentrations. *Powder Technology* 387, 22–30. doi:10.1016/j.powtec.2021.04.014

Bai, B., Zhou, R., Cai, G., Hu, W., and Yang, G. (2021b). Coupled thermo-hydro-mechanical mechanism in view of the soil particle rearrangement of granular thermodynamics. *Computers and Geotechnics* 137, 104272. doi:10.1016/j.compgeo.2021.104272

Brezzi, L., Cola, P. E. S., and Gabrieli, F. (2018). Collapse of granular–cohesive soil mixtures on a horizontal plane. *Acta Geotechnica* 15, 695–714. doi:10.1007/s11440-018-0725-7

Fang, Y. (2014). Theoretical and experimental investigation on size effect characteristic of strength and deformation of soil. *Rock and Soil Mechanics* 35, 41–47.

Gao, Y., Chen, Q., Yuan, Q., and Wang, Y.-H. (2023). The kinematics and micro mechanism of creep in sand based on DEM simulations. *Computers and Geotechnics* 153, 105082. doi:10.1016/j.compgeo.2022.105082

Gu, R., and Fang, Y. (2009a). Experiment Study of the Effects of Organic Matter on the rheological Characteristics of Soft Soils. *China Civil Engineering Journal* 6.

Gu, R., and Fang, Y. (2009b). Exploration of substance bases and mechanism of soft soil rheology. *Rock and Soil Mechanics* 6.

Huang, W., Wen, K., Deng, X., Li, J., Jiang, Z., Li, Y., et al. (2020). Constitutive Model of lateral unloading Creep of Soft Soil under Excess pore water pressure. *Mathematical Problems in Engineering* 2020, 1–13. doi:10.1155/2020/5017546

Huang, X. (2018). *Division of energy scale and analysis of engineering properties for soil granular group*. Guangzhou, China: South China University of Technology.

Kuhn, M. R., and Mitchell, J. K. (1993). New perspectives on soil creep. *Journal of Geotechnical Engineering* 119, 507–524. doi:10.1061/(asce)0733-9410(1993)119:3(507)

Liu, Z., Shao, J., Xie, S., Conil, N., and Zha, W. (2018). Effects of relative humidity and mineral compositions on creep deformation and failure of a claystone under compression. *International Journal of Rock Mechanics and Mining Sciences* 103, 68–76. doi:10.1016/j.ijrmms.2018.01.015

Naeini, S. A., and Mohammadi, S. "An investigation on the Effect of deep Mixing columns and geogrid on embankment Settlement on the Soft Soil," in Proceedings of the International Conference on Geotechnical Engineering Investigation Methods and Applications, Miami. United States, March 2022.

Ni, H., and Huang, Y. (2020). Rheological study on influence of mineral composition on viscoelastic properties of clay. *Applied Clay Science* 187, 105493. doi:10.1016/j.clay.2020.105493

Tang, S. H. (2021). Analysis of bound water and its influence factors in Mixed clayey Soils. *Water* 13.

Tsugawa, J. K., Romano, R., Pileggi, R. G., and Boscov, M. (2019). Review: Rheology concepts applied to geotechnical engineering. *Applied Rheol.* 29, 202–221. doi:10.1515/arh-2019-0018

Wei, H., Liu, D. Y., Zhao, B. Y., Feng, Y. B., and Xia, Y. C. (2014). Study on the rheological properties and constitutive Model of shenzhen mucky Soft Soil. *Journal of Engineering Science and Technol. Review* 7, 55–61. doi:10.25103/jestr.073.09

Wu, Q. (2015). *Research on influence of bond water on secondary consolidation and long term strength of soft clay*. Changchun, China: Jilin University.

Xiang, G., Yin, D., Cao, C., and Gao, Y. (2021). Creep modelling of soft soil based on the fractional flow rule: Simulation and parameter study. *Applied Mathematics and Computation* 403, 126190. doi:10.1016/j.amc.2021.126190

Xiao, S., Fang, H., and Wang, Q. (2014). The bound water, consolidation and creep behavior of soft soil. *Journal of Engineering Geol* 22, 531–535.

Yang, Q. (2017). A Study on influence of bound water on viscosity Coefficient of Clays during Consolidation. *Science Technol. and Engineering* 17, 92–96.

Yuan, J., Lin, W., Liu, Z., Fu, Q., Ye, L., and Zhao, J. (2022). An improved Model to describe the Creep behavior of Soft Soil. *Soil Mechanics and Foundation Engineering* 59, 475–483. doi:10.1007/s11204-022-09839-y

Yuan, J., 2014. *Test and analysis on influence of rheological phase material on soft soil rheological property* Guangzhou. China: South China University of Technology.

Zhang, X., and Wang, C. (2011). Viscosity coefficient of structural soft clay. *Rock and Soil Mechanics* 32, 3276–3282.

Zhu, G., Zhu, L., and Yu, C. (2017). Rheological properties of soil: A review. *IOP Conference Series: Earth and Environmental Science* 64, 012011.

Zhu, Y., Kang, B., Fang, C., Wu, G., and Zhang, F. (2019). Analysis of Creep behavior of coastal Soft-soil based on Microstructure features. *Foundation and Basement* 46, 3.

frontiers | Frontiers in Materials

TYPE Original Research
PUBLISHED 16 March 2023
DOI 10.3389/fmats.2023.1137758

Check for updates

OPEN ACCESS

EDITED BY
Xianze Cui,
China Three Gorges University, China

REVIEWED BY
Mingxun Hou,
Guangdong Construction Vocational and Technical College, China
Xiaodan Cai,
Huizhou University, China

*CORRESPONDENCE
Jie Yuan,
Jiey8904@163.com

SPECIALTY SECTION
This article was submitted to Structural Materials, a section of the journal Frontiers in Materials

RECEIVED 04 January 2023
ACCEPTED 27 February 2023
PUBLISHED 16 March 2023

CITATION
Chen J, Tong H, Yuan J, Fang Y and Huang X (2023), Energy multi-scale method to analyze the scale effect of soil particles.
Front. Mater. 10:1137758.
doi: 10.3389/fmats.2023.1137758

COPYRIGHT
© 2023 Chen, Tong, Yuan, Fang and Huang. This is an open-access article distributed under the terms of the Creative Commons Attribution License (CC BY). The use, distribution or reproduction in other forums is permitted, provided the original author(s) and the copyright owner(s) are credited and that the original publication in this journal is cited, in accordance with accepted academic practice. No use, distribution or reproduction is permitted which does not comply with these terms.

Energy multi-scale method to analyze the scale effect of soil particles

Jian Chen[1], Huawei Tong[1], Jie Yuan[1]*, Yingguang Fang[2] and Xiaofeng Huang[2]

[1]School of Civil Engineering, Guangzhou University, Guangzhou, China, [2]School of Civil Engineering & Transportation, South China University of Technology, Guangzhou, China

As a common geological material, soil is a key aspect of construction engineering. Soil has typical multi-scale characteristics, but current multi-scale methods analyze these characteristics only in regard to geometric space. More exploration of the coupling influence mechanism of the basic properties of particles on the microstructure and macroscopic properties of soil is needed. This study analyzed the influence of geometric scale and mineral composition on the surface energy of particles at the microscopic level for development of the energy multi-scale method. Experiments were performed to determine the influence of mineral composition and particle size on the plasticity index (I_p) of the soil, and experimental results are discussed and interpreted quantitatively using the energy multi-scale method. The conclusions derived from this work are as follows: 1) the mineral composition and particle size of the soil can cause interface and surface effects; 2) the comprehensive ratio of micro-force to weight (CRFW) of the particles can be determined using the energy multi-scale method and quantitatively reflects the influence of particle size and mineral composition on the microscopic properties of the soil; and 3) the energy multi-scale method explains the mechanism of the plasticity index of soil and has allowed identification of a new division of soil plasticity. When the CRFW was used as the control index, the plasticity index of the three materials was practically the same, even if the mineral composition and particle sizes of the three materials were different.

KEYWORDS

scale effect, microstructure, energy multi-scale method, adsorbed water, plasticity index

1 Introduction

Soil is one of the most common geological materials and it has clear effects on human life; slope slides, debris flow, and the collapse of building foundations are all due to soil failure (Guzzetti and Peruccacci, 2008; Pham and Kim, 2018; Li and Zhao, 2022; Samprada Pradhan and Toll, 2022; Liang and Ge, 2023). Particles in soils span about five orders of magnitude in size, from rubble to clay, and show obvious cross-scale characteristics in geometric space. Soil particles also show mineral composition diversity, with varying ratios that indicate differences in primary and secondary minerals. These particles, with irregular shapes, different sizes, and varying mineral content, accumulate to form the complex spatial structure of soil (Mitchell and Soga, 2005). During the soil deformation process, particles of different sizes and different mineral composition in different scale-spaces vary in mechanical and deformation performance. Therefore, there is an obvious size effect on soil behavior (Fang and Bo, 2016; Yang and Liu, 2017).

A series of studies showed that particles with different size and mineral composition influenced the force transmission and coordination of deformation between particles at the contact surface between particles at the micro-level and demonstrated the properties of soils at the macro-level. Monkul and Ozden (2007) found that, in the microstructure of fine mixed sand, the interactions between fine and coarse particles affected the overall stress–strain behavior of soils. Chang and Yin (2010) also suggested that the soil was an assembly of particles and that the stress–strain relationship of the assembly was determined by integrating the behavior of the interparticle contacts in all orientations. Sabbar and Chegenizadeh (2017) found that fine soil particles formed a certain structure to reduce the pores between the particles, thereby changing the soil's resistance to liquefaction. Dai and Yang (2015) revealed that the occurrence of liquefaction and temporary reduction of soil strength was mainly ascribed to loss of support from the contacts between fine particles, as well as those between fine and large particles. Li and Zhang (2016) used CT images and FEM to demonstrate that the first cracks usually appeared at soil–gravel interfaces, which is the weak part of a soil–rock mixture. Chen and Fang (2019) found that the diffuse double layers formed on particle surfaces at the microscopic level affected the effective pore for seepage, thereby leading to non-Darcy flow in some clay soils. Gong and Nie (2019) analyzed the type of contact between particles, including coordination number and normal contact force, at the microscopic level, to reveal the contribution of each contact type to the residual shear strength of the soil. Ni and Huang (2020) indicated that, according to the electric double layer theory, mineral particles have an important impact on the properties of soil due to their strong surface electrical characteristics. Phan and Bui (2021) suggested that the shear resistance of the soil is governed mainly by particle contact type and the current fractions of those types. Zhu and Zhang (2020) believed that larger particles were more likely to form an occlusal structure and provide higher frictional force, and that sand was more likely to slide when the particle size was smaller. Bai and Zhou (2021) built a coupled thermo-hydro-mechanical mechanism to explore the soil particle rearrangement of granular thermodynamics. Chen and Tong (2022) found that the charges on particle surfaces adsorb water into the pores, thereby affecting surface characteristics between the particles and thus the permeability characteristics of the soil. Therefore, it is necessary to establish a multi-scale research method linking macro and micro scales to explore the microcosmic mechanism behind the complex scale phenomenon of soil; this endeavor has become the frontier of current geotechnical field research (Mingjing, 2019).

Scholars have proposed different multi-scale methods to research the scale phenomenon of soil. First, the strain gradient theory and the couple stress theory (Cosserat, 1909; Ashby, 1970) were proposed to solve the problem of the granularity of materials and rotation of particles, as well as the discontinuity in the stress and strain transformation between the contact interface of the particles when entering a certain microscopic space scale. Researchers continued to improve these two theories for use in soil. For example, Mühlhaus (1989) derived a continuous model of regular structures within the framework of the Cosserat theory. Based on this model, the ultimate load problem of tunnel statics was solved by using the finite element method. After homogenization, Mühlhaus and Oka (1996) introduced continuous concepts, such as stress and couple stress, to directly homogenize discrete motion equations to obtain a general continuous model for granular media. Oda and Iwashita (2000), through tests on sand, found that couple stresses existed in a shear band in a manner consistent with the change of the particle rotation gradient from negative to positive. The presence of small couple stress still plays an important role in the development of microstructure in shear bands. Wang and Zhang (2003) theoretically analyzed the stability and instability sliding of an elastic rock mass in a shear zone and introduced the strain gradient plasticity theory, which allowed determination of the theoretical relationship between shear stress and the relative displacement of the upper and lower walls of a shear zone. Lu and Cui (2003) processed numerical simulation to investigate the influences of shear strain gradient and other factors on the evolution of a shear band. In the framework of a Cosserat continuum, Gudehus and Nuebel (2004) explored the evolution of a sand shear band trough using a numerical method, and the results showed that shear bands can evolve spontaneously in the interior of a granular body, even under homogeneous stress or displacement boundary conditions. Riahi and Curran (2009) used the finite element method to implement the adopted Cosserat formulation in buckling analysis of three-dimensional layered continua. Research in this area has continued to increase (Chu and Yu, 2012; Tang and Song, 2015; Tang and Wei, 2020; Tang and Wei, 2021; Borst and Alizadeh, 2022). The couple stress and strain gradient theories may be used to solve some problems with scale effects of the soil caused by the change in research scale, but these theories are based on the continuum; therefore, the anisotropy problem caused by granularity and mineral composition are not solvable using the same methods.

The discrete element method (DEM) takes the soil particle as the basic research unit, clearly describes the particle properties of the soil, and describes the macroscopic properties of the soil through the interaction of particle groups (Thornton, 2000). This method has become popular for studying multi-scale phenomena of soil. Zeghal and Shamy (2008) analyzed the liquefaction of saturated soil particles in loosely cemented sediments through the coupling of discrete elements and continuous elements. Li and Wan (2011) combined the DEM with the finite element method (FEM) and proposed a method for multi-scale analysis of granular materials at two macroscopic levels. Nguyen and Combe (2014) proposed a multi-scale modeling method for cohesive granular materials; at the micro-level, the DEM was used to simulate dense particle accumulation, and at the macro level, the numerical solution was obtained through the FEM. Zhao and Feng (2017) conducted a 3D numerical study on the formation of landslide dams in open fluid channels by using the DEM combined with computational fluid dynamics. Additionally, Liu and Zhixiang (2021) constructed a numerical model capable of reproducing the estimation of the impact of debris flow by coupling FEM and DEM, Zhang and Zhang (2022) conducted DEM simulations to quantify the relationship between fine particle loss and upscaling from particle to cell

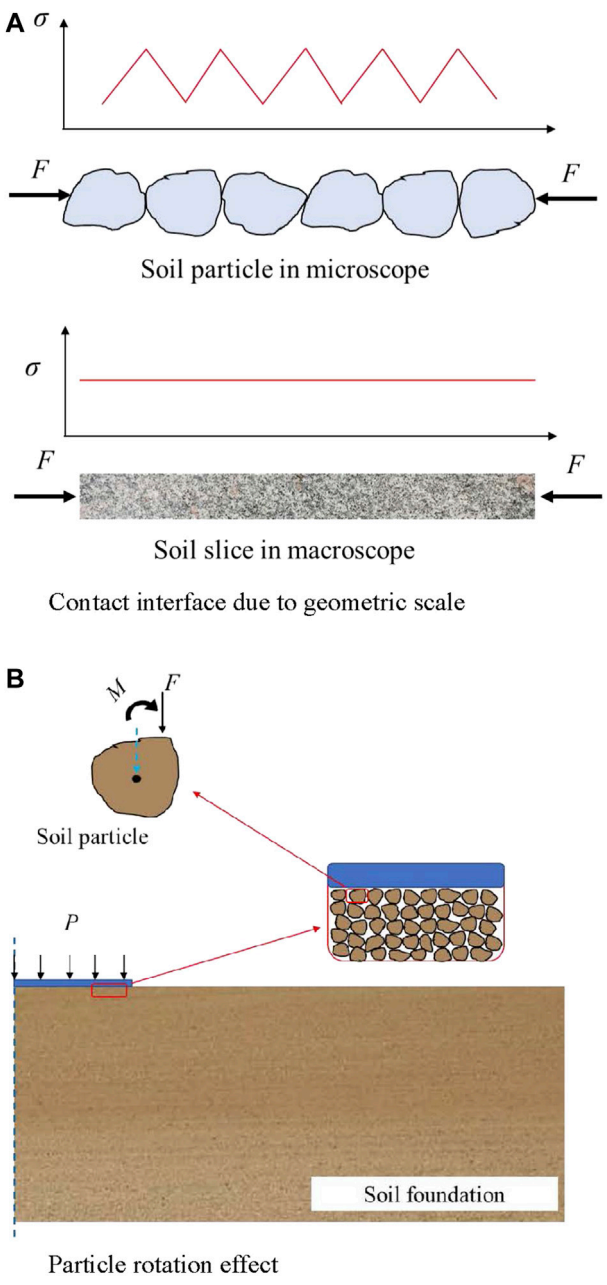

FIGURE 1
Scale effect of soil.

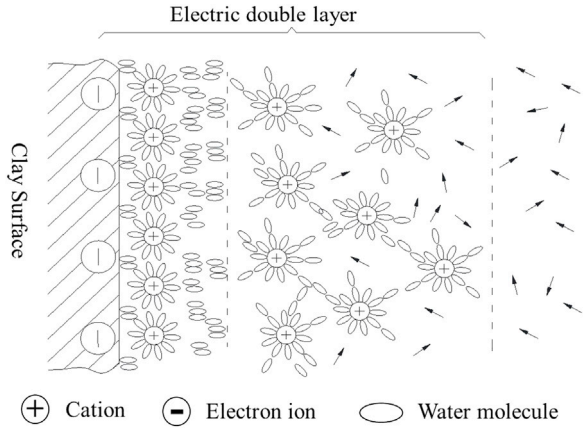

FIGURE 2
Diffuse electric double layer.

and then revealed the multi-scale response of seepage erosion in sandy strata, and Fang and Yang (2023) analyzed the progressive failure process of the stratified rock mass through the analysis of contact fracture events and the evolution of contact forces using the DEM-FEM numerical method. DEM and the DEM-FEM coupling method can intuitively display the particle properties of soil. However, limited by current computing capability, the scale of DEM or DEM-FEM models is generally small (Yang and Wang, 2023) and the particles in the models are greatly simplified. For example, for fine-grained sand–gravel mixed soil, the DEM method only models large particles and simplifies fine particles into contact parameters between particles to reduce the amount of calculation required. Clearly, this method cannot reflect the effect of gradation of particles on soil properties. In addition, due to the unclear mechanism of the coupling effects of factors such as particle size and mineral composition on the particle contact surface, the various mineral compositions and the complex contact properties between the particles result in cumbersome calibration of contact parameters in the DEM that ultimately lacks credibility.

The multi-scale phenomenon of soil has long been known, and a variety of multi-scale analysis methods have been developed. However, there are still defects in these methods when used for solving some multi-scale problems with soil. Regardless of the kind of model that is constructed to connect the macro and micro, the transmission of force between particles, the coordination of strain, and even the construction of soil microstructure are realized through the contact surface. The impact of various characteristics of soil particles at the microscopic level on soil engineering properties should be directly reflected on the contact surface between particles, and the surface energy of soil particles determines the surface of particles and the contact surface between particles. Therefore, in this study, the comprehensive ratio of micro-force to weight was proposed to quantitatively analyze the coupled influence of size and mineral composition of particles on the surface energy of soil particles. We used this energy multi-scale method of analysis to reveal the mechanism of the soil plasticity index. Our results are significant as they support accurate calibration of contact parameters of the DEM method and in promoting the application of the DEM method in soil.

2 Energy multi-scale method

2.1 Energy multi-scale property of soil

Materials are not infinitely separable, and the intrinsic properties of a particle in the internal length range will affect the mechanical properties of the microstructure. Interface effects and surface effects are ignored at the macroscopic level, but they

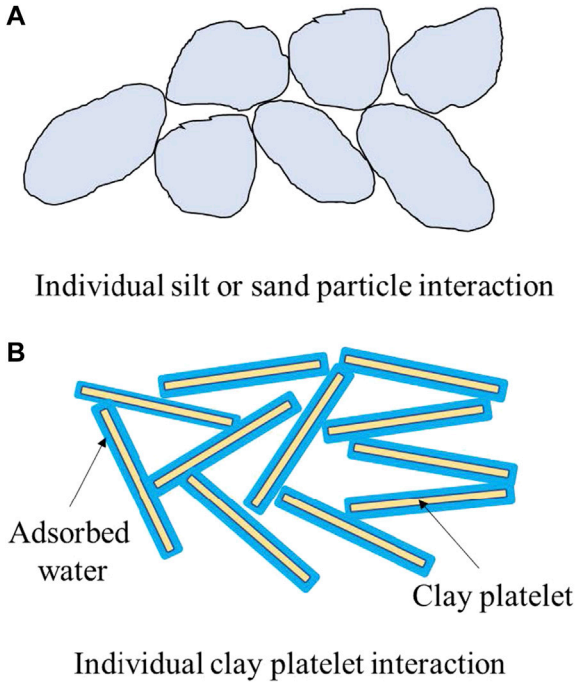

FIGURE 3
Contact states of different particles.

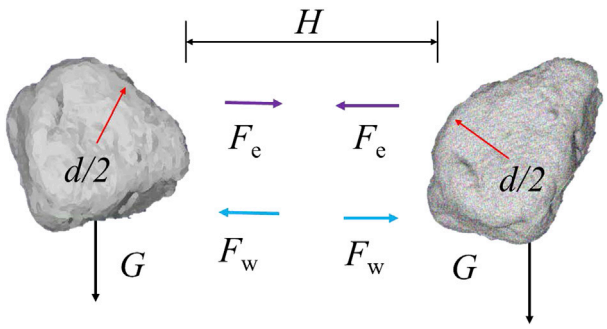

FIGURE 4
Microscopic force between particles.

play important roles at the microscopic level (Chiu and Chen, 2011; Li and Mi, 2019; Lu and Guo, 2019; Wang and Zhang, 2019). Soil shows a typical multi-scale property; that is, the stress and deformation of soil are different in each scale space. A continuous soil slice at the macroscopic level is shown in Figure 1A, which demonstrates that the stress distribution in the soil slice is nearly uniform under the load. However, at the microscopic level, where the research focus is a single soil particle, contact surface discontinuity causes the stress to appear abruptly on the contact surfaces of the particles. In Figure 1B, the cross-scale deformation behavior of the foundation from the macro-level to the micro-level is illustrated. At the macroscopic level, the foundation produced continuous compressive deformation under uniform load, whereas at the microscopic level, the soil particles showed an obvious rotational effect. Microscopically, the particles appeared in individual forms and the contact between particles was highlighted. However, macroscopically, the number of particles in a soil slice is huge and the individuality of particles is weakened; therefore, particle groups are treated as a continuous medium and the contact between particles is no longer considered. In general, the effects of interface properties between particles on soil properties change at different scales.

For soil particles, when particle size decreases, the specific surface area of particles and the proportion of charges on the surface of particles increase gradually; thus, the ability to adsorb ions and water molecules increases. As a result, the adsorbed water and the electric double layer formed on the surface of the particles are more obvious, which in turn affects the contact surface between the particles. At the same time, a typical soil mixture contains clay minerals and non-clay minerals. Most clay minerals have excess negative charges on the surface of particles due to isomorphous replacement. The negative charges adsorb the polar water molecules and cations to form an electric double layer (Figure 2). Clay particles tend to be smaller in size and have a larger specific surface area; therefore, the volume of adsorbed water and the electric double layer on the surface of particles is considerably larger than the volume of the particles. When clay particles are in contact, the contacts occur mainly between the water films on the particle's surface. For non-clay minerals, the ability to adsorb ions and water molecules is very weak because the excess charges on the surface of the non-clay minerals are less; the adsorbed water on the surface of such mineral particles is so thin that the contact between particles is mainly direct contact between mineral crystals. For soil materials, both particle size and mineral composition influence the properties of the particle surface, thereby affecting the contact surface between particles, as shown in Figure 3. Therefore, as a granular medium, soil particles also exhibit the surface effects and interface effects.

The surface and interface effects of soil particles affect the soil microstructure (Guo and Yu, 2019) and thereby affect the soil engineering properties at the macroscopic level, which is the basis for the soil-scale phenomenon. For example, particle size affects the occlusion between sand particles; increased coarse particle content leads to increased microstructure rolling and increased internal friction angle of the soil at the macroscopic level; the electric double layer (DEL) and the adsorbed water on the surface of clay particles result in a cohesive effect among the particles with increased cohesive force and increased clay mineral content; the balance between the microscopic force and the gravity of the particles affects the formation of the microscopic and macroscopic structure of the soil; at the same time, the mineral components have different adsorption water states on the surface, which will also directly affect the state of the liquid flowing over its surface, thereby affecting the permeability characteristics of the soil.

2.2 Energy multi-scale equation for soil particles

The surface state of a particle is largely determined by the particle's ability to adsorb water or other ions, and this ability is

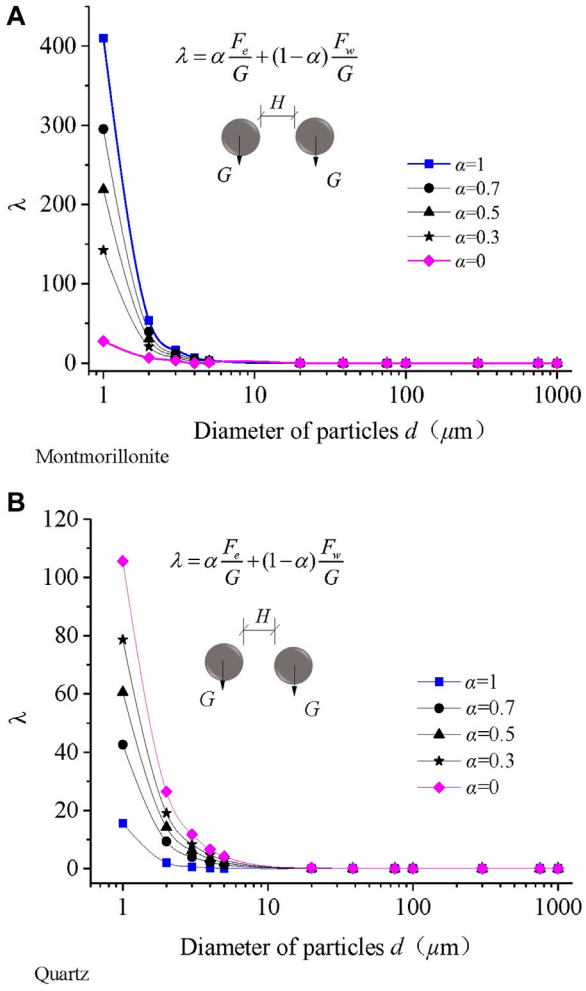

FIGURE 5
Relationship of CRFW with particle diameter.

called the particle's surface energy. This adsorption energy is mainly manifested as the van der Waals force between particles and the electric field force generated by the excess charges on the particle surface. At the micro-level, the forces with high size factor power, such as gravity and inertial force, are relatively small; while the forces with low size factor power, such as surface tension, van der Waals force, and electric field force, are relatively large, as shown in Figure 4. The surface and contact interface features of the particles are produced mainly by the direct action of these forces. Among these forces, gravity, van der Waals force, and Coulomb force can be used to characterize both the particle size and the mineral composition of soil particles.

In this study, a relationship between gravity, van der Waals force, and Coulomb force was established. As introduced previously, these forces can be used to characterize the adsorption energy of the particle surface. Therefore, our energy multi-scale method involves calculation of the ratio of the micro-Coulomb force to gravity and the ratio of the micro-van der Waals force to gravity. The equations used for these calculations are expressed as follows:

$$\lambda_e = \frac{F_e}{G} = \frac{1}{4\pi\varepsilon_0}\frac{q_1 q_2}{r^2}\Big/\frac{\rho g\pi d^3}{6} = \frac{3q_1 q_2}{2\pi^2\varepsilon_0 r^2 \rho g d^3}, \quad (1)$$

$$\lambda_w = \frac{F_w}{G} = \frac{Ad}{24H^2}\Big/\frac{\rho g\pi d^3}{6} = \frac{A}{4\rho g\pi d^2 H^2}, \quad (2)$$

where λ_e and λ_w are the ratio of micro-Coulomb force to gravity and the ratio of micro-van der Waals force to gravity, respectively, F_e is Coulomb force, F_w is van der Waals force, G is gravity, ε_0 is vacuum permittivity, q_1 and q_2 are particle charge, r is particle center spacing, ρ is the particle density, d is the particle diameter, A is the Hamaker constant, and H is the clear particle spacing. Soil particles exist mainly in a water environment, and the amount of charge associated with the particles can be obtained according to colloid and interface chemistry and electrostatic theory (Helmy, 1998; Missana and Adell, 2000):

$$q = 2\pi\varepsilon_0\phi_0, \quad (3)$$

where φ_0 is the particle surface potential and the clay particle surface potential can be determined by the cation exchange capacity (CEC) method. For the convenience of calculation and the unification of measurement indicators, the adjustment coefficient α is used to combine λ_e and λ_w as one parameter, and this parameter is called the comprehensive ratio of micro-force to weight (CRFW). The expression of λ is as follows:

$$\lambda = \alpha\lambda_e + (1-\alpha)\lambda_w = \alpha\frac{F_e}{G} + (1-\alpha)\frac{F_w}{G}. \quad (4)$$

The adjustment coefficient α must be determined according to the properties of the material. Taking the common soil minerals montmorillonite and quartz as examples, the CRFW of these two mineral particles were calculated. When the value of the adjustment coefficient α was varied, the CRFW of montmorillonite and quartz particles also changed according to particle size; these data are displayed in Figure 5. As shown in the figure, when α is 0 the λ degenerates as λ_w and when α is 1 the λ degenerates as λ_e, respectively.

Figure 5 demonstrates that the relationships between λ and the particle sizes of quartz and montmorillonite were basically the same, and when particle size decreased, λ increased gradually. The specific surface area of particles is relative to particle size. As a result, the amount of negative charge on the particle surface increased and the surface energy increased; therefore, the thickness of the water film on the particle surface became larger and the interface between particles was mainly soft contact between water layers. In contrast, with increased particle size, the effect of adsorbed water on the particle surface decreased, and the contact between particles was mainly hard contact between mineral crystals. It is reasonable to use the CRFW to describe the variation of soil properties with particle size. At the same time, it can be seen from Figure 5 that, although the particle size of two different mineral particles is the same, their CRFW values can be very different. As demonstrated previously, compared with non-clay minerals, the isomorphic replacement of clay minerals is more obvious, and the negative charge density of particle surfaces is higher, so the surface effect is more obvious. This also shows the rationality of the formula for CRFW. In summary, the CRFW in the energy multi-scale method reflects the mechanism of property changes based on particle size and mineral composition at the micro-level.

TABLE 1 Sample characteristics.

Sample No.	Composition	Sample No.	Composition
YSX-1	100%, montmorillonite (M)	YSX-8	M (60%) + Q (20%) + F (20%)
YSX-2	100%, illite (I)	YSX-9	I (20%) + Q (40%) + F (40%)
YSX-3	100%, kaolinite (K)	YSX-10	I (40%) + Q (30%) + F (30%)
YSX-4	100%, quartz (Q)	YSX-11	M (60%) + Q (20%) + F (20%)
YSX-5	100%, feldspar (F)	YSX-12	K (20%) + Q (40%) + F (40%)
YSX-6	M (20%) + Q (40%) + F (40%)	YSX-13	K (40%) + Q (30%) + F (30%)
YSX-7	M (40%) + Q (30%) + F (30%)	YSX-14	K (60%) + Q (20%) + F (20%)

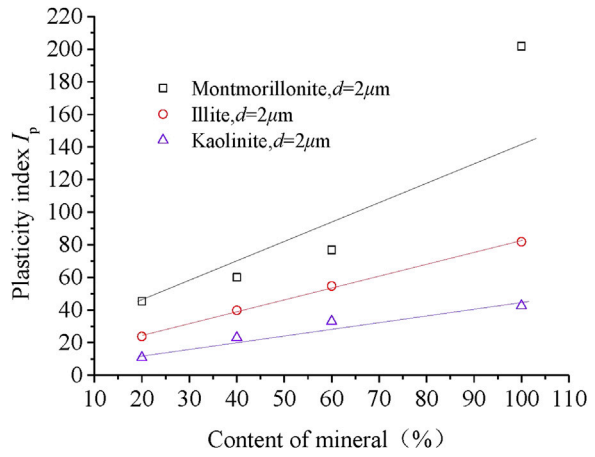

FIGURE 6
Influence of soil mineral content on sample plasticity index.

3 The plasticity index of soil explained by the energy multi-scale method

3.1 Experimental plan

The plasticity index of soil is important for engineering endeavors involving soils such as clay and silty clay. A large number of studies have found that the shear strength, permeability coefficient, and liquefaction index of plastic soils were directly or indirectly related to the plasticity index of soil. Furthermore, the plasticity index of plastic soil reflects the water adsorption capacity of the surface of the particles, which is a direct reflection of the surface energy of the particles. At the same time, the mineral composition and the diameter of the soil particle are the main factors in the calculation of the CRFW by the energy multi-scale method. Therefore, in this study, the surface potential and the diameter of the particles were tested first. Next, the samples with different mineral compositions and relative content, as well as different particle sizes, were prepared to assess the plasticity index of the soil. In terms of soil mineral composition, three typical clay minerals, montmorillonite, kaolinite, and illite, and two non-clay minerals, quartz and feldspar, were selected for these experiments. Due to the high purity of commercial soil minerals, customized commercial soil mineral powders were selected as test material. Samples with clay mineral content of 100%, 60%, 40%, 20%, and 0% were assessed, and the diameter of all mineral particles was 2 μm. Sample characteristics are summarized in Table 1.

The dried mineral powders were mixed evenly according to the designed mass ratio, then a small amount of water was added to wet the mineral particles of the soil; the samples were left to stand overnight. Finally, the liquid and plastic limits of the aforementioned soil samples were measured using a liquid–plastic limit tester, and the plasticity index of each group of samples was calculated using the liquid and plastic limit data.

3.2 Results and discussion

After the liquid–plastic test, the plasticity index (I_p) of each sample was assessed, as shown in Figure 6; the I_p of all soil samples increased with increased clay mineral content, but the three clay mineral samples had substantially different I_p values despite having the same particle size and content.

According to the energy multi-scale method, the ratio of micro-Coulomb force to gravity and the ratio of micro-van der Waals force to gravity can be calculated using equations 1 and 2 and the elements

TABLE 2 CRFW and I_p of three types of mineral particles (d = 2 μm).

Type	Diameter (μm)	λ_e	λw	λ_e/λ_e (K)	$\lambda w/\lambda w$ (K)	Ip/Ip (K)
Montmorillonite	2	53.8	6.89	6.91	0.73	4.8
Illite	2	17.2	7.54	2.21	0.79	1.68
Kaolinite	2	7.79	9.49	1	1	1

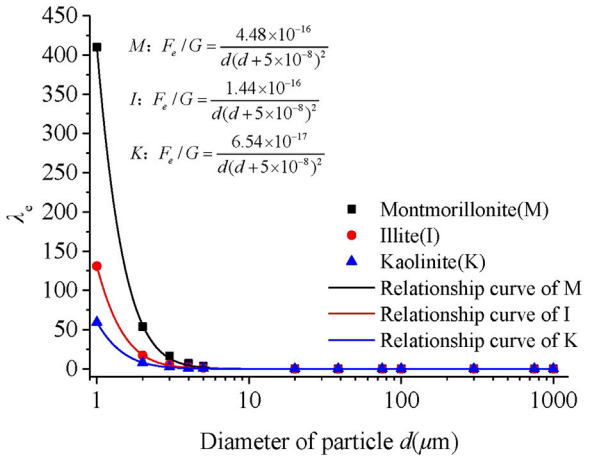

FIGURE 7
Relationship of λ_e with particle size.

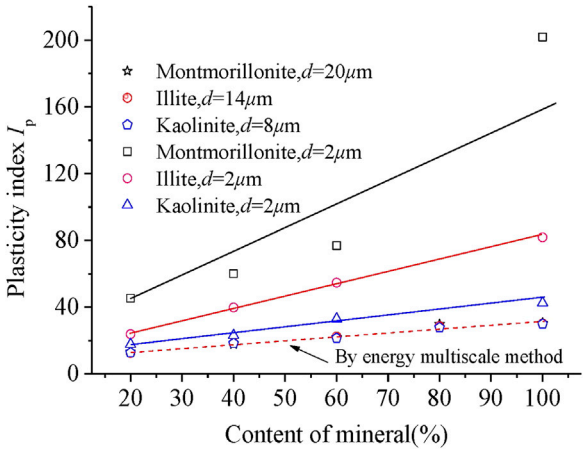

FIGURE 8
Plasticity index of soil samples with different mineral contents using the energy multi-scale method.

TABLE 3 λ_e **of mineral particles with different diameters.**

Type	Montmorillonite	Illite	Kaolinite
Diameter (μm)	20	14	8
λ_e	0.0557	0.0525	0.0558

from the literature (Huang, 2018). When d = 2 μm, λ_e, and λ_w of the three materials could be calculated and is shown in Table 2; the λ_e values of montmorillonite and illite were 6.91 and 2.1 times the value of kaolinite, respectively, whereas the λ_w values of montmorillonite and illite were 0.73 and 0.79 times that of kaolinite, respectively, and the I_P values of montmorillonite and illite were 4.8 and 1.68 times that of kaolinite, respectively. The difference in λ_w between these minerals was not large. All samples were composed of clay minerals; therefore, the adjustment coefficient α could be set to 1 for the test. As showed in Figure 5, the λ_e is bigger than λ_w for montmorillonite , while λ_e is samller than λ_w for Quartz ,within a certain particle size range. These data indicate that, in clay, the Coulomb force of particles has a greater influence on the particle surface adsorption energy, and the contribution value of λ_e to λ is larger for clay.

As described previously, the surface state and interface state are the basis of stress transfer and deformation coordination, and the surface state and contact state of the particles at the microscopic level determine the internal structure and engineering properties of the soil. The adsorbed water and the electric double layer are mainly caused by the negative charges on the surface of the particles. The more charges on the particle surface, the stronger the surface adsorption energy of the particle, and the relatively thicker the adsorbed water layer. For clay minerals, the charge density of the particles is high, and the particle size is small, so the thickness of the adsorbed water layer on the surface of the particles is relatively large for a particle with such a tiny diameter. Currently, the properties of the interface between particles are generally determined by the adsorbed water layer. Therefore, many engineering properties of clay soils are affected by the adsorbed water layer. The plasticity index of clay minerals in this study was typical, and the plasticity index refers to the relative water content of plastic soil from the plastic state to the flowing state. It is an important index for measurement of surface adsorption capacity of mineral particles to free water in the soil, and it is also a typical measure of performance of the microscopic adsorption energy of mineral particles at the macroscopic level. The surface charge density of clay mineral particles such as montmorillonite is largest, illite has the second largest, and kaolinite has the smallest, so the plasticity index of each of the three minerals decreases accordingly, as shown in Figure 6. As shown in Table 2, λ_e of montmorillonite is the largest, that of illite is the second largest, and that of kaolinite is the smallest. These data indicate that the energy multi-scale method quantitatively reflects the adsorption capacity of the microscopic surface of particles. The adsorbed water layer discussed in this paper is relatively thick compared to the particle diameter. When the particle size is large, even if the adsorbed water layer on the surface of the particle is of the same thickness as that of a smaller particle, the relative thickness can be easily ignored compared to the huge particle size. Therefore, using the energy multi-scale method, both λ_e and λ_w decreased with increased particle size, as shown in Figure 5. In addition, we assessed the plasticity index of each of the three clay minerals when the λ_e parameter was controlled. First, according to Eq. 1 and Eq. 2, the relationship curves between the λ_e and particle size of each of the three materials were calculated, as shown in Figure 7.

The particle diameters of montmorillonite, illite, and kaolinite were set to 20 μm, 14 μm, and 8 μm, respectively, and the λ_e of each of the three materials were caculated from the fitted equation in Figure 7 and the results were shoud in Table 3.

Figure 8 indicates that the plasticity indices of these three clay minerals, calculated using the energy multi-scale method, are very close to each other and nearly on the same straight line.

Therefore, there are benefits to use of this method to classify clay soil samples, as the parameter λ in the energy multi-scale method accounts for the influence of mineral composition and particle size on the microscopic surface and interface states of the particles.

4 Conclusion

Soil has an obvious scale effect, and the microscopic characteristics of particles affect the macroscopic properties of soil. This study proposed an energy multi-scale method based on the microscopic properties of particles and established a formula for calculating the CRFW. Additionally, the mechanism of clay plasticity index change was quantitatively explained by the CRFW. The conclusions of this study are as follows:

(1) Both mineral composition and particle size can influence the surface energy of particles and cause interface and surface effects. Higher clay content is associated with greater surface charge of the soil, which results in greater surface adsorption energy and greater relative thickness of the adsorbed water layer on the particle surface. At the same time, when soil particle size is very small, the specific surface area of the particles is large and the thickness of the adsorbed water layer is large. At the microscopic level, the interaction between particles occurs primarily at the contact interface, so these two factors affect the surface characteristics of the particle and thereby affect macroscopic soil properties.

(2) The CRFW of the particles calculated using the energy multi-scale method quantitatively reflects the influence of particle size and mineral composition on the microscopic properties of the soil. The energy multi-scale method takes the microscopic force of the particle as the research object and establishes the CRFW. When the particle size increases, the CRFW of the particle decreases. When the type of the particle changes, the CRFW increases with an increase in particle surface charge.

(3) The energy multi-scale method explains the mechanism of the plasticity index of plastic soil and allowed identification of a new division of soil plasticity. The CRFW quantitatively predicts the influence of mineral composition on the soil plasticity index. When the CRFW is used as the control index, even if mineral composition and particle size of materials are different, the plasticity index of the materials is the same. The multi-scale method may also solve the scale effect of soils in terms of energy scale.

Data availability statement

The original contributions presented in the study are included in the article/supplementary material; further inquiries can be directed to the corresponding author.

Author contributions

Conceptualization, JC and FY; methodology, JC; resources, HT; data curation, XH; writing—original draft preparation, JC; writing—review and editing, JY; supervision, YF; funding acquisition, JY.

Funding

The study was supported by the following fundations: Guangdong Basic and Applied Basic Research Fundation No.20223A1515030051 Funder:JY. Guangdong Basic and Applied Basic Research Fundation No.2022A1515110793 Funder: JC.

Conflict of interest

The authors declare that the research was conducted in the absence of any commercial or financial relationships that could be construed as a potential conflict of interest.

Publisher's note

All claims expressed in this article are solely those of the authors and do not necessarily represent those of their affiliated organizations, or those of the publisher, the editors, and the reviewers. Any product that may be evaluated in this article, or claim that may be made by its manufacturer, is not guaranteed or endorsed by the publisher.

References

Ashby, M. F. (1970). The deformation of plastically non-homogeneous materials. *Philos. Mag.* 21 (170), 399–424. doi:10.1080/14786437008238426

Bai, B., Zhou, R., Cai, G., Hu, W., and Yang, G. (2021). Coupled thermo-hydro-mechanical mechanism in view of the soil particle rearrangement of granular thermodynamics. *Comput. Geotechnics* 137 (8), 104272. doi:10.1016/j.compgeo.2021.104272

Borst, R. D., Alizadeh, S. S., and Hageman, T. (2022). Non-associated Cosserat plasticity. *Int. J. Mech. Sci.* 230, 107535. doi:10.1016/j.ijmecsci.2022.107535

Chang, C. S., Yin, Z. Y., and Hicher, P. Y. (2010). Micromechanical analysis for interparticle and assembly instability of sand. *J. Eng. Mech.* 137 (3), 155–168. doi:10.1061/(asce)em.1943-7889.0000204

Chen, J., Fang, Y., Gu, R., Shu, H., Ba, L., and Li, W. (2019). Study on pore size effect of low permeability clay seepage. *ARABIAN J. GEOSCIENCES* 12 (7), 238. doi:10.1007/s12517-019-4375-3

Chen, J., Tong, H., Chen, J., Tong, H., Yuan, J., et al. (2022), Permeability prediction model modified on kozeny-carman for building foundation of clay soil. *Buildings* 12(11), 1798. doi:10.3390/buildings12111798

Chiu, M., and Chen, T. (2011). Higher-order surface stress effects on buckling of nanowires under uniaxial compression. *Procedia Eng.* 10, 397–402. doi:10.1016/j.proeng.2011.04.067

Chu, X., Yu, C., and Xu, Y. (2012). The dilatancy and numerical simulation of failure behaviorof granular materials based on Cosserat model. *Interact. Multiscale Mech. Int. J.* 5 (2), 157–168. doi:10.12989/imm.2012.5.2.157

Cosserate, E. (1909). *Théorie de corps deformable*. Pairs: Herman.

Dai, B., and Yang, J. (2015). A numerical analysis of the shear behavior of granular soil with fines. *Particuolog* 2015(4), 13. doi:10.1016/j.partic.2014.08.010

Fang, X., Yang, J., Zhang, X., Zhang, C., Wang, S., and Xie, Y. (2023). Numerical modeling of open TBM tunneling in stratified rock masses using a coupled FDM-

DEM method. *Comput. Geotechnics* 156, 105251. doi:10.1016/j.compgeo.2023.105251

Fang, Y. G., and Bo, L. (2016). Multiscale problems and analysis of soil mechanics. *Mech. Mater.* 103, 55–67. doi:10.1016/j.mechmat.2016.09.003

Gong, J., Nie, Z., Zhu, Y., Liang, Z., and Wang, X. (2019). Exploring the effects of particle shape and content of fines on the shear behavior of sand-fines mixtures via the DEM. *Comput. Geotechnics* 10, 161–176. doi:10.1016/j.compgeo.2018.10.021

Gudehus, G., and Nuebel, K. (2004). Evolution of shear bands in sand. *Geotechnique* 54 (3), 187–201. doi:10.1680/geot.54.3.187.36346

Guo, Y., and Yu, X. (2019). "A holistic computational model for prediction of clay suspension structure." *Int. J. Sediment Res.* 34 (34), 345. doi:10.1016/j.ijsrc.2018.12.002

Guzzetti, F., Peruccacci, S., Rossi, M., and Stark, C. P. (2008). The rainfall intensity–duration control of shallow landslides and debris flows: An update. *Landslides* 5 (1), 3–17. doi:10.1007/s10346-007-0112-1

Helmy, A. K. (1998). The limited swelling of montmorillonite. *J. Colloid & Interface Sci.* 207 (1), 128–129. doi:10.1006/jcis.1998.5739

Huang, X. (2018). *Division of energy scale and analysis of engineering properties for soil granular group*. Guangzhou: South China University of Technology.

Li, C. S., Zhang, D., Du, S. S., and Shi, B. (2016). Computed tomography based numerical simulation for triaxial test of soil–rock mixture. *Comput. Geotechnics* 73, 179–188. doi:10.1016/j.compgeo.2015.12.005

Li, X., and Mi, C. (2019). Effects of surface tension and Steigmann–Ogden surface elasticity on Hertzian contact properties. *Int. J. Eng. Sci.* 145, 103165. doi:10.1016/j.ijengsci.2019.103165

Li, X., and Wan, K. (2011). A bridging scale method for granular materials with discrete particle assembly – Cosserat continuum modeling. *Comput. Geotechnics* 38 (8), 1052–1068. doi:10.1016/j.compgeo.2011.07.001

Li, Z., Zhao, G., Deng, X., Zhu, J., and Zhang, Q. (2022). Further development of distinct lattice spring model for stability and collapse analysis of deep foundation pit excavation. *Comput. geotechnics* 144, 104619. doi:10.1016/j.compgeo.2021.104619

Liang, X., Ge, Y., Zeng, L., Lyu, L., Sun, Q., Sun, Y., et al. (2023). Debris flow susceptibility based on the connectivity of potential material sources in the Dadu River Basin. *Eng. Geol.* 312, 106947. doi:10.1016/j.enggeo.2022.106947

Liu, C., Zhixiang, Y., and Zhao, S. (2021). A coupled SPH-DEM-FEM model for fluid-particlestructure interaction and a case study of Wenjia gully debris flow impact estimation. *Landslides* 18 (7), 2403–2425. doi:10.1007/s10346-021-01640-6

Lu, L., Guo, X., and Zhao, J. (2019). A unified size-dependent plate model based on nonlocal strain gradient theory including surface effects. *Appl. Math. Model.* 68, 583–602. doi:10.1016/j.apm.2018.11.023

Lu, X., and Cui, P. (2003). The influence of strain gradient on the shear band in a saturated soil. *Iran. J. Sci. Technol. Transaction B Eng.* 27 (1), 57–62.

Mingjing, J. (2019). New paradigm for modern soil mechanics: Geomechanics from micro to macro. *Chin. J. Geotechnical Eng.* 41 (2), 195–254. doi:10.11779/CJGE201902001

Missana, T., and Adell, A. (2000). On the applicability of DLVO theory to the prediction of clay colloids stability. *J. Colloid Interface Sci.* 230 (1), 150–156. doi:10.1006/jcis.2000.7003

Mitchell, J. K., and Soga, K. (2005). *Fundamentals of soil behavior*. Hoboken: John Wiley & Sons.

Monkul, M. M., and Ozden, G. (2007). Compressional behavior of clayey sand and transition fines content. *Eng. Geol.* 89 (3-4), 195–205. doi:10.1016/j.enggeo.2006.10.001

Mühlhaus, Dr. (1989). Application of Cosserat theory in numerical solutions of limit load problems. *Ingenieur-Archiv* 59 (2), 124–137. doi:10.1007/bf00538366

Mühlhaus, H. B., and Oka, F. (1996). Dispersion and wave propagation in discrete and continuous models for granular materials. *Int. J. Solids Struct.* 33 (19), 2841–2858. doi:10.1016/0020-7683(95)00178-6

Nguyen, T. K., Combe, G., Caillerie, D., and Desrues, J. (2014). FEM × DEM modelling of cohesive granular materials: Numerical homogenisation and multi-scale simulations. *Acta Geophys.* 62 (5), 1109–1126. doi:10.2478/s11600-014-0228-3

Ni, H., and Huang, Y. (2020). Rheological study on influence of mineral composition on viscoelastic properties of clay. *Appl. Clay Sci.* 187, 105493. doi:10.1016/j.clay.2020.105493

Oda, M., and Iwashita, K. (2000). Study on couple stress and shear band development in granular media based on numerical simulation analyses. *Int. J. Eng. Sci.* 38 (15), 1713–1740. doi:10.1016/s0020-7225(99)00132-9

Pham, K., Kim, D., Choi, H. J., Lee, I. M., and Choi, H. (2018). A numerical framework for infinite slope stability analysis under transient unsaturated seepage conditions. *Eng. Geol.* 243, 36–49. doi:10.1016/j.enggeo.2018.05.021

Phan, Q. T., Bui, H. H., Nguyen, G. D., and Bouazza, A. (2021). Effect of particle rolling resistance on drained and undrained behaviour of silty sand. *Acta Geotech.* 16 (3), 2657–2682. doi:10.1007/s11440-020-01128-y

Riahi, A., Curran, J. H., and Bidhendi, H. (2009). Buckling analysis of 3D layered structures using a Cosserat continuum approach. *Comput. Geotechnics* 36 (7), 1101–1112. doi:10.1016/j.compgeo.2009.03.012

Sabbar, A. S., Chegenizadeh, A., and Nikraz, H. (2017). Static liquefaction of very loose sand-slag-bentonite mixtures. *Soils Found. -Tokyo-* 57 (3), 341–356. doi:10.1016/j.sandf.2017.05.003

SampradaPradhan, T., Toll, D. G., Rosser, N. J., and Brain, M. J. (2022). An investigation of the combined effect of rainfall and road cut on landsliding. *Eng. Geol.* 307, 106787. doi:10.1016/j.enggeo.2022.106787

Tang, H., and Song, C. (2015). Cosserat continuum model and its application to the studies of progressive failure. *Jpn. Geotech. Soc. Spec. Publ.* 2 (18), 703–708. doi:10.3208/jgssp.chn-57

Tang, H., Wei, W., Liu, F., and Chen, G. (2020). Elastoplastic Cosserat continuum model considering strength anisotropy and its application to the analysis of slope stability. *Comput. Geotechnics* 117, 103235. doi:10.1016/j.compgeo.2019.103235

Tang, H., Wei, W., Song, X., and Liu, F. (2021). An anisotropic elastoplastic Cosserat continuum model for shear failure in stratified geomaterials. *Eng. Geol.* 293 (1), 106304. doi:10.1016/j.enggeo.2021.106304

Thornton, C. (2000). Numerical simulations of deviatoric shear deformation of granular media. *Geotechnique* 50 (1), 43–53. doi:10.1680/geot.2000.50.1.43

Wang, X., and Zhang, Z. (2003). Unified criterion for stability failure of rock specimens subject to uniaxial tension, direct shear and uniaxial compression based on gradient-dependent plasticity. *Rock Soil Mech.* 24S, 138–142. doi:10.16285/j.rsm.2003.s2.032

Wang, Y., Zhang, B., Zhang, X., Liu, J., and Shen, H. (2019). Two-dimensional fretting contact analysis considering surface effects. *Int. J. Solids Struct.* 170, 68–81. doi:10.1016/j.ijsolstr.2019.04.027

Yang, T., Liu, H. Y., and Tang, C. (2017). Scale effect in macroscopic permeability of jointed rock mass using a coupled stress–damage–flow method. *Eng. Geol.* 228, 121–136. doi:10.1016/j.enggeo.2017.07.009

Yang, W., Wang, S., Kang, W., Yu, T., and Li, Y. (2023). A unified high-order model for size-dependent vibration of nanobeam based on nonlocal strain/stress gradient elasticity with surface effect. *Int. J. Eng. Sci.* 182, 103785. doi:10.1016/j.ijengsci.2022.103785

Zeghal, M., and Shamy, U. E. (2008). Liquefaction of saturated loose and cemented granular soils, *Powder Technol.*, 184 254–265.doi:10.1016/j.powtec.2007.11.032

Zhang, D., Zhang, X., and Du, W. (2022). DEM-FEM based numerical analysis on mechanical responses of sandy soil and pipeline to seepage erosion. *Eng. Geol.* 310 (5), 106868. doi:10.1016/j.enggeo.2022.106868

Zhao, T., and Feng, D., (2017). Coupled DEM-CFD investigation on the formation of landslide dams in narrow rivers. *Landslides* 14 (1), 189–201. doi:10.1007/s10346-015-0675-1

Zhu, Z., Zhang, F., Dupla, J. C., Canou, J., and Foerster, E. (2020). Investigation on the undrained shear strength of loose sand with added materials at various mean diameter ratios. *Soil Dyn. Earthq. Eng.* 137, 106276. doi:10.1016/j.soildyn.2020.106276

Frontiers in Materials

Investigates the discovery and design of materials for future application

A multidisciplinary journal that explores the breadth of materials science, engineering and mechanics - from carbon-based materials to smart materials.

Discover the latest Research Topics

See more →

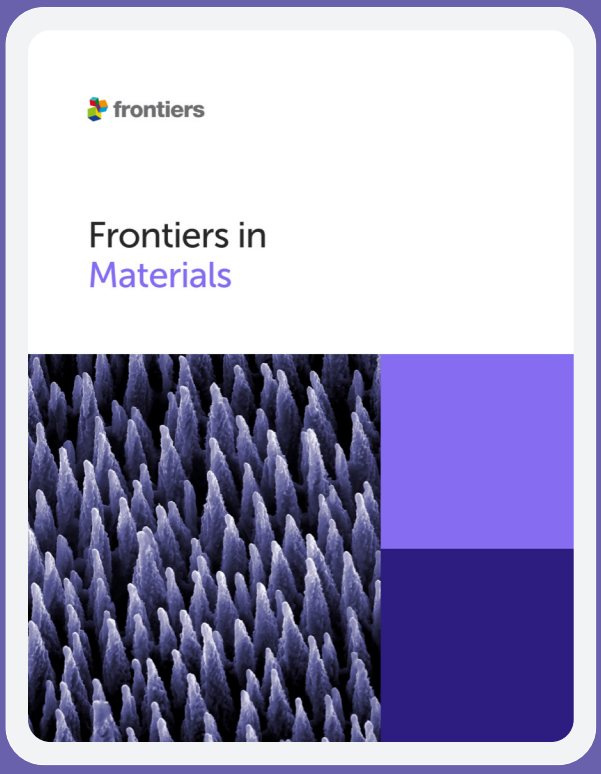

Frontiers

Avenue du Tribunal-Fédéral 34
1005 Lausanne, Switzerland
frontiersin.org

Contact us

+41 (0)21 510 17 00
frontiersin.org/about/contact